Out-of-plane seismic response and modelling of unreinforced masonry infill walls

Mariano Di Domenico

Università degli Studi di Napoli Federico II
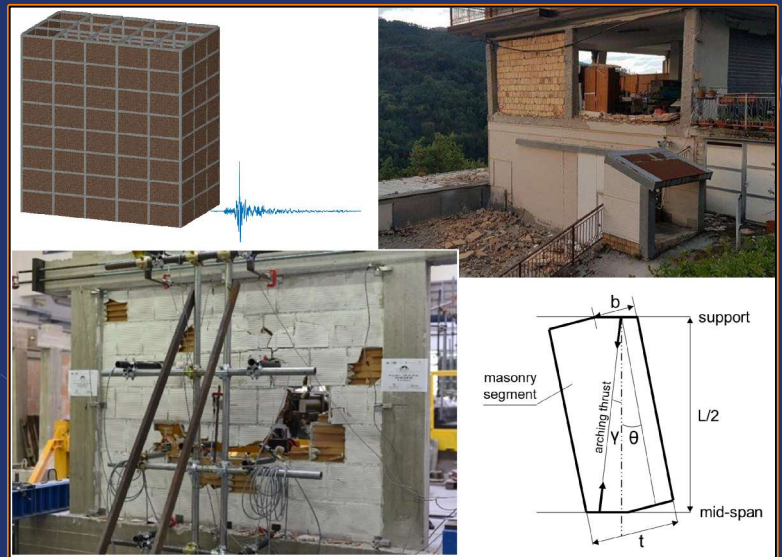
XXXI Ph.D. Programme
in Industrial Product and Process Engineering

UNIVERSITY OF NAPLES FEDERICO II

PH.D. PROGRAM
IN INDUSTRIAL PRODUCT AND PROCESS ENGINEERING
COORDINATOR PROF. GIUSEPPE MENSITIERI
XXXI CYCLE

MARIANO DI DOMENICO

PH.D. THESIS

Out-of-plane seismic response and modelling of unreinforced masonry infill walls

TUTOR
PROF. A. PROTA
PROF. G.M. VERDERAME
PROF. P. RICCI

2018

Acknowledgements/Ringraziamenti

> "*Sentir, riprese, e meditar: di poco*
> *Esser contento: da la meta mai*
> *Non torcer gli occhi: conservar la mano*
> *Pura e la mente: de le umane cose*
> *Tanto sperimentar, quanto ti basti*
> *Per non curarle: non ti far mai servo:*
> *Non far tregua coi vili: il santo Vero*
> *Mai non tradir: né proferir mai verbo*
> *Che plauda al vizio, o la virtù derida.*"
>
> Alessandro Manzoni

Sin da bambino, studiare è stata la cosa che più ho amato fare e non ho timore di scrivere che è stato lo studio, insieme a qualcuno, a salvarmi la vita. Per questo motivo, negli ultimi anni di Università, ho coltivato il desiderio di partecipare ad un programma di dottorato di ricerca. Realizzare questo desiderio nel 2015 è stata una delle più grandi gioie che ho vissuto e completare questa esperienza, oggi, rappresenta per me un grande orgoglio. Vorrei ringraziare chi ha reso possibile tutto questo e chi ha contribuito a rendere meravigliosa questa esperienza.

Vorrei ringraziare il professore Gerardo Verderame, del cui gruppo di ricerca faccio orgogliosamente parte. La sua grande sensibilità scientifica e umana sono state e saranno per me di esempio e fonte di ispirazione. Queste sue qualità mi hanno insegnato a guardare oltre ciò che è visibile, una dote estremamente rara e assolutamente imprescindibile per un buon ricercatore. Vorrei inoltre ringraziare il professore Andrea Prota, per avermi dato la possibilità di entrare a far parte della grande famiglia del DIST.

Vorrei ringraziare i revisori di questa tesi per il loro contributo cortese, attento e costruttivo.

Vorrei ringraziare ancora una volta tutti gli insegnanti che hanno contribuito alla mia formazione e a rendermi la persona, l'ingegnere e il ricercatore che sono. In rappresentanza di tutti loro vorrei ringraziare in particolare i professori Luciano Nunziante, Maria Rosaria Irace, Maria Pia Tanucci.

Vorrei ringraziare i miei colleghi di gruppo: Carlo Del Gaudio, per la serenità e

Information

Part of the content of this thesis has been already published on research journals, as reported in the list below.

− P. Ricci, M. Di Domenico, G. M. Verderame, 2018. Empirical-based out-of-plane URM infill wall model accounting for the interaction with in-plane demand. Earthquake Engineering and Structural Dynamics 2018;47.3:802-827. doi: 10.1002/eqe.2992

− M. Di Domenico, P. Ricci, G.M. Verderame, 2018. Experimental assessment of the influence of boundary conditions on the out-of-plane response of unreinforced masonry infill walls. Journal of Earthquake Engineering. doi: 10.1080/13632469.2018.1453411

− P. Ricci, M. Di Domenico, G. M. Verderame, 2018. Experimental assessment of the in-plane/out-of-plane interaction in unreinforced masonry infill walls. Engineering Structures. 2018;173:960-978. doi: 10.1016/j.engstruct.2018.07.033

− P. Ricci, M. Di Domenico, G. M. Verderame, 2018. Experimental investigation of the influence of slenderness ratio and of the in-plane/out-of-plane interaction on the out-of-plane strength of URM infill walls. Construction and Building Materials 2018;191:507-5222. doi: https://doi.org/10.1016/j.conbuildmat.2018.10.011.

Table of Contents

List of Figures

List of Tables

Introduction

Past and recent earthquakes showed that the seismic performance of buildings is strongly influenced by the presence and contribution of unreinforced masonry (URM) infills, which are usually considered as non-structural elements. Such enclosures are used – especially in Mediterranean countries – to provide buildings with thermic, visual and acoustic insulation.

On one hand, URM infills can stand significant lateral loads and, so, they contribute to the lateral strength capacity of structures. In addition, they are provided with a high in-plane stiffness. For this reason, the assessment of a construction modelled as bare frame can yield to a significant underestimation of its lateral strength and stiffness.

On the other hand, it is well-known that the high force demand that URM enclosures attract and then transfer to the confining elements can yield to unexpected failures of structural members designed without accounting for infills' presence. For example, Reinforced Concrete (RC) columns (and beams, potentially) not designed addressing seismic and capacity design provisions sometimes exhibit brittle failures during strong earthquakes due to the so-called "frame-infill interaction", i.e., due to the shear forces transferred by infills and not considered in the design. Moreover, the absence of infills at a certain storey of a building (typically, the first) produces a non-negligible stiffness variation of the structure lateral stiffness along its height, leading, in this way, to potential peaks of inelastic demand at that storey yielding to a sidesway collapse due to a soft-storey mechanism. In addition, infills' damaging due to IP actions and their repair or refurbishment produces most of the financial losses consequent to earthquakes.

In other words, neglecting infills' presence and their contribution to the seismic response of structures can be both conservative and unconservative. For these reasons, the interest in the characterization of the seismic response of URM infills has significantly grown in the engineering and research community in the last decades.

It should be noted that these bi-dimensional non-structural elements are subjected to the seismic action both in the in-plane (IP) and in the out-of-plane (OOP) direction. The expulsion or overturning from the confining frame due to OOP actions of URM infills is potentially highly detrimental for human life safety and amplifies the economic losses consequent to earthquakes. The OOP collapse of URM infills is promoted by the damage due to IP actions, which can reduce their OOP strength, stiffness and displacement capacity. This phenomenon is called IP/OOP interaction.

This PhD thesis is dedicated to the characterization and modelling of the OOP behaviour of URM infills and to the study of the effects of the IP/OOP interaction both at the level of the single (non-structural) component and at the level of the infilled structure seismic performance.

Chapter I is dedicated to the existing literature concerning this issue and investigating the definition of the OOP strength, stiffness and displacement capacity of URM infills. In addition, existing formulation for the prediction and reproduction of the IP/OOP interaction effects are addressed. Finally, existing URM infills' modelling strategies accounting for their OOP behaviour and for the IP/OOP interaction effects are described in detail.

Chapter II constitute the second part of the previous literature recall, as it is dedicated to a detailed description of the experimental tests carried out in the past to investigate the OOP behaviour of URM infills and the IP/OOP interaction effects. It is observed that the experimental database allowing evaluating the effectiveness and robustness of literature formulations and models described in Chapter I is extremely poor.

For this reason, a comprehensive and extended experimental program has been carried out at the Department of Structures for Engineering and Architecture of University of Naples Federico II. The experimental program main aim is the characterization of the effects of the panel height-to-thickness slenderness ratio, of the boundary conditions at edges and of the IP/OOP interaction on the OOP strength, stiffness and displacement capacity of URM infills. A total of fifteen tests has been carried out to enrich the available experimental database. Chapter III is dedicated to a detailed description of the experimental program and of its results.

In Chapter IV, the experimental database collected in Chapter II and III is analysed and discussed, in order to compare the prediction of literature formulations and models aimed at assessing the OOP response of URM infills and/or its significant parameters, such as the force at first macro-cracking and at maximum, as well as their secant stiffness at the first macro-cracking and at maximum and the displacement capacity/ductility. The

predicting capacity of the available IP/OOP interaction models is assessed, too. This comparison is aimed at evaluating the effectiveness of the available models for the prediction of the OOP response of both IP-undamaged and IP-damaged URM infills. Based on the results of this comparison, original and mechanical based proposals are described for a robust and effective modelling of URM infills' OOP response. In addition, empirical formulation for the prediction of the IP/OOP interaction are proposed. With Chapter IV, the characterization of the OOP behaviour of the single panel, which is the first part of this thesis, is completed.

Chapter V is dedicated to a simple state-of-the-art concerning the current provisions given by international technical codes and standards for the assessment of URM infills safety with respect to OOP seismic demands. More specifically, demand and capacity models provided by codes are described and discussed. This is preliminary to the assessment of the seismic performance of RC buildings accounting for the OOP response of infills and for the IP/OOP interaction effects, which is the second part of this thesis.

To this aim, a set of sixteen case-study buildings has been designed according to Eurocodes' provisions. The case-study buildings are described and commented in detail in Chapter VI. The case-study buildings are different for the number of storeys, which is equal to 2, 4, 6 or 8, and for the design peak ground acceleration (PGA) at Life Safety Limit State.

In Chapter VII, the case-study buildings described in the previous section are used to assess the PGA at the first OOP collapse of different infill layouts in a non-linear static framework by using both a simplified "Designer (code-based) Approach" and a refined "Reference Approach". Only the least accounts, in evaluating the OOP force demand and capacity of infills, for the structural nonlinearity as well as for the IP/OOP interaction effects. The dependence of such the PGA capacity with respect to the first OOP collapse on the number of storeys and on the design PGA is discussed. In addition, the PGA at the first OOP collapse is compared with the design PGA of the case-study buildings as well as to the PGA corresponding to their conventional structural collapse. It is shown that weak infills in mid- and high-rise buildings can collapse for OOP actions and due to the IP/OOP interaction effects at PGA demand lower than the PGA at structural collapse or even than the design PGA. In addition, simplified criteria to evaluate, based on infills geometric and mechanical properties, if the OOP safety check is necessary or not are presented.

In Chapter VIII, the seismic performance of the case-study buildings accounting and

not accounting for the IP/OOP interaction effects on URM infills is assessed by means of non-linear incremental dynamic analysis. Also in this case, the overall capacity of buildings with respect to the first OOP collapse is investigated. In addition, the OOP behaviour factor and effective stiffness of URM infills accounting for the IP/OOP interaction effects is evaluated. Such values can be used for a simplified OOP safety check of URM infills in a linear elastic framework.

In the appendix section, some theoretical considerations and experimental data supporting the discussions above proposed are reported in detail.

Chapter I
Out-of-plane strength, stiffness and displacement capacity models for URM infills

1.1   INTRODUCTION

The first part of this thesis is focused on the characterization of the out-of-plane (OOP) behaviour of unreinforced masonry (URM) infills. This first chapter is dedicated to the literature review. More specifically, the existing OOP strength, stiffness and displacement capacity models are described and commented in detail for both in-plane (IP)-undamaged and IP-damaged infills.

As will be demonstrated in Chapter II, based on experimental data, the OOP behaviour of infills can be represented by a force-displacement relationship that is defined through three characteristic points, which correspond to the attainment of the following conditions: first visible cracking or macro-cracking, peak load or maximum and collapse or ultimate condition. Therefore, the review presented in this chapter will be focused on provisions, formulations and models that predict the OOP response corresponding to these points.

The first cracking point is defined as the point in the OOP force-displacement relationship corresponding to the opening of the first noticeable crack in the infill that is subjected to an OOP action, generally due to mortar detachment from bricks. This condition corresponds to the beginning of visible panel damage and to a progressive and significant reduction in its stiffness exhibited against OOP actions, while prior to it, the infill undergoes a pseudo-elastic linear response and behaves as an orthotropic plate under flexure. For these reasons, the first cracking point is also recognizable as the point

of the experimental OOP behaviour diagram at which the first significant non-linearity occurs and the load corresponding to such condition is associated with the flexural resistance of a plate based on the tensile strength of its material.

Timoshenko and Woinowsky Krieger (1959) proposed a relationship aimed at evaluating the central displacement of a uniformly loaded elastic isotropic plate as a function of its geometry and material elastic properties. This relationship can be used to obtain an expression of the initial stiffness of the infill considered as an elastic isotropic plate, i.e., of the initial stiffness up to the first micro-cracking point. In addition, the authors provided formulations based on bending analysis to assess the OOP strength of infills considered as elastic isotropic plates under flexure. Moreover, yield-line theory was used to predict the flexural resistance of plates by Hendry (1973), Haseltine et al. (1977) and Drysdale and Essawy (1988). The OOP flexural resistance of URM infills is defined by masonry tensile strength. However, analytical studies and experimental evidences showed, as reported, e.g., by Pasca et al. (2017), that infills have strength capacity greater than the one predicted based on their flexural behaviour. In fact, only up to first cracking the infill undergoes a pseudo-elastic linear response and behaves as an orthotropic plate. For this reason, models and formulations described in this work principally refer to post-cracking strength mechanisms.

Under certain conditions, i.e., if the infill is sufficiently thick and confined by sufficiently stiff and resistant structural elements (according to ASCE-SEI 41/13 2013), soon after first cracking, the formation of vertical and horizontal compressive struts forming resistant arches in the panel thickness occurs. The strength against external OOP loads is mainly attributed to this post-cracking resistant mechanism called "arching action", first individuated by McDowell et al. (1956) and based on masonry compressive strength. Based on the infill boundary conditions at edges and on its slenderness ratios (height (h)-to-thickness (t) for the vertical direction, width (w)-to-thickness (t) for the horizontal direction), arching action can be mono-directional (vertical or horizontal) or bi-directional (both vertical and horizontal). For instance, one-way arching action occurs if two parts of the masonry infill rotate about their ends thus producing a compressive thrust in each infill part. Based on a limit analysis lower bound theorem approach, the panel OOP strength is the lateral load in equilibrium with the maximum thrust value that the infill parts can withstand based on masonry compressive strength. One-way arching occurs in infills bounded to the confining frame elements only along two edges (hereinafter, 2E infills). In infills bounded along all four edges (hereinafter, 4E infills), two-way arching action can occur. In this case, both arches contribute to the infill

strength. However, as will be shown later in this thesis, the activation of two-way or one-way arching also influences significantly the post-peak behaviour of infill walls. Strength models and formulations based on the formation of one-way or of two-way arching will be described in this section. Mechanical-based models and formulations depend on the assumed OOP load shape: this issue will be investigated, too. Moreover, existing formulations for the prediction of the secant stiffness at maximum will be also discussed.

After the attainment of the peak load point, the panel undergoes a severe and extended damage that, together with the collapse of the resistant three-hinged arch(es) in its thickness, produces a progressive reduction of its lateral load bearing capacity. For this reason, generally, after peak load, in the OOP force-displacement relationship, a softening branch is expected. It will be shown that the definition of the OOP collapse displacement and/or ductility capacity is an open issue. However, the currently available mechanical- or judgment-based potential definition of a conventional OOP ultimate displacement will be discussed.

All the above is referred to IP-undamaged infills. At the end of the chapter, the existing formulations aimed at predicting the in-plane (IP)/OOP interaction effects are presented and described, as well as the currently available modelling strategies proposed to account for the OOP behaviour of URM infills and for the IP/OOP interaction effects during structural analyses.

1.2   OOP STRENGTH MODELS BASED ON ARCHING ACTION

As already stated, An URM infill constrained by sufficiently stiff and resistant structural elements (as stated, e.g., in ASCE-SEI 41/13 2013) exhibit an OOP strength greater than the one associated to flexure, which is based on masonry tensile strength, due to arching action, which is based on masonry compressive strength, instead. In this section, OOP strength models based on one-way and two-way arching will be presented and discussed. All of them are derived based on mechanical principles, such as the lower bound theorem of limit analysis or the principle of virtual works. The least is applied in the framework of the so-called yield line theory.

As reported by Kennedy and Goodchild (2004), yield line theory was born for the analysis and design of reinforced concrete (RC) slabs. In that case, a yield line is a large crack that concurs, with other large cracks, to the definition of a cracking pattern that allows considering the slab as constituted by rigid parts rotating around cracks. Such

cracking or fracture lines are named "yield lines" as it is assumed that the slab's rebars passing through them have yielded. Plastic moments develop around such yield lines and the rotations around them are plastic rotations. In this framework, the application of virtual work equation allows calculating the strength of such slabs with respect to gravity uniformly distributed loads. In the second half of last century, efforts to extend the feasibility of the yield line theory to masonry structures and, namely, to masonry walls under lateral (e.g., wind) loads, were carried out by different authors (see, for example, Hendry 1973 and Haseltine 1977). Clearly, in this case the definition of the moment acting along cracking lines and working for the rotation of the masonry wall's parts around them is not straightforward and yield line theory should be called, more properly, "fracture line analysis", as done in Hendry et al. (2003). Nevertheless, such approach is consolidated also for masonry walls, as was introduced in different standard codes, such as BS 5628 (1992) and Eurocode 6 (2005). In these cases, the moment acting around fracture lines is calculated based on masonry flexural strength. The use of masonry flexural strength within the application of the fracture line/yield line analysis usually leads to highly underestimated values of lateral strength (as observed, e.g., by Brincker 1984). However, as first individuated by McDowell et al. (1956), arching action can occur in masonry elements. If arching action occurs, moments acting along cracking lines are not limited to those associated with masonry linear elastic behaviour, but are defined by arching thrusts forming in the wall thickness and by the lever arm associated with them. As this lever arm depends on the deformed shape of the masonry wall, the moment acting along fracture lines varies along them, as well as at increasing OOP displacement. So, in the literature, fracture line analysis methods for masonry walls and for masonry infill walls accounting for arching action were proposed based on the discretization of such walls or infill walls into vertical and horizontal stripes. The first ones allow accounting for vertical arching and to the moments along fracture lines associated with it; the second ones allow accounting for horizontal arching and to the moments along fracture lines associated with it.

Clearly, in 2E infills, in which only one-way arching occurs, only vertical stripes should be considered. This is the most simple case, while more complex discussions are needed to apply the yield-line theory for 4E infills in which two-way arching action occurs.

1.2.1. Strength models based on one-way arching action

The first model based on one-way arching provided in the literature is the one by McDowell et al. (1956), which is based on the principle of virtual works applied in the framework of the so-called yield line theory.

Note that in the derivation of McDowell et al.'s strength formulation, masonry global mechanical properties are used, with no distinction between the mechanical behaviour of mortar and bricks. Considering masonry as a homogeneous anisotropic material, based on the mechanical properties determined on wallet specimens with standardized dimensions, is a consolidated and usual approach in the application of fracture line analysis to masonry walls and infill walls. However, it is worth to remember that in recent times, models for the prediction of the OOP response of masonry walls accounting for the different properties of bricks and mortar were presented in the literature (e.g., Edri and Yankelevsky 2017, Vaculik and Griffith 2017).

To derive McDowell et al.'s OOP strength formulation for infills in which one-way arching occurs, consider a unit-width masonry stripe (i.e., a 2E infill) with length equal to L subjected to lateral loading. The stripe is crossed by one or more cracking lines that form the considered cracking pattern. In the derivation of McDowell et al.'s strength formulation, the stripe is crossed by three cracking lines and separates in two equal-length parts rotating around their ends, as shown in Figure 1.1. At increasing OOP displacement at the infill mid-span, increasing compressive stresses develops at the ends of each infill part. Such compressive stresses produce arching thrusts opposite in their horizontal component to the external load.

Note that McDowell et al. assume indeed that the infill bounding elements are stiff and that the considered unit-width infill stripe is subjected to a uniformly distributed lateral load.
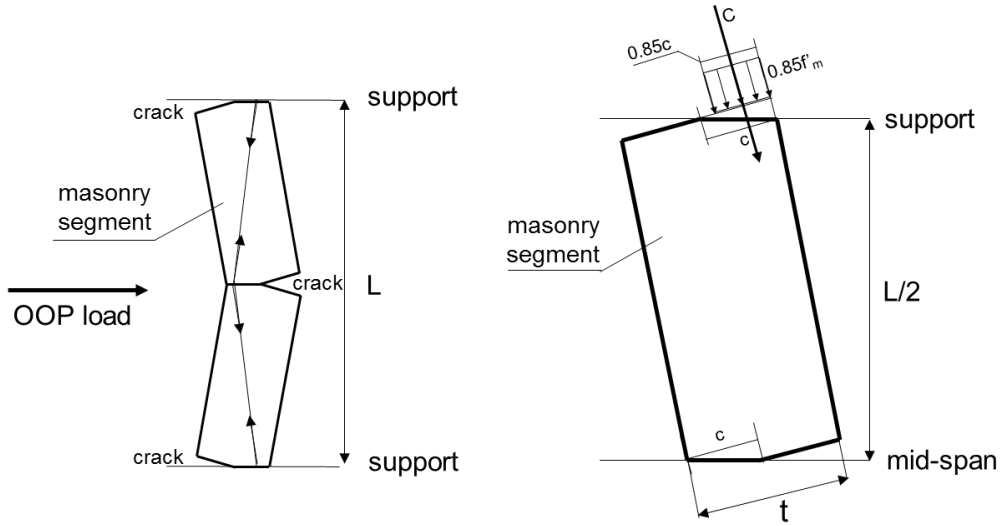
Figure 1.1. One-way arching action according to McDowell et al. (1956).

A compressive rectangular stresses distribution acting at the ends of each infill's rigid part, as shown in Figure 1.1, is considered. The distance of the arching thrust resultant from this stresses distribution from the stripe cross-section produces a moment, M_y, which the application of the principle of virtual works is referred to. The contact length, c, is determined in order to maximize C value. The distance between the compressive forces, C, is equal to the infill's thickness reduced of the OOP displacement x_y corresponding to the attainment of peak load and of two times one half of the contact length itself. One half of the resultant moment is applied at each rigid part's end and acts along the linear fracture line as M_y. So, M_y is expressed as reported in Equation 1.

$$M_y = \frac{1}{8} 0.85 f'_m t^2 \left(1 - \frac{f'_m}{E\varepsilon_c} \right)^2 \qquad (1)$$

In Equation 1, E is the Young modulus of masonry in the direction of arching thrusts, ε_c is the limit strain of the panel depending on panel length and on its thickness through Equation 2a or directly on the panel slenderness through Equation 2b. It represents the theoretical strain associated with the diagonal single rotating infill part when the OOP central displacement of the infill stripe is equal to the infill thickness, t.

$$\varepsilon_c = \frac{\sqrt{(L/2)^2 + t^2} - L/2}{\sqrt{(L/2)^2 + t^2}} \qquad (2a) \qquad \varepsilon_c = \frac{\sqrt{0.25(L/t)^2 + 1} - 0.5(L/t)}{\sqrt{0.25(L/t)^2 + 1}} \qquad (2b)$$

As shown in Equation 2b, the limit strain reduces for increasing slenderness.

By equating the external work due to the uniformly distributed load, $q_{max,2E}$, and the internal work due to M_y, an upper bound value of the infill specific strength (strength force per unit area) is derived and reported in Equation 3.

$$q_{max,2E} = 16 \frac{M_y}{L^2} \tag{3}$$

By substituting Equation 1 in Equation 3, Equation 4 is obtained.

$$q_{max,2E} = 1.7 \frac{f'_m}{(L/t)^2} \left(1 - \frac{f'_m}{E\varepsilon_c}\right)^2 \tag{4}$$

A more detailed derivation of the above equations is reported in Appendix A.

Angel et al. (1994), defined an analytical model for estimating the OOP behaviour of URM infills based on one-way arching action. For instance, an URM stripe simply supported at edges by stiff boundary elements is considered. The lateral uniformly distributed load, $q_{max,2E}$, first produces cracking at edges and at the infill mid-height; after that, arching action occurs. In post-cracking condition, the reference masonry stripe can be represented through two equal-length segments rigidly rotating about their ends and producing a compressive thrust in each infill part. Stresses and strains due to the stripe flexural behaviour are neglected. Based on equilibrium, the out-of-plane load is expressed as a function of the resultant of compressive stresses distribution due to arching action along the boundary stiff-element/masonry segment contact length, which is assumed to be triangular. It is assumed that the length of the outermost fiber of the masonry segment is reduced due to a linear strain distribution, with maximum value at edges and zero point at mid-height crack. Based only on geometric compatibility principles, closed-form relationships are defined for calculating the compressed zone thickness, which ranges from 0.3t to 0.5t, the rotation of the stripe segment and the thrust direction with respect to a vertical reference line as a function of the maximum strain attained and of the panel slenderness. Based on an experimental or assigned stress-strain relationship for masonry compressive behaviour in the direction of arching thrust, the

reconstruction of the entire lateral load-deflection curve of the stripe is possible up to masonry crushing or infill collapse for arching action vanishing (also called "snap-through"). A more detailed description of the analytical model is reported in Appendix A.

Based on the assumption of a certain relationship, depending on the infill slenderness, between the outermost compressed fiber strain at OOP peak load and masonry crushing strain, which is set to 0.4%, Angel et al. provided a simplified formulation aimed at calculating the OOP strength of URM infills (Equation 5).

$$q_{max,2E} = \frac{2f'_m}{(L/t)} R_1 R_2 \lambda \qquad\qquad (5)$$

Equation 5 expresses, so, in a simplified form, the uniformly distributed load per unit width in equilibrium with the maximum thrust that the infill parts could withstand. In other word, Angel et al.'s formulation is the result of an application of the lower bound limit analysis theorem.

In Equation 5, λ is a parameter accounting for the actual width of the compressed part of the infill cross section due to arching and for the direction of arching thrust. Through all these terms, λ can be expressed as a function of the infill slenderness ratio, L/t, according to Table 12 reported in Angel et al. or calculated through an expression by Flanagan and Bennett (1999) reported in Equation 6.

$$\lambda = 0.154 \exp(-0.0985(L/t)) \qquad\qquad (6)$$

Equation 6 is effective for L/t slenderness values between 10 and 30. R_1 is a strength-reducing factor accounting for IP damage, always equal to 1 for IP-undamaged infills. R_1 expression will be shown in section 1.5, concerning literature provision for modelling IP damage effects on infills' OOP strength. R_2 is a factor accounting for deformability of the infill-bounding frame and is reported in Equation 7.

$$R_2 = 0.357 + 2.49\text{x}10^{-14}EI \leq 1 \qquad\qquad (7)$$

This term has been defined as ratio of the OOP strength calculated through the analytical approach proposed by Angel et al. for stiff bounding frame and the OOP strength calculated through the stripe method proposed by Dawe and Seah (1989), which

accounts for the confining frame deformability and will be described in detail in the next subsection.

In Equation 7, EI is the smaller flexural stiffness expressed in Nmm^2 calculated for the structural elements of the confining frame confined by an infill wall on only one side; otherwise, i.e., if all the structural elements confining the considered infill wall are themselves confined by other infill walls on both sides, R_2 is assumed equal to unit. The condition of stiff bounding elements is normally assured, according to Angel et al., if the infill is confined by common RC members: for instance, an RC element with 30000 N/mm^2 elastic modulus for concrete and 300x400 mm^2 cross-section grants an R_2 value equal to 1. If Angel et al.'s formulation is applied for 4E infills, i.e., if only one resistant arch is considered despite the fact that in infills bounded along four edges two-way arching can occur, Flanagan and Bennett suggest to evaluate R_2 for horizontal and vertical arching and to assume the largest to be used, considering that the panel will arch mainly in the direction with the greatest stiffness of boundary elements.

Dawe and Seah (1989) defined a procedure to calculate the OOP response of URM infills in which one-way or two-way arching action occurs. This procedure consists in the application, for increasing values of the infill OOP central displacement, of the equation of virtual works. The model will be described in detail in the next subsection, as its general definition is dedicated specifically to 4E infills. However, the simplification of the described procedure for 2E infills, in which only one-way arching occurs, is straightforward.

It has been already stated that Chapter V of this thesis will be dedicated to code provisions for the calculation of the OOP force capacity and seismic demand on URM infills. For what concerns capacity models, non-European standards provide, in general, formulations based on Angel et al.'s model or on Dawe and Seah's model. It is worth to anticipate in this section the discussion on Eurocode 6 (2005) strength model, which is original and based on a very simple application of the lower bound theorem of limit analysis.

Eurocode 6, in section 6.3.2, proposes an expression to calculate the lateral specific strength of masonry walls in which arching action can occur; this relationship can be extended, potentially, to URM infills. Clearly, this relationship, which is reported in Equation 8, accounts only for one-way arching and, so, it could be rigorously applied only on infills bounded along two edges under a uniformly distributed load.

$$q_{max,2E} = f_d \left(\frac{t}{l_a}\right)^2 \tag{8}$$

In this relationship f_d is the design compressive strength of masonry in the direction of arching thrust while l_a is the panel dimension in the same direction. Such ultimate load is the 93% of the one that equilibrates the maximum thrust that can form in the masonry wall thickness as expressed in Equation 9.

$$N_{ad} = 1.5 f_d \left(\frac{t}{10}\right) \tag{9}$$

This thrust value is obtained as the expression of the resultant of a triangular compressive stress distribution assumed in the panel thickness: this distribution has maximum value equal to the masonry compressive strength and resultant applied at a distance equal to $t/10$ from the panel intrados. This also means that the depth of the compressed zone from the panel intrados is assumed equal to $0.30t$, which is, according to Angel et al., the minimum compressed zone that allows the horizontal component of arching thrust being opposite to OOP loads. This is a conservative assumption, as expected for a code provision, given that, according to Angel et al.'s analytical model, the compressed zone width normally ranges from a lower and an upper bound respectively equal to $0.3t$ and $0.5t$. Moreover, note that also this approach is based on the lower bound theorem of limit analysis, i.e. on the determination of the maximum specific load that the infill can withstand as the maximum load in equilibrium with internal thrusts, as also pointed out for Angel et al.'s strength model.

1.2.2. Strength models based on two-way arching action

For 4E infills, mechanical-based OOP strength models (by Dawe and Seah) and formulations (by Bashandy et al. 1995) have been proposed, as well as empirical-based formulations (by Dawe and Seah and by Flanagan and Bennett).

As already stated, Dawe and Seah defined a procedure to calculate the OOP response of URM infills in which one-way or two-way arching action occurs. Consider an infill wall divided in unit-width stripes with length equal to L and subjected to lateral loading. Given a cracking pattern, each stripe is crossed by one or more fracture lines.
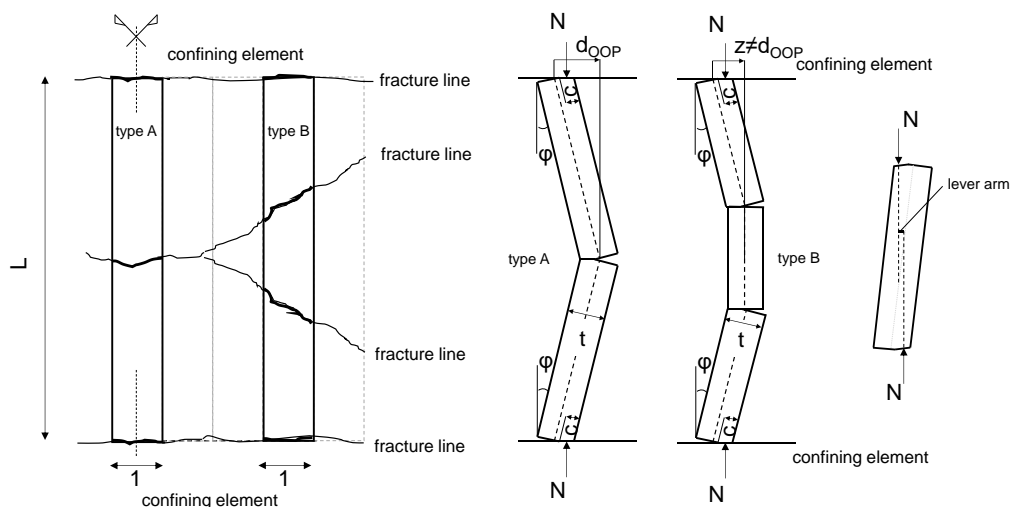
Figure 1.2. Deformed shape of a type A and type B stripes divided by fracture lines in separate parts rigidly rotating about their ends. On the right, a particular of a stripe single part.

As shown in Figure 1.2, it is usual considering two types of stripes, as also done in this study. A "type A" stripe is crossed by one fracture line at its centre. Such fracture line separates type A stripes in two equal length parts rigidly rotating around their ends. A "type B" stripe is crossed by two fracture lines, both of them at the same distance from the stripe nearer end. The two fracture lines separate type B stripes in three parts, with the two exterior parts rigidly rotating around their ends. Clearly, if d_{OOP} is the OOP central displacement of the infill, e.g., the central and maximum displacement of a type A stripes, type B stripes have a maximum displacement z which is different from d_{OOP} due to geometric compatibility. Hence, as the infill will be considered as divided in separate parts rigidly rotating around fracture lines, the reference deformed shape defined for the application of the method is a linear relation among z (OOP maximum displacement of the generic stripe) and d_{OOP} (OOP central displacement of the infill).

At a certain value of z, a certain rotation φ is defined for each stripe, as reported in Equation 8.

$$\varphi = \frac{2z}{L} \tag{8}$$

At increasing d_{OOP} (and, therefore, for each stripe, at increasing z and φ), increasing

compressive stresses develop at the ends of each stripe part. Such compressive stresses produce arching thrusts opposite in their horizontal component to the external load. The compressive stresses develop in the stripe thickness along the contact length between the masonry segment and the confining elements. The contact length, c, is calculated as reported in Equation 8.

$$c = \frac{2t\tan\varphi - L(1 - \cos\varphi)}{4\tan\varphi + (k_1 k_2 f_m L/tE_m)\cos\varphi} \tag{9}$$

In Equation 9, k_1 and k_2 are stress block parameters both set to 0.85, f_m and E_m are masonry compressive strength and elastic modulus, respectively, in the direction examined.

According to Dawe and Seah, the resultant of compressive stresses acting, per unit length, in the depth of contact is equal to N, which is calculated as reported in Equation 10.

$$N = k_1 k_2 f_m c \tag{10}$$

This force acts at a distance equal to 0.5c from the outermost compressed fibre of the stripe cross-section. Note that, through c, N depends only on the rotation, which is equal for all stripes oriented in the same direction, and on the infill geometric and mechanical properties. As shown in Figure 1.2, N generates a moment with respect to the stripe cross section centroid which is calculated as reported in Equation 11.

$$M = 0.5N(t - c - z) \tag{11}$$

Note that the moment depends on the OOP maximum displacement of the considered stripe, so it varies for each stripe, as already stated (however, note that for 2E infills, z is equal for all stripes hence also N is equal for all stripes). For each value of d_{OOP}, z can be calculated for all stripes as a reference deformed shape has been defined, φ can be calculated through Equation 8, c through Equation 9, N through Equation 10 and M through Equation 11. The internal work for each infill stripe is calculated as reported in Equation 12.

$$L_{I,stripe} = 2N(t - c - z)\varphi = 4N(t - c - z)\frac{d_{OOP}}{L} \tag{12}$$

Given a certain value of the OOP central displacement d_{OOP}, the sum of the internal works calculated for both horizontal and vertical stripes must be calculated and equated to the external work, which depends on the external load shape. This equation provides the OOP force corresponding to the fixed OOP central displacement d_{OOP} and, so, the OOP force-displacement curve for the considered infill.

All the above described approach can be applied also when considering the presence of a gap g between the infill confining elements and the infill edges (as for "3E" infills, that are detached from the upper structural element). To account for this, only Equation 9 should be modified as reported in Equation 13.

$$c = \frac{2t\,\tan\varphi - L(1 - \cos\varphi) - g}{4\tan\varphi + (k_1 k_2 f_m L/tE_m)\cos\varphi} \tag{13}$$

Note that g is assumed as a constant, i.e., is equal to the initial gap existing between the infill wall and the confining elements and does not evolves explicitly at increasing value of d_{OOP}. It should be noted that, when accounting for the presence of g, c can result lower than zero. This means that the considered stripe is actually not in contact with the adjacent structural element and that arching thrusts do not form. However, at increasing value of d_{OOP}, c can become greater than zero. This means that the rotation of the infill stripe has "filled" the gap and that the stripe and the adjacent element came in contact, allowing the formation of arching thrusts. This circumstance occurred during the experimental program carried out at the Department of Structures of Engineering and Architecture of University of Naples Federico II, as will be shown in Chapter III.

Equation 9 can be modified to consider also the deformability of the confining frame elements. In fact, due to arching thrusts, the structural elements that support infills deform and it is possible to associate with each stripe the total outward displacement of the confining elements, f, in correspondence with the considered stripe. Note that f is calculated as the algebraic sum of the outward displacements calculated at both ends of the stripe, according to the reference system reported in Figure 1.3 in the case of an infill wall that encloses a simple one-bay one-storey frame. The beam outward displacement is assumed as positive when it has the same direction of vertical thrusts, while columns' outward displacements are assumed as positive when they have the same direction of

horizontal thrusts acting on each element.
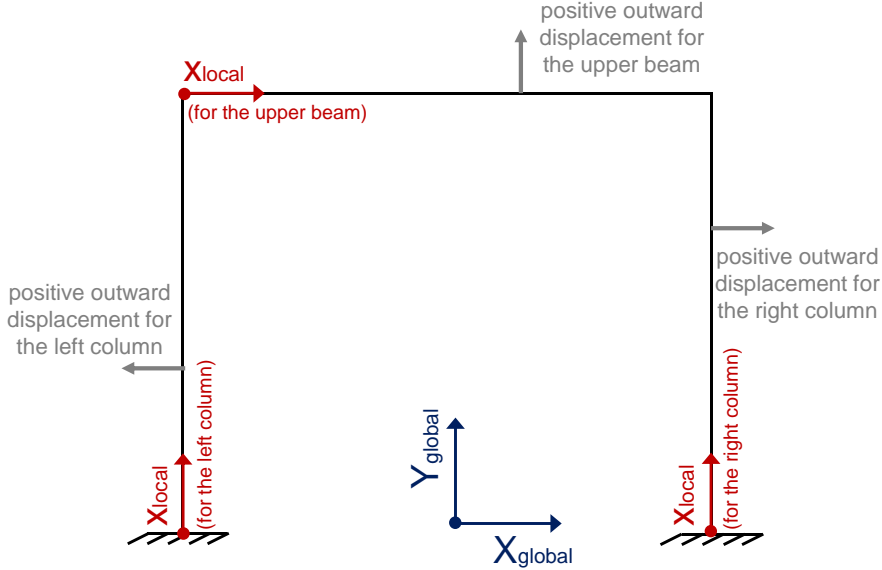
Figure 1.3. Global and local reference systems that should be used to correctly define the f value for each stripe.

To account for the frame deformability, only Equation 9 should be modified as reported in Equation 14.

$$c = \frac{2t\,\tan\varphi - L(1 - \cos\varphi) - g - f}{4\tan\varphi + (k_1 k_2 f_m L/tE_m)\cos\varphi} \tag{14}$$

Differently from g, f is a function of d_{OOP}, as at increasing OOP central displacement arching thrusts vary and, so, also the outward displacement of the confining frame elements, which is subjected to arching thrusts applied by the infill, varies. Note that, as f is different for each stripe, when the deformability of the confining frame is considered, the depth of contact c is different for each stripe, and, therefore, also N is different for each stripe. In other words, when the infill is confined by stiff elements, the vertical and/or horizontal arching thrusts are uniformly distributed along its width/height. On the contrary, if the confining elements are deformable, such thrusts are no more uniformly distributed and are lower where the confining elements maximum deflections are

expected. It will be shown in the next Chapters that arching thrusts in the central part of very thick and robust infills can even be zero due to the frame elements' deformations.

As explained by Dawe and Seah themselves and herein recalled, when introducing the frame deformability in the model, it is necessary to implement an iterative procedure to calculate, for each stripe, the correct value of c corresponding to a certain value of d_{OOP}.

The steps of the iterative procedure are reported in the following. Note that in the following discussions, it is assumed that the considered infill walls encloses a simple one-bay one-storey structural frame. This is assumed for two reasons: first, Dawe and Seah's model accounting for the frame deformability will be applied in Chapter IV on the results of experimental tests carried out on infills enclosing simple one-bay one-storey frames; second, in real buildings, the effects of the frame deformability on the OOP response of URM infills can be often neglected, as the deformation of structural elements due to arching thrusts is prevented by the confinement provided by other structural and non-structural elements

i.   The OOP force-displacement must be calculated under the hypothesis of stiff confining elements. For a specific value of d_{OOP}, this leads to a distribution of arching thrusts N acting on the confining structural elements. As already stated, at this stage N is equal for all stripes with the same direction. Therefore, a uniformly distributed outward load acts on the RC frame structural elements.

ii.   To introduce the frame deformability in the OOP response model, it is necessary to calculate the frame deformed shape under the load distribution evaluated at the first step. This leads to the definition of a value of f for each stripe.

iii.   A new compression-bearing width value must be calculated for each stripe by means of Equation 14. Clearly, this yields to a new distribution of arching thrusts, which is no more uniform even when associated with stripes with the same direction.

iv.   The new outward load distribution leads to a new deformed shape of the confining frame, which leads to a new value of c for all stripes and, so, to a new distribution of arching thrusts.

Steps iii. and iv. should be reiterated until no significant variation in the value of

arching thrusts is observed between successive iterations. As this iterative procedure must be performed for each value of d_{OOP}, when accounting for the frame deformability it is not possible to provide a closed-form final relationship between the OOP force and the OOP central displacement. So, in this case, the OOP force-displacement relationship is found numerically: the higher the number of vertical and horizontal stripes, the lower the error made in the discretization of the infill wall in stripes.

To achieve all these goals, it is necessary to introduce in the routine a matrix containing the deformability coefficients of the structural frame, Δ. If *n* is the number of horizontal stripes and *m* is the number of vertical stripes, the frame elements' outward displacements must be calculated in *n* control section of each column and in *m* control section in the upper beam. Each control section corresponds to the centre of a stripe. For all these reasons, the deformability matrix that must be implemented is a $(2n+m)\times(2n+m)$ square matrix. The generic term of the Δ matrix, δ_{ij}, represents the outward displacement in the *i*-th control section when a unit-force with the direction of arching thrusts is applied in the *j*-th control section. For each value of d_{OOP}, for each iteration, the trial value of the arching thrust acting in the *j*-th stripe, N_j, must be multiplied for the *j*-th column of Δ to obtain the outward displacement of all control sections due to N_j.

When this has been done for all columns of Δ, the actual outward displacement in the *i*-th control section, f_i, which enters Equation 14, is provided by the sum of all $N_j\delta_{ij}$ products, as reported in Equation 15.

$$f_i = \sum_{j=1}^{2n+m} N_j \, \delta_{ij} \tag{15}$$

To express in a closed form all the δ_{ij} terms, it is convenient to divide Δ in sub-matrices, as shown in Figure 1.4.

Figure 1.4. Partitioned deformability matrix.
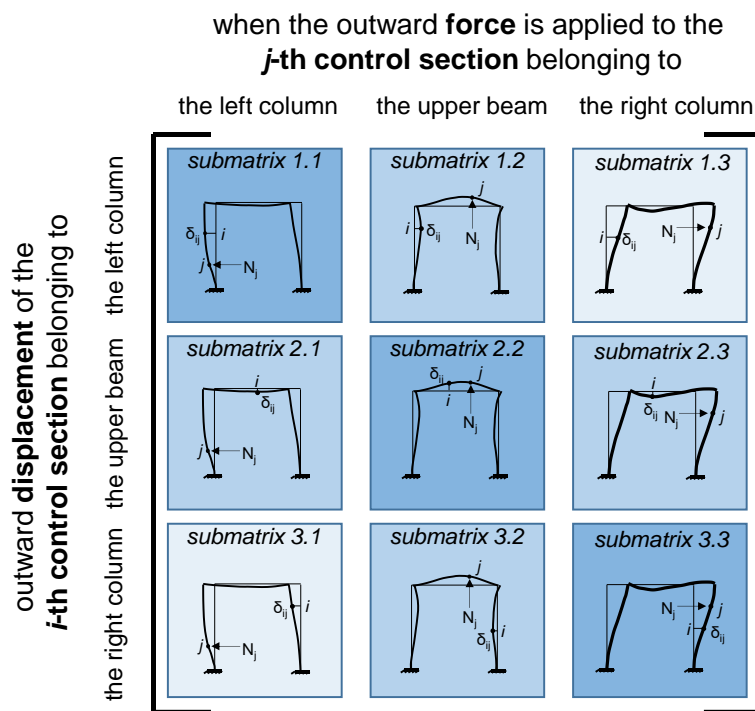
Namely, both lines and columns are divided in three groups. The first group is constituted by *n* lines/columns and is related to the RC frame left column. The second group is constituted by m lines/columns and is related to the RC frame upper beam. The third group is constituted by n lines/columns and is related to the RC frame right column. Therefore, a total of 9 submatrices is defined. For the sake of clarity, they are numbered in Figure 1.4. The generic submatrix carries the outward displacement of a control section belonging to the left column/upper beam/right column when a unit-force is applied, in the direction of arching thrusts, to a control section belonging to the left column/upper beam/right column.

The values of the frame deformability coefficients are reported in the following equations and are determined by considering only the frame flexural deformability.

submatrix 1.1

$$\frac{(x_i^2(-2(6a+b)(a+2b)h^3x_j+6(6a+b)(a+2b)h^3x_j+3h(-(15a^2+26ab+3b^2)h+(a+b)(6a+b)x_i)x_j^2+(6a+b)(3(a+b)h-(2a+b)x_i)x_j^3))}{(12(6a+b)(a+2b)EI_ch^3)} \qquad x_i \le x_j$$

$$\frac{(x_j^2(3hx_i(2(6a+b)(a+2b)h^2-(15a^2+26ab+3b^2)hx_i+(a+b)(6a+b)x_i^2)-(6a+b)(2(a+2b)h^3-3(a+b)hx_i^2+(2a+b)x_i^3)x_j))}{(12(6a+b)(a+2b)EI_ch^3)} \qquad x_i > x_j$$

submatrix 1.2

$$\frac{x_i^2(bh-x_j)x_j(b(b(h+x_i)+a(-5h+6x_i))-2(a+2b)x_j)}{4b(6a+b)(a+2b)EI_ch^2}$$

submatrix 1.3

$$\frac{(x_i^2x_j^2(3h(-(9a^2+14ab+3b^2)h+(a+b)(6a+b)x_i)+(6a+b)(3(a+b)h-(2a+b)x_i)x_j))}{(12(6a+b)(a+2b)EI_ch^3)}$$

submatrix 2.1

$$\frac{(bh-x_i)x_ix_j^2(a(-5bh-2x_i+6bx_j)+b(-4x_i+b(h+x_j)))}{4b(6a+b)(a+2b)EI_ch^2}$$

submatrix 2.2

$$\frac{-(x_i(bh-x_j)(2b(6a+b)(a+2b)h^2x_i^2-bh(3ab(8a+5b)h^2+3b(13a+4b)hx_i-2(a+2b)x_i^2)x_j+2(a+2b)(6abh^2+(3bh-2x_i)x_i)x_j^2))}{(12ab^2(6a+b)(a+2b)EI_ch^3)} \qquad x_i \le x_j$$

$$\frac{((bh-x_i)x_j(3abh^2x_i(b(8a+5b)h-4(a+2b)x_i)+3bhx_i(b(13a+4b)h-2(a+2b)x_i)x_j-2(a+2b)(b(6a+b)h^2+bhx_i-2x_i^2)x_j^2))}{(12ab^2(6a+b)(a+2b)EI_ch^3)} \qquad x_i > x_j$$

submatrix 2.3

$$\frac{-(bh-x_i)x_ix_j^2(7abh+3b^2h-2ax_i-4bx_i-b(6a+b)x_j)}{4b(6a+b)(a+2b)EI_ch^2}$$

submatrix 3.1

$$\frac{(x_i^2x_j^2(3h(-(9a^2+14ab+3b^2)h+(a+b)(6a+b)x_i)+(6a+b)(3(a+b)h-(2a+b)x_i)x_j))}{(12(6a+b)(a+2b)EI_ch^3)}$$

submatrix 3.2

$$\frac{(x_i^2(bh-x_j)x_j(a(-7bh+6bx_i+2x_j)+b(b(-3h+x_i)+4x_j)))}{(4b(6a+b)(a+2b)EI_ch^2)}$$

submatrix 3.3

$$\frac{(x_i^2(-2(6a+b)(a+2b)h^3x_j+6(6a+b)(a+2b)h^3x_j+3h(-(15a^2+26ab+3b^2)h+(a+b)(6a+b)x_i)x_j^2+(6a+b)(3(a+b)h-(2a+b)x_i)x_j^3))}{(12(6a+b)(a+2b)EI_ch^3)} \qquad x_i \le x_j$$

$$\frac{(x_j^2(3hx_i(2(6a+b)(a+2b)h^2-(15a^2+26ab+3b^2)hx_i+(a+b)(6a+b)x_i^2)-(6a+b)(2(a+2b)h^3-3(a+b)hx_i^2+(2a+b)x_i^3)x_j))}{(12(6a+b)(a+2b)EI_ch^3)} \qquad x_i > x_j$$

Figure 1.5. Deformability coefficient for the RC frame shown in Figure 1.4. In the above Equations, $a=EI_b/EI_c$ and $b=w/h$. EI_b and EI_c are the flexural stiffness of the beam and of the columns' cross sections, respectively.

A second issue should be considered when dealing with URM infills in RC frames. Clearly, for steel members, it is possible to assume a constant value of the flexural deformability coefficients up to yielding. However, the deformation of RC elements depends on their initial elastic stiffness only at low load levels. If the non-linear behaviour of concrete and steel rebars is not explicitly modelled, as in the present case, an effective deformability of members should be defined to obtain a realistic evaluation of the frame displacements given that a linear elastic behaviour is assumed for them.

The application of the above procedure in a parametric study allowed the identification of the more important parameters in determining infills' OOP strength. Based on the experimental results of the tests performed by Dawe and Seah, an empirical relationship (Equation 16) involving these parameters was then proposed to compute the resistant OOP uniformly distributed load for concrete blocks infills bounded on four

edges in a pinned frame.

$$q_{max,4E} = 4.5f_m'^{0.75}t^2 \left(\frac{\alpha}{w^{2.5}} + \frac{\beta}{h^{2.5}}\right) \tag{16}$$

Clearly, Equation 16 is an additive formulation, in which the contributions of vertical and horizontal arching to $q_{max,4E}$ can be separately evaluated. Masonry compressive strength, f'_m, is different perpendicular and parallel to bricks' holes. According to Flanagan and Bennett, the value determined perpendicular to bricks' holes should be used, as this is often the only one available. The factors α and β are two parameters accounting for flexural (EI) and torsional (GJ) stiffness of the surrounding columns (*c* subscript) and beams (*b* subscript) determined as reported in Equations 17 and 18.

$$\alpha = \frac{1}{h}(E_cI_ch^2 + G_cJ_cth)^{0.25} \leq 50 \tag{17}$$

$$\beta = \frac{1}{w}(E_bI_bw^2 + G_bJ_btw)^{0.25} \leq 50 \tag{18}$$

For infills detached from the confining frame along the upper edge (3E infills), Equation 16 is substituted by Equation 12.

$$q_{max,3E} = 4.5f_m'^{0.75}t^2 \left(\frac{\alpha}{w^{2.5}}\right) \tag{19}$$

In addition, Equation 17 is substituted by Equation 20.

$$\alpha = \frac{1}{h}(E_cI_ch^2 + G_cJ_cth)^{0.25} \leq 75 \tag{20}$$

The upper bounds applied on α and β values were determined through the application of the step-by-step procedure proposed by the authors to evaluate infills' OOP force-displacement relationship on infills surrounded by stiff elements. Note that the application of Equations 16 and 19 on infills realized in a moment-resisting frame could produce underestimating predictions of their OOP strength. In fact, as will be shown in Chapter II, Dawe and Seah tested infilled steel frames with structural members pinned

at ends. Steel members constituting infills' confining frames were provided of relatively low flexural and torsional stiffness. For this reason, α and β values close to their maximum are usually obtained for infills in RC frames. In other words, common RC confining members usually reproduce a "stiff boundary elements" condition.

Flanagan and Bennett also proposed a modification reported in Equation 21 of Equation 16 to best-fit additional experimental data.

$$q_{max,4E} = 4.1 f'_m{}^{0.75} t^2 \left(\frac{\alpha}{w^{2.5}} + \frac{\beta}{h^{2.5}} \right) \tag{21}$$

In Equation 21, all parameters keep the already discussed meaning, except for α and β that are determined by neglecting the torsional stiffness terms.

Bashandy et al. (1995), extended McDowell et al.'s approach to infills bounded along four edges with width equal to w and height equal to h through a stripe method. The collapse mechanism shown in Figure 1.6 is considered, with θ=45°.
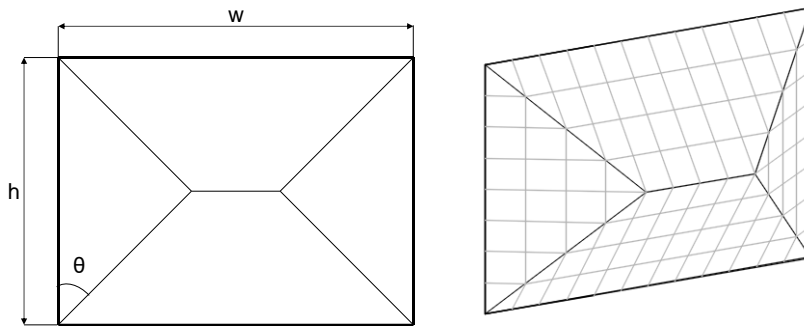
Figure 1.6. Collapse mechanism considered by Bashandy et al.

The infill is divided in vertical and horizontal non-interacting stripes. The first ones account for vertical arching, the second ones account for horizontal arching. A maximum displacement equal to the one that produces the attainment of peak load due to vertical arching, x_{yv}, is assigned to the central horizontal fracture line of the infill, i.e., the maximum OOP displacement associated with each central vertical stripes is equal to x_{yv}. Given the regularized deformed shape considered, non-central vertical stripes, as well as all horizontal stripes, are associated with a maximum OOP displacement lower than x_{yv}. In correspondence with fracture lines, moments due to vertical and horizontal arching act. Such moments are different for each stripe. Namely, moments due to

vertical arching are equal to M_{yv} for central vertical stripes as to these stripes a displacement equal to x_{yv} is assigned. For non-central vertical stripes, whose maximum OOP displacement varies from zero (edge stripes) to x_{yv}, moments due to vertical arching vary linearly from zero to M_{yv}. For what concerns horizontal stripes, the maximum moment can be attained only if the maximum displacement of the considered stripe is equal to x_{yh}. However, no horizontal stripe is associated with a maximum OOP displacement equal to x_{yh}, as the maximum OOP displacement for the central horizontal stripe is, for geometric compatibility, equal to x_{yv}. Hence, moments due to horizontal arching are linearly dependent on the maximum displacement attained by the considered horizontal stripe and, so, vary from zero to x_{yv}/x_{yh} times M_{yh}, which is the moment due to horizontal arching acting around the fracture lines crossing the central horizontal stripe. For each vertical and horizontal stripe, a uniformly distributed load whose external work is equal to the internal work due to moments acting in correspondence of fracture lines crossing the considered stripe is calculated. As moments are linearly variable from zero to the maximum value when passing from boundary stripes to central stripes, also the uniformly distributed load calculated for each stripe is different from stripe to stripe. Namely, it equals zero on the infill edges and is maximum for central stripes. In this way, the external load shape reproduces the deformed shape itself. In other words, the load distribution is shaped as a hipped roof as the deformed shape itself, so it will be defined as "hipped-shaped" in the following. Note that within this approach, moments due to arching action and acting in correspondence of fracture lines are null at the infill edges and maximum at the infill centre. This assumption has no mechanical basis (note in fact that Dawe and Seah's model is based on completely opposite assumptions), and yields to strongly underestimated values of the OOP strength of URM infills, as also noted by Bashandy et al. themselves.

M_{yv} and M_{yh} can be calculated through the application of Equation 1, with masonry mechanical properties adapted to the considered direction of arching thrusts. Also ε_c should be calculated separately for vertical and horizontal stripes by using Equation 2a or 2b. The OOP resistance obtained is expressed through Equation 22. In Equation 22, x_{yv} and x_{yh} are calculated as reported in Equation 23.

$$F_{max} = 16 \frac{M_{yv}}{h^2} \left[h^2 \ln 2 + h^2 \left(\frac{w-h}{h} \right) + wh \left(\frac{M_{yh}}{M_{yv}} \frac{x_{yv}}{x_{yh}} \right) \ln \left(\frac{w}{w - 0.5h} \right) \right] \qquad (22)$$

$$x_{yv} = \frac{tf'_{mv}}{E_{mv}\varepsilon_{cv}} \qquad (23a) \quad x_{yh} = \frac{tf'_{mh}}{E_{mh}\varepsilon_{ch}} \qquad (23b)$$

The "equivalent" uniformly distributed load whose resultant on the infill surface produces the resistance expressed in Equation 22 is reported in Equation 24.

$$q_{max,4E} = 16\frac{M_{yv}}{h^2}\left[\frac{h}{w}\ln2 + \left(\frac{w-h}{w}\right) + \left(\frac{M_{yh}}{M_{yv}}\frac{x_{yv}}{x_{yh}}\right)\ln\left(\frac{w}{w-0.5h}\right)\right] \qquad (24)$$

Note that for w that tends to infinity, $q_{max,4E}$ expressed in Equation 24 becomes $q_{max,2E}$ expressed in Equation 3, i.e., the specific resistance of a panel bounded along four edges tends, independently on masonry mechanical properties, to the specific resistance of a panel bounded only along two edges as the panel width increases.

Equation 22 can be generalized for θ varying between 0 and 45°, as reported in Equation 25.

$$F_{max} = 16\frac{M_{yv}}{h^2}\left[\frac{h^2}{tg\theta}\ln2 + h^2\left(\frac{w-htg\theta}{h}\right) + \frac{wh}{tg^2\theta}\left(\frac{M_{yh}}{M_{yv}}\frac{x_{yv}}{x_{yh}}\right)\ln\left(\frac{w}{w-0.5htg\theta}\right)\right] \qquad (25)$$

Independently on θ value, also in this case $q_{max,4E}$ tends to $q_{max,2E}$ if w tends to infinity. Consider also that the formulation reported in Equation 25 does not have an absolute minimum for varying θ, i.e., it cannot be used to individuate the optimal value of θ that minimize the predicted OOP strength.

1.2.3. Influence of the load shape on the theoretical OOP strength of infills

In Table 1, all the OOP strength models described in the previous sections are recalled. Each model refers to a specific boundary condition for the infill, to one-way or two-way arching action and to a specific external load shape.

As shown in Table 1.1, all strength models allow calculating the uniformly distributed load corresponding to the considered infill's OOP strength, except for Bashandy et al.'s model, in which the calculated load is hipped-shaped as the considered collapse mechanism/deformed shape. Not all experimental tests were carried out by applying on test specimens a uniformly distributed load. So, in order to assess all literature and code formulations predictive capacity by using the collected experimental results, which is the scope of Chapter IV of this thesis, it is necessary to "adapt" them

to different load shapes. In this section, separately for infills bounded along two and four edges, the relationships associated to different strength models are reformulated for different load shapes, in order to show the effect of different loading condition on the theoretical OOP strength of infills. In addition, it is worth to mention that adapting the OOP strength formulations to different load shapes is useful for the interpretation of experimental tests' results, but also preliminary to the proposal of efficient, robust and reliable strength formulations. Namely, a formulation valid for uniformly distributed lateral load can be effective for a safety assessment of URM infills under wind load. A different load shape should be used for infills under seismic load, as will be shown in Chapter IV.

Table 1.1. OOP strength models based on one-way and two-way arching action.

Author/Code	formulation/model type	arching action	external load shape
McDowell et al.	mechanical	one-way	uniform
Angel et al.	mechanical	one-way	uniform
Eurocode 6	mechanical	one-way	uniform
Dawe and Seah	mechanical	two-way	whichever
Dawe and Seah	empirical	two-way	uniform
Bashandy et al.	mechanical	two-way	hipped
Flanagan and Bennett	empirical	two-way	uniform

Note that Dawe and Seah's and Flanagan and Bennett's formulations are empirical, so their expressions cannot be adapted to different loading conditions by using an analytical approach. For what concerns Dawe and Seah's stripe model, its application can be always performed by accounting for the OOP load actual shape within the calculation of the virtual work of external forces.

1.2.3.1. Strength models accounting for one-way arching

Consider an URM infill wall with height h and width w, bounded only along the lower and upper horizontal edges. Consider for this infill a collapse mechanism defined by horizontal fracture lines along the lower and upper edges, as well as along the infill's mid-height. The maximum moment per unit width along linear hinges, M_y, is calculated according to McDowell et al.'s formulation reported in Equation 1. If φ is the rotation of the infill rigid parts around the fracture lines at edges and 2φ is the relative rotation

of infill parts around the central fracture line, as shown in Figure 1.7, the internal virtual work is expressed as in Equation 28.
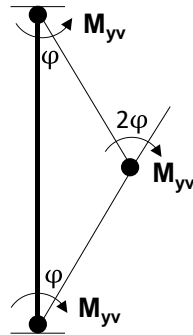
Figure 1.7. Assumed deformed shape at maximum for 2E infills.

$$L_I = 4M_{yv}\varphi \tag{28}$$

The external virtual work L_E due to loads applied on the infill depends on the external load shape. The external virtual work for uniformly distributed load (Figure 1.8a), for a concentrated load applied on two points, each one distant γh from the nearest edge (Figure 1.8b), and for concentrated load applied at the infill mid-height (Figure 1.8c) are reported in Equations 29-30 and 31, respectively.
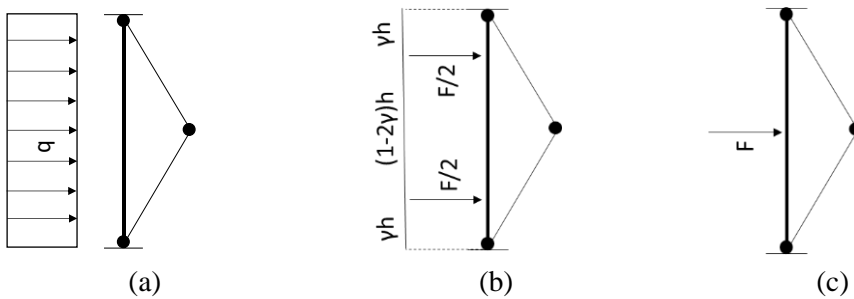
Figure 1.8. Load shapes considered for the calculation of the external virtual work.

$$L_E = q\frac{h^2}{4}\varphi \tag{29}$$

$$L_E = F\gamma h\varphi \tag{30}$$

$$L_E = F \frac{h}{2} \varphi \tag{31}$$

By equating virtual works, the following expressions, reported in Equations 32-34 are derived for the OOP strength, F_{max}, of the considered infill. As expected, Equation 20 corresponds to McDowell et al.'s formulation.

uniformly distributed load $F_{max} = (q_{max}hw) = 16M_{yv} \dfrac{w}{h}$ $\qquad$ (32)

concentrated load on two points $F_{max} = \dfrac{4}{\gamma} M_{yv} \dfrac{w}{h}$ $\qquad$ (33)

concentrated load at mid-height $F_{max} = 8M_{yv} \dfrac{w}{h}$ $\qquad$ (34)

Equations 32-34 show that an infill subjected to uniformly distributed load exhibits an OOP strength equal to two times the resistance exhibited under concentrated load applied at mid-height, and to 4γ times the resistance exhibited under concentrated load applied on two points, each one distant γh from the nearest edge.

As already stated, Eurocode 6's strength model is based on the assumption of a maximum value for vertical arching thrust and on the calculation of the maximum uniformly distributed load in equilibrium with that thrust value. In other words, it is based on one-way arching and on the lower bound theorem of limit analysis. The resultant load in equilibrium with the maximum arching thrust reported in Equation 9 calculated for different load shapes is reported in Equations 35-37. As expected, Equation 35 corresponds to Eurocode 6's formulation (except for the 1.08 factor, which is dropped in Eurocode 6 formulation for simplicity).

uniformly distributed load $F_{max} = 1.08f_m \left(\dfrac{t}{h}\right)^2 wh$ $\qquad$ (35)

concentrated load on two points $F_{max} = \dfrac{0.27}{\gamma} f_m \left(\dfrac{t}{h}\right)^2 wh$ $\qquad$ (36)

concentrated load at mid-height $F_{max} = 0.54f_m \left(\dfrac{t}{h}\right)^2 wh$ $\qquad$ (37)

As Equations 32-34, also Equations 35-37 show that an infill subjected to uniformly

distributed load exhibits an OOP strength equal to two times the resistance exhibited under concentrated load applied at mid-height, and to 4γ times the resistance exhibited under concentrated load applied on two points, each one distant γh from the nearest edge.

The same results are obtained by "adapting" Angel et al.'s formulation to different load shapes. For all these reasons, it is possible to conclude that the conversion factor between one loading shape to another for infills in which one-way arching occurs does not depend on the infill mechanical or geometric properties and, above all, does not depend on the specific mechanical-based strength model used.

1.2.3.2. Strength models accounting for two-way arching

Now, consider an URM infill bounded along all edges. In this case, Bashandy et al.'s model can be adapted to different loading schemes by equating internal and external works calculated by applying the hypotheses of Bashandy et al.'s approach, especially in terms on moment distribution along fracture lines.

Equations 38-40 report the calculated value of F_{max} for different loading schemes obtained by applying all the hypotheses of Bashandy et al.'s model, which were presented in the previous section. The four loading points considered in Equation 39 are placed on the infills' diagonal, at distance equal to γh from the nearer horizontal edge for each horizontal couple of loading points.

uniformly distributed load
$$F_{max} = 16M_{yv}\left[\frac{3}{2}\frac{w}{h}\frac{(2w-h)}{(3w-h)} + \frac{3}{2}\frac{M_{yh}}{M_{yv}}\frac{x_{yv}}{x_{yh}}\left(\frac{w}{3w-h}\right)\right] \quad (38)$$

concentrated load
on four points
$$F_{max} = 16M_{yv}\left[\frac{1}{8\gamma}\left(2\frac{w}{h} - 1 + \frac{M_{yh}}{M_{yv}}\frac{x_{yv}}{x_{yh}}\right)\right] \quad (39)$$

concentrated load
at mid-height
$$F_{max} = 16M_{yv}\left[\frac{1}{2}\frac{w}{h} - \frac{1}{4} + \frac{1}{4}\frac{M_{yh}}{M_{yv}}\frac{x_{yv}}{x_{yh}}\right] \quad (40)$$

If the assumptions reported in Equation 41 are made:

$$S = \frac{w}{h}; \quad (41a); \qquad T = \frac{M_{yh}}{M_{yv}}\frac{x_{yv}}{x_{yh}} \quad (41b)$$

Equations 38-40 can be rewritten as:

uniformly distributed load	$$F_{max} = 16M_{yv}\left[\frac{3}{2}S\frac{(2S-1)}{(3S-1)} + \frac{3}{2}T\left(\frac{S}{3S-1}\right)\right]$$	(42)
concentrated load on four points	$$F_{max} = 16M_{yv}\left[\frac{1}{8\gamma}(2S-1+T)\right]$$	(43)
concentrated load at mid-height	$$F_{max} = 16M_{yv}\left[\frac{1}{2}S - \frac{1}{4} + \frac{1}{4}T\right]$$	(44)

As can be observed through Equations 42-44, it is not possible, for infills bounded along four edges, to define a "conversion factor" of the OOP resistance in passing from one loading scheme to another independently on the infill geometrical (represented by S) and mechanical (represented by T) properties. A sensitivity analysis to S and T variation for the ratios of F_{max} under a hipped load ($F_{max,hl}$) over F_{max} under uniformly-distributed load ($F_{max,ud}$), 4-points load with $\gamma=1/3$ ($F_{max,4p}$) and under central 1-point load ($F_{max,1p}$) is shown in Figure 1.9.
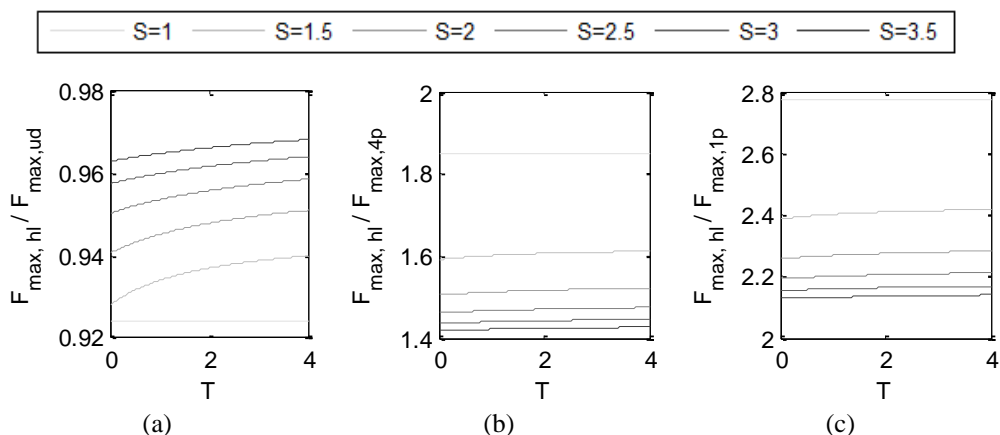
Figure 1.9. Conversion factor of OOP strength under hipped load to uniformly distributed load (a), to concentrated 4 points with $\gamma=1/3$ load (b) and to concentrated 1 point load (c).

In all cases, the conversion factor shown in Figure 1.9 is independent on masonry mechanical properties for square panels. A slight variability with both S and T is observed for $F_{max,hl}/F_{max,ud}$, with conversion factor meanly equal to 0.94, while a significant variability with S, but not with T, is observed for both $F_{max,hl}/F_{max,4p}$ and $F_{max,hl}/F_{max,1p}$.

1.3   OOP STIFFNESS MODELS

As already stated, infill walls under lateral loads behave, in the initial loading stages, as an elastic orthotropic plate.

Timoshenko and Woinowsky-Krieger proposed a relationship aimed at evaluating the central displacement of a uniformly-loaded elastic plate, δ, as reported in Equation 45.

$$\delta = \alpha \frac{qa^4}{D} \tag{45}$$

In Equation 45 α is a parameter accounting for the aspect ratio and bounding condition of the plate (see Tables 8, 29 and 47 in Timoshenko and Woinowsky-Krieger); a is the shorter dimension of the plate (typically, in an infill wall, the height, h); D is the well-known flexural stiffness of the plate per unit width, expressed according to Equation 46.

$$D = \frac{Et^3}{12(1 - v^2)} \tag{46}$$

 The previous relationship can be used to obtain an expression of the initial stiffness of the infill considered as an elastic plate, i.e., of the initial stiffness up to the first cracking point, as reported in Equation 47, in which b is the longer dimension of the plate (typically, in an infill wall, the width, w).

$$K_{el} = \frac{F}{\delta} = \frac{qab}{\alpha \frac{qa^4}{D}} = \frac{bD}{\alpha a^3} = \frac{1}{\alpha} \frac{w}{h^3} \frac{Et^3}{12(1 - v^2)} = \frac{1}{12\alpha(1 - v^2)} \frac{Ew}{(h/t)^3} \tag{47}$$

As Equation 47 is dedicated to isotropic plates, E is the elastic modulus of the material. It is well known that masonry is an orthotropic material. Hence, the application of Equation 47 to masonry infills is not immediate.

It is worth mentioning, as it will be useful when dealing with infills under seismic loads, that with the same approach above shown it is possible to derive from Timoshenko's work also the elastic stiffness of a rectangular plate under sinusoid load, as reported in Equation 48.

$$K_{el} = \frac{\pi^2}{3(1-v^2)} Ewt^3h \left(\frac{1}{w^2} + \frac{1}{h^2}\right)^2 \tag{48}$$

The literature provides a formulation for the calculation of the secant stiffness at maximum. Kadysiewski and Mosalam (2009), in fact, propose to calculate this stiffness value using an approach based on the first out-of-plane natural frequency of the panel considered pinned only at the top and bottom edges given by Blevins and Plunkett (1980) and reported in Equation 49. Clearly, for this reason, the formulation is rigorously applicable only to 2E infills.

$$f = \frac{\pi}{2L^2} \sqrt{\frac{\xi EI}{m/L}} = \frac{\pi}{2h^2} \sqrt{\frac{\xi Ewt^3}{12m/h}} \tag{49}$$

In Equation 49, L is the infill length and E is masonry elastic modulus, both of them evaluated in the direction perpendicular to the pinned edges: typically, L is the infill height, h; m is the infill mass; I is the infill cross-section area moment; ξ is a coefficient defining the effective flexural stiffness of the infill cross section.

For such a type of 2E infill, the mass participating to the first out-of-plane mode, m_p, is equal to ψ times the infill total mass, with ψ equal to 0.81, as reported by Kadysiewski and Mosalam. It is well known that for a Single Degree of Freedom (SDOF) dynamic system the fundamental vibration frequency is calculated as reported in Equation 50.

$$f = \frac{1}{2\pi} \sqrt{\frac{k}{m_p}} = \frac{1}{2\pi} \sqrt{\frac{k}{\psi m}} \tag{50}$$

In Equation 50, k is the SDOF elastic stiffness. If the URM infill is considered as an SDOF with respect to OOP excitations, k is its elastic stiffness in the OOP direction. By comparing Equations 49 and 50, the value of k can be determined. According to Kadysiewski and Mosalam, this is the value of the OOP secant stiffness at maximum and is reported in Equation 51.

$$K_{max} = \frac{\pi^4}{12} \psi \xi \frac{Ew}{(h/t)^3} \tag{51}$$

If, according to Kadysiewski and Mosalam, ψ is assumed equal to 0.81 and ξ is assumed equal to 0.50 (to account for the cross-section cracking), Equation 52 is derived.

$$K_{max} = 3.28 \frac{Ew}{(h/t)^3} \tag{52}$$

It is worth to mention that Equation 52 and 47 has the same structure, as if K_{max} can be expressed as a fraction of K_{el} depending on the infill boundary condition and effective stiffness due to cracking.

1.4   OOP DISPLACEMENT CAPACITY MODELS

Usually, the collapse displacement of a structural or non-structural member is conventionally defined based on a fixed reduction of its resistance. This reduction is commonly related to a certain damage state of the element or to a significant variation in its response. A unique and commonly accepted definition of OOP displacement capacity for URM infills is not available. However, according to previous studies and code provisions the OOP displacement capacity can be calculated by associating it to different phenomena.

First, it is commonly accepted that for geometric compatibility the OOP displacement cannot be greater than the infill thickness, t.

In addition, based on Angel et al. (1994)'s analytical model, two candidate expression for the definition of the OOP collapse displacement can be derived. The first one is associated to an instability phenomenon called "snap-through", which occurs when arching action vanishes. The second one is associated to masonry mechanical properties, i.e., to masonry crushing due to the compressive stresses associated with arching thrusts.

To derive such expressions, a masonry stripe simply supported at ends is considered. Indefinitely stiff and resistant supports are assumed. As shown in Figure 1.10, masonry stripes are supposed to crack at ends and mid-height and to divide in two equal-length masonry segments.
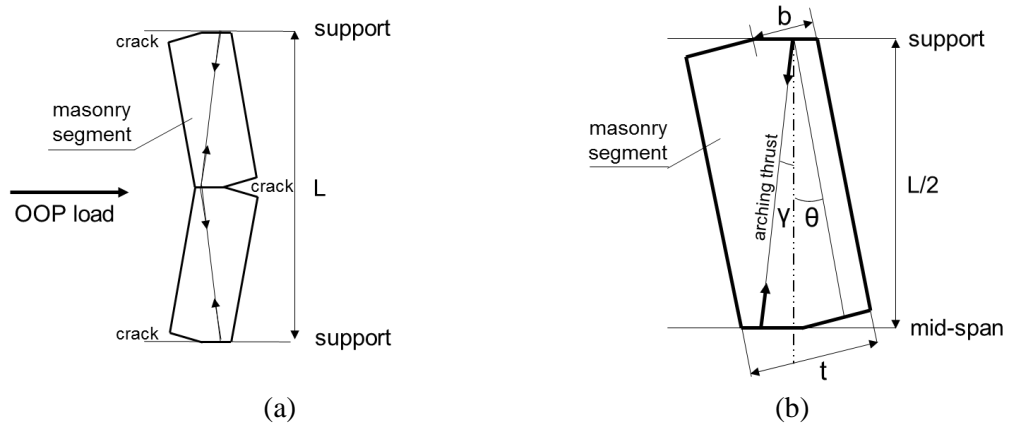
Figure 1.10. Cracked masonry stripe deformed shape at arching action occurrence (a) and masonry segment detail (b).

Based only on equilibrium and geometrical compatibility, the expressions reported in Equations 53-55 are derived for the compression bearing width in the infill thickness normalized with respect to the infill thickness itself, b/t, for the rotation of masonry segments, θ, and for the angle of arching thrust direction with respect to vertical direction, γ, in the hypothesis of small displacements and rotations.

$$\frac{b}{t} = 0.25 \left(1 + \sqrt{1 - 2c\left(\frac{L}{t}\right)^2} \right) \tag{53}$$

$$\theta = c\frac{L/t}{b/t} \tag{54}$$

$$\gamma = \frac{2\left(1 - 2k_2(b/t)\right)}{(L/t)} - c\frac{L/t}{b/t} \tag{55}$$

In Equations 53-55, L is the length of the infill panel in which arching action occurs, k_2 is assumed equal to 0.33 for triangular compression stresses distribution in the bearing width, c is a dimensionless parameter defined as reported in Equation 56.

$$c = \frac{1}{4}\varepsilon_{max} \qquad (56)$$

In Equation 56, ε_{max} is the strain attained at the outermost compressed fiber in the panel thickness. The masonry stripe central displacement is calculated as reported in Equation 57.

$$d = \theta\frac{L}{2} \qquad (57)$$

As shown in section 6.2 of Angel et al., when c is equal to the value reported in Equation 58, the direction of arching thrust becomes vertical, i.e., γ equals 0.

$$c_{lim} = \frac{0.481}{(L/t)^2} \qquad (58)$$

At this point, if a little displacement increment is applied to the masonry stripe, arching thrusts assume horizontal component with the same direction of OOP loads, i.e., a little increment of lateral displacement produces a sudden snap-through collapse of the stripe as arching action separates masonry segments from each other.

If c=c_{lim}, the b/t ratio assumes a limit value as reported in Equation 59.

$$\frac{b}{t} = \left(\frac{b}{t}\right)_{lim} = 0.25\left(1 + \sqrt{1 - 2c_{lim}\left(\frac{L}{t}\right)^2}\right) = 0.30 \qquad (59)$$

In the same case, also the masonry segment rotation attains a limit value, as reported in Equation 60.

$$\theta = \theta_{lim} = c_{lim}\frac{L/t}{(b/t)_{lim}} = \frac{1.60}{(L/t)} = 1.60\frac{t}{L} \qquad (60)$$

The displacement at snap-through is obtained by substituting Equation 60 in Equation 57, as reported in Equation 61.

$$d = d_{lim} = \theta_{lim} \frac{L}{2} = 1.60 \frac{t}{L} \frac{L}{2} = 0.80t \tag{61}$$

So, both vertical and horizontal arching vanish if the infill central displacement is equal to 0.80 times the infill thickness.

For what concerns the displacement at masonry crushing due to arching thrusts, in this case, c assumes the value reported in Equation 62.

$$c_{crush} = \frac{1}{4}\varepsilon_{crush} \tag{62}$$

The masonry segments' rotation at masonry crushing is reported in Equation 63.

$$\theta = \theta_{crush} = c_{crush} \frac{L/t}{b/t} = 0.25\varepsilon_{crush} \frac{L/t}{b/t} \tag{63}$$

In Equation 63, b/t should be equal to the value reported in Equation 64.

$$\left(\frac{b}{t}\right)_{crush} = 0.25\left(1 + \sqrt{1 - 2c_{crush}\left(\frac{L}{t}\right)^2}\right) \tag{64}$$

In order to provide a conservatively simplified equation for d_{crush} prediction, it is necessary to assume for b/t the maximum possible value for b/t, equal to 0.50. In this case, Equation 63 can be rewritten as reported in Equation 65.

$$\theta = \theta_{crush} = c_{crush} \frac{L/t}{(b/t)_{crush}} = 0.50\varepsilon_{crush} \frac{L}{t} \tag{65}$$

The displacement at masonry crushing can be expressed as reported in Equation 66.

$$d = d_{crush} = \theta_{crush} \frac{L}{2} = 0.50\varepsilon_{crush} \frac{L}{t} \frac{L}{2} = \left(0.25\varepsilon_{crush} \frac{L}{t}\right) L \tag{66}$$

Moreover, the OOP displacement at the attainment of peak load for infills with slenderness equal to 20 and masonry crushing strain equal to 0.004 should be lower than 3% of the infill height to ensure that such infills can reach their maximum load-bearing

capacity without snapping through according to Angel et al. and FEMA 274 (1997). This height percentage is assumed as OOP displacement capacity by ASCE/SEI 41-13 (2013) at Life Safety Limit State.

Finally, Kadysiewski and Mosalam (2009), based on judgment, suggest assuming the OOP collapse displacement equal to 5 times the OOP displacement at peak load. In other words, they assume an OOP ductility capacity for the infill equal to 5.

1.5   IP/OOP INTERACTION MODELLING FORMULATIONS

As already stated, the damage of infills due to IP actions affects their OOP response and vice-versa. This phenomenon is called IP/OOP interaction.

For what concerns the IP damage effects on the OOP response, previous works mainly investigate the effects on the OOP strength. The IP damage entity is usually represented by a main displacement demand parameter such as the Interstorey Drift Ratio (IDR) and, in some cases, by the infill vertical slenderness ratio, h/t. In fact, it is assumed that at equal IP displacement demand, less slender infills should be less damaged and then that their OOP capacity should be less compromised. The same result was observed by Agnihotri et al. (2013) through numerical FEM analyses.

An OOP strength model accounting for IP/OOP interaction was proposed by Angel et al. (1994(based on experimental data. In this case, the pure OOP resistance of the undamaged infill is reduced using an R_1 factor that will be called R in this thesis. R is expressed as a function of the infill height over thickness slenderness ratio and of the maximum IP drift (IDR) attained normalized with respect to the IP drift corresponding to the infill IP first cracking (IDR_{crack}), as reported in Equation 67.

$$R = 1 \qquad\qquad \frac{IDR}{2IDR_{crack}} < 0.5$$

$$R = \left[1.08 + (h/t)\left(-0.015 + (h/t)\left(-0.00049 + 0.000013(h/t)\right)\right)\right]^{\frac{IDR}{2IDR_{crack}}} \qquad \frac{IDR}{2IDR_{crack}} \geq 0.5 \tag{67}$$

OOP strength reduces for increasing IP displacement and reduces faster for higher slenderness values, as intuitively expected.

Morandi et al. (2013) based on Calvi and Bolognini (2001)'s tests, proposed

empirical stepwise (Equation 68) and linear (Equation 69) formulations for the calculation of the OOP strength reduction factor due to IP damage. In the "stepwise" formulation, the onset of IP/OOP interaction effects on the OOP strength for thin infills is set corresponding to an IDR equal to 0.30%, which is the threshold IDR for infilled RC buildings at the attainment of Damage Limitation limit state according to the Italian building code NTC2008 (2008).

$$R = \begin{cases} 1.00 & \text{IDR} \leq 0.30\% \\ 0.20 & 0.30\% < \text{IDR} \leq 1.00\% \\ 0 & \text{IDR} > 1.00\% \end{cases} \tag{68}$$

$$R = \begin{cases} 1\text{-}2.67\text{IDR} & \text{IDR} \leq 0.30\% \\ 0.20 & 0.30\% < \text{IDR} \leq 1.00\% \\ 0 & \text{IDR} > 1.00\% \end{cases} \tag{69}$$

Based on Guidi et al. (2013)'s tests on unreinforced masonry strong and thick infills, Verlato et al. (2014) proposed an empirical relationship for the evaluation of the R factor. Such relationship is reported in Equation 70.

$$R = \begin{cases} 1\text{-}0.86\text{IDR} & \text{IDR} \leq 0.70\% \\ 0.40 & 0.70\% < \text{IDR} \leq 1.20\% \\ 0 & \text{IDR} > 1.20\% \end{cases} \tag{70}$$

For what concerns the effects of damage due to OOP action on the IP response of infills, based on numerical analysis, Al-Chaar (2002) states that the effects of OOP loads on the IP capacity of infills could be neglected if these loads do not exceed a threshold fixed at 20% of the corresponding capacity; otherwise, a formulation based on FEM analysis is provided and is reported in Equation 71.

$$\frac{\text{IP}_{\text{red}}}{\text{IP}_{\text{cap}}} = 1 + \frac{1}{4}\frac{\text{OP}_{\text{dem}}}{\text{OP}_{\text{cap}}} - \frac{5}{4}\left(\frac{\text{OP}_{\text{dem}}}{\text{OP}_{\text{cap}}}\right)^2 \tag{71}$$

In Equation 71, IP_{red} is a general parameter of IP capacity reduced due to OOP action; IP_{cap} is the same parameter of IP capacity in absence of OOP action; OP_{dem} is the OOP demand acting on the infill corresponding to the IP capacity parameter under exam; OP_{cap} is the same parameter of OOP capacity in absence of IP action.

Further formulations and approaches dedicated to the prediction of the IP/OOP interaction effects will be shown in the next subsection, in which the available modelling approaches and strategies to account for the OOP behaviour of infills and for the IP/OOP interaction effects during structural analyses are presented and discussed.

1.6   IP/OOP INTERACTION MODELLING STRATEGIES

Hashemi and Mosalam (2007) proposed a strut and tie macro-model of infills based on the results of FEM analyses. In this model, the infill is represented by eight no-tension truss elements joined in the center by a no-compression truss element. The coordinates of the characteristic points of the constitutive law together with the geometric characteristics of struts and tie are calibrated in order to obtain an interaction domain of IP action, P_H, and OOP action, P_N, which follows the one obtained through numerical analysis. In order to obtain this domain, several numerical analyses at finite two-dimensional elements were carried out, during which the infill was subjected to a constant OOP action P_N and to an IP action P_H increasing up to the panel collapse. The pushover curves and the resulting interaction domain obtained are shown in Figure 1.11.

(a)   (b)
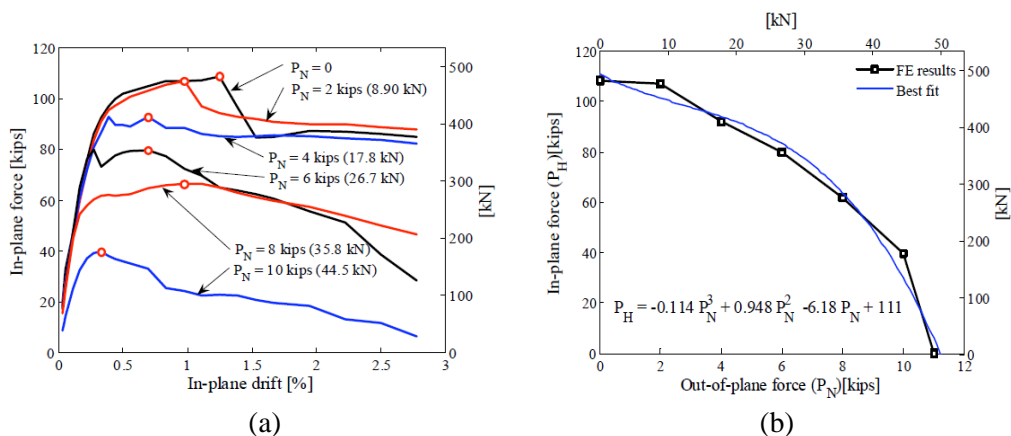
Figure 1.11. IP/OOP interaction represented through IP pushover curves at assigned OOP forces (a) and through a static IP/OOP interaction domain (b). Adapted from Hashemi and Mosalam (2007).

Kadysiewski and Mosalam (2009) introduced a macro-model alternative to the one proposed by Hashemi and Mosalam. In this case, the infill is modelled through one diagonal beam element pinned at the edges and provided with a lumped mass in the

center active only in the OOP direction. Kadysiewski and Mosalam calculate the OOP strength of the undamaged infill by applying FEMA356 (2000) provisions, based on Angel et al.'s formulation, as will be explained in Chapter V, while the stiffness is determined following the indications based on OOP frequency of the panel discussed the previous subsections. Then, the OOP displacement at peak load Δ_{Ny0} is determined as the peak force resulting from the peak load to the above-mentioned stiffness ratio, while the ultimate displacement is set equal to 5 times the peak load displacement. In order to take into account the IP/OOP interaction, the authors introduce a convex relationship derived from numerical analysis and represented in Figure 1.12; moreover, an interaction domain in terms of yielding and collapse displacements is defined as reported in Equation 72.

$$\left(\frac{P_N}{P_{N0}}\right)^{3/2} + \left(\frac{P_H}{P_{H0}}\right)^{3/2} = 1 \tag{72}$$
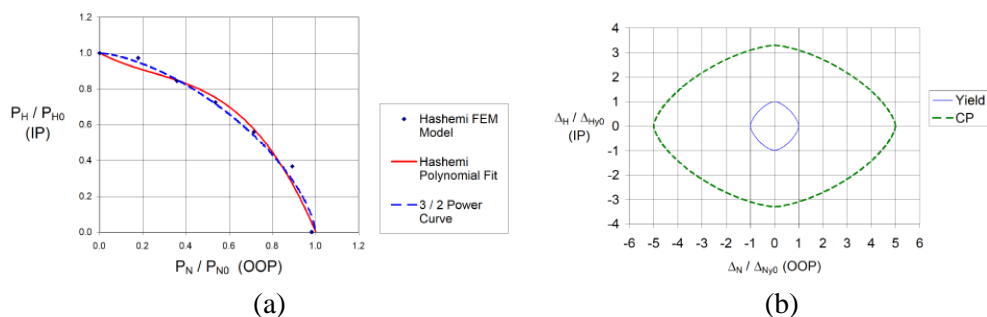
Figure 1.12. IP/OOP interaction domains in terms of forces (a) and displacements (b). Adapted from Kadysiewski and Mosalam (2009)

Given that until yielding the IP and OOP behaviour of infill is assumed to be linear elastic, the interaction domain in terms of yielding displacement is expressed through the same convex relationship used for the domain in terms of forces; moreover, given the lack of specific indications in literature, the authors postulate that the same 3/2 power relationship can be used to model the interaction in terms of ultimate displacement. Integral part of the discussed model is a routine that removes from the structural model the elements representative of the infill when their IP/OOP displacement history exceeds the interaction domain in terms of ultimate displacement.

Dolatshahi et al. (2014) carried out three-dimensional FEM analyses resulting in

interaction domains in terms of yielding and peak load. The analytical relationship proposed to represent the elliptical yielding curve, which is shown in Figure 1.13, is reported in Equation 73.
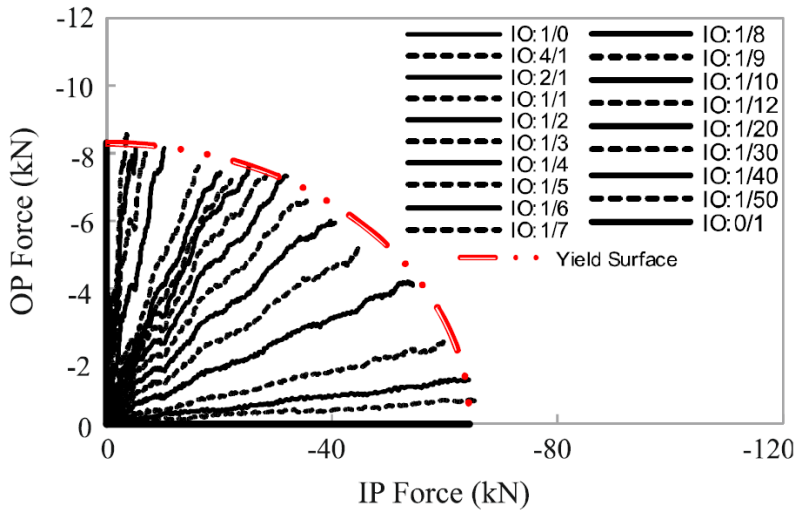
Figure 1.13. IP/OOP interaction domain in terms of forces. Adapted from Dolatshahi et al. (2014).

$$\left(\frac{P_N}{P_{N0}}\right)^2 + \left(\frac{P_H}{P_{H0}}\right)^2 = 1 \tag{73}$$

Furtado et al. (2016) defined an infill model inspired by the proposal of Kadysiewski and Mosalam. In this model, the infill is represented by 4 diagonal rigid elements joined in the center by one element which takes into account the non-linearity of the infill behaviour. The central element is joined to the diagonal struts through 2 nodes in which the OOP mass is lumped. The OOP behaviour is assumed as elastic-plastic with strength and stiffness calculated accordingly to Kadysiewski and Mosalam's approach. Also in this case, part of the model is an algorithm that removes the elements representative of the infill from the structural model if its IP/OOP displacement history exceeds an interaction domain in terms of ultimate displacement. The domain is linear and is based on the assumption that, for the undamaged panel, the maximum IP drift is equal to 1.5% while the maximum OOP drift is equal to 3%.

A macro-model based on the one defined by Kadysiewski and Mosalam was also

proposed by Longo et al. (2016). The interaction domains previously considered were derived through numerical analysis. Maheri et al. (2012) carried out a sequence of tests aimed at determining an experimental IP/OOP interaction domain in terms of strength of infills. Fifteen masonry panels were tested until collapse under combined IP/OOP action. Each of these panels was subjected to a fixed OOP load monotonically applied and kept constant while IP diagonal action was applied until the panel collapse. At increasing values of the previously imposed OOP load, a reduction of strength and stiffness under IP action was registered, as reported in Figure 1.14.
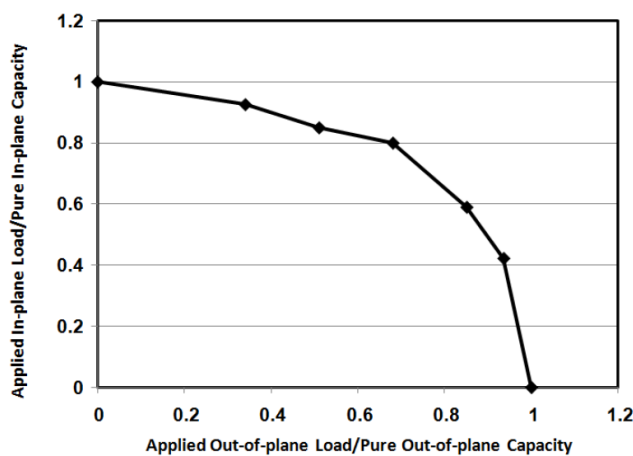
Figure 1.14. IP/OOP interaction experimental domains in terms of force. Adapted from Maheri and Najafgholipour (2012).

Di Trapani et al. (2018) proposed a macro-model in which the infill wall is represented by two fiber-section diagonals accounting for the IP/OOP interaction and through a vertical and a horizontal element accounting for the bi-directional arching action.

An infill wall model accounting for the IP/OOP interaction was proposed by Oliaee and Magenes (2016). The infill is represented by 2 diagonals, each one divided into 2 non-interacting in-series no-tension elements, an inelastic truss representing IP behaviour and a distributed inelasticity fiber element representing OOP behaviour. The IP/OOP interaction is introduced through the updating of the strain at peak load of the material assigned to fibers (OOP stiffness reduction) and through the reduction of the fiber elements' thickness (OOP strength reduction) depending on the maximum IP displacement registered. The reduction of the fiber elements' thickness represents the

expulsion of outer shells of masonry units due to IP damage. The effort made to provide the model's features of a physical meaning, unlike Kadysiewski and Mosalam-based models, has to be highlighted.

REFERENCES

- Agnihotri P, Singhal V, Rai DC. Effect of in-plane damage on out-of-plane strength of unreinforced masonry walls. Engineering Structures 2013;57:1-11.
- Al-Chaar G. Evaluating strength and stiffness of unreinforced masonry infill structures. Engineer research and development center Champaign (IL) Construction Engineering Research Lab, 2002.
- Angel R, Abrams DP, Shapiro D, Uzarski J, Webster M. Behaviour of reinforced concrete frames with masonry infills. University of Illinois Engineering Experiment Station. College of Engineering. University of Illinois at Urbana-Champaign., 1994.
- ASCE/SEI 41-13. Seismic rehabilitation of existing buildings. Reston, VA: American Society of Civil Engineers; 2013.
- Bashandy T, Rubiano NR, Klingner RE. Evaluation and analytical verification of infilled frame test data. Phil M. Ferguson Structural Engineering Laboratory, University of Texas at Austin. 1995.
- Brincker R. Yield-Line Theory and Material Properties of Laterally Loaded Masonry Walls. MASONRY INT. Masonry Int., 1984, 1: 8.
- Calvi GM, Bolognini D. Seismic response of reinforced concrete frames infilled with weakly reinforced masonry panels. Journal of Earthquake Engineering 2001;5.2:153-185.
- Code of practice for use of masonry. Part 1: Structural use of unreinforced masonry. BS 5628 Part 1, British Standards Institution, London, 1992.
- Dawe JL, Seah CK. Out-of-plane resistance of concrete masonry infilled panels. Canadian Journal of Civil Engineering 1989;16(6):854–864.
- Di Trapani F, Cavaleri L, Shing PB. A macro-element model for in-plane and out-of-plane responses of masonry infills in frame structures. Journal of Structural Engineering (ASCE) 2018;144(2). doi: 10.1061/(ASCE)ST.1943-541X.0001926.
- Dolatshahi KM, Aref AJ, and Yekrangnia M. Bidirectional behaviour of unreinforced masonry walls, Earthquake Engineering & Structural Dynamics 2014;30: 2377–2397. DOI: 10.1002/eqe.2455.

- Drysdale, RG, Essawy AS. Out-of-plane bending of concrete block walls. Journal of Structural Engineering 1988;114.1:121-133.
- Edri IE, Yankelevsky DZ. An analytical model for the out-of-plane response of URM walls to different lateral static loads. Engineering Structures 2017;136:194-209.
- Eurocode 6. EN 1996-1-1: Design of masonry structures - Part 1-1: General rules for reinforced and unreinforced masonry structures, 2005.
- FEMA 274. ATC, 1997, NEHRP Commentary on the Guidelines for the Seismic Rehabilitation of Buildings, prepared by the Applied Technology Council (ATC-33 project) for the Building Seismic Safety Council, published by the Federal Emergency Management Agency, Report No. FEMA274, Washington, D.C.
- FEMA 356. Prestandard and commentary for the seismic rehabilitation of buildings. Washington, DC: Federal Emergency Management Agency; 2000.
- Flanagan RD, Bennett RM 1999. Arching of masonry infilled frames: Comparison of analytical methods. Practice Periodical on Structural Design and Construction 1999;4.3:105-110.
- Furtado A, Rodrigues H, Arêde A, Varum H 2016. Simplified macro-model for infill masonry walls considering the out-of-plane behaviour. Earthquake Engineering and Structural Dynamics 2016;45.4:507-524.
- Guidi G, da Porto F, Dalla Benetta M, Verlato N, Modena C. Comportamento sperimentale nel piano e fuori piano di tamponamenti in muratura armata e rinforzata. Proceedings of the XV ANIDIS, L'Ingegneria Sismica in Italia, Padua, Italy, 2013, 30. (in Italian).
- Haseltine BA, West HW, Tutt JN. Design of walls to resist lateral loads. The Structural Engineer. 1977;55.10:422-430.
- Hashemi SA, Mosalam KM. Seismic evaluation of reinforced concrete buildings including effects of infill masonry walls. Pacific Earthquake Engineering Research Center 2007;100:1026-1037.
- Hendry AW. The lateral strength of unreinforced brickwork. The Structural Engineer. 1973;51.2:43-50.
- Hendry AW. The lateral strength of unreinforced brickwork. The Structural Engineer. 1973;51.2:43-50.
- Kadysiewski S, Mosalam KM. Modelling of unreinforced masonry infill walls considering in-plane and out-of-plane interaction. Pacific Earthquake Engineering Research Center 2009.

- Kennedy G, Goodchild C. Practical yield line design. The concrete centre, Camberley, United Kingdom. 2004.
- Longo F, Granello G, Tecchio G, da Porto F, Modena C. A masonry infill wall model with in-plane out-of-plane interaction applied to pushover analysis of RC frames. Brick and Block Masonry: Proceedings of the 16th International Brick and Block Masonry Conference, Padova, Italy, 26-30 June 2016.
- Maheri MR, Najafgholipour MA, In-plane shear and out-of-plane bending capacity interaction in brick masonry walls. 15th World Conference on Earthquake Engineering, Lisbon, Portugal; 09/2012.
- McDowell EL, McKee KE, Sevin E. Arching action theory of masonry walls. J. Struct. Div 1956;82.2:915.
- Morandi P, Hak S, Magenes G. Simplified out-of-plane resistance verification for slender clay masonry infills in RC frames. Proceedings of the XV ANIDIS, L'Ingegneria Sismica in Italia, Padua, Italy, 2013.
- NTC2008. Decreto ministeriale 14 gennaio 2008 - Norme Tecniche per le Costruzioni NTC2008. Supplemento ordinario n. 30 Gazzetta Ufficiale 4 febbraio 2008, n 29. (in Italian).
- Oliaee M, Magenes G. In-plane out-of-plane interaction in the seismic response of masonry infills in RC frames. Brick and Block Masonry: Proceedings of the 16th International Brick and Block Masonry Conference, Padova, Italy, 26-30 June 2016.
- Pasca M., Liberatore L., Masiani R. Reliability of analytical models for the prediction of out-of-plane capacity of masonry infills. Structural Engineering and Mechanics 2017;64.6:765-781. doi: 10.12989/sem.2017.64.6.765
- Timoshenko SP, Woinowsky Krieger S. Theory of plates and shells. McGraw-Hill, New York, 1959.
- Vaculik J, Griffith MC. Out-of-plane load-displacement model for two-way spanning masonry walls. Engineering Structures 2017;141:328-343.
- Verlato N, Guidi G, da Porto F. Experimental testing and numerical modelling of infill masonry walls subjected to in-plane damage. Proc. of the Second European Conference on Earthquake Engineering and seismology, 25-29 August 2014, Istanbul, Turkey.

Chapter II
Experimental state-of-the-art

2.1   INTRODUCTION

The first Chapter of this thesis was dedicated to the presentation, analysis and discussion of the OOP strength, stiffness and displacement capacity models for IP-undamaged and IP-damaged URM infills. In order to assess the effectiveness of these models, in this Chapter the experimental tests previously carried out and presented in the literature aimed at assessing the pure OOP behaviour of such types of infills as well as the IP/OOP interaction effects are described.

First, it is worth to mention that, with respect to the number of IP tests (which is, according to De Risi et al. 2018, in the order of hundreds), the number of OOP or combined IP/OOP tests performed on URM infills is very small, i.e., in the order of the dozens. In this Chapter, only pseudo-static tests on URM infills will be considered.

The first section of this Chapter is dedicated to the pseudo-static OOP tests carried out on 2-edges (2E) infills, i.e., on infills bounded only along the upper and the lower edges also indicated, sometimes, as masonry stripes, in which only one way arching occurs. The second section is dedicated to the pseudo-static OOP tests carried out on 4-edges (4E) infills, i.e., on infills bounded along all edges to the confining structural elements. In this second section, also some specimens that will be defined as 3-edges (3E) infills, i.e., infills bounded along three out of four edges to the confining structural elements, will be presented. A third section is dedicated to other experimental programs that will not enter the database discussed in Chapter IV for reasons that will be explained for each of them.

The experimental programs will be presented in chronological order. Within the

description of each experimental program, pure OOP tests and combined IP/OOP tests will be described. For each experimental program, test specimens' characteristics, tests' procedure and tests' remarkable results will be described. Geometric and mechanical properties of specimens are reported, if provided by the authors or procurable in the literature. More specifically, masonry compressive strength in the vertical (f_{mv}) and in the horizontal (f_{mh}) direction are reported, as well as masonry elastic modulus in the vertical (E_{mv}) and in the horizontal (E_{mh}) direction. An overall collection of geometric and mechanical properties of specimens is reported in Appendix D.

In addition, for what concerns the OOP response of specimens, information concerning the load and displacement corresponding to the first visible crack/first significant non-linearity (F_{crack} and d_{crack}, respectively), and to the maximum (F_{max} and d_{max}, respectively), as well as the displacement at the end of the test (d_{end}) are collected. Based on F and d values, the secant stiffness at first visible crack (K_{crack}) and at maximum (K_{max}) are calculated. If such data are not directly provided by the authors, they are derived, if possible, from the observation of the OOP force-displacement relationships, based on the tests' description provided by the authors and, sometimes, on judgment.

2.2   EXPERIMENTAL TESTS ON 2E INFILLS

In this section, the pure OOP experimental tests carried out on 2E infills, i.e., on masonry stripes by da Porto et al. (2007) and by Hak et al. (2014) are described. The report by Modena et al. (2005) is also considered at support of the description of the tests by da Porto et al. (2007).

2.2.1. da Porto et al., 2007

Single-wythe panels made of clay hollow bricks were built between the ceiling and the floor of laboratory and used as test specimens. Each specimen was 2520 mm high, 1000 mm wide and 300 mm thick, with a slenderness equal to 8.4 and aspect ratio equal to 0.40. Bricks were jointed through 10 mm thick M3 cementitious mortar layers.

The tested specimens differed for the direction of bricks' holes (O – horizontal, V – Vertical) and for the bed joint type (A, B, C). More specifically, stripes with type A mortar joints were characterized by non-continuous vertical and horizontal joints; stripes with type B mortar joints were characterized by non-continuous vertical joints and continuous horizontal joints; stripes with type C mortar joints were characterized by

non-continuous vertical and horizontal joints. Three classes of panels were so defined: FOA, FOB and FVC; for each one of these classes, three specimen were realized and tested 28 days after their construction. Characterization tests on brick units and mortar specimens were performed. Their results are reported in Modena et al. (2005). Based on these results, masonry compressive strength and elastic modulus are determined based on Eurocode 6 (2005) formulations (section 3.6.1.2 and 3.7.2, respectively). Such average values determined and provided for FOA, FOB and FVC specimens are reported in Table 2.1.

Table 2.1. Mechanical properties of the specimens by da Porto et al. (2007).

specimen	f_{mv} [N/mm^2]	E_{mv} [N/mm^2]	f_{mh} [N/mm^2]	E_{mh} [N/mm^2]
FOA	1.87	1870	-	-
FOB	2.62	2620	-	-
FVC	5.22	5220	-	-

Test were performed by applying a concentrated load at the infill mid-height. Such load was distributed along a horizontal line through an horizontal steel beam. In addition, the load was applied monotonically and in displacement control at 0.01 mm/sec velocity. A picture of the experimental program setup is reported in Figure 2.1. All tests were interrupted soon after the attainment of peak load, at which the specimen collapsed.

The experimental evidences showed that the out-of-plane strength of panels was mainly influenced by brick units' compressive strength and by their general robustness: in fact, panels made of bricks with vertical cores showed a global collapse mechanism instead of the local (at the edges) mechanism exhibited by panels made of bricks with horizontal cores. Moreover, panels with continuous horizontal bed joints exhibited a peak load greater by about 30% with respect to the one exhibited by panels with interrupted joints. In this study, given the boundary conditions of the specimens, there was no significant contribution of vertical joints typology to the ultimate load of panels.

A summary of tests' results is reported in Table 2.2.
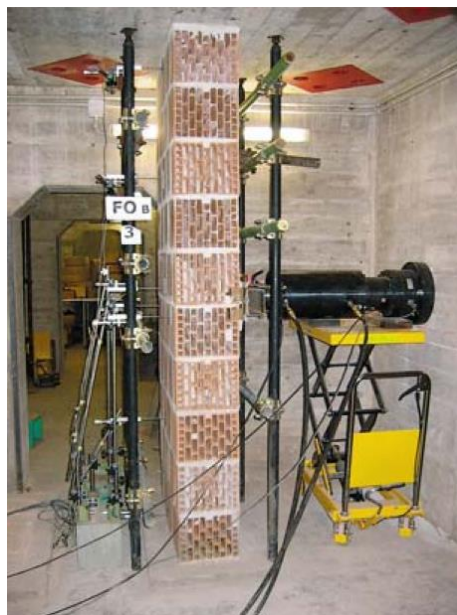
Figure 2.1. Experimental setup by da Porto et al. (2007).

Table 2.2. Summary of tests' results by da Porto et al. (2007).

| | F_{crack} | d_{crack} | K_{crack} | F_{max} | d_{max} | K_{max} | d_{end} |
specimen	[kN]	[mm]	[kN/mm]	[kN]	[mm]	[kN/mm]	[mm]
FOA1	13.0	0.35	37.1	43.2	2.3	18.8	2.3
FOA2	13.0	0.35	37.1	43.8	2.4	18.3	2.4
FOA3	13.0	0.35	37.1	45.1	2.3	19.6	2.3
FOB1	14.5	0.35	41.4	63.9	2.9	22.0	2.9
FOB2	14.5	0.35	41.4	55.3	2.6	21.3	2.6
FOB3	14.5	0.35	41.4	58.0	2.3	25.2	2.3
FVC1	23.4	0.20	117	174	3.4	51.2	3.4
FVC2	23.4	0.20	117	193	4.4	43.9	4.4
FVC3	23.4	0.20	117	179	3.4	52.6	3.4

2.2.2. Hak et al., 2014

Hak et al. (2014) tested thick real-scale URM infills both in the in-plane and in the OOP direction. Among these, specimen TA5 was bounded only along the upper and the lower edges to the confining RC frame. The specimen was realized with clay hollow bricks placed with vertical cores and vertical and horizontal mortar joints. It was 350

mm thick, 2950 mm high and 1380 mm wide. The aspect ratio was equal to 0.47, the vertical slenderness was equal to 8.4. The mechanical properties provided for specimen TA5 are reported in Table 2.3.

Table 2.3. Mechanical properties of specimen TA5 by Hak et al. (2014).

specimen	f_{mv} [N/mm^2]	E_{mv} [N/mm^2]	f_{mh} [N/mm^2]	E_{mh} [N/mm^2]
TA5	4.64	5299	1.08	494

The OOP test was performed by applying the load at the specimens' mid-height by means of two horizontal beams. Being the infill detached from structural elements at both lateral edges, this loading type can be schematized with two concentrated forces acting at distance from the infill mid-height equal to one-half the distance between the horizontal beams. However, the distance between the two horizontal beams is not provided, although it seems to be very small from graphical sketches of the experimental setup. Hence, also in this case, the external load will be considered as concentrated at the infill mid-height.

In this case, differently from da Porto et al.'s tests, the OOP load was applied to the infill surface with load-unload cycles. In addition, the infill stripe was bounded to the upper and to the foundation beam of an RC frame. The compressive strength of da Porto et al.'s masonry predicted, based on the compressive strength of bricks with vertical holes and mortar, through EC6 formulation and equal to 5.22 N/mm^2 was similar to the compressive strength parallel to bricks' holes declared by Hak et al. for their masonry wallets, equal to 4.64 N/mm^2. Moreover, the two masonry stripes had similar slenderness ratio. However, da Porto et al.'s stripes had an OOP strength equal to around 2.5 times that exhibited by the similar stripe by Hak et al. and a displacement at peak load equal to 1/5 of that shown by Hak et al.'s stripe. Moreover, Hak et al.'s specimen did not show a brittle failure at peak load. First, such significant differences can be due to the cyclic nature of Hak et al. tests. Second, such differences can also be due, for some part at least, to the deformability of the bounding elements for Hak et al.'s specimen.

A summary of the test results is reported in Table 2.4.

Table 2.4. Summary of test TA5 results by Hak et al. (2014).

specimen	F_{crack} [kN]	d_{crack} [mm]	K_{crack} [kN/mm]	F_{max} [kN]	d_{max} [mm]	K_{max} [kN/mm]	d_{end} [mm]
TA5	35.0	1.0	35.0	67.0	18.0	3.72	75

A picture of the specimen at the end of the test is reported in Figure 2.2.

Figure 2.2. Specimen TA5 by Hak et al. (2014) after tests.

2.3 EXPERIMENTAL TESTS ON 4E INFILLS

In this section, the pure OOP and combined IP/OOP experimental tests carried out on 4E infills, i.e., on URM infills bounded to the confining structural elements along all edges are described.

The tests considered are those by Dawe and Seah (1989), Angel et al. (1994), Flanagan and Bennett (1999a), Calvi and Bolognini (2001), Varela-Rivera et al. (2012), Guidi et al. (2013), Hak et al. (2014), Furtado et al. (2016).

2.3.1. Dawe and Seah, 1989

Steel frames infilled by real-scale single-wythe walls made of concrete hollow

bricks were used as test specimens. Each infill was 2800 mm high and 3600 mm wide, with aspect ratio equal to 1.29. The concrete units were jointed by a type S mortar.

The tested infills were 90, 140 or 190 mm thick, with a vertical slenderness ranging from 14.7 to 31. Specimens WE2, WE4, WE5 and WE8 were realized with plain unreinforced masonry and were mortared along all edges to the confining steel elements. Specimen WE3 was constituted by a dry-stack unreinforced masonry panel. Specimen WE1 was reinforced with trust type joint reinforcement at alternate courses. Specimens WE6 and WE7 were unreinforced and reinforced, respectively, infills provided with a 20 mm gap between the upper edge and the upper beam of the steel frame (i.e., they were 3E infills). Specimen WE9 was a plain masonry panel provided with a central opening. The mechanical properties provided for the specimens are reported in Table 2.5. Note that the f_{mv} and E_{mv} values are provided in detail by Flanagan and Bennett (1999b) while the average value of f_{mh} and E_{mh}, equal for all specimens, is provided by Dawe and Seah.

Table 2.5. Mechanical properties for the specimens by Dawe and Seah (1989).

specimen	f_{mv} [N/mm^2]	E_{mv} [N/mm^2]	f_{mh} [N/mm^2]	E_{mh} [N/mm^2]
WE1	3.1	24600	18.4	17400
WE2	28.1	23000	18.4	17400
WE3	24.3	17575	18.4	17400
WE4	22.7	13800	18.4	17400
WE5	20.2	15600	18.4	17400
WE6	22.3	17200	18.4	17400
WE7	23.0	16100	18.4	17400
WE8	27.4	16200	18.4	17400
WE9	24.3	17575	18.4	17400

A uniform pressure normal to the panel surface was applied gradually in increments of 0.2 kPa prior to first cracking and 0.4 kPa thereafter. At the end of each load increment, the pressure was maintained at a constant level to allow the system to stabilize before deflection readings were taken. The tests were interrupted, presumably, when each specimen attained an extreme damage condition preventing the prosecution of the test itself. Combined IP/OOP tests were not performed.

It was observed that, after cracking, the lateral strength of infill is granted by arching

action, whose effectiveness did not result influenced by the presence of the opening. They also observed that the out-of-plane strength increases with the square of the panel thickness and reduces as its width and height increase.

In general, the study was dedicated to the influence of the boundary conditions at edges on the pure OOP response of infills. It was observed that the presence of gaps or the panel slippage at edge could influence the cracking pattern and the deformed shape exhibited by the infill: according to Dawe and Seah's response model, this circumstance has a great influence on the OOP stiffness and strength exhibited by infills. In addition, the presence of a gap can prevent the formation of arching action in a specific direction, provided that the infill deformation during loading does not make the infill itself come in contact with the confining structural element despite the initial gap. In this case, arching action does not occur at the initial loading steps, but can form successively. All the above considerations are summarized in Figure 2.3. Note that, e.g.., WE2 specimen, which was bounded along four edges, exhibited an OOP strength 1.8 times higher than WE6 specimen, which was bounded along three edges.

. A summary of the tests' results is reported in Table 2.6.
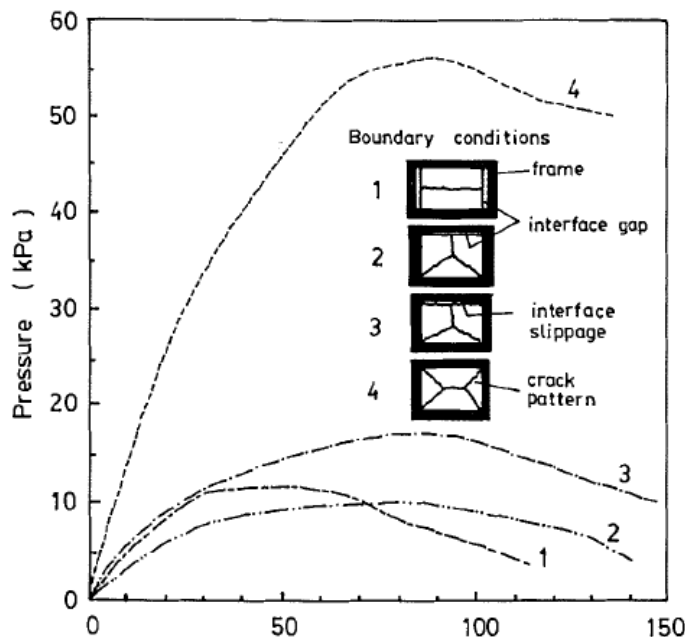
Figure 2.3. Effect of boundary conditions at the edges of infills on their deformed shape and OOP response. Adapted from Dawe and Seah (1989).

Table 2.6. Summary of tests' results by Dawe and Seah (1989).

specimen	F_{crack} [kN]	d_{crack} [mm]	K_{crack} [kN/mm]	F_{max} [kN]	d_{max} [mm]	K_{max} [kN/mm]	d_{end} [mm]
WE1	26.2	-	-	225	-	-	-
WE2	38.3	-	-	194	-	-	-
WE3	-	-	-	78.6	-	-	-
WE4	24.2	-	-	113	-	-	-
WE5	22.2	-	-	78.6	-	-	-
WE6	52.4	-	-	107	-	-	-
WE7	68.5	6.2	11.1	148	70.0	2.1	110
WE8	48.4	-	-	135	-	-	-
WE9	32.3	-	-	175	-	-	-

2.3.2. Angel et al., 1994

Eight one-half scaled RC infilled frames were tested. The infill specimens were 1625 mm high and 2440 mm wide, with aspect ratio equal to 1.5. Except for one specimen, the columns were subjected to an axial load simulating the presence of upper storeys. The infills were made of clay bricks placed with horizontal holes (specimens 1, 2, 3, 6, 7 and 8) or concrete masonry units (CMU, shown in Figure 2.4, specimens 4 and 5). Half-wythe (specimens 1, 2 and 3), single-wythe (specimens 4, 6 and 7) and double-wythe (specimens 5 and 8) panels were tested: their thickness ranged from 48 mm (specimens 1, 2, 3) to 190 mm (specimens 5 and 8) while their vertical slenderness varied between 9 and 34. The bed joints were realized with various (N, S or lime) types of cementitious mortar. Some specimens (2, 3 and 6) were repaired after the out-of-plane test and then tested again under lateral actions. A summary of masonry mechanical properties provided by the authors is reported in Table 2.7.

Figure 2.4. Concrete Masonry Unit (CMU).

Table 2.7. Mechanical properties for the specimens by Angel et al. (1994).

specimen	f_{mv} [N/mm^2]	E_{mv} [N/mm^2]	f_{mh} [N/mm^2]	E_{mh} [N/mm^2]
1	11.6	7848	-	-
2b	10.9	8046	-	-
2c	10.9	8046	-	-
3b	10.1	5212	-	-
3c	10.1	5212	-	-
4b	22.9	12438	-	-
5b	21.5	11625	-	-
5d	21.5	11625	-	-
6b	4.6	2137	-	-
6b2	4.6	2137	-	-
6c	4.6	2137	-	-
6d	4.6	2137	-	-
6t	4.6	2137	-	-
7b	11.0	2923	-	-
8b	3.5	2358	-	-

Specimen 1 was tested under pure OOP load. For all the other specimens, a preliminary in-plane test was carried out. Specimens were subjected to a cyclic in-plane load until the attainment of a maximum displacement equal to two times the displacement at first cracking Δ_{cr}; then, each infill was in-plane unloaded and the panel was tested with a monotonically increasing out-of-plane uniformly distributed pressure until the attainment of an out-of-plane displacement to infill height ratio equal to 3%. Actually, for specimens 4b, 5b, 5d, 7c, 7b and 8b, the out-of-plane strength was higher than the lateral load that the actuator could apply: in these cases, a lower bound of the lateral strength and displacement capacity is obtained as a result of the test. Specimens 2, 3 and 6 were repaired after the out-of-plane test with a 12 mm thick plaster layer reinforced with a wire mesh. Specimens 5 and 6 were tested out-of-plane at a fixed in-plane displacement equal to two times the displacement at first cracking, that is, in presence of an in-plane load equal to 1.5 times the in-plane force at first cracking.

This experimental program allowed validating the out-of-plane strength predicted at various IDRs by the analytical relationship proposed by Angel et al.. Note that, for what concerns the pure OOP behaviour, Angel et al.'s strength model is defined for 2E infills; however, the horizontal slenderness of the specimens tested only under pure OOP load,

specimen 1, was significantly high, being equal to around 51, and then, most likely, the authors assumed that arching action in that direction cannot occur.

With reference to URM infills made with solid clay bricks, test specimen 1 was tested under pure OOP loading and exhibited an OOP strength equal to 31.3 kN and a final cracking pattern defined by diagonal cracks developing at the interface between mortar and bricks. Test specimens 2b and 3b, equal to the reference specimen for geometric and nominal mechanical properties, were IP tested with the application of an IP drift equal to 0.34% and 0.22%, respectively. Both of them showed noticeable horizontal cracks between mortar joints and bricks at the end of the IP test. Specimens 2b and 3b attained an OOP strength equal to 15.9 and 23.7 kN, respectively. Also in this case, OOP loading produced noticeable diagonal cracking developing at the interface between mortar and bricks. Some observations about the effectiveness of the repairing method applied are also discussed.

A summary of the tests' results is reported in Table 2.8.

Table 2.8. Summary of tests' results by Angel et al. (1994).

specimen	F_{crack} [kN]	d_{crack} [mm]	K_{crack} [kN/mm]	F_{max} [kN]	d_{max} [mm]	K_{max} [kN/mm]	d_{end} [mm]
1	17.1	3.3	5.2	31.3	16.0	2.0	48.0
2b	7.5	7.2	1.0	15.9	16.0	1.0	48.0
2c	37.9	1.6	23.7	79.2	26.0	3.0	48.0
3b	12.7	7.9	1.6	23.7	23.0	1.0	48.0
3c	52.3	1.4	37.3	83.0	18.0	4.6	48.0
4b	118	6.7	17.6	118	7.0	16.9	-
5b	129	1.7	75.9	129	1.7	75.9	-
5d	128	1.2	107	128	1.5	85.4	-
6b	28.9	8.4	3.4	49.2	32.0	1.5	52.0
6b2	-	-	-	42.0	52.0	0.8	-
6c	121	-	-	122	1.7	71.9	-
6d	-	-	-	36.8	56.0	0.7	-
6t	-	-	-	121	-	-	-
7b	127	8.2	15.4	122	8.0	15.2	-
8b	128	7.3	17.5	127	8.0	15.9	-

2.3.3. Flanagan and Bennett, 1999

Real scale steel frames infilled with square panels made of structural clay tiles were tested. The units had horizontal cores and were jointed with type N cementitious mortar; bed joints were 19 mm thick. The infill panels were 2240 mm high and wide. During the experimental campaign, single wythe and double wythe infills were tested; their thickness was 100 (specimen 25), 200 (specimen 2, 11, 13, 18, 19, 20 and 23) or 330 mm (specimen 22) and their slenderness ranged from 6.8 to 22.4. The double-wythe specimen 22 was realized with no plaster between layers. Moreover, the structural frames were realized by using two types of beam and column cross section. A summary of masonry mechanical properties provided by the authors in Flanagan and Bennett (1999b) is reported in Table 2.9.

Table 2.9. Mechanical properties for the specimens by Flanagan and Bennett (1999).

specimen	f_{mv} [N/mm^2]	E_{mv} [N/mm^2]	f_{mh} [N/mm^2]	E_{mh} [N/mm^2]
18	5.59	5300	3.01	2160
19	5.59	5300	3.01	2160
20	5.59	5300	3.01	2160
22	2.29	5040	-	-
23	5.59	5300	3.01	2160
25	5.59	5300	3.01	2160

Some pure in-plane (specimen 2) and out-of-plane tests (specimens 18, 22, 25) were performed in order to estimate the infills capacity under unidirectional load. The OOP tests were carried out by applying a uniformly distributed pressure with load-unload cycles. The test on specimen 19 was carried out first by applying a cyclic in-plane displacement history and then, after in-plane unloading, by applying a monotonically increasing out-of-plane pressure. Some infills were subjected first to a load-unload out-of-plane cycles, with the actuator acting on the top of the specimen or to load-unload out of plane cycles first applied at half-height of the specimen, then to its top edge, and then to a cyclic in-plane load (specimens 11, 13 and 20). Moreover, one test was carried out first by applying a cyclic in-plane load and then, at a fixed and kept constant value of in-plane displacement, a cyclic uniformly distributed out-of-plane pressure and so on (specimen 23, whose state at the end of the test is shown in Figure 2.5). It is worth to mention that this test is the only one presented in the literature allowing the evaluation

of the IP force reduction due to OOP damage given by OOP actions applied on the entire infill wall.
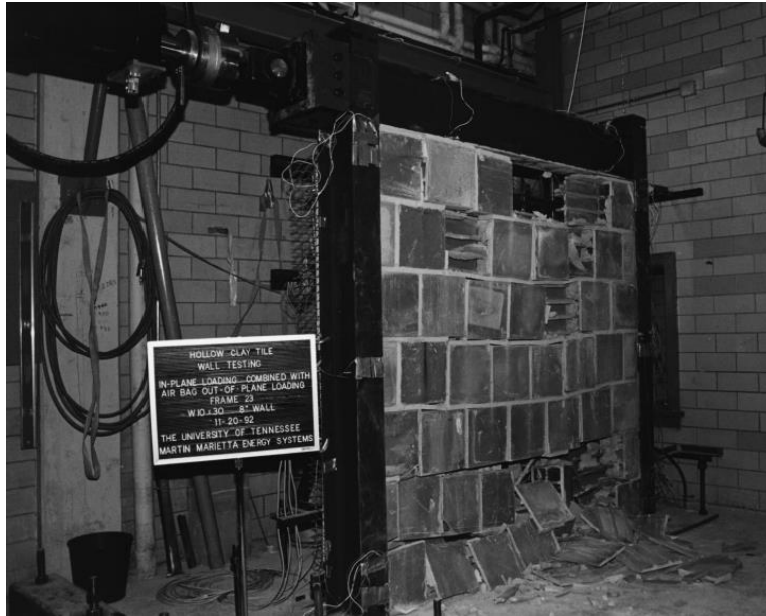
Figure 2.5. State of specimen 23 by Flanagan and Bennett at the end of the test.

The in-plane/out-of-plane interaction seems to be negligible for specimens 18, 22 and 25 which were 200 mm and 330 mm thick and had a slenderness ratio ranging from 6.8 to 11.2. However, Shing and Mehrabi (2002) pointed out that this result was probably due to the small slenderness of the specimens: in this case, the arching action in the panel thickness is so robust that in-plane damage cannot deteriorate it, unless very high drift demands are applied. The main effect of the in-plane damage previous to lateral loading is the out-of-plane stiffness reduction, therefore the out-of-plane displacements are greater for damaged panels than for undamaged infills. To be more specific, specimen 18 exhibited an OOP strength equal to 133.5 kN, while its "twin" specimen 19, IP-damaged up to a drift equal to 0.85%, exhibited a reduced strength equal to 108.9 kN. Actually, specimen 23, which was nominally equal to specimen 18, was IP-damaged up to a drift equal to 0.20% and exhibited a strength equal to 75.4 kN, which is quite unexpected and difficultly explainable with other reason than experimental variability.

Prior out-of-plane damaging can modify the in-plane collapse mechanism by preventing diagonal cracking and promoting corner crushing. An in-plane action about 80% of the correspondent capacity leads to a 20% out-of-plane strength reduction; on the contrary, a lateral action about 75% of out-of-plane strength do not determine a significant reduction of capacity against in plane actions.

A summary of tests' results is reported in Table 2.10.

Table 2.10. Summary of tests' results by Flanagan and Bennett (1999a).

specimen	F_{crack} [kN]	d_{crack} [mm]	K_{crack} [kN/mm]	F_{max} [kN]	d_{max} [mm]	K_{max} [kN/mm]	d_{end} [mm]
18	40.6	1.2	33.9	133	11.5	11.6	38.0
19	7.5	1.6	4.7	109	19.3	5.6	56.0
20	-	-	-	104	10.9	9.5	-
22	85.3	1.2	71.1	198	49.5	4.0	71.0
23	-	-	-	76.8	10.0	7.7	-
25	-	-	-	40.6	25.3	1.6	94.0

2.3.4. Calvi and Bolognini, 2001

Real scale RC infilled frames designed by applying the capacity design rules and dispositions provided by Eurocode 8 were tested. Infill wall panels were made of clay bricks with horizontal cores; they were 2750 mm high, 4200 mm wide, hence with aspect ratio equal to 1.53, 115 mm thick and vertical slenderness ratio equal to 20.4. Two plaster layers, each of which with 10 mm thickness, were applied to the specimens' surface. Brick units were jointed through a cementitious mortar.

The specimens differed mainly for the possible presence and typology of reinforcement. Specimens 2, 6 and 10 were non-reinforced. Specimen 10 was tested under pure OOP load, while specimens 2 and 6 were first IP cyclically loaded up to drift levels equal to 1.20 and 0.40%, respectively; then, they were subjected to OOP loading. Specimens 3 and 7 were reinforced with steel bars embedded in the horizontal mortar layers; specimen 3 was tested under pure OOP load, while specimen 7 was first IP cyclically tested up to 0.40% drift and then OOP tested. Specimens 4, 8 and 11 were reinforced with Murfor reinforcing system, shown in Figure 2.6, which consists in two parallel wires welded together with a continuous truss wire embedded in bed joints. A summary of the average masonry mechanical properties provided by the authors is reported in Table 2.11.

Figure 2.6. Murfor reinforcing system. Picture from: www.ilnuovocantiere.it.

Table 2.11. Mechanical properties for the specimens by Calvi and Bolognini (2001).

specimen	f_{mv} [N/mm^2]	E_{mv} [N/mm^2]	f_{mh} [N/mm^2]	E_{mh} [N/mm^2]
All	1.10	1873	1.11	991

More specifically, specimen 11 was tested under pure OOP load; specimens 4 and 8 were first IP tested, both up to a drift equal to 0.40%, and then OOP tested. Specimens 5 and 9 were reinforced with a wire mesh embedded in the external plaster layer. Both tests were aimed at investigating the IP/OOP interaction effects. The IP tests were carried out up to a drift level equal to 1.20% and 0.40%, respectively. All out-of-plane tests were performed by means of a monotonic increasing load applied on 4 points placed on the infills' diagonals at one-third of the diagonal length. During tests, an axial load was applied on the top of the columns.

The tests were mainly aimed at assessing the IP/OOP interaction effects and the influence on them of various reinforcement types. Focusing on URM infills' performance, the IP-undamaged test specimen 10 exhibited a resistance equal to 33.7 kN, while specimens 6 and 2, IP-damaged up to 0.40% and 1.20% drifts, respectively, exhibited an OOP strength equal to 9 kN and 6 kN, respectively. The authors observed that the external reinforcement was considerably more efficient than internal reinforcement, both in terms of undamaged strength and OOP strength degradation due to previous IP damaging limitation.

A summary of the tests' results is reported in Table 2.12.

Table 2.12. Summary of tests' results by Calvi and Bolognini (2001).

specimen	F_{crack} [kN]	d_{crack} [mm]	K_{crack} [kN/mm]	F_{max} [kN]	d_{max} [mm]	K_{max} [kN/mm]	d_{end} [mm]
2	-	-	-	6.0	-	-	-
4	-	-	-	17.2	-	-	53.0
5	-	-	-	21.4	-	-	22.0
6	6.5	10.0	0.7	9.0	18.4	0.5	37.0
7	-	-	-	19.7	16.1	1.2	44.0
8	8.2	5.5	1.5	17.5	18.4	1.0	48.0
9	32.0	4.0	8.0	46.6	25.7	1.8	28.0
10	29.0	2.4	12.1	33.7	5.2	6.5	13.0
11	29.0	2.4	12.1	36.8	11.2	3.3	46.0

2.3.5. Varela-Rivera et al., 2012

Six full scale RC infilled frames were tested. Note that, differently from all other experimental programs, in this case the infills were built prior than the RC frame. The RC frame itself was restrained at its base to the floor of the laboratory in different ways. More specifically, specimens E-2, E-3, E-5 and E-6 were attached to the laboratory strong floors by means of rollers along the entire length of the RC frame lower beam. On the other hand, specimens E-1 and E-4 were not attached to the laboratory floor but simply connected to it through a fixed support place at the mid-length of the RC frame lower beam. The least technique was used to significantly reduce the IP stiffness of the infilled frame system.

For what concerns infill walls, they were realized with concrete hollow bricks with vertical holes and horizontal and vertical mortar joints Specimens E-1, E-2 and E-3 were roughly 3700 mm high and 2800 mm wide, with aspect ratio roughly equal to 1.33; specimens E-4, E-5 and E-6 were roughly 2900 mm high and 2700 mm high, with aspect ratio roughly equal to 1.1. Specimens E-1, E-2, E-4 and E-5 were 150 mm thick, with vertical slenderness ratio roughly equal to 19; specimens E-3 and E-6 were 120 mm thick, with vertical slenderness ratio roughly equal to 23. Also the confining structural elements' cross-section varied among different specimens; however, note that they were usually small, with one dimension equal to the infill thickness (120 or 150 mm) and the other dimension typically equal to 200 or 250 mm. In other words, such elements were characterized by a significant flexural deformability. A summary of masonry mechanical properties provided by the authors is reported in Table 2.13.

Table 2.13. Mechanical properties for the specimens by Varela-Rivera et al. (2012).

specimen	f_{mv} [N/mm^2]	E_{mv} [N/mm^2]	f_{mh} [N/mm^2]	E_{mh} [N/mm^2]
E-1	2.84	-	-	-
E-2	2.84	-	-	-
E-3	2.45	-	-	-
E-4	2.84	-	-	-
E-5	2.84	-	-	-
E-6	2.45	-	-	-

Only pure OOP tests were performed. All specimens were tested under uniformly distributed load applied on a surface centered with respect to the infill and provided with length equal to 3.00 m and height equal to 2.40 m. A picture of the specimens at the end of tests is reported in Figure 2.7.

The experimental program main aim was investigating, at fixed infill aspect ratio and vertical slenderness ratio, the effect of the frame deformability on the OOP response of the infills, especially in terms of strength, damage and collapse mechanism. This circumstance will be recalled in the next Chapter, dedicated to the application of currently available strength and response models on these and other specimens. Actually, the authors observed that the OOP strength of infills with equal slenderness ratio and aspect ratio was lower when they were enclosed in more deformable RC frames. This is consistent with Dawe and Seah's findings.

A summary of the tests' results is reported in Table 2.14.

Table 2.14. Summary of tests' results by Varela-Rivera et al. (2012).

specimen	F_{crack} [kN]	d_{crack} [mm]	K_{crack} [kN/mm]	F_{max} [kN]	d_{max} [mm]	K_{max} [kN/mm]	d_{end} [mm]
E-1	-	-	-	63.1	38.6	1.6	38.6
E-2	-	-	-	93.4	36.0	2.6	36.0
E-3	-	-	-	86.4	38.6	2.2	38.6
E-4	-	-	-	105	25.2	4.2	26.3
E-5	-	-	-	130	12.2	10.6	20.0
E-6	-	-	-	111	15.1	7.4	25.2

Wall specimen E-1

Wall specimen E-2

Wall specimen E-3

Wall specimen E-4

Wall specimen E-5

Wall specimen E-6
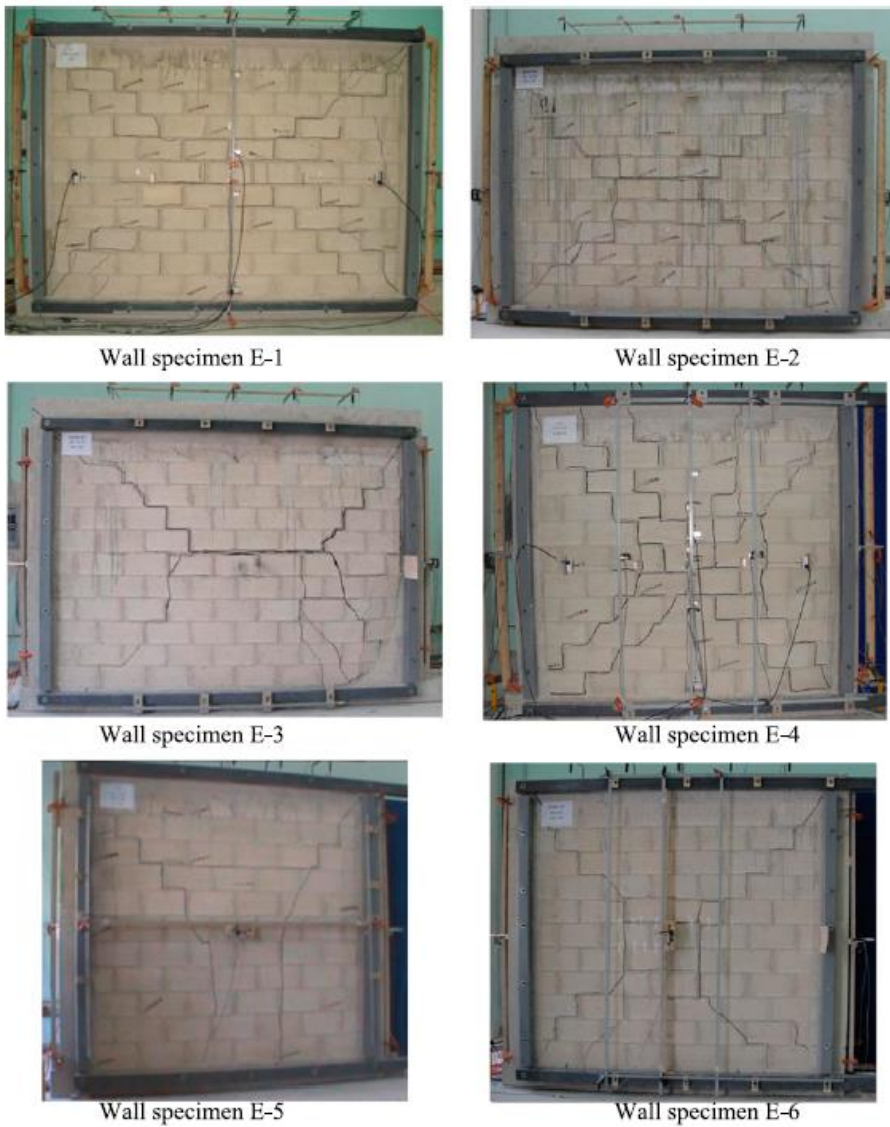
Figure 2.7. Specimens' state at the end of the OOP tests by Varela-Rivera et al. (2012).

2.3.6. Guidi et al., 2013

Full scale RC frames infilled with single-wythe infills were tested. The specimens were 2650 mm high, 4150 mm wide (hence, with aspect ratio equal to 1.57); they were realized with clay hollow bricks type POROTON P69TA jointed with a 10 mm thick horizontal layer of cementitious mortar. No vertical mortar was used, given that each brick unit can slot in the one that stands beside it. The frame was designed as if it was part of a three-storeys building designed in accordance to 2008 Italian technical code and by applying capacity design; even the infill wall panel was designed in accordance to modern technical codes provisions and taking into account the IP and OOP actions as will be explained in Chapter V, dedicated to current code provisions for the OOP safety check of infills.

Thick and thin infills were tested. The first ones were 300 mm thick (i.e., with vertical slenderness equal to 8.8) and were distinguished in unreinforced masonry infills (URM) and reinforced masonry infills (RM). The RM specimens were reinforced with vertical and horizontal reinforcing bars, as shown in Figure 2.8.
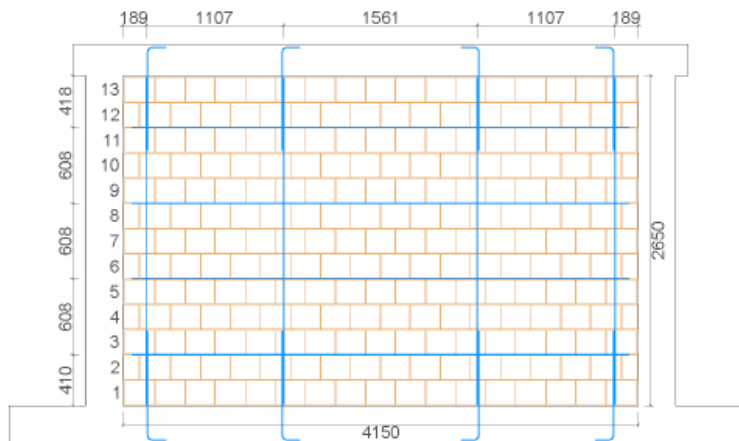
Figure 2.8. Reinforcement layout used for thick infills by Guidi et al. (2013). Adapted from Guidi et al. (2013).

As already stated, also thin infills were tested. They were 120 mm thick (i.e., with vertical slenderness ratio equal to 22.1). In addition, they were provided of a 15 mm thick layer of external plaster and were distinguished in unstrengthened (USM) and strengthened (SM), the least provided with a quadriaxial fiberglass embedded in an 8

mm-thick additional plaster layer.

A summary of the average masonry mechanical properties provided by the authors is reported in Table 2.15.

Table 2.15. Mechanical properties for the specimens by Guidi et al. (2013).

specimen	f_{mv} [N/mm^2]	E_{mv} [N/mm^2]	f_{mh} [N/mm^2]	E_{mh} [N/mm^2]
All	6.00	4384	1.19	1767

First, a cyclic displacement history is applied in the in-plane direction: it consists in sinusoidal cycles with increasing amplitude and three times repeated peaks for each displacement amplitude. After the in-plane loading and unloading, the infill wall was loaded out-of-plane through a monotonic increasing lateral force applied by means of four loading points placed along the infill diagonals, each one at one-third of the diagonal length. All tests were performed with an axial load applied on columns. Two in-plane maximum drift levels were established prior to out-of-plane tests: "D", corresponding to the attainment of Damage Limitation Limit State (IDR=0.50%) according to the Italian building code for bare RC frames, and "U", corresponding, according to the authors, to the Ultimate Limit State (IDR=1.2%). Unfortunately, no OOP test on an IP-undamaged reference specimen was performed. The main aim of the experimental program was the assessment of the effectiveness of the strengthening and reinforcing techniques tested at various drift levels.

According to the authors, thick panels' strength was mainly due to vertical arching while thin panels exhibited a flexural mechanism parallel to bed joints: for these reasons, the first ones took advantage of a greater lateral strength.

The reinforcing and strengthening techniques turned out effective to prevent the OOP partial or global expulsion and to grant damage distribution. Reinforced thick panels were stronger than the unreinforced ones at different drift levels (+32% at ultimate limit state, +14% at damage limit state); moreover, they exhibited a smaller strength reduction in passing from damage to ultimate limit state (reinforced: -6%, unreinforced, -23%). Similar observations can be extended also to USM and SM panels and for the OOP stiffness of infills. Moreover, it was observed that, with a prior in-plane maximum attained drift equal to 1.2%, the displacement correspondent to a 20% strength degradation is greater than the one registered for unstrengthened panels.

A summary of tests' results is reported in Table 2.16.

Table 2.16. Summary of tests' results by Guidi et al. (2013).

	F_{crack}	d_{crack}	K_{crack}	F_{max}	d_{max}	K_{max}	d_{end}
specimen	[kN]	[mm]	[kN/mm]	[kN]	[mm]	[kN/mm]	[mm]
URM-D	201	15.0	13.4	201	15.0	13.4	29.9
URM-U	159	19.4	8.2	159	19.4	8.2	48.2
RM-D	272	20.4	13.3	272	20.4	13.3	28.2
RM-U	195	18.2	10.7	195	18.2	10.7	38.0
USM-U	10.0	20.3	0.5	10.0	20.3	0.5	73.5
SM-U	15.0	24.9	0.6	15.0	24.9	0.6	99.6

2.3.7. Hak et al., 2014

Five full scale single-wythe panels made of clay hollow bricks with vertical holes and class M5 cementitious mortar were used as test specimens. Each infill wall was realized in an RC frame. Each specimen was 2950 mm high and 350 mm thick, with vertical slenderness ratio equal to 8.4. Specimen TA5, a masonry stripe spanning from the upper beam to the foundation beam of the RC frame has been already described in the previous section. Four other specimens were tested. Specimen TA1, TA2 and TA3 were fully infilled, while specimen TA4 was partially infilled, as it was realized with a central opening spanning along the entire height of the RC frame. Focusing on the fully infilled specimens, they were 4220 mm wide, with aspect ratio equal to 1.43.

Only combined IP and OOP tests were performed. Specimens TA1, TA2 and TA3 were first cyclically tested in the IP direction up to three different drift levels equal to 1.50%, 2.50% and 1.00%, respectively. Then, the specimens were tested by applying load-unload OOP cycles. The OOP load was applied by means of 16 loading points aligned in two horizontal rows at the center of the infill wall. All OOP tests were interrupted at the attainment of an infill central displacement equal to 75 mm. The average mechanical properties provided for all specimens are reported in Table 2.17.

Table 2.17. Mechanical properties of the specimens by Hak et al. (2014).

	f_{mv}	E_{mv}	f_{mh}	E_{mh}
specimen	[N/mm^2]	[N/mm^2]	[N/mm^2]	[N/mm^2]
All	4.64	5299	1.08	494

The experimental program was aimed at the assessment of the IP/OOP interaction effects on very thick and robust infills. The damage state of the specimens at the end of

the IP tests is sketched. In addition, a detailed description of damage propagation in the infill wall during OOP load-unload cycles is provided. It is observed that infills TA1 and TA3 a similar damage state, manly visible at the upper corners of the specimens, at the end of the IP tests. Hence, it is not surprising that they exhibit a very similar OOP strength. More specifically, specimen TA3 exhibited a strength slightly higher than that observed for specimen TA1 (168.5 kN versus 163.9 kN), even if the IP drift attained by specimen TA3 was lower. This is due, most likely, to experimental variability. On the other hand, the OOP stiffness of specimen TA1 is lower than that of specimen TA3, as expected. Specimen TA2 strength and stiffness is significantly lower than those shown by specimens TA1 and TA3, being specimen TA2 IP tested up to the maximum IP drift. More specifically, the OOP strength of specimen TA2 was equal to 102.7 kN, with a 37% reduction with respect to specimen TA1. A picture of specimen TA2 at the end of the test is reported in Figure 2.9.

Figure 2.9. State of specimen TA5 at the end of the OOP test by Hak et al. (2014).

It should be noted that, even at very high previously imposed IP drift and at very high OOP displacement demand, the thick and robust specimens tested by Hak et al. exhibit an excellent OOP response, both in terms of strength and in terms of observed damage state, which seems to be quite controlled.

A summary of tests' results on the fully infilled specimens is reported in Table 2.18.

Table 2.18. Summary of tests' results by Hak et al. (2014).

specimen	F_{crack} [kN]	d_{crack} [mm]	K_{crack} [kN/mm]	F_{max} [kN]	d_{max} [mm]	K_{max} [kN/mm]	d_{end} [mm]
TA1	-	-	-	168.5	60.0	2.8	82.0
TA2	-	-	-	102.7	70.0	1.5	90.0
TA3	-	-	-	163.9	28.0	5.9	78.0

2.3.8. Furtado et al., 2016

Three full-scale RC infilled frames were tested. The infills were 2300 mm high, 4200 mm wide (i.e., with aspect ratio equal to 1.83); they were realized with clay hollow bricks with horizontal cores. All specimens were constituted by a 150 mm thick single-wythe layer, with vertical slenderness ratio equal to 15.3. Only during the IP test, for Inf_03 panel, an internal 110 mm thick leaf (with vertical slenderness equal to 20.9) was added by leaving a hollow with thickness equal to 40 mm. The average mechanical properties provided for all specimens are reported in Table 2.19.

Table 2.19. Mechanical properties of the specimens by Furtado et al. (2016).

specimen	f_{mv} [N/mm^2]	E_{mv} [N/mm^2]	f_{mh} [N/mm^2]	E_{mh} [N/mm^2]
All	0.53	1418	-	-

All the OOP tests were performed by means of air-bags. With an axial load equal to 300 kN applied on columns, Inf_01 specimen was subjected to an out-of-plane monotonic increasing displacement up to the end of the test, which was interrupted at the incipient collapse for overturning of the infill. Without axial load on columns (such as for Inf_03), Inf_02 was subjected to a sequence of three load-unload cycles characterized by the same maximum lateral displacement target, which ranged from 2.5 to 70 mm. The same cyclic out-of-plane displacement path was applied to Inf_03, which had been previously cyclically loaded in-plane up to the attainment of a 0.5% IDR; moreover, the in-plane test was performed in presence of the above mentioned internal leaf, which was removed prior to out-of-plane testing.

First, it was observed that the OOP response of specimens Inf_01 and Inf_02 was similar, despite the different OOP loading path and the presence of axial load on the

columns of specimen Inf_01. More specifically, the two specimens exhibited a very similar OOP strength equal to 75 kN and 70 kN, respectively. A picture of the specimens at the end of tests is reported in Figure 2.10.
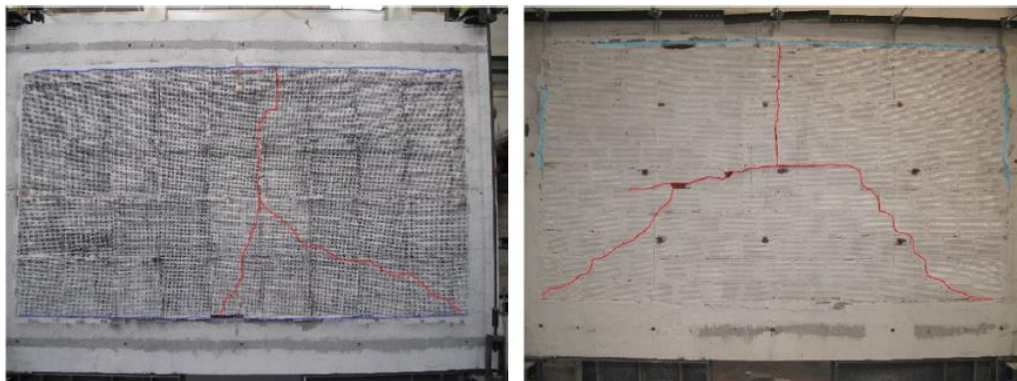
Figure 2.10. IP-undamaged Inf_01 (left) and Inf_02 (right) specimens by Furtado et al. (2016) at the end of tests.

For what concerns the effects of the IP/OOP interaction, it was observed that the lateral strength of the IP-damaged panel was four times smaller than the one registered for undamaged panels. The undamaged panel exhibited a softening branch in the force-displacement relationship that was absent in the one obtained for the previously damaged panel: this is due to the rigid-body mechanism observed for the second one, whose testing was interrupted at the onset of the OOP collapse for overturning, as shown in Figure 2.11. In addition, first cracking occurred at the same OOP drift (0.1%) for both undamaged and damaged panels, but in the first case the correspondent load was about 50 kN (similar for both Inf_01 and Inf_02), while in the second case it was about 18 kN.

Figure 2.11. IP-damaged specimen Inf_03 by Furtado et al. (2016) at the end of test.

No significant effect of axial load on columns was observed in terms of OOP strength. However, through further tests carried out by Furtado et al. (2018a) it was observed that the presence of axial load can influence the OOP cracking pattern, while it can have contradictory effects on infills' initial stiffness, as Angel et al. observe its increase in presence of axial load while Furtado et al. (2018b) observe its decrease in presence of axial load.

A summary of tests' results is reported in Table 2.20.

Table 2.20. Summary of tests' results by Furtado et al. (2016).

specimen	F_{crack} [kN]	d_{crack} [mm]	K_{crack} [kN/mm]	F_{max} [kN]	d_{max} [mm]	K_{max} [kN/mm]	d_{end} [mm]
Inf_01	50.0	2.3	21.7	75.0	21.0	3.6	70.0
Inf_02	50.0	2.3	21.7	69.0	13.0	5.3	53.0
Inf_03	18.0	2.3	7.8	18.0	13.0	1.4	37.0

2.4 OTHER EXPERIMENTAL PROGRAMS

In this subsection, other significant experimental programs presented in the literature are described. For reasons that will be explicitly explained for each of them, they will be neither included in the experimental database used in Chapter IV for the assessment of the existing literature models/formulations nor used for the proposal of new formulations/modelling approaches.

The tests herein presented are those by Beconcini (1997) on 2E masonry stripes, and those by Griffith and Vaculik (2007) and by Pereira et al. (2011) on 4E infills.

2.4.1. Beconcini, 1997

Single-wythe panels made of clay hollow bricks were built between the ceiling and the floor of the laboratory and used as test specimens. Each specimen was 1000 mm wide. 33 infills were tested. They differed in their height (2800 mm – aspect ratio w/h equal to 0.36 – or 3500 mm – aspect ratio w/h equal to 0.29) and thickness (80 or 120 mm, slenderness ratio h/t ranging from 23.3 to 43.7), as well as for unit dimensions, cores and bed joints direction and for the possible presence of a 10 mm thick plaster on the wall surface. Unfortunately, the information concerning masonry mechanical properties is very poor. The author only state that for specimens 3, 5, 6, 18 and 19 masonry mean compressive strength, presumably perpendicular to bricks' holes, is 0.69 N/mm^2. For this reason, such test will be not included in the database.

28 days after their construction, the panels were tested by applying a monotonically increasing OOP load at 1250 mm height from the floor. Such load was distributed along a horizontal line through an horizontal steel beam.

The author reports the out-of-plane behaviour diagrams for all specimens up to the attainment of the peak load, at which the test was interrupted due to the specimen collapse. The state of some specimens at the end of the tests is shown in Figure 2.12.

In general, first cracking appears in correspondence to a bed joint and arises due to mortar detachment from bricks. In absence of vertical joints, cracking load is around one half of the cracking load of panels provided of them, while their presence do not affect the value of peak load, given that the panel always arches in the vertical direction. Cracking load was greater for panels made of bricks with vertical cores: in fact, according to the authors, in this case the interlocking effect due to mortar into the cores delayed cracks' opening.

For panels characterized by the same thickness, the dimensions of brick units did

not affect ultimate load, which was influenced by cores direction instead. More specifically, brick units with vertical cores made panels stronger with respect to lateral actions, as well as plaster on the panel surface did.

Figure 2.12. Some specimens by Beconcini (1997) after tests.

2.4.2. Griffith and Vaculik, 2007

Full scale single-wythe panels made of clay hollow bricks with horizontal holes were used as test specimens. Each infill wall was 2500 mm high and 110 mm thick, i.e., provided with vertical slenderness ratio equal to 22.7. The units were jointed by 10 mm thick cementitious mortar layers. The infills were not realized in a real and "ordinary" structural frame, but they were restrained at edges by steel elements, as shown in Figure 2.13.

Figure 2.13. Experimental setup by Griffith and Vaculik (2007).

All panels were clamped on vertical edges and simply supported at the inferior edge. Specimens 1 to 6 were 4000 mm wide, with aspect ratio equal to 1.60, while specimens 7 and 8 were 2500 mm wide, i.e., with unit aspect ratio. The specimens differed also for the boundary condition on the superior edge (free for specimen 6, simply supported for all the other specimens;, for the possible presence (for all specimens except for specimen 6) of a vertical compressive stress σ_v that ranged from 0 to 0.10 N/mm^2; for the possible presence of an opening (specimens 3 to 8), as well as for its position in the infill panel (central for specimens 7 and 8, non-central in all the other cases). Combined IP/OOP tests were not performed. A uniformly distributed monotonically increasing load was applied to the specimens through an air-bag system. When the specimen was significantly damaged, the panel was unloaded and the test was interrupted.

The great number of variables introduced in this experimental study do not allow the comparison between the OOP response of equal plain and solid URM infill with different boundary conditions at edges. For this reason, these test do not enter the experimental database.

However, it is of great interest the fact that an plastic behavior after peak load was observed and registered during tests for all specimens. According to Lawrence (1986), this is due to the presence of constraints against rotation active on the vertical panel edges. In fact, it seems that this circumstance allows the redistribution of bending moment along diagonal cracks towards vertical edges in the post-peak response. Assuming, as advised by Willis et al. (2004) and Griffith et al. (2005), an elastic-brittle moment-rotation relationship for the "plastic hinges" represented by cracks, the panel is

preserved from brittle failure at peak load mainly due to this redistribution phenomenon. Such redistribution cannot occur for da Porto et al.'s and Beconcini's specimens, which are not restrained on lateral edges: hence, they collapse at peak load. However, it will be shown in the next Chapters that the redistribution allowing a post-peak displacement capacity for URM infills is not only depending on the boundary conditions, but also to masonry own stress-strain response, which is usually brittle in compression perpendicular to holes, somehow ductile in compression parallel to bricks' holes.

The pre-stressed specimen exhibited a greater stiffness and strength than the others, as well as a smaller elastic recovery at unloading. The energy dissipation capacity was significant and not negligible.

2.4.3. Pereira et al., 2011

RC infilled frames designed in accordance to Eurocode 2 (2004) and Eurocode 8 (2004) and 2:3 scaled were tested. The specimens were made with clay hollow bricks with horizontal cores; they were 1700 mm high, 3500 mm wide (aspect ratio equal to 2.06), and 150 mm thick (vertical slenderness ratio equal to 11.3). An M5 class cementitious mortar was used to joint brick units.

This experimental program is similar to the one performed by Calvi and Bolognini (2001). Namely, it was mainly aimed at assessing the beneficial effects of two types of reinforcement on the OOP response of IP-damaged infills. In fact, specimens differed mainly for the possible presence and typology of reinforcement: an unreinforced panel (REF specimen) was tested, as well as two infills reinforced with a couple of bars embedded in bed joints (JAR specimen), and two infills reinforced with Murfor system (RAR specimen). Moreover, REF panel lacked of an external plaster layer, differently from the other specimens.

It is worth to mention that no pure OOP test on a reference unreinforced infill was performed. For this reason, the tests are not included in the database. First, an in-plane test was performed by applying a cyclical horizontal displacement history up to the attainment of an IDR about 0.5%. During tests, an axial load was applied on the columns in order to simulate the presence of upper storeys. Then, the specimens was IP unloaded and loaded out-of-plane through a couple of actuators active on 4 air-bags that applied cyclic lateral displacement to the specimens.

As already stated, the main purpose of this study was estimating and comparing the

effectiveness of the adopted reinforcement. A significant increase in the OOP strength of reinforced specimens, which was nearly 5 times that observed for the reference unreinforced specimen, which was IP-damaged up to the same drift level, was observed. In addition, a significant variation in the OOP collapse mechanism was observed, as the unreinforced REF specimens failed with a separation of the masonry wall from the confining RC frame, as shown in Figure 2.14. An increase in the IP strength for the reinforced specimens was observed, too.

Figure 2.14. OOP incipient collapse for REF specimen by Pereira et al. (2011).

REFERENCES

- Angel R, Abrams DP, Shapiro D, Uzarski J, Webster M. Behaviour of reinforced concrete frames with masonry infills. University of Illinois Engineering Experiment Station. College of Engineering. University of Illinois at Urbana-Champaign., 1994.
- Beconcini ML. Sulla resistenza a forze orizzontali di pareti in elementi forati in laterizio. Costruire in laterizio 1997;55:60-69. (in Italian).
- Calvi GM, Bolognini D. Seismic response of reinforced concrete frames infilled with weakly reinforced masonry panels. Journal of Earthquake Engineering 2001;5.2:153-185.
- Dawe JL, Seah CK. Out-of-plane resistance of concrete masonry infilled panels. Canadian Journal of Civil Engineering 1989;16(6):854–864.

- da Porto F, Barbiero E, Dalla Benetta C, Modena C. Sperimentazione sul comportamento fuori piano di tamponamenti in muratura di laterizio. Murature Oggi 2007;94. (in Italian).
- De Risi MT, Del Gaudio C, Ricci P, Verderame GM. In-plane behaviour and damage assessment of masonry infills with hollow clay bricks in RC frames. Engineering Structures 2018;168:257-275.
- Eurocode 2. Design of Concrete Structures. Part 1-1: General Rules and Rules for Buildings. Brussels, 2004. 225 p.
- Eurocode 6. Design of Masonry Structures. Part 1-1: General Rules for Reinforced and Unreinforced Masonry Structures. Brussels, 2005. 123 p.
- Eurocode 8. Design of structures for Earthquake Resistance. Part 1-1: General Rules, Seismic Actions and Rules for Buildings. Brussels, 2004. 229 p.
- Flanagan RD, Bennett RM 1999a. Bidirectional behaviour of structural clay tile infilled frames. Journal of Structural Engineering 1999;125.3:236-244.
- Flanagan RD, Bennett RM 1999b. Arching of masonry infilled frames: Comparison of analytical methods. Practice Periodical on Structural Design and Construction 1999;4.3:105-110.
- Furtado A, Rodrigues H, Arêde A, Varum H. Experimental evaluation of out-of-plane capacity of masonry infill walls. Engineering Structures 2016;111:48-63.
- Furtado A, Rodrigues H, Arêde A, Varum H 2018a. Effect of the Panel Width Support and Columns Axial Load on the Infill Masonry Walls Out-Of-Plane Behavior. Journal of Earthquake Engineering 2018.
- Furtado A, Rodrigues H, Arêde A, Varum H 2018b. Out-of-plane behavior of masonry infilled RC frames based on the experimental tests available: A systematic review. Construction and Building Materials 2018;168:831-848.
- Griffith MC, Lawrence SJ, Willis CR. Diagonal bending of unreinforced clay brick masonry. Journal of the British Masonry Society–Masonry International 2005;18.3.
- Griffith MC, Vaculik J. Out-of-plane flexural strength of unreinforced clay brick masonry walls. TMS Journal 2007;25.1:53-68.
- Guidi G, da Porto F, Dalla Benetta M, Verlato N, Modena C. Comportamento sperimentale nel piano e fuori piano di tamponamenti in muratura armata e rinforzata. Proceedings of the XV ANIDIS, L'Ingegneria Sismica in Italia, Padua, Italy, 2013, 30. (in Italian).

- Hak S, Morandi P, Magenes G. Out-of-plane experimental response of strong masonry infills. 2nd European Conference on Earthquake Engineering and Seismology, 2014.
- Lawrence SJ. Behaviour of brick masonry walls under lateral loading. Dissertation Abstracts International Part B: Science and Engineering [DISS. ABST. INT. PT. B-SCI. & ENG.] 1986, 47.1.
- Modena C, da Porto F. Ricerca sperimentale sul comportamento fuori piano di tamponamenti in muratura in zona sismica. Test report. Dipartimento di Costruzioni e Trasporti, University of Padova, 2005. (in Italian)
- Pereira MFP, Pereira MFN, Ferreira JED, Lourenço PB. Behaviour of masonry infill panels in RC frames subjected to in plane and out of plane loads. 7th International Conference on Analytical Models and New Concepts in Concrete and Masonry Structures. 2011.
- Shing PB, Mehrabi AB. Behaviour and analysis of masonry-infilled frames. Progress in Structural Engineering and Materials 2002;4.3:320-331.
- Varela-Rivera J, Moreno-Herrera J, Lopez-Gutierrez I, Fernandez-Baqueiro L. Out-of-plane strength of confined masonry walls. Journal of Structural Engineering 2012;138.11:1331-1341.
- Willis CR, Griffith MC, Lawrence SJ. Horizontal Bending of Unreinforced Clay Brick Masonry Walls, Masonry International 2004;17(3):109-121.

Chapter III
DIST-UNINA experimental program

3.1   INTRODUCTION

In the previous Chapter, the experimental tests currently available in the literature and performed to assess the OOP behaviour of URM infills and the IP/OOP interaction effects have been presented and discussed. The aim of the experimental state-of-the-art was collecting an experimental database that will be used, in Chapter IV, to assess the predicting capacity of strength, stiffness and displacement capacity formulations described in Chapter I and to propose efficient original formulation for modelling the pure OOP response of infills and the IP/OOP interaction effects. However, it is undeniable that the experimental database collected is quite small, with only some dozens of pure OOP tests on plain URM infills and a dozen of combined IP/OOP tests. To make more robust the evaluations that will be performed in the next chapter, it is necessary to enrich the experimental database.

For this reason, a wide experimental program has been performed in the Department of Structures for Engineering and Architecture (DIST) of University of Naples Federico II (UNINA). This experimental program will be referenced, hereafter, as DIST-UNINA experimental program.

A total of fifteen OOP pseudo-static tests on URM infills in 2:3 scaled RC frames has been performed (Figure 3.1). The experimental program had two main aims:

    i.   the assessment of the OOP behaviour of URM infills previously damaged by the cyclic application of in-plane (IP) displacements up to different drift levels (i.e., the investigation of the IP/OOP interaction);

ii.   ii. the assessment of the OOP behaviour of URM infills with different boundary conditions at edges.

The first aim has been achieved through a reference pure OOP test associated with three combined IP/OOP tests, each of which carried out up to three different drift levels (L, low; M, intermediate; H, high). This set of tests has been performed two times on infills equal for nominal mechanical and geometric properties, except for the thickness, which was equal to 80 mm for the first set and to 120 mm for the second set.
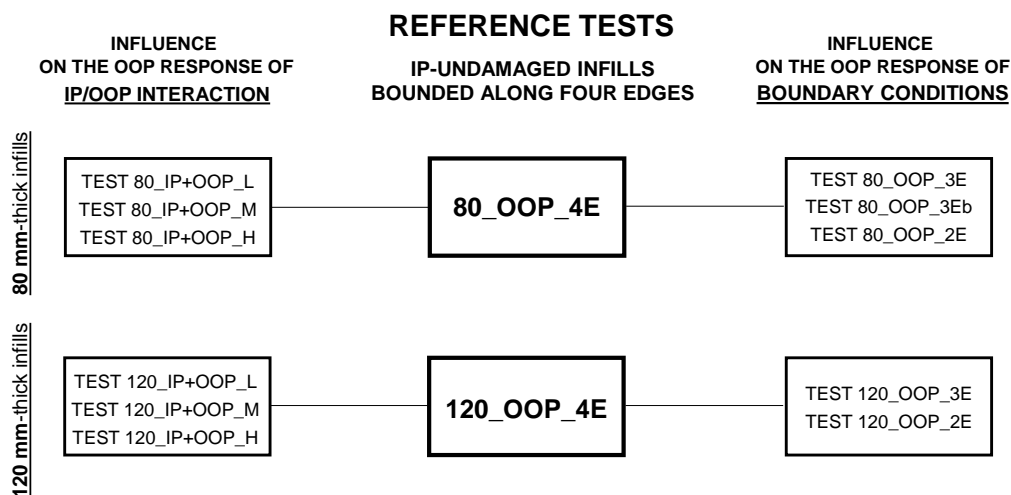
Figure 3.1. Overview of the experimental program carried-out at the Department of Structures for Engineering and Architecture of the University of Naples Federico II.

For what concerns the second aim, i.e. the investigation of the influence of boundary conditions on the OOP response of URM infills, a first set of experimental tests on 80 mm-thick infills has been performed. Namely, specimen 80_OOP_2E was mortared to the confining RC frame along the upper and the lower edge. In this case, the OOP strength of the specimen was granted by one-way arching action along the vertical direction. Specimen 80_OOP_4E was bounded to the confining RC elements along all the edges. In this case, the OOP strength of the specimen was due to two-way (horizontal and vertical) arching action. In addition, specimen 80_OOP_3E was bounded along three edges to the confining frame, as it was detached from the RC frame upper beam.

First, during the test, it exhibited one-way horizontal arching; then, the infill wall came in contact with the upper beam allowing the occurrence, also in this case, of double – both horizontal and vertical – arching. To complete the assessment of the OOP strength of 80 mm-thick infills in which only one-way (horizontal or vertical) arching occurs, the experimental behaviour of a second 80 mm-thick infill bounded along three edges is presented (specimen 80_OOP_3Eb). Then, the experimental behaviour of three 120 mm-thick infills is described. Specimen 120_OOP_4E was bounded along four edges to the elements of the confining RC frames, while specimens 120_OOP_3E and specimen 120_OOP_2E were respectively bounded along three and two edges.

In addition, two other tests have been performed on URM infills bounded along four edges: first, a preliminary pure OOP "pilot" test; second, a cyclic pure OOP test. The results of these tests will be presented, too.

In section 3.2, some preliminary issues are discussed. More specifically, the specimens are described, material properties are reported and the experimental setup is described, as well as the instrumentation layout and the loading path used for the IP tests and for the OOP tests.

In section 3.3, the preliminary pure OOP "pilot" test is described, as well as the reference pure OOP tests on the 80 mm thick and on the 120 mm thick infills mortared along four edges to the confining frame.

In section 3.4, the combined IP/OOP tests on the 80 mm thick and on the 120 mm thick infills are presented and discussed.

In section 3.5, the pure OOP tests on the 80 mm thick and on the 120 mm thick infills bounded along three and two edges are presented and discussed.

In section 3.6, the pure OOP cyclic test is presented and discussed.

Further details on the experimental tests' results are reported in Appendix B (cracking patterns and damage evolution) and in Appendix C (instrumentation measurements).

3.2   EXPERIMENTAL PROGRAM GENERAL INFORMATION

In this section, some general information on the experimental program are provided. Namely, the RC frames are described, as well as material properties. The experimental setup is presented, together with the instrumentation layout ant the loading path.

3.2.1. Specimens' description and construction materials' properties

The experimental tests herein described were carried out on 2:3 scaled infilled RC frames designed according to the seismic Italian building code NTC2008 (2008). The RC frames were realized using class C28/35 and C32/40 concrete for the RC frames realized for the tests on the 80 mm and on the 120 m thick infills, respectively, and steel reinforcement bars with nominal characteristic yielding stress equal to 450 N/mm^2. Construction drawings of the RC frame, with geometric and reinforcement details are reported in Figure 3.2.

For the tests on the 80 mm thick infills, infill walls with thickness equal to 80 mm were realized by using 250x250x80 mm^3 clay hollow bricks with nominal percentage of voids equal to 60%, nominal thickness of internal tiles equal to 7.4 mm and nominal thickness of external tiles equal to 8.0 mm. Brick units were placed with horizontal holes and with 1 cm thick horizontal and vertical courses of class M5 mortar. A picture of the brick unit is reported in Figure 3.3. Similar properties are associated with the 250x250x120 mm^3 clay hollow bricks. A picture of the brick unit is reported in Figure 3.4.

The bricks used had lower bound compressive strength equal to 2 N/mm^2 perpendicular to holes and to 5 N/mm^2 parallel to holes.

Recent studies have shown that the absolute dimensions – which are modified through scaling – of URM walls can have a significant influence on the IP response of URM walls and on the IP/OOP interaction effects due to the so-called size-effect. Namely, in Petry and Beyer (2014) and in Frumento et al. (2009), it is shown on empirical basis that smaller walls are characterized by a less steep softening branch and, so, by a higher IP drift capacity. This can influence the damage evolution due to IP action and, potentially, the OOP response of IP-damaged URM walls. Namely, at equal IP drift, a lower damage can be exhibited by smaller infills and, so, a lower OOP strength/stiffness reduction, too. On the other hand, in TU-DELFT (1997) and in Najafgholipour et al. (2013-2014) it was shown through numerical FEM analyses that smaller URM walls can exhibit a lower IP strength and a more significant entity of IP/OOP interaction. In the Authors' opinion, it is not possible to immediately extend these – somehow contradictory – results obtained for URM walls to URM infill walls. In addition, to the Authors' knowledge, no specific study was dedicated, concerning these issues, to URM infill walls. Further experimental and numerical investigation is needed on this topic. However, note that the specific scale factor used for this study, which is relatively near to the unit, should somehow limit the potential influence of size

effect on tests' results.

Mean properties of construction materials are reported in Table 3.1 and 3.2. Masonry compressive strength f_m and elastic modulus E_m were determined by vertical and horizontal compression tests on 770x770x80 mm³ masonry wallets, according to EN 1052-1 (1999) standard, while its tensile strength f_t and shear modulus G_m were determined by performing diagonal compression tests on 1280x1280x80 mm³ wallets, according to ASTM E519 – 02 (2002) standard.
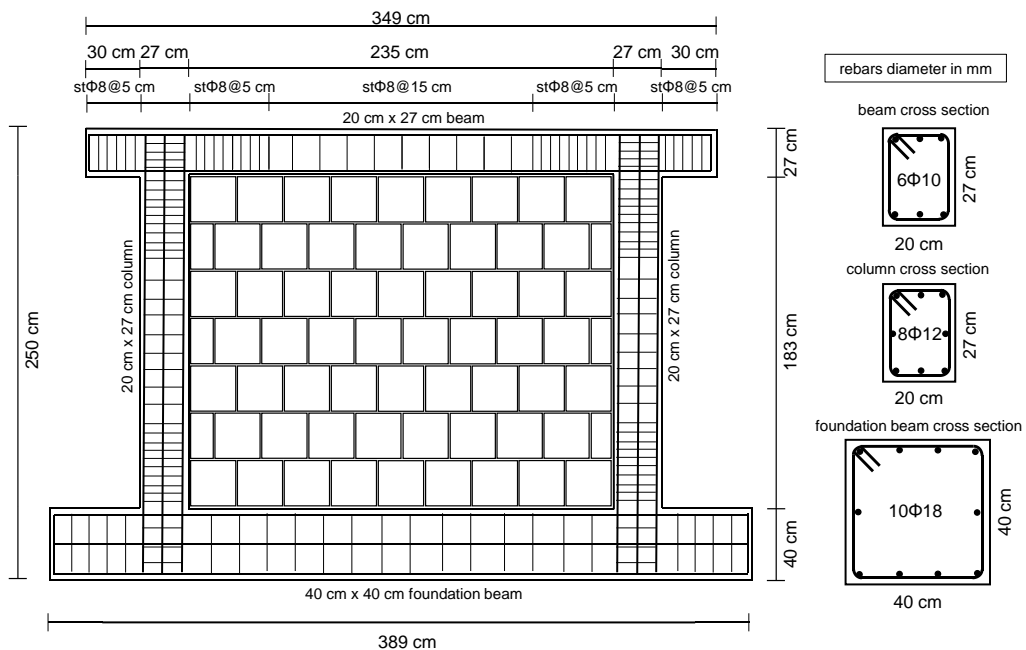
Figure 3.2. Construction drawings of the RC frame specimen.

Figure 3.3. Picture of the 250x250x80 mm³ clay bricks used for this study.

Figure 3.4. Picture of the 250x250x120 mm^3 clay bricks used for this study.

Table 3.1. Average RC frames mechanical properties.

specimen	f_{cm} [N/mm^2]	f_{ym} [N/mm^2]	E_{cm} [N/mm^2]
frames used for tests on the 80 mm-thick infills	36.0	552	32308
frames used for tests on the 120 mm-thick infills	46.2	497	34819

Table 3.2. Average masonry mechanical properties.

specimen	f_{mv} [N/mm^2]	E_{mv} [N/mm^2]	f_{mh} [N/mm^2]	E_{mh} [N/mm^2]	f_t [N/mm^2]	G_m [N/mm^2]	f_j [N/mm^2]
pilot	1.74	1015	2.97	1966			10.4
80_OOP_4E	1.80	1517	2.21	1188			10.4
80_OOP_3E	1.80	1517	2.21	1188			10.4
80_OOP_3Eb	2.44	1846	2.88	2502			
80_OOP_2E	1.81	1090	2.45	1255			8.3
80_IP+OOP_L	1.81	1090	2.45	1255	0.23	315	8.3
80_IP+OOP_M	1.81	1090	2.45	1255	0.23	315	8.3
80_IP+OOP_H	1.81	1090	2.45	1255	0.23	315	8.3
120_OOP_4E	1.65	1455	2.12	1262			
120_OOP_3E	2.21	1770					
120_OOP_2E	2.21	1770					
120_IP+OOP_L	1.65	1455	2.12	1262			
120_IP+OOP_M	1.65	1455	2.12	1262			
120_IP+OOP_H	1.65	1455	2.12	1262			
120_OOP_4E_cyclic	2.21	1770					

A picture of the infilled RC frame is shown in Figure 3.5.

Figure 3.5. Picture of an infilled RC frame used for this study.

3.2.2. Test setup and loading system

The experimental setup was constituted by two parts. First, an IP setup was realized. A cantilever vertical beam was used as reaction structure for the IP hydraulic actuator. Steel plates were placed at each end of the RC frame upper beam and connected to the hydraulic actuator. Such plates were connected through four quenched steel rebars, each one post-tensioned by applying a 55 kN load, in order to apply positive and negative displacements during cyclic IP tests previous to OOP monotonic tests. Two steel stiff members transverse to the RC foundation beam were fixed at the rigid floor in order to prevent rigid body rotations of the RC frame during IP tests. Moreover, two stiff steel

members were fixed to the rigid floor and placed at each end of the foundation beam to prevent rigid body translations of the RC frame during IP tests. Second, the OOP setup was constituted by steel members and clamps aimed at preventing OOP drifts of the RC frame during OOP tests and at functioning as reaction structure for the OOP hydraulic actuator. A rendering of the experimental setup is reported in Figure 3.6. A picture of the experimental setup is reported in Figure 3.7.

LEGEND		
1. Infill wall	7. Posterior columns	14. IP reaction cantilever beam
2. RC frame	8. Diagonal stiffening members	15. IP hydraulic actuator
3. OOP lower clamps	9. Reaction beam	16. Plates for post-tensioned rebars
4. OOP upper clamps	10. OOP hydraulic actuator	
5. Transverse beams for OOP upper clamps connection to anterior columns	11. OOP load transfer system	17. Post-tensioned rebars for IP cyclic loading
	12. Constraints against IP translation	
6. Anterior columns	13. Constraints against IP rotation	

Figure 3.6. Rendering of the experimental setup.

Figure 3.7. Picture of the experimental setup.

IP cyclic loads were applied in displacement control at one end of the RC frame upper beam, according to the loading path reported in Table 3.3.

Table 3.3. IP loading path defined by nominal target IP drifts and displacements.

cycle	target IP drift	target IP displacement	n. of sub-cycles	velocity
#	[%]	[mm]	[-]	[mm/s]
1	+/-0.1	+/-1.97	3	0.25
2	+/-0.2	+/-3.93	3	0.25
3	+/-0.3	+/-5.90	3	0.25
4	+/-0.4	+/-7.86	3	0.50
5	+/-0.5	+/-9.83	3	0.50
6	+/-0.6	+/-11.79	3	0.50
7	+/-0.8	+/-15.72	3	0.50
8	+/-1.0	+/-19.65	3	0.50
9	+/-1.2	+/-23.58	3	1.00
10	+/-1.4	+/-27.51	3	1.00
11	+/-1.6	+/-31.44	3	1.00
12	+/-1.8	+/-35.37	3	1.00
13	+/-2.0	+/-39.30	3	1.00
14	+/-2.4	+/-47.16	3	1.00

According to consolidated analytical studies (Blevins and Plunkett 1980), the deformed shape associated to the first OOP vibration mode of an elastic plate simply-supported at edges is well described, along the vertical and horizontal direction in the plate's plane, through a sinusoidal shape function. Thus, the first mode-proportional static load equivalent to the seismic action has the same shape, under the reasonable hypothesis of uniform-mass dynamic system, and, so, is characterized by a null load along the infill edges. This means that all load distributions applied in the OOP direction during pseudo-static tests not shaped as a sinusoid are approximation of the real static load equivalent to the seismic action. In this study, OOP loads were applied in displacement control monotonically increasing at 0.02 mm/s velocity (except for the cyclic test, whose OOP loading protocol will be described in section 3.6) on four points/spherical hinges using a loading scheme two times symmetric with respect to the horizontal and vertical directions in the infill's plane. This loading scheme has the advantage to reproduce the seismic condition of null load along the infill edge and was also adopted by Calvi and Bolognini (2001) and by Guidi et al. (2013) for OOP tests and combined IP+OOP tests. The loading points are placed on the infill's diagonals, at a distance from both diagonal's ends equal to one-third of the diagonal length, as shown in Figure 3.8. The loading system was statically determined in order to grant an equal partition between the four loading points of the resultant load applied.

No axial load was applied on columns. The presence of axial load on columns seems to not affect significantly the pure OOP strength of URM infills, as shown by Furtado et al. (2016, 2018a-b). However, the presence of axial load can influence the OOP cracking pattern, as shown by Furtado et al. (2018a-b), while contradictory effects on infills' initial stiffness, as Angel et al. (1994) observe its increase in presence of axial load while Furtado et al. (2018b) observe its decrease in presence of axial load. Further investigation is needed on this topic.

For what concerns the IP response, only a very small number of experimental tests has been performed investigating the different performance of RC infilled frames in presence and absence of axial load. Namely, Stylianidis (2012) tested five couples of identical RC infilled frames with and without axial load on columns. Based on these results, Del Gaudio et al. (2017) showed that the IDRs corresponding to the attainment of Damage States associated with light, medium, severe and heavy damage for the specimens tested in presence of axial load on columns can be both higher and lower than those obtained for specimens tested in absence of axial load on columns. On average, it

seems that the presence of axial load can make higher the IDRs associated with all Damage States: in this sense, the choice of performing the tests for the present study without the application of the axial load can be considered conservative. However, the small number of tests carried out to investigate this issue do not allow a robust judgement on the effects of the presence/absence of the axial load on columns on the evolution of damage in RC infilled frames during IP tests. Further investigation is needed on this topic.

3.2.3. Instrumentation layout

As shown in Figure 3.8, twelve LVDTs were placed along the infills' edges to read OOP displacements due to potential detachment of the infill from the surrounding frame.

Five laser displacement transducers were placed to read OOP displacements of the infill centre and of the four loading points. Moreover, two LVDTs were placed at the centre of the RC frame upper and foundation beam (OOP_top and OOP_bot, respectively), in order to read potential OOP translation or drifts of the RC frame during tests.

A horizontal LVDT was placed at the upper beam's end opposite to the IP-loaded end (IP_top) to read IP displacements of the upper beam cross-section centroid. Moreover, a horizontal LVDT was placed at the foundation beam's end to read potential rigid translation of the RC frame during IP tests (IP_bot).
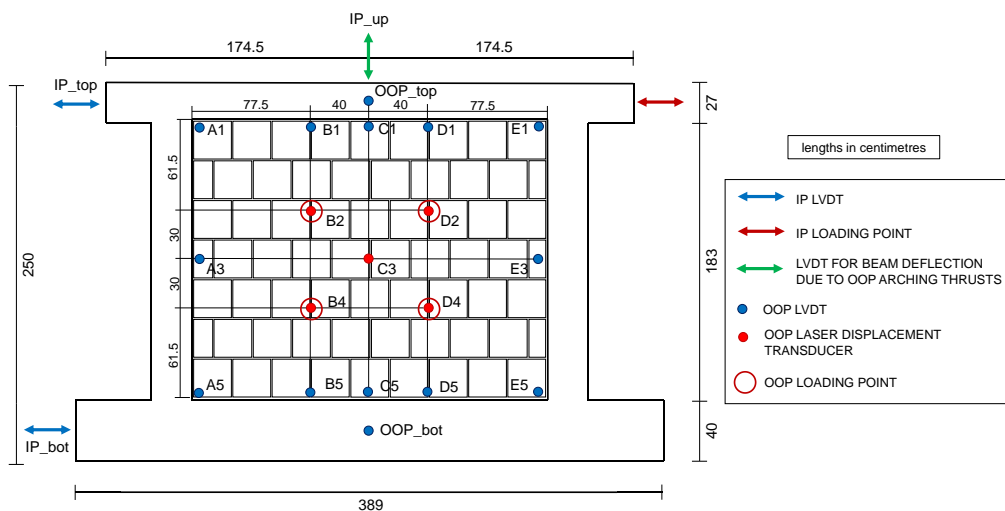
Figure 3.8. Instrumentation layout.

Only for the tests on the 120 mm-thick infills, a vertical LVDT (IP_up) was placed at the centre of the upper beam upper edge to read potential deflections of the beam due to arching thrusts.

3.3   REFERENCE TESTS

This section is dedicated to the description and discussion of the reference pure OOP tests carried out on the IP-undamaged URM infills mortared along four edges to the confining RC frame.

Namely, the pilot test on an 80 mm thick infill is described, as well as the pure OOP test on the IP-undamaged specimen 80_OOP_4E and the pure OOP test on the IP-undamaged specimen 120_OOP_4E.

The experimental tests are described with the support of the OOP force-central displacement (or drift, with OOP drift defined as the OOP central displacement of the infill divided by one-half of the infill height) diagrams and with the representation of the evolution of cracking patterns during the tests. Further details are reported in Appendices B-C.

3.3.1. Pilot test

A pilot OOP test was performed prior to the beginning of the experimental program. The main aims of this test were:

i.   Evaluating the OOP behaviour of the infill with special attention to the post-peak response, above all to check the potential necessity of safeguards against a particularly brittle or abrupt failure at the end of the test;

ii.   Evaluating the order of magnitude of the OOP strength of the infill and compare it with the design load for the experimental setup and for the maximum load that it can bear (90 kN and 128 kN, respectively);

iii.   Evaluating the OOP displacement read by LVDTs OOP_top and OOP_bot (see the instruments' layout in Figure 3.8), in order to verify the absence of OOP rigid translation and drifts of the RC frame during tests, i.e., the effectiveness of the experimental setup lower and upper OOP clamps;

iv.   Assessing the effectiveness of the instrumentation layout adopted that, for this test, was constituted also by instruments placed on the posterior face of the infill.

The pilot test provided a positive feedback for what concerns all these issues. However, for a homogeneous reading of the OOP displacements of the specimens, all instruments were placed in the successive tests on the anterior face of the infill.

As the experimental results had not to be used for comparison with other experimental tests in this experimental program, nor with literature formulation etc., the test was performed at higher velocity (0.05 mm/s), with no white painting on the infill wall. So, no significant or detailed information is available on the damage evolution of the specimen during the test, which was very brief (about 10/15 minutes). However, for the sake of completeness, the OOP force-displacement response of the pilot infill is reported in Figure 3.9. A picture of the specimen at the end of the test is reported in Figure 3.10.
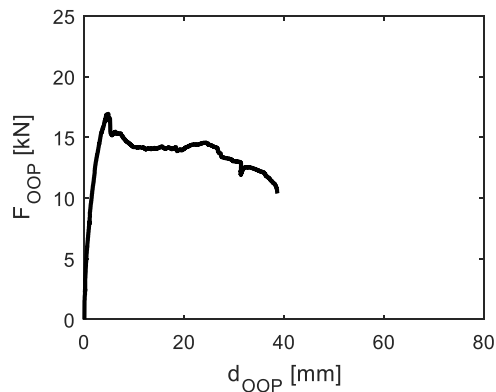
Figure 3.9. OOP force vs infill's central displacement for the pilot specimen.

Figure 3.10. Pilot specimen at the end of test.

3.3.2. Test 80_OOP_4E

The OOP force-infill's centre displacement diagram obtained for OOP_4E specimen is shown in Figure 3.11. Since very low load levels, micro-cracks formation was announced by cracking noises. However, the first visible diagonal crack appeared in the upper part of the infill only at a central displacement equal to 3.3 mm, corresponding to a 19.4 kN load, as shown in Figure 3.12, in which the evolution of cracking pattern during the test is shown.

A second diagonal crack in the lower part of the infill appeared at the attainment of the infill resistance, equal to 22.0 kN, corresponding to a central displacement equal to 5.4 mm. After the attainment of peak load, the infill resistance decreased up to 18.1 kN at a displacement equal to 10.3 mm. During this phase, pre-existing diagonal cracks extended and noticeable horizontal cracks in the lower part of the infill, along the bottom course of bricks, appeared. So, a pseudo-plastic phase in the OOP response of the infill was observed up to a displacement of 28.7 mm, with new vertical and horizontal cracks opening in the central part of the infill. After that, a softening branch in the OOP response diagram was observed. In this phase, pre-existing cracks became wider, especially in the lower part of the infill. The test ended at a central displacement equal to 76.9 mm, corresponding to a load equal to 2.8 kN, i.e., a resistance loss of the infill equal to 87%. During the test, no detachment of the infill from the surrounding frame was read by LVDTs and no significant displacement was registered in the OOP direction for the foundation and upper beams of the RC frame. A summary of test results is

reported in Table 3.4.

Based on the OOP displacements read by instruments, the evolution of the reconstructed deformed shape of the specimen is shown in Figure 3.13. A picture of the specimen at the end of the test is reported in Figure 3.14.
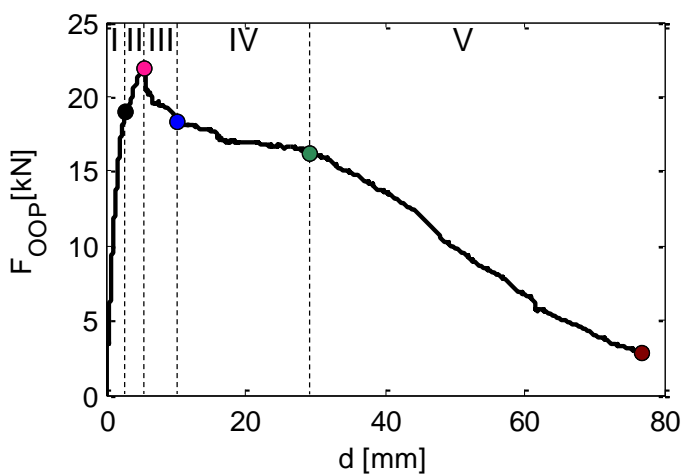
Figure 3.11. OOP force vs infill's central displacement for specimen 80_OOP_4E.

Table 3.4. Summary of test 80_OOP_4E results.

specimen	F_{crack}	d_{crack}	K_{crack}	F_{max}	d_{max}	K_{max}	d_{end}
	[kN]	[mm]	[kN/mm]	[kN]	[mm]	[kN/mm]	[mm]
80_OOP_4E	19.4	3.3	5.9	22.0	5.4	4.1	76.9

a) F_{OOP} =19.4 kN d_{OOP}=3.3 mm

b) F_{OOP} =22.0 kN d_{OOP}=5.4 mm

c) F_{OOP} =2.8 kN d_{OOP}=76.9 mm
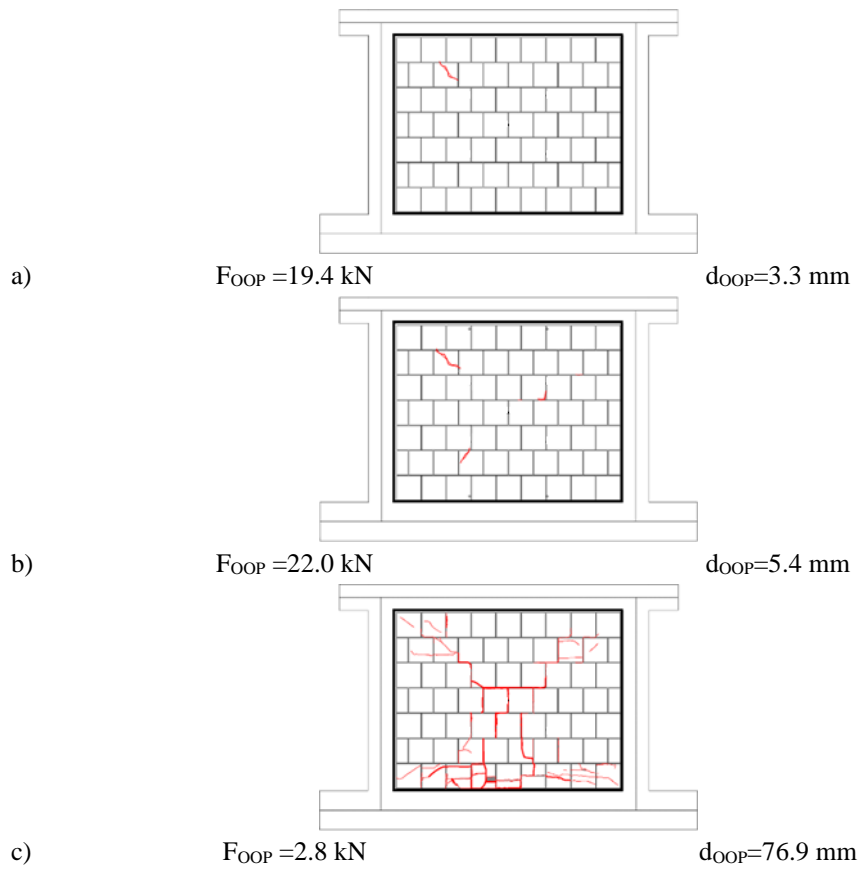
Figure 3.12. Cracking pattern evolution at first macro-cracking (a), peak load (b) and at the end of the test (c) for specimen 80_OOP_4E.
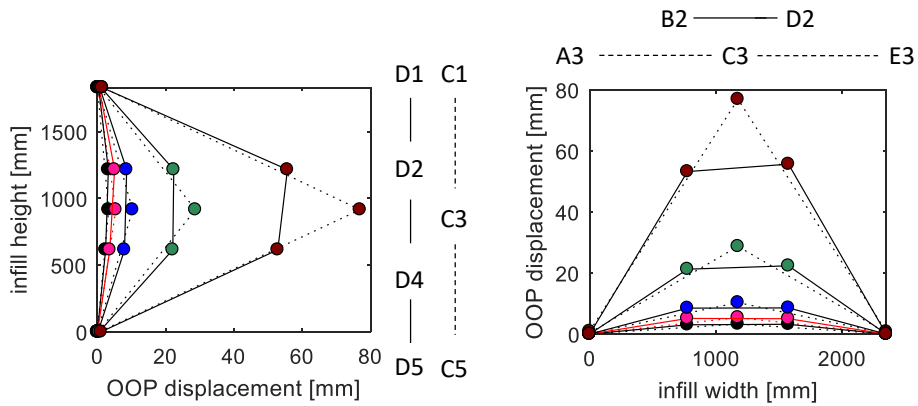
Figure 3.13. Deformed shape evolution along vertical and horizontal alignments (see the instruments' layout in Figure 3.8) for specimen 80_OOP_4E at the end of each one of the five phases individuated in Figure 3.11. The deformed shape corresponding to the attainment of peak load is highlighted with a red line.

Figure 3.14. Specimen 80_OOP_4E at the end of test.

3.3.3. Test 120_OOP_4E

The OOP force-central displacement response of the specimen 120_OOP_4E is shown in Figure 3.15. It is observed that the general behaviour of this specimen is similar

to that exhibited by specimen 80_OOP_4E. A first pseudo-elastic branch was observed up to the first visible diagonal crack formation in the upper part of the infill, which occurred for a load equal to 27.5 kN, which was attained at a displacement equal to 2.5 mm. Then, the response of the specimen was non-linear up to the attainment of peak load, equal to 41.9 kN, which occurred for a central OOP displacement equal to 8 mm. Differently from specimen 80_OOP_4E, in this case the peak load was significantly higher than the first macro-cracking load. As for specimen 80_OOP_4E, immediately after the attainment of peak load a drop in the load-bearing capacity of the specimen occurred, as the load reduced to 37.7 kN for a displacement equal to 8.4 mm. Then, a smooth softening branch was observed up to a central displacement equal to 26.8 mm and to a load equal to around 30 kN. During this phase, a rapid evolution of the cracking pattern was observed, with the formation of further diagonal cracks in the upper part of the infill, then of horizontal cracks along the lower course of bricks and finally with the formation of vertical cracks at mid-width of the infill, in its lower part. After that, a steeper softening branch was observed up to the end of the test, which was interrupted at an OOP central displacement equal to 64.6 mm, at a force equal to 4.7 kN, with a reduction of the OOP load-bearing capacity equal to 89% with respect to the registered strength. This last phase was characterized by the formation of horizontal cracks in the upper part of the infill and by the further opening of previously-formed cracks, especially in the lower part of the infill, where the exterior tiles of lower bricks were failing and overturning at the end of the test. A summary of test results is reported in Table 3.5.

During the test, no significant displacement was registered in the OOP direction at the edges of the infill and also for the foundation and upper beams of the RC frame. Based on the OOP displacements read by instruments, the evolution of the reconstructed deformed shape of the specimen is shown in Figure 3.16. The evolution of cracking pattern in the specimen is reported in Figure 3.17. A picture of the specimen at the end of the test is reported in Figure 3.18.
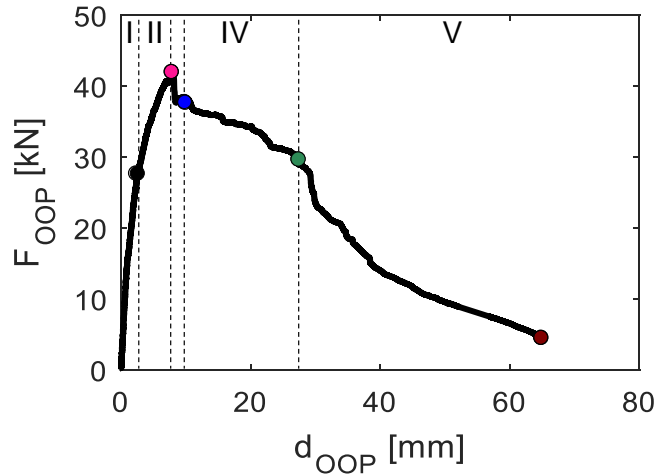
Figure 3.15. OOP force vs infill's central displacement for specimen 120_OOP_4E.

Table 3.5. Summary of test 120_OOP_4E results.

	F_{crack}	d_{crack}	K_{crack}	F_{max}	d_{max}	K_{max}	d_{end}
specimen	[kN]	[mm]	[kN/mm]	[kN]	[mm]	[kN/mm]	[mm]
120_OOP_4E	27.5	2.5	11.0	41.9	8.0	5.2	64.6
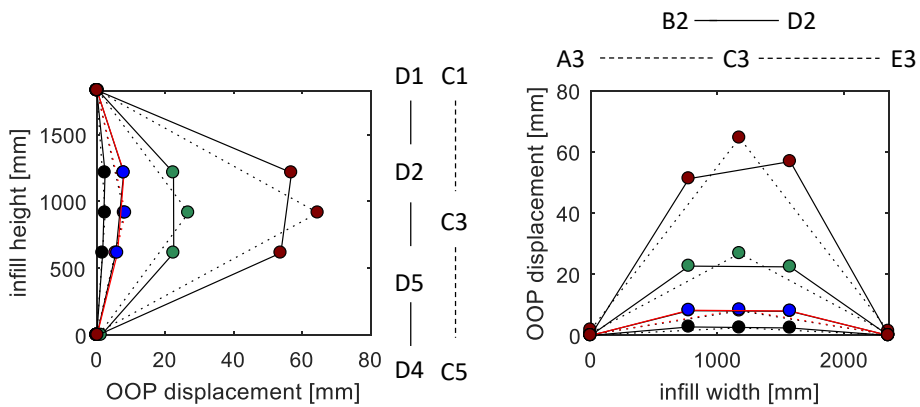
Figure 3.16. Deformed shape evolution along vertical and horizontal alignments (see the instruments' layout in Figure 3.8) for specimen 120_OOP_4E at the end of each one of the five phases individuated in Figure 3.15. The deformed shape corresponding to the attainment of peak load is highlighted with a red line.

a) $F_{OOP} = 27.5$ kN $d_{OOP} = 2.5$ mm

b) $F_{OOP} = 41.9$ kN $d_{OOP} = 8.0$ mm

c) $F_{OOP} = 4.7$ kN $d_{OOP} = 64.6$ mm
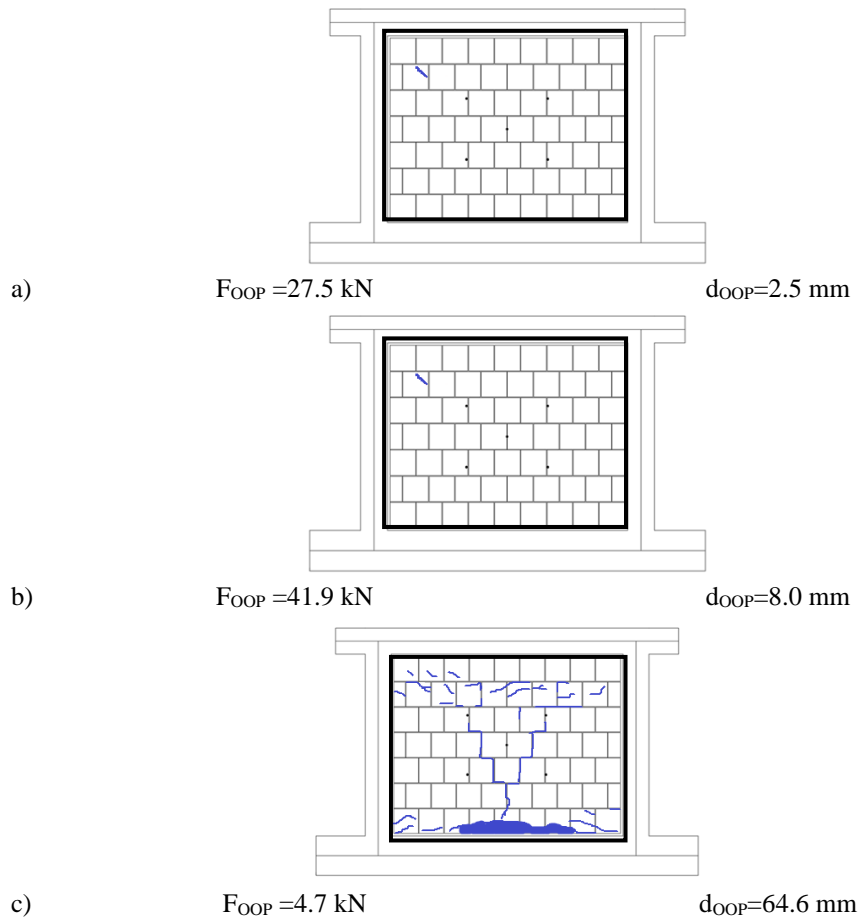
Figure 3.17. Cracking pattern evolution at first macro-cracking (a), peak load (b) and at the end of the test (c) for specimen 120_OOP_4E.
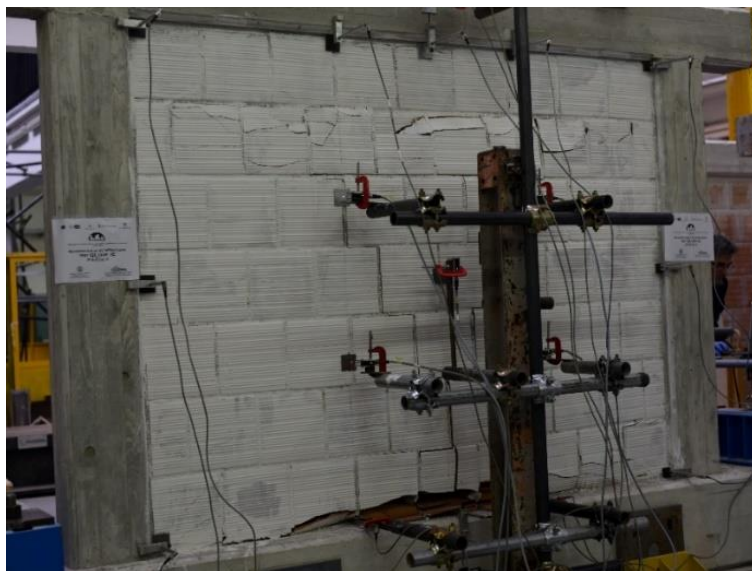
Figure 3.18. Specimen 120_OOP_4E at the end of test.

3.4   COMBINED IP/OOP TESTS

This section is dedicated to the description and discussion of the experimental tests carried out on infills mortared along all the edges to the confining frame elements to investigate the IP/OOP interaction. For each specimen, first, a cyclic IP test is performed up to a certain drift level. Then, the specimen is unloaded and, after IP unloading, tested in the OOP direction. Note that, due to the slight deformability of the reaction cantilever beam part of the IP setup, the actual IP drifts attained during tests are slightly lower than the nominal ones.

For what concerns 80 mm thick infills, three combined IP/OOP tests are presented. Test 80_IP+OOP_L was performed at maximum nominal IP drift equal to 0.20%; test 80_IP+OOP_M was performed at maximum nominal IP drift equal to 0.40%; test 80_IP+OOP_H was performed at maximum nominal IP drift equal to 0.60%.

For what concerns 120 mm thick infills, three combined IP/OOP tests are presented. Test 120_IP+OOP_L was performed at maximum nominal IP drift equal to 0.30%; test 120_IP+OOP_M was performed at maximum nominal IP drift equal to 0.60%; test 120_IP+OOP_H was performed at maximum nominal IP drift equal to 1.00%. A summary of the experimental tests carried out and presented in this section is reported in Table 3.6.

Table 3.6. Summary of the combined IP/OOP tests.

test	nominal maximum IP drift	actual maximum IP drift
80_IP+OOP_L	0.20%	0.16%
80_IP+OOP_M	0.40%	0.37%
80_IP+OOP_H	0.60%	0.58%
120_IP+OOP_L	0.30%	0.21%
120_IP+OOP_M	0.60%	0.50%
120_IP+OOP_H	1.00%	0.89%

The experimental tests are described with the support of IP cyclic response diagrams and OOP force-central displacement diagrams. In addition, the evolution of cracking patterns during the tests is shown. Further details are reported in Appendices B-C.

3.4.1. Test 80_IP+OOP_L

Test 80_IP+OOP_L was performed first by imposing to the test specimen an IP cyclic displacement history up to the attainment of a maximum nominal drift equal to 0.20%. Due to the deformability of the IP reaction cantilever beam, the actual maximum IP drift attained by the specimen, read by the LVDT at the end of the frame's upper beam, was equal to 0.16%, corresponding to a maximum IP displacement equal to 3.14 mm. The IP cyclic response of specimen IP+OOP_L is reported in Figure 3.19a.

First masonry cracking occurred for a positive IP drift equal to 0.068%, corresponding to a 56.3 kN load, and for a negative IP drift equal to 0.067%, corresponding to an IP force equal to 58.0 kN. First crack appeared due to mortar detachment from bricks in the lower part of the infill. The test was interrupted after the attainment of a maximum displacement equal to 3.1 mm, corresponding to a 0.16% drift and to a 79.4 kN load. At this point, further cracks due to mortar detachment from bricks appeared also in the upper part of the infill. During the IP tests, the instrumentation read very small and absolutely negligible displacements of the foundation beam of the RC frame. The evolution of the IP cracking pattern for the specimen is reported in Figure 3.20.

Test specimen was IP unloaded and then loaded in the OOP direction. The OOP monotonic response of specimen 80_IP+OOP_L is reported in Figure 3.19b.
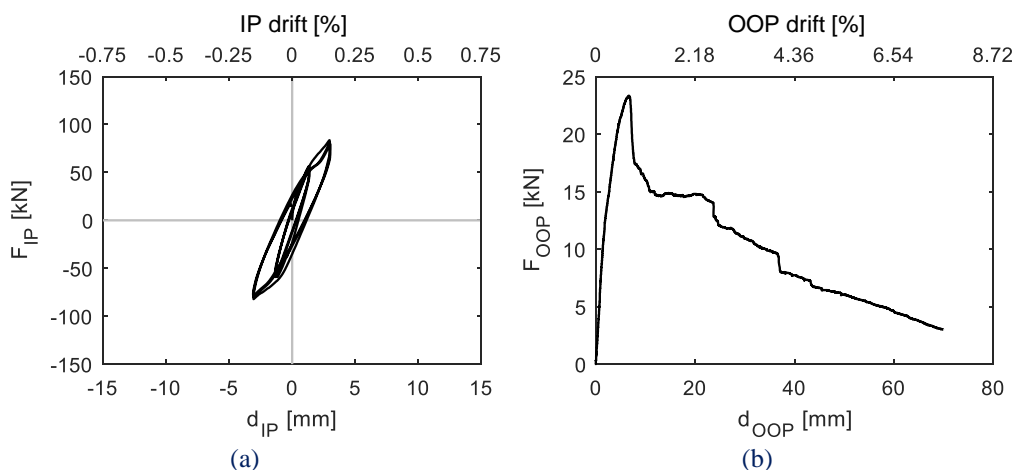
Figure 3.19. IP (a) and OOP (b) response of specimen 80_IP+OOP_L.

The first visible diagonal crack due to OOP loading appeared in the upper part of the infill, at a central displacement equal to 1.8 mm (0.20% drift), corresponding to a load equal to 12.6 kN. After first macro-cracking, further cracks opened along the infill's diagonals up to the attainment of the peak load equal to 23.4 kN for an OOP central displacement equal to 6.8 mm (0.74% drift). After peak load, a sudden decrease of the OOP load-bearing capacity occurred with the formation of cracks in the lower part of the infill. The load decreased to 15.2 kN for a central displacement equal to 10.9 mm (1.19% drift). After that, a pseudo-plastic behaviour was observed, up to a load equal to 14.9 kN for a central displacement equal to 21.7 mm (2.37% drift). Then, a softening branch was registered, first with the opening of previously-formed cracks in the lower part of the infill, then with the formation and opening of new cracks in the central part and in correspondence of the infill upper corners. The test ended at a central displacement equal to 70.5 mm (7.70% drift), corresponding to an OOP load equal to 3.2 kN and, so, to a load-bearing capacity reduction, with respect to peak load, about 86%. At the end of the test, the exterior tiles of the infill's lower brick were failing and overturning. No significant OOP displacement was read by LVDTs along the infill's edges. A summary of the OOP test results is reported in Table 3.7. The evolution of the OOP cracking pattern for the specimen is reported in Figure 3.21.

A picture of the test specimen 80_IP+OOP_L at the end of the test is reported in Figure 3.22.

a) F_{IP} =56.3 kN d_{IP}=1.32 mm

IP peak load not reached

b) F_{IP} = - d_{IP}= -

c) F_{IP} =79.4 kN d_{IP}=3.10 mm
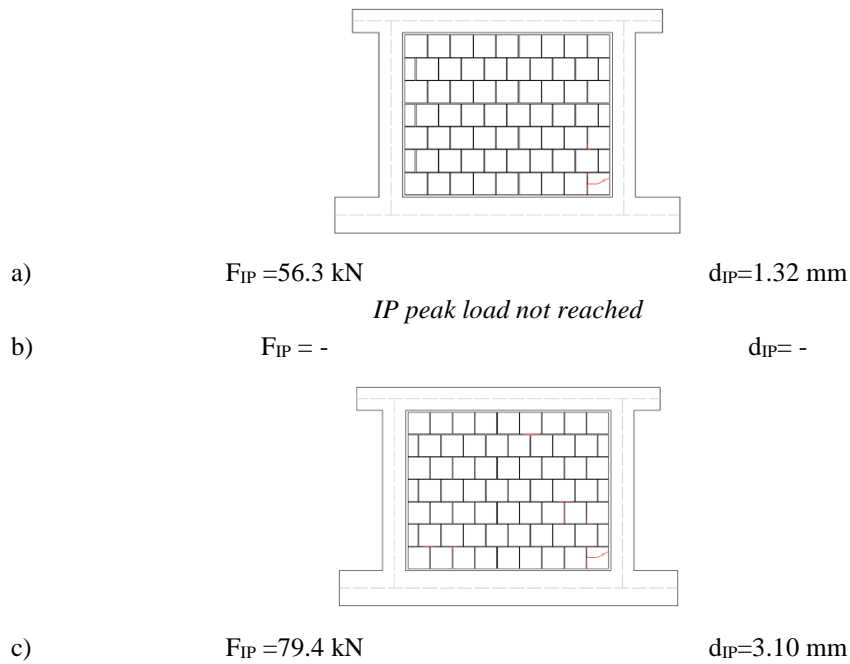
Figure 3.20. Cracking pattern evolution during the IP test at first macro-cracking (a), peak load (b) and at the end of the test (c) for specimen 80_IP+OOP_L.

a) F_{OOP} =12.6 kN d_{OOP}=1.8 mm

b) F_{OOP} =23.4 kN d_{OOP}=6.8 mm

c) F_{OOP} =3.2 kN d_{OOP}=70.5 mm
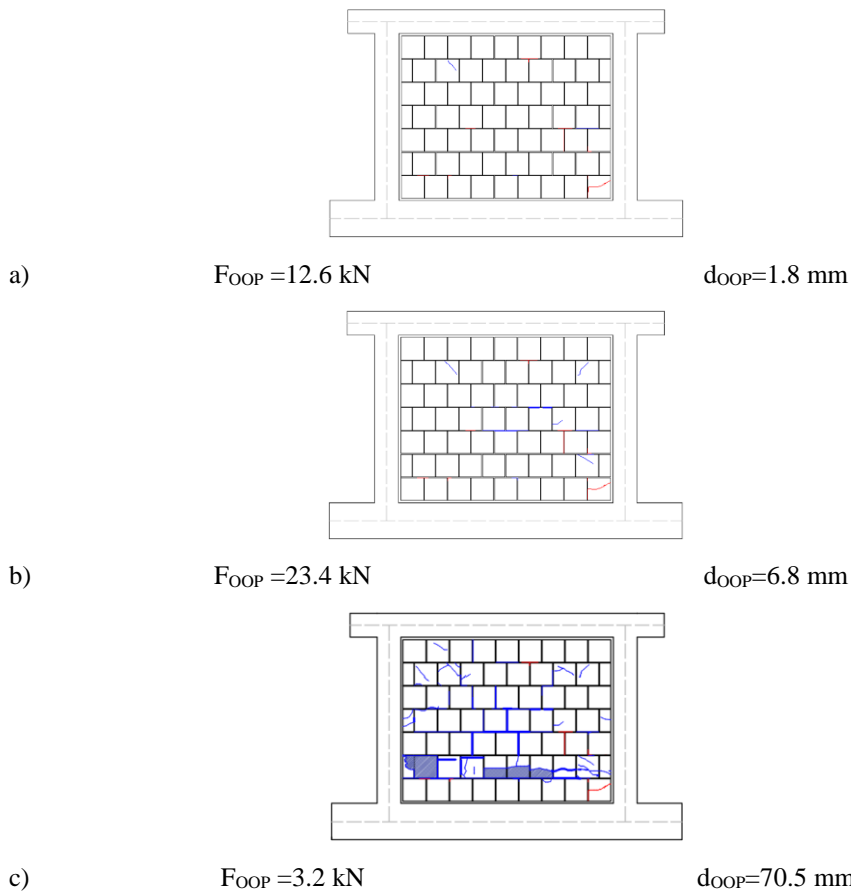
Figure 3.21. Cracking pattern evolution during the OOP test at first macro-cracking (a), peak load (b) and at the end of the test (c) for specimen 80_IP+OOP_L.

Table 3.7. Summary of test 80_IP+OOP_L (IP IDR=0.16%) results.

	F_{crack}	d_{crack}	K_{crack}	F_{max}	d_{max}	K_{max}	d_{end}
specimen	[kN]	[mm]	[kN/mm]	[kN]	[mm]	[kN/mm]	[mm]
80_IP+OOP_L	12.6	1.8	7.0	23.4	6.8	3.4	70.5
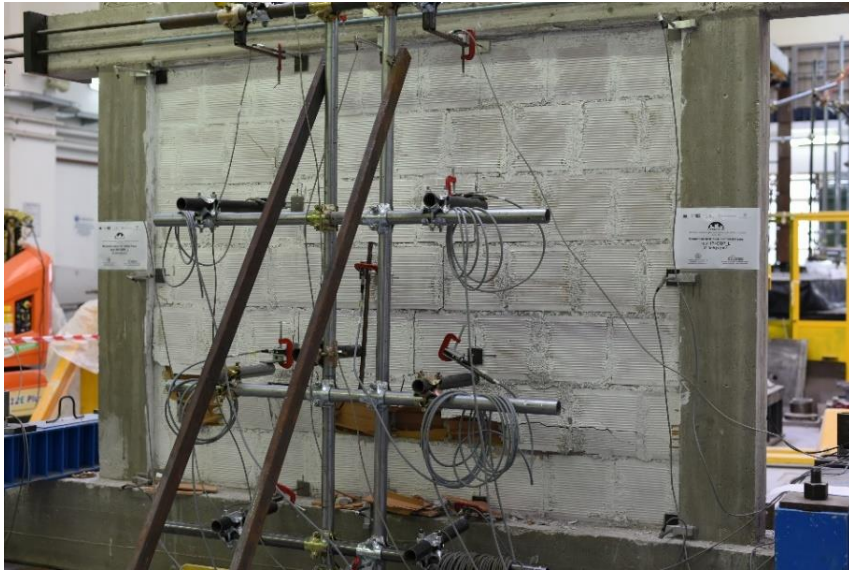
Figure 3.22. Specimen 80_IP+OOP_L at the end of test.

3.4.2. Test 80_IP+OOP_M

Test 80_IP+OOP_M was performed first by imposing to the test specimen an IP cyclic displacement history up to the attainment of a maximum nominal drift equal to 0.40%. Also in this case, due to the test setup slight deformability, the actual maximum IP drift attained by the specimen was lower than the nominal one and equal to 0.37%, corresponding to a maximum IP displacement equal to 7.3 mm. The IP force-displacement diagram of specimen IP+OOP_M is reported in Figure 3.23a.

First masonry cracking occurred with mortar detachment from bricks in the lower part of the infill, for a positive IP drift equal to 0.064%, corresponding to a 62.2 kN load, and to a negative drift equal to 0.062%, corresponding to a 62.1 kN. Up to the attainment of an IP displacement equal to 4.8 mm and of an IP force equal to 101.9 kN, cracks formed and opened in the central part of the infill, along the two diagonals. The test was interrupted at the attainment of a maximum displacement equal to 7.3 mm, corresponding to a 0.37% drift and to a load decreasing, within the same cycle, from 102.5 to 88.6 kN. At this point, the exterior tiles of the central bricks were failing and overturning. No significant IP translation of the RC frame was read by the LVTD at its base. The evolution of the IP cracking pattern for the specimen is reported in Figure 3.24.

The specimen was IP unloaded and then monotonically loaded in the OOP direction.

The OOP force-central displacement behaviour diagram of specimen 80_IP+OOP_M is reported in Figure 3.23b.
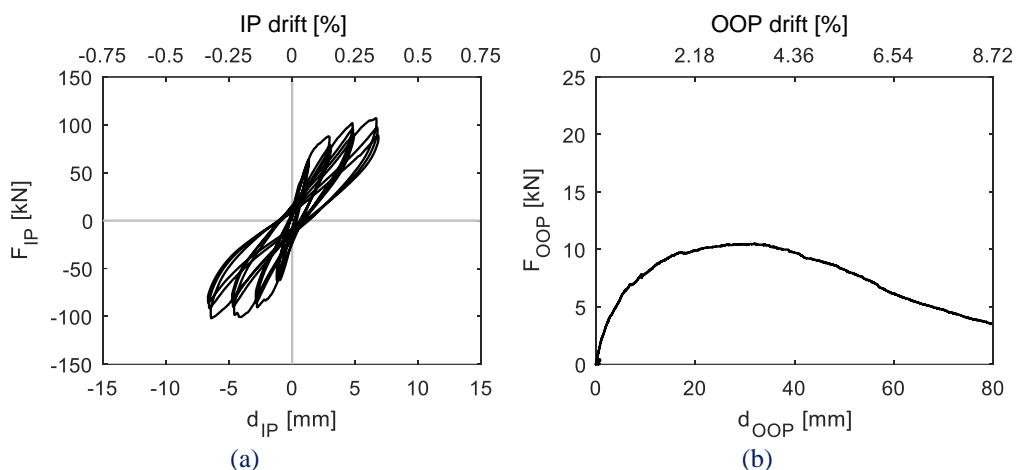
Figure 3.23. IP (a) and OOP (b) response of specimen 80_IP+OOP_M.

Up to the attainment of a central displacement equal to 11.7 mm (1.28% drift), corresponding to an 8.5 kN load no visible cracking due to OOP loading was observed. At this point some cracks appeared in the centre of the infill. At the attainment of peak load, equal to 10.5 kN for a central displacement of 32.0 mm (3.50% drift), diagonal cracks appeared at the infill's corners. The test ended at a central displacement equal to 81.2 mm (8.87% drift), corresponding to an OOP load equal to 3.3 kN and, so, to a load-bearing capacity reduction, with respect to peak load, about 69%. The post-peak behaviour was defined by a smooth softening branch. During the load-bearing capacity reduction, new diagonal cracks formed and opened along the specimen's diagonals. Also in this case, no significant OOP displacement was read by LVDTs along the infill's edges. A summary of the OOP test results is reported in Table 3.8. The evolution of the OOP cracking pattern for the specimen is reported in Figure 3.25.

A picture of the test specimen 80_IP+OOP_M at the end of the test is reported in Figure 3.26.

a) $F_{IP} = 62.2$ kN $d_{IP} = 1.26$ mm

IP peak load not reached

b) $F_{IP} = -$ $d_{IP} = -$

c) $F_{IP} = 102$ kN $d_{IP} = 7.30$ mm

Figure 3.24. Cracking pattern evolution during the IP test at first macro-cracking (a), peak load (b) and at the end of the test (c) for specimen 80_IP+OOP_M.

a) F_{OOP} =8.5 kN d_{OOP}=11.7 mm

b) F_{OOP} =10.5 kN d_{OOP}=0.3 mm

c) F_{OOP} =3.3 kN d_{OOP}=81.2 mm

Figure 3.25. Cracking pattern evolution during the OOP test at first macro-cracking (a), peak load (b) and at the end of the test (c) for specimen 80_IP+OOP_M.

Table 3.8. Summary of test 80_IP+OOP_M (IP IDR=0.37%) results.

	F_{crack}	d_{crack}	K_{crack}	F_{max}	d_{max}	K_{max}	d_{end}
specimen	[kN]	[mm]	[kN/mm]	[kN]	[mm]	[kN/mm]	[mm]
80_IP+OOP_M	8.5	11.7	0.73	10.5	32.0	0.33	81.2

Figure 3.26. Specimen 80_IP+OOP_M at the end of test.

3.4.3. Test 80_IP+OOP_H

An IP cyclic displacement history up to a nominal drift equal to 0.60% was applied to specimen 80_IP+OOP_H. The actual maximum IP displacement, due to the reaction cantilever beam slight deformability, was equal to 11.4 mm, corresponding to a 0.58% drift. The IP response diagram of specimen IP+OOP_H is reported in Figure 3.27a.

First cracks due to IP action formed at the infill's corner for a positive IP drift equal to 0.063%, at an IP load equal to 49.1 kN, and for a negative IP drift equal to 0.070%, corresponding to an IP load equal to 43.1 kN. The infilled frame attained its negative peak load equal to -95.6 kN for an IP displacement equal to 6.3 mm, during the 4th cycle, and its positive peak load equal to 112.3 kN at a displacement equal to 8.4 mm during the 5th loading cycle. Up to the attainment of the positive peak load, cracks formed and opened first along the infills diagonal, then in the infill's lower part. During the 5th loading cycle exterior tiles of the infill's brick along diagonals failed. During the 6th loading cycle some bricks in the central part of the specimen, along the lower bricks courses, collapsed and were expelled from the infill. The 6th loading cycle ended at a displacement equal to 11.4 mm, with an IP load ranging from 104.5 to 82.9 kN due to intra-cycle softening. Also in this case, the instrumentation read very small and absolutely negligible displacements of the foundation beam of the RC frame. The evolution of the IP cracking pattern for the specimen is reported in Figure 3.28.

Test specimen was IP unloaded and then monotonically loaded in the OOP direction.

The OOP force-central displacement behaviour diagram of specimen 80_IP+OOP_H is reported in Figure 3.27b.

<div align="center">(a)   (b)</div>
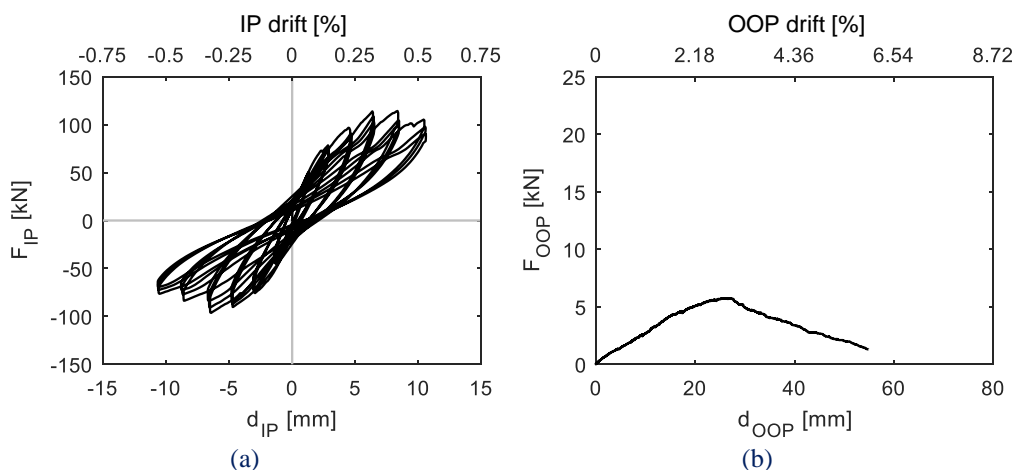
Figure 3.27. IP (a) and OOP (b) response of specimen 80_IP+OOP_H.

First visible cracks due to OOP loading appeared in the central part of the infill, near the RC frame columns, at a central displacement equal to 9.4 mm (1.03% drift), for an OOP load equal to 2.6 kN. Such cracks became wider up to the attainment of the infill's OOP strength equal to 5.9 kN at a central displacement equal to 25.8 mm (2.82% drift). During the softening response after peak load, new cracks appeared in the central and upper part of the infills, especially due to mortar detachment from bricks. The test was interrupted at an OOP load equal to 0.7 kN, corresponding to a displacement equal to 64.0 mm (6.99% drift). Also in this case, no significant OOP displacement was read by LVDTs along the infill's edges. A summary of the OOP test results is reported in Table 3.9. The evolution of the OOP cracking pattern for the specimen is reported in Figure 3.29.

A picture of the test specimen 80_IP+OOP_M at the end of the test is reported in Figure 3.30.

a) F_{IP} =49.1 kN d_{IP}=1.24 mm

b) F_{IP} = 112.3 kN d_{IP}= 8.4 mm

c) F_{IP} =105 kN d_{IP}=11.4 mm

Figure 3.28. Cracking pattern evolution during the IP test at first macro-cracking (a), peak load
(b) and at the end of the test (c) for specimen 80_IP+OOP_H.

a) F_{OOP} =2.6 kN d_{OOP}=9.4 mm

b) F_{OOP} =5.9 kN d_{OOP}=25.8 mm

c) F_{OOP} =0.7 kN d_{OOP}=64.0 mm

Figure 3.29. Cracking pattern evolution during the OOP test at first macro-cracking (a), peak load (b) and at the end of the test (c) for specimen 80_IP+OOP_H.

Table 3.9. Summary of test 80_IP+OOP_H (IP IDR=0.58%) results.

	F_{crack}	d_{crack}	K_{crack}	F_{max}	d_{max}	K_{max}	d_{end}
specimen	[kN]	[mm]	[kN/mm]	[kN]	[mm]	[kN/mm]	[mm]
80_IP+OOP_H	2.6	9.4	0.28	5.9	25.8	0.23	64.0
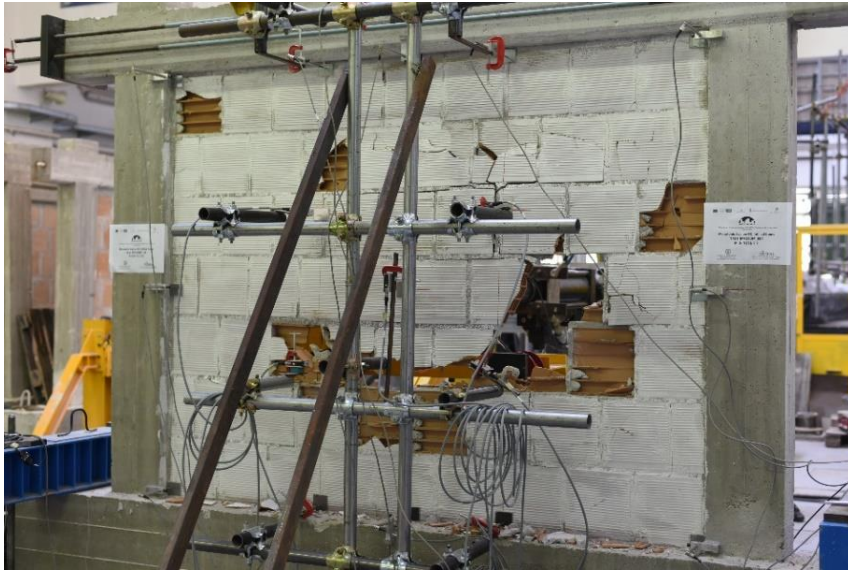
Figure 3.30. Specimen 80_IP+OOP_H at the end of test.

3.4.4. General considerations on the results of tests on the 80 mm thick infills

A comparison between the experimental IP and OOP force-displacement diagrams for the reference 80_OOP_4E specimen and the three IP+OOP tests above described is shown in Figures 3.31 and 3.32.

For what concerns the IP response (Figure 3.31), it is observed that the behaviour of the three specimens, that are equal for workmanship and nominal geometric and mechanical properties, is actually very similar, especially for positive loads/displacements. Specimens 80_IP+OOP_L and 80_IP+OOP_M were not tested up the attainment of the infilled frame strength, which was observed for specimen 80_IP+OOP_H and was roughly equal to 100 kN and was registered for an IP drift roughly equal to 0.4%. In addition, specimen 80_IP+OOP_H, which was tested up to the maximum IP drift, showed the beginning of the softening branch of the infill wall, as can be observed by the strength degradation after the attainment of peak load. The similar IP behaviour in terms of force-displacements diagrams is confirmed and supported by the evolution of damage in the specimens, which was very similar for all of them.. Namely, it seems that all specimens failed under IP loading for diagonal compression (Asteris et al., 2011), i.e., for exceeding compression stresses developing along diagonal directions in the central part of the infill.
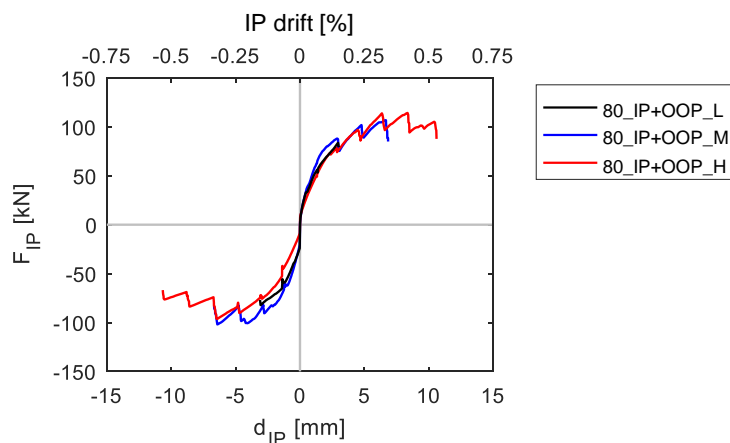
Figure 3.31. Comparison of the IP responses of the 80 mm thick infills.

For what concerns the OOP response of specimens (Figure 3.32), infill 80_IP+OOP_L exhibited an almost bilinear OOP behaviour, with a pseudo-linear response up to peak load and a steep softening branch up to the complete OOP resistance loss. A smother OOP response was observed for specimen 80_IP+OOP_M, with a sort of pseudo-plastic phase over the attainment of peak load, while a nearly bilinear response was again observed for specimen 80_IP+OOP_H. First, it is observed that specimen 80_IP+OOP_L, which was previously damaged at the lowest IP drift, exhibited an OOP strength (F_{max}) slightly greater than that exhibited by reference specimen 80_OOP_4E. This is quite unexpected but acceptable considering also the low IP drift imposed prior to the OOP test. Considering that the IP response of the specimen was not significantly different from that exhibited by specimens 80_IP+OOP_M and 80_IP+OOP_H, the slightly higher strength of specimen 80_IP+OOP_L is due, most likely, to experimental variability, which is typical of URM infills. Similar considerations can be extended to the secant stiffness at first macro-cracking, K_{crack}, of the same specimen. Except for these unexpected but acceptable results, secant stiffness at first macro-cracking and at peak load (K_{max}), as well as force at first macro-cracking (F_{crack}) and at peak load, decrease at increasing previously applied IP displacement, as expected. Moreover, all specimens seem to exhibit a similar softening negative stiffness and a reduced displacement capacity at increasing IP damage.
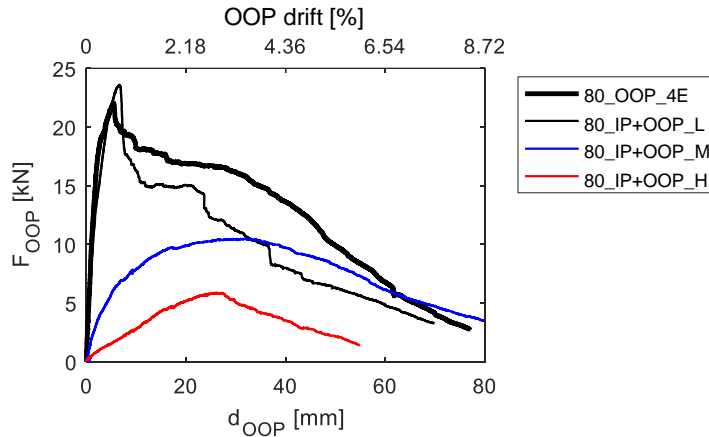
Figure 3.32. Comparison of the OOP responses of the 80 mm thick infills.

3.4.5. Test 120_IP+OOP_L

Test 120_IP+OOP_L was performed first by imposing to the specimen an IP cyclic displacement history up to the attainment of a maximum nominal drift equal to 0.30%. Due to the deformability of the test setup, the actual maximum IP drift attained by the specimen, read by the LVDT at the end of the frame's upper beam, was equal to 0.21%, corresponding to a maximum IP displacement equal to 4.13 mm and corresponding to a maximum load equal to 106.8 kN. The IP cyclic response of specimen 120_IP+OOP_L is reported in Figure 3.33a.

During the IP test no significant damage involved the specimen (Figure 3.33a), as only hairline cracks appeared at the interface with the upper beam. This occurred roughly in correspondence with the first significant non-linearity in the cyclic force-displacement diagram, which occurred for a positive drift equal to 0.083%, corresponding to a load equal to 71.0 kN and for a negative drift equal to 0.067%, corresponding to a load equal to 68.1 kN. Due to these cracks, the infill was detached from the upper beam, as confirmed during the OOP test. During the IP tests, no specimen's rigid translation was read by the instrumentation. The evolution of the IP cracking pattern for the specimen is reported in Figure 3.34.

The specimen was IP unloaded and then monotonically loaded in the OOP direction. The OOP force-central displacement behaviour diagram of specimen 120_IP+OOP_L is reported in Figure 3.33b.
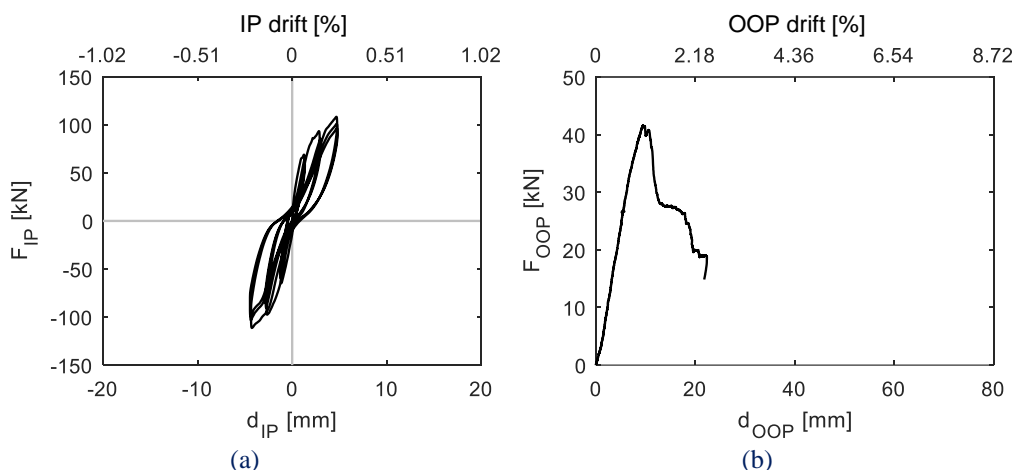
Figure 3.33. IP (a) and OOP (b) response of specimen 120_IP+OOP_L.

During the OOP test, the infill had a linear pseudo-elastic behaviour up to a central displacement equal to 2.8 mm (0.31% drift) and to an OOP load equal to around 1 kN. Then, a second linear pseudo-elastic phase with higher stiffness was observed. This occurred as during the first phase the infill wall slipped in the OOP direction along the upper edge, while the second phase begun when, due to the infill flexural deflection in the vertical direction, the upper edge came in contact with the upper beam and no more slippage occurred, allowing the formation of two-way arching action. This second linear pseudo-elastic phase ended at the attainment of peak load.

First horizontal cracks appeared in the upper part of the infill at the interface between bricks and mortar joints only at the attainment of the peak load (Figure 3.34b-c). The infill exhibited an OOP strength equal to 41.6 kN in correspondence of a central displacement equal to 9.7 mm (1.06% drift). Then, a steep softening branch was observed. In this phase, further horizontal cracks opened in the upper part of the infill, involving both bricks and the interface between mortar and bricks. The test was interrupted at a central displacement equal to 22 mm (2.40% drift), at which the OOP load was equal to 19 kN, with a reduction in the load-bearing capacity with respect to the OOP strength equal to 54%. At that point, the exterior tiles of the bricks in the upper part of the infill were failing and overturning. A summary of the OOP test results is reported in Table 3.10. The evolution of the OOP cracking pattern for the specimen is reported in Figure 3.35.

A picture of the test specimen 120_IP+OOP_L at the end of the test is reported in

Figure 3.36.

a)   F$_{IP}$ =69.6 kN   d$_{IP}$=1.47 mm

IP peak load not reached

b)   F$_{IP}$ = -   d$_{IP}$= -

c)   F$_{IP}$ =107 kN   d$_{IP}$=4.1 mm
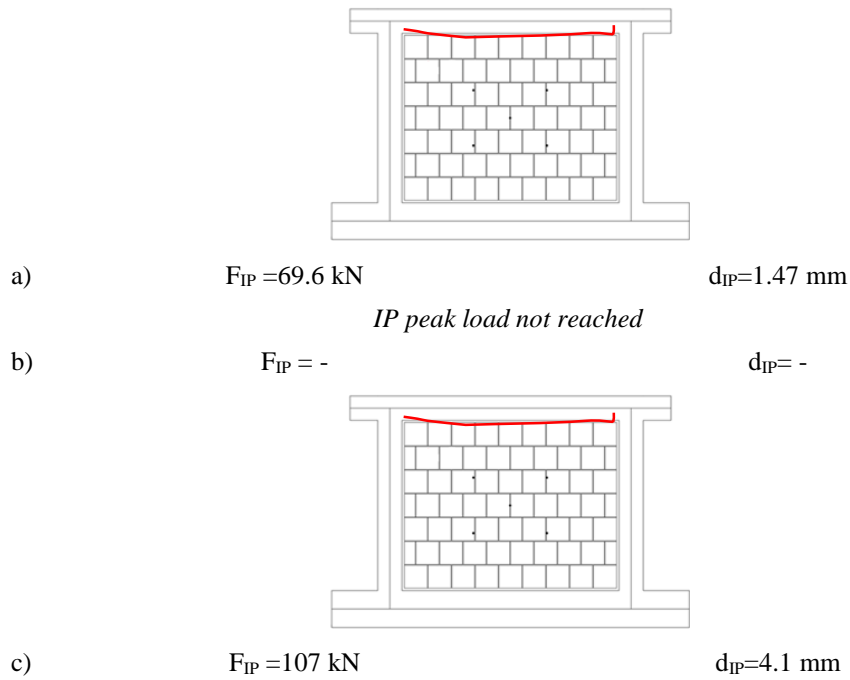
Figure 3.34. Cracking pattern evolution during the IP test at first macro-cracking (a), peak load
(b) and at the end of the test (c) for specimen 120_IP+OOP_L.

a) F_{OOP} =41.6 kN d_{OOP}=9.7 mm

b) F_{OOP} =41.6 kN d_{OOP}=9.7 mm

c) F_{OOP} =19.0 kN d_{OOP}=22.0 mm

Figure 3.35. Cracking pattern evolution during the OOP test at first macro-cracking (a), peak load (b) and at the end of the test (c) for specimen 120_IP+OOP_L.

Table 3.10. Summary of test 120_IP+OOP_L (IP IDR=0.21%) results.

	F_{crack}	d_{crack}	K_{crack}	F_{max}	d_{max}	K_{max}	d_{end}
specimen	[kN]	[mm]	[kN/mm]	[kN]	[mm]	[kN/mm]	[mm]
120_IP+OOP_L	41.6	9.7	4.3	41.6	9.7	4.3	22.0
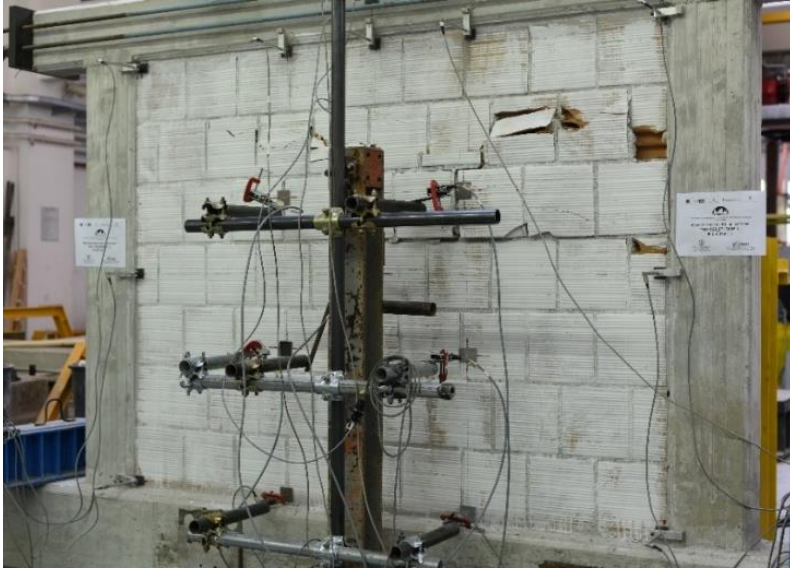
Figure 3.36. Specimen 120_IP+OOP_L at the end of test.

3.4.6. Test 120_IP+OOP_M

In this case, prior to the OOP loading, the specimen was subjected to an IP cyclic displacement history up to the attainment of a maximum nominal IP drift equal to 0.60%, corresponding to an actual maximum IP drift equal to 0.50%, i.e., to a maximum IP displacement equal to 9.7 mm corresponding to a maximum load equal to 120.4 kN. The IP force-displacement diagram of specimen 120_IP+OOP_M is reported in Figure 3.37a.

Also in this case, despite the quite high drift achieved, no significant damage occurred except from the formation of cracks at the interface with the upper beam. The formation of such cracks begun in correspondence of the first significant non-linearity in the IP force-displacement response, which was registered for a positive drift equal to 0.087%, with a load equal to around 100 kN, and for a negative drift equal to 0.073%, with a load equal to about 73 kN. During the following cycles, such cracks opened and damaged some of the exterior tiles of the upper bricks. In addition, at the attainment of the target displacement, further cracks appeared at the interface between the upper part of the infill and the left column of the RC frame. No significant IP translation of the RC frame was read by the LVTD at its base. The evolution of the IP cracking pattern for the specimen is reported in Figure 3.38.

The specimen was IP unloaded and then monotonically loaded in the OOP direction.

The OOP force-central displacement behaviour diagram of specimen 120_IP+OOP_M is reported in Figure 3.37b.

(a)   (b)
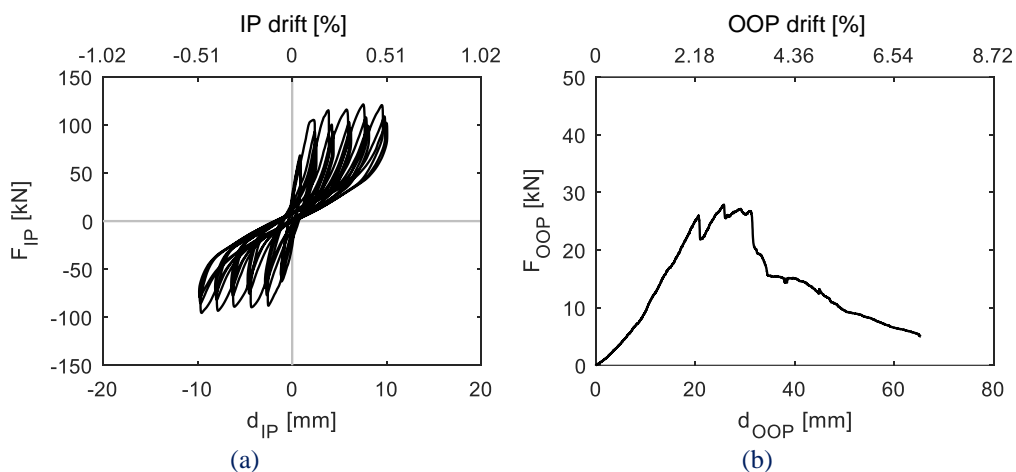
Figure 3.37. IP (a) and OOP (b) response of specimen 120_IP+OOP_M.

Also in this case, up to a central displacement equal to 10 mm (1.09% drift) and to a load equal to 8.9 kN, the infill slipped along the upper edge in the OOP direction. When the upper edge of the infill came in contact with the upper beam due to its vertical flexural deflection, an increase of the OOP stiffness was registered and two-way arching formed. At a central displacement equal to 21.1 mm (2.31% drift), for a load equal to 26.3 kN, a noticeable horizontal crack appeared in the upper part of the infill, along the almost entire interface between a course of bricks and the lower mortar joint. After that, the load dropped to 22.4 kN, with the formation of some diagonal cracks in the upper part of the infill. Then, the load increased up to the attainment of the OOP strength of the specimen, equal to 27.9 kN, at a central displacement equal to 26.3 mm (2.87% drift). During this phase, further horizontal and vertical cracks formed and opened in the upper part of the infill, in correspondence of the interface between bricks and mortar joints. Then, the load was pseudo-constant up to a displacement equal to 31.5 mm (3.44% drift), from which a steep softening branch begun leading the load to around 15 kN at a central OOP displacement equal to 36 mm (3.93% drift). During this phase, horizontal cracks damaging bricks' tiles formed and opened in the lower part of the infill. Then, a less steep softening branch was observed up to the end of the test, which was interrupted at a central displacement equal to 66 mm (7.21% drift) and at a load equal to 5.4 kN, with

a reduction of the load bearing capacity with respect to the infill OOP strength equal to 81%. During the last part of the test, horizontal cracks in the lower part of the infill widened and some exterior tiles of bricks failed. A summary of the OOP test results is reported in Table 3.11. The evolution of the OOP cracking pattern for the specimen is reported in Figure 3.39.

A picture of the test specimen 120_IP+OOP_M at the end of the test is reported in Figure 3.40.

a) F_{IP} =86.5 kN d_{IP}=1.57 mm

b) F_{IP} = 120.4 kN d_{IP}= 9.7 mm

c) F_{IP} = 120.4 kN d_{IP}= 9.7 mm
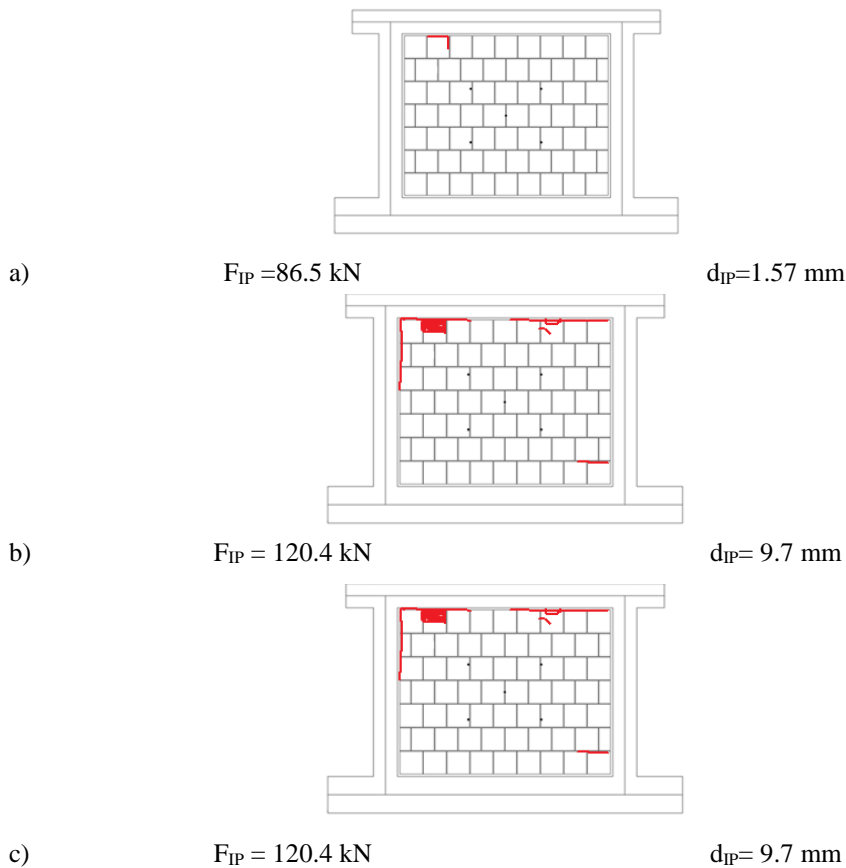
Figure 3.38. Cracking pattern evolution during the IP test at first macro-cracking (a), peak load (b) and at the end of the test (c) for specimen 120_IP+OOP_M.

a) F_{OOP} =26.3 kN d_{OOP}=21.1 mm

b) F_{OOP} =27.9 kN d_{OOP}=26.3 mm

c) F_{OOP} =5.4 kN d_{OOP}=66.0 mm
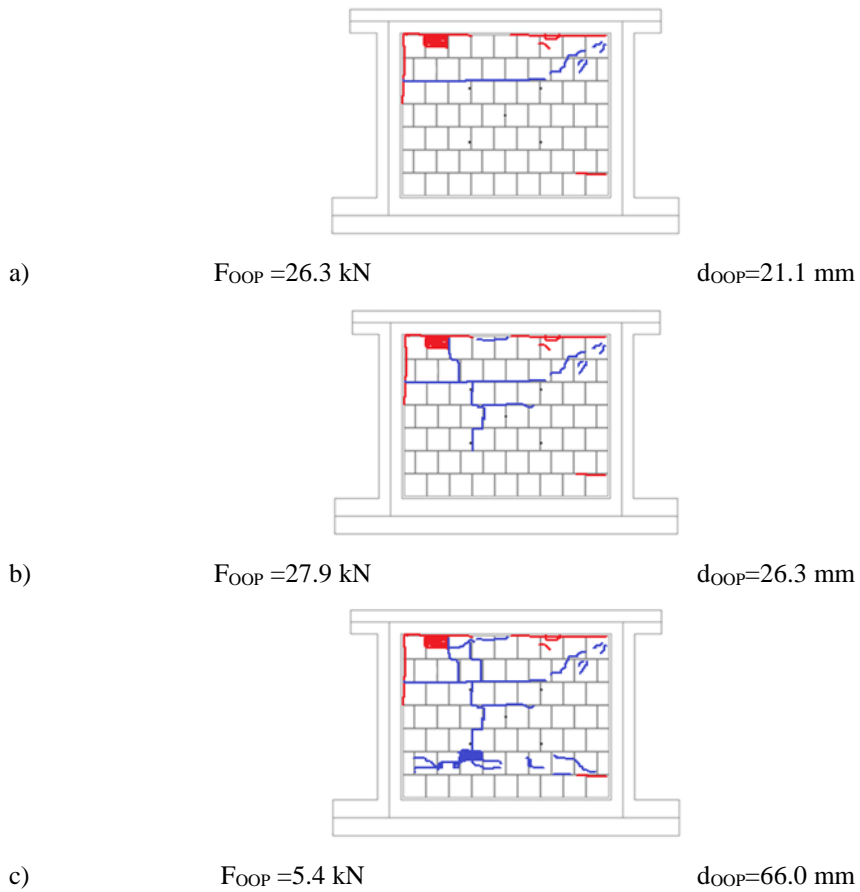
Figure 3.39. Cracking pattern evolution during the OOP test at first macro-cracking (a), peak load (b) and at the end of the test (c) for specimen 120_IP+OOP_M.

Table 3.11. Summary of test 120_IP+OOP_M (IP IDR=0.51%) results.

	F_{crack}	d_{crack}	K_{crack}	F_{max}	d_{max}	K_{max}	d_{end}
specimen	[kN]	[mm]	[kN/mm]	[kN]	[mm]	[kN/mm]	[mm]
120_IP+OOP_M	26.3	21.1	1.2	27.9	26.3	1.1	66.0
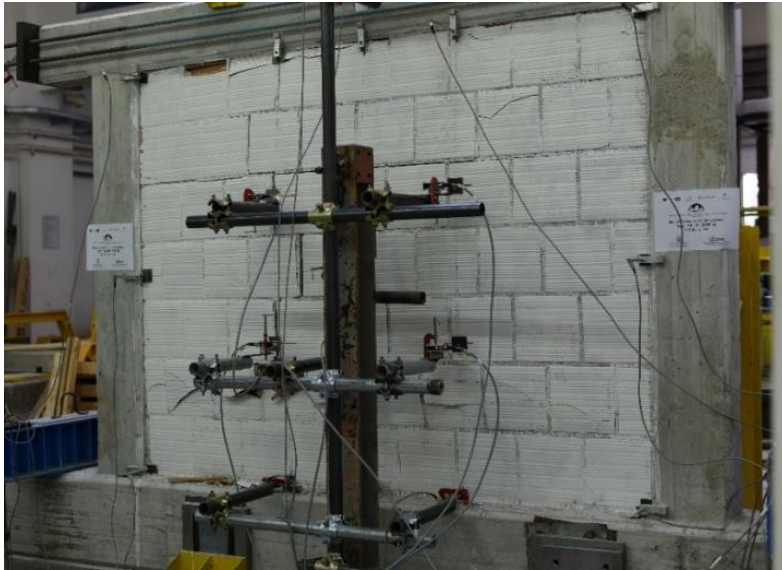
Figure 3.40. Specimen 120_IP+OOP_M at the end of test.

3.4.7. Test 120_IP+OOP_H

Specimen 120_IP+OOP_H was loaded in the IP direction through a cyclic displacement history up to a maximum nominal IP drift equal to 1.00%, corresponding to an actual IP drift equal to 0.89% and to a maximum IP displacement equal to 17.6 mm. The IP force-displacement diagram of specimen 120_IP+OOP_H is reported in Figure 3.41a.

The first horizontal crack in the infill formed between the right corner brick and the corresponding lower mortar joint. This occurred in correspondence of the first significant non-linearity in the IP force-displacement diagram, for a positive IP drift equal to 0.086% and for a load equal to 72 kN. The first significant non-linearity for negative loads occurred for a negative IP drift equal to 0.069% and for a load equal to 61 kN. From the 3rd to the 6th cycle, respectively carried out up to a nominal IP drift equal to 0.30% and 0.60%, the maximum IP positive load was constant and roughly equal to 100 kN, while the maximum IP negative load was constant and roughly equal to 93 kN. During this phase, the infill wall failed for crushing of the upper corner on the right. In addition, horizontal cracks at the interface between the infill and the upper beam occurred. As these cracks widened, some of the exterior tiles of the upper bricks failed and overturned. During the 7th and 8th loading cycle, respectively carried out up to a nominal IP drift equal to 0.80% and 1.00%, no significant crack appeared in the infill,

while pre-existing cracks where furtherly opening. During the last cycle, a maximum positive load equal to 116 kN and a maximum negative load equal to 119 kN where registered. Also in this case, the instrumentation did not show horizontal rigid translations of the RC specimen due to IP loading. The evolution of the IP cracking pattern for the specimen is reported in Figure 3.42.

The specimen was IP unloaded and then monotonically loaded in the OOP direction. The OOP force-central displacement behaviour diagram of specimen 120_IP+OOP_H is reported in Figure 3.41b.

(a)   (b)
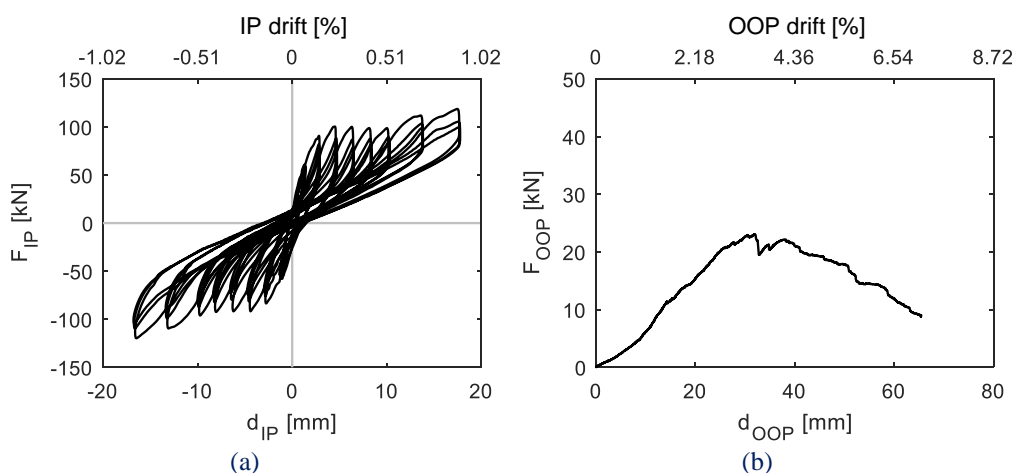
Figure 3.41. IP (a) and OOP (b) response of specimen 120_IP+OOP_H.

As for the other IP-damaged specimens, also in this case the infill slipped along the upper edge in the OOP direction up to a central displacement equal to 8 mm (0.87% drift), corresponding to a load equal to 4.3 kN. Then, an increase in the OOP stiffness was observed when slippage stopped and two-way arching occurred. First horizontal cracks due to OOP loading appeared at the interface between bricks and mortar in the upper part of the infill for a central displacement equal to 14.2 mm (1.55% drift) and for a load equal to 11.2 kN. The OOP strength of the specimen, which was equal to 23.1 kN, was reached for a central displacement equal to 31.7 mm (3.46% drift). Up to this load, further horizontal cracks appeared at the interface between bricks and mortar in the upper part of the infill, together with sub-vertical cracks in the central part of the specimen. After a little drop in the OOP load-bearing capacity, load increased again and reached 22.1 kN at a central displacement equal to 38.1 mm (4.16% drift). Then, a

softening branch was observed up to the end of the test, which was interrupted at a central displacement equal to 65 mm (7.10% drift) and at a load equal to 9.1 kN, with a reduction in the load-bearing capacity with respect to the specimen OOP strength equal to 60%. After the attainment of peak load, no further significant crack formed, while existing cracks opened and widened. A summary of the OOP test results is reported in Table 3.12. The evolution of the OOP cracking pattern for the specimen is reported in Figure 3.43.

A picture of the test specimen 120_IP+OOP_H at the end of the test is reported in Figure 3.44.

a) $F_{IP} = 66.5$ kN $d_{IP} = 1.53$ mm

b) $F_{IP} = 119$ kN $d_{IP} = 17.6$ mm

c) $F_{IP} = 119$ kN $d_{IP} = 17.6$ mm
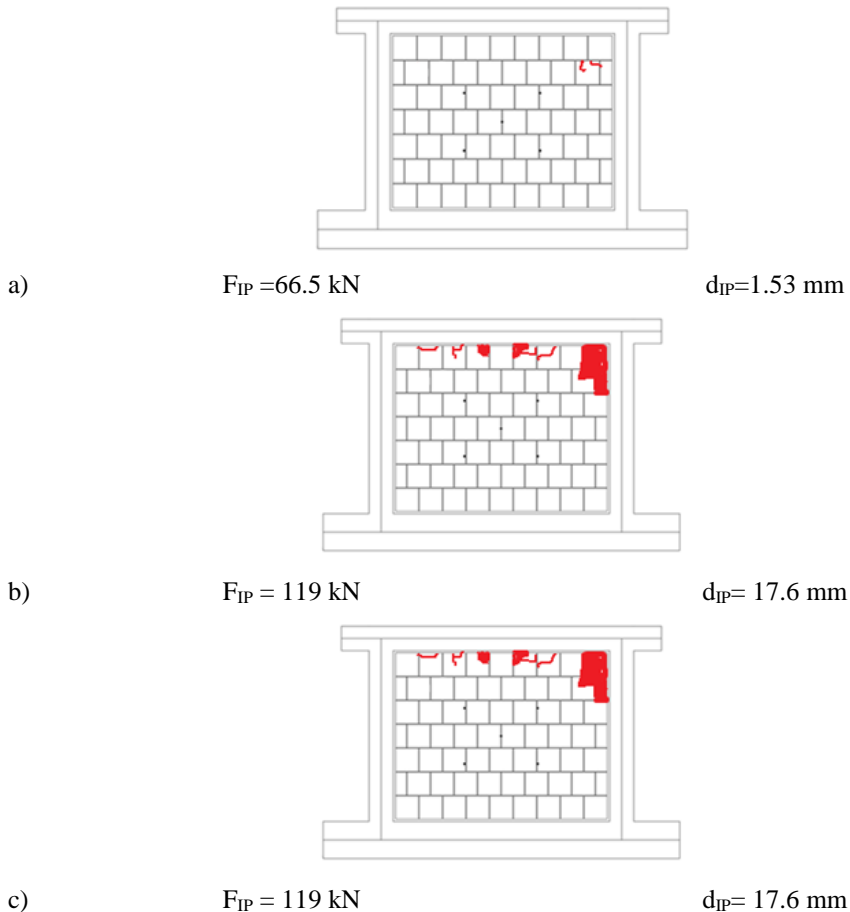
Figure 3.42. Cracking pattern evolution during the IP test at first macro-cracking (a), peak load (b) and at the end of the test (c) for specimen 120_IP+OOP_H.

a) F_{OOP} =11.2 kN d_{OOP}=14.2 mm

b) F_{OOP} =23.1 kN d_{OOP}=31.7 mm

c) F_{OOP} =9.1 kN d_{OOP}=65.0 mm
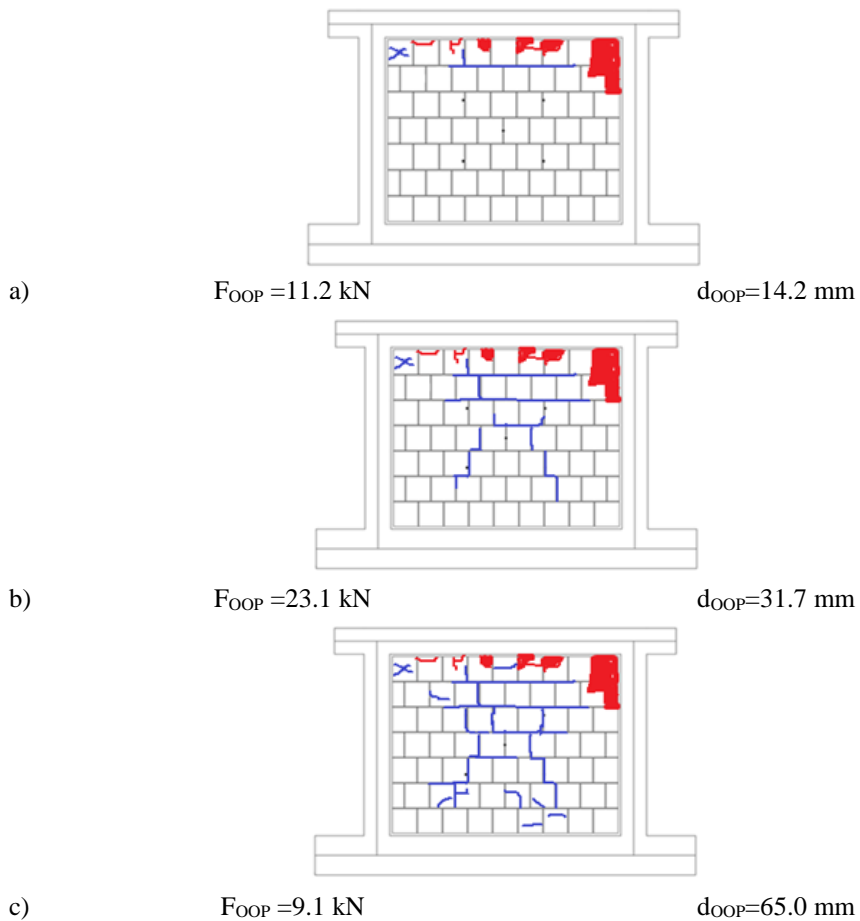
Figure 3.43. Cracking pattern evolution during the OOP test at first macro-cracking (a), peak load (b) and at the end of the test (c) for specimen 120_IP+OOP_H.

Table 3.12. Summary of test 120_IP+OOP_H (IP IDR=0.89%) results.

	F_{crack}	d_{crack}	K_{crack}	F_{max}	d_{max}	K_{max}	d_{end}
specimen	[kN]	[mm]	[kN/mm]	[kN]	[mm]	[kN/mm]	[mm]
120_IP+OOP_H	11.2	14.2	0.79	23.1	31.7	0.73	65.0
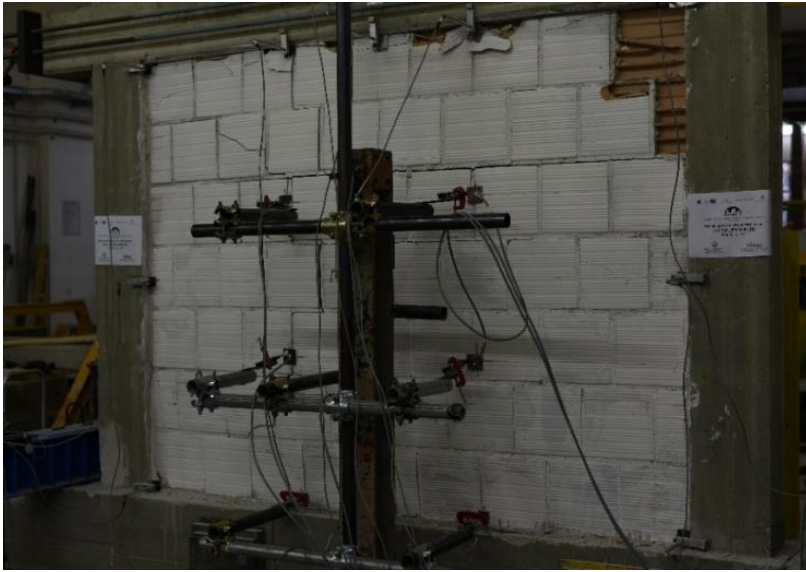
Figure 3.44. Specimen 120_IP+OOP_H at the end of test.

3.4.8. General considerations on the results of tests on the 120 mm thick infills

A comparison between the experimental IP and OOP force-displacement diagrams for the reference 120_OOP_4E specimen and the three IP+OOP tests above described is shown in Figures 3.45 and 3.46.

The IP behaviour of specimens 120_IP+OOP_L, 120_IP+OOP_M and 120_IP+OOP_H was similar in terms of force-displacement response and failure mode (Figure 3.45). In fact, all the specimens showed an almost equal initial stiffness and, when attained, an almost equal strength roughly equal to 120 kN. As already stated, the similarity in the force-displacement response is associated with a similarity in the failure mode of specimens, that was a sliding shear failure at the interface between the infill and the RC frame upper beam for all of them, together with a corner crushing for specimen 120_IP+OOP_H (Asteris et al., 2011).
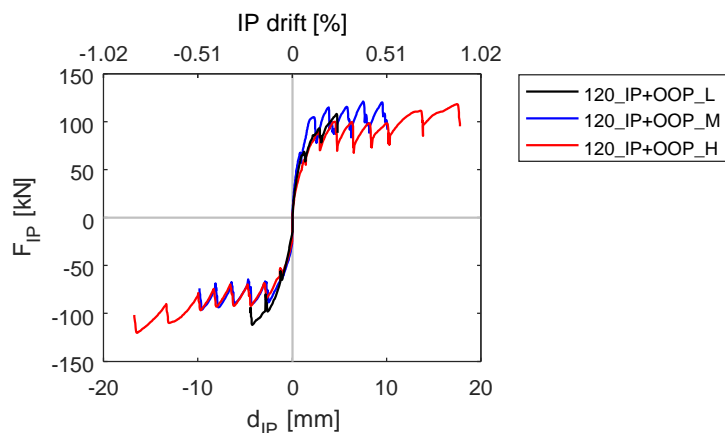
Figure 3.45. Comparison of the IP responses of the 120 mm thick infills.

For what concerns the OOP response (Figure 3.46), the reference IP-undamaged specimen 120_OOP_4E showed a force-displacement response similar to that observed for the 80 mm-thick reference specimen 80_OOP_4E, even if with higher stiffness and strength, of course. For what concerns combined IP and OOP tests, differently from the 80 mm-thick infills, all the tests carried out on the 120 mm-thick infills showed a certain slippage of the infill along the upper edge as this edge was detached from the upper beam due to IP actions. This was confirmed by the instruments placed along the infill upper edge. Namely, LVDT C1 (see the instruments' layout in Figure 3.8), read a maximum OOP displacement equal to around 0 for specimen 120_OOP_4E (no slippage) and equal to around 0.6 mm, 7 mm and 5 mm for specimens 120_IP+OOP_L, 120_IP+OOP_M and 120_IP+OOP_H, respectively.

The specimen subjected to the lowest IP drift prior to the OOP test, 120_IP+OOP_L, exhibited a very steep and quite unexpected post-peak behaviour. However, at least up to the attainment of the maximum load, its behaviour was not different from the OOP response of the corresponding 80 mm-thick specimen, which showed a reduced initial stiffness but an unvaried strength with respect to the reference IP-undamaged specimen. This confirms the existence of a sort of "critical" IP drift, as already intuited by Angel et al., from which the OOP strength begins reducing, while it is not varied before. As will be shown in section 7, the statistical regression of the experimental data – from this and from other literature works – shows that such a "critical" drift depends on the infill slenderness and that it is lower for slender infills, as intuitively expected. Clearly, as already observed for the tests on the 80 mm-thick infills, the OOP strength and stiffness

reduces at increasing previously-applied IP maximum drift, with the minimum strength and stiffness observed for specimen 120_IP+OOP_H. Only the first cracking load for specimen 120_IP+OOP_L was higher than that observed for the reference IP-undamaged specimen, most likely due to experimental variability.

A quite uncertain behaviour is observed for all specimens on the post-peak branch, with no clear relationship of its slope with the amount of IP damage previously achieved.
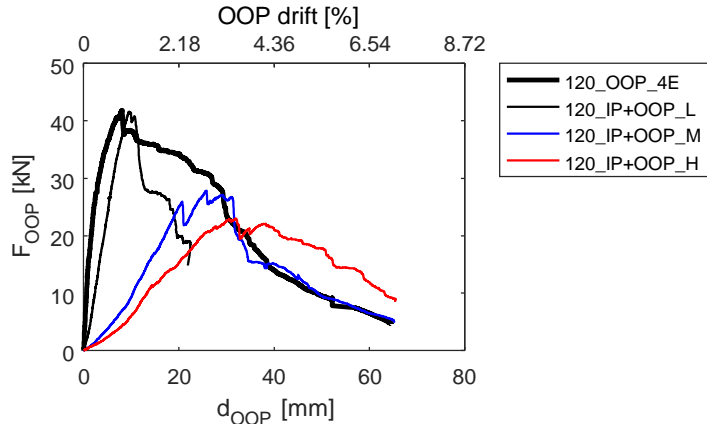
Figure 3.46. Comparison of the OOP responses of the 120 mm thick infills.

3.5 OOP TESTS ON INFILLS WITH DIFFERENT BOUNDARY CONDITIONS

This section is dedicated to the description and discussion of the experimental tests carried out on infills mortared along three (3E specimens) or two (2E infills) to the confining RC frames.

These tests have been carried out to assess the influence of different boundary conditions on the OOP response of URM infills. First of all, this yields to the occurrence of one-way horizontal arching in 3E specimens, of one-way vertical arching in 2E specimens. Clearly, the results of these tests are compared with those obtained for the reference tests on infills mortared along all edges to the confining structural elements, in which two-way arching (both vertical and horizontal) occurs.

For what concerns 80 mm thick infills, three tests are presented. Note that these infills were provided of a gap with respect to the confining RC elements equal to 2 mm, except for specimen 80_OOP_3Eb, for which the gap between the infill and the RC upper beam was equal to 40 mm. Test 80_OOP_3E was performed on an infill bounded along three

edges to the confining frame elements; however, during the tests, the upper edge of the infill came in contact with the upper RC beam: hence, two-way arching occurred. For this reason, the test was repeated to assess the OOP behaviour of a nominally identical specimen in which only one-way horizontal arching occurred. This test is named 80_OOP_3Eb. Also the results of this test are presented and discussed. Test 80_OOP_2E was performed on an infill in which only the upper and the lower edges were mortared to the confining frame elements. In this infill, only one-way vertical arching occurred.

For what concerns 120 mm thick infills, two tests are presented. Note that these infills were provided of a gap with respect to the confining RC elements equal to 40 mm (test 120_OOP_3E) or to 30 mm (test 120_OOP_2E). Test 120_OOP_3E was performed on an infill bounded along three edges to the confining frame elements in which only one-way horizontal arching occurred. Test 120_OOP_2E was performed on an infill in which only the upper and the lower edges were mortared to the confining frame elements. In this infill, only one-way vertical arching occurred.

A summary of the tests presented in this section is reported in Table 3.13.

Table 3.13. Summary of the OOP tests on infills with different boundary conditions.

test	details
80_OOP_3E	detached from the RC upper beam, two-way arching
80_OOP_3Eb	detached from the RC upper beam, one-way horizontal arching
80_OOP_2E	detached from the RC columns, one-way vertical arching
120_OOP_3E	detached from the RC upper beam, one-way horizontal arching
120_OOP_2E	detached from the RC columns, one-way vertical arching

The experimental tests are described with the support of the OOP force-central displacement (or drift, with OOP drift defined as the OOP central displacement of the infill divided by one-half of the infill height) diagrams and with the representation of the evolution of cracking patterns during the tests. Further details are reported in Appendices B-C.

3.5.1. Test 80_OOP_3E

The infill wall is realized with a 2 mm gap with respect to the upper beam. The OOP force-infill's centre displacement diagram obtained for specimen 80_OOP_3E specimen is shown in Figure 3.47. Also in this case, micro-cracks formation was announced by cracking noises since the test beginning. First vertical cracking occurred in the upper

part of the infill, at a central displacement equal to 5.5 mm, corresponding to a 12.3 kN load, as shown in Figure 3.48, in which the evolution of cracking pattern during the test is reported. This vertical hairline crack is consistent with the expected cracking pattern and failure mode for an infill bounded along three edges in which only horizontal arching can occur as reported, e.g., by Dawe and Seah (1989). However, immediately after first macro-cracking, the upper edge of the infill made contact with the upper beam, which prevented further OOP free displacements at that edge. This is demonstrated in the evolution of the deformed shape along vertical and horizontal alignments reported in Figure 3.49, as well as by the diagonal cracks that appeared in the infill up to the attainment of the infill resistance, and by the tangent stiffness increase registered immediately after first macro-cracking visible in Figure 3.47. So, soon after first macro-cracking, the OOP_3E specimen begun behaving as a 4E specimen, with the occurrence of vertical arching. The OOP strength of the infill was equal to 17.6 kN and corresponded to a central displacement equal to 14.6 mm. After the attainment of peak load, the infill resistance decreased up to 11.4 kN at a displacement equal to 21.8 mm. During this phase, noticeable horizontal cracks in the lower part of the infill appeared. As occurred during Test OOP_4E, a pseudo-plastic phase in the OOP response of the infill was observed up to a displacement of 34.6 mm, with new vertical and horizontal cracks opening in the central part of the infill. After that, a softening branch in the OOP response diagram was observed, with the enlargement of pre-existing cracks. The test ended at a displacement equal to 58.4 mm, corresponding to a load equal to 6.5 kN, i.e., a resistance loss of the infill equal to 63%. At this point, exterior tiles of brick in the lower part of the infill were crushing and overturning. During the test, no detachment of the infill from the surrounding frame was read by LVDTs and no significant displacement was registered in the OOP direction for the foundation and upper beams of the RC frame. A summary of test results is reported in Table 3.14.

Based on the cracking pattern reported in Figure 3.48 and on the evolution of the profile of OOP displacements reported in Figure 3.49, it seems reasonable to assume that the deformed shape of the panel evolved during the test according to a hipped deformed shape. A picture of the specimen at the end of the test is reported in Figure 3.40.
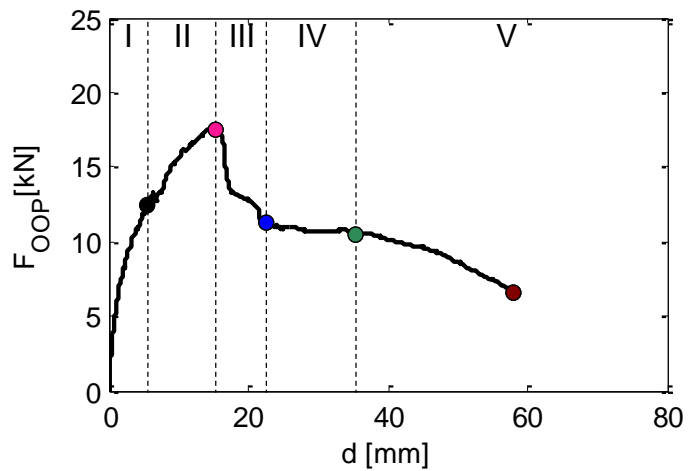
Figure 3.47. OOP force vs infill's central displacement for specimen 80_OOP_3E.

Table 3.14. Summary of test 80_OOP_3E results.

	F_{crack}	d_{crack}	K_{crack}	F_{max}	d_{max}	K_{max}	d_{end}
specimen	[kN]	[mm]	[kN/mm]	[kN]	[mm]	[kN/mm]	[mm]
80_OOP_3E	12.3	5.5	2.2	17.6	14.6	1.2	58.4

a) F_{OOP} =12.3 kN d_{OOP}=5.5 mm

b) F_{OOP} =17.6 kN d_{OOP}=14.6 mm

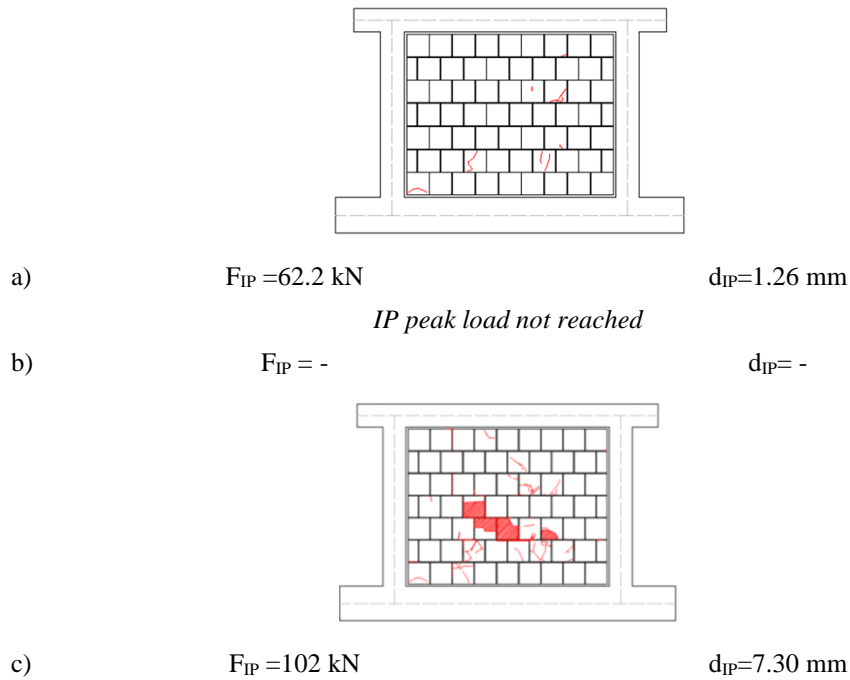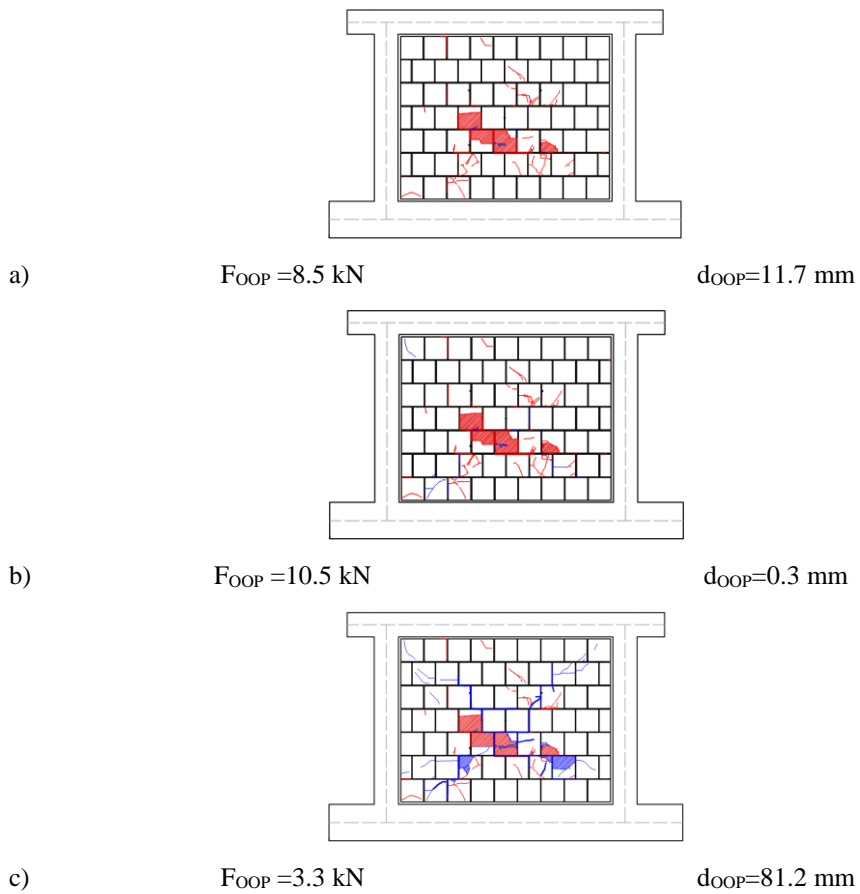c) F_{OOP} =6.5 kN d_{OOP}=58.4 mm
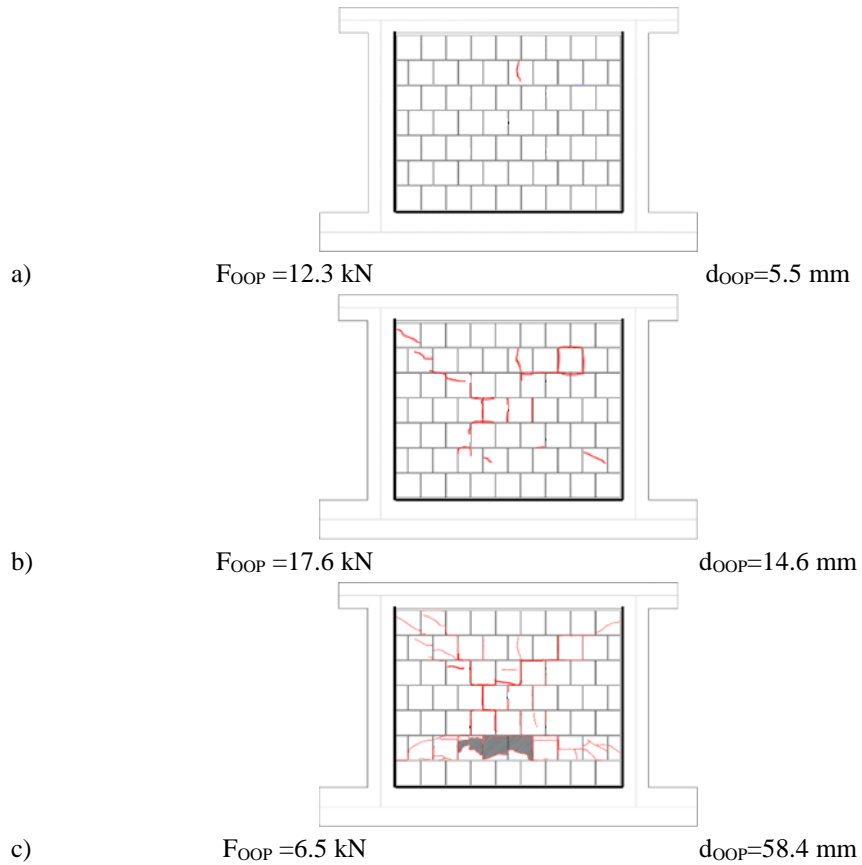
Figure 3.48. Cracking pattern evolution at first macro-cracking (a), peak load (b) and at the end of the test (c) for specimen 80_OOP_3E.
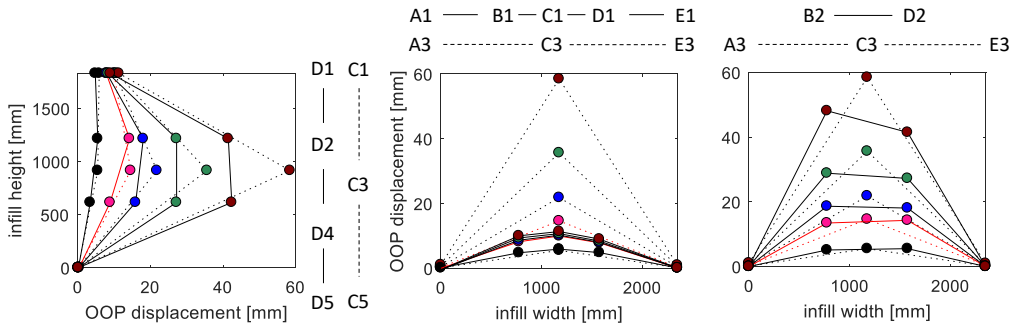
Figure 3.49. Deformed shape evolution along vertical and horizontal alignments (see the instruments' layout in Figure 3.8) for specimen 80_OOP_3E at the end of each one of the five phases individuated in Figure 3.47. The deformed shape corresponding to the attainment of peak load is highlighted with a red line.
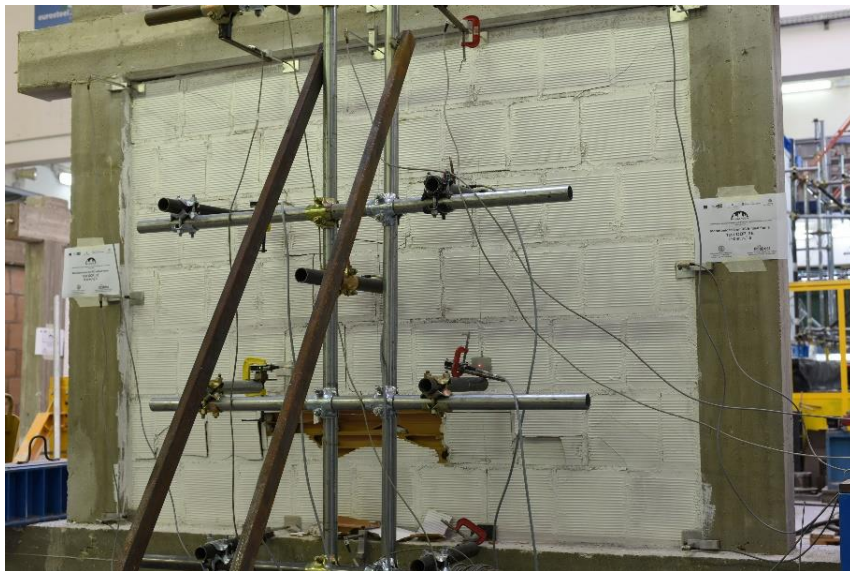
Figure 3.50. Specimen 80_OOP_3E at the end of test.

3.5.2. Test 80_OOP_3Eb

In this case, the infill wall was provided of a 40 mm gap from the RC upper beam. The OOP force-central displacement diagram is shown in Figure 3.51.

The OOP behaviour of the specimen was characterized by five phases, as shown in Figure 3.51. First, the infill wall behaved as linear elastic up to the first non-linearity in

the force-displacement diagram, which occurred for an OOP central displacement equal to around 2.5 mm and for a force equal to around 8.5 kN. However, during this phase, no visible damage was observed. Then, a second roughly linear, but with reduced tangent stiffness, phase begun. This second phase ended at a central OOP displacement equal to 14.8 mm, corresponding to a load equal to 18.2 kN, at which the first visible vertical cracks formed in the central upper part of the infill. After that, a non-linear behaviour was registered over the attainment of the peak load, which was equal to 18.4 kN and was registered at an OOP displacement equal to 20 mm. The first smooth softening branch was registered up to a central displacement equal to 34 mm, corresponding to an OOP force equal to 15 kN. During this phase, further vertical and horizontal cracks appeared in the central and upper part of the infill. A second linear softening branch was registered up to the end of the test. During this phase, further vertical cracks at the interface between mortar and bricks appeared in the lower part of the infill. The test ended at a central displacement equal to 65 mm and at an OOP force equal to 4.6 kN, corresponding to a reduction of the OOP load bearing capacity of the infill with respect to its strength equal to -75%. During the test, no significant displacement was registered in the OOP direction for the foundation and upper beams of the RC frame. A summary of test results is reported in Table 3.15.

The evolution of cracking pattern in the specimen is reported in Figure 3.52. Based on the OOP displacements read by instruments, the evolution of the reconstructed deformed shape of the specimen is shown in Figure 3.53. A picture of the specimen at the end of the test is reported in Figure 3.54.
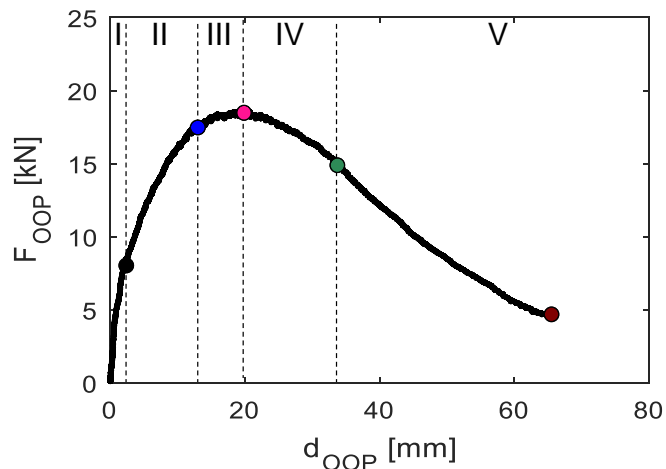
Figure 3.51. OOP force vs infill's central displacement for specimen 80_OOP_3Eb.

Table 3.15. Summary of test 80_OOP_3Eb results.

specimen	F_{crack} [kN]	d_{crack} [mm]	K_{crack} [kN/mm]	F_{max} [kN]	d_{max} [mm]	K_{max} [kN/mm]	d_{end} [mm]
80_OOP_3Eb	8.5	2.5	3.4	18.4	20.0	0.92	65.0

a) $F_{OOP} = 8.5$ kN $d_{OOP} = 2.5$ mm

b) $F_{OOP} = 18.4$ kN $d_{OOP} = 20.0$ mm
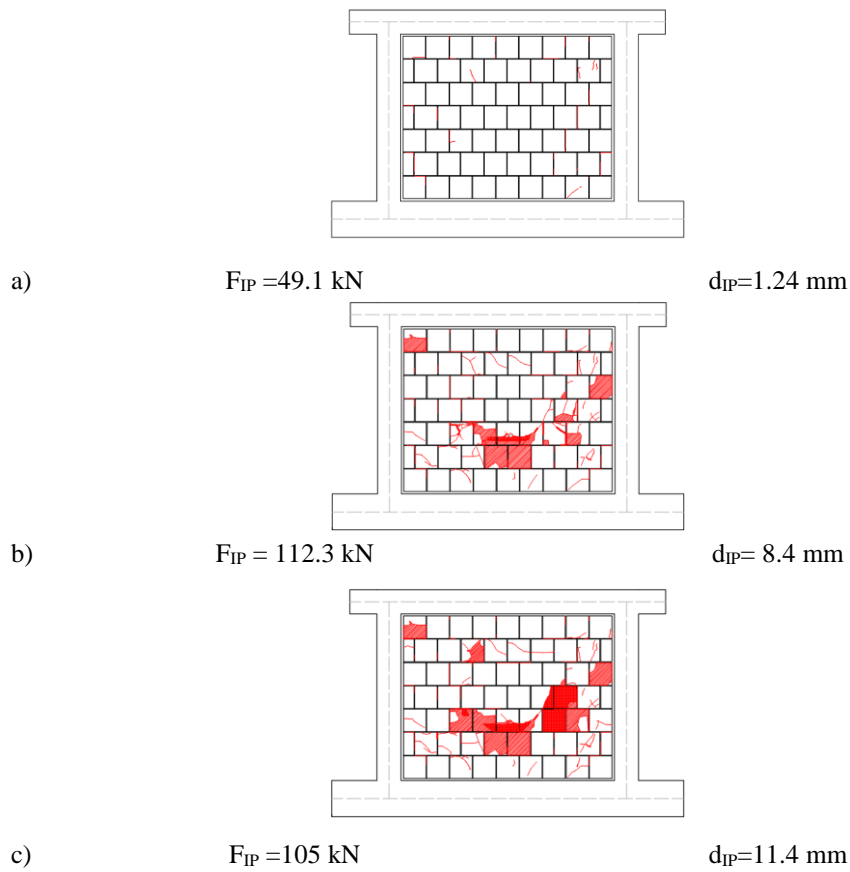

c) $F_{OOP} = 4.6$ kN $d_{OOP} = 65.0$ mm
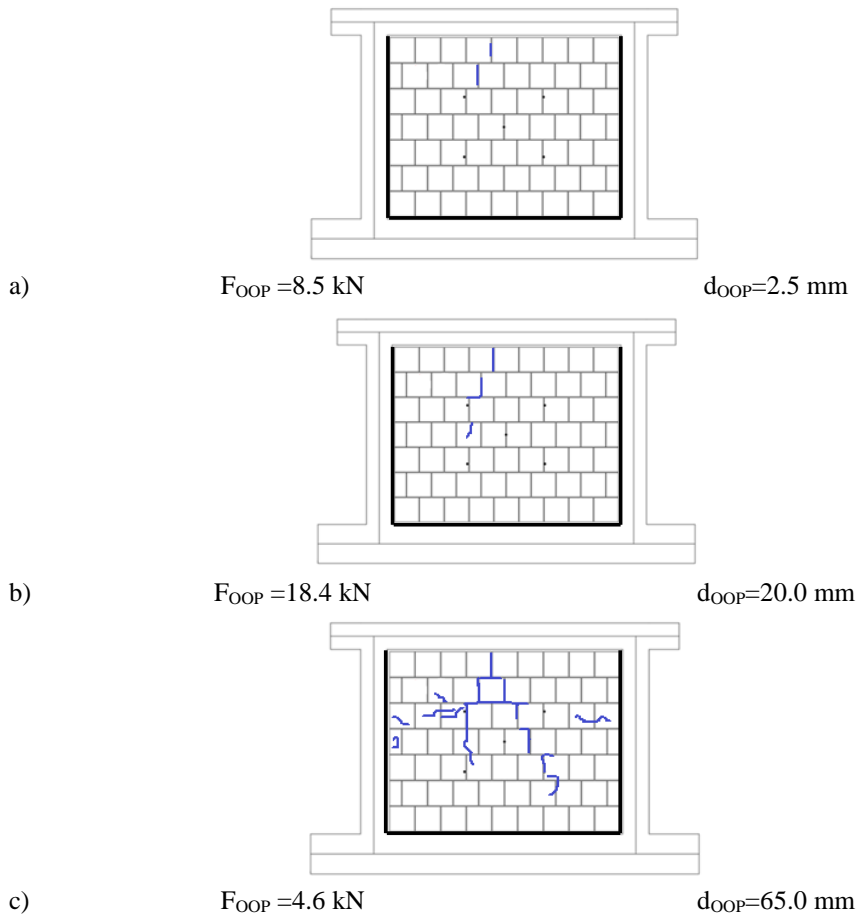
Figure 3.52. Cracking pattern evolution at first macro-cracking (a), peak load (b) and at the end of the test (c) for specimen 80_OOP_3Eb.
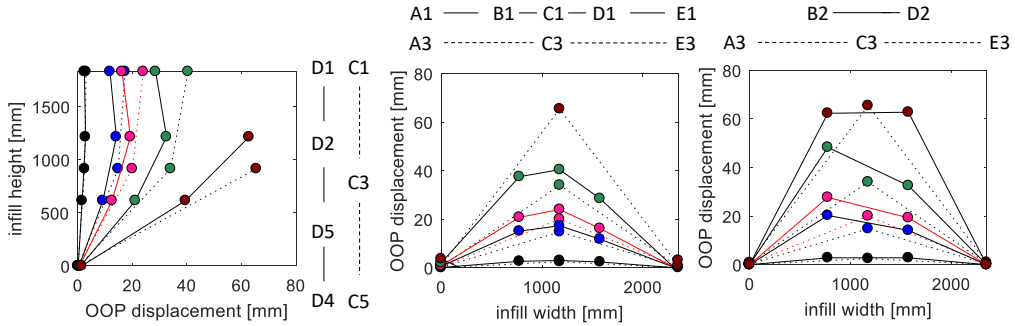
Figure 3.53. Deformed shape evolution along vertical and horizontal alignments (see the instruments' layout in Figure 3.8) for specimen 80_OOP_3Eb at the end of each one of the five phases individuated in Figure 3.51. The deformed shape corresponding to the attainment of peak load is highlighted with a red line. Some readings are missing as some instruments reached the end of their measuring range.
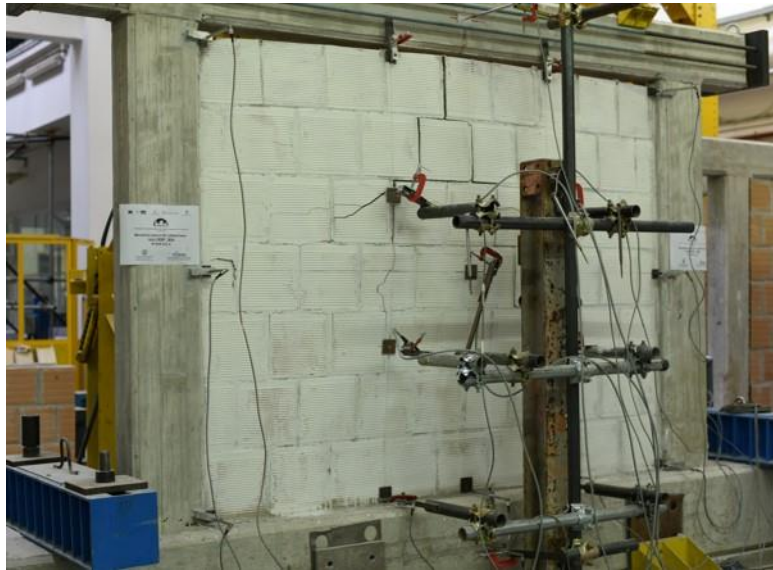
Figure 3.54. Specimen 80_OOP_3Eb at the end of test.

3.5.3. Test 80_OOP_2E

The OOP force-infill's centre displacement diagram obtained for specimen 80_OOP_2E is shown in Figure 3.55. First diagonal cracking occurred in the upper part of the infill, near to its mid-height, at a central displacement equal to 6.9 mm,

corresponding to a 12.9 kN load, as shown in Figure 3.56, in which the evolution of cracking pattern is reported. Diagonal cracks in the upper part of the infill appeared until the attainment of the infill resistance, equal to 14.6 kN, corresponding to a central displacement equal to 17 mm. At this point, a new horizontal crack between a mortar and a brick horizontal course appeared, in the upper part of the infill, near mid-height. After the attainment of peak load, at a central displacement equal to 18.7 mm, the infill resistance suddenly dropped from 13.9 to 4.1 kN, with a load bearing capacity reduction of 72%. During the test, no detachment of the infill from the surrounding frame was read by LVDTs and no significant displacement was registered in the OOP direction for the foundation and upper beams of the RC frame. A summary of test results is reported in Table 3.16.

Based on the OOP displacements read by instruments, the evolution of the reconstructed deformed shape of the specimen is shown in Figure 3.57. A picture of the specimen at the end of the test is reported in Figure 3.58, with a detail of the crack at the infill centre shown in Figure 3.59.
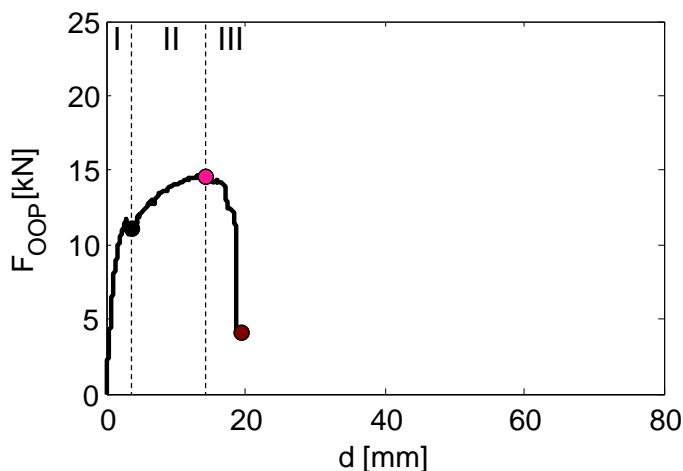
Figure 3.55. OOP force vs infill's central displacement for specimen 80_OOP_2E.

Table 3.16. Summary of test 80_OOP_2E results.

	F_{crack}	d_{crack}	K_{crack}	F_{max}	d_{max}	K_{max}	d_{end}
specimen	[kN]	[mm]	[kN/mm]	[kN]	[mm]	[kN/mm]	[mm]
80_OOP_2E	12.9	6.9	1.9	14.6	17.0	0.86	18.7

a) F_{OOP} =12.9 kN d_{OOP}=6.9 mm

b) F_{OOP} =14.6 kN d_{OOP}=17.0 mm

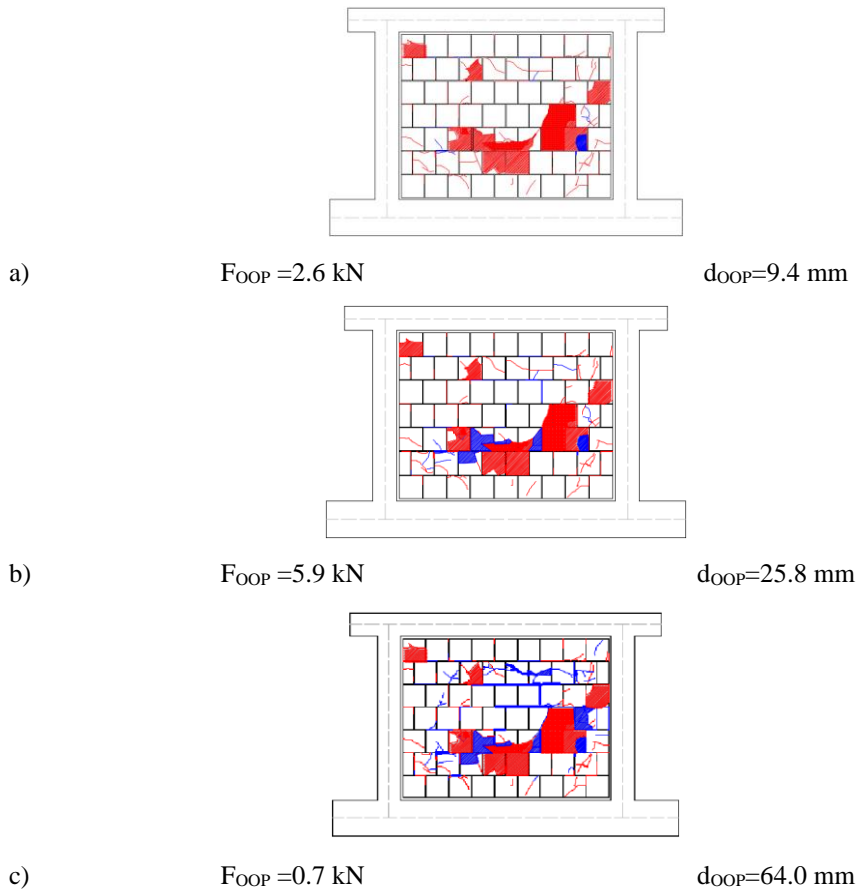c) F_{OOP} =4.1 kN d_{OOP}=18.7 mm
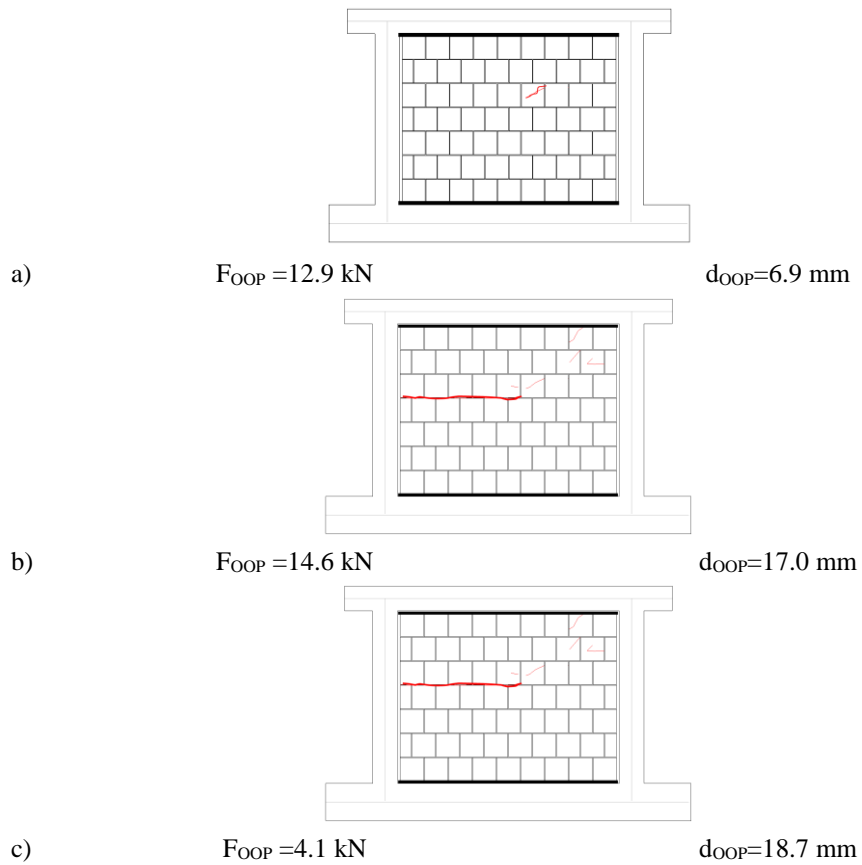
Figure 3.56. Cracking pattern evolution at first macro-cracking (a), peak load (b) and at the end of the test (c) for specimen 80_OOP_2E.
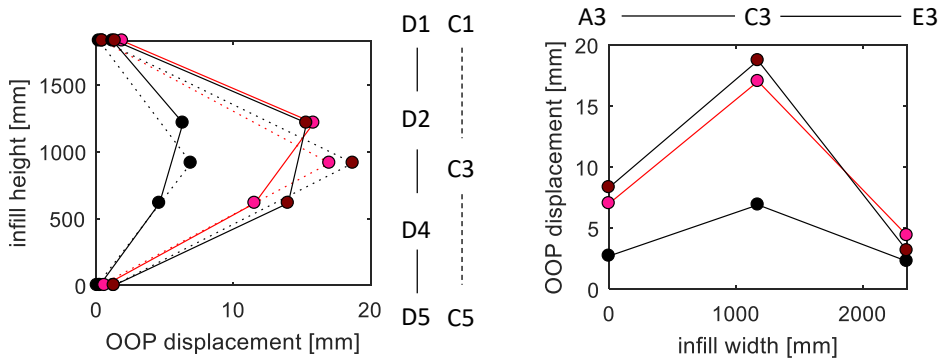
Figure 3.57. Deformed shape evolution along vertical and horizontal alignments (see the instruments' layout in Figure 3.8) for specimen 80_OOP_2E at the end of each one of the three phases individuated in Figure 3.55. The deformed shape corresponding to the attainment of peak load is highlighted with a red line.
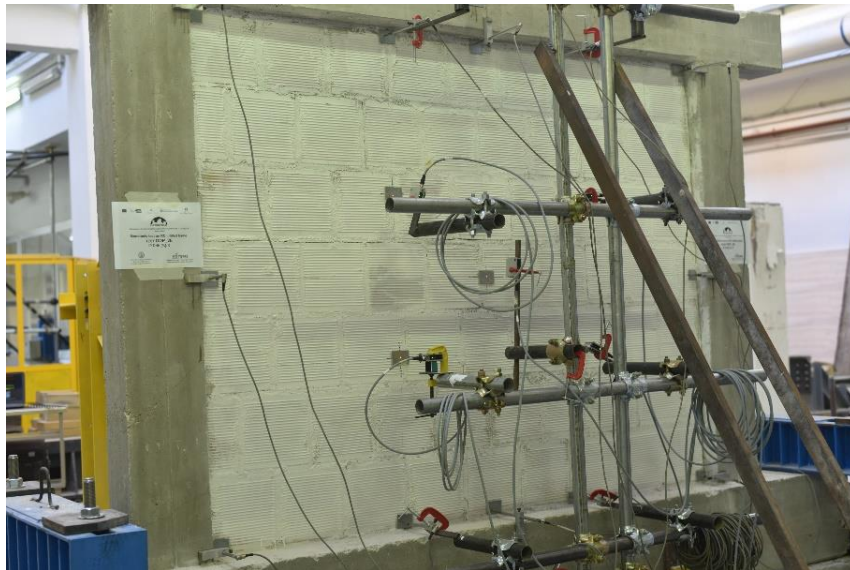
Figure 3.58. Specimen 80_OOP_2E at the end of test.

Figure 3.59. Detail of specimen 80_OOP_2E at the end of test.

3.5.4. Test 120_OOP_3E

The infill wall was provided of a 40 mm gap from the RC upper beam. The OOP force-central displacement diagram is shown in Figure 3.60.

The infill showed since the beginning of the test a clear non-linear behaviour, similarly to specimen 80_OOP_3Eb. First cracking occurred with the formation of a vertical crack at the center of the infill upper part. First cracking load was equal to 19.5 kN and was attained at a central displacement equal to 4.3 mm. The infill exhibited an OOP strength equal to 33.6 kN. This load was attained for a central displacement equal to 16.4 mm. A rapid evolution of the cracking patter was observed from a displacement equal to 11.5 mm up to the attainment of the peak load displacement, with the formation of further vertical cracks and then of a horizontal crack in the center of the upper part of the infill as well as of hairline diagonal cracks in the infill lower corners. Unfortunately, due to a technical problem, the test was interrupted at a central displacement equal to 28 mm, corresponding to a 22.5 kN load. During this third and last part of the test, further hairline diagonal cracks formed and opened in both the central and the lower part of the infill. During the test, no significant displacement was registered in the OOP direction for the foundation and upper beams of the RC frame. A summary of test results is reported in Table 3.17.

The evolution of cracking pattern in the specimen is reported in Figure 3.61. Based on the OOP displacements read by instruments, the evolution of the reconstructed deformed shape of the specimen is shown in Figure 3.62. A picture of the specimen at the end of the test is reported in Figure 3.63.
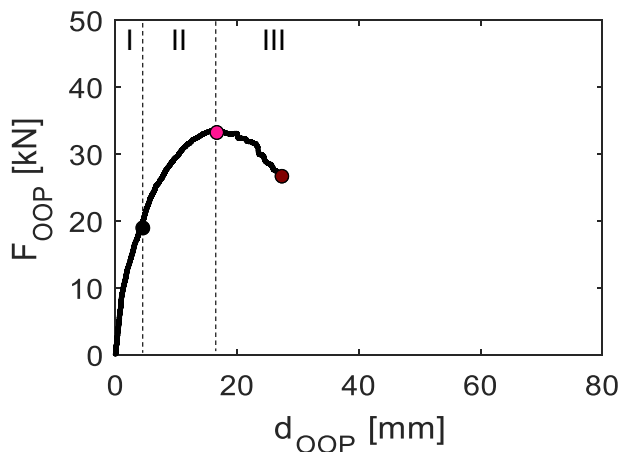
Figure 3.60. OOP force vs infill's central displacement for specimen 120_OOP_3E.

Table 3.17. Summary of test 120_OOP_3E results.

specimen	F_{crack} [kN]	d_{crack} [mm]	K_{crack} [kN/mm]	F_{max} [kN]	d_{max} [mm]	K_{max} [kN/mm]	d_{end} [mm]
120_OOP_3E	19.5	4.3	4.5	33.6	16.4	2.0	28.0

a) $F_{OOP} = 19.5$ kN $d_{OOP} = 4.3$ mm

b) $F_{OOP} = 33.6$ kN $d_{OOP} = 16.4$ mm

c) $F_{OOP} = 22.5$ kN $d_{OOP} = 28.0$ mm
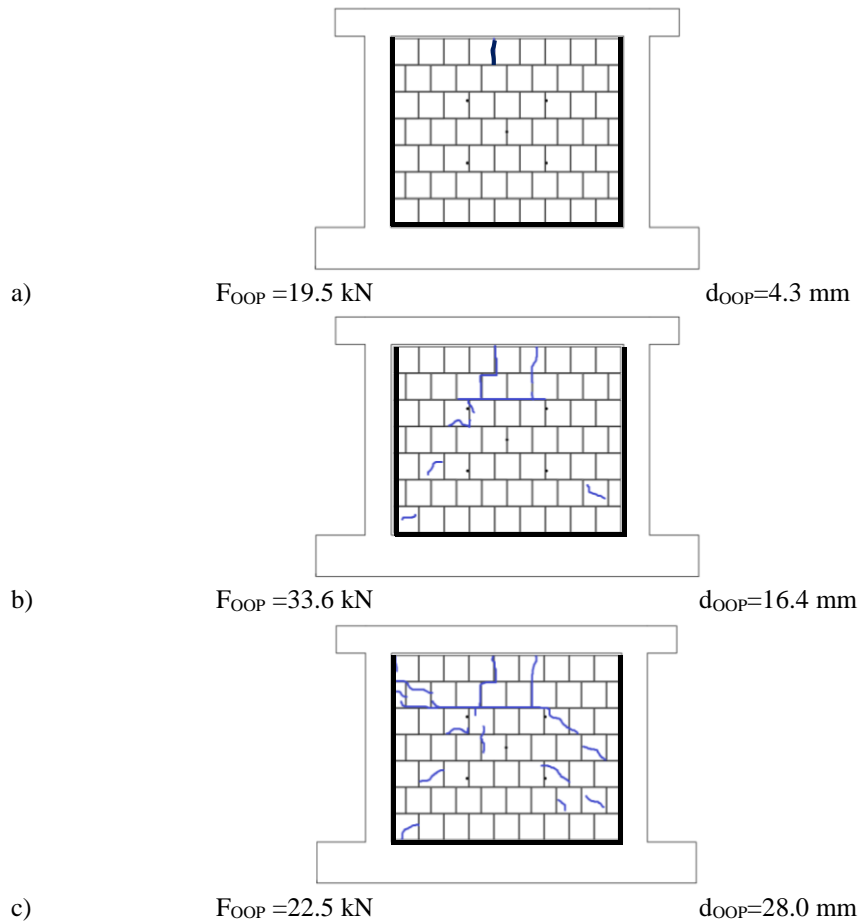
Figure 3.61. Cracking pattern evolution at first macro-cracking (a), peak load (b) and at the end of the test (c) for specimen 120_OOP_3E.
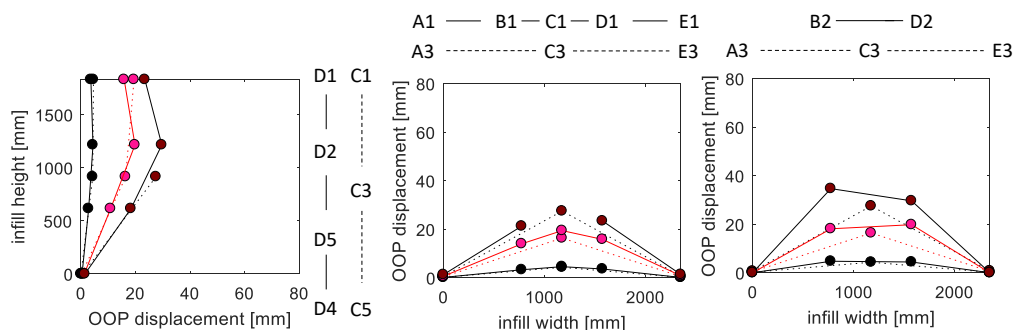
Figure 3.62. Deformed shape evolution along vertical and horizontal alignments (see the instruments' layout in Figure 3.8) for specimen 120_OOP_3E at the end of each one of the three phases individuated in Figure 3.60. The deformed shape corresponding to the attainment of peak load is highlighted with a red line. Some readings are missing as some instruments reached the end of their measuring range.
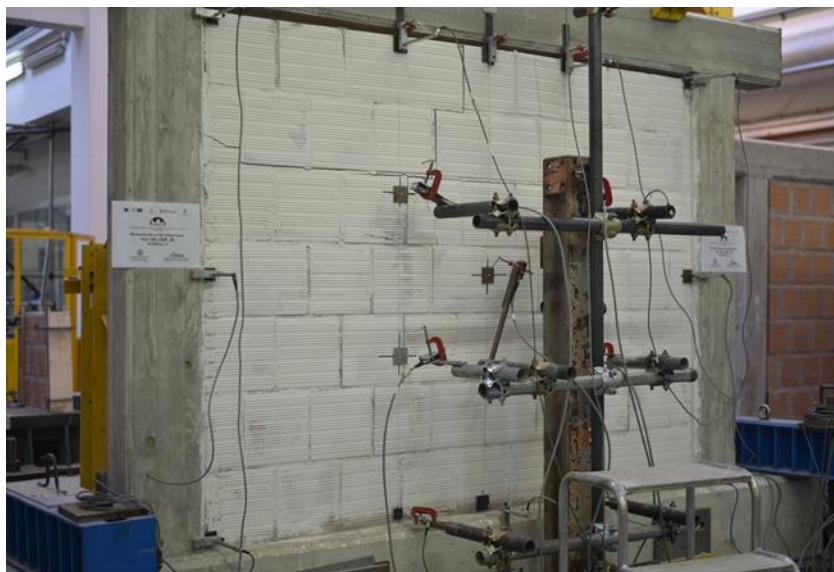
Figure 3.63. Specimen 120_OOP_3E at the end of test.

3.5.5. Test 120_OOP_2E

The infill was provided with a 30 mm gap from both the two RC columns. The OOP force-infill's centre displacement diagram obtained for 120_OOP_2E specimen is shown in Figure 3.64. The OOP response of the infill was characterized by four phases.

The first pseudo-elastic linear phase ended at the attainment of an OOP central displacement equal to around 1.5 mm, corresponding to a load equal to about 9 kN. At this point, at which a loud cracking noise was heard, a reduction of the specimen's tangent stiffness was registered, even if no visible damage was observed. After that, a second linear phase was registered, which ended at the infill first macro-cracking with the formation of a long horizontal crack between bricks and mortar joints near the infill mid-height. This occurred for a load equal to 18.5 kN, at a central displacement equal to 5.5 mm. After that, a third non-linear phase was observed up to the attainment of peak load, equal to 24 kN, at a displacement equal to 9.5 mm. During this phase, the pre-existing horizontal crack widened. After that, the load was pseudo-constant up to the attainment of a central displacement equal to 13 mm. Then, it suddenly dropped to 14 kN at a central displacement equal to 14.5 mm. With the reduction of the OOP load-bearing capacity equal to -42% with respect to the peak load, the test was interrupted. During the test, no significant displacement was registered in the OOP direction for the foundation and upper beams of the RC frame. A summary of test results is reported in Table 3.18.

The evolution of cracking pattern in the specimen is reported in Figure 3.65. Based on the OOP displacements read by instruments, the evolution of the reconstructed deformed shape of the specimen is shown in Figure 3.66. A picture of the specimen at the end of the test is reported in Figure 3.67.
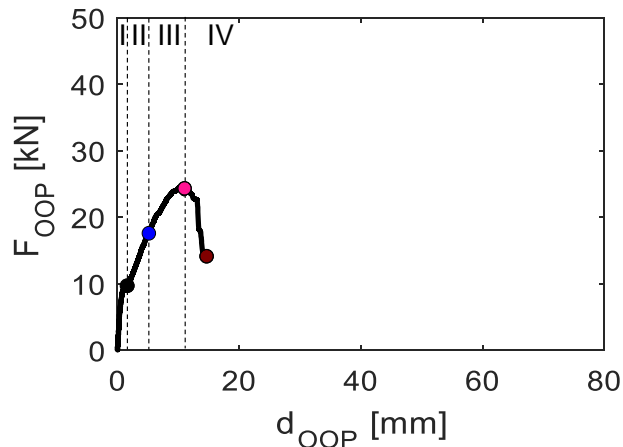
Figure 3.64. OOP force vs infill's central displacement for specimen 120_OOP_2E.

Table 3.18. Summary of test 120_OOP_2E results.

specimen	F_{crack} [kN]	d_{crack} [mm]	K_{crack} [kN/mm]	F_{max} [kN]	d_{max} [mm]	K_{max} [kN/mm]	d_{end} [mm]
120_OOP_2E	18.5	5.5	3.4	24.0	9.5	2.5	14.5

a) $F_{OOP} =18.5$ kN $d_{OOP}=5.5$ mm

b) $F_{OOP} =24.0$ kN $d_{OOP}=9.5$ mm

c) $F_{OOP} =14.0$ kN $d_{OOP}=14.5$ mm

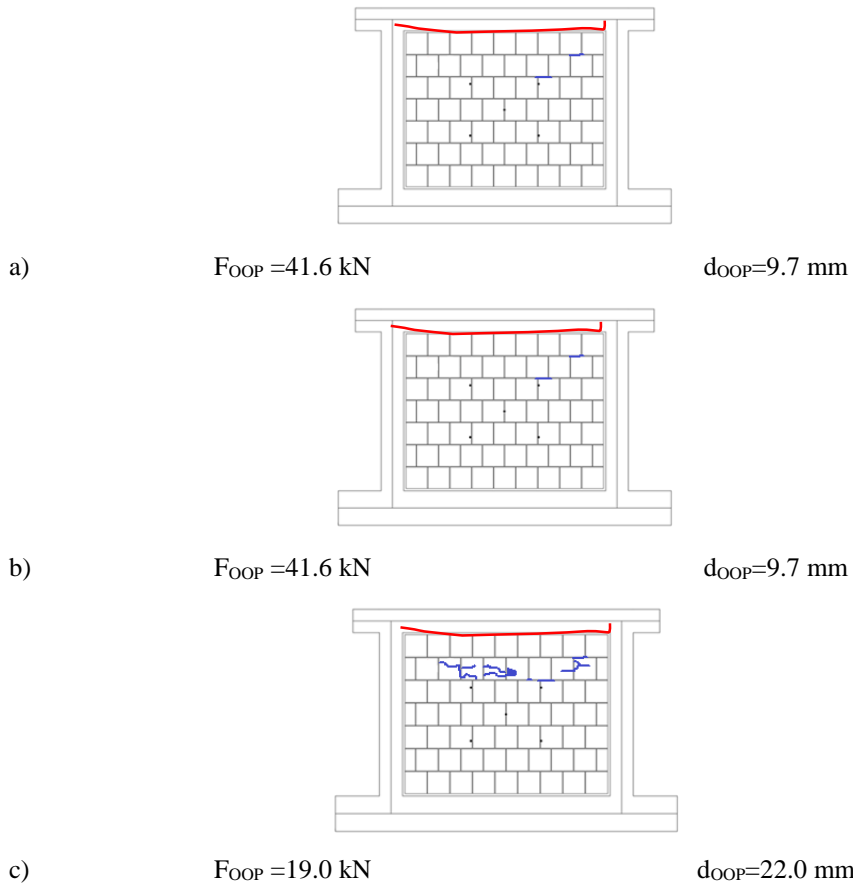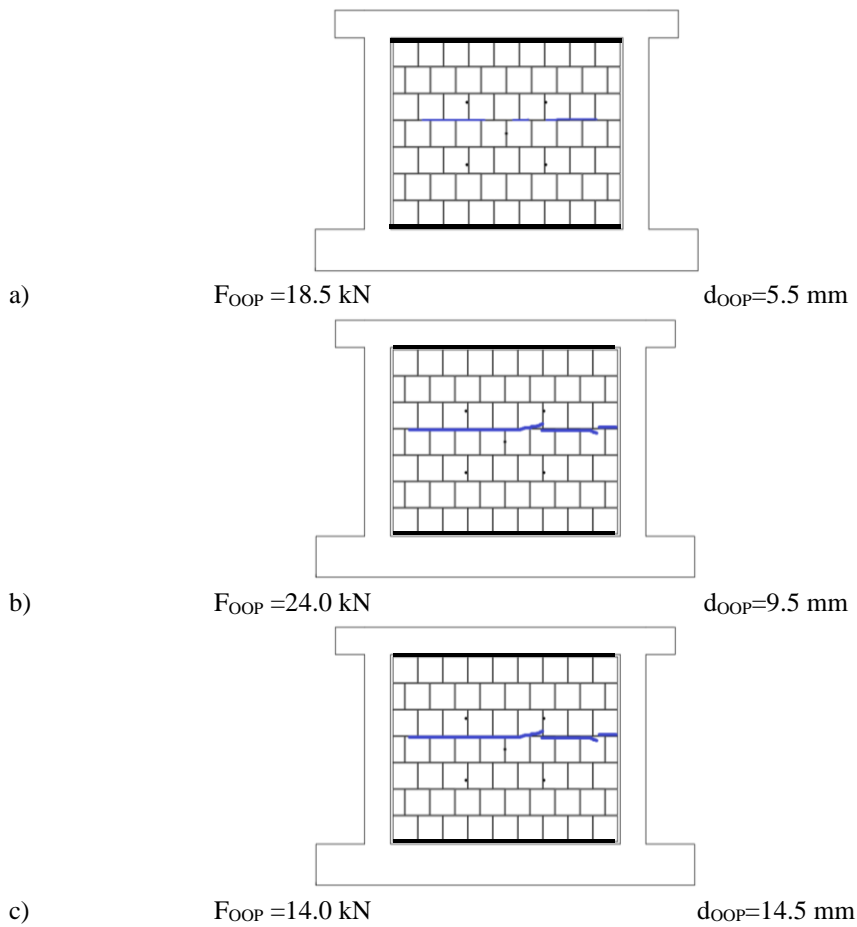Figure 3.65. Cracking pattern evolution at first macro-cracking (a), peak load (b) and at the end of the test (c) for specimen 120_OOP_2E.
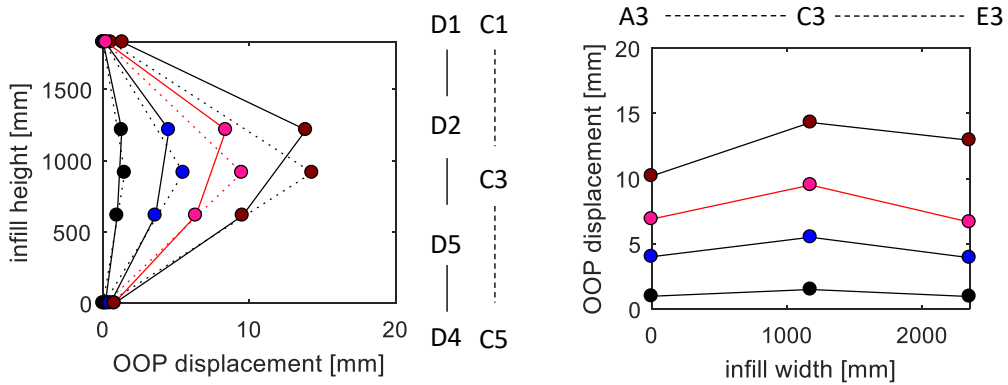
Figure 3.66. Deformed shape evolution along vertical and horizontal alignments (see the instruments' layout in Figure 3.8) for specimen 120_OOP_2E at the end of each one of the four phases individuated in Figure 3.64. The deformed shape corresponding to the attainment of peak load is highlighted with a red line.
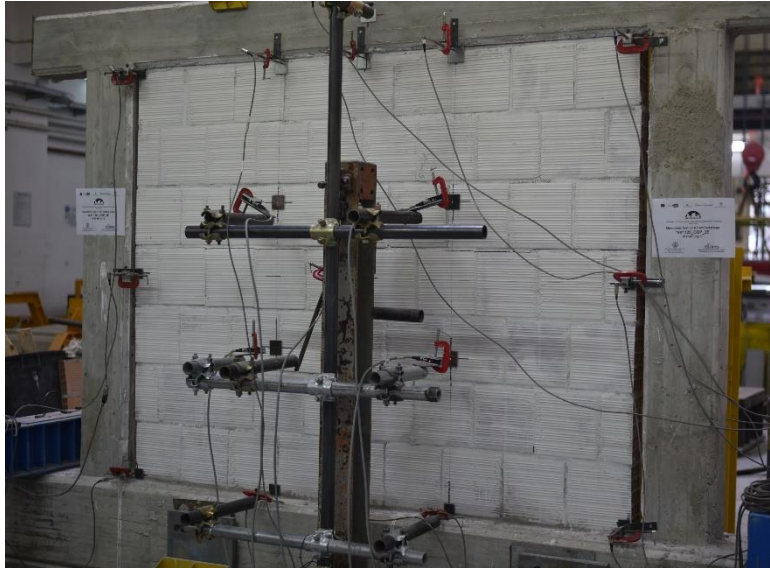
Figure 3.67. Specimen 120_OOP_2E at the end of test.

3.5.6. General considerations on tests' results

The OOP response of specimens is compared in Figure 3.68 and in Figure 3.70.

For both the 80 mm- and the 120 mm-thick infills, the following considerations can be drawn from Figure 3.68. First, it is observed that the OOP strength granted by two-

way arching action is greater than that assured by one-way arching, of course. In addition, the OOP resistance granted by one-way vertical arching is lower than that associated with horizontal arching. Clearly, this last evidence is not a general rule, as the hierarchy between the two resistant mechanisms is determined by both masonry mechanical properties and the infill aspect ratio. Second, it is observed that the post-peak behaviour of infills bounded along three edges is smoother than that registered for infills bounded along two or four edges.
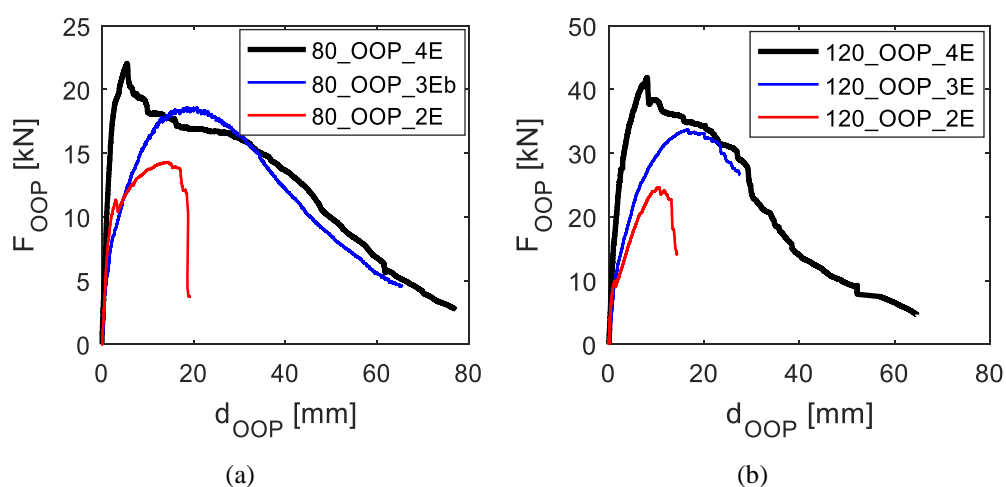
Figure 3.68. Experimental response of the 80 mm-thick specimens (a) and of the 120 mm-thick specimens (b).

As already stated, the OOP load-bearing capacity of specimens is granted by arching action. The infill walls tested were realized with mortar and hollow clay bricks with horizontal holes. Therefore, vertical arching thrusts act perpendicularly to bricks' holes, while horizontal arching thrusts act parallel to bricks' holes. For this reason, the different OOP response of infills in which one-way (horizontal or vertical) arching or two-way arching occurs is likely to be related to the different response of unreinforced masonry loaded perpendicularly or parallel to bricks' holes. For example purposes, the axial stress-strain relationships obtained for some of the masonry wallets tested for the mechanical characterization of test specimens' masonry are shown in Figure 3.69. It can be observed that wallets tested under axial load perpendicular to bricks' holes exhibited a brittle failure due to masonry crushing at the attainment of the maximum stress, while

wallets tested under axial load parallel to bricks' holes showed, in most cases, a certain post-peak deformation capacity up to the wallet collapse due to crushing.
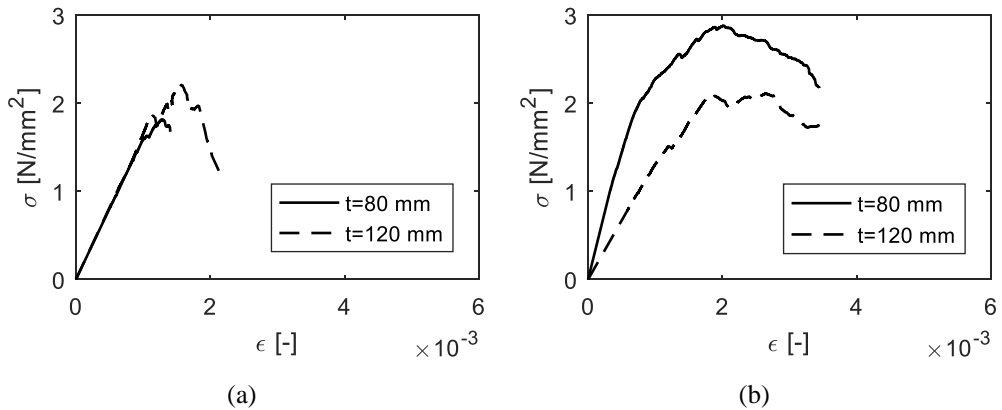
Figure 3.69. Axial stress-strain relationships for some of the masonry wallets tested for the mechanical characterization of test specimens' masonry. Results for wallets tested under compressive load perpendicularly to bricks' holes (a) and parallel to bricks' holes (b).

In "2E" and "4E" specimens, in which vertical arching occurs, the attainment of peak load is followed by a non-negligible drop of the load-bearing capacity of test specimens. Most likely, based also on the evidence shown in Figure 3.69a, this occurs at masonry crushing due to vertical arching thrusts. In "2E" specimens, this event corresponds to the collapse of the infill wall panel, as the stresses acting in masonry cannot redistribute towards restrained edges of the infills other than those directly involved in the abovementioned crushing due to vertical arching. For "4E" specimens, even if masonry seems to crush at the attainment of peak load, a significant post-peak displacement capacity is observed. This is likely to be due to the existence of horizontal arching.

In fact, if "3E" specimens are considered, it can be noted that their OOP response is smoother than that of "2E" and "4E" specimens, and that a significant post-peak displacement capacity is granted. The smoother response over the attainment of peak load is consistent with the response of masonry wallets under compressive load parallel to bricks' holes. In other words, the smoother behaviour of specimens characterized by one-way horizontal arching seems to be due to the absence of vertical arching and, so, of vertical crushing soon after the attainment of peak load. In addition, this seems to be

confirmed by the fact that the "zone" over the attainment of peak load of "3E" specimens is consistent or corresponding with the "pseudo-plastic" branch (in the 80 mm-thick specimen) and with the "smooth" softening branch (in the 120 mm-thick specimen) registered for "4E" specimens after the attainment of peak load. Moreover, it is observed that the last branch of the force-displacement response of specimens is consistent for the "3E" and the "4E" 80 mm-thick specimens and, even if with some extrapolation, also for the 120 mm-thick specimens. This seems to indicate that the last part of the force-displacement curves was determined, in both cases, only by the progressive collapse of masonry due to horizontal arching.

In other words, from tests results it seems that:

i. The failure of the resistant mechanism constituted by vertical arching is brittle as the response of masonry loaded perpendicularly to bricks' holes (as shown in Figure 3.69a): "2E" and "4E" specimens show a load-bearing capacity drop at the attainment of peak load due to the occurrence of vertical arching failure;

ii. As all the restrained edges are involved in masonry crushing and in the consequent failure of the one-way vertical arching resistant mechanism, vertical arching failure corresponds to the collapse of the entire infill wall if it is bounded only along the upper and the lower edges ("2E" specimens);

iii. In "4E" specimens, after the brittle failure of vertical arching, stresses move towards vertical restrained edges: this allows the infill taking advantage of the "ductility", associated with horizontal arching, that masonry exhibits under compressive loads applied parallel to bricks' holes (as shown in Figure 3.69b). For this reason, "4E" specimens do not collapse at vertical arching failure but have a certain post-peak displacement capacity;

iv. In "3E" specimens, the "ductility" associated with horizontal arching is "directly" invoked (without passing from stresses' redistributions). For these reasons, "3E" specimens exhibit a smoother response over the attainment of peak load and a certain post-peak displacement capacity.

These circumstances partially confirm the statement by Flanagan and Bennett, that affirmed that vertical arching provide infills with OOP strength, while horizontal arching provide them with OOP post-peak displacement capacity. From the results herein

presented, it is clear that infills bounded along two edges, in which only vertical arching occurs, have a significantly smaller strength than infills in which two-way arching occurs. However, it seems proved that the post-peak OOP displacement capacity of URM infills is due, for the most, by the existence of horizontal arching. Clearly, these are only qualitative considerations: further theoretical and experimental investigation is needed to achieve a deeper knowledge on these issues.

From Figure 3.70 it is observed that, as expected, the 120 mm-thick infills are characterized by greater stiffness and strength than the 80 mm-thick infills. For instance, the ratio between the OOP strength of specimens with the same boundary conditions and different slenderness ratio ranges from 1.64 to 1.90, with mean value equal to 1.79.

Only 2E specimens allow a straightforward comparison in terms of ultimate/collapse displacement, as they with no doubt collapsed soon after the attainment of peak load. In Chapter IV, it will be shown that this occurred, most likely, at masonry crushing due to vertical arching thrusts. Based on Equation 66 reported in Chapter I, for equal masonry crushing strain ε_{crush}, a lower vertical crushing displacement is expected for thicker, i.e., less slender, infills. This is consistent with the experimental evidence, which showed a lower displacement capacity for specimen 120_OOP_2E than for specimen 80_OOP_2E.
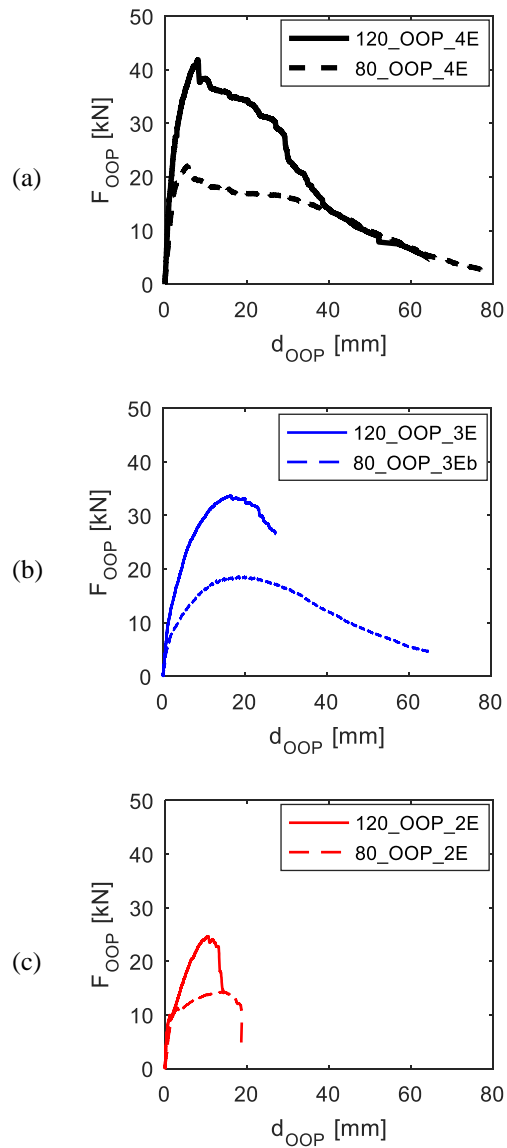
Figure 3.70. Experimental response of the specimens bounded along four (a) three (b) and two (c) edges.

3.6   OOP CYCLIC TEST

This section is dedicated to the description and discussion of a cyclic pure OOP test on a 120 mm thick infill mortared along all edges to the confining RC frame elements, nominally identical to the specimens presented in the previous section for mechanical and geometric characteristics.

In the first subsection, some preliminary issues are discussed. More specifically, the modifications of the experimental setup necessary to perform the test are presented, as well as the cyclic loading path adopted.

In the second subsection, the results of the test are presented with the support of the force-displacement diagram for the specimen and of the evolution of cracking pattern. A simple comparison with the monotonic reference test 120_OOP_4E is also discussed.

3.6.1. Test setup and loading path

To perform the test, eight holes were made in the mortar beds of the specimen, two holes corresponding to each one of the four loading points. Two holes were realized in each one of the four plates belonging to the loading system described in section XXX, which were in contact with the posterior surface of the specimen. Then, four steel plates equal to those belonging to the loading system were realized and provided each one with two holes. These plates were placed in contact with the anterior surface of the specimen. Four steel rebars with 10 mm diameter were realized. These rebars passed through the holes realized in the four posterior and in the four anterior steel plates, as well as in the holes realized in the specimen. In this way, positive and negative displacements were imposed to the specimen.

A picture of the front and back view of the specimen with the above described plates and rebars is reported in Figure 3.71.

<center>(a)   (b)</center>
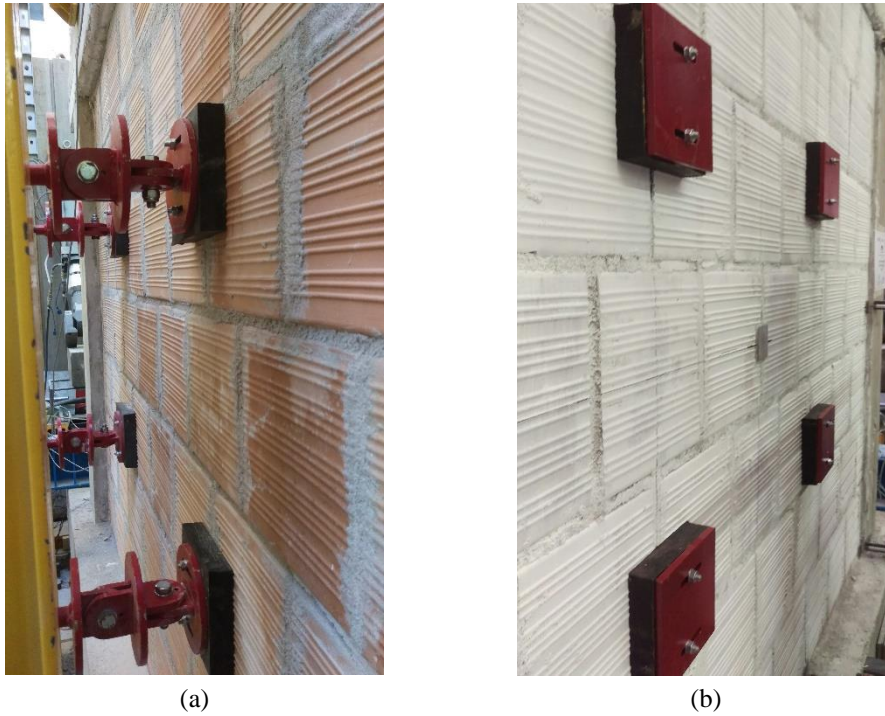
Figure 3.71. Back (a) and front (b) view of the specimen tested under cyclic pure OOP load.

To decide the loading path for this test, the OOP response diagram of the reference monotonic test 120_OOP_4E was considered. The significant points highlighted in Figure 3.15 were considered. The displacements of the actuator corresponding to those points were assumed as target positive and negative displacements for the cyclic test. The velocity of the test was equal to that of the monotonic test in the first three cycles, to allow some comparison with the results of the monotonic reference test. Then, it was doubled in the fourth cycle and again doubled in the fifth cycle, in order to limit the test duration. No sub-cycle was performed.

The loading path is summarized in Table 3.19.

Table 3.19. OOP loading path defined by nominal target OOP displacements imposed by the actuator.

cycle	target OOP displacement	velocity
#	[mm]	[mm/s]
1	+/-7.00	0.02
2	+/-14.0	0.02
3	+/-32.0	0.02
4	+/-44.0	0.04
5	+/-66.0	0.08

3.6.2. Test 120_OOP_4E_cyclic

The first significant non-linearity in the force-displacement response of the specimen was observed for a load equal to 13.2 kN, corresponding to a displacement equal to 1.0 mm. However, during the entire first cycle, no visible crack was observed in the specimen. During the first cycle, a maximum load equal to 22.8 kN was attained at a central displacement equal to 4.7 mm, while a minimum load equal to -24.5 kN was attained at a central displacement equal to -4.3 mm. A residual displacement equal to -0.9 mm was registered at load equal to zero, at the beginning of the second cycle.

During the second cycle, the first diagonal cracks appeared in the upper part of the infill together with a horizontal crack in the infill centre at a load equal to 29.5 kN and at a displacement equal to 7.7 mm. The second cycle was characterized by a maximum load equal to 36.4 kN attained for a central displacement equal to 11.0 mm and by a minimum load equal to -39.4 kN attained for a central displacement equal to -9.0 mm. At the end of the second cycle, a residual displacement equal to -1.6 mm was registered. Further diagonal cracks appeared in the lower part of the infill.

The third cycle was characterized by local maximum load equal to 36.2 kN attained for a central displacement equal to 12.6 mm. At the attainment of maximum, a small drop occurred. This drop yield the load to 33.0 kN. Then, the load increased again up to 36.7 kN attained at a central displacement equal to 32.2 mm. During this phase, further diagonal cracks formed in the lower part of the infill, as well as a horizontal crack near the infill lower edge. The minimum load attained was equal to -34.5 kN corresponding to a central displacement equal to -25.6 mm. During the unloading phase, the horizontal bottom crack widened and expanded also along the lower part of the vertical edges of the infill. In addition, a further horizontal crack appeared at the centre of the lower course of bricks. At the attainment of the minimum load, a load bearing capacity drop occurred yielding the OOP load to -23.0 kN at a central displacement equal to -26.8 mm. This

abrupt load reduction was equal to 33%. The third cycle ended with a residual displacement equal to -13.1 mm. During the reloading phase, a wide horizontal crack appeared in the central part of the upper course of bricks.

The fourth cycle was characterized by a very fast damaging of the infill, with the crushing of the exterior tiles of bricks in the upper and lower part of the infill. The maximum load was equal to 20.4 kN and was attained for a central displacement equal to 25.1 mm. The target displacement associated with the fourth cycle was attained for a central displacement equal to 50.8 mm, corresponding to a load equal to 16.8 kN. The unloading phase was characterized by the collapse and overturning of the exterior tiles of bricks. A zero load, with a residual central displacement equal to 20.6 mm, the test was interrupted.

The OOP strength of the infill was equal to 36.7 kN and was attained for a central displacement equal to 32.2 mm, during the third cycle. A summary of test results is reported in Table 3.20. No significant OOP translation of the RC frame was registered by the LVDTs at the base of the RC frame. The OOP force-displacement diagram for the specimen is reported in Figure 3.72. The evolution of cracking pattern is shown in Figure 3.73. A picture of the specimen at the end of the test is reported in Figure 3.74.
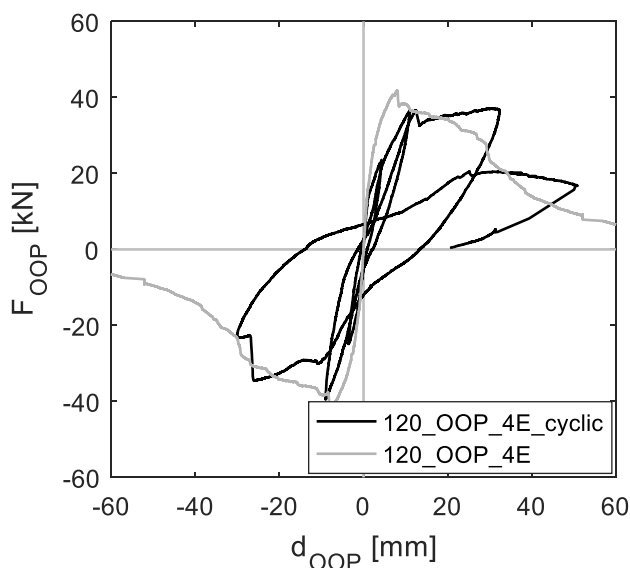
Figure 3.72. OOP force vs infill's central displacement for specimen 120_OOP_4E_cyclic (black line) compared with the monotonic response of specimen 120_OOP_4E (grey line).

Table 3.20. Summary of test 120_OOP_4E_cyclic and test 120_OOP_4E results.

specimen	F_{crack} [kN]	d_{crack} [mm]	K_{crack} [kN/mm]	F_{max} [kN]	d_{max} [mm]	K_{max} [kN/mm]	d_{end} [mm]
120_OOP_4E_cyclic	29.5	7.7	3.8	36.7	32.2	1.1	50.8
120_OOP_4E	27.5	2.5	11.0	41.9	8.0	5.2	64.6

a) F_{OOP} =29.5 kN d_{OOP}=7.7 mm

b) F_{OOP} =36.7 kN d_{OOP}=32.2 mm

c) F_{OOP} =16.8 kN d_{OOP}=50.8 mm
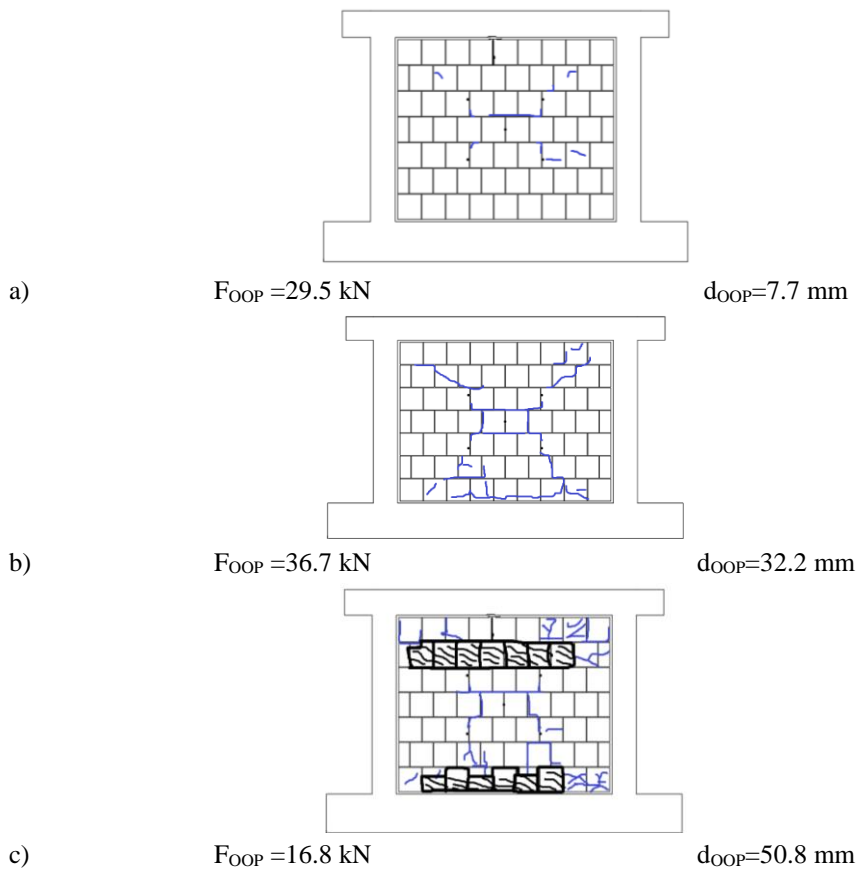
Figure 3.73. Cracking pattern evolution at first macro-cracking (a), peak load (b) and at the end of the test (c) for specimen 120_OOP_4E_cyclic.

Figure 3.74. Specimen 120_OOP_4E_cyclic at the end of test.

It is observed from Figure 3.72 and Table 3.20 that the monotonic and cyclic test had quite different responses, especially after the first non-linearity. More specifically, the first cracking load and the strength of the specimens were similar, but the one tested under cyclic load exhibited a significantly greater deformability, especially in terms of secant stiffness at peak load. On the other hand, the softening branch of the monotonic test and the negative stiffness defined by the envelope of the positive peaks of the third and fourth cycles seem to be quite similar.

Most likely, such differences in the infills' deformability is due to the different nature of the loading path. Note also that, as reported in Table 3.2, the infills tested had not exactly the same mechanical properties. Also this difference may have had some role in the different response of specimens. Clearly, this is the result of the comparison of two tests only: further investigation is needed on this issue.

REFERENCES

- Angel R, Abrams DP, Shapiro D, Uzarski J, Webster M. Behaviour of reinforced concrete frames with masonry infills. University of Illinois Engineering Experiment Station. College of Engineering. University of Illinois at Urbana-Champaign., 1994.

- Asteris PG, Kakaletsis DJ, Chrysostomou CZ, Smytous EE. Failure modes of in-filled frames. Electronic Journal of Structural Engineering 2011;11.1.
- ASTM E519-02, Standard Test Method for Diagonal Tension (Shear) in Masonry Assemblages, ASTM International, West Conshohocken, PA, 2002, www.astm.org.
- Blevins RD, Plunkett R. Formulas for natural frequency and mode shape. Journal of Applied Mechanics 1980;47:461.
- Calvi GM, Bolognini D. Seismic response of reinforced concrete frames infilled with weakly reinforced masonry panels. Journal of Earthquake Engineering 2001;5.2:153-185.
- Dawe JL, Seah CK. Out-of-plane resistance of concrete masonry infilled panels. Canadian Journal of Civil Engineering 1989;16(6):854–864.
- Del Gaudio C, De Risi MT, Ricci P, Verderame GM. Drift-based fragility functions for hollow clay masonry infills in RC buildings under in-plane seismic actions, Proceedings of the XVII ANIDIS, L'Ingegneria Sismica in Italia, Pistoia, Italy, 2017.
- EN 1052-1 CEN 1999: Methods of test for masonry. Part 1: determination of compressive strength. European Committee for Standardization, Brussels.
- Frumento S, Magenes G, Morandi P, Calvi GM (2009). Interpretation of experimental shear tests on clay brick masonry walls and evaluation of q-factors for seismic design. Research Report EUCENTRE 2009/02, IUSS Press, Pavia, Italy: 2009, ISBN: 978-88-6198-034-1.
- Furtado A, Rodrigues H, Arêde A, Varum H. Experimental evaluation of out-of-plane capacity of masonry infill walls. Engineering Structures 2016;111:48-63.
- Furtado A, Rodrigues H, Arêde A, Varum H 2018a. Effect of the Panel Width Support and Columns Axial Load on the Infill Masonry Walls Out-Of-Plane Behavior. Journal of Earthquake Engineering 2018.
- Furtado A, Rodrigues H, Arêde A, Varum H 2018b. Out-of-plane behavior of masonry infilled RC frames based on the experimental tests available: A systematic review. Construction and Building Materials 2018;168:831-848.
- Guidi G, da Porto F, Dalla Benetta M, Verlato N, Modena C. Comportamento sperimentale nel piano e fuori piano di tamponamenti in muratura armata e rinforzata. Proceedings of the XV ANIDIS, L'Ingegneria Sismica in Italia, Padua, Italy, 2013, 30. (in Italian).
- Najafgholipour MA, Maheri MR, Lourenço PB. Capacity interaction in brick masonry under simultaneous in-plane and out-of-plane loads. Construction and Building Materials 2013;38:619-626.

- Najafgholipour MA, Maheri MR, Lourenço PB. Definition of interaction curves for the in-plane and out-of-plane capacity in brick masonry walls. Construction and Building Materials 2014;55:168-182.
- NTC2008. Decreto ministeriale 14 gennaio 2008 - Norme Tecniche per le Costruzioni NTC2008. Supplemento ordinario n. 30 Gazzetta Ufficiale 4 febbraio 2008, n 29. (in Italian).
- Petry S, Beyer K.Influence of boundary conditions and size effect on the drift capacity of URM walls. Engineering Structures 2014; 65: 76–88. DOI: 10.1016/j.engstruct.2014.01.048.
- Stylianidis KC. Experimental investigation of masonry infilled R/C frames. The Open Construction and Building Technology Journal 2012;6:194-212.
- TU-DELFT. Two aspects related to the analysis of masonry structures: Size effect and parameter sensitivity. Technical report TU-DELFT No 03.21.1.31.25/TNO-BOUW No 97-NM-R1533. Faculty of Engineering, TU Delft, Netherlands; 1997.

Chapter IV
Experimental database analysis and modelling proposals

4.1. INTRODUCTION

In Chapter I, mechanical and empirical-based OOP strength, stiffness and displacement capacity models for IP-undamaged and IP-damaged infills were presented. In Chapter II, the OOP and IP/OOP tests carried out on URM and RM infills were described. Considering the fact that the number of experimental tests carried out on URM infills and available in the literature was very small, a wide experimental program herein named DIST-UNINA was carried out at the Department of Structures for Engineering and Architecture of University of Naples Federico II.

The collection of the experimental tests available in the literature and the realization of new experimental tests was aimed at the definition of a wide experimental database that can be used for the assessment of the predictive capacity of the literature models presented in Chapter I and, if necessary, the proposals of the formulations for modelling the OOP behaviour of URM infills and of the IP/OOP interaction effects. This chapter is dedicated to both these aims.

In section 4.2, the experimental database is defined. More specifically, eligibility criteria are defined and the experimental tests satisfying these criteria are selected.

In section 4.3, the models available in the literature for the prediction of the secant stiffness at first macro-cracking and at peak load for IP-undamaged URM infills are applied to the experimental database. Based on the results of this comparison, modelling proposals are provided.

In section 4.4, the models available in the literature for the prediction of OOP strength for IP-undamaged URM infills are applied to the experimental database. Based on the results of this comparison, modelling proposals are provided, also for what concerns the force at first macro-cracking.

In section 4.5, the models available in the literature for the potential definition of a conventional OOP collapse displacement of URM infills are applied to the experimental database. Based on the results of this comparison, modelling proposals are provided.

In section 4.6, the models available in the literature for the prediction of the OOP strength reduction due to the IP damage are applied to the experimental database. Based on the results of this comparison, empirical formulations are proposed to model the stiffness and strength reduction due to IP damage are proposed. Further proposals are discussed for the prediction of the variation of the displacement capacity due to the IP damage.

In section 4.7, the issue of the IP response variation due to OOP damage is discussed. A modelling proposal, based on the experimental data, is provided.

In section 4.8, a summary of the proposed OOP model for URM infills accounting for the IP/OOP interaction effects is described.

4.2. DEFINITION OF THE EXPERIMENTAL DATABASE

In this section, the experimental database is defined. The first subsection is dedicated to the definition of the eligibility criteria for entering the database concerning pure OOP tests; the second subsection is dedicated to the definition of the eligibility criteria for entering the database concerning IP/OOP tests.

4.2.1. Database of pure OOP tests

This section is dedicated to the definition of the experimental database constituted by pure OOP tests that will be used for the assessment of the effectiveness of literature strength, stiffness and displacement capacity models as well as for the proposal, if necessary, of new models and formulations.

First, consider that the number of pure OOP tests described in Chapter II and II is 43. Among these, 12 were carried out on 2E infills, 4 on 3E infills, 27 on 4E infills. Considering 2E infills, 3 tests were carried out on infills in RC frames, 9 on infills built between the floor and the ceiling of the laboratory. Considering 3E infills, 3 tests were carried on infills in RC frames, 1 on an infill in a steel frame. Considering 4E infills, 15

tests were performed on infills in RC frames, 12 tests were performed on infills in steel frames.

To define the experimental database, only some of the above specimens were considered based on the following criteria:

i.   All the experimental tests presented in the literature aimed at investigating the OOP response and strength of plain URM infills constituted by clay/concrete units with vertical and horizontal mortar joints are considered;

ii.   Tests performed on reinforced, repaired, retrofitted or in-plane damaged infills are excluded;

iii.   Innovative infills with sliding joints or other devices aimed at reducing their in-plane vulnerability are excluded;

iv.   Infills tested in the OOP direction with the presence of pre-compression stresses were excluded;

v.   Specimens with non-continuous mortar joints are excluded;

vi.   Specimens with openings are excluded;

vii.   Only one-leaf specimens completely bounded/mortared along two edges, in which one-way arching can occur, or completely bounded/mortared along four edges, in which two-way arching can occur, are considered;

viii.   Only monotonic and load-unload tests are considered: in fact, the cyclic test 120_OOP_4E_cyclic revealed that the behaviour of a specimen under "real" cyclic load (i.e., tested under cyclic positive and negative imposed displacements) can be significantly different, in terms of OOP deformability, from that of a specimen under monotonic or load-unload loading path. As specimen 120_OOP_4E_cyclic is a singularity with respect to all the other tests, it was not included in the database to prevent the introduction of a singular source of heterogeneity.

Based on the above-listed criteria, the specimens listed in Table 4.1 entered the pure OOP tests database. The database is separated between 2E (6 out 12 infills were selected) and 4E specimens (17 out of 27 infills were selected); for 4E specimen, a further separation is made between infills in RC frames (11 out of 15 infills were selected) and infills in steel frames (6 out of 12 infills were selected).

Table 4.1. Experimental database of pure OOP tests.

#	Author	Specimen	Boundary condition	Frame material
1	da Porto et al.	FOB1	2E	-
2	da Porto et al.	FOB2	2E	-
3	da Porto et al.	FOB3	2E	-
4	Hak et al.	TA5	2E	RC
5	DIST-UNINA	80_OOP_2E	2E	RC
6	DIST-UNINA	120_OOP_2E	2E	RC
7	Angel et al.	1	4E	RC
8	Calvi and Bolognini	10	4E	RC
9	Varela-Rivera et al.	E-1	4E	RC
10	Varela-Rivera et al.	E-2	4E	RC
11	Varela-Rivera et al.	E-3	4E	RC
12	Varela-Rivera et al.	E-4	4E	RC
13	Varela-Rivera et al.	E-5	4E	RC
14	Varela-Rivera et al.	E-6	4E	RC
15	Furtado et al.	Inf_02	4E	RC
16	DIST-UNINA	80_OOP_4E	4E	RC
17	DIST-UNINA	120_OOP_4E	4E	RC
18	Dawe and Seah	WE2	4E	Steel
19	Dawe and Seah	WE4	4E	Steel
20	Dawe and Seah	WE5	4E	Steel
21	Dawe and Seah	WE8	4E	Steel
22	Flanagan and Bennett	18	4E	Steel
23	Flanagan and Bennett	25	4E	Steel

4.2.2. Database of combined IP/OOP tests

Among the OOP tests carried out after a cyclic IP test reported in Chapter II and III, only those carried out on URM plain infills were considered. Also in this case, reinforced, repaired, retrofitted, engineered, strengthened infills were excluded. Combined IP/OOP tests with no reference IP-undamaged specimen were excluded, of course. In addition, only experimental programs in which at least two combined IP/OOP tests at two different IP IDR levels were considered. This criterion was necessary to check the consistency of the results proposed by the experimental programs and to prevent the introduction in the database of potential outliers.

Based on the above criteria, the database of combined IP/OOP tests is constituted only by ten 4E infills in RC frames, as reported in Table 4.2.

Table 4.2. Experimental database of combined IP/OOP tests.

#	Author	Specimen	Reference specimen	IP IDR [%]
1	Angel et al.	3b	1	0.22
2	Angel et al.	2b	1	0.34
3	Calvi and Bolognini	6	10	0.40
4	Calvi and Bolognini	2	10	1.20
5	DIST-UNINA	80_IP+OOP_L	80_OOP_4E	0.16
6	DIST-UNINA	80_IP+OOP_M	80_OOP_4E	0.37
7	DIST-UNINA	80_IP+OOP_H	80_OOP_4E	0.58
8	DIST-UNINA	120_IP+OOP_L	120_OOP_4E	0.21
9	DIST-UNINA	120_IP+OOP_M	120_OOP_4E	0.50
10	DIST-UNINA	120_IP+OOP_H	120_OOP_4E	0.89

4.3. ASSESSMENT OF THE OOP STIFFNESS

In this section, the secant stiffness at first macro cracking and at peak load of the specimens considered in the experimental database is compared with the predictions of literature models. Based on the results of this comparison, proposals for modelling the pure OOP behaviour of URM infills are presented.

4.3.1. Prediction of secant stiffness at first macro-cracking

In Chapter II and III, data concerning the load, F_{crack}, and the OOP displacement, d_{crack}, at the appearance of the first visible crack in the specimens were collected. If such data were not directly provided by the authors, the first macro-cracking point was read on the OOP force-displacement diagram, if provided, at the first significant non-linearity. The secant stiffness at first macro-cracking, K_{crack}, is derived as the ratio between F_{crack} and d_{crack}.

In this section, K_{crack} is compared with the prediction of Timoshenko (1959)'s formulation, reported in Equation 47 in Chapter I, for 4E infills and with the prediction of Kadysiewski and Mosalam (2009)'s formulation, reported in Equation 51 in Chapter I, for 2E infills, with ξ equal to one (i.e., by assuming the gross value for the flexural stiffness of the infill horizontal cross section).

Within this comparison, an assumption is implied. In fact, rigorously, K_{crack} is not equal to K_{el} predicted by Timoshenko and by Kadysiewski and Mosalam with ξ equal to one, as the initial elastic stiffness of the infill should be greater than K_{crack} and roughly equal to the secant stiffness at first micro-cracking. However, the first micro-cracking

cannot be individuated visually nor on the experimental force-displacement response of specimens; on the other hand, specific models for the prediction of the secant stiffness at first macro-cracking are not available. For all these reasons, it is assumed that the propagation of micro-cracks in the infill panel occurring between the formation of the first micro-crack and the opening of the first macro-crack does not produce a significant reduction in stiffness, as shown in Figure 4.1.

In Table 4.3, K_{crack} is compared with the predicted value of K_{el} for 2E infills; the same is done in Table 4.4 for 4E infills. Note that for 2E infills, the elastic modulus in the vertical direction is always provided and used in the application of Kadysiewski and Mosalam formulation. The same is done for the application of Timoshenko's formulation on 4E infills, as masonry elastic modulus in the vertical direction is always provided by the authors, differently from masonry elastic modulus in the horizontal direction. This is also consistent with the fact that, given the specimens' aspect ratio, the main contribution to their overall OOP stiffness is expected to be provided in the shorter, i.e., the vertical direction. Note also that in the application of Timoshenko's formulation, the Poisson coefficient is assumed equal to 0.30, as the values of the α coefficient provided are referred to that value of ν.

The experimental-to-predicted ratio is calculated for each experimental results. The mean, the median and the Coefficient of Variation (CoV) of these ratios is then calculated.
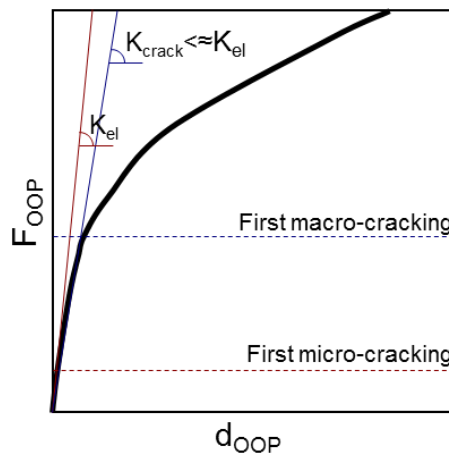
Figure 4.1. OOP Elastic vs secant at first macro-cracking stiffness of URM infills.

Table 4.3. Comparison of the experimental and predicted values of K_{crack} for 2E specimens.

Author	Specimen	K_{crack} [kN/mm]		
		experimental	predicted	exp/pred
da Porto et al. (2007)	FOB1	41.4	29.0	0.70
da Porto et al. (2007)	FOB2	41.4	29.0	0.70
da Porto et al. (2007)	FOB3	41.4	29.0	0.70
Hak et al. (2014)	TA5	35.0	70.4	2.01
DIST-UNINA	80_OOP_2E	1.9	1.4	0.74
DIST-UNINA	120_OOP_2E	3.4	7.7	2.26
			mean	1.19
			median	0.72
			CoV	63%

As expected, the elastic stiffness predicted by Kadysiewski and Mosalam's formulation overestimates K_{crack} for 2E infills in terms of median value. A median equal to one of the experimental-to-predicted ratios is obtained if the predicted K_{el} is multiplied for a reduction factor equal to 0.84. In other words, it seems that, for 2E infills, K_{crack} is equal to 0.84 times the initial elastic stiffness K_{el}. However, note that the quality of the prediction is not good, as the CoV associated with the experimental-to-predicted ratios is very high and equal to 63%.

For 4E specimens, note that Flanagan and Bennett (1999a)'s specimen 18 is associated with an experimental-to-predicted ratio that is an outlier according to Peirce (1852) criterion. Most likely, this occurs because the confining steel frame has a too high deformability to allow considering the restraints at the edges of the infill wall simply supported on fix supports. This value is hence dropped from the table.

However, it is worth to observe that for 4E infills in RC frames Timoshenko's prediction is quite good, with a median of the experimental-to-predicted ratio near to the unit and a low CoV. Most likely, the error of the prediction is due to the orthotropic nature of masonry.

Table 4.4. Comparison of the experimental and predicted values of K_{crack} for 4E specimens.

Author	Specimen	K_{crack} [kN/mm]		
		experimental	predicted	exp/pred
Angel et al.	1	5.2	5.9	0.89
Calvi and Bolognini	10	12.1	11.0	1.10
Varela-Rivera et al.	E-1	-	-	-
Varela-Rivera et al.	E-2	-	-	-
Varela-Rivera et al.	E-3	-	-	-
Varela-Rivera et al.	E-4	-	-	-
Varela-Rivera et al.	E-5	-	-	-
Varela-Rivera et al.	E-6	-	-	-
Furtado et al.	Inf_02	21.7	16.2	1.34
DIST-UNINA	80_OOP_4E	5.9	4.3	1.38
DIST-UNINA	120_OOP_4E	11.0	13.8	0.79
Dawe and Seah	WE2	-	-	-
Dawe and Seah	WE4	-	-	-
Dawe and Seah	WE5	-	-	-
Dawe and Seah	WE8	-	-	-
Flanagan and Bennett	18	33.9	190.6	-
Flanagan and Bennett	25	-	-	-
			mean	0.95
			median	1.10
			CoV	28%

4.3.2. Prediction of secant stiffness at peak load

In this section, the secant stiffness at maximum K_{max} is compared with the prediction of Kadysiewski and Mosalam's formulation, reported in Equation 51 in Chapter I, for 2E infills, with ξ equal to 0.50, as suggested by the authors.

The elastic modulus in the vertical direction is always provided and used in the application of Kadysiewski and Mosalam formulation.

The experimental-to-predicted ratio is calculated for each experimental results. The mean, the median and the Coefficient of Variation (CoV) of these ratios is then calculated. The results of the comparison are shown in Table 4.5.

Table 4.5. Comparison of the experimental and predicted values of K_{max} for 2E specimens.

Author	Specimen	K_{max} [kN/mm]		
		experimental	predicted	exp/pred
da Porto et al. (2007)	FOB1	22.0	14.5	0.66
da Porto et al. (2007)	FOB2	21.3	14.5	0.68
da Porto et al. (2007)	FOB3	25.2	14.5	0.58
Hak et al. (2014)	TA5	3.72	35.2	-
DIST-UNINA	80_OOP_2E	0.86	0.7	0.82
DIST-UNINA	120_OOP_2E	2.5	3.8	1.54
			mean	0.85
			median	0.68
			CoV	46%

Note that Hak et al.'s specimen TA5 is associated with an experimental-to-predicted ratio that is an outlier according to Peirce (1852) criterion. Most likely, this occurs because the confining RC frame has a too high deformability under the arching thrusts forming the infill thickness to allow considering the restraints at the edges of the infill wall simply supported on fix supports. This value is hence dropped from the table.

The value of ξ fixed by Kadysiewski and Mosalam to 0.50 is defined based on judgment. Hence, it is possible to calibrate it based on this, even if small, experimental database. A median of the experimental to predicted ratio equal to 1.00 is obtained if ξ is set to 0.73. However, note that the prediction is associated with a quite high value of the CoV, which is equal to 46%.

The assessment of the secant stiffness at peak load for 4E infills is not possible, as no literature formulation to this aim exists.

4.3.3. Modelling proposals

Based on the above comparisons the following empirical-mechanical modelling proposals are provided.

For what concerns 2E infills, the secant stiffness at first macro-cracking can be predicted by means of Kadysiewski and Mosalam's formulation, provided that ξ is assumed equal to one and that the resulting elastic stiffness is reduced by means of a factor equal to 0.84. The secant stiffness at maximum can be predicted by means of Kadysiewski and Mosalam's formulation with ξ equal to 0.73. In other words, to predict the secant stiffness at first macro-cracking and at peak load for 2E infills, Equation 1 and 2 can be used.

$$K_{crack} = 5.51 \frac{Ew}{(h/t)^3} \tag{1}$$

$$K_{max} = 4.79 \frac{Ew}{(h/t)^3} \tag{2}$$

In Equation 1 and 2, E is masonry elastic modulus in the direction in which the 2E infill spans. For what concerns 4E infills, the secant stiffness at first macro-cracking can be predicted by means of Timoshenko's formulation with quite good results. No literature formulation is available to predict the secant stiffness at maximum. However, from the experimental database collected, it is observed that the experimental value of K_{max} is equal, on average, to 0.40 times K_{crack}. Hence, it is suggested to assume K_{max} equal to 0.40 times the value of K_{crack} predicted through Timoshenko's formulation.

4.4. ASSESSMENT OF THE OOP STRENGTH

In this section, the OOP strength of the specimens considered in the experimental database is compared with the predictions of literature models. Based on the results of this comparison, proposals for modelling the pure OOP behaviour of URM infills are presented, also for what concerns the prediction of the first macro-cracking load.

Clearly, models based on two-way arching and adapted to the specific loading condition (uniformly distributed or concentrated on one or four points) are applied only on specimens bounded along four edges, models based on one-way arching and adapted to the specific loading condition are applied only on specimens bounded along two edges.

Due to the impossibility of adapting Dawe and Seah (1989)'s and Flanagan and Bennett (1999b)'s formulations to different loading schemes, as these formulations are empirical, Equations 7 and 11 are applied only on infills bounded along four edges tested through the application of a uniformly distributed load.

In addition, Dawe and Seah's response model is applied to all test specimens considering the deformability of the confining structural elements. For all specimens, the experimental strength is also compared with that predicted by Dawe and Seah's response model. For the application of this model, a very large number of geometric and mechanical properties for both the infill and the confining frames are necessary.

Note that in Appendix D, the specimens included in the experimental database are

listed with some of the specimens' main properties. For what concerns the confining frame properties, data concerning the upper beam (b subscript) and the columns (c subscript) are provided. The data concerning the lower beam are not reported as, in most cases, it cannot deform as it is attached to the laboratory floor as foundation beam. Only specimens E-1 and E-4 by Varela-Rivera et al. (2012) are provided with a deformable lower beam not attached to the floor. For these specimens, the lower beam has a 150 mm×200 mm cross section and its deformability will be considered in the application of Dawe and Seah's model. However, as already above stated, some necessary mechanical properties for some specimens are missing. In these cases, some assumptions are necessary. Namely:

i.   when masonry strength parallel to bricks' holes is missing for 4E specimens, it is assumed equal to the product of masonry compressive strength perpendicular to bricks' holes times the average of the parallel-to-perpendicular strength ratios calculated, when both values were available, for each specimen of the entire database. Such average is equal to 1.21;

ii.   when masonry elastic modulus is missing in a certain direction, it is assumed equal to the product of masonry compressive strength in the same direction times the average of the E_m/f_m ratios in the same direction calculated, when both values were available, for each specimen of the entire database. Such average is equal to 809 parallel to bricks' holes and to 1038 perpendicular to bricks' holes;

iii.   the shear modulus G of the confining frame materials is always calculated by applying the simple elastic relation $G=E/(2(1+\nu))$, in which the Poisson coefficient ν is assumed equal to 0.10 for concrete and to 0.30 for steel.

When the abovementioned assumptions are made to complete the Table 4.6, the assumption is marked with an asterisk (*).

To apply Dawe and Seah's response model, as reported in Chapter I, it is necessary to define a certain OOP deformed shape exhibited during OOP loading. In general, the deformed shape exhibited by the infill wall during the tests can be deduced by means of the evolution of local displacement during tests (if provided) or through the regularized and idealized crack patterns provided by the authors. The main deformed shapes individuated in the database are shown in Figure 4.2 and associated with the specimens of the experimental database in Table 4.6.
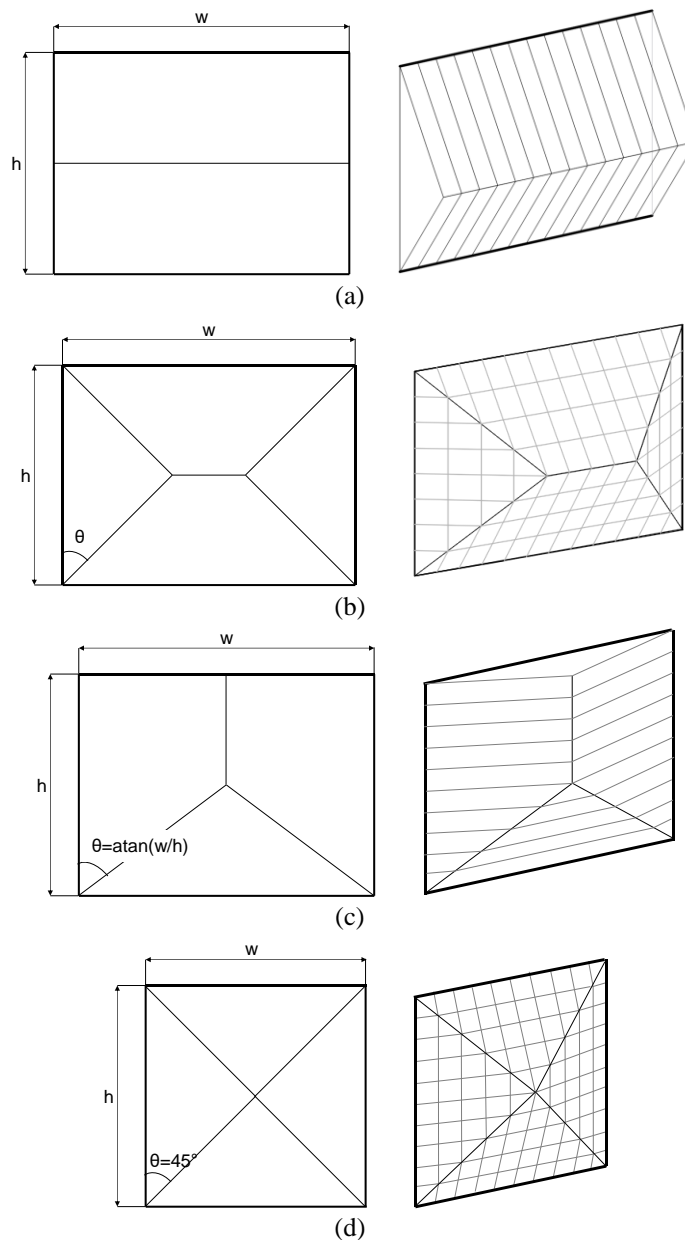
Figure 4.2. Regularized and idealized deformed shapes of the infills of the experimental database collected: the deformed shape shown in (a) is typical of 2E infills; the one shown in (b) is typical of rectangular 4E infills; the one shown in (c) is observed for some 4E infills in case of slippage at the upper edge; the one shown in (d) is typical of square 4E infills.

Table 4.6. Association of the specimens to the regularized and idealized deformed shapes reported in Figure 4.2.

#	Author	Specimen	Boundary condition	Deformed shape
1	da Porto et al.	FOB1	2E	a
2	da Porto et al.	FOB2	2E	a
3	da Porto et al.	FOB3	2E	a
4	Hak et al.	TA5	2E	a
5	DIST-UNINA	80_OOP_2E	2E	a
6	DIST-UNINA	120_OOP_2E	2E	a
7	Angel et al.	1	4E	b
8	Calvi and Bolognini	10	4E	b*
9	Varela-Rivera et al.	E-1	4E	b
10	Varela-Rivera et al.	E-2	4E	b
11	Varela-Rivera et al.	E-3	4E	b
12	Varela-Rivera et al.	E-4	4E	d
13	Varela-Rivera et al.	E-5	4E	d
14	Varela-Rivera et al.	E-6	4E	d
15	Furtado et al.	Inf_02	4E	c
16	DIST-UNINA	80_OOP_4E	4E	b
17	DIST-UNINA	120_OOP_4E	4E	b
18	Dawe and Seah	WE2	4E	c
19	Dawe and Seah	WE4	4E	c
20	Dawe and Seah	WE5	4E	b
21	Dawe and Seah	WE8	4E	b
22	Flanagan and Bennett	18	4E	b*
23	Flanagan and Bennett	25	4E	b*

When such deformed shape is neither provided by the Authors nor can be deduced by the description of the fracture pattern, it seems reasonable to assume that it is a hipped deformed shape (the most common for 4E specimens) as the one shown in Figure 4.2b with $\theta=45°$. This assumption is marked with an asterisk (*) in Table 4.2.

For each strength-predicting formulation/model, the experimental-to-predicted strength ratios are calculated for all specimens. Mean, median and Coefficient of Variation of these ratios are calculated for all OOP capacity models in order to assess their effectiveness. The results of the assessment carried out for all models are then discussed and compared.

A preliminary judgment on the most influent parameters in determining the OOP strength of URM infills can be provided by observing Figure 4.3, in which the experimental OOP strength of specimens is reported as a function of the infill thickness, vertical slenderness and vertical masonry compressive strength both for infills bounded

along two edges and for infills bounded along four edges. Clearly, similar trends are observed also when relating the OOP strength with the horizontal slenderness and compressive strength of masonry.

URM infills' OOP strength increases with the panel thickness and masonry compressive strength. In fact, for increasing t and f_m, the maximum thrust due to arching action increases and so also the maximum lateral load in equilibrium with maximum thrust increases. The slenderness ratio increases when h increases and t reduces. When t reduces, arching thrusts reduce. In addition, when h increases, arching thrusts approach the vertical direction: hence, their component opposite to the OOP external load reduces. For both of these reasons, clearly, the OOP strength reduces with increasing panel slenderness.
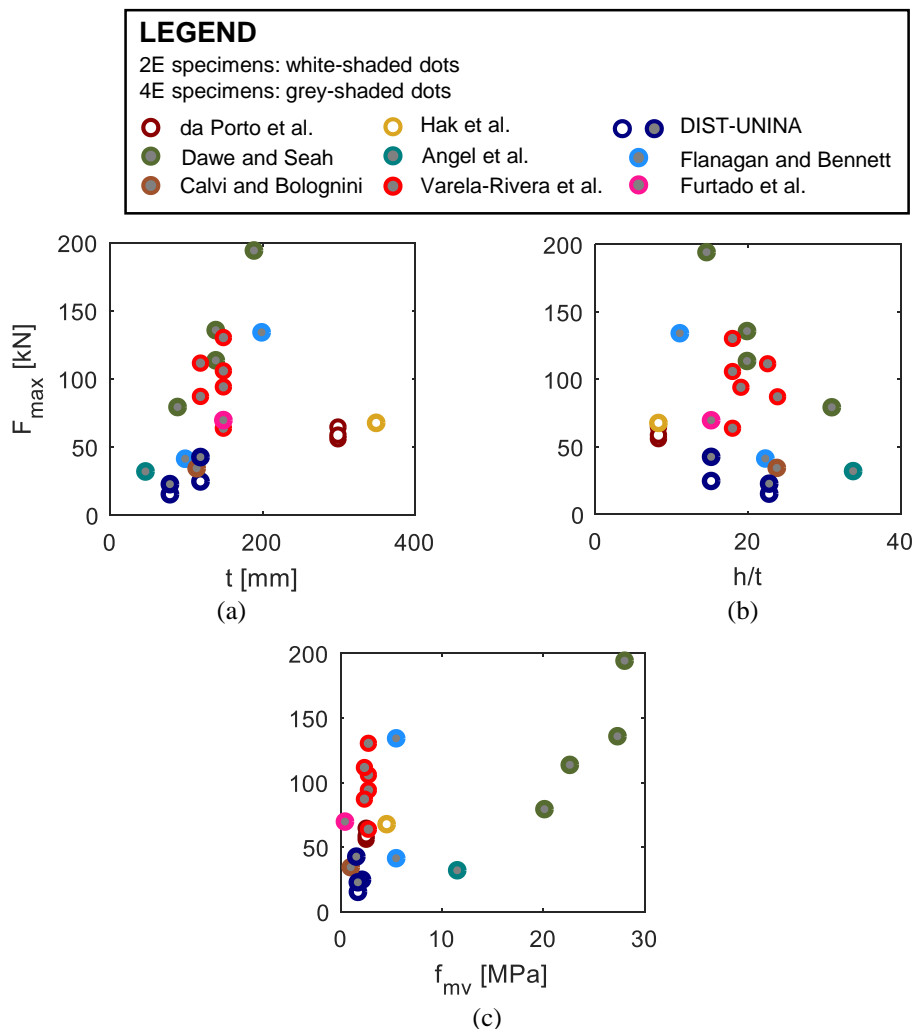
Figure 4.3. Trends of the experimental value of the OOP strength of the specimens included in the database with the specimens' thickness (a), vertical slenderness (b) and masonry vertical compressive strength (c).

4.4.1. Prediction of the OOP strength of 2E infills

In this section, OOP strength models based on one-way arching are applied to predict the resistance of test specimens bounded along two edges. In Table 4.7 and 4.8, the observed and predicted values of the OOP strength of all specimens are reported as well as the mean, median and CoV of the experimental-to-predicted strength ratios.

Table 4.7. Experimental strength, Fmax [kN], of infills bounded along two edges compared to the predicted value by McDowell et al., Angel et al. and Eurocode 6.

		F_{max} [kN]						
			predicted					
			McDowell et al.		Angel et al.		Eurocode 6	
Author	specimen	exp.	pred	exp/pred	pred	exp/pred	pred	exp/pred
da Porto et al.	FOB1	63.9	71.6	0.87	52.9	1.21	50.5	1.27
da Porto et al.	FOB2	55.3	71.6	0.75	52.9	1.04	50.5	1.09
da Porto et al.	FOB3	58.0	71.6	0.79	52.9	1.10	50.5	1.15
Hak et al.	TA5	67.0	212	0.32	150	0.45	144	0.47
DIST-UNINA	80_OOP_2E	14.6	6.0	2.43	5.1	2.85	12.0	1.21
DIST-UNINA	120_OOP_2E	24.0	37.9	0.63	20.6	1.17	33.1	0.73
			mean	0.96	mean	1.30	mean	1.01
			median	0.77	median	1.13	median	1.12
			CoV	77%	CoV	62%	CoV	32%

On the entire database, on average, Eurocode 6 (2005)'s and Angel et al. (1994)'s models underestimate the OOP strength of test specimens, which is expected as they are based on limit analysis lower bound theorem. It is worth to note that all models significantly overestimate Hak et al.'s specimen strength.

Note that the application of Dawe and Seah (1989)'s model (Table 4.8) is performed also by accounting for the deformability of the confining elements (except for da Porto et al. (2007)'s specimens, of course). It is worth to mention that for specimen 120_OOP_2E, the evolution of the outward displacement of the RC frame upper beam during the OOP test is provided. This allow calibrating an effective stiffness of the RC elements' section equal to one-half their elastic flexural stiffness, in order to obtain a predicted maximum beam deflection equal to the experimental one.

For this reason, in all cases, RC members are considered as provided with both an elastic flexural stiffness (EI) and with an effective flexural stiffness equal to one-half the elastic one ($EI_{eff}=0.5EI$).

Table 4.8. Experimental strength, Fmax [kN], of infills bounded along two edges compared to the predicted value by Dawe and Seah's model under the hypothesis of stiff confining elements (stiff), of deformable confining elements with elastic stiffness (elastic) and of deformable confining elements with effective flexural stiffness equal to one-half the elastic one (effective).

		F_{max} [kN]						
			predicted by Dawe and Seah's model					
Author	specimen	exp.	stiff	exp/pred	elastic	exp/pred	effective	exp/pred
da Porto et al.	FOB1	63.9	61.9	1.03	-	1.03	-	1.03
da Porto et al.	FOB2	55.3	61.9	0.89	-	0.89	-	0.89
da Porto et al.	FOB3	58.0	61.9	0.94	-	0.94	-	0.94
Hak et al.	TA5	67.0	181	0.37	172	0.39	164	0.41
DIST-UNINA	80_OOP_2E	14.6	10.9	1.34	9.9	1.47	9.8	1.49
DIST-UNINA	120_OOP_2E	24.0	36.0	0.67	31.8	0.75	28.9	0.83
			mean	0.87	mean	0.91	mean	0.93
			median	0.92	median	0.92	median	0.92
			CoV	38%	CoV	39%	CoV	37%

The application of Dawe and Seah's model shows that it works quite well on 2E specimens and that accounting, when necessary, for the frame elements' deformability improves the quality of its performance.

Therefore, it can be concluded that the best prediction of the OOP strength is provided by both Eurocode 6 formulation adapted to the real loading condition, which is associated with a median of the experimental-to-predicted strength ratios equal to 1.12 and with a CoV equal to 32%, and Dawe and Seah's model, which is associated with a median of the experimental-to-predicted strength ratios equal to 0.92 and with a CoV ranging from 37% to 39%.

However, being Eurocode 6 model application very simple and straightforward, it seems reasonable to suggest its application on 2E infills, provided that its formulation is adapted to the real loading condition.

4.4.2. Prediction of the OOP strength of 4E infills

In this section, OOP strength models based on two-way arching are applied to predict the resistance of test specimens bounded along four edges. In Tables 4.9-4.10, the observed and predicted values of the OOP strength of all specimens as well as the mean,

median and CoV of the experimental-to-predicted strength ratios are reported for specimens in RC frames and in steel frames, respectively.

Remember that the empirical formulations by Dawe and Seah and Flanagan and Bennett (1999b) were applied only to test specimens loaded under uniformly distributed load, as they are empirical and cannot be adapted to different loading conditions. Remember also that they were defined for infills in pinned steel frames and that, for this reason, they can underestimate the OOP strength of infills in moment-resisting (such as RC) frames. Bashandy et al. (1995)'s formulation is adapted to the specific loading condition used during tests.

Table 4.9. Experimental strength, F_{max} [kN], of infills bounded along four edges to RC frames compared to the predicted value by Dawe and Seah (empirical formula), Flanagan and Bennett and Bashandy et al.

			F_{max} [kN]					
			predicted					
			D&S formula		F&B		Bashandy et al.	
Author	specimen	exp.	exp.	exp/pred	exp.	exp/pred	exp	exp/pred
Angel et al.	1	31.3	26.8	1.17	24.4	1.29	8.1	3.89
Calvi and Bolognini	10	33.7	-	-	-	-	13.3	2.53
Varela-Rivera et al.	E-1	63.1	17.1	3.68	11.3	5.56	101	0.62
Varela-Rivera et al.	E-2	93.4	20.5	4.57	14.5	6.43	94.3	0.99
Varela-Rivera et al.	E-3	86.4	10.2	8.51	7.6	11.32	37.2	2.32
Varela-Rivera et al.	E-4	105	23.4	4.49	17.1	6.14	103	1.02
Varela-Rivera et al.	E-5	130	23.8	5.44	17.3	7.50	101	1.28
Varela-Rivera et al.	E-6	111	12.7	8.75	9.7	11.46	42.1	2.63
Furtado et al.	Inf_02	69.0	23.6	2.93	21.4	3.23	30.4	2.27
DIST-UNINA	80_OOP_4E	22.0	-	-	-	-	5.6	3.94
DIST-UNINA	120_OOP_4E	41.9	-	-	-	-	21.5	1.95
			mean	4.94	mean	6.62	mean	2.13
			median	4.53	median	6.28	median	2.27
			CoV	53%	CoV	53%	CoV	52%

Table 4.10. Experimental strength, F_{max} [kN], of infills bounded along four edges to steel frames compared to the predicted value by Dawe and Seah (empirical formula), Flanagan and Bennett and Bashandy et al.

F_{max} [kN]							
			predicted				
			D&S formula		F&B		Bashandy et al.
Author	specimen	exp.	exp.	exp/pred	exp.	exp/pred	exp	exp/pred
Dawe and Seah	WE2	194	368	0.53	335	0.58	1720	0.11
Dawe and Seah	WE4	113	170	0.66	155	0.73	523	0.22
Dawe and Seah	WE5	78.6	64.5	1.22	58.8	1.34	43.6	1.80
Dawe and Seah	WE8	135	196	0.69	179	0.76	590	0.23
Flanagan et al.	18	133	163	0.82	148	0.90	324	0.41
Flanagan et al.	25	40.6	37.0	1.10	33.7	1.20	38.4	1.06
			mean	0.84	mean	0.92	mean	0.64
			median	0.75	median	0.83	median	0.32
			CoV	32%	CoV	32%	CoV	104%

The application of Dawe and Seah's model is performed by accounting for the deformability of the confining elements as well as for the specific load shape adopted during tests and for the deformed shape shown by infills during tests. It is worth to mention that for specimen 120_OOP_4E and for all Varela-Rivera et al.'s specimens, the evolution of the outward displacement of the RC frame upper beam during the OOP test is reported. This allow calibrating an effective flexural stiffness of the RC elements' section equal to 0.30 times the elastic flexural stiffness for specimen 120_OOP_4E, in order to obtain a predicted maximum beam deflection equal to the experimental one. In all the other cases, RC members are considered as provided with an elastic flexural stiffness or by an effective flexural stiffness equal to one-half the elastic one.

In addition, the following assumptions were made when applying Dawe and Seah's model:

i.   For what concerns Angel et al.'s specimen 1, only vertical arching was considered. In fact, the horizontal slenderness ratio w/t, which is greater than 50 for this specimen, is more than two times the slenderness upper bound (25, according to Eurocode 6 and ASCE 41-13) allowing considering possible the occurrence of arching action in that direction: based on this, it

seems that the occurrence of horizontal arching should be excluded;

ii.   For what concerns Furtado et al. (2016a)'s specimen Inf_02, the predicted experimental-to-predicted ratio ranges from 2.50 (stiff boundary elements) to 2.62 (deformable boundary elements with effective stiffness). These values have been classified as outliers according to Peirce's criterion (Peirce 1852) and, so, have been dropped from Table 4.11;

iii.   For what concerns Dawe and Seah's specimens WE2, WE4, WE5 and WE8, the experimental-to-predicted ratios calculated by the Authors of this study are equal to 0.86, 0.95, 0.90 and 0.57, respectively. These values are different from those presented by Dawe and Seah's themselves, which are equal to 1.02, 0.96, 0.88 and 0.99, respectively. To the Authors' knowledge, this difference cannot be explained with other reason than the fact that Dawe and Seah's knowledge level of material properties, boundary conditions of infills and assumed deformed shape was of course higher than the knowledge level of the Authors of this study: e.g., for what concerns masonry properties in the horizontal direction, only an average of the compressive strength and of the elastic modulus is provided in the reference paper. For this reason, in Table 4.8, the experimental-to-predicted ratios presented for Dawe and Seah's specimens are those declared by Dawe and Seah themselves. This circumstance has been pointed out with an asterisk (*) in Table 4.12.

The results of the application of Dawe and Seah's model is reported in Table 4.11 for infills in RC frames and in Table 4.12 for infills in steel frames.

Table 4.11. Experimental strength, F_{max} [kN], of infills bounded along four edges to RC frames compared to the predicted value by Dawe and Seah mechanical model under the hypothesis of stiff confining elements (stiff), of deformable confining elements with elastic stiffness (elastic) and of deformable confining elements with effective flexural stiffness equal to one-half the elastic one (effective).

		F_{max} [kN]						
			predicted by Dawe and Seah's model					
Author	specimen	exp.	stiff	exp/pred	elastic	exp/pred	effective	exp/pred
Angel et al.	1	31.3	46.5	0.67	38.1	0.82	33.4	0.94
Calvi and Bolognini	10	33.7	31.0	1.08	29.9	1.13	28.4	1.19
Varela-Rivera et al.	E-1	63.1	267	0.24	102	0.62	84.5	0.75
Varela-Rivera et al.	E-2	93.4	272	0.34	140	0.67	115	0.81
Varela-Rivera et al.	E-3	86.4	142	0.61	71.4	1.21	55.9	1.55
Varela-Rivera et al.	E-4	105	260	0.40	115	0.92	93.7	1.12
Varela-Rivera et al.	E-5	130	259	0.50	125	1.04	99.5	1.30
Varela-Rivera et al.	E-6	111	137	0.82	89.3	1.24	64.8	1.71
Furtado et al.	Inf_02	69.0	27.6	-	26.9	-	26.3	-
DIST-UNINA	80_OOP_4E	22.0	22.3	0.99	21.4	1.03	21.0	1.05
DIST-UNINA	120_OOP_4E	41.9	55.0	0.76	51.9	0.81	46.2	0.91
			mean	0.64	mean	0.95	mean	1.13
			median	0.64	median	0.97	median	1.08
			CoV	43%	CoV	23%	CoV	28%

Table 4.12. Experimental strength, Fmax [kN], of infills bounded along four edges to steel frames compared to the predicted value by Dawe and Seah mechanical model under the hypothesis of stiff confining elements (stiff), of deformable confining elements with elastic stiffness (elastic) and of deformable confining elements with effective flexural stiffness equal to one-half the elastic one (effective).

F_{max} [kN]						
			predicted by Dawe and Seah's model			
Author	specimen	exp.	stiff	exp/pred	elastic	exp/pred
Dawe and Seah	WE2	193.5	1731	0.11	189.7*	1.02*
Dawe and Seah	WE4	112.9	761.1	0.15	117.4*	0.96*
Dawe and Seah	WE5	78.6	479.4	0.16	89.6*	0.88*
Dawe and Seah	WE8	135.1	1597	0.08	136.4*	0.99*
Flanagan and Bennett	18	133.5	642.9	0.21	269.8	0.49
Flanagan and Bennett	25	40.6	126.4	0.32	65.5	0.62
			mean	0.17	mean	0.73
			median	0.16	median	0.74
			CoV	49%	CoV	26%

*Values provided by Dawe and Seah.

As shown in Table 4.11, Dawe and Seah's, Flanagan and Bennett (1999b)'s and Bashandy et al.'s formulations significantly underestimate the OOP strength of infills in RC frames, as expected, with median of the experimental-to-predicted ratios ranging from 2.27 to 6.28. On the contrary, Dawe and Seah's model with elastic flexural stiffness of confining members performs, on average, very well, with a median of the experimental-to-predicted strength ratios equal to 0.97 associated with a CoV equal to 23%. For all these reasons, it seems that the prediction of the OOP strength of URM infills bounded along four edges to RC frames can be successfully achieved by applying Dawe and Seah's response model, provided that the deformability of the confining elements is considered. However, it is worth to mention the labor-intensive nature of the model application, for which some simplification is needed.

As shown in Table 4.10, Bashandy et al.'s formulation predicts an OOP strength of URM infills in steel frames equal to, on average, two times the experimental value. On the contrary, Dawe and Seah's model and formulation, as well as Flanagan and Bennett

(1999b)'s formulation, on average, produce similar results, with median of the experimental-to-predicted ratios ranging from 0.75 to 0.83. Therefore, using the simpler Flanagan and Bennett (1999b)'s formulation seems to be the best predicting approach for URM infills in steel frames; however, it is applicable, only under uniformly distributed lateral loads. For this reason, it is suggested also in this case the use (with no significant loss in the predictive capacity) of Dawe and Seah's response model, provided that the deformability of the confining elements is considered.

It is worth to mention that the deformability of the confining elements plays a fundamental role in predicting the OOP strength of URM infills, especially in steel frames, as expected. The ratio between the strength calculated under the hypothesis of deformable confining elements (F_{def}) and the strength calculated under the hypothesis of stiff confining elements (F_{stiff}) is equal to, on average, 0.67 for infills in RC frames and to 0.25 for infills in steel frames. Clearly, the value of the F_{def}/F_{stiff} ratio somehow depends on the element-infill "relative" stiffness. In fact, for a given OOP displacement, the entity of the frame actual deformation due to arching thrusts increases with increasing value of thrust forces. Such a value depends on the infill thickness and on masonry compressive strength, which is strongly related to its elastic modulus. Hence, the value of arching thrusts depends on the OOP stiffness of the infill, which is strongly related to the infill thickness and to masonry elastic modulus. Of course, for a given OOP displacement, the entity of the frame actual deformation due to arching thrusts decreases with increasing flexural stiffness of the confining elements.

4.4.3. Final remarks on the predictive capacity of literature formulations/models

Based on the findings above shown, it can be concluded that:

i.   The OOP strength of infills bounded along two edges is well predicted by Eurocode 6 formulation adapted to the real loading condition (experimental-to-predicted strength ratios' mean equal to 1.01, median equal to 1.12, CoV equal to 32%);

ii.   The OOP strength of infills bounded along four edges to RC frames is well predicted only by Dawe and Seah's response model accounting for the confining elements' elastic deformability (experimental-to-predicted strength ratios' mean equal to 0.95, median equal to 0.97, CoV equal to

23%):

iii.   The OOP strength of infills bounded along four edges to steel frames is predicted by Dawe and Seah's response model with some overestimation (experimental-to-predicted strength ratios' mean equal to 0.73, median equal to 0.74, CoV equal to 26%). As an alternative, the simpler Flanagan and Bennett (1999a)'s formulation can be used (experimental-to-predicted strength ratios' mean equal to 0.92, median equal to 0.83, CoV equal to 32%), but only in the case of uniformly distributed load.

For all these reasons, it seems that the prediction of the OOP seismic strength of URM infills can significantly benefit from the simplification of Dawe and Seah's model in a reliable and robust way, especially for URM infills bounded along four edges to RC frames. Namely, it is useful to define, if possible, a direct formulation to determinate the strength that Dawe and Seah's model would predict. Different attempts showed that this cannot be done in closed form: a numerical approach will be used in the following subsections.

This effort is aimed at proposing a formulation that can be used for the assessment of 4E URM infills' OOP strength also in a code-based framework. To achieve this goal, as already stated, it seems appropriate to begin from Dawe and Seah's response model, which is robust and reliable: in fact, its effectiveness has been demonstrated based on experimental results; in addition, it is a mechanical model, based on consolidated principles and reasonable hypotheses. However, prior to this simplification, it is worth to discuss some issues reported in the following list.

i.   *Load shape*. It has been shown that experimental tests have been performed by using different loading conditions and that Dawe and Seah's response model works quite well for all of them. Hence, the direct and simplified strength formulation that will be derived in the following subsections will be proposed for the assessment of URM infills in both "experimental" and "real" cases, i.e., under realistic loading conditions. For this reason, it seems reasonable to perform the simplification effort herein proposed for three different load shapes. The first one is a four-point load, with each horizontal couple of points distant h/3 from the nearest horizontal edge. This loading condition is considered exclusively for comparison with experimental tests' results. The second one is a uniform load, which can represent, e.g., wind

load, and also for the comparison with experimental tests. The third one is a sinusoid-shaped load, which is representative of seismic loads, as will be shown in section 6.

ii. *Frame deformability.* It has been shown that when dealing with experimental results the confining frame deformability cannot be neglected to obtain a good prediction of the OOP strength of URM infills. However, as stated by Flanagan and Bennett (1999b), too, in real buildings infill walls are confined by structural elements whose deformability is usually neutralized as they are themselves confined by other structural and non-structural elements. For this reason, in real buildings, adopting the hypothesis of stiff confining elements when calculating URM infills' OOP strength seems reasonable. So, in the simplified formulations that will be proposed, the confining elements deformability will be neglected. However, it seems appropriate that the proposed formulations can be applied also for comparison with experimental tests results, in which, as demonstrated, the frame elements' deformability cannot be neglected. Therefore, once a direct strength formulation has been obtained for all load shapes, an empirical correction factor will be calibrated to reduce the OOP strength for a given "frame-to-infill relative stiffness ratio".

iii. *Assumption of a deformed shape.* It has been shown that to apply Dawe and Seah's model it is necessary to fix a regularized deformed shape of the infill. In addition, it has been shown that for infills bounded along two edges the experimental deformed shape can be always regularized with that represented in Figure 4.2a. For what concerns infills bounded along four edges, the experimental database herein collected shows that two deformed shapes are commonly observed: the one shown in Figure 4.2b, which transforms in the one represented in Figure 4.2d for square panels, and the one shown in Figure 4.2c when the infill detaches from the upper beam during OOP loading. In the simplification effort herein proposed, the deformed shape shown in Figure 4.2a will be used for 2E infills, both the deformed shapes shown in Figure 4.2b (or Figure 4.2d) and in Figure 4.2c will be considered for 4E infills.

Remember that the empirical formulations by Dawe and Seah and Flanagan and Bennett (1999b) were applied only to test specimens loaded under uniformly distributed

load, as they are empirical and cannot be adapted to different loading conditions. Remember also that they were defined for infills in pinned steel frames and that, for this reason, they can underestimate the OOP strength of infills in moment-resisting (such as RC) frames. Bashandy et al.'s formulation is adapted to the specific loading condition used during tests.

4.4.4. Some considerations on the OOP strength of infills under seismic load

As above mentioned, before showing the derivation of a simplified direct formulation for the OOP strength of URM infills, it is worth to discuss the shape of the lateral load acting on URM infills when subjected to seismic actions.

Consider an infill wall bounded only along the upper and lower edges. Such a panel can be considered, with acceptable approximation, as a uniformly-distributed mass beam pinned at edges, whose first vibration mode in the OOP direction is shaped as a sinusoid function, according to expression reported in Equation 3.

$$\varphi(y) = \Phi \sin\left(\frac{\pi}{h}y\right) \qquad\qquad 0 \le y \le h \tag{3}$$

In Equation 3, Φ is the maximum displacement attained at the infill mid-height due to the first vibration mode; y is the axis denoting the vertical direction. For this boundary condition, the participating mass associated to the first vibration mode is the 81% of the infill total mass. For a uniformly-distributed mass dynamic system, the static load for unit-width equivalent to the seismic action, $q_{seismic,2E}$, corresponding to the first vibration mode, is shaped as the first vibration mode itself, as shown in Equation 4.

$$q_{seismic,2E}(y) = q_{s,2E} \sin\left(\frac{\pi}{L}y\right) \qquad\qquad 0 \le y \le L \tag{4}$$

In Equation 4, $q_{s,2E}$ is the maximum value attained at the infill mid-height by the sinusoidal-distributed load $q_{seismic,2E}$, y is the direction in which arching action occurs and L is the infill length in the direction of arching action. Given this load shape, under the hypothesis of Eurocode 6's approach and of McDowell et al.'s approach the values of $q_{s,2E}$ reported in Equations 5a-b are obtained. Consequently, the OOP strength $F_{max,seismic,2E}$ reported in Equations 6a-b are calculated by integrating Equation 4 on the entire infill height and width.

McDowell et al.'s approach   Eurocode 6 approach

$$q_{s,2E} = \frac{\pi^2}{L^2} M_{yv} \qquad \text{(a)}; \qquad q_{s,2E} = 0.85 f_m \left(\frac{t}{L}\right)^2 \qquad \text{(b)} \qquad \text{(5)}$$

$$F_{seismic,2E} = 4\pi M_{yv} \frac{w}{L} \qquad \text{(a)}; \qquad F_{seismic,2E} = 0.85 f_m \left(\frac{t}{L}\right)^2 wh \quad \text{(b)} \qquad \text{(6)}$$

Based on the above results, the OOP resistance of an infill bounded along two edges under seismic load is equal to around 0.78 times the resistance calculated for the same infill subjected to a uniformly distributed load, i.e., is always lower than that associated with a uniformly distributed load. In this sense, calculating the OOP strength of URM infills for a seismic safety check by means of a formulation defined for a uniformly distributed load can be not conservative. In addition, note that the OOP strength of 2E infills under seismic load is theoretically almost equal to that shown under two concentrated forces, each of which distant L/3 from the nearest bounded edge ($\gamma=1/3$).

Now, consider an infill bounded along four edges. According to consolidated analytical studies (Blevins and Plunkett, 1980) the deformed shape associated to the first OOP vibration mode of an elastic plate simply-supported at edges is well described, along the vertical and horizontal direction in the plate's plane, through a sinusoidal shape function. Given these conditions, the deformed shape associated to the first mode in the OOP direction of such a plate can be expressed as reported in Equation 7 and represented in Figure 4.4.

$$\varphi(x,y) = \Phi \sin\left(\frac{\pi}{w}x\right) \sin\left(\frac{\pi}{h}y\right) \qquad \begin{array}{l} 0 \le x \le w \\ 0 \le y \le h \end{array} \qquad \text{(7)}$$

In Equation 7, Φ is the maximum displacement attained at the infill center due to the first vibration mode. For this boundary condition, the participating mass associated to the first vibration mode is the 66% of the infill total mass. Also in this case, given the hypothesis of uniformly-distributed mass system, the static load for unit-surface equivalent to the seismic action, $q_{seismic,4R}$, corresponding to the first vibration mode is shaped as the first vibration mode itself, as shown in Equation 8.

$$q_{seismic,4E}(x,y) = q_{s,4E} \sin\left(\frac{\pi}{w}x\right) \sin\left(\frac{\pi}{h}y\right) \qquad \begin{array}{l} 0 \le x \le w \\ 0 \le y \le h \end{array} \qquad \text{(8)}$$

In Equation 8, $q_{s,4E}$ is the maximum value attained at the infill center by the sinusoidal-distributed load $q_{seismic,4E}$.
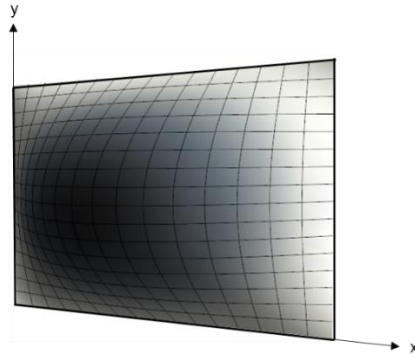
Figure 4.4. First mode sinusoid deformed shape of an infill bounded along all edges.

Clearly, for both 2E and 4E infills, independently on the deformed shape shown at peak load, the sinusoid load shape can be considered rigorous only in the first loading stages; in the post-elastic range, infills' modal deformed shape is expected to change gradually up to becoming similar to the shape defined by the collapse mechanism exhibited. Neither the evolution of the load shape nor the variation of the deformed shape can be considered when applying Dawe and Seah's model, as both of them must be fixed since the beginning of the procedure application. For this reason, it is assumed that the seismic load shape does not vary at increasing central displacement demand acting on the infill, with some analogy with the classical procedure for the application of non-linear static pushover analysis, in which the modification of the lateral deformed shape of the structure, and consequently of the lateral load shape, and are not considered. Note that, nevertheless, in the comparison with experimental tests' results, the model effectiveness is demonstrated despite the assumption of a fixed deformed shape.

4.4.5. Proposed direct mechanical-based formulations

It has been shown in the previous sections that Dawe and Seah's mechanical-based model works quite well when predicting the OOP strength of URM infills. However, the application of the model is, actually, very labor-intensive. With the aim of calculating straightforwardly the OOP strength of URM infills without renouncing to the quality of the mechanical-based predictions of Dawe and Seah's model, simplified but robust and

reliable formulations are herein proposed.

As already stated, these proposed formulations are first calculated by applying Dawe and Seah's response model under the hypothesis of stiff confining elements (as in real buildings) for 2E and 4E infills under four-point load, uniformly distributed load (which can represent, e.g., a wind load) and sinusoid load (which represents, as shown in subsection 4.4.4, seismic load). The two deformed shapes observed during experimental tests are considered: a hipped deformed shape (Figure 4.2b) and a trilinear deformed shape (Figure 4.2c).

To propose these simplified strength formulations, a parametric study is carried out. Namely, sets of:

i. 11 values of possible height (ranging from 1000 to 3000 mm with 200 mm steps);

ii. 17 values of possible width (ranging from 1400 to 4600 mm with 200 mm steps);

iii. 9 values of possible thickness (ranging from 40 to 360 mm with 40 mm steps);

iv. 24 values of possible masonry vertical compressive strength (ranging from 0.40 to 5.00 N/mm^2, which are values typical for hollow clay brick and mortar masonry, with 0.20 N/mm^2 steps);

v. 24 values of possible masonry horizontal compressive strength (with the same range and steps used for vertical compressive strength);

are considered. The elastic moduli of masonry have been defined based on the E_m/f_m ratios calculated on the collected experimental database. Based on these sets of geometric and mechanical properties, 969408 "simulated" 4E infills were defined. However, among these, those defined by unrealistic geometric properties were not considered. Namely, infills with vertical or horizontal slenderness ratio lower than 5 or greater than 35 were excluded, as well as infills with width lower than height, as they are not typical of real buildings (and, potentially, can be considered as infills with horizontal height and vertical width). Hence, 530496 "simulated" 4E infills were actually considered.

Then, Dawe and Seah's response model was applied on the simulated infills. The calculated values of strength were related to the simulated infills' geometric and mechanical properties by means of a non-linear least square regression analysis. In this

way, simple and direct strength formulations were obtained which reproduce, although with a certain approximation, the mechanical-based and reliable result that Dawe and Seah's model would have provided.

To perform non-linear regressions, a model function must be defined. First, the model function should be the one that allows reducing the regression error as much as possible. However, in the Authors' opinion, it should be provided with two more characteristics: first, the model function should be simple and simply applicable; second, even if derived through a numerical analysis, the model function should be defined by predictive parameters that can be immediately and straightforwardly related to the mechanical phenomena that determinate the predicted variable, i.e., in this case, the OOP strength of infills.

Also considering that Eurocode 6 formulation, which has clear and simple mechanical basis, works quite well on 2E specimens, the model function reported in Equation 9 – similar to that of Eurocode 6 – was chosen.

$$F_{max} = \left[\theta_{1v} f_{mv}{}^{\theta_{2v}} \left(\frac{t}{h}\right)^{\theta_{3v}} + \theta_{1h} f_{mh}{}^{\theta_{2h}} \left(\frac{t}{w}\right)^{\theta_{3h}} \right] wh \tag{9}$$

In Equation 9, in the summation in square brackets, the first term accounts for vertical arching, the second term for horizontal arching. In this equation, lengths are expressed in millimeters and forces in Newtons.

In Equation 9, θ_1, θ_2 and θ_3 are coefficients determined by means of the non-linear regression analysis of the numerical values of the OOP strength predicted by means of Dawe and Seah's model. The values of the regression coefficients are reported in Table 4.13 for different loading shapes and deformed shapes; in addition, the mean, median and CoV of the theoretical-to-simplified strength ratios are reported.

It is observed that for all deformed shapes, load shapes and boundary conditions the capacity of the proposed equation in substituting the application of Dawe and Seah's model is good, as the median of the theoretical-to-simplified ratios ranges from 0.98 to 1.01 while the CoV range from 3 to 12%.

Table 4.13. Regression coefficients for Equation 9 for different load and deformed shape, together with mean, median and CoV of the ratios of the OOP strength calculated for the "simulated" infills through Dawe and Seah's model and by applying the regression formulations (simplified).

#	load shape	deformed shape	values of the regression coefficients						model-to-simplified ratios		
			θ_{1v}	θ_{2v}	θ_{3v}	θ_{1h}	θ_{2h}	θ_{3h}	mean	median	CoV
1	4-pt	hipped	2.20	0.85	2.25	0.35	1.27	1.62	0.97	0.99	10%
2	unif.	hipped	2.36	0.97	2.15	2.17	0.94	1.89	0.97	0.98	8%
3	sin.	hipped	2.86	0.82	2.28	0.23	1.39	1.48	0.97	0.99	12%
4	4-pt	trilinear	0.61	0.99	2.08	1.19	1.00	2.09	0.99	1.00	3%
5	unif.	trilinear	0.97	0.99	2.08	1.91	1.00	2.09	0.99	1.01	3%
6	sin.	trilinear	2.58	0.84	2.24	0.39	1.29	1.62	0.97	0.99	10%

The proposed direct strength formulation has been derived for 4E infills for different deformed shapes and load shapes under the hypothesis of stiff boundary structural elements. The latter is the condition typical of "real" infill walls in "real" buildings, as the deformation of structural elements due to arching thrusts is prevented by the confinement provided by other structural and non-structural elements. However, it seems reasonable to provide some tool allowing the analyst of experimental data applying the proposed formulations also accounting for the frame deformability, based on the experimental data, i.e., through an empirical approach (as also done by Dawe and Seah, Flanagan and Bennett 1999b).

As already stated, it seems reasonable to assume as predictor parameter some factor dependent on the "relative stiffness" of the structural elements and of the infill wall. As vertical arching thrusts act on the frame beam(s) and horizontal arching thrusts act on the frame columns, the predictor parameters reported in Equation 10 are defined with forces expressed in Newtons and lengths in millimeters.

$$\lambda_v = \frac{(EI)_b}{1000 t f_{mv}} \qquad\qquad \lambda_h = \frac{(EI)_c}{1000 t f_{mh}} \qquad\qquad (10)$$

Clearly, the application of Dawe and Seah's model under the hypothesis of deformable confining frame accounts also for the axial and torsional deformability of elements. For the sake of simplicity, the predictor parameters are expressed only in terms of the flexural stiffness of the elements. In other words, it is assumed that the axial and torsional deformability of elements is related to the flexural one. In addition, the stiffness of the infill wall is represented by the compressive strength, not by the elastic modulus.

This is because the elastic modulus is not always available in the considered database. Also in this case, it is implied that the elastic modulus is (linearly) related to the compressive strength, as also assumed by different codes (e.g., Eurocode 6, ASCE 41-13).

The application of Dawe and Seah's model with confining members provided with elastic stiffness provides, on average, the best prediction for both infills in steel frames and in RC frames. Hence, for each specimen of the database, the ratio R_d between the experimental strength and that calculated by the proposed direct strength formulations (Equation 9), which are defined under the hypothesis of stiff confining elements, is calculated.

Through a non-linear regression analysis the experimental values of R_d are related to the values of λ_v and λ_h. The non-linear regression showed that only the parameter λ_h is significant, because in the considered specimens only one beam deforms (as the lower one is attached to the laboratory floor), while two columns deflect; therefore, the columns' deformability is more responsible for the OOP strength reduction. Based on all these considerations, the formulation reported in Equation 11 was determined.

$$R_d = \min(1; k_s(6.73 \times 10^{-3})\lambda_h^{0.27}) \tag{11}$$

In Equation 11, k_s is a coefficient accounting for the static scheme of the confining frame and is equal to 0.60 for infills in steel pinned frames, to 1.00 for infills in moment-resisting RC frames.

The experimental and predicted values of R_d are shown in Tables 4.14-4.15. In the same tables, the experimental values of the OOP strength of specimens is compared with that predicted by Equation 9 (with regression coefficient associated with the specific loading condition and observed/assumed deformed shape) multiplied for the calculated value of the R_d factor. The experimental-to-predicted ratios are slightly different from those reported in Tables 4.11-4.12, which are derived with the application of Dawe and Seah's complete model. On average, it is observed that the proposed simplified formulation, with the introduction of the deformability factor, actually allow predicting the OOP strength in a straightforward way, without significant lost in the predictive capacity compared to the complete model. The comparison between the experimental and predicted values of R_d and F_{max} is also shown in Figure 4.5.

Table 4.14. Experimental and predicted values of the deformability factor R_d and of the OOP

strength derived from the proposed simplified approach for infills in RC frames.

Author	specimen	λ_h [mm^3]	R_d			F_{max} [kN]		
			exp.	predicted	exp/pred	exp.	predicted	exp/pred
Angel et al.	1	3.92E+07	0.82	0.76	0.97	31.3	39.2	0.80
Calvi and Bolognini	10	1.61E+08	0.96	1.00	0.85	33.7	35.4	0.95
Varela-Rivera et al.	E-1	1.87E+06	0.38	0.33	1.05	63.1	96.9	0.65
Varela-Rivera et al.	E-2	3.32E+06	0.52	0.39	1.24	93.4	113.4	0.82
Varela-Rivera et al.	E-3	3.13E+06	0.50	0.38	1.15	86.4	62.1	1.39
Varela-Rivera et al.	E-4	3.71E+06	0.44	0.40	0.94	105.1	121.8	0.86
Varela-Rivera et al.	E-5	3.95E+06	0.48	0.41	1.02	129.6	122.8	1.06
Varela-Rivera et al.	E-6	5.11E+06	0.65	0.44	1.21	110.9	73.6	1.51
DIST-UNINA	80_OOP_4E	5.99E+07	0.96	0.85	1.03	22.0	26.2	0.84
DIST-UNINA	120_OOP_4E	4.49E+07	0.94	0.78	0.43	41.9	49.4	0.85
				mean	0.99		mean	0.97
				median	1.02		median	0.86
				CoV	23%		CoV	28%

Table 4.15. Experimental and predicted values of the deformability factor R_d and of the OOP strength derived from the proposed simplified approach for infills in steel frames.

Author	specimen	λ_h [mm^3]	R_d			F_{max} [kN]		
			exp.	pred.	exp/pred	exp.	pred.	exp/pred
Dawe and Seah	WE2	1.08E+06	0.11	0.17	0.63	193.5	299.4	0.65
Dawe and Seah	WE4	1.46E+06	0.15	0.19	0.77	112.9	153.5	0.74
Dawe and Seah	WE5	2.27E+06	0.19	0.21	0.73	78.6	123.5	0.64
Dawe and Seah	WE8	1.46E+06	0.09	0.19	0.44	135.1	311.7	0.43
Flanagan and Bennett	18	2.34E+06	0.42	0.21	1.91	133.5	141.2	0.95
Flanagan and Bennett	25	4.67E+06	0.52	0.26	1.56	40.6	42.0	0.97
				mean	1.01		mean	0.73
				median	0.75		median	0.69
				CoV	58%		CoV	28%
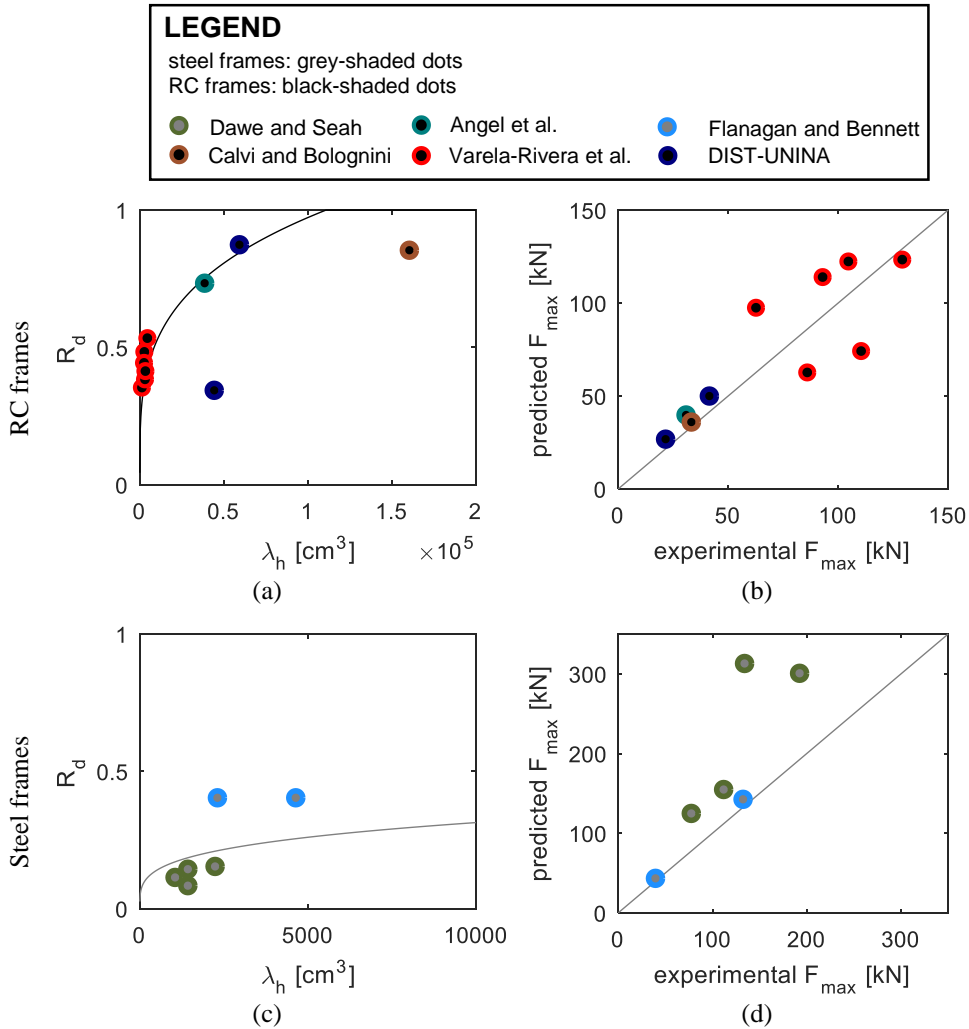
Figure 4.5. Comparison of the experimental and predicted values of the R_d deformability factor for infills in RC frames (a) and in steel frames (c). Comparison of the experimental and predicted values of the OOP strength of specimens in RC frames (b) and of specimens in steel frames (d).

The proposed formulations have been derived based on the application of Dawe and Seah's model. This was possible as it was demonstrated that Dawe and Seah's model well predicts the OOP strength of specimens tested in the literature. For this reason, it is necessary to recall that the reliability of Dawe and Seah's model has been tested only with reference to infills with mechanical and, above all, geometric properties defined in

specific ranges. Namely, only infills with slenderness ratio greater than 15 and thickness lower than 200 mm were considered. Therefore, the Authors cannot grant the reliability of such model, and of the proposed simplified formulations, outside these bounds. In addition, note that Flanagan and Bennett (1999b) express some doubts on the fact that in very thick infills arching action can develop as predicted by Dawe and Seah's model, given that thick infills' behaviour, such as in thick plates and shells, "may be less influenced by membrane forces".

In new RC buildings, infill walls bounded along four edges to the confining elements are usually "thick" and "robust", being characterized by:

    i.   High thickness (e.g., t>300 mm), i.e., very low height-over-thickness slenderness ratio (e.g., h/t<10);

    ii.   High masonry compressive strength in the direction parallel to holes (e.g., f_m>5 N/mm^2);

    iii.   Construction with vertical holes.

This choice of such type of infills is very useful to guarantee good acoustic and, above all, thermic insulation, i.e., a good energetic performance of buildings. Clearly, such a type of infill walls is expected also to be provided with very high OOP strength, and, so, to exhibit a good seismic performance under lateral actions.

The OOP behaviour of this type of infills has been studied in recent years mainly by da Porto and co-workers (Guidi et al. 2013) and by Magenes and co-workers (Hak et al.). Unfortunately, these experimental programs do not include IP-undamaged infills, as they were performed to investigate the effects of IP damage on the OOP response of URM infills, i.e., the effects of the so-called IP/OOP interaction. Based also on these tests, many experimental and modelling studies have been published in past and recent years in the literature concerning the IP/OOP interaction (e.g., Angel et al., Mosalam and Günay 2015, Furtado et al. 2016b among many others). However, there is no experimental test reporting the OOP strength of thick and robust IP-undamaged URM infills in which two-way arching can occur.

In Authors' opinion, further research is absolutely necessary on this topic. Given the current absence of experimental data, it is suggested for this type of infills the use Eurocode 6 (2005) formulation that, being dedicated to 2E infills in which only one-way arching can occur, should provide conservative prediction of the OOP strength of such type of infills.

4.4.6. Modelling proposals

In the previous section, mechanical-based OOP strength formulations have been proposed for different deformed shape, loading and boundary conditions at edges. In addition, it has been suggested to use Eurocode 6 strength model, adapted to the specific loading condition, for 4E robust and thick infills, widely used in new RC constructions.

Unfortunately, there is no formulation in the literature to predict the OOP load corresponding to the first macro-cracking/significant non linearity. Hence, an empirical-based proposal is herein provided.

The experimental value collected for F_{crack} are reported in Table 4.16. The empirical relationship proposed herein was defined by correlating the observed values of F_{crack} with $n=5$ geometric and mechanical properties of infills (t, h, w, f_{mv}, and E_{mv}) using a linear least-squares regression. The regressions were carried out by correlating the natural logarithm of each observed variable with a set constituted by *i (i=1,…,n)* candidate parameters.

First, the full model (*i=n*) was selected as the "reference model". Then, F-tests were performed comparing the reference full model with all reduced models *(i=1,…,n-1)* to associate with each reduced model a p-value related to the null hypothesis of statistical equivalence between the considered reduced model and the reference model. Models with a p-value lower than the significance level, α, were immediately rejected, because in this case the null hypothesis itself should be rejected. Among all possible reduced models, the one with a minimum number of parameters and a higher p-value was accepted and is herein proposed. Note that α was set to 0.10 to conservatively reduce the risk of a Type II error (i.e., not rejecting a false null hypothesis – in this case, accepting a reduced model with a statistically significant difference from the reference model) according to Draper and Smith (1998).

The formulation obtained is reported in Equation 12, in which forces are expressed in Newtons and lengths in millimetres. In addition, in the experimental database it is observed that F_{crack} is never greater than 0.90 times F_{max}. This upper bound is introduced in Equation 12 to avoid modelling issues. Note that no specific relationship can be proposed for 2E infills, as the database is constituted only by four data. Prior to further investigations, Equation 12 should be used also for them.

$$F_{crack} = \min\left(3.50 f_{mv}^{0.14} \frac{t}{h^{1.48}} wh; 0.90 F_{max}\right) \tag{12}$$

Table 4.16. Comparison of the experimental and predicted values of F_{crack} for 4E specimens.

Author	Specimen	F_{crack} [kN]		
		experimental	predicted	exp/pred
Angel et al.	1	17.1	16.0	0.89
Calvi and Bolognini	10	29.0	36.5	1.10
Varela-Rivera et al.	E-1	-	-	-
Varela-Rivera et al.	E-2	-	-	-
Varela-Rivera et al.	E-3	-	-	-
Varela-Rivera et al.	E-4	-	-	-
Varela-Rivera et al.	E-5	-	-	-
Varela-Rivera et al.	E-6	-	-	-
Furtado et al.	Inf_02	50.0	46.7	1.34
DIST-UNINA	80_OOP_4E	19.4	18.6	1.38
DIST-UNINA	120_OOP_4E	27.5	27.4	0.79
Dawe and Seah	WE2	-	-	-
Dawe and Seah	WE4	-	-	-
Dawe and Seah	WE5	-	-	-
Dawe and Seah	WE8	-	-	-
Flanagan and Bennett	18	40.6	49.2	0.82
Flanagan and Bennett	25	-	-	-
			mean	0.98
			median	1.04
			CoV	12%

The formulation proposed in Equation 12 has quite good predictive capacity, with a median of the experimental-to-predicted ratio equal to 1.04 and a CoV equal to 12%.

4.5. ASSESSMENT OF THE OOP DISPLACEMENT CAPACITY

For 2E infills made with clay hollow bricks with horizontal holes the OOP collapse occurs at the attainment of peak load, due to the fact that masonry does not exhibit ductility when arching thrusts act perpendicular to bricks' holes and to the fact that, for such boundary condition, the redistribution of stresses after the attainment of peak load is not possible.

For what concerns 4E infills, due to the small number of experimental tests carried out to investigate the OOP behaviour of URM infills which lack, in most cases, of a clear and detailed description of damage evolution, the definition of the OOP collapse displacement of URM infill walls, d_u, is currently an open issue. For instance, experimental tests carried out on infilled RC frames do not allow a unique definition of

d_u, and the authors of those tests, in most cases, do not discuss this topic and define as "collapse displacement" the OOP central displacement at which the test was interrupted.

In Chapter I, formulations for the prediction of candidate values of the OOP conventional collapse associated with specific phenomena or to limit values of the ductility were presented and discussed. With reference to 4E infills for which the experimental OOP force-displacement diagram is available and presents a post-peak branch, the values of these candidate collapse displacements were calculated. The position of such values of candidate collapse displacement with respect to the overall OOP response of specimens is shown in Figure 4.6 and 4.7. Note that for the prediction of the displacement at masonry crushing, a conventional value of εcrush was used. Such value is equal to 0.004, as suggested by Angel et al. (1994).
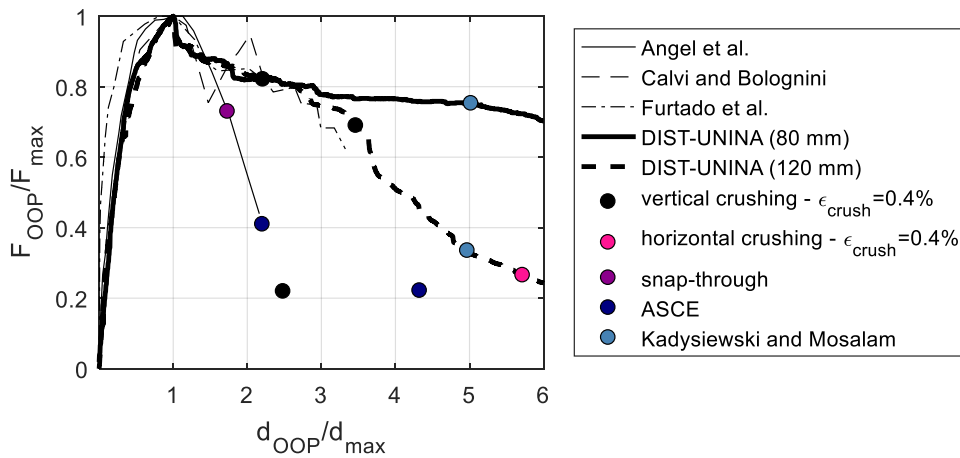
Figure 4.6. Normalized OOP force-displacement diagrams (d_{OOP} normalized with respect to d_{max}) and position of the candidate collapse displacements described in Chapter I.
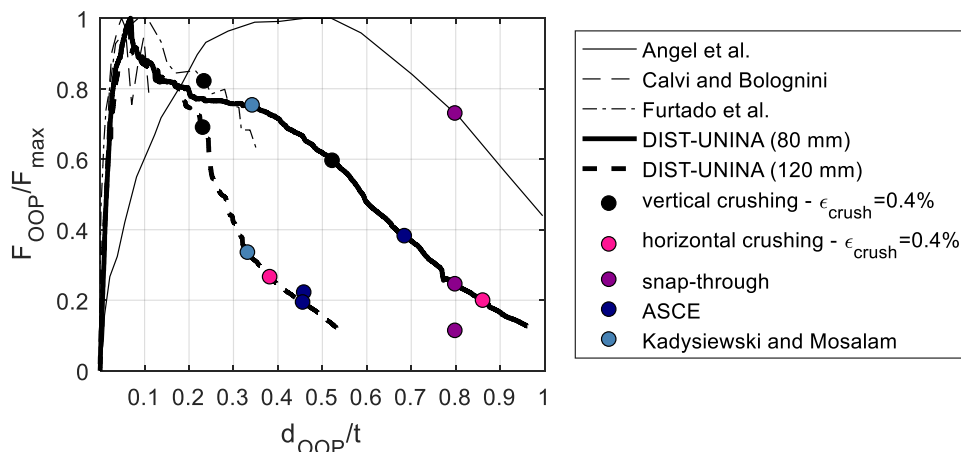
Figure 4.7. Normalized OOP force-displacement diagrams (d_{OOP} normalized with respect to t) and position of the candidate collapse displacements described in Chapter I.

It is clear from Figures 4.6 and 4.7 that there is no evidence of a recurrent trend that allows considering one of the candidate collapse displacements as the more robust and efficient.

The collapse displacement of a structural or non-structural member is conventionally defined based on a fixed reduction of its resistance. This reduction is commonly related to a certain damage state of the element or to a significant variation in its response. Similarly to the assumption usually made for the definition of the displacement capacity of members realized with brittle materials, it is suggested to assume as conventional OOP collapse displacement, d_u, the infill central displacement at which, in the softening branch of the OOP response, the infill exhibit a 20% reduction of the lateral resistance, d_{80}.

As shown in Figures 4.8 and 4.9, this displacement corresponds, based on the results of OOP tests on URM infills for which the experimental OOP force-displacement diagram is available and presents a post-peak branch, to a ductility capacity which is equal to, at least, 1.40 (based on Calvi and Bolognini 2001's results). In addition, a potential correlation of d_u with the infill geometric and mechanical properties was investigated. Among the possible ones, it was observed that the most clear and straightforward was the correlation with the infill thickness – which is also related – and sufficiently distant – to the infill central displacement at which arching action is expected to vanish according to Angel et al., 0.80t.
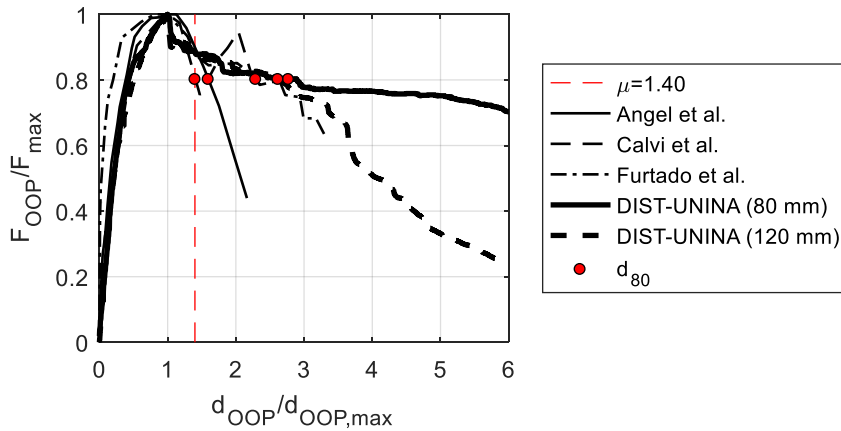
Figure 4.8. Normalized OOP force-displacement diagrams (d_{OOP} normalized with respect to d_{max}) and position of the OOP displacement at 20% strength degradation.
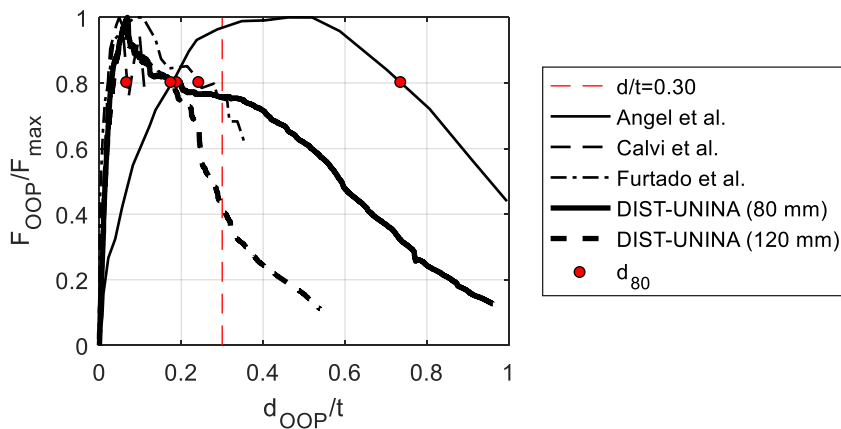
Figure 4.9. Normalized OOP force-displacement diagrams (d_{OOP} normalized with respect to t) and position of the OOP displacement at 20% strength degradation.

Namely, d_u is equal, on average, to 0.30 times the infill thickness. For these reasons, based on experimental data, it is assumed that the OOP ductility capacity of the infill wall is equal to $0.30t/d_{max}$ and that such ductility cannot be lower than 1.40 or greater than t/d_{max}, as the infill central OOP displacement cannot overcome the infill thickness for geometric compatibility.

4.6. ASSESSMENT OF THE IP/OOP INTERACTION EFFECTS

This section is dedicated to the assessment of the IP/OOP interaction effects in terms of OOP strength, stiffness and displacement capacity variation due to the IP displacement demand and vice-versa.

In the first subsection, the formulations aimed at predicting the OOP strength reduction factor R due to the IP displacement demand presented in Chapter I are applied to the experimental database collected in section 4.2.2 in order to assess their effectiveness.

In the second subsection, based on the experimental database collected, more robust and efficient empirical formulations are proposed not only for the prediction of the R factor, but also for modelling the first macro-cracking load, the secant stiffness at first macro-cracking and at maximum, as well as the displacement capacity variation due to IP displacement demands.

In the third subsection, the effects of the OOP displacement demand on the IP response are discussed. Based on experimental data, a modelling proposal is presented.

4.6.1. Assessment of literature formulations

In this subsection, the formulations proposed in the literature by Angel et al., Morandi et al. and Verlato et al. to predict the OOP strength reduction factor, R, which is defined as the ratio between the OOP strength of the IP-damaged infill and the OOP strength of the IP-undamaged infill, are applied to the experimental database collected. This application is aimed at assessing their predicting capacity. Note that the application of Angel et al.'s formulation requires, as input datum, the IDR corresponding to the infill first visible cracking due to IP actions. As this information is available only for DIST-UNINA specimens (as the mean of the IDR_{crack} values evaluated for positive and negative displacements), Angel et al.'s formulation will be applied only to these specimens.

The experimental values of the R factor are reported in Table 4.17. They are compared with the corresponding predicted values in Tables 4.18 and 4.19. A graphical comparison of experimental and predicted R factors is shown in Figures 4.10 and 4.11.

Table 4.17. Experimental values of the R factor ($F_{max,dam}/F_{max,und}$).

Author	specimen	h/t	IP drift [%]	IDR_{crack} [%]	reference specimen	F_{max} IP-und [kN]	IP-dam [kN]	R
Angel et al.	2b	33.9	0.34	-	1	31.3	15.9	0.51
Angel et al.	3b	33.9	0.22	-	1	31.3	23.7	0.76
Calvi and Bolognini	6	20.4	0.40	-	10	33.7	9.0	0.27
Calvi and Bolognini	2	20.4	1.20	-	10	33.7	6.0	0.18
Furtado et al.	Inf_03	15.3	0.50	-	Inf_02	69.0	18.0	0.26
DIST-UNINA	80_IP+OOP_L	22.9	0.16	0.068	80_OOP_4E	22.0	23.4	1.06
DIST-UNINA	80_IP+OOP_M	22.9	0.37	0.063	80_OOP_4E	22.0	10.5	0.48
DIST-UNINA	80_IP+OOP_H	22.9	0.58	0.067	80_OOP_4E	22.0	5.9	0.27
DIST-UNINA	120_IP+OOP_L	15.2	0.21	0.075	120_OOP_4E	41.9	41.6	0.99
DIST-UNINA	120_IP+OOP_M	15.2	0.50	0.080	120_OOP_4E	41.9	27.9	0.67
DIST-UNINA	120_IP+OOP_H	15.2	0.89	0.078	120_OOP_4E	41.9	23.1	0.55

Table 4.18. Comparison of the experimental values of the R factor ($F_{max,dam}/F_{max,und}$) with the value predicted by Angel et al.'s formulation.

Author	specimen	experimental R	Angel et al.'s R	exp/pred
DIST-UNINA	80_IP+OOP_L	1.06	0.59	1.81
DIST-UNINA	80_IP+OOP_M	0.48	0.27	1.82
DIST-UNINA	80_IP+OOP_H	0.27	0.14	1.92
DIST-UNINA	120_IP+OOP_L	0.99	0.71	1.39
DIST-UNINA	120_IP+OOP_M	0.67	0.47	1.45
DIST-UNINA	120_IP+OOP_H	0.55	0.25	2.24
			mean	1.77
			median	1.81
			CoV	19%

Table 4.19. Comparison of the experimental values of the R factor ($F_{max,dam}/F_{max,und}$) with the values predicted by Morandi et al.'s (stepwise and linear) and by Verlato et al.'s formulations.

		R	predicted R					
			Morandi et al. (stepwise)		Morandi et al. (linear)		Verlato et al.	
Author	specimen	exp.	pred.	exp/pred	pred.	exp/pred	pred.	exp/pred
Angel et al.	2b	0.51	0.20	2.55	0.20	2.55	0.71	0.72
Angel et al.	3b	0.76	1.00	0.76	0.41	1.84	0.81	0.94
Calvi and Bolognini	6	0.27	0.20	1.35	0.20	1.35	0.66	0.41
Calvi and Bolognini	2	0.18	0.00	-	0.00		0.40	0.45
Furtado et al.	Inf_03	0.26	0.20	1.30	0.20	1.30	0.57	0.46
DIST-UNINA	80_IP+OOP_L	1.06	1.00	1.06	0.57	1.85	0.86	1.23
DIST-UNINA	80_IP+OOP_M	0.48	0.20	2.40	0.20	2.40	0.68	0.70
DIST-UNINA	80_IP+OOP_H	0.27	0.20	1.35	0.20	1.35	0.50	0.54
DIST-UNINA	120_IP+OOP_L	0.99	1.00	0.99	0.44	2.25	0.82	1.21
DIST-UNINA	120_IP+OOP_M	0.67	0.20	3.35	0.20	3.35	0.57	1.18
DIST-UNINA	120_IP+OOP_H	0.55	0.20	2.75	0.20	2.75	0.40	1.38
			mean	1.79	mean	2.10	mean	0.84
			median	1.35	median	2.05	median	0.72
			CoV	50%	CoV	33%	CoV	43%
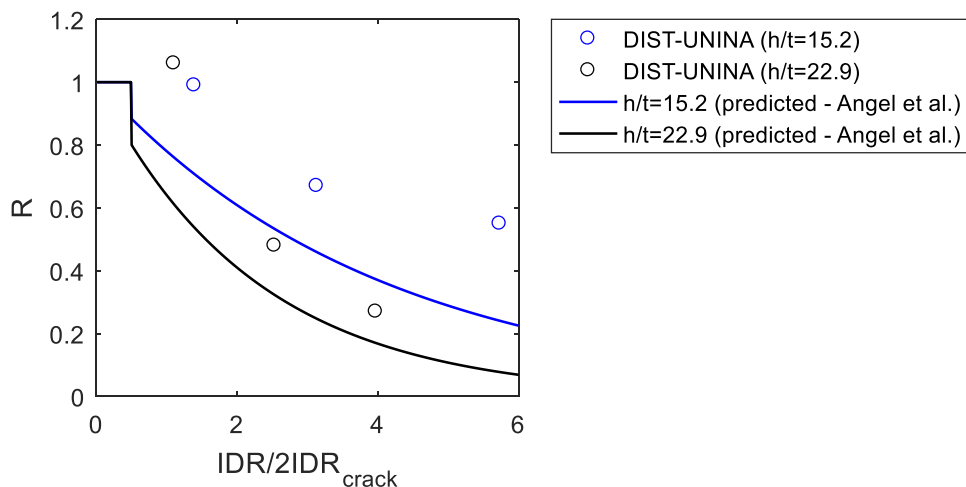
Figure 4.10. Comparison of the R factor of DIST-UNINA specimens with those predicted by applying Angel et al.'s formulation.
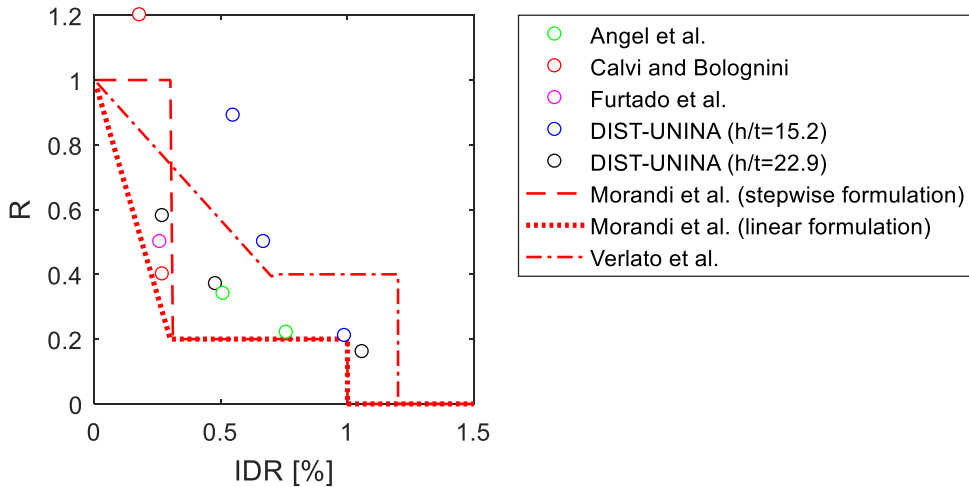
Figure 4.11. Comparison of the R factors calculated for the entire database with those predicted by applying Morandi et al.'s and Verlato et al.'s formulations.

It is observed that Angel et al. (1994)'s and Morandi et al. (2013)'s are quite conservative. On the other hand, Verlato et al. (2014)'s formulation, based on the median of the experimental-to-predicted R ratios, is unconservative, most likely because it has been derived based on experimental tests' results on very thick and robust URM infills.

4.6.2. Modelling proposals (IP effects on OOP)

In the previous subsection, it was observed that the currently available literature formulations for the prediction of the R factor are not sufficiently efficient. In addition, no relationship exists to predict the variation due to the IP damage of the first macro-cracking load and of the secant stiffness at first macro-cracking and at maximum.

In this subsection, empirical formulations aimed at predicting the variation of such significant response parameters are proposed. In addition, an empirical approach for the prediction of the variation of the OOP collapse displacement due to IP damage is presented.

At first, it is worth to consider only DIST-UNINA experimental data to discuss the predictive parameters entering the proposed formulations. Clearly, one of them is the IP displacement demand represented by the IDR demand. However, the OOP strength and

stiffness variation due to the IP/OOP interaction is due, more generally, to the entity of the IP damage. It is intuitive that, at equal IP drift, the entity of the IP damage depends also on the infill geometric and mechanical properties. Angel et al. and Agnihotri et al. (2013) already observed that, at equal IP drift, less slender infills are expected to show a lower OOP strength reduction with respect to slender infills. This is confirmed also by DIST-UNINA results, not only for what concerns the OOP strength, but also for the other significant response parameters, except for K_{crack}, as shown in Figure 4.12.
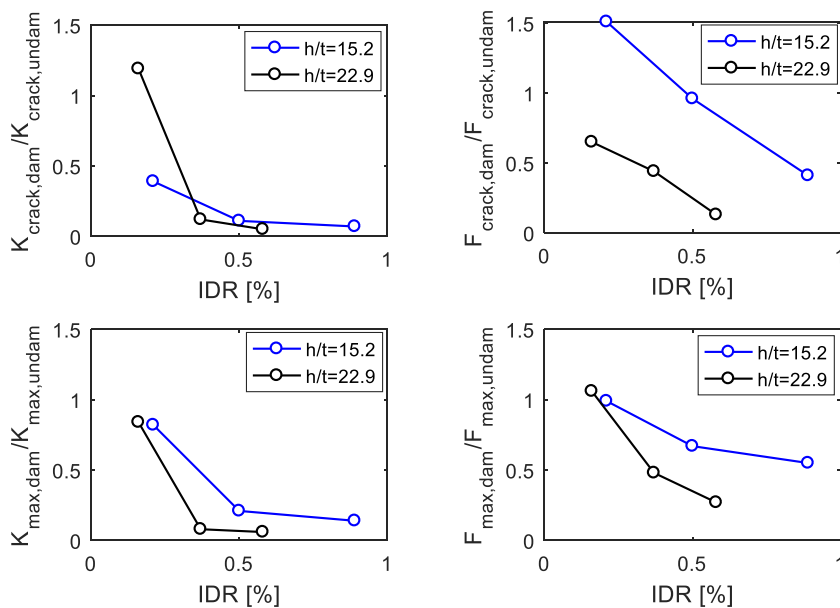
Figure 4.12. Experimental values of the reduction factors for secant stiffness and force at first macro-cracking and at peak load for DIST-UNINA specimens.

As it is clear from Figure 4.12, there is a strong influence of the vertical slenderness ratio (h/t) on the reduction of the significant OOP response parameters of the tested infills, except for K_{crack}. Namely, at a fixed IDR, the secant stiffness at peak-load and force (both at first macro-cracking and at peak-load) reduction factors are generally lower for slender infills.

In this section, empirical formulations aimed at predicting such factors are derived through least-square regressions in the logarithmic space. The predictor parameters chosen are the maximum IP IDR attained during the IP test and the slenderness ratio

(h/t) of the considered infills. Further investigation is needed to evaluate the introduction of further predictor parameters, such as the infill aspect ratio (w/h, as Agnihotri et al. demonstrate through numerical analyses that square infills exhibit lower effects of the IP/OOP interaction with respect to rectangular infills) or masonry mechanical properties.

The experimental data used to carry out regressions are those included in the experimental database. These results are recalled in Table 4.20.

Table 4.20. Experimental values of the reduction factors for secant stiffness and force at first macro-cracking and at peak load for the entire database collected.

Authors	specimen	h/t	IP drift [%]	experimental damaged-over-undamaged ratios			
				F_{crack}	K_{crack}	F_{max}	K_{max}
Angel et al.	3b	33.9	0.22	0.74	0.31	0.76	0.53
Angel et al.	2b	33.9	0.34	0.44	0.20	0.51	0.51
Calvi and Bolognini	6	20.4	0.40	0.22	0.05	0.27	0.08
Calvi and Bolognini	2	20.4	1.20	-	-	0.18	-
DIST-UNINA	80_IP+OOP_L	22.9	0.16	0.65	1.19	1.06	0.84
DIST-UNINA	80_IP+OOP_M	22.9	0.37	0.44	0.12	0.48	0.08
DIST-UNINA	80_IP+OOP_H	22.9	0.58	0.13	0.05	0.27	0.06
DIST-UNINA	120_IP+OOP_L	15.2	0.21	1.51	0.39	0.99	0.82
DIST-UNINA	120_IP+OOP_M	15.2	0.50	0.96	0.11	0.67	0.21
DIST-UNINA	120_IP+OOP_H	15.2	0.89	0.41	0.07	0.55	0.14

To perform the non-linear regression analysis, a model function had to be defined. Consider now Figure 4.13, in which the experimental R factors calculated for the entire database shown in Table 4.20 are represented as a function of the IDR. From Figure 4.13, it can be observed that the values of the R ratio for infills with (h/t) ratio equal or greater than 20.4 (black-filled dots) seem to follow a unique trend, while a significantly different, less degrading trend characterizes the infills with (h/t) ratio equal to 15.2 (blue dots). In both cases, the relationship between R and IDR can be well-described by a negative power function.
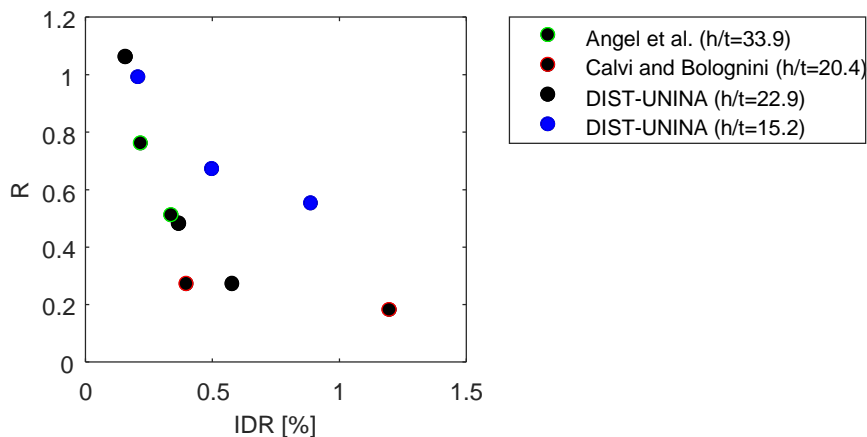
Figure 4.13. Experimental strength reduction factors reported in Table 4.20.

In other words, it seems that the slenderness ratio actually affects the entity of IP/OOP interaction effects only if it is lower than 20. This is consistent with the results of Angel et al.'s formulation, which indicates a lower sensitivity of R to the slenderness ratio for larger values of (h/t), as also shown by Agnihotri et al. through numerical FEM analyses. Similar observations can be extended to the relation existing between force and stiffness reduction factors and IDR.

So, based on a trial-and-error procedure, the model function reported in Equation 13 is assumed. In Equation 13, P is the generic significant OOP response parameter (force/stiffness at first macro-cracking or at peak load).

$$\frac{P_{dam}}{P_{undam}} = \min\left\{\left[a + b \min\left(20.4; \frac{h}{t}\right)\right] \cdot (IDR)^c; 1.00\right\} \tag{13}$$

In Figure 4.14, the observed and predicted values of the stiffness and force at first macro-cracking and at peak load reduction factors are compared for the entire database shown in Table 4.20.

In Table 4.21, the values obtained through the least-square regression for the coefficients a, b and c in Equation 8 are reported; in addition, the mean, median and CoV of the observed-over-predicted ratios are also shown. As expected, the formulations derived provide lower reduction factors for higher IP displacement demand at equal h/t and for higher h/t at equal IP displacement demand.
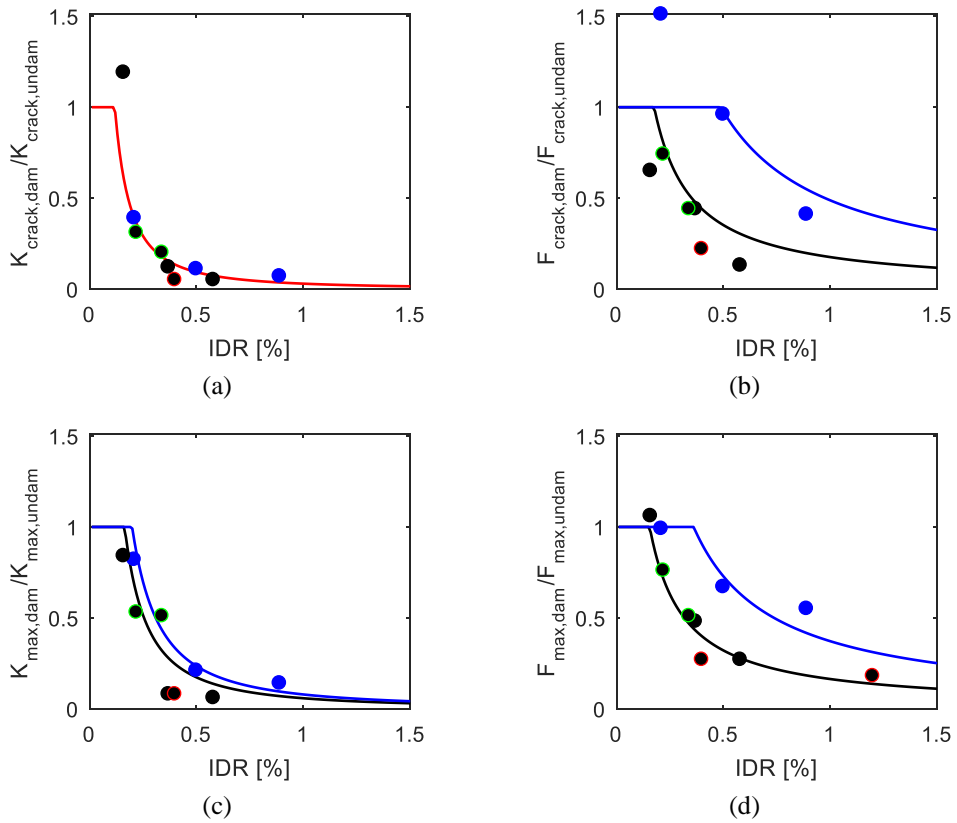
Figure 4.14. Comparison of the experimental values of the reduction factors for secant stiffness and force at first macro-cracking and at peak load for the entire database collected. Black curves are obtained by means of Equation 13 referred to specimens with slenderness ratio equal to or greater than 20.4. Blue curves are obtained by means of Equation 13 referred to specimens with slenderness ratio equal to 15.2. Red curves are determined independently on h/t. For the experimental points, see the legend in Figure 4.13.

Table 4.21. Values of the coefficients of Equation 13 and mean, median and CoV of the ratios between the experimental values of K_{crack}, F_{crack}, K_{max} and F_{max} reduction factors and those predicted by means of Equation 13.

experimental damaged-over-undamaged ratios	Coefficients of Eq. 13			experimental/predicted		
	a	b	c	mean	median	CoV
K_{crack}	0.03	0.00	-1.65	1.10	1.01	49%
F_{crack}	1.40	-0.06	-1.00	0.83	0.85	38%
K_{max}	0.14	-0.004	-1.57	0.85	0.85	55%
F_{max}	0.98	-0.04	-0.97	1.06	1.08	18%

Consider now the OOP strength degradation factor. Equation 13 can be used for a correct assessment and safety check of URM infills with respect to OOP seismic demands accounting for the IP/OOP interaction effects. In addition, from Equation 13, it is possible to derive the "critical" IDR, IDR_{crit}, from which IP displacement demand is effective in reducing the OOP strength, i.e., the value of the IDR demand at the onset of the activation of IP/OOP interaction effects. Such values of IDR_{crit} calculated for different values of h/t are shown in Figure 4.15.

For example, consider the OOP safety check of URM infills at Damage Limitation limit state (DL). The attainment of DL is usually related to the attainment of a certain threshold IDR demand in the IP direction. So, such an IDR value should also be the one used for the evaluation of the OOP strength reduction factor. The IDR corresponding to the attainment of this limit state is set to 0.50% by the current Italian building code NTC2008 (2008) and by Eurocode 8 (2004). The commentary to the Italian building code, Circolare 617/2009 (2009), states that such threshold should be reduced to 0.30% if infill walls are considered in the structural model. In the literature, different suggestions have been proposed to define such threshold. Morandi et al. (2013) suggest to assume a limit IDR at DL equal to 0.30% for RC buildings with thin infills. In addition, the attainment of DL is associated by different Authors with the attainment of a Damage State (DS) corresponding to an intermediate/severe damage of the infill (DS2). Based on the description of the evolution of damage in URM infills tested in the IP direction, a threshold IDR corresponding to a 50% probability of DS2 exceedance equal to 0.40%, 0.46% and 0.34% was defined by Cardone and Perrone (2015), Sassun et al. (2016), and De Risi et al. (2018), respectively. In addition, drift ranges in which the DL is probably attained were proposed, among many others, by Rossetto and Elnashai (2003), Dolšek and Fajfar (2008a-b), Colangelo (2013a-b).

Among the abovementioned threshold drifts for DL exceedance, consider now the

higher one, proposed by Sassun et al., equal to 0.46%. It is shown in Figure 4.15 that only for slenderness ratios roughly lower than 12.5 it is possible to avoid the reduction of the OOP strength at DL, i.e., given the usual values of h, only for very thick infills (e.g., t>=250mm). Therefore, for thin infills, which are common in existing RC buildings, it is not safe to neglect the effects of the IP/OOP interaction in the seismic OOP safety check of URM infills even at DL. Clearly, this is even truer for whichever performance level higher than DL.
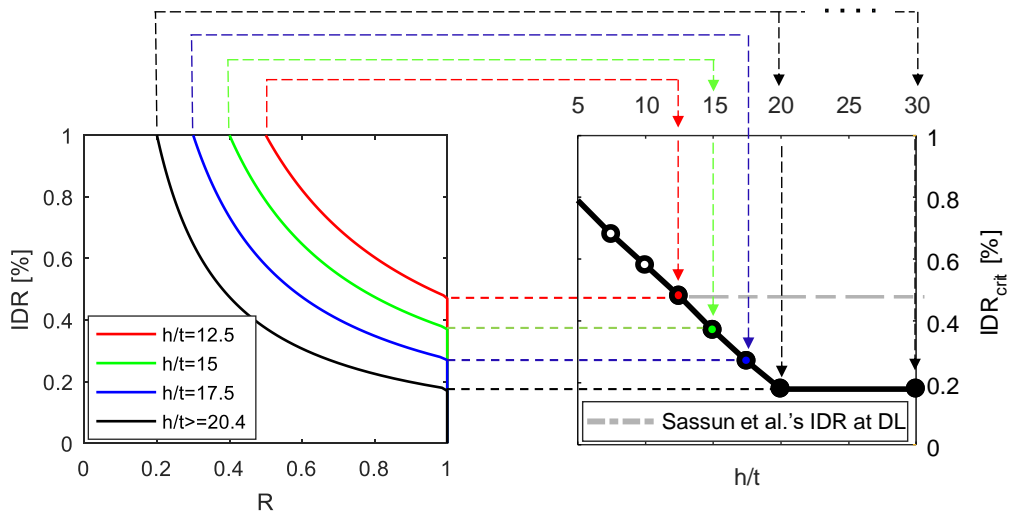
Figure 4.15. Values of the IDR at the onset of the reduction of the OOP strength as a function of the slenderness ratio.

Consider the OOP strength reduction due to IP/OOP interaction effects. To predict the R factor, an empirical formulation based on experimental data has been proposed and reported in Equation 13, which should be applied with the regression coefficients reported in Table 4.21. Due to its empirical nature, the proposed relationship is fully reliable in the range of h/t and IDR values included in the database, i.e., for slenderness ratio greater than 15.2 and IDR lower than 1.20%. Its results outside these bounds must be considered an extrapolation, of course.

As already stated, thick infills (i.e., with thickness typically around 300 mm) with low slenderness ratio are nowadays commonly used in RC buildings. Such infills have h/t equal to about 10, a value that is outside the abovementioned bounds. So, for such a type of infills, the formulation proposed could not be reliable (even if on the side of

safety).

However, based on some hypotheses and assumptions, it is possible to propose a formulation for the prediction of the R factor also accounting for tests' results obtained by testing thick and robust infills made of bricks with vertical holes, such as those tested by Guidi et al. (2013). As already stated, these results were not included in the original database as they are not provided of a reference IP-undamaged OOP strength, i.e., there is no OOP test at zero IP drift. The experimental results on URM infills by Guidi et al. are recalled in Table 4.22.

Table 4.22. Experimental results by Guidi et al.

Author	specimen	h/t	IP drift [%]	F_{max} [kN]
Guidi et al.	URM-D	8.8	0.50	250
Guidi et al.	URM-U	8.8	1.20	203

In the previous section, the concept of critical IDR was introduced. From Figure 4.15, it can be observed that, even if determined with some extrapolation, the IDR_{crit} for a slenderness ratio equal to 8.8 is equal to 0.62%. The combined IP+OOP test carried out at the lowest drift by Guidi et al. was performed after the application of an IP displacement demand corresponding to a drift equal to 0.50%. Therefore, potentially, one could assume that, being 0.50% lower than the critical IDR for h/t=8.8 (although extrapolated), the OOP strength of specimen URM-D is equal to the OOP strength of the IP-undamaged infill.

If this assumption is accepted, the R factor for specimen URM-D is equal to 1.00, while it is equal to 0.81 for specimen URM-U. With the same approach and methodology described in the previous section, a regression analysis of the experimental data is performed accounting for the R factors already considered and reported in Table 4.5 as well as those associated with Guidi et al.'s tests.

The values of the coefficient a, b, and c in Equation 13 are reported in Figure 4.16. In the same figure, a comparison between the predicted R curves for h/t equal to 20.4, 15.2 and 8.8 and the experimental data is shown.
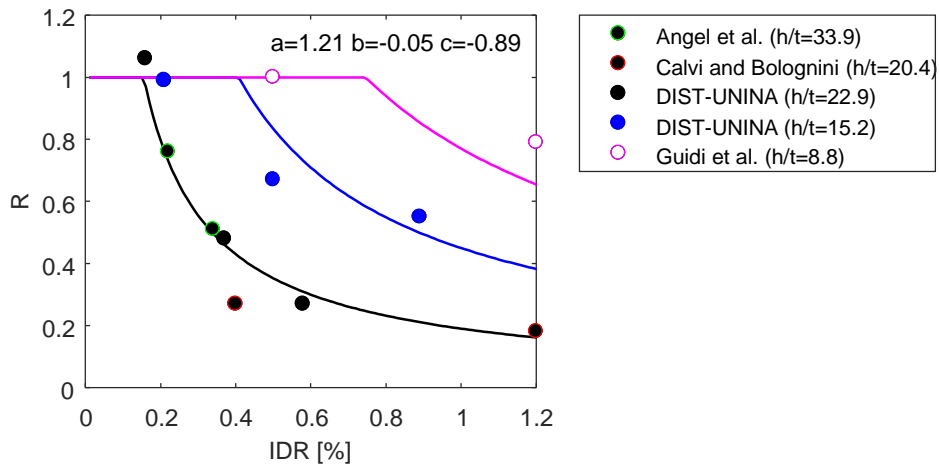
Figure 4.16. Experimental and predicted R ratios accounting also for Guidi et al.'s tests. The pink curve is associated with h/t=8.8, the blue curve to h/t=15.2 and the black curve to h/t≥20.4.

The experimental-over-predicted ratios, in this case, have mean equal to 0.99, median equal to 1.03 and CoV equal to 16%.

The OOP displacement ductility has been defined in section 4.5 for IP-undamaged infills and its value has been fixed. Now, assume that the same definition is applied for the displacement ductility of IP-damaged infills, i.e., assume the displacement ductility of IP-damaged infill equal to the ratio of d_{80}/d_{max}.

Based on DIST-UNINA experimental results., as shown in Figure 4.17, it is observed that the displacement ductility of IP-damaged URM infills is equal to, at least, 1.10 (based on specimen 120_IP+OOP_L performance). In addition, it is equal, on average, to 0.50 times the displacement ductility of the IP-undamaged infill, roughly independently on the infill slenderness ratio h/t and on the IP displacement demand.

Based on this, it is assumed that the OOP displacement ductility of IP-damaged infills is equal to a certain fraction, dependent on the IDR, of the IP-undamaged infill displacement ductility according to the simplified linear function shown in Figure 4.17, but never lower than 1.10 or greater than t/d_{max}, as the infill central OOP displacement cannot overcome the infill thickness for geometric compatibility.
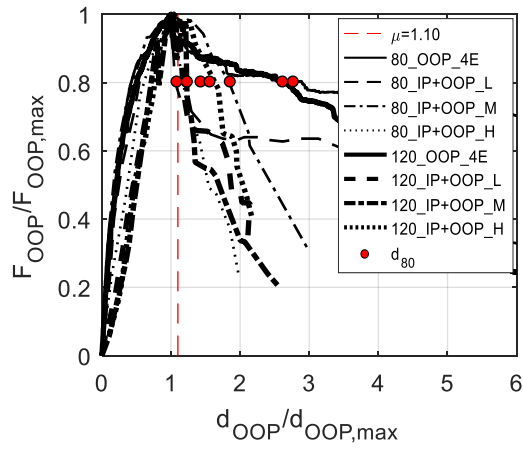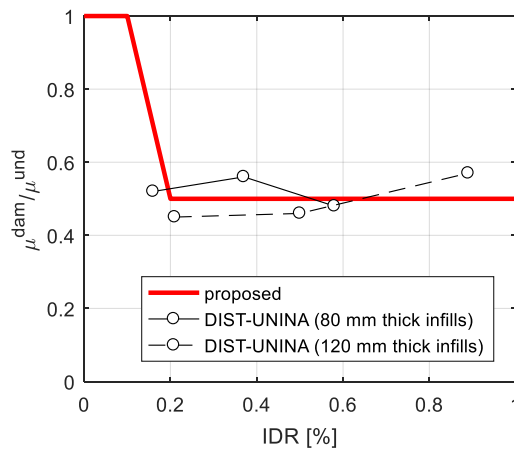
Figure 4.17. Conventional OOP collapse displacement for IP-damaged infills (a) and relation with the IDR of the damaged ductility over the undamaged ductility (b).

Note that these assumptions yield, in general, to a displacement ductility which reduces due to the IP damage and to a displacement capacity that increases at increasing IP drift demand. This occurs because, in general, the OOP central displacement at the attainment of peak load of the IP-damaged infill, which is calculated as the ratio between the "damaged" strength and the "damaged" secant stiffness, increases with the IDR demand. The increase of d_u, i.e., of the displacement at 20% strength degradation, at increasing IP displacement demand is consistent with the recent experimental results

proposed in the literature.

Also for this reason, as well as to avoid numerical issues during the analyses, it is assumed that the OOP collapse displacement cannot decrease at increasing IDR. This circumstance can occur sometimes at very low IDR levels.

4.6.3. Modelling proposals (OOP effects on IP)

The experimental tests aimed at investigating the IP/OOP interaction mainly examined the IP damage effects on the OOP behaviour rather than vice versa. Flanagan and Bennett (1999a) tested an infill (specimen 20) first by pushing it through an OOP action that increased up to the 75% of the undamaged infill lateral strength and then by applying an IP action up to collapse. This test allowed us to observe, during the IP response, a 50% stiffness reduction with respect to the one exhibited by the undamaged panel, while no IP strength reduction was observed. However, an identical infilled frame, specimen 23, was tested through a "combined" IP/OOP procedure. For instance, the specimen was subjected first to a cyclic IP test in displacement control and then, as the IP displacement was kept constant, to an OOP test carried out in load control. Later, while the OOP load was kept constant at zero, a new cyclic IP test was carried out and so on, for a total of six IP tests and five OOP tests.

It was observed that during the OOP tests, the IP load, which maintained a constant IP displacement, decreased. It is possible to reconstruct the IP force-displacement relationship for specimen 23, as shown in Figure 4.18. The obtained IP backbone can be compared with the one defined for the control specimen 2, which was identical to specimen 23 and tested only IP up to collapse.
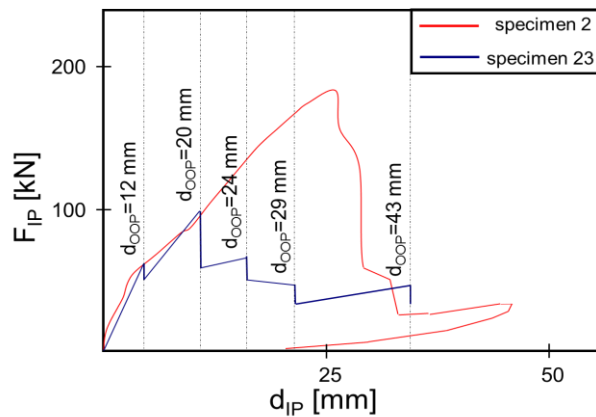
(a)
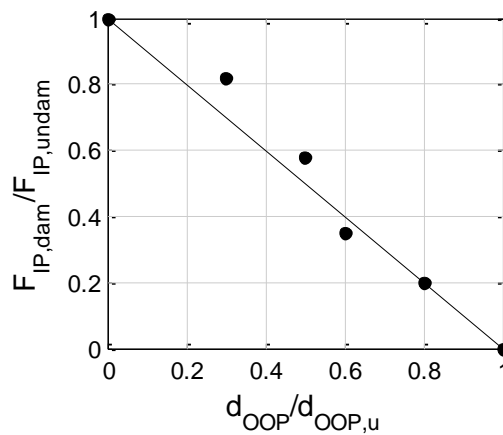
(b)

Figure 4.18. Extrapolated IP force degradation based on Flanagan and Bennett's specimens 2 and 23 behaviour (b) shown in (a).

In Figure 4.18a, for each drop of the IP load at a fixed IP displacement, the maximum OOP displacement attained during the OOP test, which produced that drop, is indicated. Clearly, the reduction of the IP load necessary to reach a certain IP displacement is due also to the cumulative effects of damage. However, the lack of experimental data on this issue makes the use of evidence of this combined test very useful to define the IP backbone degradation. First, it is possible to associate IP displacements at which the IP tests were stopped to the maximum OOP displacement attained during the

corresponding OOP test normalized with respect to the undamaged infill OOP collapse displacement declared by the authors. Then, to each OOP displacement ratio, it is possible to associate the ratio of the force on specimen 23's reconstructed IP backbone and the force on specimen 2's IP backbone for the corresponding IP displacement. Note that in the diagram shown in Figure 4.18a, the point corresponding to d_{OOP}=43 mm was dropped, given that that OOP displacement was greater than the OOP ultimate displacement declared by the authors for the undamaged panel (specimen 18).

Based on this experimental evidence, if the infill has been damaged by the OOP action represented by the OOP maximum displacement d_{OOP}, the IP force that produces the IP displacement d_{IP}, $F_{IP,dam}(d_{IP}, d_{OOP})$ can be expressed through a simplified linear relationship reported in Equation 14.

$$\frac{F_{IP,dam}(d_{IP}, d_{OOP})}{F_{IP,undam}(d_{IP})} = 1 - \frac{d_{OOP}}{d_{OOP,u}} \tag{14}$$

In Equation 14, $F_{IP,undam}(d_{IP})$ is the IP force that produces the IP displacement d_{IP} of the undamaged panel and $d_{OOP,u}$ is the undamaged infill ultimate OOP displacement.

Experimental data that allow defining the variation in the IP ultimate displacement due to the OOP action damage are not provided in the literature: further experimental tests should be carried out on this topic.

4.7. SUMMARY OF THE PROPOSED OOP MODEL FOR URM INFILLS

In the previous sections, the comparison of the experimental results proposed in Chapter II and III with the predictions of the formulations described in Chapter I has been presented. Based on the results of this comparison, mechanical-based or empirical formulations have been proposed to predict the significant response parameters for URM infills, i.e., the secant stiffness at first macro-cracking and at maximum, the force at first macro-cracking and at maximum, the conventional collapse displacement.

In addition, based on the experimental results, the variation of all these parameters due to the IP/OOP interaction effects has been modelled through empirical formulations.

With these findings, the first part of this thesis, which was dedicated to the characterization of the OOP response of URM infills and of the IP/OOP interaction effects, is complete. The second part of the thesis will be dedicated to the assessment,

through non-linear static and dynamic analyses, of the OOP behaviour of infills and of the IP/OOP interaction effects on the seismic response of URM infills and of infilled RC buildings. To this aim, the OOP response model accounting for the IP/OOP interaction effects defined in this Chapter will be used.

For all these reasons, it is worth to sum up, at the end of this Chapter, the proposed OOP model for URM infills as shown in Figure 4.19.
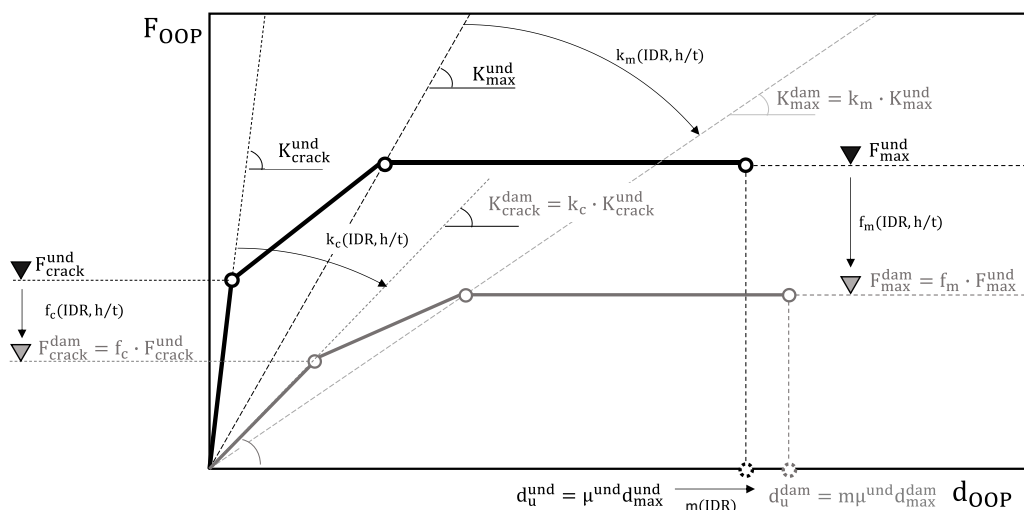
Figure 4.19. Proposed OOP response model for IP-undamaged and IP-damaged infills.

Some considerations have to be discussed.

i. The analyses will be carried out to assess the seismic response of URM infills and of RC buildings; hence, the loading condition considered is the seismic one. For this reason, the strength formulation adopted is the one proposed in section 4.4.5 for seismic load and hipped deformed shape, which is the most recurrent in the experimental database;

ii. For what concerns K_{crack}, it has been shown that Timoshenko's formulation for plates under uniformly distributed load is quite effective in its prediction independently on the real load shape. However, for consistency with the strength model, K_{crack} is calculated through the formulation derived from Timoshenko's closed-form solution for elastic isotropic plates under sinusoid load, i.e., under seismic load;

iii. As already discussed, due to the confinement provided by other structural

and non-structural elements to the structural elements at the edges of infills, in real buildings the effect of the frame deformability on the OOP response of infill can be neglected. Hence, also in the model used for the numerical analysis such effect will not be considered;

iv.   Note that the assumption of a conventional OOP collapse displacement defined at 20% strength degradation, which is quite small, allows the use of a response model plastic between the maximum and the conventional collapse point.

The formulations defining the characteristic points in Figure 4.19 for URM infills under seismic load in RC buildings are summarized in Tables 4.23 and 4.24.

Table 4.23. Formulations defining the seismic response of IP-undamaged URM infills in a stiff confining frame adopted for the numerical analyses.

$$F_{crack} = \min\left(0.9F_{max}; 3.50f_{mv}^{0.14}\frac{t}{h^{1.48}}wh\right) \tag{15}$$

$$K_{crack} = \frac{\pi^2}{3(1-\nu^2)}E_{mv}wt^3h\left(\frac{1}{w^2}+\frac{1}{h^2}\right)^2 \tag{16}$$

$F_{max} =$
for thin infills
$$= \left[2.86f_{mv}^{0.82}\left(\frac{t}{h}\right)^{2.28} + 0.23f_{mh}^{1.39}\left(\frac{t}{w}\right)^{1.48}\right]wh \tag{17a}$$
for thick infills
$$= \left[0.85f_{mv}\left(\frac{t}{h}\right)^2\right]wh \tag{17b}$$

$$K_{max} = 0.40K_{crack} \tag{18}$$

$$d_u = \mu^{und}d_{max} = \max\left(1.4; \frac{0.30t}{d_{max}}\right)d_{max} \tag{19}$$

Table 4.24. Formulations defining the reduction factors (as shown in Figure 4.19) for the assessment of the seismic response of IP-damaged URM infills in a stiff confining frame.

$$f_c = \min\{[1.40 - 0.06 \min(20.4; h/t)] \cdot IDR^{-1.00}; 1\} \tag{20}$$

$$k_c = \min\{0.03 \cdot IDR^{-1.65}; 1\} \tag{21}$$

$$f_m = \min\{[1.21 - 0.05 \min(20.4; h/t)] \cdot IDR^{-0.89}; 1\} \tag{22}$$

$$k_m = \min\{[0.14 - 0.004 \min(20.4; h/t)] \cdot IDR^{-1.57}; 1\} \tag{23}$$

$$m = \begin{cases} 1.00, & IDR \leq 0.10\% \\ 1.5 - 5IDR, & 0.10\% < IDR \leq 0.20\%, \\ 0.50, & IDR > 0.20\% \end{cases} \quad m\mu^{und} \geq 1.10 \tag{24}$$

REFERENCES

- Agnihotri P, Singhal V, Rai DC. Effect of in-plane damage on out-of-plane strength of unreinforced masonry walls. Engineering Structures 2013;57:1-11.
- Angel R, Abrams DP, Shapiro D, Uzarski J, Webster M. Behaviour of reinforced concrete frames with masonry infills. University of Illinois Engineering Experiment Station. College of Engineering. University of Illinois at Urbana-Champaign., 1994.
- Blevins RD, Plunkett R. Formulas for natural frequency and mode shape. Journal of Applied Mechanics 1980;47:461.
- Calvi GM, Bolognini D. Seismic response of reinforced concrete frames infilled with weakly reinforced masonry panels. Journal of Earthquake Engineering 2001;5.2:153-185.
- Cardone D, Perrone G. Developing fragility curves and loss functions for masonry infill walls. Earthquakes and Structures 2015;9.1:257-279.
- Circolare 617/2009. Istruzioni per l'applicazione delle nuove norme tecniche per le costruzioni. Ministero delle infrastrutture e dei trasporti, 2009. (in Italian).
- Colangelo F (2013a). Probabilistic characterization of an analytical fuzzy-random model for seismic fragility computation. Structural Safety 2013;40:68-77.
- Colangelo F (2013b). Drift-sensitive non-structural damage to masonry-infilled reinforced concrete frames designed to Eurocode 8. Bulletin of Earthquake Engineering 2013;11.6:2151-2176.
- Dawe JL, Seah CK. Out-of-plane resistance of concrete masonry infilled panels. Canadian Journal of Civil Engineering 1989;16(6):854–864.

- da Porto F, Barbiero E, Dalla Benetta C, Modena C. Sperimentazione sul comportamento fuori piano di tamponamenti in muratura di laterizio. Murature Oggi 2007;94. (in Italian).
- De Risi MT, Del Gaudio C, Ricci P, Verderame GM. In-plane behaviour and damage assessment of masonry infills with hollow clay bricks in RC frames. Engineering Structures 2018;168:257-275.
- Dolšek M, Fajfar P (2008a). The effect of masonry infills on the seismic response of a four-storey reinforced concrete frame – a deterministic assessment. Engineering Structures 2008;30.7:1991-2001.
- Dolšek M, Fajfar P (2008b). The effect of masonry infills on the seismic response of a four-storey reinforced concrete frame – a probabilistic assessment. Engineering Structures 2008;30.11:3186-3192
- Draper NR, Smith, H. Fitting a straight line by least squares. Applied Regression Analysis, Third Edition, John Wiley & Sons, Inc. New York,1998.
- Eurocode 6. Design of Masonry Structures. Part 1-1: General Rules for Reinforced and Unreinforced Masonry Structures. Brussels, 2005. 123 p.
- Eurocode 8. Design of structures for Earthquake Resistance. Part 1-1: General Rules, Seismic Actions and Rules for Buildings. Brussels, 2004. 229 p.
- Flanagan RD, Bennett RM 1999a. Bidirectional behaviour of structural clay tile infilled frames. Journal of Structural Engineering 1999;125.3:236-244.
- Flanagan RD, Bennett RM 1999b. Arching of masonry infilled frames: Comparison of analytical methods. Practice Periodical on Structural Design and Construction 1999;4.3:105-110.
- Furtado A, Rodrigues H, Arêde A, Varum H. Experimental evaluation of out-of-plane capacity of masonry infill walls. Engineering Structures 2016;111:48-63.
- Furtado A, Rodrigues H, Arêde A, Varum H 2016b. Simplified macro-model for infill masonry walls considering the out-of-plane behaviour. Earthquake Engineering and Structural Dynamics 2016;45.4:507-524.
- Guidi G, da Porto F, Dalla Benetta M, Verlato N, Modena C. Comportamento sperimentale nel piano e fuori piano di tamponamenti in muratura armata e rinforzata. Proceedings of the XV ANIDIS, L'Ingegneria Sismica in Italia, Padua, Italy, 2013, 30. (in Italian).
- Hak S, Morandi P, Magenes G. Out-of-plane experimental response of strong masonry infills. 2nd European Conference on Earthquake Engineering and Seismology, 2014.
- Kadysiewski S, Mosalam KM. Modelling of unreinforced masonry infill walls considering in-plane and out-of-plane interaction. Pacific Earthquake Engineering Research Center 2009.
- Morandi P, Hak S, Magenes G. Simplified out-of-plane resistance verification for slender clay masonry infills in RC frames. Proceedings of the XV ANIDIS, L'Ingegneria Sismica in Italia, Padua, Italy, 2013.

- Mosalam K.M., Günay S. Progressive collapse analysis of reinforced concrete frames with unreinforced masonry infill walls considering in-plane/out-of-plane interaction. Earthquake. Spectra 2015;31.2,921-943.
- NTC2008. Decreto ministeriale 14 gennaio 2008 - Norme Tecniche per le Costruzioni NTC2008. Supplemento ordinario n. 30 Gazzetta Ufficiale 4 febbraio 2008, n 29. (in Italian).
- Peirce B. Criterion for the rejection of doubtful observations. The Astronomical Journal 1852;2.45:161-163.
- Rossetto T, Elnashai A. Derivation of vulnerability functions for European-type RC structures based on observational data. Engineering Structures 2003;25.10:1241-1263.
- Sassun K, Sullivan TJ, Morandi P, Cardone D. Characterising the in-plane seismic performance of infill masonry. Bulletin of the New Zealand Society for Earthquake Engineering 2016;49.1:100-117.
- Timoshenko SP, Woinowsky Krieger S. Theory of plates and shells. McGraw-Hill, New York, 1959.
- Varela-Rivera J, Moreno-Herrera J, Lopez-Gutierrez I, Fernandez-Baqueiro L. Out-of-plane strength of confined masonry walls. Journal of Structural Engineering 2012;138.11:1331-1341.
- Verlato N, Guidi G, da Porto F. Experimental testing and numerical modelling of infill masonry walls subjected to in-plane damage. Proc. of the Second European Conference on Earthquake Engineering and seismology, 25-29 August 2014, Istanbul, Turkey.

Chapter V
Out-of-plane code-based safety assessment of URM infills

5.1. INTRODUCTION

In the previous Chapters, OOP strength, stiffness and displacement capacity models for IP-undamaged and IP-damaged URM infills were presented (Chapter I), the experimental tests carried out in the literature were described (Chapter II), the results of new experimental tests were introduced (Chapter III), the reliability of the above-mentioned models and formulations was assessed and an empirical-mechanical OOP response model for IP-undamaged and IP-damaged infill was presented (Chapter IV).

The first four Chapters constitute the first part of this thesis and they were dedicated to the characterization of the OOP response of IP-undamaged and IP-damaged URM infills, with particular attention to their behaviour under seismic load.

The second part of the thesis, which begins with this Chapter, is dedicated to the seismic assessment of the OOP response of URM infills accounting for the IP/OOP interaction effects as well as to the assessment of the seismic response of infilled RC buildings accounting for the OOP response of infills and for the IP/OOP interaction. A special attention is dedicated to the evaluation of the seismic Intensity Measure (IM) corresponding to the OOP collapse of infills and, more specifically, to the value of IM corresponding to the attainment of the first OOP collapse. Such assessment is aimed at the assessment of the seismic safety of RC buildings with respect to the attainment of Life Safety Limit State and, in general, at the seismic safety check of URM infills through numerical analyses in a non-linear static (Chapter VII) and dynamic (Chapter

VIII) framework.

Prior to this, it is worth to recall how the OOP safety check of URM infills is carried out based on current code provisions, if available, which are expected to be simplified on the side of safety. This recall is aimed at providing a more conscious approach to the description and comment of the results of the numerical analyses presented in the next chapter, in order to define more robust and reliable recommendations for a really safety-sided check of URM infills under seismic load.

In section 5.2, a general introduction to the issue of the seismic safety assessment of non-structural elements is provided.

In section 5.3, OOP capacity models provided in current building codes are presented and discussed.

In section 5.4, OOP demand models provided in current building codes are presented and discussed.

In section 5.5, some open issues on which codes are not clear or immediately applicable are discussed.

5.2. GENERAL CONSIDERATIONS ON THE SEISMIC SAFETY ASSESSMENT OF URM INFILLS

Despite their significant contribution to the seismic response of structures, infill walls are currently considered in building codes as non-structural elements. Hence, whichever provision for their seismic safety check should be searched, in such codes, in the section dedicated to non-structural elements.

The seismic safety check of non-structural elements is typically force-based, as they are considered sensitive to accelerations. However, their inelastic capacity is sometimes considered by means of a behaviour/response modification factor.

Generally, seismic codes do not provide capacity models for non-structural elements. However, considering their wide diffusion and their clear prominence with respect to other non-structural elements, some codes provide capacity models for URM infills under seismic OOP actions. This issue will be addressed in the next subsection: in general, they are simplified versions of the strength models proposed in the literature and described in detail in Chapter I. On the other hand, demand models have never been discussed in this thesis, so they deserve some introductory words.

It is well known that, with extreme simplification, the seismic demand on structures – when a force-based approach is used, as in the design process according to current

codes – is calculated first in terms of maximum shear demand at its base, with reference to an equivalent Single Degree of Freedom (SDOF) system. Such base shear is then distributed to each floor according to a more or less simplified distribution consistent with the fundamental vibration mode shape of the structure itself.

A slightly different approach is adopted for non-structural elements and, among them, for infill walls. In fact, the seismic demand acting on them cannot be calculated by neglecting their exact position in the building. More specifically, the force demand acting on them is calculated in general, by multiplying their mass by the so-called floor spectral acceleration, which is calculated by means of floor acceleration spectra.

To understand in few words what a floor acceleration spectrum is, consider whichever building with *n* floors and consider that, at the mass centre of each floor, both the translational and the rotational mass are lumped. If such a building is subjected to an acceleration time-history at its base, each lumped mass will respond with an acceleration time-history at each storey, which will be different from the base acceleration time-history due to stiffness and damping properties of the building. If an SDOF is placed at a certain floor of the building it will be subjected, at its base, to the acceleration time-history associated with that floor and it will respond, based on its mass, stiffness and damping properties, with a certain acceleration time-history. The function that, at fixed damping ratio and at varying vibration period of such an SDOF, provides the maximum acceleration acting on such a SDOF subjected to the floor acceleration history is the floor spectrum of the building at the selected storey. Clearly, one can calculate the floor spectrum at each floor.

In general, based on the above discussion, the floor spectrum at each floor depends on the base acceleration, on the building height, on the considered floor height, on the period of the building, on the period of the SDOF, on the damping properties of the building and on the damping properties of the SDOF.

Non-structural elements, also called appendages, are considered as SDOF placed at a certain floor of buildings. Hence, the acceleration demand acting on them is calculated as the floor spectral acceleration at the floor on which the non-structural element is placed as a function of its dynamic properties, of the building dynamic properties and of the acceleration at the building base.

Clearly, as simplified design spectra are provided for the design of buildings, also direct and simplified floor spectra depending only of the base acceleration in terms of Peak Ground Acceleration (PGA) and on the dynamic properties of the non-structural elements and of the building/supporting structure are provided. Simplified – i.e., based

on the results of numerical analyses – or theoretical formulations for the calculation of floor spectra have been proposed in the literature by different authors (e.g., Politopoulos 2010, Sullivan et al. 2013, Petrone et al. 2015, Vukobratovic and Fajfar 2016-2017, Surana et al. 2018, among others). In this Chapter, those proposed by current seismic codes are presented.

The acceleration demand so calculated, multiplied for the mass of the non-structural elements and potentially reduced by a behaviour factor is compared with the force capacity of the non-structural element to assess its safety against seismic actions.

Note that not all standards provide indication about both capacity and demand as reported in Table 5.1.

Table 5.1. Code provisions on the OOP safety check of URM infills.

Code	EC6	EC8	FEMA 306	FEMA 356	ASCE-SEI 41-13	ASCE 7-10	NZSEE 2017
Strength capacity	✓		✓	✓	✓		✓
Force demand		✓				✓	✓

5.3. OOP STRENGTH MODELS IN BUILDING CODES

In this section, the OOP strength models provided in current building codes are discussed. More specifically, the strength model provided by Eurocode 6 (2005), FEMA 306 (1998), FEMA 356 (2000), ASCE/SEI 41-13 (2013) and NZSEE 2017 (2017) are introduced.

It is worth to note that all the proposed models refer to URM infills under uniformly distributed load. It has been demonstrated that, actually, the load shape has a significant influence on the strength exhibited by URM infills and that the uniformly distributed load is more representative of a wind load than of a seismic load, which is sinusoid-shaped.

5.3.1. Eurocode 6 strength model

Eurocode 6 (2005), in section 6.3.2, proposes an expression to calculate the lateral specific strength of masonry walls in which arching action can occur; this relationship can be extended, potentially, to URM infills and is reported in Equation 1.

$$q_{max} = f_d \left(\frac{t}{l_a}\right)^2 \tag{1}$$

In this relationship f_d is the design compressive strength of masonry in the direction of arching thrust while l_a is the panel dimension in the same direction. Such ultimate load is the 93% of the one that equilibrates the maximum thrust that can form in the masonry wall thickness as expressed in Equation 2.

$$N_{ad} = 1.5 f_d \left(\frac{t}{10}\right) \tag{2}$$

This thrust value is obtained as the expression of the resultant of a triangular compressive stress distribution assumed in the panel thickness: this distribution has maximum value equal to the masonry compressive strength and resultant applied at a distance equal to t/10 from the panel intrados. This also means that the depth of the compressed zone from the panel intrados is assumed equal to 0.30t, which is, according to Angel et al. (1994), the minimum compressed zone that allows the horizontal component of arching thrust being opposite to OOP loads. This is a conservative assumption, given that, according to Angel et al.'s analytical model, the compressed zone width normally ranges from a lower and an upper bound respectively equal to 0.3t and 0.5t. Moreover, note that also this approach is based on the lower bound theorem of limit analysis, i.e. on the determination of the maximum specific load that the infill can withstand as the maximum load in equilibrium with internal thrusts. Hence, it is expected to provide a lowed bound of the actual OOP strength of the infill. In addition, it neglects the presence of two-way arching, which usually occurs in URM infills in real buildings. Also for these reasons, it is expected to provide conservative values of the strength, as it is expected for a code provision. However, such conservativeness can be at least partially neutralized by the fact that the IP/OOP interaction effects are not explicitly considered.

5.3.2. FEMA 306 strength model

FEMA 306 (1998), in section 8.3.3 suggests evaluating the OOP specific strength of URM infills by means of Angel et al. (1994)'s formulation, as reported in Equation 3.

$$q_{max} = \frac{2f'_{me}}{(h/t)} R_1 R_2 \lambda \tag{3}$$

Equation 3 expresses the uniformly distributed load per unit width in equilibrium with the maximum thrust that the infill parts could withstand. In other word, Angel et al.'s formulation provided by FEMA306 is the result of an application of the lower bound limit analysis theorem. In Equation 5, λ is a slenderness parameter reported in Table 8-5 of FEMA 306 as a function of the infill vertical slenderness, h/t; f_{me} is masonry expected compressive strength; R_2 is a factor accounting for deformability of the infill-bounding frame and is reported in Equation 4.

$$R_2 = 0.357 + 2.49x10^{-14}EI{\leq}1 \tag{4}$$

In Equation 4, EI is defined as flexural rigidity of the weakest frame on the non-continuous side of the infill panel expressed in Nmm^2.

It is worth to note that in this case the effect of the IP damage is explicitly considered through the R_1 factor, which is tabulated as a function of the infill vertical slenderness h/t and on the entity of IP damage (moderate or severe) in Table 8-5 of FEMA 306.

5.3.3. FEMA 356 and ASCE/SEI 41-13 strength model

First, it is worth to note that FEMA 356 (2000) lists the conditions allowing the occurrence of arching action in URM infills in section 7.5.3.1. Namely, the panel must be in full contact with the surrounding elements that must have sufficient strength and stiffness to resist arching thrusts. In addition, the panel must have a vertical slenderness ratio lower than 25.

Based on these hypothesis, the code suggests evaluating the OOP specific strength of URM infills by means of a simplified version of Angel et al. (1994)'s formulation, as reported in Equation 5.

$$q_{max} = \frac{0.7f'_m}{(h/t)} \lambda_2 \tag{5}$$

In Equation 5, λ_2 is a slenderness parameter reported in Table 7-11 of FEMA 356; f'_m is the lower bound of the compressive strength of masonry calculated by dividing by 1.3 (1.6 in FEMA273 1997) its average compressive strength. FEMA274 (1997) points

out that the previous expression, which was already provided in FEMA273 (1997), is the relationship by Angel et al. (1994) simplified to evaluate a lower bound of the infills lateral strength. For instance, according to Flanagan and Bennett (1999), a 24% reduction of the undamaged infill's strength due to IP damage is assumed, as well as a 39% reduction due to confining frame deformability.

Identical provisions are given by ASCE/SEI 41-13 (2013) in section 11.4.3.2.

5.3.4. NZSEE 2017 strength model

The guidelines for the seismic assessment of moment resisting frames with infill panels currently applied in New Zealand (NZSEE 2017, section C7.6.1.1) suggest the use of Dawe and Seah (1989)'s empirical formulation modified by Flanagan and Bennett (1999) and with further corrections to calculate the probable OOP strength of solid URM infills in terms of resisting OOP pressure, as reported in Equation 6.

$$q_{max,solid}[kPa] = 730\gamma(f'_m)^{0.75}t^2 \left(\frac{\alpha_{arch}}{L_{inf}^{2.5}} + \frac{\beta_{arch}}{h_{inf}^{2.5}}\right) \tag{6}$$

In Equation 6 f'_m is the compressive strength of masonry expressed in N/mm^2; t is the infill thickness expressed in mm and not exceeding 1/8 of the infill height, according to Flanagan and Bennett. The coefficients α_{arch} and β_{arch} are the α and β factors defined by Dawe and Seah modified by Flanagan and Bennett, as reported in Equations 7 and 8. L_{inf} is the infill width expressed in mm.

Remember that masonry is an orthotropic material, hence it has two different compressive strength involved in vertical and in horizontal arching; in general, if clay hollow bricks are used, the compressive strength perpendicular to bricks' holes is different, and lower than, the compressive strength parallel to bricks' holes. The code does not provide indications on which one of these should be used. Remember that Flanagan and Bennett suggest using masonry compressive strength perpendicular to bricks' holes. Considering that it is usually the minimum one, it should provide a lower bound of the probable OOP strength. This is consistent with a code-based approach to the strength calculation. Hence, it seems reasonable to accept Flanagan and Bennett (1999) suggestion and use masonry compressive strength perpendicular to bricks' holes when applying Equation 6.

$$\alpha_{arch} = \frac{1}{h}(E_c I_c h^2)^{0.25} \leq 50 \tag{7}$$

$$\beta_{arch} = \frac{1}{L_{inf}}(E_b I_b L_{inf}^2)^{0.25} \leq 50 \tag{8}$$

In Equations 7 and 8, length are expressed in mm and forces in N. E is the elastic modulus and I is the cross-section inertia of the confining beam (b subscript) and of the confining column (c subscript). NZSEE suggests to assume α_{arch} equal to zero if a side gap greater than 0.02t exists; the same for β_{arch} if a top gap greater than 0.02t exists.

The coefficient γ accounts for the strength reduction due to the IP damage as a function of the infill vertical slenderness ratio. It is expressed as reported in Equation 9.

$$\gamma = \min\left(1.1\left(1 - \frac{h/t}{55}\right); 1\right) \tag{9}$$

The γ coefficient is obtained through a linearization of Angel et al.'s formulation at IDR demand equal to 2 times the IDR at first visible cracking of the infill wall due to IP actions, i.e., at moderate damage according to Angel et al.

In addition, NZSEE suggests reducing the OOP strength calculated by means of Equation 6 in presence of openings. Hence, for infills with openings, Equation 10 should be used.

$$q_{max} = q_{max,solid}\left(1 - \frac{A_{op}}{A_{wtot}}\right) \tag{10}$$

In Equation 10, A_{op} is the area of the opening, A_{wtot} is the total area of the infill. This expression for the strength reduction factor in presence of openings is reported by Flanagan and Bennett (1999) citing Mays et al. (1998). The code states that such formulation has not been validated a sufficient number of experimental results. In addition, it should be used with caution when $A_{op} > 0.2 A_{wtot}$: in this case, in fact, the occurrence of two-way arching is not certain.

5.4. OOP DEMAND MODELS IN BUILDING CODES

In this section, the OOP demand models provided in current building codes are

discussed. More specifically, the demand model provided by Eurocode 8 (2004), ASCE/SEI 7-10 (2010) and NZSEE 2017 (2017) are introduced. Of course, demand models herein presented are acceleration floor spectra and formulations aimed at defining, based on the acceleration demand, the force demand acting on URM infills.

5.4.1. Eurocode 8 demand model

Eurocode 8 (2004), in section 4.3.5, proposes an expression of the design force demand acting on non-structural elements, as reported in Equation 11.

$$F_{Ed} = \frac{S_a W_a \gamma_a}{q_a} \tag{11}$$

In Equation 11, W_a is the weight of the non-structural element, γ_a is the importance factor, q_a is the behaviour factor, S_a is the seismic coefficient, which is equal to the pseudo-spectral acceleration acting on the non-structural element divided by the acceleration of gravity g and is calculated as shown in Equation 12.

Note that for infill walls the importance factor is assumed equal to 1 according to section 4.3.5.3 of EC8 while the behaviour factor is assumed equal to 2, as suggested for exterior walls in section 4.3.5.4 of EC8.

$$S_a = \alpha S \left[\frac{3(1 + z/H)}{1 + (1 - T_a/T_1)^2} - 0.5 \right] \tag{12}$$

The floor acceleration has a linear distribution along the building height. In Equation 12, α is the design acceleration on type A soil, a_g, divided by the acceleration of gravity g, S is the soil factor, hence, αS is equal to PGA/g. In addition, z is the height of the non-structural element above the building base, H is the total height of the building. T_1 is the fundamental vibration period of the building in the relevant direction, T_a is the non-structural element vibration period.

Some considerations have to be discussed. First, what is z? American standards are more clear on this issue: z is the height, above the building base, of the point in which the non-structural element is attached to the building. For infill walls, such attachment is "diffused" along the building edges. One could assume that, "on average", the attachment point corresponds to the infill barycentre.

Second, what is T_1? As Equation 12 should be used in design and assessment of buildings, it seems that T_1 should be consistent with the framework in which the Equation is used. In other words, if it is used in the design process, T_1 is the design period of the building in the direction of interest (e.g., for RC buildings, the elastic period calculated for the bare frame with elements provided with halved inertia – according to Eurocode 8). On the other hand, if Equation 12 is used in the assessment process, T_1 should be the period of the building as it has been modelled for the assessment procedure, e.g., the effective period of the building if a non-linear static analysis is performed.

For what concerns T_a, no indication is provided in the code for non-structural elements in general and for infill walls in particular. This issue will be discussed in section 5.5.

However, it is worth to note that for stiff non-structural element T_a equals zero. Hence, in this case, the floor spectral acceleration ranges from PGA at z equal to zero to 2.5PGA at z equal to H. The floor spectral acceleration is obtained if T_a equals T_1. In this case, the floor spectral acceleration ranges from 2.5PGA at z equal to zero to 5.5PGA at z equal to H.

5.4.2. ASCE/SEI 7-10 demand model

ASCE/SEI 7-10 (2010), in section 13.3.1, proposes an expression of the design force demand acting on non-structural elements, F_p, as reported in Equation 13.

$$F_p = \frac{0.4a_p S_{DS} W_p}{\left(R_p/I_p\right)}\left(1 + 2\frac{z}{H}\right)$$

(13)

For the sake of clarity, Equation 13 can be re-written as reported in Equation 14. In this way, it can be simply compared with Eurocode 8 formulation.

$$F_{Ed} = \frac{S_a W_p I_p}{R_p}$$

(14)

In Equation 14, I_p is the component importance factor varying from 1.00 to 1.50. Values higher than one should be used, as reported in section 13.1.3, only for non-structural elements in strategical buildings and in buildings containing hazardous substances. R_p is the component response modification factor (equivalent to the

behaviour factor q_a) that varies from 1.00 to 12 as reported in Table 13.5-1 and 13.6-1. It should be assumed equal to 2.50 for URM infills. W_p is, of course, the weight of the non-structural element. In Equation 14, S_a is the floor acceleration acting on the non-structural element, as reported in Equation 15.

$$S_a = 0.4S_{DS}\left(1 + 2\frac{z}{H}\right)a_p \qquad\qquad (15)$$

In Equation 15, S_{DS} is the so-called spectral acceleration at short period: $0.4S_{DS}$ is the PGA; H is the average building height above its base, z is the height of the non-structural element attachment to the building; a_p is a factor accounting for the amplification of accelerations due to the deformability of the non-structural element reported in Table 13.5-1. It is worth to note that the American approach, with this factor, simplifies the calculation of the seismic demand acting on non-structural elements, as there is no need of a more or less detailed dynamic characterization of the non-structural elements required for the determination of its period, T_a, which enters Eurocode 8 formulation. Exterior non-structural wall elements, such as URM infills, are associated with an ap factor equal to 1.00, which is equivalent to consider them as stiff elements or, in other words, as non-structural elements with period equal to zero.

According to the ASCE/SEI 7-10 approach, the floor spectral acceleration on non-structural elements is varies linearly along the building height. For stiff non-structural elements, such as infill walls, it ranges from PGA at z equal to zero to 3PGA at z equal to H, i.e., it provides higher floor spectral acceleration on stiff non-structural elements with respect to Eurocode 8 formulation. The maximum value of a_p reported in Table 13.5-1 is equal to 2.5. Hence, the maximum floor spectral acceleration acting on very deformable non-structural elements ranges from 2.5PGA at z equal to zero to 5PGA at z equal to H. Hence, such approach provides lower floor spectral acceleration of deformable non-structural elements with respect to Eurocode 8 formulation.

However, note that the code also provides lower and upper bounds for the force demand acting on non-structural elements, i.e., with some manipulation of the formulations provided in ASCE/SEI 7-10, on the floor spectral acceleration: the lower bound is equal to $0.4PGA \cdot R_p$, while the upper bound is equal to $4PGA \cdot R_p$.

5.4.3. NZSEE 2017 demand model

NZSEE 2017 (2017), in section C7.6.2, explicitly refer to the loading code NZS

1170.5 – 2004 (2004) for the calculation of the OOP seismic demand on URM and RM infills. More specifically, the formulations proposed in NZS 1170.5 – 2004 are dedicated to non-structural elements in general; NZSEE 2017 provides some indications for an application of such formulations in the case of URM and RM infills.

NZS 1170.5 – 2004, in section 8.5.1, provides the formulation reported in Equation 16 to calculate the force demand on non-structural elements, F_{ph}.

$$F_{ph} = C_p(T_p)C_{ph}R_pW_p \leq 3.6W_p \tag{16}$$

In Equation 16, C_{ph} is the non-structural element response factor, which is equivalent to the inverse of the behaviour factor. Its value is expressed in Table 8.2 as a function of the expected ductility demand acting on the non-structural element, μ_p, and ranges from 0.45 (for μ_p equal to or greater than 3) to 1 (for μ_p equal to 1). NZSEE 2017 suggests assuming μ_p equal to 1 for URM infills and to 1.25 for RM infills; hence, C_{ph} is assumed equal to 1 for URM infills and to 0.85 for RM infills: this is equivalent to assume a behaviour factor equal to 1 for URM infills and to 1/0.85≈1.18 for RM infills.

In Equation 16, R_p should not be confused with the R_p factor used in the American approach. In fact, in this case, R_p is the non-structural element risk factor, which is equivalent to the importance factor I_p. The values for R_p are listed in table 8.1. This factor is greater than one only when the hazard due to the non-structural component failure is "disproportionately great". W_p is the weight of the non-structural element, of course.

The term $C_p(T_p)$ is the horizontal design coefficient of the non-structural element, i.e., in other words, the design floor spectral acceleration. It is calculated according to a formulation provided in section 8.2 of NZS 1170.5 – 2004, as reported in Equation 17.

$$C_p(T_p) = C(0)C_{Hi}C_i(T_p) \tag{17}$$

In Equation 17, $C(0)$ is the so-called hazard coefficient at period T equal to zero. It should be evaluated "for the modal response spectrum method and numerical integration time history methods" as reported in table 3.1 and is equal to 1.00 g for type A and B soil (strong rock and rock, respectively), to 1.33 g for type C soil (shallow soil) and to 1.12 for type D and E (soft and very soft soils, respectively). In other words, $C(0)$ is the equivalent of PGA.

In Equation 17, $C_i(T_p)$ is the spectral shape coefficient of the non-structural elements.

It accounts for the non-structural element dynamic properties through the period T_p. $C_i(T_p)$ is expressed as a function of the period T_p in section 8.4 and ranges from 0.5 for T_p higher than 1.50 s to 2.0 for T_p lower than 0.75 s. NZSEE 2017 suggests assuming, for URM infills, T_p lower than 0.75 s, and, so, $C_i(T_p)$ equal to 2.0.

C_{Hi} is a coefficient accounting for the height of the attachment of the non-structural part to the supporting structure, h_i, and for to the maximum height of the building h_n. C_{Hi} is calculated through the formulations provided in section 8.3 and reported in Equation 18.

$$C_{Hi} = \left(1 + \frac{h_i}{6}\right) \qquad \text{for all } h_i<12 \text{ m} \qquad (18a)$$

$$C_{Hi} = \left(1 + 10\frac{h_i}{h_n}\right) \qquad \text{for } h_i<0.2h_n \qquad (18b)$$

$$C_{Hi} = 3.0 \qquad \text{for } h_i \geq 0.2h_n \qquad (18c)$$

In addition, the code states that for elevations that satisfy the height limitations of both Equations 18a and 18b, the lower value of C_{Hi} shall be used.

Note that also in this case the distribution of floor accelerations is linear along the building height.

5.5. CRITICAL ASPECTS AND OPEN ISSUES

In the above sections, strength capacity and force demand models provided by current building codes have been presented and discussed. With the aid of the literature review reported in Chapter 1, the comprehension of the strength capacity models provided is quite simple. More specifically, the conservativeness of the assumptions at the base of such models has been described as well as the issues that are neglected (e.g., two-way arching and the possible presence of opening in the European and American approach, the IP/OOP interaction in the European approach, the influence of the load shape on the OOP strength in all the approaches).

For what concerns the calculation of the seismic demand, it has been clarified that URM infills are considered as non-structural elements sensitive to accelerations in the OOP direction. Hence, the force demand acting on them is calculated by means of floor spectra. The acceleration demand acting on non-structural elements in general and on

URM infills in particular depends, roughly, on three main aspects: the seismic acceleration demand at the building base; the position of the non-structural element/infill in the building; the dynamic properties of the non-structural element/infill. In addition, the force demand on non-structural elements depends on their ductility capacity, as a behaviour factor (or equivalent) is introduced in all the force demand models above presented.

In this section, further discussion is presented on two of the above aspects that are not exhaustively addressed in current building codes: the calculation of the OOP vibration period of the specific class of non-structural elements herein considered, i.e., URM infill walls, as well as the evaluation of the most appropriate value of the behaviour factor. Both issues are introduced in this section. A robust and reliable proposal for their evaluation is provided in the next Chapters, dedicated to the numerical assessment of the seismic response of infills and of infilled RC structures through non-linear static and dynamic analyses.

5.5.1. OOP vibration period of URM infills

In the calculation of the seismic demand acting on non-structural elements by means of floor response spectra, it is obvious that the acceleration demand acting on a certain non-structural element at a certain floor must depend on its dynamic properties summarized in the vibration period, T_a. In fact, a stiff non-structural element is expected to respond exactly as the floor at which it is attached, while a deformable non-structural element is expected to respond differently from such floor, with dynamic amplification or de-amplification of the acceleration demand.

It is worth to note that both the American and the New Zealand loading codes bypass the problem of the calculation of T_a for URM infills. ASCE/SEI 7-10 assume that the seismic response of the infill as non-structural element is equal to the response of the supporting floor: in other words, ASCE/SEI 7-10 assumes that URM infills can be considered as stiff elements with period equal to zero. On the other hand, NZSEE 2017 assumes that URM infills have, presumably, period lower than 0.75 s and that, for this reason, the acceleration acting on them is two times that associated with the supporting floor. More complex is the approach of Eurocode, which requires an explicit calculation of the vibration period of the non-structural element through the introduction of Ta in the formulation for the calculation of the acceleration demand; no further indication is provided concerning how to calculate such period. Hence, the designer is supposed to

refer to the consolidated literature.

In this regard, the first question that should be addressed is: T_a should be considered as an elastic "initial" period of the infill or an "effective" period? In the second case, there is no study available in the literature that allows the use of whichever specific formulation: this issue will be addressed in Chapter VIII of this thesis. If an elastic period should be used, some considerations can be discussed, as reported in the following.

The elastic period of an infill wall is the vibration period associated with the first vibration mode of an elastic orthotropic plate. Clearly, for its calculation, a numerical approach can be used, with the FEM modelling of the infill wall. However, as pointed out also in recent studies (De Angelis and Pecce 2018), the boundary conditions at the edges of the infill play a fundamental role in the definition of its first OOP vibration period. Such conditions depend, of course, on the construction quality, but also, and primarily, on the modal deformed shape of the entire building. In fact, the deflection or torsional rotation of the structural elements surrounding the infill can allow/prevent the rotation of the infill edges and, so, reproduce an intermediate (and undetermined *a priori*) condition between a simple support and a clamp acting on the infill edges.

The determination of the real boundary conditions at the edges of an infill in a real building is crucial, as its vibration period strongly depends on them, also considering that all the closed-form formulations for the calculation of such a period assume certain boundary conditions at the edges of the plate. Hence, to use the correct formulation, further numerical studies concerning the modal deformed shape of infills in buildings should be performed.

In addition, note that all the closed-form formulations available in the literature are dedicated to isotropic plates: the effect of the material orthotropy is neglected, too.

Remembering that the above open issues (real boundary condition at edges; material orthotropy) still remain, it is worth to recall the closed-form approaches available for a straightforward calculation of T_a.

Blevins and Plunkett (1980) report closed-form formulations for the vibration frequencies of elastic isotropic plates with different boundary conditions at edges. For what concerns the first vibration mode, Equation 19 applies for simply supported along all edges rectangular plates, Equation 20 for clamped along all edges rectangular plates.

$$f = \frac{\pi(1 + (w/h)^2)}{2w^2} \sqrt{\frac{Et^2}{12\rho(1 - \nu^2)}} \tag{19}$$

$$f = \frac{\lambda^2}{2\pi w^2} \sqrt{\frac{Et^2}{12\rho(1 - \nu^2)}} \tag{20}$$

In Equations 19 and 20, w, h and t are the infill width, height and thickness, respectively; E is masonry elastic modulus, ρ is masonry density, ν is Poisson coefficient, λ is a coefficient depending on the infill aspect ratio. The use of a simplified version of Equation 19, with ν equal to zero, is proposed by Penna et al. (2007).

On the other hand, consistently with a possible modelling approach, the OOP period of the infill wall can be calculated by applying the classical SDOF formulation with mass equal to the participating mass to the first vibration mode, which is equal to 66% of the total mass for an infill simply-supported along all edges, and stiffness equal to the initial elastic stiffness of the infill under seismic load calculated, for example, by using Timoshenko (1959)'s formulation.

5.5.2. OOP behaviour factor

It has been already stated that when calculating the OOP seismic demand acting on an infill wall, the infill wall is considered an SDOF placed on a certain floor of the building provided with a certain mass and with a certain stiffness. Hence, it undergoes a certain maximum acceleration, the floor spectral acceleration, that multiplied for the infill/SDOF mass provides the OOP force acting on the infill/SDOF.

However, it should be remembered that this is the force demand acting on the infill/SDOF only if it has an indefinitely elastic behaviour. Of course, infill walls under OOP action are not indefinitely elastic, as shown also through experimental tests' results in Chapter II and III. In addition, they are provided with a certain ductility equal to, at least, 1.4 for IP-undamaged infills and to 1.1 for IP-damaged infills, as shown in Chapter IV.

The ratio between the OOP seismic demand on the infill/SDOF calculated as it was elastic and the OOP strength capacity of the infill/SDOF is the OOP behaviour factor of the infill, q. Of course, it is used in a force-based seismic-safety design of infills to take advantage of the infill post-peak displacement capacity by forcing it entering in the non-linear behaviour range. Clearly, the value of the behaviour factor strongly depends on the ductility capacity of the infill wall under OOP actions: the higher the ductility capacity, the higher the behaviour factor that can be used.

Different values of the behaviour factor (also called response factor) are proposed in

codes. Eurocode 8 suggests assuming q equal to 2.0; ASCE/SEI 7-10 suggests assuming q equal to 2.5; NZSEE 2017 suggests assuming q equal to 1.0 for URM infills.

Some issues should be pointed out. First, there is no numerical or analytical study justifying the above values. Maybe, if it is assumed that infills have an OOP elastic-plastic behaviour and the applicability of the equal displacement rule is accepted, these q values are fixed by assuming a ductility capacity equal to 2.0, 2.5 or 1.0. However, as already stated, there is no study in the literature justifying such an assumption.

If it assumed that infills have the same ductility capacity and that the calculated OOP seismic demand acting on them is equal, independently on the code provisions applied to evaluate it, the OOP safety check should provide equal results by using ASCE/SEI 41-13 strength model or Eurocode 6 if the ratio between the strength provided by Eurocode 6 model and the one provided by ASCE/SEI 41-13 is equal to the inverse of the ratio of the corresponding behaviour factors, which is equal to 1.25.

The ratio between the strength provided by Eurocode 6 model (Equation 1) over that provided by ASCE/SEI 41-13 (Equation 5) is shown, for varying values of the vertical slenderness h/t and under the hypothesis of f_d equal to f_{me}, in Figure 7.1.
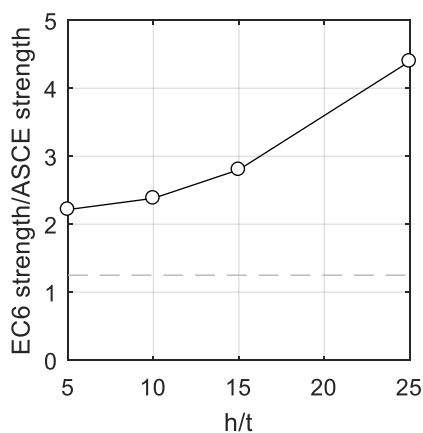
Figure 5.1. Ratio of the OOP strength provided by Eurocode 6 and ASCE models at varying h/t values.

The values of the strength ratios are highly different from 1.25, hence, the two safety checks are different also in terms of results obtained.

A second issue should be discussed. One of the effects of the IP/OOP interaction is the OOP strength and stiffness reduction, as well as a displacement capacity variation.

Do the q-factors provided by codes account for this circumstance?

In Chapter VIII, all these issues will be covered based on the results of non-linear dynamic analyses. An OOP effective stiffness and period for URM infills will be defined and, consistently, a unique value of the behaviour factor accounting for the IP/OOP interaction effects.

REFERENCES

- Angel R, Abrams DP, Shapiro D, Uzarski J, Webster M. Behaviour of reinforced concrete frames with masonry infills. University of Illinois Engineering Experiment Station. College of Engineering. University of Illinois at Urbana-Champaign., 1994.
- ASCE/SEI 7-10. Minimum Design Loads for Buildings and Other Structures. ASCE 7-10. Reston, VA: ASCE, 2010.
- ASCE/SEI 41-13. Seismic rehabilitation of existing buildings. Reston, VA: American Society of Civil Engineers; 2013.
- Blevins RD, Plunkett R. Formulas for natural frequency and mode shape. Journal of Applied Mechanics 1980;47:461.
- Dawe JL, Seah CK. Out-of-plane resistance of concrete masonry infilled panels. Canadian Journal of Civil Engineering 1989;16(6):854–864.
- De Angelis A, Pecce MR. Out-of-plane structural identification of a masonry infill wall inside beam-column RC frames. Engineering Structures 2018;173:546-558.
- Eurocode 6. Design of Masonry Structures. Part 1-1: General Rules for Reinforced and Unreinforced Masonry Structures. Brussels, 2005. 123 p.
- Eurocode 8. Design of structures for Earthquake Resistance. Part 1-1: General Rules, Seismic Actions and Rules for Buildings. Brussels, 2004. 229 p.
- FEMA273. ATC, 1997, NEHRP Guidelines for the Seismic Rehabilitation of Buildings, prepared by the Applied Technology Council (ATC-33 project) for the Building Seismic Safety Council, published by the Federal Emergency Management Agency, Report No. FEMA273, Washington, D.C.
- FEMA 274. ATC, 1997, NEHRP Commentary on the Guidelines for the Seismic Rehabilitation of Buildings, prepared by the Applied Technology Council (ATC-33 project) for the Building Seismic Safety Council, published by the Federal Emergency Management Agency, Report No. FEMA274, Washington, D.C.
- FEMA 306. ATC, 1998, Evaluation of Earthquake Damaged Concrete and Masonry Wall Buildings, Basic Procedures Manual, prepared by the Applied Technology Council (ATC-33 project) for the Partnership for Response and Recovery, published by the Federal Emergency Management Agency, Report No. FEMA306, Washington, D.C.
- FEMA 356. Prestandard and commentary for the seismic rehabilitation of buildings. Washington, DC: Federal Emergency Management Agency; 2000.

- Flanagan RD, Bennett RM 1999b. Arching of masonry infilled frames: Comparison of analytical methods. Practice Periodical on Structural Design and Construction 1999;4.3:105-110.
- Mays G, Hetherington JG, Rose TA. Resistance-deflection functions for concrete wall panels with openings. Journal of Structural Engineering 1998;124.5:579-587.
- NZS 1170.5:2004. Structural design actions. Earthquake design Actions. New Zealand Society for Earthquake Engineering (NZSEE), 2004.
- NZSEE 2017. New Zealand Society for Earthquake Engineering (NZSEE), Structural Engineering Society New Zealand Inc. (SESOC), New Zealand Geotechnical Society Inc., Ministry of Business, Innovation and Employment, Earthquake Commission. The Seismic Assessment of Existing Buildings (the Guidelines), Part C – Detailed Seismic Assessment, 2017. http://www.eq-assess.org.nz/
- Penna A, Calvi GM, Bolognini D. Design of masonry structures with bed joint reinforcement. Seminar Paredes de Alvenaria Inovaçao e possibilidades actuais, Lisbona, Portugal, 2007.
- Petrone C, Magliulo G, Manfredi G. Seismic demand on light acceleration-sensitive nonstructural components in European reinforced concrete buildings. Earthquake Engineering and Structural Dynamics 2015;44:1203–1217. doi: 10.1002/eqe.2508.
- Politopoulos I. Floor spectra of MDOF nonlinear structures. Journal of Earthquake Engineering 2010;14.5:726-742.
- Sullivan TJ, Calvi PM, Nascimbene R. Towards improved floor spectra estimates for seismic design. Earthquakes and Structures 2013;4.1:109-132.
- Surana M, Pisode M, Singh Y, Lang DH. Effect of URM infills on inelastic floor response of RC frame buildings. Engineering Structures 2018;175:861-878.
- Timoshenko SP, Woinowsky Krieger S. Theory of plates and shells. McGraw-Hill, New York, 1959.
- Vukobratović V, Fajfar P. A method for the direct estimation of floor acceleration spectra for elastic and inelastic MDOF structures. Earthquake Engineering and Structural Dynamics 2016;45:2495–2511. doi: 10.1002/eqe.2779.
- Vukobratović V, Fajfar P. Code-oriented floor acceleration spectra for building structures. Bulletin of Earthquake Engineering 2017;15.7:3013-3026.

Chapter VI
Description of the case-study RC buildings

6.1. INTRODUCTION

In the previous Chapter, the code provisions aimed at the OOP safety assessment of URM infills have been presented and discussed. In general, it has been observed that the strength capacity and force demand models provided are extremely simplified, most likely on the side of safety, and that they neglects many issues, such as a complete characterization of the two-way arching strength mechanism, the influence on the OOP strength of the load shape, the detailed characterization of the IP/OOP interaction effects, the dynamic properties of infills, the definition of their ductility capacity and behaviour factor. Such aspects, which are not included in currently applied formulations and models, have been deeply discussed in the first part of the thesis, with a complete characterization of the OOP response of IP-undamaged and IP-damaged infills based on mechanical models and on experimental data.

As already stated, the second part of this thesis is dedicated to the assessment of the seismic response of URM infills and of infilled RC buildings with non-linear static and dynamic analyses. This effort is also aimed to the comparison of the results of such detailed analyses with the results of code-based safety check, in order to provide robust and reliable, although simplified, provisions for a correct and safe assessment of URM infills under seismic loads.

To achieve this goal, it is necessary to define, design and model a wide set of RC buildings.

In this Chapter, the design in Ductility Class "High" (DCH) of 16 Category A (Domestic and Residential activities according to Eurocode 1 2002 (EC1), section 6.3.1)

RC buildings with a two-times symmetric rectangular plan is presented. In the following, the X and Z global axes define the horizontal reference plan while the Y global axis is vertical and perpendicular to that plan. The case-study buildings are provided with 5 bays in the X direction and of 3 bays in the Z direction. All bays spans are 4.5 m long, so the structural plan dimensions are 22.5 m along X axis and 13.5 m along Z axis. The 16 buildings designed are different for the number of storeys, which is equal to 2, 4, 6 or 8, and for the design PGA (PGA_d) at Life Safety Limit State (LS), equal to 0.05, 0.15, 0.25 or 0.35 g. The inter-storey height is always equal to 3 m. Each building has been designed for gravity and seismic loads by applying the Response Spectrum Analysis (RSA) according to Eurocode 2 (2004) (EC2) and Eurocode 8 (2004) (EC8).

A simplified reproduction of the case-study buildings plan is reported in Figure 6.1.
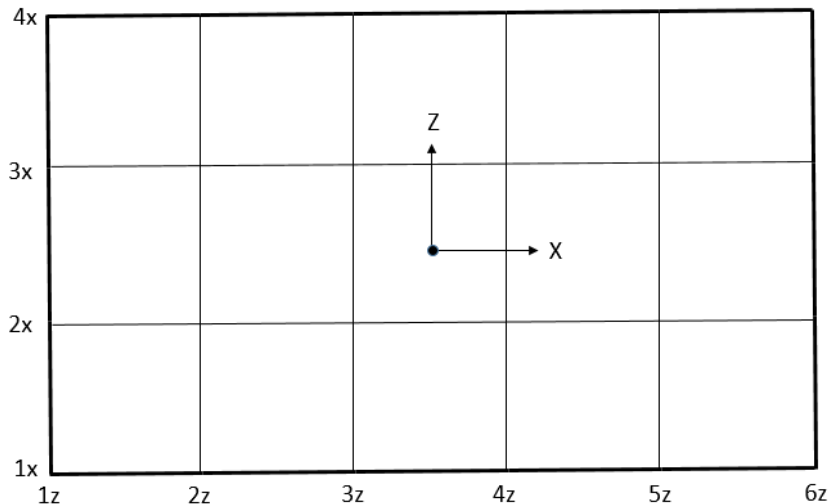
Figure 6.1. Structural plan of the case-study buildings, together with the names of the 6 frames parallel to the Z axis and of the 4 frames parallel to the X axis.

In section 6.2, the general procedure used to design buildings is described.

In section 6.3, some general considerations on the results of design are discussed.

6.2. DESIGN PROCEDURE OF THE CASE-STUDY BUILDINGS

In this section, the procedure used to design buildings according to Eurocodes is presented. Namely, design material properties are presented, the design spectra are

shown, the basic modelling and design criteria are discussed, the rationale for dimensioning structural elements is presented, loads and load combinations used in the design process are shown.

Finally, the global verification of the building performance is performed at LS and at Damage Limitation limit state. The design and verification of beams and columns is briefly presented.

6.2.1. Materials' properties

The materials used for the design of buildings were class C28/35 concrete and rebars with nominal characteristic yielding tensile strength equal to 450 N/mm^2. The details of material properties are reported in Table 1.

Table 6.1. Materials' properties used for the design and assessment of the case-study buildings.

property	symbol	value
concrete characteristic compressive strength	f_{ck}	28.0 N/mm^2
concrete mean compressive strength	f_{cm}	36.0 N/mm^2
concrete design compressive strength	f_{cd}	15.9 N/mm^2
concrete mean tensile strength	f_{ctm}	2.77 N/mm^2
concrete design tensile strength	f_{ctd}	1.29 N/mm^2
concrete ultimate strain	ε_{cu}	0.00350
concrete elastic modulus	E_{cm}	32308 N/mm^2
steel characteristic yielding stress	f_{yk}	450 N/mm^2
steel mean yielding stress	f_{ym}	517 N/mm^2
steel design yielding stress	f_{yd}	391 N/mm^2
steel elastic modulus	E_s	210000 N/mm^2

The concrete mean compressive strength f_{cm} has been obtained from its characteristic value for the cylindrical specimen f_{ck} by applying the relationship proposed by EC2 in Tab. 3.1, as reported in Equation 1.

$$f_{cm} = f_{ck} + 8 \text{ N/mm}^2 \tag{1}$$

The design compressive strength f_{cd} has been determined by applying the strain-rate coefficient α_{cc} equal to 0.85 and the partial safety factor for concrete γ_c equal to 1.5 for persistent and transient design conditions (as reported in Eurocode 2, section 2.4.2.4), according to the relation proposed by EC2 in section 3.1.6, as reported in Equation 2.

$$f_{cd} = \alpha_{cc} \frac{f_{ck}}{\gamma_c} \tag{2}$$

The mean, f_{ctm}, characteristic, f_{ctk}, and design, f_{ctd}, tensile strength of the concrete were calculated by applying the relationships proposed by Eurocode 2 in Tab. 3.1 and Eurocode 2, section 3.1.6, as reported in Equations 3-5.

$$f_{ctm} = 0.3 f_{ck}{}^{2/3} \tag{3}$$

$$f_{ctk} = 0.7 f_{ctm} \tag{4}$$

$$f_{ctd} = \alpha_{ct} \frac{f_{ctk}}{\gamma_c} \tag{5}$$

In Equation 5, α_{ct} is set equal to one.

The concrete mean elastic modulus in compression has been calculated by applying the formulation proposed in Eurocode 2, Table 3.1, as reported in Equation 6.

$$E_{cm} = 22000 \left(\frac{f_{cm}[N/mm^2]}{10} \right)^{0.3} \tag{6}$$

The reinforcing steel design yielding stress f_{yd} has been determined from its characteristic value f_{yk} by applying the relationship proposed in Eurocode 2, section 3.2.7, as reported in Equation 7.

$$f_{yd} = \frac{f_{yk}}{\gamma_s} \tag{7}$$

In Equation 7, the safety factor for steel γ_s for persistent and transient design conditions is assumed equal to 1.15 according to Eurocode 2, section 2.4.2.4.

The constitutive laws adopted in the design process for modelling the materials' behaviour are the elastic-plastic model for the reinforcement steel (according to Eurocode 2, section 3.2.7) and the rectangular stress distribution (according to Eurocode 2, section 3.1.7) for concrete, with λ, the coefficient that defines the effective height of the compression zone, equal to 0.8 and η, the coefficient that defines the effective compression strength, equal to 1. All the assumptions and relationships above presented

are effective for concretes with $f_{ck}<50$ N/mm^2, as in the present case.

6.2.2. Elastic and design response spectra

For the seismic design of buildings, the response spectra provided for horizontal motion by Eurocode 8, section 3, have been used. The vertical seismic component was neglected, as no one of the conditions that make necessary to take into account for it (as reported in Eurocode 8, section 4.3.3.5.2) was realized. The buildings were designed on a stiff and horizontal type A soil, with soil factor S equal to 1. Moreover, the importance factor γ_I was set equal to 1, which is proper for buildings with domestic and residential use, the damping ratio was set equal to the 5%. The values for the periods T_B, T_C and T_D were set equal to the ones suggested for the Type 1 elastic spectrum, which is recommended for high-seismicity zones, and were equal to 0.15, 0.40 and 2.00 s, respectively.

The PGA associated to LS elastic spectrum was set to 4 different values: 0.05, 0.15, 0.25 and 0.35 g for a return period T_R of 475 years. The elastic spectra for a return period of 50 years, which were used for the design at Damage Limitation Limit State (DL), were determined by multiplying for 0.4 the PGA adopted for the elastic spectra at LS (Hak et al. 2012).

The elastic spectra at LS and at DL used for design are reported in Figure 6.2.
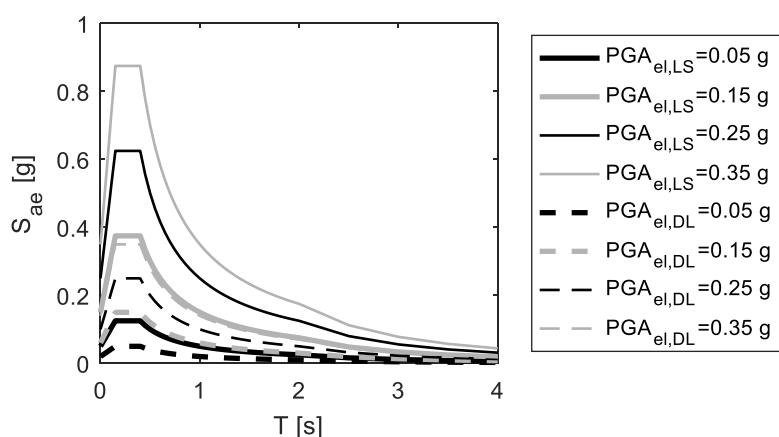
Figure 6.2. Elastic response spectra at LS and DL

Within the application of the RSA, for the force-based safety check of the structural elements at LS, the elastic response spectra were reduced by applying the behavior factor

q. It was determined according to section 5.2.2.2 of Eurocode 8 for multi-storey and multi-bays RC frame system, for which α_u/α_1 is equal to 1.3, designed in DCH, for which μ is equal to 4.5. It was assumed that the buildings were regular in plan but not in elevation: these assumptions will be verified in the following. For this reason, the behavior factor reduction coefficient k_R=0.8 was applied. The behavior factor applied was then equal to 4.68.

The design response spectra were obtained by dividing by q all the spectral pseudo-accelerations, as shown in Figure 6.3. Note that they cannot be lower than β times the PGA, with β equal to 0.2, as suggested in EC8, section 3.2.2.
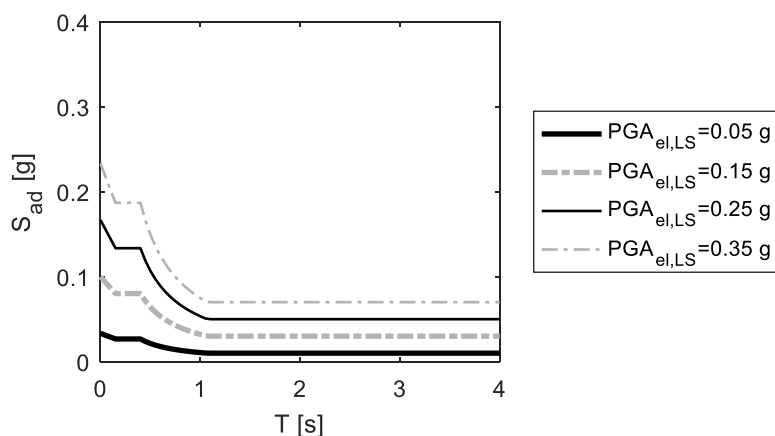
Figure 6.3. Design response spectra at LS.

6.2.3. Basic design and modelling criteria

The design of buildings was carried out by applying the basic principles presented in section 4.2.1 of Eurocode 8. Among all, the diaphragmatic behavior of the storey levels was assured and introduced in the structural model. In addition, a somehow equal lateral elastic stiffness along the X and Z directions has been pursued. Therefore, the storey masses were lumped in the barycentre of floors, except for the masses of the structural elements, which were assigned as linear masses distributed along them, and except for the infill walls' masses, which were introduced in the model as linear masses distributed on the perimeter beams. In order to take into account for the structural elements cracking, the flexural stiffness of columns and beams were reduced by 50% according to Eurocode 8, section 4.3. Elements representative of infill walls were not introduced

in the structural model, so the buildings were designed as bare RC frames.

6.2.4. Dimensioning of structural elements

The structural elements dimensioning was carried out by applying three main criteria.

First, the lateral deformability at LS was checked based on the results of a linear lateral force analysis, according to Eurocode 8, section 4.3.3.2, that was carried out by assigning a distributed load of 12 kN/m^2 to each floor and by adopting a 5‰ limitation for the interstorey drift according to Eurocode 8, section 4.4.3.2.

Second, the prevention of the bond failure for the anchorage of beams reinforcement was ensured. In fact, in section 5.6.2.2, Eurocode 8 sets some lower bounds for the ratio between the maximum diameter of longitudinal bars used in beams and the dimension of the columns cross section, in order to prevent the bond failure under seismic actions of the anchorage of the reinforcement passing through beam-column joints. This control, which is very strict, will be discussed again in the next section. To take into account for it in the dimensioning of columns sections, it has been assumed that the longitudinal bars' diameter was equal to 16 mm, that the normalized axial load was equal to zero, which is on the side of safety, and that the ratio between the compression steel ratio and the maximum allowed tension steel ratio was equal to 0.8.

Third, the dimensions of elements was set in order to inhibit P-δ effects.

6.2.5. Gravity load determination and combination

Gravity loads were determined with reference to a 25 cm thick concrete and masonry floor realized with a 4 cm thick concrete slab in order to guarantee the diaphragmatic behavior of the storey levels. The materials' weight per unit volume used for the calculation of gravity loads are reported in Table 7.2.

Table 6.2. Construction materials' weight per unit volume.

material	value
reinforced concrete	25 kN/m^3
masonry	8 kN/m^3
mortar/plaster	15 kN/m^3

The partitions and the pavement were taken into account through distributed loads equal to 1.2 kN/m^2 and 0.4 kN/m^2, respectively, while the live load was assumed equal to 2 kN/m^2. These assumptions are in accordance to the values suggested for residential

buildings in Eurocode 1, section 6.3.1.2. The weight of infills was not considered on the perimeter beams at the roof level, of course. However, the presence of a 1.2 m high protection wall realized along the roof perimeter was considered.

For all buildings, the floor seismic weight per unit area, which was calculated by accounting for the weight of structural and non-structural elements, as well as for the 30% of the live loads, is between 9 and 10 kN/m^2, which is consistent with the assumptions made in the phase of structural elements' dimensioning.

For the safety check of structural members with respect to gravity loads the following load combinations were considered according to Eurocode 0 (2002), section 6.4.3.

- For the resistance verifications at Ultimate Limit State (ULS), the load combination reported in Equation 8 has been used.

$$E_d = 1.3G_{k1} + 1.5G_{k2} + 1.5Q_k \qquad (8)$$

- For the stresses limitation, cracking and deformability verifications at Serviceability Limit State (SLS), the load combination reported in Equation 9 has been used.

$$E_d = G_{k1} + G_{k2} + \psi Q_k \qquad (9)$$

In Equation 9, the ψ factor was set to 1, 0.7 or 0.5 according to the specific verification to carry out.

For the verification with respect to the seismic actions, the combination reported in Equation 10 has been used.

$$E_d = G_{k1} + G_{k2} + 0.3Q_k + E \qquad (10)$$

In Equation 10, E is the seismic action applied in the two direction in the horizontal plan according to the 30% combination rule. To account for accidental torsional effects, the floor mass centre is set in four different positions, as shown in Figure 6.4.
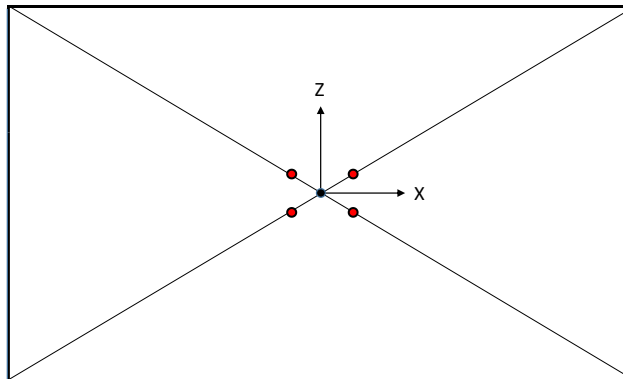
Figure 6.4. Centre of mass positions assumed in the design process.

Each one of the four application points is 5% of the structural plan dimensions in the X and Z direction distant from the floor geometric centre according to Eurocode 8, section 4.3.2.

6.2.6. Global verifications of the case-study buildings

After the definition and elastic modelling of the structures, of the loads and of the masses, some global verifications were carried out.

First, a check of the regularity in plan was performed. The plan regularity criteria are listed in section 4.2.3.2 of Eurocode 8. In the present case, all buildings have a rectangular compact and two times symmetric structural plan, lacking of any set-back. The ratio between the two dimensions of the structural plan is 1.67, which is lower than the limit value, 4. The calculation of the radius of gyration of the floor mass in plan l_s and of the torsional radii r_x and r_y for each floor allowed verifying that all buildings were not torsionally flexible, as the ratio r/l_s was equal, on average, to 1.2. For these reasons, all designed buildings were regular in plan.

Second, a check of the regularity in elevation was performed. The elevation regularity criteria are listed in section 4.2.3.3 of Eurocode 8. In the present case, all buildings are provided of a framed lateral load-resistant structure that runs without interruptions or set-backs from the foundation to the roof. Moreover, the mass variation between successive floors are always conveniently limited. Based on the results of the linear lateral load analysis, i.e., by applying a lateral forces distribution whose shape is consistent with a simplified linear deformed shape of the structure, it was possible to calculate the lateral interstorey stiffness in the X and Z directions for each building as

the ratio between the storey seismic shear force and the correspondent interstorey drift. For all buildings, in passing from the first to the second storey, a reduction of the lateral stiffness upper than the 30% was observed: it is assumed that such a reduction can be classified as "non-gradual", so all buildings are not regular in elevation. This was already assumed in the dimensioning phase.

Third, a check on P-δ effects was performed. In order to verify the negligibility of geometric non-linearity second order effects, according to Eurocode 8, section 4.4.2.2, the following steps were followed. Said h the Interstorey height, for each storey, the vertical action due to gravity loads in the seismic combination, P, was calculated. Hence, the storey seismic shear force, V, given by a lateral load linear analysis carried out with reference to the spectral pseudo-acceleration associated at LS to the first vibration period of the structure in the considered direction given by a modal analysis was calculated. Then, the floor barycentre displacement in the two horizontal direction, δ, obtained by multiplying the one given as result by the linear lateral load analysis for the ductility factor μ_δ, according to Eurocode 8, section 4.3.4, was calculated. Such ductility factor was assumed equal to the behavior factor q, as in all the considered cases, the first vibration period of the structure was lower than T_C, according to Eurocode 8, section 5.2.3. From these displacement values, the interstorey drifts, d, were obtained. For all buildings, for all storeys and in all the horizontal directions it was verified that the second-order effects were negligible, as the inequality reported in Equation 11 was satisfied.

$$\frac{Pd}{Vh} < 0.1 \tag{11}$$

Fourth, for all buildings, lateral deformability verifications at DL limit state were performed. More specifically, for each floor and in correspondence of two points diametrically opposed of the structural plan perimeter, P1 and P2 in Figure 6.5, it was verified that in any one of the 32 seismic load combinations the interstorey drift ratio (IDR) was upper than the 5‰, according to Eurocode 8, section 4.4.3.2.

The displacements values were obtained through an elastic response spectrum analysis. In all the considered cases, for all buildings and in all directions, the maximum IDR was never upper than the 2-3‰, so the verification was satisfied.
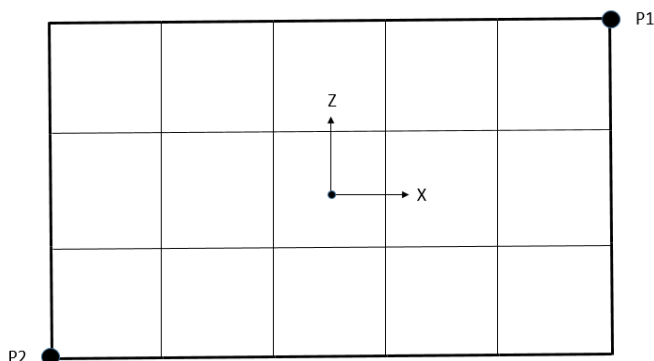
Figure 6.5. Points for the calculation of the buildings' displacements for their verification at DL.

6.2.7. Design of beams

The concrete cover thickness was defined accordingly to section 4.4.1 of Eurocode 2. For instance, a distance of 40 mm from the longitudinal reinforcement centroid closest to the concrete surface and the concrete surface itself was considered sufficient to guarantee an adequate protection of the reinforcement from aggressive external factors.

The longitudinal reinforcement of each beam was determined based on the envelope of the bending moment diagrams given by the 32 seismic load combinations plus the one given by the gravity load combination at ULS. The quantity of steel reinforcement this way calculated was then compared with the upper and lower limitations provided by Eurocode 2 in section 9.2.2.1 6.2.3 and by Eurocode 8 in section 5.4.3.1.2 and potentially modified based on them. Each beam is provided of longitudinal web reinforcement. Given that all dispositions about seismic local detailing for longitudinal and transversal reinforcement were respected, the local ductility verification proposed in section 5.4.3.1.2(4)b of Eurocode 8 was neglected. According to section 5.6.2.2 of Eurocode 8, the anchorage of bars passing through beam-columns joints was verified.

The shear force acting on beams was determined by applying capacity design rules according to section 5.5 of Eurocode 8 while the shear strength was calculated by applying the truss model proposed in section 6.2.3 of Eurocode 2. This allowed the determination of the transversal reinforcement, which was constituted by vertical stirrups with 8 mm diameter whose spacing was verified, and eventually modified, also according to the limitations stated in section 9.2.2 of Eurocode 2 and in section 5.5 of Eurocode 8. In any case the additional diagonal reinforcement discussed in section

5.5.3.1.2 of Eurocode 8 was necessary.

6.2.8. Design of columns

The concrete cover thickness was defined accordingly to section 4.4.1 of Eurocode 2. For instance, a distance of 40 mm from the longitudinal reinforcement centroid closest to the concrete surface and the concrete surface itself was considered sufficient to guarantee an adequate protection of the reinforcement from aggressive external factors.

The longitudinal reinforcement of each column was determined based on the bending moment calculated by applying the beam-column capacity design rules according to section 5.5 of Eurocode 8. The number of reinforcing bar used was set in order to respect the maximum distance among them accordingly to the maximum distance allowed for restrained bars set to 150 mm according to section 5.5.3.2 of Eurocode 8.

The shear transverse reinforcement constituted by stirrups and ties was calculated by applying the truss model proposed in section 6.2.3 of Eurocode 2 based on the shear actions obtained by applying capacity design rules and according to the restrictions on stirrups spacing and mechanical percentage of transversal reinforcement provided in section 9.5.3 of Eurocode 2 and in section 5.5.3.2.2 of Eurocode 8. In all cases, stirrups with 8 mm diameter were used for the transverse reinforcement.

6.3. SOME CONSIDERATIONS ON THE DESIGN RESULTS
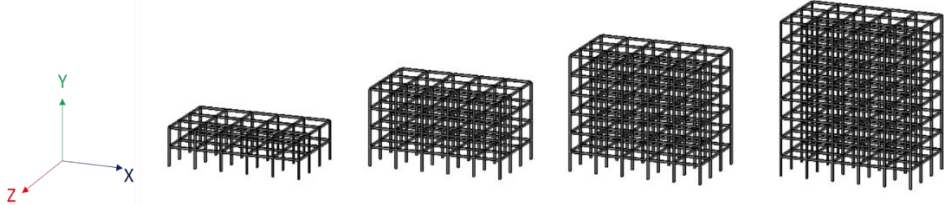
In this section, some considerations on the results of the design process are discussed. First, modal analysis results showing buildings' modal characteristics are shown. Second, some suggestions on frame elements' dimensioning are derived.

In addition, considerations and comments on the structural sections of beams and columns and their dependency on the number of floors and on the design seismic acceleration are presented, similarly to the discussion presented in Panagiotakos and Fardis (2004).

6.3.1. Results of modal analysis

The design vibration periods of the case-study buildings are reported in Table 6.3 and in Figure 6.6. Note that the periods shown are calculated with a modal analysis on the bare frame models with halved inertia of the structural elements' cross-section.

Table 6.3. Design fundamental periods in the X and Z global directions of the case-study bare buildings.

	Number of storeys of the bare frames							
	2		4		6		8	
	$T_{1,Z}$	$T_{1,X}$	$T_{1,Z}$	$T_{1,X}$	$T_{1,Z}$	$T_{1,X}$	$T_{1,Z}$	$T_{1,X}$
design PGA at LS	[s]	[s]	[s]	[s]	[s]	[s]	[s]	[s]
0.05 g	0.418	0.406	0.578	0.554	0.775	0.743	1.070	1.023
0.15 g	0.418	0.406	0.538	0.520	0.741	0.712	1.022	0.977
0.25 g	0.418	0.406	0.476	0.459	0.693	0.665	0.961	0.919
0.35 g	0.345	0.336	0.403	0.389	0.566	0.542	0.762	0.728
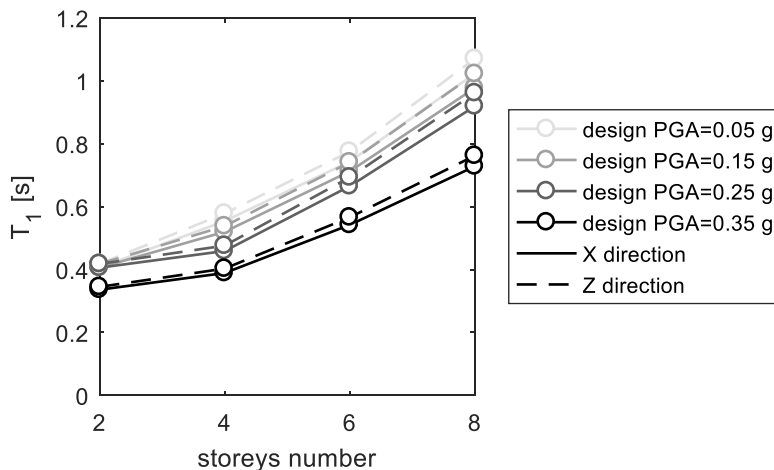
Figure 6.6. First vibration period in X and Z directions of the case-study buildings.

A quite clear and expected hierarchy between the periods of the case-study buildings is observed, with a straightforward trend of the periods with both the number of storeys and the design PGA at LS. Note that the periods in the Z direction are always slightly higher than the corresponding in the X direction. This occurs because buildings are less long in the Z direction, so they tend to be more deformable with respect to X direction;

however, in section 6.2.3 it has been stated that the design was oriented at ensuring, as much as possible, an equal lateral stiffness in both the horizontal directions, according to Eurocode 8 general design principles. However, note also that stairs were not introduced, for simplicity, in the structural models.

6.3.2. A proposal for dimensioning criteria

In section 6.2.4 it has been stated that for dimensioning of structural members in general and of columns in particular, the prevention of the bond failure for the anchorage of beams reinforcement was ensured. In fact, in section 5.6.2.2, Eurocode 8 sets some lower bounds for the ratio between the maximum diameter of longitudinal bars used in beams and the dimension of the columns cross section, in order to prevent the bond failure under seismic actions of the anchorage of the reinforcement passing through beam-column joints. This control is very strict and, in most cases, was the most influent in determining the dimensions of columns cross-sections. To take into account for it in the dimensioning of columns sections, it has been assumed that the longitudinal bars' diameter was equal to 16 mm, that the normalized axial load was equal to zero, which is on the side of safety, and that the ratio between the compression steel ratio and the maximum allowed tension steel ratio was equal to 0.8.

However, based on the results of the design process, it is possible to define some more specific and less conservative assumptions for dimensioning of elements. For what concerns ν_d, which is defined as the maximum normalized axial load given by the seismic load combinations, it is suggested to use the values reported in Tables 6.4 and 6.5 for the first and last floor of buildings and to linearly interpolate for intermediate floors.

Table 6.4. Value of the design normalized axial load to use in columns' dimensioning at first floor.

building number of storeys	interior joints	exterior joints
2-3	0.08	0.04
4-7	0.20	0.05
8 or more	0.30	0.10

Table 6.5. Value of the design normalized axial load to use in columns' dimensioning at last floor.

building number of storeys	interior joints	exterior joints
2-3	0.05	0.02
4-7	0.05	0.02
8 or more	0.05	0.02

For what concerns ρ'/ρ_{max}, which is defined as the ratio between the compression steel ratio and the maximum allowed tension steel ratio based on the verification requested in section 5.4.3.1.2 of Eurocode 8, the use of the value 0.8 is suggested.

For what concerns d_{bL}, the maximum diameter of longitudinal bars, the use of the values reported in Tables 6.6 and 6.7 is suggested.

Table 6.6. Value of the maximum diameter of longitudinal bars to use in columns' dimensioning for design PGA at LS lower than 0.20 g.

building number of storeys	from 1st to 4th storey	for upper storeys
1-4	14 mm	-
more than 4	16 mm	14 mm

Table 6.7. Value of the maximum diameter of longitudinal bars to use in columns' dimensioning for design PGA at LS equal to or greater than 0.20 g.

building number of storeys	interior joints	exterior joints
1-4	16 mm	-
more than 4	18 mm	16 mm

6.3.3. Structural members' characteristics

To enter more deeply the results of the design of the case-study buildings, in this section the average values of:

i. the depth of beams' cross section, h_b;
ii. the area of columns' cross section, A_c;
iii. the top reinforcement ratio of beams' cross sections, ρ_{top};
iv. the bottom reinforcement ratio of beams' cross section, ρ_{bot};
v. the total reinforcement ratio of columns' cross sections, ρ_{tot};

for each storey and for each case-study building are reported in Figure 6.7.
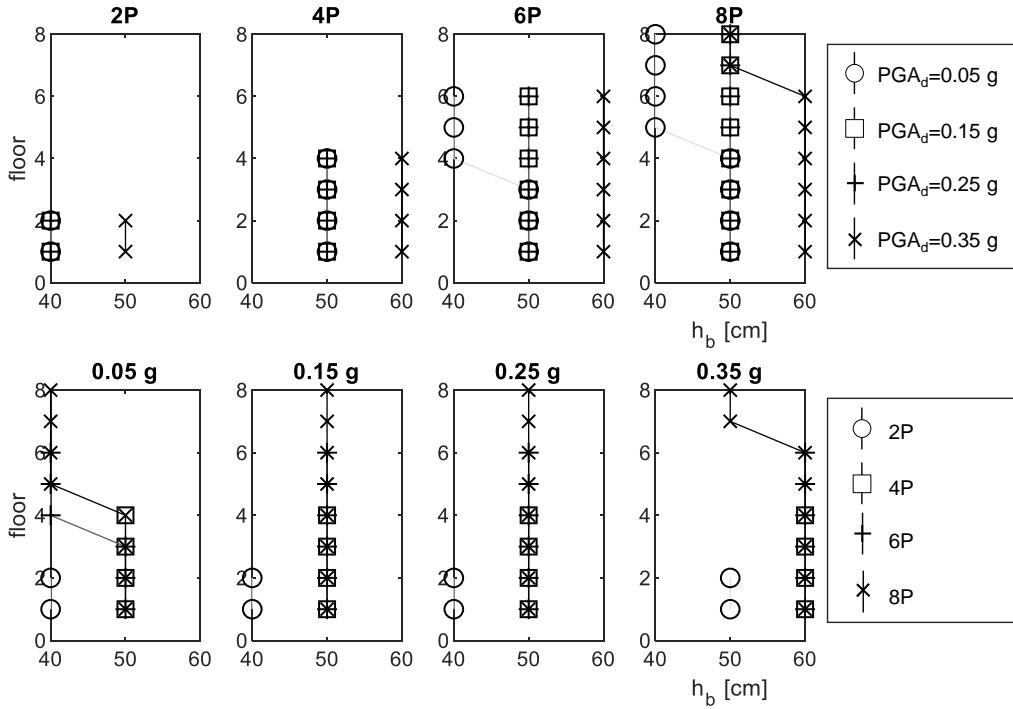
Figure 6.7. Average depth of beams' cross-sections.

In the first row of Figure 6.7, the average depth of beams' cross-sections is shown, for each floor, at varying design PGA in bins homogeneous in terms of number of storeys. In the second row of Figure 6.7, the same property is represented for varying number of storeys in bins homogeneous in terms of PGA. Some lines are not visible, as they often overlap. The average depth ranges from 40 to 60 cm.

It can be observed that, with the exception of low-rise buildings, beams' cross-section depth is quite independent on the total number of storeys of the building and is equal, on average, to 50 cm for low-intermediate design PGA and to 60 cm for high PGA. The depth of beams' cross-sections varies sensitively at increasing design PGA. It is observed that, as expected, beams' cross-section depth is lower at upper storeys of mid- and high-rise buildings designed for lower design PGA.
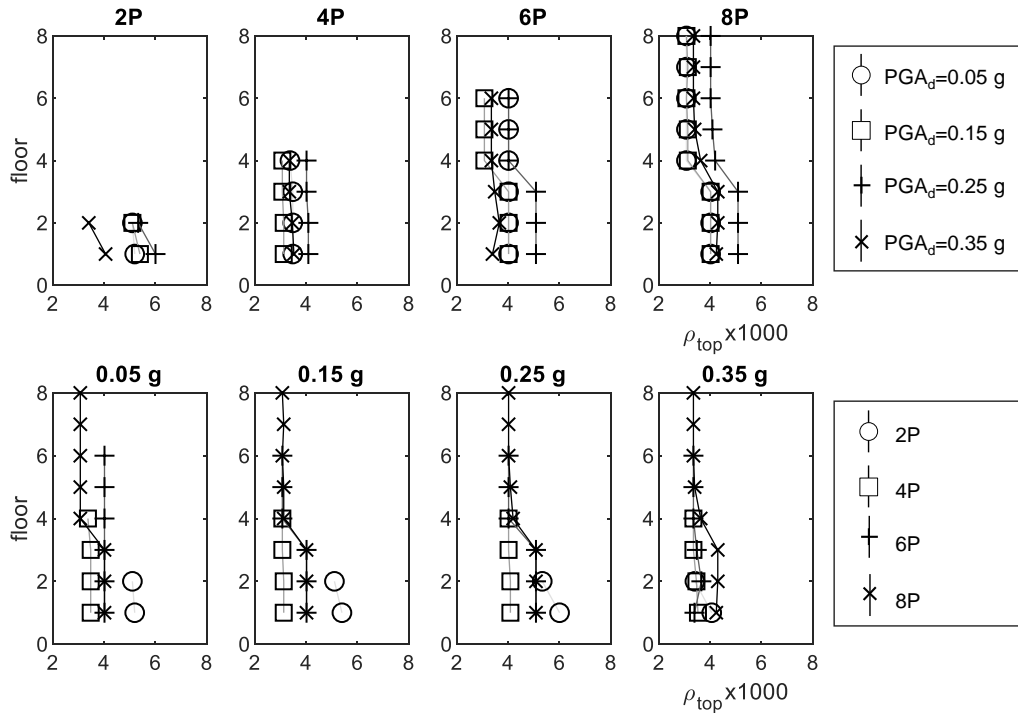
Figure 6.8. Average top reinforcement ratio of beams' cross-sections.

In the first row of Figure 6.8, the average top reinforcement ratio of beams' cross-sections is shown, for each floor, at varying design PGA in bins homogeneous in terms of number of storeys. In the second row of Figure 6.8, the same property is represented for varying number of storeys in bins homogeneous in terms of PGA. Some lines are not visible, as they overlap. The average top reinforcement ratio ranges from 0.3% to 0.6%.

It can be observed that, at the upper storeys of mid- and high-rise buildings, the top reinforcement ratio of beams' cross-sections is independent on the total number of storeys and is equal, on average, to 0.3% for low-intermediate design PGA and to 0.4% for intermediate-high PGA. For low- and mid-rise buildings as well as at the lower storeys of mid- and high-rise buildings, there is a certain dependence of the average top reinforcement ratio on the total number of storeys, as well as on the design PGA. However, there is no clear trend with neither of them. This occurs because the reinforcement ratio is equal to the ratio between the reinforcement area and the cross-section area. Both quantities increase, in general, at increasing design PGA and total

number of storeys. However, they not increase with the same rate and this rate depends, above all, on the practitioner judgment, so, sometimes, the lines represented in Figure 6.8 intersect. In general, it is observed that such ratio reduces in passing from lower to upper storeys, due to a reduction of the necessary reinforcement steel area.
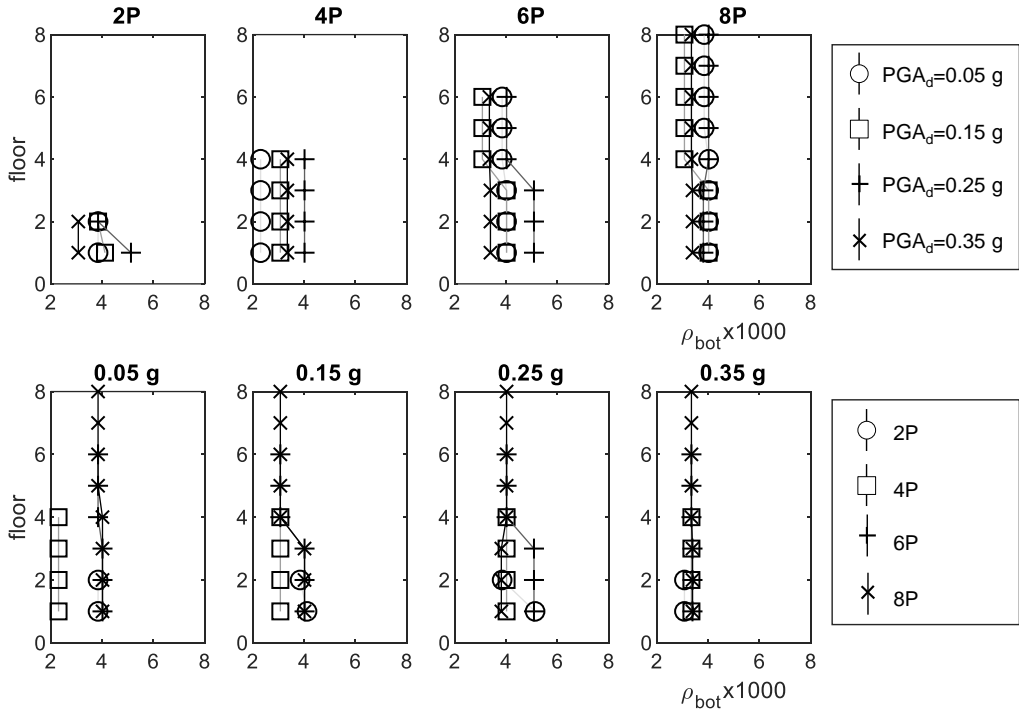
Figure 6.9. Average bottom reinforcement ratio of beams' cross-sections.

In the first row of Figure 6.9, the average bottom reinforcement ratio of beams' cross-sections is shown, for each floor, at varying design PGA in bins homogeneous in terms of number of storeys. In the second row of Figure 6.9, the same property is represented for varying number of storeys in bins homogeneous in terms of PGA. Some lines are not visible, as they overlap. The average bottom reinforcement ratio ranges from 0.2% to 0.5%.

It can be observed that, at the upper storeys of mid- and high-rise buildings, the bottom reinforcement ratio of beams' cross-sections is independent on the total number of storeys and is equal, on average, to 0.3%. For low- and mid-rise buildings as well as at the lower storeys of mid- and high-rise buildings, there is a certain dependence of the

average bottom reinforcement ratio on the total number of storeys, as well as on the design PGA. However, there is no clear trend with neither of them. This occurs because the reinforcement ratio is equal to the ratio between the reinforcement area and the cross-section area. Both quantities increase, in general, at increasing design PGA and total number of storeys. However, they not increase with the same rate and this rate depends, above all, on the practitioner judgment, so, sometimes, the lines represented in Figure 6.8 intersect. In general, it is observed that such ratio, differently from the top reinforcement ratio, is quite constant in passing from lower to upper storeys.
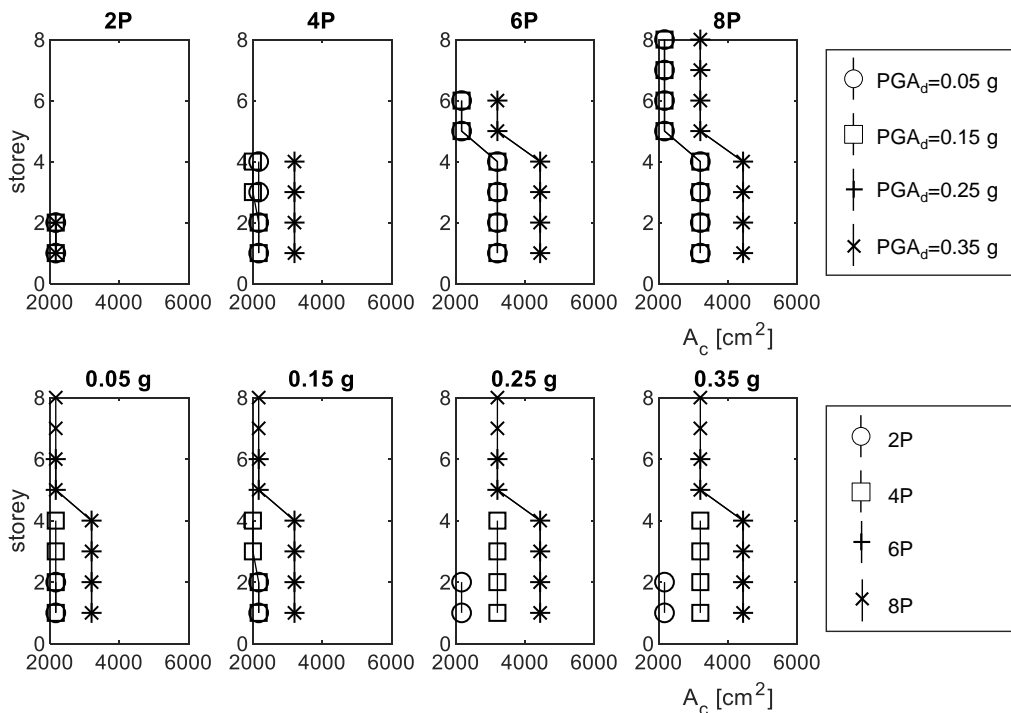
Figure 6.10. Average area of columns' cross-sections.

In the first row of Figure 6.10, the average area of columns' cross-sections is shown, for each floor, at varying design PGA in bins homogeneous in terms of number of storeys. In the second row of Figure 6.10, the same property is represented for varying number of storeys in bins homogeneous in terms of PGA. Some lines are not visible, as they overlap. The average area of columns ranges from 2000 cm² to 4500 cm².

Differently from the previous quantities, clear and straightforward trends are visible in Figure 6.10. It is observed that the area of columns is quite independent on the specific design PGA for low-intermediate PGA and on the specific number of storeys for low- and mid-rise buildings.
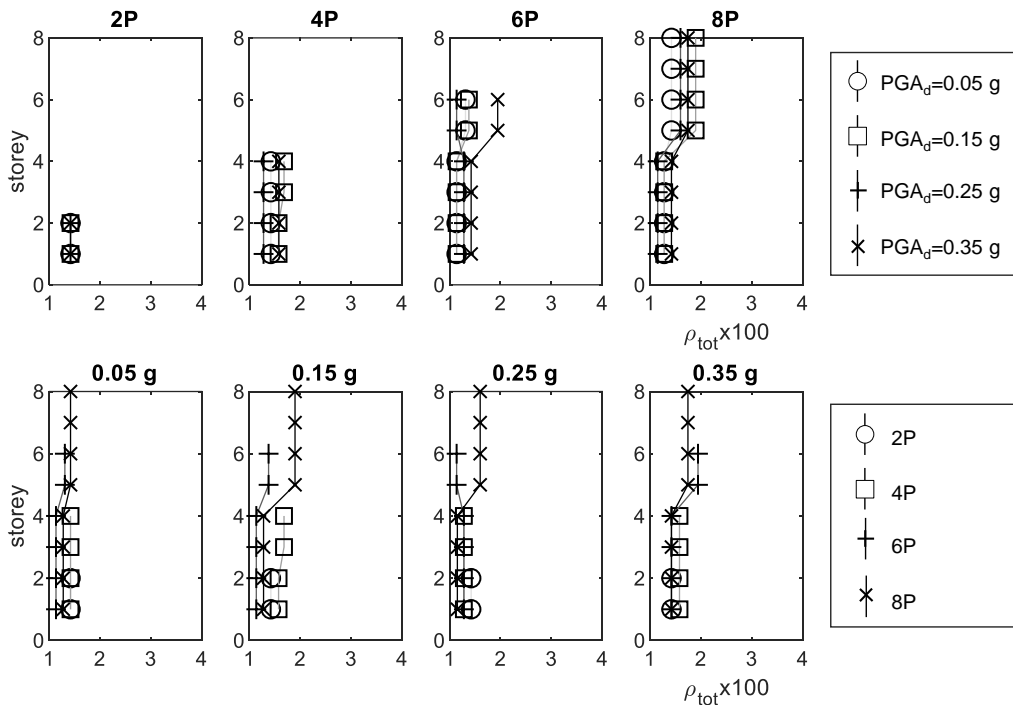
Figure 6.11. Average total reinforcement ratio of columns' cross-sections.

In the first row of Figure 6.11, the average total reinforcement ratio of columns' cross-sections is shown, for each floor, at varying design PGA in bins homogeneous in terms of number of storeys. In the second row of Figure 6.11, the same property is represented for varying number of storeys in bins homogeneous in terms of PGA. Some lines are not visible, as they overlap. The average total reinforcement ratio ranges from 1% to 2%.

It can be observed that, at the upper storeys of mid- and high-rise buildings, the bottom reinforcement ratio of beams' cross-sections is independent on the total number of storeys and is equal, on average, to 1.5% for low design PGA and to 2% for intermediate and high design PGA. For low- and mid-rise buildings as well as at the

lower storeys of mid- and high-rise buildings, there is a certain dependence of the average total reinforcement ratio, which increases at fixed total number of storeys for increasing design PGA and decreases, at fixed design PGA, at increasing number of storeys. Most likely, this occurs because the necessary reinforcement ratio increases at higher rate than the cross-section area at fixed number of storeys and at increasing design PGA, while the contrary occurs at fixed design PGA and at increasing number of storeys. However, remember that part of these trends is certainly due to the practitioner judgment. In addition, the reinforcement ratio in intermediate and high-rise buildings increases in passing from lower to upper storeys due to the reduction of columns' cross-section area. In addition, the reinforcement ratio also tends to increase at upper storeys due to the lower axial load ratio and, hence, to the lower beneficial effect of it on the moment strength of columns.

REFERENCES

- Eurocode 0. Basis of structural design. Brussels, 2002.
- Eurocode 1. Actions on structures. Brussels, 2002.
- Eurocode 2. Design of Concrete Structures. Part 1-1: General Rules and Rules for Buildings. Brussels, 2004. 225 p.
- Eurocode 8. Design of structures for Earthquake Resistance. Part 1-1: General Rules, Seismic Actions and Rules for Buildings. Brussels, 2004. 229 p.
- Hak S, Morandi P, Magenes G, Sullivan TJ. Damage control for clay masonry infills in the design of RC frame structures. Journal of Earthquake Engineering 2012;16:sup1, 1-35.
- Panagiotakos TB and Fardis MN. Seismic performance of RC frames designed to Eurocode 8 or to the Greek Codes 2000. Bulletin of Earthquake Engineering 2004;2:221-259.

Chapter VII
Out-of-plane seismic safety assessment of URM infills in a non-linear static framework

7.1. INTRODUCTION

In this Chapter, the 16 RC case-study infilled buildings presented in Chapter VI and different for number of storeys (2, 4, 6 and 8) and for the design Peak Ground Acceleration (0.05, 0.15, 0.25 and 0.35 g) at Life Safety Limit State (LS) are examined. Two different infill layouts are considered, i.e., a double leaf 'weak' infill layout (WL) and a one leaf 'strong' infill layout (SL). First, for each case study building, the Peak Ground Acceleration (PGA) at which the first OOP collapse of infills occurs (PGA_c) is assessed according to a "Designer Approach" (i.e., a "code-based" approach) applied in a linear elastic framework on bare frame models and using code provision for the assessment of infills' OOP capacity and demand. Second, the PGA_c is evaluated by using non-linear static analyses carried out on infilled models of the case-study buildings, according to the procedure assumed as "Reference Approach", and literature formulations for OOP capacity and demand accounting for the IP/OOP interaction. The influence of the number of storeys and of the design PGA of the building on the PGA_c are discussed. The overestimation of the PGA_c assessed using the "Designer Approach" is shown and discussed, as well as the overestimation of the PGA_c assessed in a linear elastic framework even if the IP/OOP interaction is considered.

Based on the "Reference Approach" results, fragility curves with respect to the first OOP collapse for all case-study buildings are shown considering both the OOP PGA and the IP inter-storey drift ratio (IDR) as demand parameter. Finally, for all the case-

study buildings, a wide range of 42 infill layouts, different for slenderness ratio and masonry compressive strength, is considered and the results of the application of the "Reference Approach" are shown in order to calculate a "limit state" curve defining the slenderness-compressive strength couples for which the OOP safety check of infills may be neglected.

7.2. DESCRIPTION OF THE PROCEDURES APPLIED FOR THE ASSESSMENT OF THE COLLAPSE PGA

As previously stated, the first aim of this Chapter is assessing the overestimation of the PGA and of the spectral pseudo-acceleration (PSA) associated with the first OOP infill collapse (PGA_c and PSA_c, respectively) calculated by neglecting the IP/OOP interaction by using a totally Eurocode-based approach for 16 RC case-study infilled buildings different for number of storeys (2, 4, 6 and 8) and for the design PGA (0.05, 0.15, 0.25 and 0.35 g) at LS. To achieve this goal, the hereafter-described procedures are applied. In the following, the X and Z global axes define the horizontal reference plan. Consider X as the 'IP direction' and Z as the 'OOP direction'; clearly, the following procedures are applied also considering X as the 'OOP direction' and Z as the 'IP direction'.

Note that the PGA_c is assumed as capacity PGA of the entire building at LS. In other words, the OOP collapse of infills is considered as the attainment of the LS. This is in accordance with section 2.2.2(6)P of Eurocode 8 (2004) (EC8), in which it is stated that at Ultimate Limit States, such as LS, "*it shall be verified that under the design seismic action the behaviour of nonstructural elements does not present risks to persons and does not have a detrimental effect on the response of the structural elements*".

7.2.1. Designer (code-based) Approach (DA)

For the application of the DA, the OOP strength of infills is calculated by applying Eurocode 6 (2005) (EC6) formulation for masonry walls under uniformly-distributed lateral load reported in section 6.3.2, herein extended to infill walls (Equation 1).

$$F_{Rd} = f_d \left(\frac{t}{l_a}\right)^2 wh \tag{1}$$

In Equation 1, t is the infill thickness, w is the infill width, h is the infill height. Infill

walls with w>h, as in the considered case, mainly arch in the vertical direction (Flanagan and Bennett, 1999). For this reason, in Equation 1 f_d is the design compressive strength of masonry in the vertical direction and l_a is the height of the infill calculated as distance between the confining beams' centrelines.

For each case-study bare frame, the OOP force demand, F_{Ed}, acting on the infills at each storey considered as non-structural elements is assessed by applying Equation 2, which is proposed in section 4.3.5 of EC8.

$$F_{Ed} = \frac{S_a W_a \gamma_a}{q_a} \tag{2}$$

In Equation 2, W_a is the weight of the infill participating to its first out-of-plane vibration mode, γ_a is the importance factor of the infill, assumed equal to 1 according to section 4.3.5.3 of EC8, q_a is the behaviour factor of the infill, assumed equal to 2, as suggested for exterior walls in section 4.3.5.4 of EC8. S_a is the seismic coefficient, which is equal to the PSA acting on the infill in the OOP direction divided by the acceleration of gravity g, and is calculated as shown in Equation 3.

$$S_a = \alpha S \left[\frac{3(1 + z/H)}{1 + (1 - T_a/T_1)^2} - 0.5 \right] \tag{3}$$

In Equation 3, α is the design acceleration on type A soil, a_g, divided by the acceleration of gravity g, S is the soil factor, z is the height of the infill barycentre above the building base, H is the total height of the building, T_1 is the fundamental vibration period of the building in the relevant direction, i.e., in our case, the design fundamental vibration period of the building in the OOP direction, calculated for the bare frame model with halved-inertia for the structural elements' section. T_a is the infill vibration period in the OOP direction. Codes do not provide indications on this issue, hence there is no code prescription that can be assumed as reference. For this reason, T_a is calculated, both when applying the DA and the RA, by applying the classical formulation for a single-degree of freedom system, with mass equal to the infill mass participating to the first OOP vibration mode (assumed as the 66% of the infill total mass), and stiffness calculated as for an elastic plate pinned along all edges according to the formulation by Timoshenko and Woinowsky-Krieger (1959). With some manipulation, Equations 2 and 3 can be written as Equations 4 and 5, respectively.

$$F_{Ed} = \frac{PSA}{g} \frac{W_a \gamma_a}{q_a} \tag{4}$$

$$PSA = PGA \left[\frac{3(1 + z/H)}{1 + (1 - T_a/T_1)^2} - 0.5 \right] \tag{5}$$

The DA consists in:

i.   Calculating, for each infill layout, the OOP strength, F_{Rd}, by applying Equation 1.

ii. Calculating, for each case study building and in each horizontal direction, the maximum demand acting on infills – which always occurs at the last floor – by using Equation 4 and matching it to the capacity calculated using Equation 1 in order to define the PSA_c.

iii. Calculating PGA_c from PSA_c using Equation 5.

7.2.2. Reference Approach (RA)

For the application of RA, literature formulations for OOP capacity and demand are applied. For the prediction of the IP-undamaged infill OOP strength under seismic load, the mechanical model by Dawe and Seah (1989) is applied for WL, i.e., for thin infills, while Eurocode 6 formulation adapted to the seismic load shape is applied to predict the OOP strength of the SL, i.e., for thick infills, as suggested in Chapter IV.

The OOP force displacement-curve for WL infills predicted by Dawe and Seah is reported in Figure 7.1.
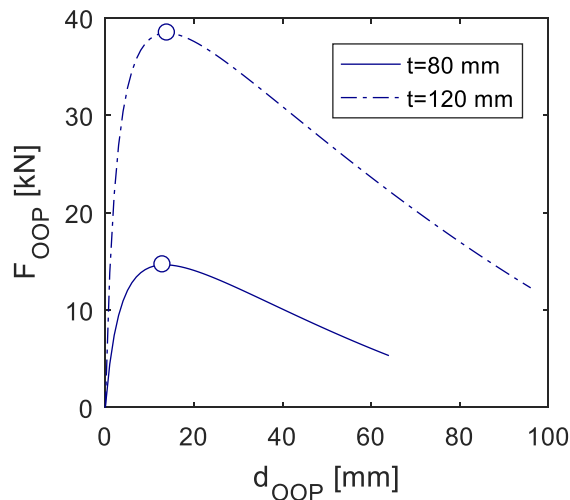
Figure 7.1. OOP response curve predicted by using Dawe and Seah's model for the 80 mm- and 120 mm-thick leaves constituting the WL infill type.

R, the OOP strength degradation factor due to the IP damage, represented by the maximum IP inter-storey drift ratio, IDR, expressed in percentage, at given infill vertical slenderness, h/t, is calculated by applying the empirical relationship derived in Chapter IV and reported in Equation 6.

$$R(IDR) = \frac{F_{Rd}(IDR| h/t)}{F_{Rd}(IDR = 0)} = \min(1; [1.21 - 0.05\min(20.4; h/t)](IDR)^{-0.89}) \qquad (6)$$

The seismic demand on infills is obtained by multiplying the demand PSA for the infill participating mass to the first OOP vibration mode, equal, also in this case, to the 66% of the infill total mass. Equation 3 proposed by EC8 does not account for the effects of the non-linear behaviour of the primary structure on floor acceleration demands while at LS the RC structure is supposed to have already exhibited a significant non-linearity (Vukobratović and Fajfar, 2016). Also for this reason, Equation 3 generally overestimates floor accelerations, especially for high structures, as observed by different authors (Pinkawa et al., 2014, Petrone et al., 2015). For this reason, within the RA, the OOP acceleration demand will be calculated by using the floor spectra proposed for inelastic MDOF by Vukobratović and Fajfar (2017). Vukobratović and Fajfar formulation of the PSA demand differs from EC8 proposal mainly for two aspects.

First, it accounts for the effects of higher vibration modes, which are neglected in

EC8 formulation: for this reason, for a given PGA – for example, 1 g - the acceleration demand may be not be monotonically increasing along the building height as shown in Figure 7.2a for a 6-storey case study-building. Second, it accounts for the inelastic structural behaviour due to the excitation of the first vibration mode using the PSA reduction factor R_μ, which in this work is obtained from the SPO2IDA tool (Vamvatsikos and Cornell, 2006). For this reason, for a given floor, the acceleration demand grows up with decreasing rate as PGA increases, as shown for the last storey of a 6-storey case-study building in Figure 7.2b.

The ductility of the non-structural element is considered by assigning to it an equivalent damping ratio, i.e., directly when calculating the PSA demand. For this reason, the force acting on infills is calculated without the application *a posteriori* of a behaviour factor. According to Vukobratović and Fajfar (2017), such equivalent damping ratio is fixed to 10%, which is appropriate for non-structural elements with expected ductility demand equal to 1.5 (i.e., with ductility capacity at least equal to 1.5) and with 1% damping ratio, while it is conservative for non-structural elements at higher ductility demand and with higher damping ratio. It is worth to mention that in Chapter IV it is shown that for both IP-undamaged and IP-damaged (up to moderate-high IDR levels) URM infills the ductility capacity is compatible with this value of minimum ductility capacity.

(a)   (b)
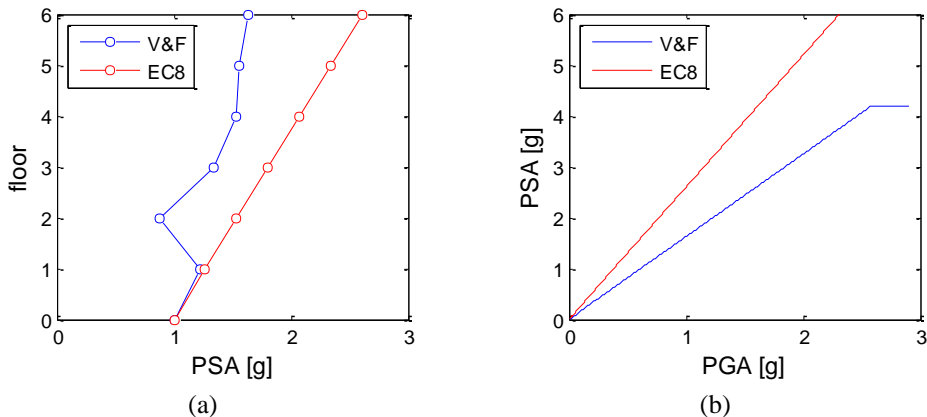
Figure 7.2. Floor distribution of demand acceleration for given PGA equal to 1.00 g (a) and PSA evolution at increasing PGA for the last storey (b) of a 6-storey case-study building obtained by applying Vukobratovic and Fajfar's and Eurocode 8's floor spectrum.

For simplicity, the procedure is described with reference to a 4-storey building.

i.   For each infill layout, the OOP strength, F_{Rd}, is calculated by applying Dawe and Seah's model (for WL) or Eurocode 6 formulation (for SL).

ii.   For each case-study infilled building, a static pushover (SPO) analysis is performed in the IP direction to obtain a base shear (V_b) vs roof displacement (Δ_{TOP}) curve. The loading path used to carry out SPO analyses is proportional to the force distribution along the frame height associated with the first vibration mode in the considered IP direction.

iii.   The SPO V_b-Δ_{TOP} curve is then multi-linearized according to the piecewise procedure described for elastic-hardening-negative systems in De Luca et al. (2013). Note that the application of the above procedure results in an effective fundamental period assigned to each case-study building equal to its elastic fundamental vibration period.

iv.   For each case-study building, the 50th percentile IDA curve is associated with each SPO curve by applying the SPO2IDA tool. This allows defining an elastic PSA vs Δ curve. The introduction of each elastic PSA in the EC8 Type I spectrum allows passing from elastic PSA to elastic PGA vs Δ curve. Using the SPO analysis results, to each Δ it is possible to associate the IDR for each storey and to define PGA vs IDR curves for each storey (Figure 7.3).

v.   To each IDR demand, for each storey, it is possible to associate the degraded strength of the infills at that storey, by means of Equation 7, and trace a PSA_c vs PGA_{IP} curve (Figure 7.3).

vi.   It is assumed that the PGA acting in the OOP direction is equal to the PGA acting in the IP direction: this assumption is discussed in the following. For each PGA_{OOP} value the PSA demand in the OOP direction is calculated by means of Vukobratović and Fajfar floor spectrum and demand PSA vs PGA_{OOP} curves for each storey can be defined (Figure 7.4a).

vii.   The set of PSA_c-vs-PGA_{IP} curves and the set of demand PSA-vs-PGA_{OOP} curves intersect at various values of PGA. The lowest of such PGAs is the PGA_c accounting for the IP/OOP interaction ($PGA_{c,W/}$ in Figure 7.4b). In addition, the set of demand PSA-vs-PGA_{OOP} curves intersect the vertical line representative of the undamaged PSA_c value at various values of PGA. The lowest of such PGAs is the PGA_c accounting for the IP/OOP interaction ($PGA_{c,W/O}$ in Figure 7.4b). For each case-study infilled building and for each infill layout the

effective PGA$_c$ is the minimum between the one calculated assuming X and Z as the IP direction, clearly. The IDR distribution associated with PGA$_c$ is the collapse IDR distribution assessed by accounting for IP/OOP interaction.

Let us call PSA$_X$ and PSA$_Z$ the PSA associated with the ground motion acting along the X and Z direction, respectively. Current building codes, such as EC8, suggest combining the effects of multidirectional ground motions by means of a linear simplification of the Square Root of Sum of Squares (SRSS) rule by applying the so-called 30% rule, independently on the value of the PSA$_X$/PSA$_Z$ ratio (Menun and Der Kiureghian, 1998), for which no indication is provided. As previously stated, an equal intensity for the seismic excitation acting along the two horizontal directions, X and Z, is assumed in this study. In absence of specific provisions given by technical standards, this conservative assumption is consistent with a code-based approach and with the suggestion provided by Wilson et al. (1995), recalled by Menun and Der Kiureghian.

Note that, for simplicity, the effects of OOP actions on the IP response of infills that are neglected. This approach, given the overestimation of the infilled structure stiffness, leads to a non-conservative underestimation of the infills IP displacement and, so, of their OOP capacity reduction due to interaction. For the same reason, the infill OOP stiffness reduction due to IP actions is neglected as well as the consequent T$_a$ elongation and the presence of openings.
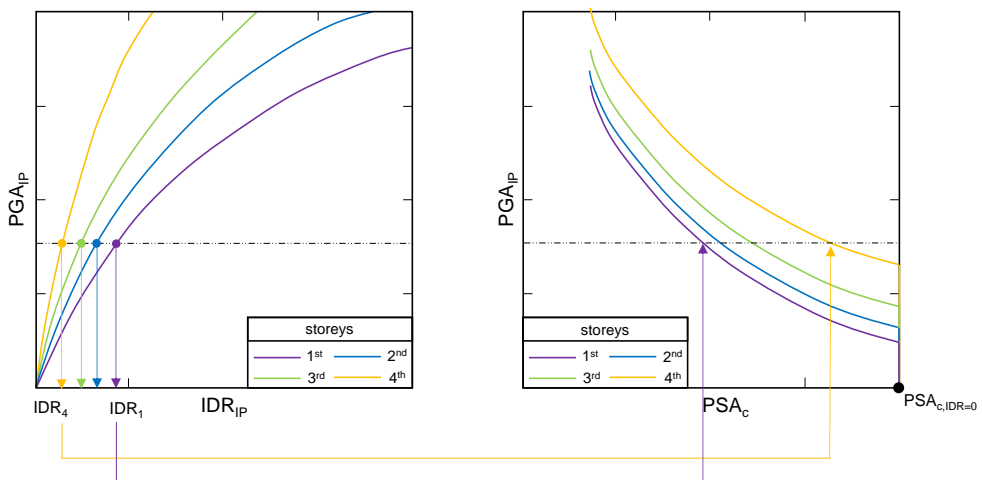
Figure 7.3. Reference approach schematic representation: definition of IP displacement demand as a function of the IP PGA and definition of the degraded OOP strength of infills corresponding to that IP PGA.

(a)   (b)
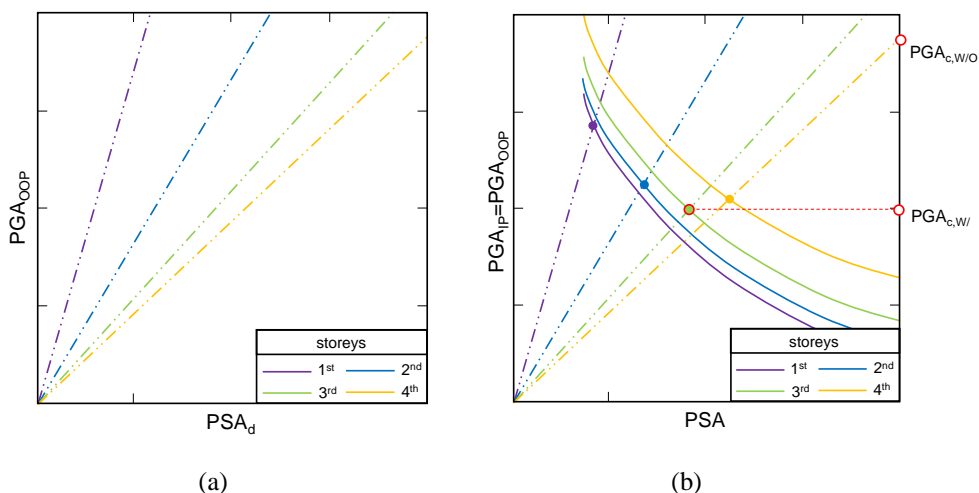
Figure 7.4. Reference approach schematic representation: definition of OOP demand (a) and matching of OOP capacity and demand (b).

7.3. MODELLING OF THE CASE-STUDY BUILDINGS

In order to apply the RA described in section 2.2, the RC elements non-linearity is modelled using a tri-linear moment-chord rotation backbone provided of the cracking point and perfectly plastic after yielding point. These points are determined using a section analysis and by applying the dispositions about yielding chord rotation given by the Annex A of EC8, part 3 (2005).

The dynamic properties of the case-study bare frames are reported in Table 6.3 in Chapter VI. For instance, the design fundamental periods assessed for the structural models with halved inertia primary elements, which enter EC8 formulation for floor acceleration spectra, are reported for bare frames. The elastic fundamental periods, which enter Vukobratović and Fajfar formulation for floor acceleration spectra, are presented for the infilled frames in Table 7.1.

Table 7.1. Elastic fundamental periods in the X and Z global directions of the case-study infilled buildings.

design PGA	Number of storeys of the infilled buildings							
	2		4		6		8	
WL	$T_{1,z}$ [s]	$T_{1,x}$ [s]	$T_{1,z}$ [s]	$T_{1,x}$ [s]	$T_{1,z}$ [s]	$T_{1,x}$ [s]	$T_{1,z}$ [s]	$T_{1,x}$ [s]
0.05 g	0.107	0.085	0.222	0.181	0.298	0.242	0.414	0.329
0.15 g	0.107	0.085	0.219	0.177	0.293	0.240	0.408	0.326
0.25 g	0.107	0.085	0.210	0.178	0.277	0.231	0.386	0.315
0.35 g	0.104	0.083	0.209	0.176	0.277	0.231	0.384	0.318
SL								
0.05 g	0.103	0.085	0.215	0.173	0.293	0.233	0.407	0.317
0.15 g	0.103	0.085	0.211	0.172	0.289	0.231	0.401	0.315
0.25 g	0.103	0.085	0.206	0.169	0.275	0.224	0.383	0.309
0.35 g	0.102	0.084	0.205	0.168	0.272	0.226	0.381	0.306

As previously stated, two infill layouts are considered. The first one is constituted by a double-leaf (thickness: 80+120 mm) URM 'weak' infill wall (weak layout, WL), the second one is constituted by a one-leaf (thickness: 300 mm) URM 'strong' infill wall (strong layout, SL). The mechanical properties of these infills are those calculated for the masonry wallets tested by Calvi and Bolognini (2001) for the WL and those by Guidi et al. (2013) for the SL (Table 7.2). Note that the value of the masonry shear strength of Guidi et al.'s specimen was not provided by the Authors and so was set to 0.30 N/mm^2 according to Table 3.4 of EC6.

Table 7.2. Geometric and mechanical properties of all infill layouts.

property	symbol	units			
leaf thickness	t	[mm]	80	120	300
height	h	[mm]	3000	3000	3000
width	w	[mm]	4500	4500	4500
slenderness ratio	h/t	[-]	37.5	25	10
total mass	m_{tot}	[kg]	864	1296	3240
shear modulus	G	[N/mm^2]	1039	1039	788
shear strength	τ_{cr}	[N/mm^2]	0.15	0.15	0.30
vertical direction					
compressive strength	f_{mv}	[N/mm^2]	1.10	1.10	6.00
elastic modulus	E_{mv}	[N/mm^2]	1873	1873	4312
horizontal direction					
compressive strength	f_{mh}	[N/mm^2]	1.11	1.11	1.19
elastic modulus	E_{mh}	[N/mm^2]	991	991	1767

Each infill wall was introduced in the structural model using a single equivalent strut whose non-linear behaviour is modelled based on Panagiotakos and Fardis (1996) proposal. According to this modelling approach, the slope of the softening branch of the force-displacement IP behavior relationship is a fraction α of the infill initial elastic stiffness, while the infill residual strength is herein set to zero. In Fardis (1996) it is suggested to set α to a value between -1.5% and -5%. For the WL and SL leaves, an α value equal to -1.6% and -3.6%, respectively, is assumed. Such values lead to predictions of the softening stiffness and ultimate IP displacement in good accordance with the experimental evidences shown by Calvi and Bolognini (specimen 2) for α=-1.6% and by Guidi et al. (specimen URM-U) for α=-3.6%. The IP behaviour characteristic points are reported in Table 7.3.

In the following, each case-study building is identified using an acronym, such as *XPY*, in which *X* is the number of storeys and *Y* the design PGA at LS expressed in g/100.

Table 7.3. Infills' IP behaviour characteristic points.

property	symbol	units			
leaf thickness	t	[mm]	80	120	300
cracking force	F_{crack}	[kN]	54.0	81.0	405
initial stiffness	K_{crack}	[kN/mm]	125	187	355
cracking displ.	d_{crack}	[mm]	0.43	0.43	1.14
cracking IDR	IDR_{crack}	[%]	0.014	0.014	0.038
maximum force	F_{max}	[kN]	70.0	105	526
secant stiffness at max.	K_{max}	[kN/mm]	7.66	11.0	42.4
displ. at maximum	d_{max}	[mm]	9.16	9.54	12.4
IDR at maximum	IDR_{max}	[%]	0.30	0.32	0.41
collapse displacement	d_u	[mm]	44.3	44.7	53.7
collapse IDR	IDR_u	[%]	1.48	1.49	1.79

7.4. APPLICATION OF DA AND RA PROCEDURES

7.4.1. Designer Approach (DA) application and results

In this section, the results of the application of the procedure reported in section 7.2.1 are presented and described. The OOP infills' properties are reported in Table 7.4.

Table 7.4. OOP infill properties for all layouts used for DA application.

property	symbol	units			
leaf thickness	t	[mm]	80	120	300
OOP strength	F_{Rd}	[kN]	10.6	23.8	810
PSA capacity	PSA_c	[g]	3.70	5.56	75.8[*]
OOP period	T_a	[s]	0.14	0.09	0.02

*: Result of the simple comparison of Equations 1 and 4, clearly without any physical acceptable meaning.

First, clearly, for given design PGA and number of storeys, a greater PGA_c is expected for SL, than for WL, due to the different OOP strength associated with them.

If the IP/OOP interaction is neglected, as in this case, the first OOP infill collapse is always expected at the last storey. In fact, Equation 5 proposed by EC8 predicts acceleration demands that monotonically grow up with the height of the barycenter of the considered non-structural element above the building base. This also means that, for our present purpose, the z/H ratio is fixed for all the case-study buildings with the same

number of storeys and that the PGA_c associated with them varies only due to the variation of the infill layout and of the T_a/T_1 ratio. Equation 5 returns acceleration demands that, for a given z/H, grows up with the T_a/T_1 ratio. So, for a given infill layout and for a given number of storeys of the considered building, PGA_c decreases for increasing T_a/T_1 ratios, i.e., for increasing stiffness of the case-study bare frames. For this reason, the lower PGA_c is expected and registered for infills built along the Z direction, i.e., subjected to the OOP acceleration in the X direction, which is the buildings' stiffer direction. However, as shown in Figure 7.5, the PGA_c in the two directions are very similar, with $PGA_{c,X}$ slightly lower than $PGA_{c,Z}$.
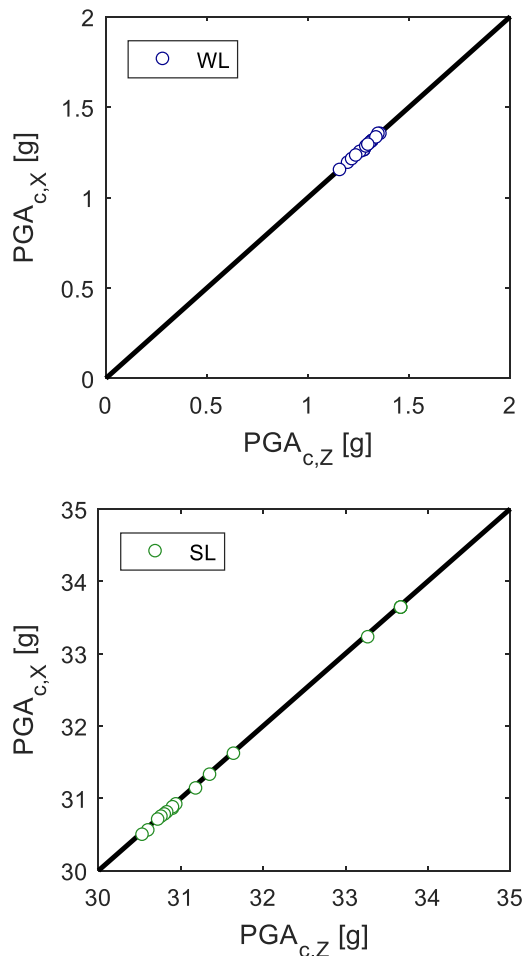
Figure 7.5. Comparison of the OOP PGA_c in X and Z directions for all case-study buildings obtained by applying the DA.

It is observed that the PGA capacity for SL infills is very much higher than that calculated for WL infills. This occurs because the OOP strength of SL infills is very much higher than that of WL infills, as reported in Table 7.4: this circumstance fully neutralize the opposite effect on the assessment of the PGA capacity given by a potential higher OOP force demand acting on the stiffer and heavier infills, such as SL infills, with respect to less stiff and heavy infills, such as WL infills.

So, in all cases, $PGA_{c,X}$ is the PGA_c of the case-study buildings. Moreover, a greater stiffness is expected for buildings designed for a greater PGA. For this reason, for a given infill layout and for a given number of storeys, PGA_c is expected to decrease for increasing design PGA (Figure 7.6).
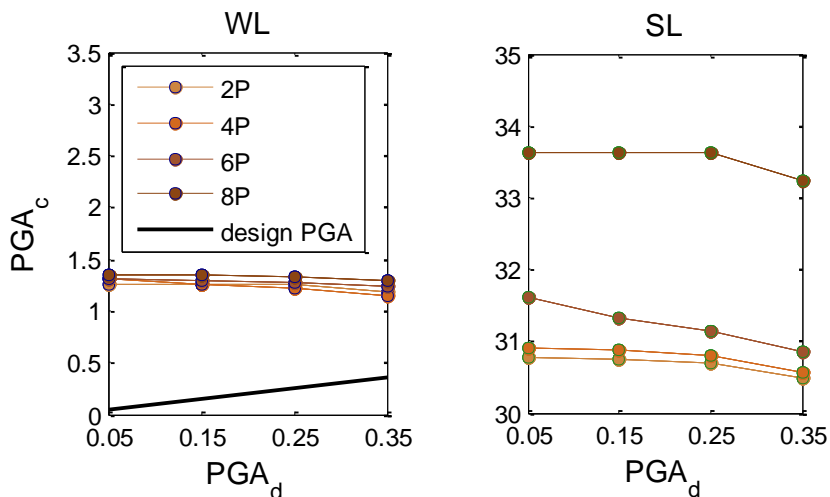
Figure 7.6. Comparison of the OOP PGA_c for all case-study buildings obtained by applying the DA. Effect of the design PGA.

It is observed, from Figure 7.6, that using DA always returns PGAs associated with the first OOP collapse of infills greater than the design PGA at LS. In other words, the DA usually makes the practitioner sure that the safety check of infills with respect to the OOP collapse is satisfied for common infill layouts with a demand-over-capacity ratio at most equal to around 0.30.

Moreover, for a given infill layout, i.e., for a given T_a, a lower T_1 is expected for buildings with a lower number of storeys, so a lower PGA_c is expected for lower case-study buildings (Figure 7.7).
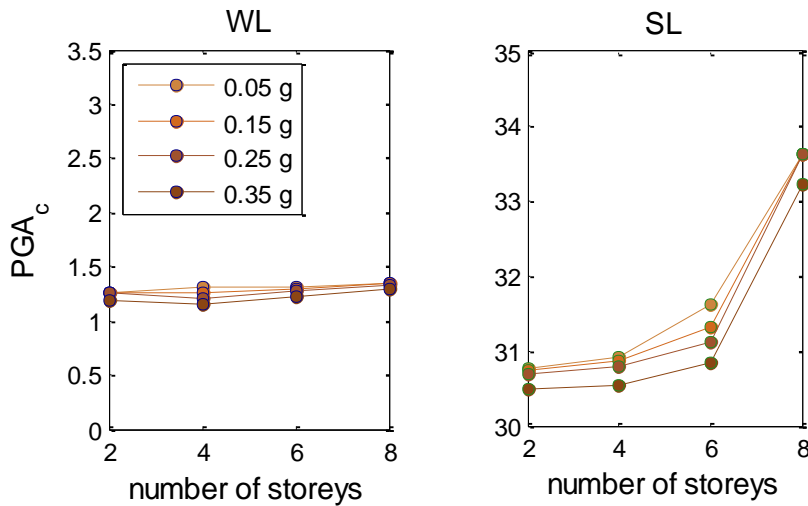
Figure 7.7. Comparison of the OOP PGA_c for all case-study buildings obtained by applying the DA. Effect of the number of storeys.

However, these are not general rules, because some T_a/T_1-z/H combinations can result in lower PGA_c values assessed for higher buildings. For example, building 2P35 with WL infills has greater PGA_c than building 4P35 with the same infills. In the first case, T_a/T_1=0.42 and z/H=0.750, while in the second case T_a/T_1=0.36 and z/H=0.875. As shown in Figure 7.8, for such T_a/T_1-z/H combination, PGA_c is expected to be lower for 4P35 building.
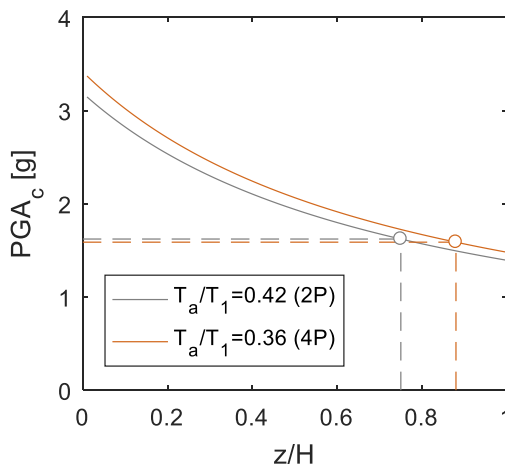
Figure 7.8. PGA_c variation with z/H for fixed T_a/T_1 ratios.

7.4.2. Reference Approach (RA) application and results

In this section, the results of the application of the procedure reported in section 7.2.2. are presented and described. The OOP infills' properties are reported in Table 7.5.

Table 7.5. OOP infill properties for all layouts used for RA application.

property	symbol	units			
leaf thickness	t	[mm]	80	120	300
OOP strength	F_{Rd}	[kN]	14.7	38.5	688
PSA capacity	PSA_c	[g]	3.58	5.23	32.8[*]
OOP period	T_a	[s]	0.14	0.09	0.02

[*]: Ratio of the OOP strength over the 66% of the infill weight, clearly without any physical acceptable meaning.

Note that the application of the RA yields to OOP strength values greater than those calculated by means of the Eurocode 6 formulation (in its original form) applied within the DA in the case of thin leaves. Mainly, this is due to the fact that Dawe and Seah's model accounts for two-way arching, while Eurocode 6 formulation accounts only for vertical arching. However, the strength obtained for the thick leaf is lower than that used for the application of the DA. This occurs because the strength model used for DA and RA is the same, but in the application of the RA the formulation by Eurocode 6 is modified to be adapted to the seismic loading condition. In addition, note that being the 80 mm- and 120 mm-thick leaves' strength greater than that obtained by applying Eurocode 6 model, the lower PGA_c obtained for them by applying the RA are only due to the different approach used in determining it, above all for the fact that in the RA the IP/OOP interaction is considered.

First, for a given design PGA and number of storeys, a greater PGA_c is expected for SL than for WL, due to the different OOP "undamaged" strength associated with them.

If the IP/OOP interaction is considered, the first OOP collapse is not expected at the last storey, given that the maximum strength degradation occurs at low-intermediate storeys, where the maximum IDR demand is expected. Moreover, for equal PGA applied in the X and Z direction, greater IDRs are expected in the less stiff direction, which is the Z direction for all the case-buildings. This means that the first OOP collapse is expected for infills built along the Z direction, i.e., for infills subjected to the OOP action in X direction. As shown in Figure 7.9, for each case-study building $PGA_{c,X}$ is lower than $PGA_{c,Z}$ and, for this reason, is assumed as PGA_c of the entire building.

Due to the IP/OOP interaction, the first infill OOP collapse is observed in the lower

part of the building, generally below the building mid-height, along the building less stiff direction, as shown in Figure 7.10. In Figure 7.10 it is also observed that the storey associated with the first OOP collapse tends to pass, in the 8-storey buildings, from the third (WL) to the fifth (SL), most likely due to significant changes in the inelastic displacement shapes and collapse mechanism of such buildings at increasing strength and stiffness of the infills.
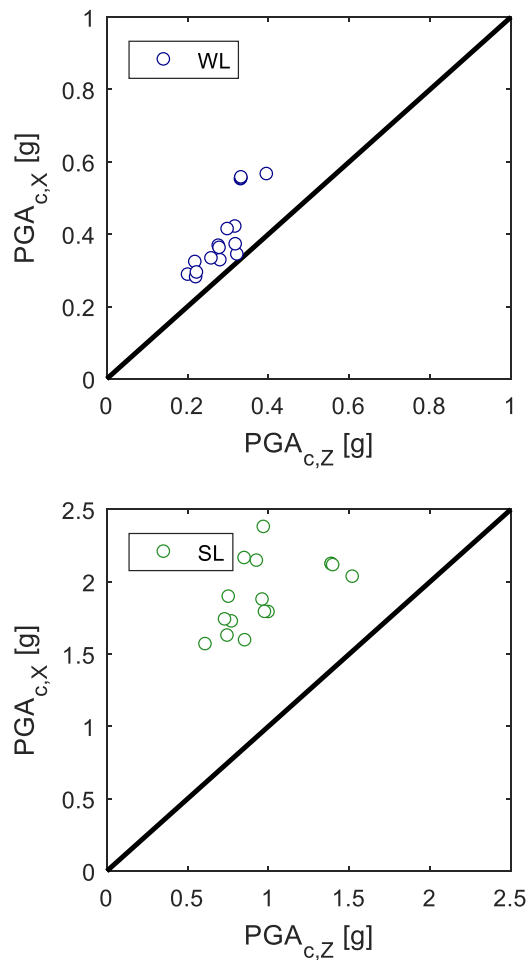
Figure 7.9. Comparison of the OOP PGA_c in X and Z directions for all case-study buildings obtained by applying the RA.
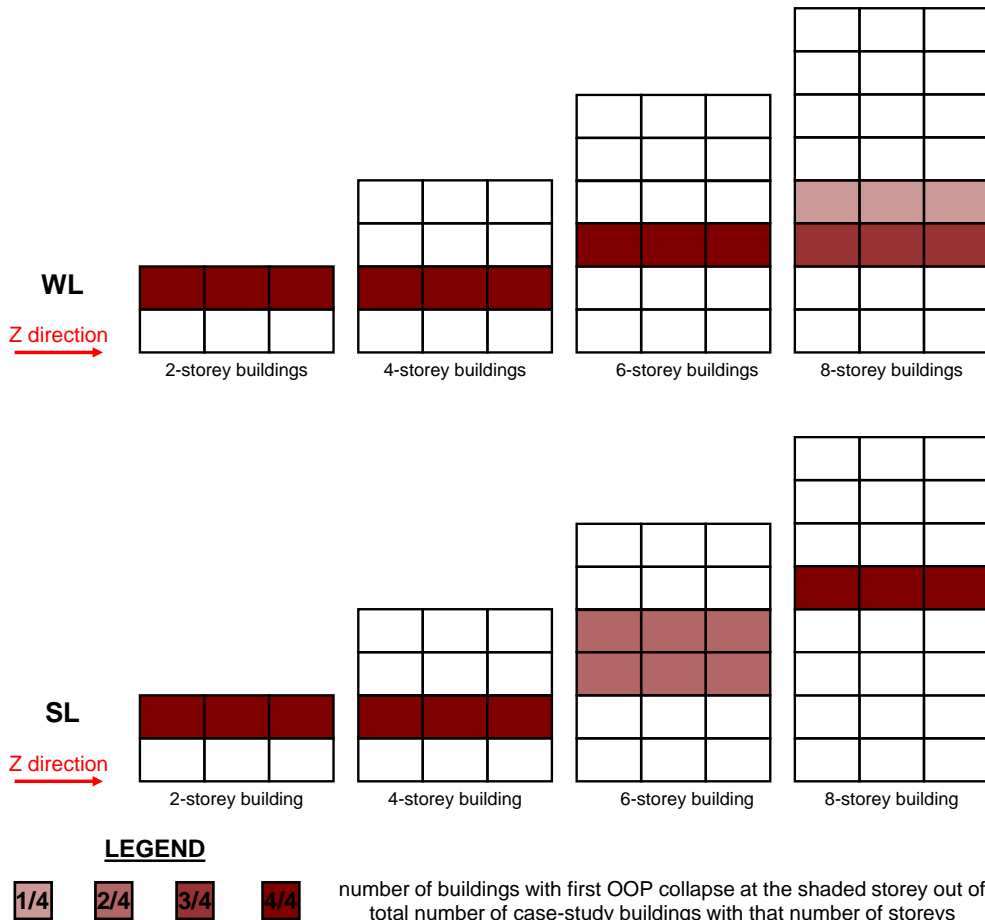
Figure 7.10. Frequency distribution for the floor at which the first OOP collapse occurs for all case-study buildings by accounting for the IP/OOP interaction.

The parameters that define the OOP demand according to EC8, z/H and T_a/T_1, also enter Vukobratović and Fajfar's floor spectrum, even if in a more complex and elaborated formulation. So, for simplicity, let us explain some trends observed for PGA_c variation among the case-study buildings with direct reference to those parameters.

First, consider that, as shown in Figure 7.10, the first OOP collapse storey, i.e., the z/H ratio, is fixed, *de facto*, for all the case-study buildings with the same number of storeys.

Due to IP/OOP interaction, the PGA_c associated with them varies only due to the variation of the IDR demand distribution, which depends on the lateral deformability of

the structure, and of the T_a/T_1 ratio. First, it is shown in Figure 7.11 that for a given infill layout and design PGA, PGA_c decreases for increasing number of storeys, which is expected given the higher lateral deformability of higher buildings.
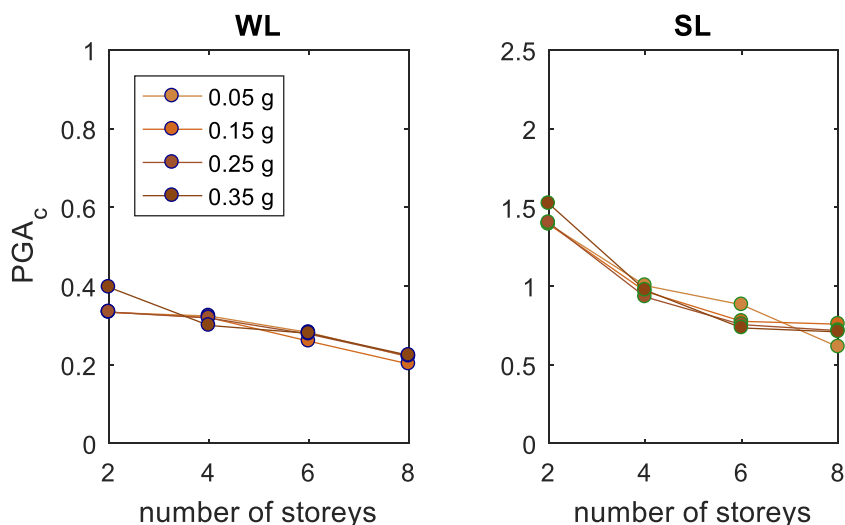
Figure 7.11. Comparison of the OOP PGA_c for all case-study buildings obtained by applying the RA. Effect of the number of storeys.

For a given infill layout, the variability of the T_a/T_1 is extremely limited for different design PGAs, due to the prevalent effect of the infills' stiffness in T_1 definition with respect to the characteristics of the RC structure. For these reasons, for a given infill layout and for a given number of storeys, the PGA_c is almost independent on the design PGA, as shown in Figure 7.12.
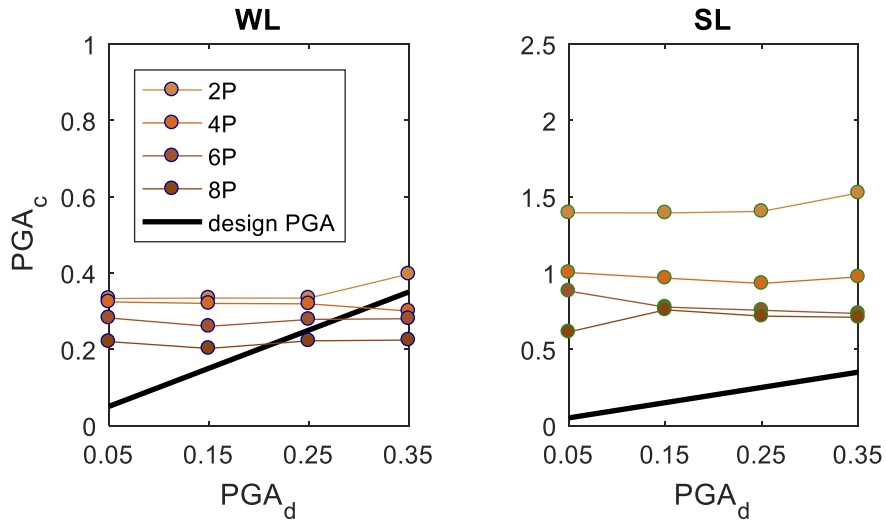
Figure 7.12. Comparison of the OOP PGAc for all case-study buildings obtained by applying the RA. Effect of the design PGA.

According to the RA results, as shown in Figure 12, thin URM infills characterized by low OOP resistance (WL) in mid- and high-rise buildings (from 4 to 8 storey) deigned for mid- and high-seismicity zones (from 0.25 g) can be unsafe with respect to the OOP collapse. This means that, in these cases, the attainment of LS is avoided in terms of structural performance at the design PGA, at which wide OOP collapses of infills are expected, instead.

Moreover, especially for WL, the PGA associated with the first OOP failure ($PGA_{c,OOP}$) can be lower than the PGA associated with the structural failure ($PGA_{c,STR}$) with respect to LS, i.e., the attainment for the first time in an RC element of the structure of a chord rotation demand equal to ¾ of the ultimate chord rotation of the element, as shown in Figure 7.13. This means that the LS can be attained due to non-structural collapse prior than for structural collapse.
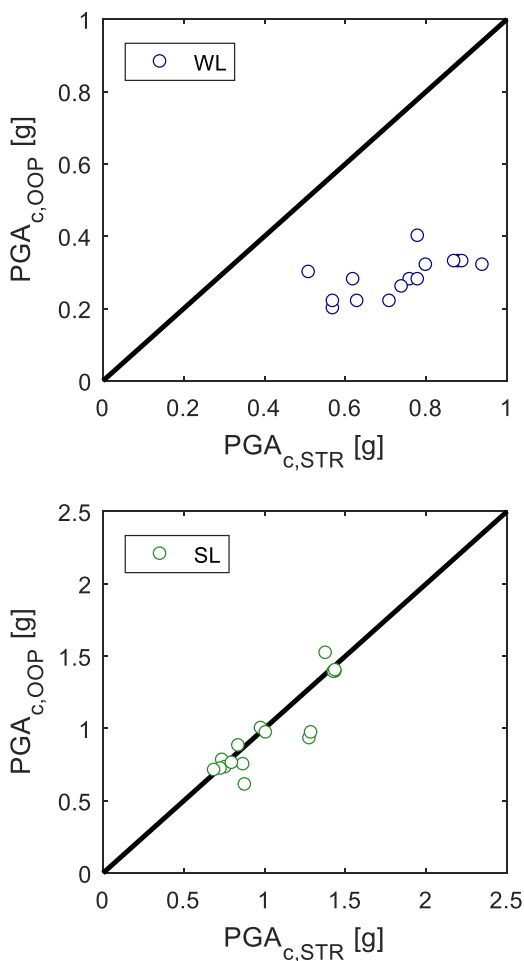
Figure 7.13. Comparison of the PGA_c for all case-study buildings with respect to structural failure and non-structural OOP failure with respect to LS.

OOP collapse due to IP/OOP interaction is expected for a maximum IDR demand in the Z direction equal to, on average, 0.44% for WL. For SL layout, first OOP collapse due to IP/OOP interaction occurs for maximum IDRs ranging between 3% and 6%, which are always greater than IDR_u. This means that the IP collapse always foreruns the OOP collapse. This also means, in the Authors' opinion, that the OOP safety check for SL layout can be neglected, as the attainment of LS due to non-structural failure occurs for IP failure first.

Actually, for a given infill layout, 16 values of IDR corresponding to the first OOP

collapse of infills were obtained, one for each case-study building. Based on these results, fragility curves relating the probability of OOP failure to the IP IDR for each infill layout were obtained and are reported in Figure 7.14.

The reader is strongly recommended to consider such fragility curves only as a concise and immediate summary of the results obtained. Such curves are aimed at highlighting the role of IP damage in promoting the OOP collapse of infills, the importance of IP/OOP interaction phenomena, and the non-negligibility of such phenomena in in assessing the safety with respect to seismic action of URM infills and of RC structures. In fact, in the Author opinion, it is not possible, nor correct, to define a "threshold IDR" at which the OOP collapse can be considered as expected, even in a simplified and code-based framework. As observed in this section, IP/OOP interaction is a complex phenomenon, whose effects are influenced by structural dynamic behaviour and structural and non-structural non-linearity. In order to assess correctly the seismic safety of URM infills, a detailed analysis, accounting for all these effects, is recommended.
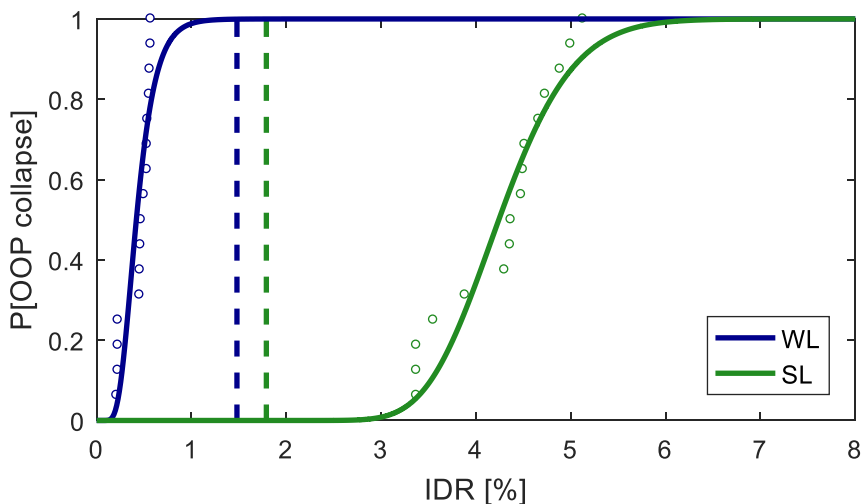
Figure 7.14. Comparison of the fragility curves (continuous lines) in terms of IDR with respect to the attainment of LS for OOP failure of infills of all case-study buildings for different infill layouts. Dashed vertical lines represent the IDR corresponding to the IP collapse of the infill, according to Panagiotakos and Fardis's model.

As expected, a greater fragility with respect to infills' OOP collapse is observed for

WL with respect to SL. Moreover, it is observed that the probability that the OOP collapse occurs for IDR lower than the IP collapse IDR, IDR_u, is around one for WL and around zero for SL. As already stated, this means that the attainment of LS due to non-structural failure occurs for OOP failure of thin/weak infills and for IP failure of thick/strong infills.

Each fragility curve contains in its parameters the variability of IDR_c associated with the variation of the buildings' number of storeys and design PGA. In other words, one can enter such fragility curves only knowing the infill typology and without knowing the building number of storeys and design PGA, i.e., by assuming an equal probability that the considered building is characterized by a number of storeys equal to 2, 4, 6 or 8 and by a design PGA equal to 0.05 g, 0.15 g, 0.25 g and 0.35 g.

7.4.3. Comparison of DA and RA results

In Figure 7.15, a comparison between the PGA_c predicted using the RA and the one obtained from the DA for each case-study building and for each infill layout is reported. As expected, PGA_c is highly overestimated using the DA. The PGA_c for WL obtained using the DA is, on average, 4.5 times the one obtained using the RA, while the PGA_c for SL obtained using the DA is, on average, 35 times the one obtained using the RA.

For a given infill layout, 16 values of PGA corresponding to the first OOP collapse of infills were obtained using both the DA and the RA, one for each case-study building. Based on these results, fragility curves relating the probability of OOP failure to the OOP PGA for each infill layout were obtained separately with reference to DA and RA results. These curves are reported in Figure 7.16. The fragility curve for SL obtained using the DA is not reported, given the high and physically unacceptable values of the assessed collapse PGAs.
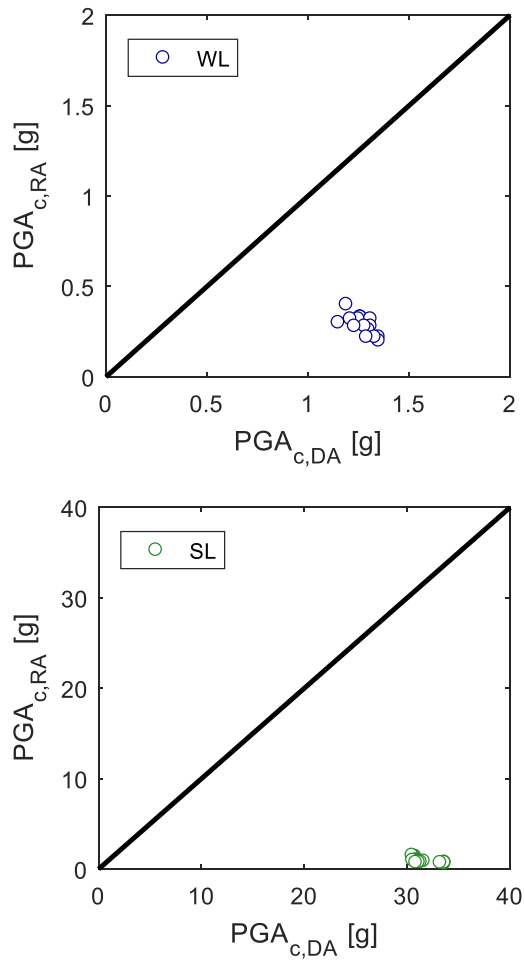
Figure 7.15. Comparison of the OOP PGA_c for all case-study buildings obtained by applying the DA and RA.
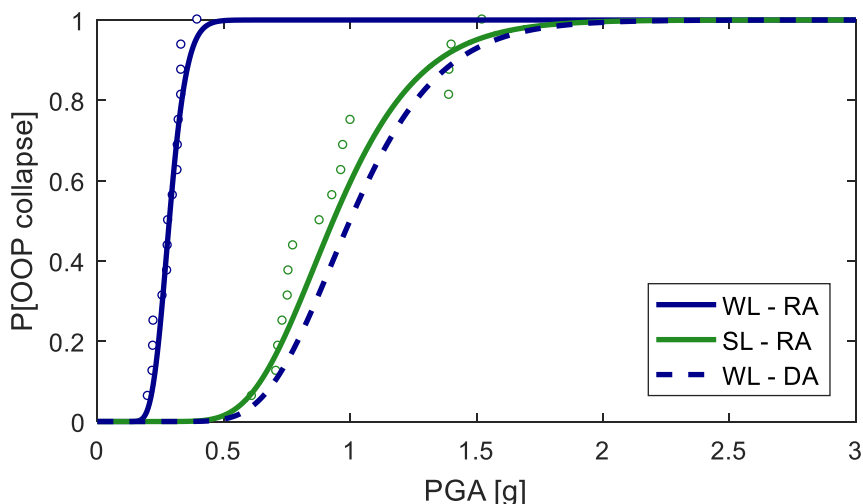
Figure 7.16. Comparison of the fragility curves in terms of PGA, obtained by using the DA and RA, with respect to the attainment of LS for OOP failure of infills of all case-study buildings for different infill layouts.

The median collapse PGA is equal to 0.29 g for WL, to 0.91 g for SL. As expected, a greater fragility with respect to infills' OOP collapse is observed if the RA is applied. A summary of all PGA_c assessed using different approaches is reported in Table 7.6, at the end of next section.

Also in this case, each fragility curve contains in its parameters the variability of PGA_c associated with the variation of the buildings' number of storeys and design PGA. In other words, one can enter such fragility curves only knowing the infill typology and without knowing the building number of storeys and design PGA, i.e., by assuming an equal probability that the considered building is characterized by a number of storeys equal to 2, 4, 6 or 8 and by a design PGA equal to 0.05 g, 0.15 g, 0.25 g and 0.35 g.

7.5. OOP SAFETY CHECK OF INFILLS IN A LINEAR ELASTIC FRAMEWORK

In this section, the PGA_c is assessed by applying an elastic RSA on the bare frame models of all case-study buildings. The OOP acceleration demand on infills is calculated by applying EC8 floor spectrum, while infills' OOP capacity is calculated using Dawe and Seah's model and the strength degradation curve proposed in Equation 6, in which

the IDR resulting from the RSA are introduced. This approach will be called Suggested Designer Approach (SDA). The main aim of this section is evaluating if the simplest and most common design procedure of RC buildings can be used to predict an accurate value of PGA_c if, at least, the IP/OOP interaction is considered. SL infills will be neglected, as it was demonstrated in the previous section that the OOP safety check for them can be omitted.

In this case, a fundamental role is played by the displacement distribution, and the consequent IDR distribution, along the building height resulting from the structural analysis. In fact, the OOP strength reduction factor is calculated based on such IDR distribution.

First, let us investigate this issue: is the elastic distribution of IDRs along the building height appropriate to carry out infills' OOP safety check? Considering that the OOP safety check is not necessary for SL, as shown in the previous section, let us consider the elastic distribution of IDRs along the WL case-study buildings' height obtained by using a RSA with Response Spectrum anchored at the PGA_c evaluated, for each case-study building, using the RA. Moreover, in Figure 7.17 the elastic IDR distribution is compared to the one obtained, at the same PGA value, using the RA.
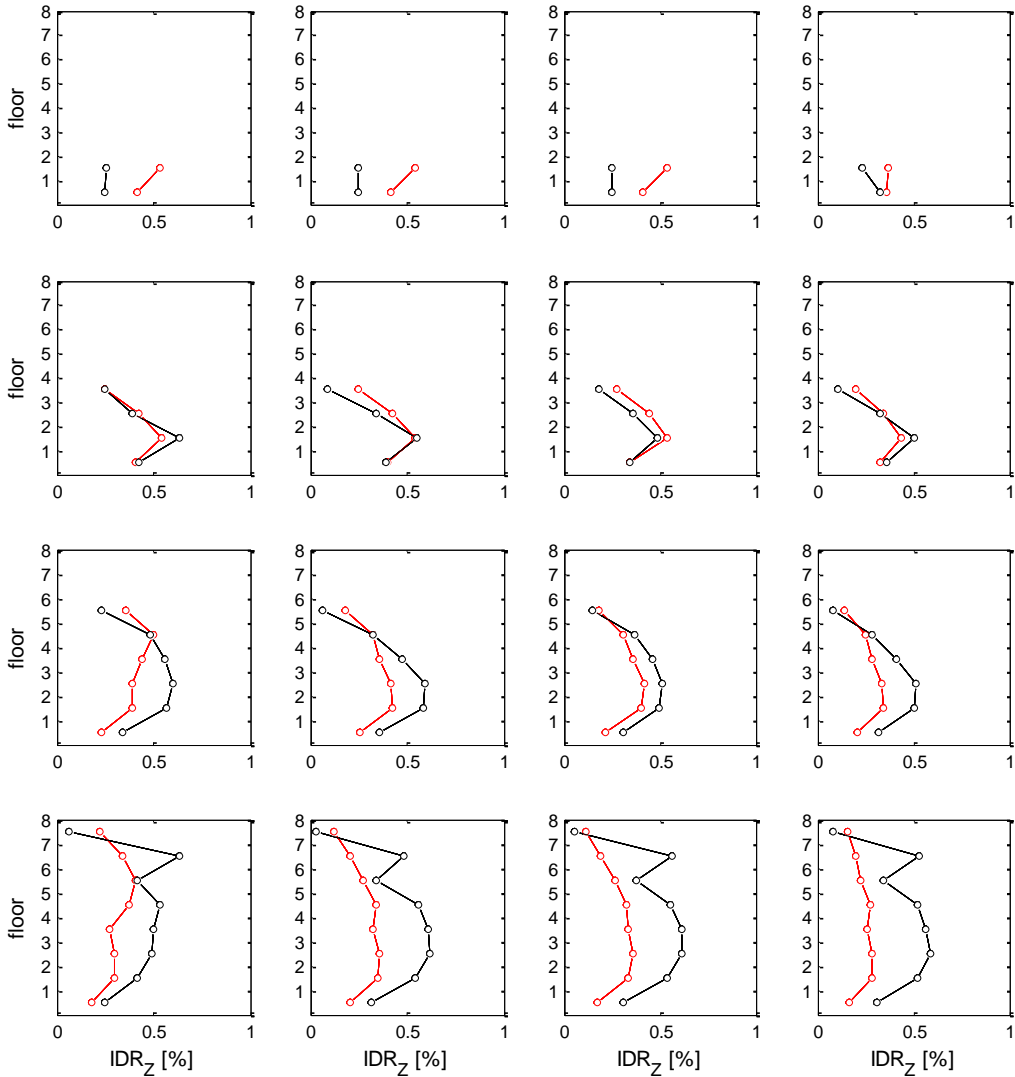
Figure 7.17. IDR distribution in Z direction for all case-study buildings with WL infills obtained by means of RSA (red line) and non-linear static analysis (black line) for $PGA=PGA_{c,RA}$.

As shown in Figure 7.17, for mid- and high-rise buildings, the OOP strength reduction factor is underestimated if it is calculated based on the elastic distribution of IDRs obtained by applying the RSA on bare frame models. This unexpected result is strictly connected to the non-linear response of the infilled frame assessed with the

application of RA. In fact, except for the 2-storey case-study buildings, the top displacement demand at PGA_c is lower for the elastic bare frame model than for the infilled model, due to the non-negligible inelastic demand acting on it at PGA_c, as schematically shown in Figure 7.18.
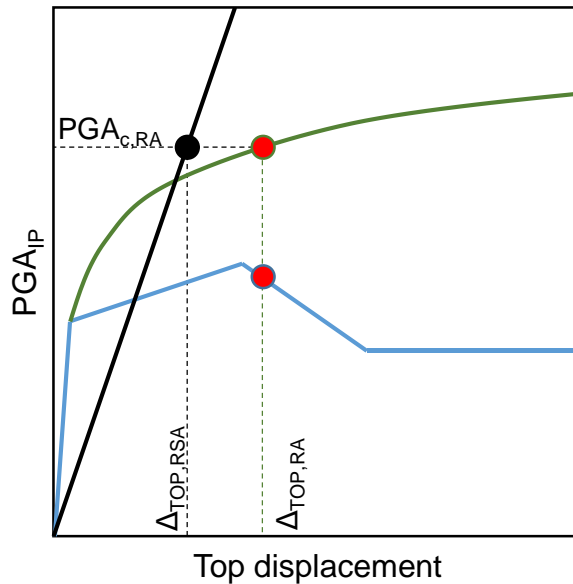
Figure 7.18. Top displacement demand at $PGA=PGA_{c,RA}$ for the infilled and bare frame building. The static pushover of the infilled building is reported in blue, the SPO2IDA for the same building in green. The incremental response of the elastic bare frame is reported in black (schematic representation).

The non-linear IDR distribution cannot be reproduced using elastic analyses on the bare frame models, which are destined to produce predictions of PGA_c, which are herein called $PGA_{c,SDA}$, greater than those obtained using the RA. In other words, a safety-check procedure not accounting for the inelastic response of the structure is not able to produce accurate values of PGA_c, for which the values obtained using the RA are assumed as benchmark in this work. The practitioner should be aware of this circumstance. Considering the observations discussed above, accounting for IP/OOP interaction, even if in a linear-elastic framework, is necessary to not overestimate PGA_c as shown in the comparison of DA and RA results, even if it is not sufficient to obtain an accurate prediction of PGA_c. In fact, such prediction cannot be other than un-conservative as long

as the OOP safety check of infills is carried out in a linear elastic framework.

The values of PGA_c obtained by using the SDA for WL are compared to those obtained by means of DA and RA in Figure 7.19.
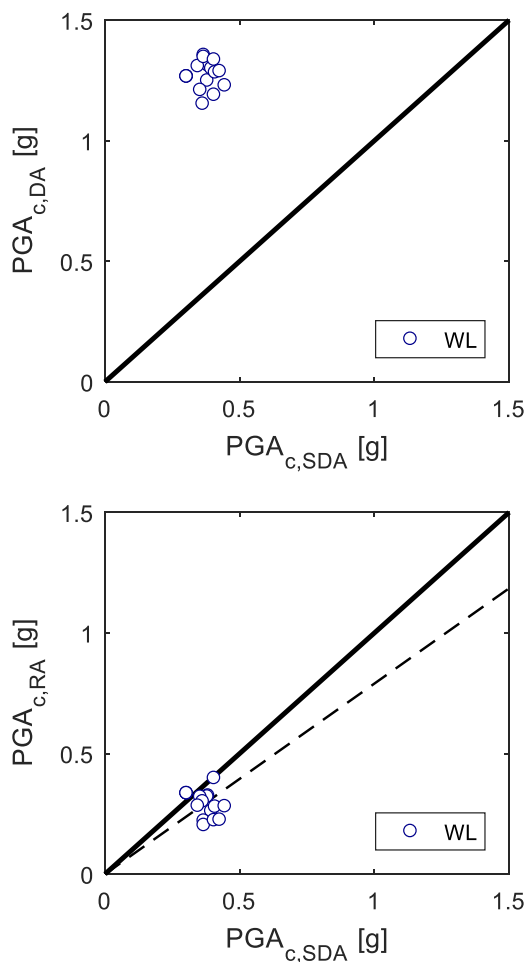
Figure 7.19. Comparison of the OOP PGA_c for all case-study buildings obtained by applying the DA, RA and SDA.

As already stated, accounting for IP/OOP interaction produces a reduction of PGA_c with respect to those predicted using the DA. However, PGA_c assessed using the SDA are generally greater than the benchmark ones assessed using the RA: the ratio between the $PGA_{c,RA}$ and the $PGA_{c,SDA}$ for each case-study building ranges from 0.52 and 1.1

and is equal, on average, to 0.79.

In Table 7.6, the PGA_c assessed using the Designer Approach, the Reference Approach and the Suggested Designer Approach are reported for all case-study buildings.

Table 7.6. PGA at first OOP infill collapse for all case-study buildings assessed by means of the Designer Approach (DA), Reference Approach (RA) and Suggested Designer Approach (SDA).

	First OOP collapse PGA [g]				
	WL			SL	
case-study building	DA	RA	SDA	DA	RA
2P05	1.265	0.333	0.305	30.8	1.359
2P15	1.265	0.334	0.304	30.7	1.358
2P25	1.265	0.334	0.304	30.7	1.367
2P35	1.189	0.397	0.406	30.5	1.411
4P05	1.311	0.324	0.384	30.9	1.234
4P15	1.248	0.320	0.381	30.9	1.278
4P25	1.209	0.319	0.355	30.8	1.273
4P35	1.152	0.300	0.364	30.6	1.291
6P05	1.308	0.282	0.346	31.6	1.253
6P15	1.298	0.260	0.396	31.3	1.250
6P25	1.282	0.278	0.410	31.1	1.276
6P35	1.228	0.280	0.446	30.8	1.228
8P05	1.354	0.220	0.368	33.6	1.135
8P15	1.346	0.202	0.368	33.6	1.177
8P25	1.335	0.222	0.406	33.6	1.210
8P35	1.287	0.224	0.427	33.2	1.190

7.6. WHEN IS THE OOP SAFETY CHECK OF INFILLS NECESSARY?

As shown in section 7.4, SL infills, which are characterized by high compressive strength of masonry and low slenderness ratio of the panel, are expected to collapse for IP failure prior to the OOP failure. Let us call $PGA_{c,OOP}$ the PGA corresponding to the first OOP collapse and $PGA_{c,IP}$ the PGA corresponding to the first IP collapse, both calculated in a non-linear static framework.

The main aim of this section is defining, for each case-study building, a sort of "limit state" surface that can be used to know *a priori*, based only on the values of h/t and f_m, if each leaf of the infill walls of the building must be verified against the OOP collapse ($PGA_{c,OOP}/PGA_{c,IP}<1$) or if the IP collapse foreruns the OOP collapse

(PGA$_{c,OOP}$/PGA$_{c,IP}$>1) and, so, the OOP safety check is not necessary, as the attainment of LS due to non-structural failure occurs for IP failure of infills.

In this section, the application of the RA is carried out on all case-study buildings considering 42 different infill layouts generated by combining 7 different values of slenderness ratio (10, 12, 15, 20, 25, 30, 37.5) and 6 different values of masonry compressive strength in the vertical direction (1, 2, 3, 4, 5 and 6 N/mm^2). Among the 42 layout considered, 6 are associated with a single-leaf panel (h/t=10) while the others are constituted by a two-leaf panel constituted by a leaf with h/t equal to 12, 15, 20, 25, 30 or 37.5 plus a second leaf with slenderness equal to 37.5. For the double-leaf layouts, both leaves are provided of identical mechanical properties and the OOP strength is calculated by means of Dawe and Seah's model, while for single-leaf layouts the OOP strength is calculated by means of Eurocode 6 formulation adapted to the seismic loading condition.

Infill walls were IP-modelled by applying Panagiotakos and Fardis's model. Some assumptions have been made to define the IP and OOP behaviour of each infill layout.

i. Based on Calvi and Bolognini and Guidi et al. experimental values of the compressive strength in the horizontal direction, which is equal to around 1 N/mm^2 for both Authors, independently on masonry compressive strength in the vertical direction, the same value was adopted for all infill layouts considered in this section;

ii. The elastic modulus of masonry in both horizontal and vertical direction has been calculated as 1000 times the masonry compressive strength in that direction, based on EC6 relationship proposed in section 3.7.2;

iii. The shear modulus of masonry has been assumed as equal to 0.4 times the elastic modulus calculated for the horizontal direction, in accordance with EC6 recommendation reported in section 3.7.3;

iv. Masonry tensile strength has been determined as a function of masonry vertical compressive strength by means of the linear interpolation of the τ_{cr}-f$_m$ couples defined for Calvi and Bolognini and for Guidi et al.;

v. For the definition of the IP backbone, the softening stiffness ratio, p, has been determined as a function of the panel slenderness by means of a linear interpolation of the p-h/t couples defined for Calvi and Bolognini and for Guidi et al..

For each case-study building, the $PGA_{c,OOP}/PGA_{c,IP}$ ratio has been calculated for all 42 infill layouts. As shown in Figure 7.20, the surface obtained by a linear least-square regression in the logarithmic space relating the considered h/t-f_m couples to the value of the $PGA_{c,OOP}/PGA_{c,IP}$ ratio can be represented in the h/t-f_m-$PGA_{c,OOP}/PGA_{c,IP}$ space. The intersection of this surface with the $PGA_{c,OOP}/PGA_{c,IP}$=1 plan is a curve whose projection on the h/t-f_m plan represents the "limit state" curve separating the h/t-f_m couples for which the IP collapse foreruns the OOP collapse from those for which the OOP collapse foreruns the IP collapse.
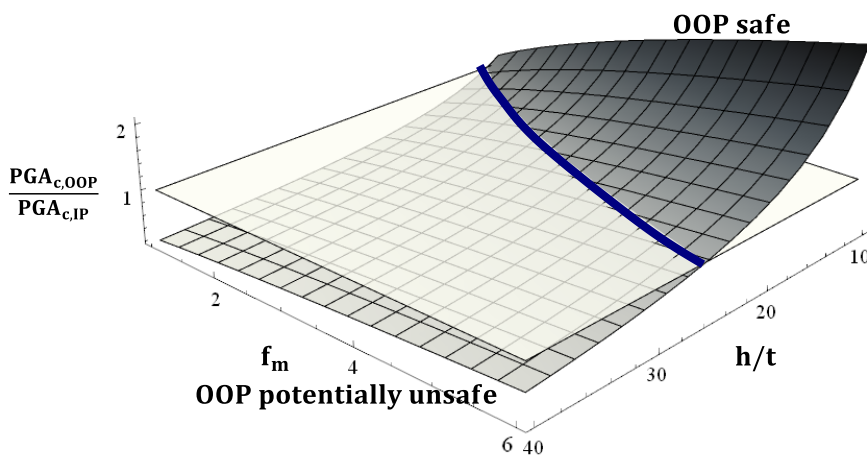
Figure 7.20. Conceptual example of predicted $PGA_{c,OOP}/PGA_{c,IP}$ ratio surface (dark grey) with limit state curve (blue) separating the h/t-f_m couples for which the IP collapse foreruns the OOP collapse from those for which the OOP collapse foreruns the IP collapse.

In Figures 7.21-7.24, for each case-study building, the results of these calculations are reported in the h/t-f_m plan. Each h/t-f_m couple is represented by a point whose color indicates a specific condition:

- Blue points are associated with h/t-f_m couples for which $PGA_{c,OOP}<PGA_{c,IP}$;
- Green points represent h/t-fm couples with $PGA_{c,OOP}>PGA_{c,IP}$ and $PGA_{c,OOP}$ greater than the design PGA at LS, i.e., h/t-f_m couples for which the OOP safety check is necessary but likely to be satisfied;
- Red points represent couples for which the OOP safety check is not satisfied, as $PGA_{c,OOP}$ is lower than the design PGA at LS.

For each case-study building, the "limit state" curve is represented in the h/t-f_m curve in blue. In addition, the curve corresponding to the intersection of the $PGA_{c,OOP}$/design PGA surface with the $PGA_{c,OOP}$/design PGA=1 plan is reported in dark red. Such curve separates h/t-f_m couples for which the OOP safety check is satisfied from those for which the OOP safety check is not satisfied.
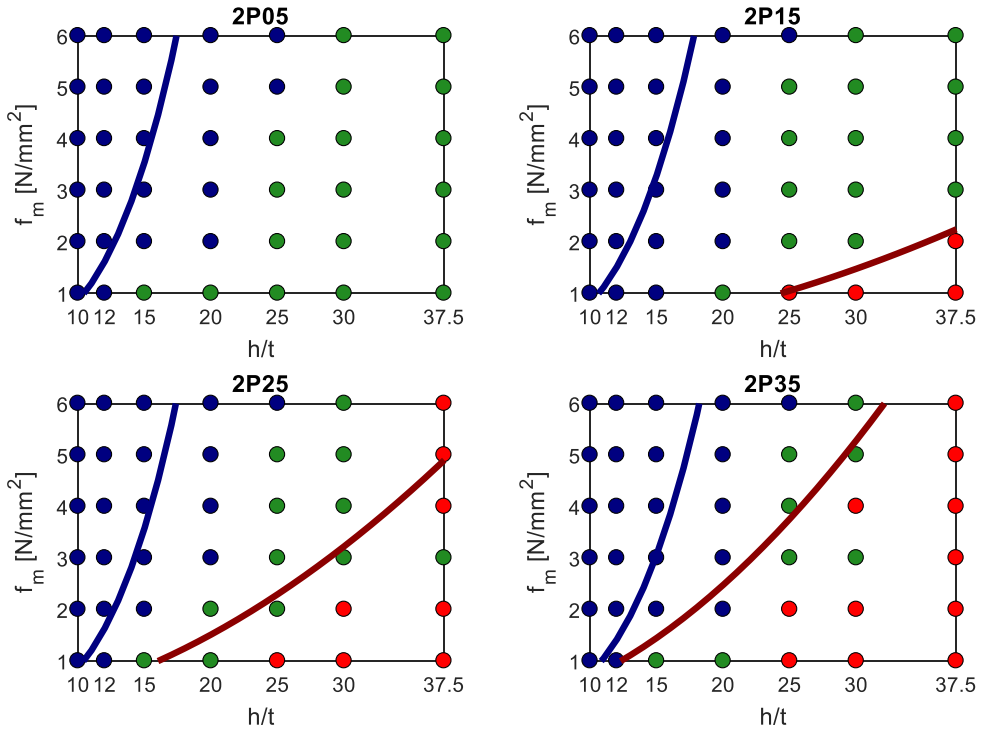
Figure 7.21. OOP safety domains in terms of slenderness ratio and masonry compressive strength obtained for the 2-storey case study buildings by applying the RA.
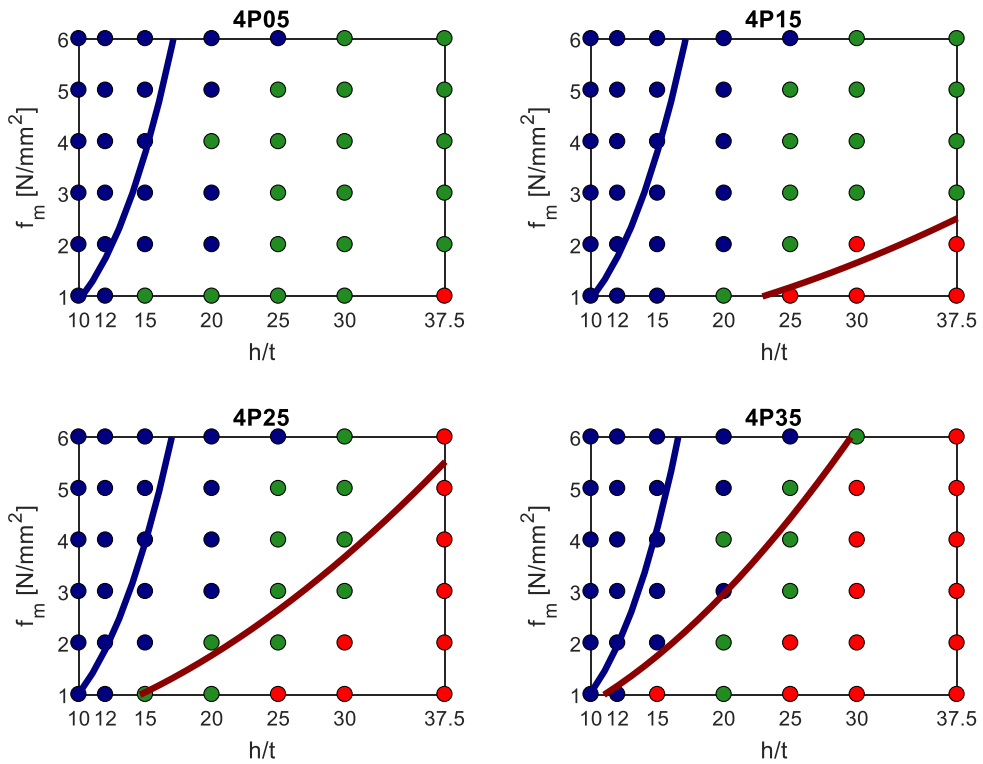
Figure 7.22. OOP safety domains in terms of slenderness ratio and masonry compressive strength obtained for the 4-storey case study buildings by applying the RA.
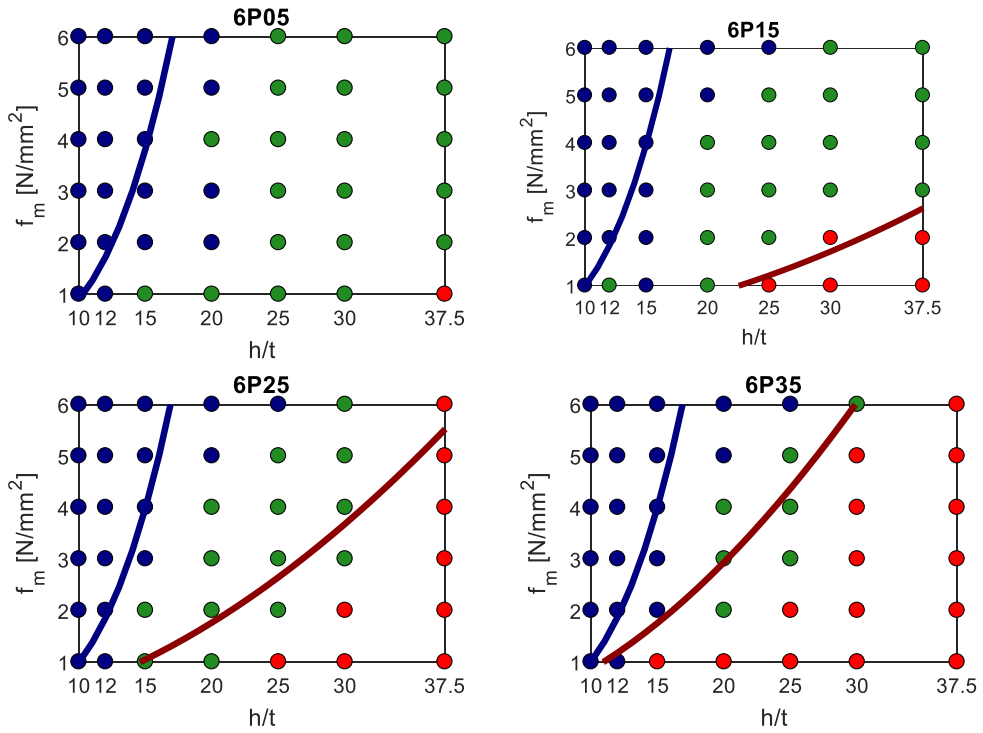
Figure 7.23. OOP safety domains in terms of slenderness ratio and masonry compressive strength obtained for the 6-storey case study buildings by applying the RA.
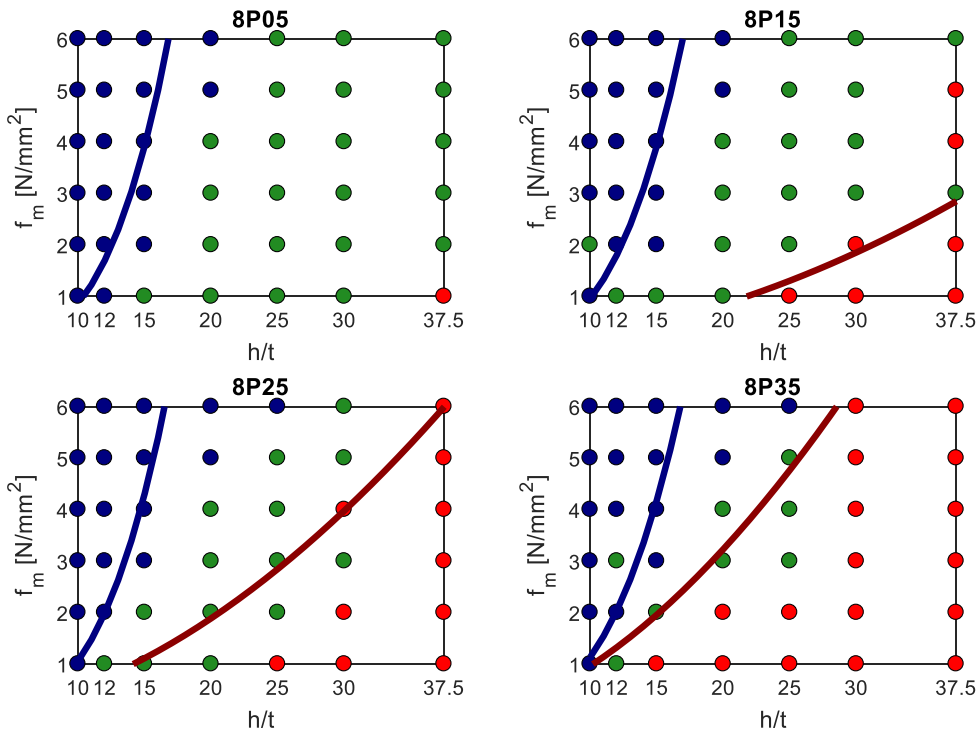
Figure 7.24. OOP safety domains in terms of slenderness ratio and masonry compressive strength obtained for the 8-storey case study buildings by applying the RA.

It is shown in Figures 7.21-7.24 that for slenderness ratios equal to or lower than 15 and masonry compressive strength in the vertical direction equal to at least 3 N/mm^{2} the OOP safety check of URM infills can be neglected independently on the number of floors of the building and on its design PGA at LS, because the infills' IP failure foreruns their OOP collapse.

Note that, according to the formulation reported in section 3.6.1.2 of Eurocode 6, such a masonry compressive strength is attained for a brick compressive strength in the vertical direction and for a mortar compressive strength both equal to at least 5 N/mm^{2}. More in general, the minimum masonry compressive strength, $f_{m,min}$, that grants that the IP failure foreruns the OOP collapse can be expressed as a function of the h/t ratio, consistently with the blue curves reported in Figures 7.21-7.24 and on the side of safety, according to Equation 7, as also shown in Figure 7.25.

$$f_{m,min}[N/mm^2] = 0.7(h/t - 10) + 1.5 \tag{7}$$
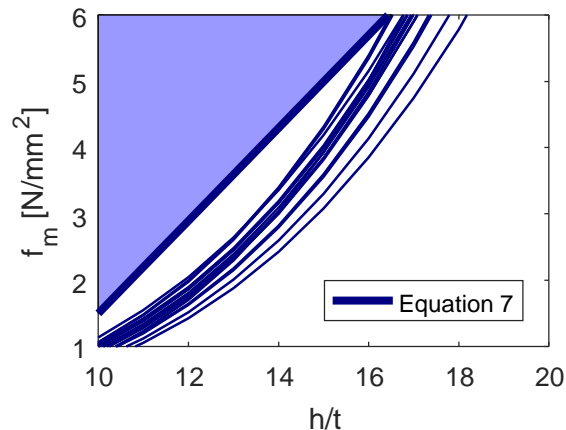
Figure 7.25. Limit state curves for all case-study buildings and their linear safety-sided simplification. The shaded area covers all the OOP safe h/t-f_m couples.

In addition, from Figures 7.21-7.24, it is observed that, independently on the number of storeys of the considered building, for low PGA demand at LS only slender and weak URM infills are going to collapse. For buildings in high-seismicity zones, widespread OOP collapses are expected for infills with slenderness ratio equal to or greater than 20 and masonry compressive strength lower than 2 N/mm² and for infills with slenderness ratio equal to or greater than 30 independently on their masonry compressive strength.

7.7. CONCLUSIVE REMARKS

In this Chapter, 16 case-study buildings designed according to EC8, different for number of storeys (2, 4, 6 and 8) and design PGA (0.05 g, 0.15 g, 0.25 g and 0.35 g) are considered as uniformly infilled by two different infill layouts, a two-leaf "weak" infill layout (WL) and a one-leaf "strong" infill layout (SL). On these case-study buildings, the PGA at which the first OOP infill collapse occurs (PGA_c) has been evaluated by means of a "Designer Approach", which does not account for the IP/OOP interaction and for the structural non-linearity, and by means of a "Reference Approach", which accounts for the IP/OOP interaction and for the structural non-linearity in a non-linear static framework.

The collapse PGAs obtained by applying the DA are similar in X and Z directions. However, panels built along Z direction, i.e., subjected to the OOP action in the building stiffer direction, are slightly more vulnerable than those aligned along X direction. A lower PGA_c is expected for stiffer buildings, i.e. for low-rise buildings and/or buildings designed for a higher PGA at LS. The first OOP collapse is always expected at the building last storey. The PGA_c is always greater than the design PGA of the building at LS.

Due to IP/OOP interaction effects, the collapse PGAs obtained by applying the RA are significantly lower for panels aligned along the building less stiff direction with respect to those built along the building stiffer direction. The PGA_c significantly decreases at increasing number of storeys of the considered building, while the effects of the different design PGA on the PGA_c are quite negligible. The first OOP collapse is expected at the second storey for 2- and 4-storeys building while it is expected between the third and the fifth storey for 6- and 8-storeys buildings. By comparing the PGA_c to the design PGA at LS, URM infills characterized by low/intermediate OOP resistance (WL and ML) in mid- and high-rise buildings (from 4 to 8 storey) deigned for mid- and high-seismicity zones (from 0.25 g) can be unsafe with respect to the OOP collapse. This means that, in these cases, the attainment of LS is avoided in terms of structural performance at the design PGA, at which wide OOP collapses of infills are expected, instead.

Based on the RA results, fragility curves relating the probability of OOP collapse to both the PGA acting in the OOP direction and the maximum IDR attained in the IP direction assumed as demand parameters are shown. Median PGA_c calculated by applying the RA are equal to 0.29 g and 0.91 g for WL and SL, respectively. Such values are equal to 0.23 and 0.03 times the corresponding median PGA_c obtained by applying the DA. Moreover, it is shown that the probability of OOP collapse for an IP IDR demand lower than the IDR corresponding to the infill IP collapse is around 0 for SL infills. In other words, for strong and robust infills, the IP collapse foreruns the OOP collapse and the OOP safety check is not necessary, given that LS is attained, considering non-structural elements, for infills' IP failure first.

It was shown that carrying out the OOP safety check of infills in a linear elastic framework and considering IP/OOP interaction produces PGA_c lower than those obtained by applying the DA but greater than those obtained by using the RA. In other words, structural non-linearity has a significant influence, which cannot be neglected, in the definition of the IP demand at infills OOP collapse.

Finally, for all case-study buildings, a wide range of 42 infill layouts, different for slenderness and masonry compressive strength, is considered and a "limit state" curve defining the h/t-f_m couples for which the IP collapse foreruns the OOP collapse is reported. Based on these results, infills with slenderness equal to or lower than 15 and masonry compressive strength equal to or greater than 3 N/mm^2 are safe with respect to the OOP collapse, as it is forerun by IP failure, and the OOP safety check for them can be neglected.

The trends and main concepts above-highlighted will be checked in the next Chapter, dedicated to non-linear dynamic analyses on the case-study buildings.

REFERENCES

- Calvi GM, Bolognini D. Seismic response of reinforced concrete frames infilled with weakly reinforced masonry panels. Journal of Earthquake Engineering 2001;5.2:153-185.
- Dawe JL, Seah CK. Out-of-plane resistance of concrete masonry infilled panels. Canadian Journal of Civil Engineering 1989;16(6):854–864.
- De Luca F, Vamvatsikos D, Iervolino I. Near-optimal piecewise linear fits of static pushover capacity curves for equivalent SDOF analysis. Earthquake Engineering and Structural Dynamics 2012;42.4:523-543.
- Eurocode 6. Design of Masonry Structures. Part 1-1: General Rules for Reinforced and Unreinforced Masonry Structures. Brussels, 2005. 123 p.
- Eurocode 8. Design of structures for Earthquake Resistance. Part 1-1: General Rules, Seismic Actions and Rules for Buildings. Brussels, 2004. 229 p.
- Eurocode 8. Design of structures for Earthquake Resistance. Part 3: Assessment and Retrofitting of Buildings. Brussels, 2005. 89 p.
- Fardis MN (editor). Experimental and numerical investigations on the seismic response of RC infilled frames and recommendations for code provisions, ECOEST/PREC8 Report No.6, Laboratorio Nacional de Engenharia Civil Publications, Lisbon, 1996.
- Flanagan RD, Bennett RM 1999. Arching of masonry infilled frames: Comparison of analytical methods. Practice Periodical on Structural Design and Construction 1999;4.3:105-110.
- Guidi G, da Porto F, Dalla Benetta M, Verlato N, Modena C. Comportamento

sperimentale nel piano e fuori piano di tamponamenti in muratura armata e rinforzata. Proceedings of the XV ANIDIS, L'Ingegneria Sismica in Italia, Padua, Italy, 2013, 30. (in Italian).

- Menun C and Der Kiureghian A. A replacement for the 30%, 40%, and SRSS Rules for multicomponent seismic analysis. Earthquake Spectra 1998;14.1:153-163.

- Panagiotakos TB, Fardis MN. Seismic response of infilled RC frames structures. 11th World Conference on Earthquake Engineering. June 23-28, 1996, Acapulco, México.

- Petrone C, Magliulo G, Manfredi G. Seismic demand on light acceleration-sensitive nonstructural components in European reinforced concrete buildings. Earthquake Engineering and Structural Dynamics 2015;44:1203–1217. doi: 10.1002/eqe.2508.

- Pinkawa M, Hoffmeister B, Feldmann M. A critical review of current approaches on the determination of seismic force demands on nonstructural components. Proceedings of the 9th International Conference on Structural Dynamics EURODYN2014. Porto, Portugal, 30 June – 2 July 2014.

- Timoshenko SP, Woinowsky Krieger S. Theory of plates and shells. McGraw-Hill, New York, 1959.

- Vamvatsikos D, Cornell, CA. Direct estimation of the seismic demand and capacity of oscillators with multi-linear static pushovers through IDA. Earthquake Engineering and Structural Dynamics 2006;35.9:1097-1117.

- Vukobratović V, Fajfar P. A method for the direct estimation of floor acceleration spectra for elastic and inelastic MDOF structures. Earthquake Engineering and Structural Dynamics 2016;45:2495–2511. doi: 10.1002/eqe.2779.

- Vukobratović V, Fajfar P. Code-oriented floor acceleration spectra for building structures. Bulletin of Earthquake Engineering 2017;15.7:3013-3026.

- Wilson EL, Suharwardy I, Habibullah A. A clarification of the orthogonal effects in a three-dimensional seismic analysis. Earthquake Spectra 1995;11:659-666.

Chapter VIII

Seismic assessment of infilled RC buildings in a non-linear dynamic framework accounting for the in-plane/out-of-plane interaction

8.1. INTRODUCTION

In this chapter, the 16 RC case-study infilled buildings presented in Chapter VI and different for number of storeys (2, 4, 6 and 8) and for the design Peak Ground Acceleration (0.05, 0.15, 0.25 and 0.35 g) at Life Safety Limit State (LS) are examined. Three different infill layouts are considered:

i.   a double leaf 'weak' infill layout constituted by an 80 mm-thick leaf and by a 120 mm-thick leaf (WL);

ii.   a double leaf 'intermediate' infill layout constituted by an 120 mm-thick leaf and by a 200 mm-thick leaf (ML);

iii.   a one leaf 'strong' infill layout constituted by a 300 mm-thick leaf (SL).

A total of 48 case-study buildings is examined by means of non-linear incremental dynamic analyses (IDA, Vamvatsikos and Cornell 2002). For each case study building, two different models are analyzed:

i.   a W/ model, in which the variation of the IP and OOP backbones due to the interaction during structural analyses is implemented, together with the

infill removal at the attainment of the IP or of the OOP collapse displacement;

ii.   a W/O model, in which the IP and OOP backbones do not vary during the analyses and only the infill removal at the attainment of the IP or of the OOP collapse displacement is implemented.

The IP behaviour of URM infills is modelled according to Panagiotakos and Fardis (1996). The OOP behaviour of URM infills is modelled according to the model proposed in Chapter IV. The OOP and IP behaviour variation due to the IP and OOP displacement demands is modelled according to the model proposed in Chapter IV. The non-linear time history analyses are carried out by using the OpenSees code (McKenna et al. 2000). The main aims of this chapter are:

i.   the assessment of the global seismic response of the case-study buildings accounting and not accounting for the IP/OOP interaction effects;

ii.   the assessment of the IDR and of the PGA associated with the first OOP collapse of infills accounting and not accounting for the IP/OOP interaction;

iii.   the assessment of the OOP effective stiffness and behaviour factor of URM infills that can be used for their seismic assessment in a simplified linear elastic framework.

In section 8.2, the modelling strategy adopted to implement in OpenSees the IP/OOP interaction model proposed in Chapter IV is described.

In section 8.3, the modelling of the case-study buildings is presented.

In section 8.4, the procedure of the non-linear time-history analysis is presented together with the selected records.

In section 8.5, the analyses' results in terms of global response of the case-study buildings are presented and discussed.

In section 8.6, the analyses' results in terms of IDR and PGA corresponding to the first OOP collapse are presented. A comparison with the same results obtained in a non-linear static framework in the previous Chapter is discussed.

In section 8.7, the analyses' results in terms of infills' OOP effective stiffness and behaviour factor are presented and discussed.

8.2. IP/OOP INTERACTION MODELLING STRATEGY

In Chapter IV, an OOP model and an IP/OOP interaction model has been presented. The proposed model has been introduced in OpenSees through the modelling strategy described in this section. The proposed modelling strategy has been conceived to:

i. reproduce the IP and OOP behaviour of infills;
ii. take into account the IP/OOP interaction effects in terms of strength, stiffness and displacement capacity variation during the structural analyses:
iii. allow the user to model IP and OOP behaviour of infills – and the corresponding degrading rules – adopting any trilinear material model as well as any hysteretic rule.

Remember that the IP behaviour of infills is herein modelled according to Panagiotakos and Fardis (1996)'s model. The OOP behaviour is modelled by means of a trilinear backbone plastic after the attainment of peak load and up to the attainment of the conventional OOP collapse displacement. As observed in Chapters III and IV, after the OOP peak load displacement, IP-undamaged infills show, actually, a softening branch, while IP-damaged infills show a plastic or a softening behaviour. Modelling both behaviours can produce physically unexplainable issues, such as a sudden increase in the OOP load bearing capacity in passing from the condition of undamaged infill to the condition of IP damaged infill, if the trespassing occurs at high OOP displacement demand, as shown in Figure 8.1.

For this reason, given the impossibility of perfectly reproducing experimental evidence without the risk of occurrence of physically unexplainable issues, the OOP behaviour of infills is modelled as plastic after peak-load displacement for both undamaged and IP-damaged infills, as was also done by Kadysiewski and Mosalam (2009). Consider that the conventional OOP collapse displacement is set to the 20% strength degradation after the attainment of peak load. Such a limited reduction is consistent with the adoption of a plastic behaviour after maximum.
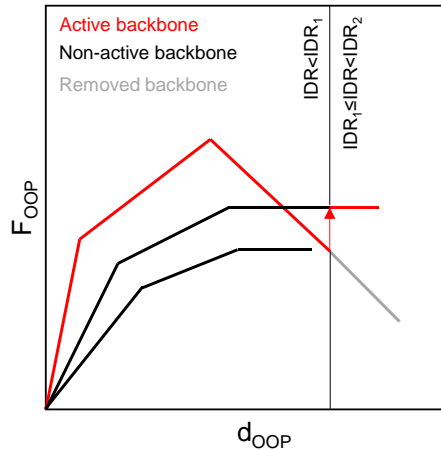
Figure 8.1. Potential physically unexplainable issues deriving from modelling a degrading behaviour for the IP-undamaged infill and a plastic behaviour for the IP-damaged infill.

First, the OOP force-displacement behaviour relationship should be defined for the undamaged panel. Given the infill geometric and mechanical properties, an OOP trilinear backbone can be defined through the semi-empirical approach described in Chapter IV. Hereafter, the above-defined OOP behaviour relationship will be referred to as the IDR=0 backbone. Then, n IDRs (IDR$_i$, with i=1, …, n) should be set as discrete IP damage thresholds. Through the degradation-modelling relationships, it is possible to define n OOP backbones, corresponding to the n IDRs: each one of these curves, which will be mentioned hereafter as IDR=IDR$_i$ backbones, represents the OOP behaviour that the infill will exhibit from the moment when the IP IDR demand exceeds the damage threshold represented by IDR$_i$.

Note that the degradation relationships are used by applying the necessary limitations to prevent some issues with no mechanical reason that can occur for low or high values of the IDR: e.g., a secant stiffness at peak load greater than the initial one or a cracking load higher than the peak one.

As shown in Figure 8.2, each infill should be represented by a diagonal element representing the IP behaviour of the infill. Each of these elements is connected through a pinned joint to the surrounding frame and is provided with a central node that is connected to a second central node in which the mass participating in the first OOP vibration mode of the infill is lumped which is assumed equal to 66% of the panel total mass. Note that the infill's OOP displacement is defined as the OOP displacement of the

mid-span mass node with respect to the chord that connects the bottom and top frames' nodes. The connection between these central nodes is ensured by $2n+1$ plastic hinges. First, a plastic hinge carrying the IDR=0 backbone must be defined (in the following analyses, a Hysteretic Material is used for this). Then, for each IDR=IDR_i backbone, a couple of plastic hinges must be defined: the first one, which will be called the "*i*-th real plastic hinge", models the OOP behaviour defined by the considered IDR_i backbone; the second one, which will be called the "*i*-th auxiliary plastic hinge", behaves according to the force-displacement relationship defined by the IDR=IDR_i backbone mirrored with respect to the displacements axis. This goal can be achieved in OpenSees by defining the "auxiliary" backbones through a Parallel Material that is referred, with scale factor equal to -1, to the constitutive relationship used to define the corresponding "real" backbone. This means that the OOP force for a given OOP displacement in the *i*-th real plastic hinge is always equal and opposite to the OOP force at the same displacement in the *i*-th auxiliary plastic hinge. This also means that as long as all plastic hinges are part of the infill model, the panel OOP behaviour is the one defined by the IDR=0 backbone, while the effects of the other plastic hinges are mutually neutralizing. Based on the experimental data provided by some authors, such as Hak et al. (2014) and Furtado et al. (2016), the β coefficient that governs the stiffness cyclic degradation of the Hysteretic Material used to model the OOP backbones seems to be included between 0.5 and 0.8. Note that in spite of the suggestion herein provided about the material models for the IP/OOP backbones, an interesting difference between the proposed modelling approach and the ones described in Chapter I is the possibility for the user to model the IP and OOP infills' behaviour (both non-degraded and degraded) with any desired trilinear material model as well as with any hysteretic rule.

To account for the degradation of infills' OOP strength, stiffness and ductility capacity, an integral part of the proposed model is a routine that removes from the structural model the IDR_{i-1} real plastic hinge and the IDR_i auxiliary plastic hinge when the IP IDR exceeds the previously defined damage threshold represented by IDR_i. In this way, as soon as the IDR exceeds IDR_i, and as long as the IDR is lower than the successive IP damage threshold IDR_{i+1}, the panel OOP behaviour is defined by the IDR=IDR_i backbone "contained" in the *i*th real plastic hinge, while the effects of the remaining plastic hinges are still mutually neutralizing.

In other words, once a certain IP displacement is attained, the OOP behaviour is definitively modified. An explanatory simplified version of the routine aimed at passing from the IDR_i to the IDR_{i+1} backbone is shown in Figure 8.3 and reproduced in a sort of

graphical workflow in Figure 8.4. As already stated, the above-mentioned backbone removal routine allows the user to implement in the structural model the OOP response parameter variation due to IP action. Moreover, similar to what has been done previously by different authors and first by Mosalam and Günay (2015), a second and different removal routine was implemented: if the OOP displacement exceeds the ultimate displacement associated with the IDR=IDR_i backbone, all the elements representative of the infill wall are removed from the structural model.
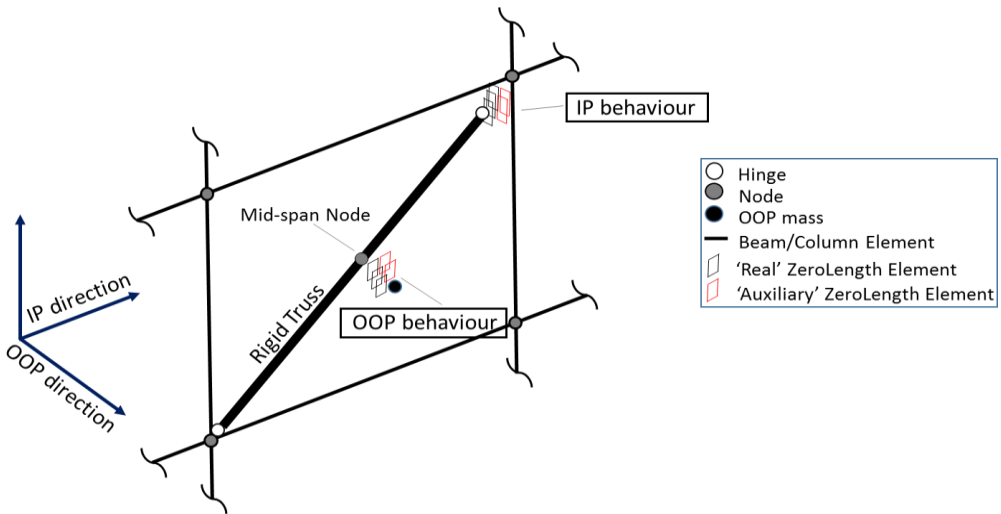
Figure 8.2. Graphical representation of the proposed modelling strategy.

```
PRIOR TO THE STRUCTURAL ANALYSIS

for each Infill Wall modeled
    set CF1, a control flag for the element removal, to 0
    for each ZeroLength element (ZL) carrying a "real" OOP backbone
        set IPLD, the value of the IP displacement at which the ZL must be removed
        set CF2, a control flag for the ZL removal, to 0
        set OOPUD, the value of the ultimate OOP displacement associated to the ZL
    end
end

DURING THE STRUCTURAL ANALYSIS, AT EACH STEP CONVERGED

for each Infill Wall modeled
    set IPD to the current in-plane displacement
    set OOPD to the current out-of-plane displacement
    if (element not already removed, i.e., CF1==0)
        if OOPD>OOPUD
            remove the whole infill wall
            set CF1 to 1
        else
            for i that skims each ZL carrying a "real" OOP backbone
                if (the i-th ZL not already removed, i.e., CF2==0)
                    if IPD>IPLD
                        remove the i-th ZL carrying the "real" OOP backbone
                        remove the ZL carrying the i+1-th "auxiliary" OOP backbone
                        set CF2 to 1
                    end
                end
            end
        end
    end
end
```

Figure 8.3. Simplified schema of the routine aimed at trespassing from one backbone to another.

Introduction of the IP-undamaged infill OOP backbone
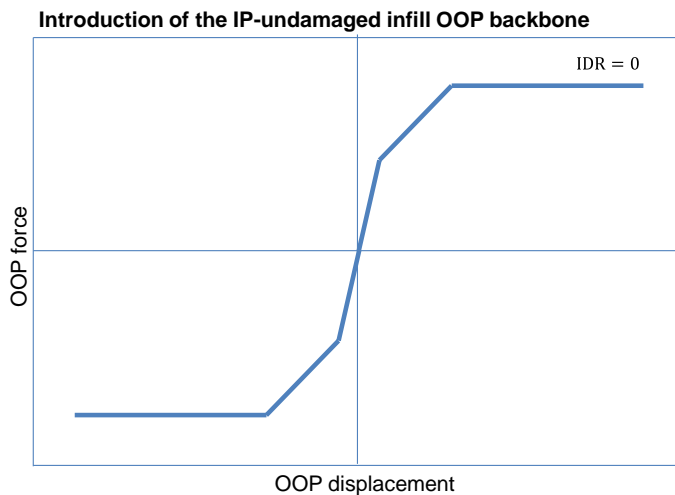
(a) Consider the OOP real backbone for the IP-undamaged infill and introduce it in the structural model (blue continuous line, backbone 1)

Introduction of the IP-damaged infill OOP real backbone
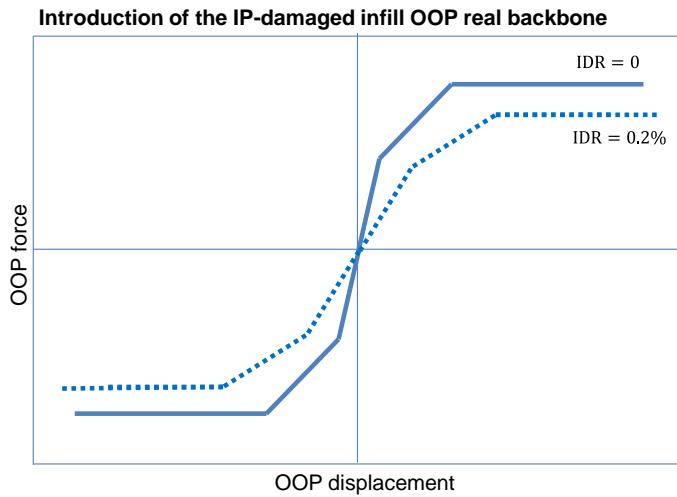
(b) Consider the OOP real backbone for the IP-damaged infill at IP drift equal to 0.2% (for example) and introduce it in the structural model (blue dotted line, backbone 2).

Introduction of the IP-damaged infill OOP auxiliary backbone
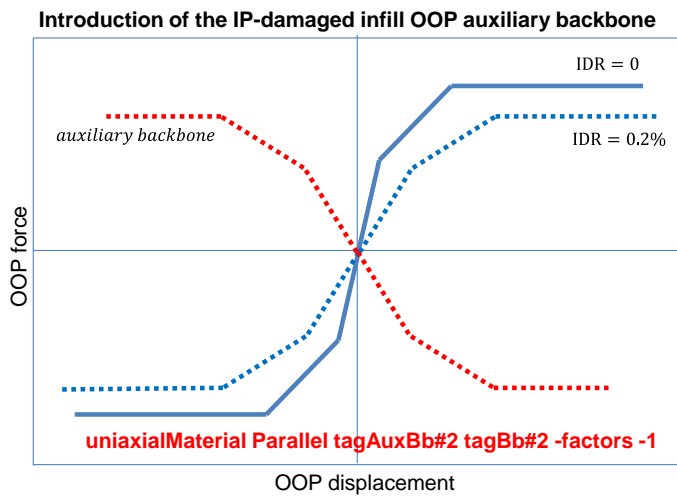
(c) Consider the OOP backbone for the IP-damaged infill at IP drift equal to 0.2% mirrored with respect to the horizontal axis and introduce it in the structural model. This is the auxiliary backbone 2 (red dotted line).

The IP-damaged infill OOP backbones are mutually neutralizing

IDR = 0

auxiliary backbone

IDR = 0.2%

OOP force

OOP displacement
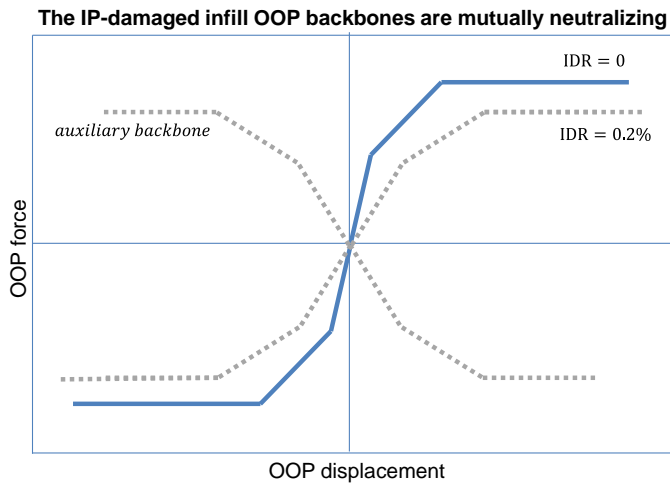
(d) At this stage, the two backbones at IDR equal to 0.2%, the real and the auxiliary one, are mutually neutralizing (grey dashed lines).

The IP-undamaged infill OOP backbone is active

active backbone   IDR = 0

auxiliary backbone

IDR = 0.2%

OOP force

OOP displacement
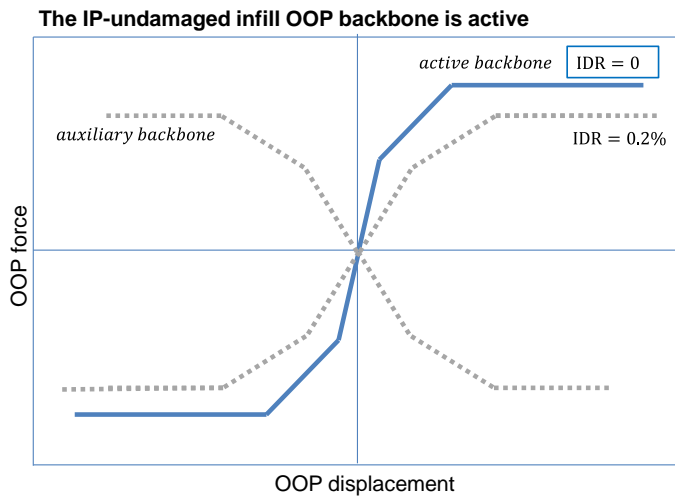
(e) At this stage, the OOP behaviour of the infill is determined by the active backbone associated with IDR=0, i.e., the real backbone of the IP-undamaged infill (backbone 1, blue continuous line).

Removal of the IP-undamaged infill OOP backbone
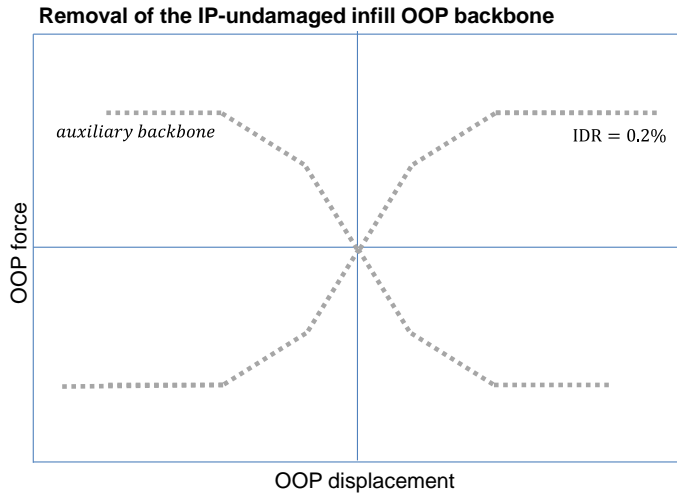
(f) At each step of the structural analysis, check if IDR is lower or greater than 0.2%. In the least case, remove backbone 1…

Removal of the IP-damaged infill OOP auxiliary backbone
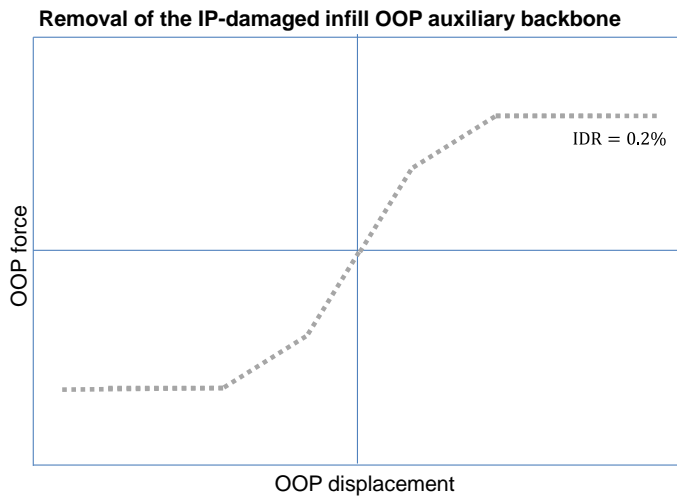
(g) … and remove also the auxiliary backbone 2.
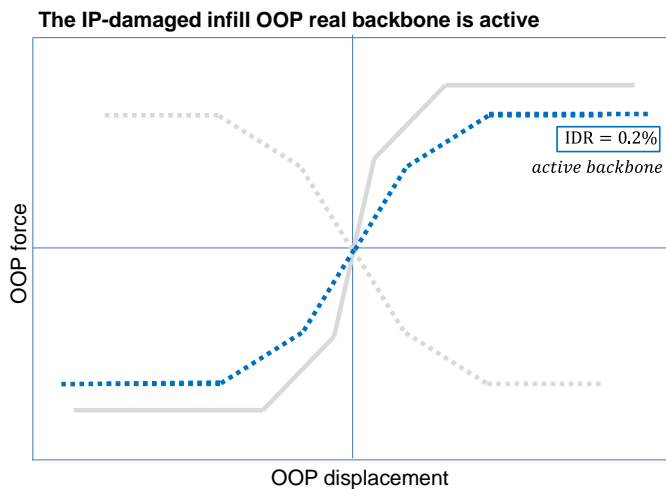
(h) The active backbone is backbone 2 (blue dotted line). The OOP behaviour of the infill is determined by it.

Figure 8.4. Modelling strategy workflow.

The IP strength and stiffness degradation can be controlled through the ratio between the OOP displacement demand and the OOP displacement capacity of the undamaged panel. It can be modelled, together with the entire infill removal due to the attainment of the IP ultimate displacement, through a procedure that is very similar the one explained in the previous lines for the modelling of the infill OOP behaviour. Moreover, the proposed model can be easily modified by modelling each infill wall through a couple of diagonal non-interacting no-tension struts: only one of these struts should be provided with a central mass node that accounts for the OOP behaviour of the infill. Additionally, in this case, the user should assume the OOP displacement of that central node as the parameter that controls the IP damage and remove, when the generic damage threshold $d_{OOP,i}$ is exceeded, the corresponding IP real and auxiliary plastic hinges from both elements. In the structural models herein analyzed, a couple of no-tension trusses is used to model each infill leaf.

The "mutually-neutralizing backbones" artifice herein described allows the user to model the IP and OOP behaviours of infills, as well as strength, stiffness and displacement capacity reduction due to the IP-OOP interaction. Clearly, the proposed implementation strategy addresses the current tools and routines available in the OpenSees code, which do not allow reproduction of the continuous strength, stiffness and displacement capacity degradation rule by updating elements' and materials'

properties step-by-step during analyses. For this reason, the passage from one backbone to another cannot be perfectly smooth - even if it can be as smoother as the number of modelled backbones increases, especially at low IDR values for the OOP infill behaviour. This issue can be solved, for example, through the implementation in the OpenSees code of interaction domains.

8.3. MODELLING OF THE CASE-STUDY BUILDINGS

The RC elements' non-linearity is modelled in OpenSees by using ModIMKPeakOriented Material with response parameters determined according to Haselton et al. (2007) with introduction of the cracking point. This moment-chord rotation empirical model was calibrated on a wide database collecting the experimental response of RC members under cyclic loading. The empirical nature of the model, together with the great number of experimental tests considered, allows reproducing accurately and reliably the softening behaviour of RC elements as well as strength and stiffness hysteretic degradation due to cyclic loading. These issues are extremely important in predicting RC buildings seismic response through incremental dynamic analyses, especially for structures controlled by ductile response up to ultimate condition as for frames designed according to Eurocode 8 (2004). For all these reasons, together with the reliability of Haselton et al.'s model in reproducing the post-peak behaviour of RC members, such approach allows the observation of the dynamic instability phenomenon in RC structures more straightforwardly than could be done using fiber-section based structural models. Note that dynamic instability is a clear and immediate indicator of the ultimate seismic performance level that can be expected for "ductile-controlled" RC structures as in the new case-study buildings it is observed, sometimes, only accounting for IP-OOP degradation in infills (i.e., only for W/ models). Even if limited only to some cases, this allows highlighting the influence of IP/OOP interaction on the seismic response of RC structures as well as the importance of considering the IP/OOP interaction phenomena in structural analyses of RC buildings, even if designed addressing seismic provisions of modern technical codes such as Eurocodes, to not incur in a potentially highly detrimental overestimation of such buildings' seismic performance.

As previously stated, three infill layout are considered. The first one is constituted by a double-leaf (thickness: 80+120 mm) URM 'weak' infill wall (weak layout, WL), the second one is constituted by a two-leaf (thickness: 120+200 mm) URM

'intermediate' infill wall (intermediate layout, ML), the third one is constituted by a one-leaf (thickness: 300 mm) URM 'strong' infill wall (strong layout, SL). The mechanical properties of these infills are those calculated for the masonry wallets tested by Calvi and Bolognini for the WL and ML and those by Guidi et al. for the SL (Table 8.1). Note that the value of the masonry shear strength of Guidi et al.'s specimen was not provided by the Authors and so was set to 0.30 N/mm² according to Table 3.4 of Eurocode 6 (2005).

Table 8.1. Infills' geometric and masonry mechanical properties.

property	symbol	units				
leaf thickness	t	[mm]	80	120	200	300
height	h	[mm]	3000	3000	3000	3000
width	w	[mm]	4500	4500	4500	4500
slenderness ratio	h/t	[-]	37.5	25	15	10
total mass	m_{tot}	[kg]	864	1296	2160	3240
shear modulus	G	[N/mm²]	1039	1039	1039	788
shear strength	τ_{cr}	[N/mm²]	0.15	0.15	0.15	0.30
vertical direction						
compressive strength	f_{mv}	[N/mm²]	1.10	1.10	1.10	6.00
elastic modulus	E_{mv}	[N/mm²]	1873	1873	1873	4312
horizontal direction						
compressive strength	f_{mh}	[N/mm²]	1.11	1.11	1.11	1.19
elastic modulus	E_{mh}	[N/mm²]	991	991	991	1767

Each infill wall was introduced in the structural model using a single equivalent strut whose non-linear behaviour is modelled based on Panagiotakos and Fardis (1996) proposal. According to this modelling approach, the slope of the softening branch of the force-displacement IP behavior relationship is a fraction α of the infill initial elastic stiffness, while the infill residual strength is herein set to zero. In Fardis (1996) it is suggested to set α to a value between -1.5% and -5%. For the 80-, 120- and 200-mm thick and for the 300-mm thick leaves, it is assumed an α value equal to -1.6% and -3.6%, respectively. Such values lead to predictions of the softening stiffness and ultimate IP displacement in good accordance with the experimental evidences shown by Calvi and Bolognini (specimen 2) for α=-1.6% and by Guidi et al. (specimen URM-U) for α=-3.6%. The IP behaviour characteristic points are reported in Table 8.2.

Table 8.2. Infills' IP behaviour characteristic points.

property	symbol	units				
leaf thickness	t	[mm]	80	120	200	300
cracking force	F_{crack}	[kN]	54.0	81.0	135	405
initial stiffness	K_{crack}	[kN/mm]	125	187	312	355
cracking displ.	d_{crack}	[mm]	0.43	0.43	0.43	1.14
cracking IDR	IDR_{crack}	[%]	0.014	0.014	0.014	0.038
maximum force	F_{max}	[kN]	70.0	105	175	526
secant stiffness at max.	K_{max}	[kN/mm]	7.66	11.0	17.5	42.4
displ. at maximum	d_{max}	[mm]	9.16	9.54	10.0	12.4
IDR at maximum	IDR_{max}	[%]	0.30	0.32	0.33	0.41
collapse displacement	d_u	[mm]	44.3	44.7	45.2	53.7
collapse IDR	IDR_u	[%]	1.48	1.49	1.51	1.79

The OOP behaviour of IP-undamaged infills has been modelled by using the lumped-plasticity empirical-based modelling strategy proposed in Chapter IV.

The OOP behaviour characteristic points of the IP-undamaged case-study infill leaves are reported in Table 8.3. Note that the mass participating to the first OOP vibration mode of each leaf has been set equal to 66% of the infill total mass.

The dynamic properties of the case-study bare frames are reported in Table 6.3 in Chapter VI. The elastic fundamental periods are presented for the infilled frames in Table 8.4.

Table 8.3. OOP-undamaged infills' OOP behaviour characteristic points.

property	symbol	units				
leaf thickness	t	[mm]	80	120	200	300
cracking force	F_{crack}	[kN]	18.0	39.5	68.4	130
initial stiffness	K_{crack}	[kN/mm]	1.20	4.06	18.8	146
cracking displ.	d_{crack}	[mm]	14.9	9.73	3.64	0.89
maximum force	F_{max}	[kN]	20.0	43.9	122.7	688
secant stiffness at max.	K_{max}	[kN/mm]	0.48	1.63	7.53	58.5
displ. at maximum	d_{max}	[mm]	41.5	27.0	16.3	11.8
collapse displacement	d_u	[mm]	58.1	37.8	60.0	90.0
initial ductility	μ^{und}	[-]	1.40	1.40	3.68	7.65
OOP participating mass	m_a	[kg]	570	855	1426	2138
OOP elastic period	T_a	[s]	0.137	0.091	0.055	0.024

Note that the WL is characterized by low IP stiffness and low OOP strength; the ML is characterized by high IP stiffness and low OOP strength (with reference to the thinner leaf); the SL is characterized by high IP stiffness and high OOP strength. For this reason,

WL infills are expected to be very prone to IP/OOP interaction and vulnerable with respect to OOP actions; ML infills are expected to be less prone to IP/OOP interaction but vulnerable with respect to OOP actions not differently than WL infills; SL infills are expected to be significantly vulnerable neither to IP/OOP interaction nor to OOP actions.

Table 8.4. Elastic fundamental periods in the X and Z global directions of the case-study infilled buildings.

	Number of storeys of the infilled buildings							
design PGA	2		4		6		8	
WL	$T_{1,Z}$ [s]	$T_{1,X}$ [s]	$T_{1,Z}$ [s]	$T_{1,X}$ [s]	$T_{1,Z}$ [s]	$T_{1,X}$ [s]	$T_{1,Z}$ [s]	$T_{1,X}$ [s]
0.05 g	0.107	0.085	0.222	0.181	0.298	0.242	0.414	0.329
0.15 g	0.107	0.085	0.219	0.177	0.293	0.240	0.408	0.326
0.25 g	0.107	0.085	0.210	0.178	0.277	0.231	0.386	0.315
0.35 g	0.104	0.083	0.209	0.176	0.277	0.231	0.384	0.318
ML								
0.05 g	0.097	0.074	0.194	0.154	0.263	0.206	0.366	0.282
0.15 g	0.097	0.074	0.189	0.153	0.260	0.205	0.362	0.280
0.25 g	0.097	0.074	0.187	0.150	0.247	0.203	0.344	0.278
0.35 g	0.095	0.073	0.184	0.145	0.248	0.198	0.348	0.271
SL								
0.05 g	0.103	0.085	0.215	0.173	0.293	0.233	0.407	0.317
0.15 g	0.103	0.085	0.211	0.172	0.289	0.231	0.401	0.315
0.25 g	0.103	0.085	0.206	0.169	0.275	0.224	0.383	0.309
0.35 g	0.102	0.084	0.205	0.168	0.272	0.226	0.381	0.306

In the following, each case-study building is identified using an acronym, such as *X*P*Y_Z*, in which *X* is the number of storeys, *Y* the design PGA at LS expressed in g/100, Z the infill layout indicator.

8.4. ANALYSIS PROCEDURE

In order to carry out the dynamic analyses, ten ground motions were selected among

the records of European earthquakes collected in the Engineering Strong-Motion (ESM) Database (Luzi et al. 2016). Some significant characteristics of the selected ground motions are reported in Table 8.5.

Table 8.5. Ground Motions selected for the Incremental Dynamic Analyses.

#	ESM ID	Country	Date	M_w	R_{epi} [km]	PGA_{NS}	PGA_{EW}
1	ME-1979-0003	Montenegro	15/04/1979	6.9	19.7	0.18 g	0.21 g
2	IT-1980-0012	Italy	23/11/1980	6.9	28.3	0.10 g	0.08 g
3	IT-1984-0004	Italy	07/05/1984	5.9	10.1	0.10 g	0.11 g
4	IT-1997-0006	Italy	26/09/1997	6.0	26.5	0.02 g	0.03 g
5	IT-1997-0137	Italy	14/10/1997	5.6	8.70	0.18 g	0.10 g
6	SI-1998-0010	Italy	12/04/1998	5.7	23.5	0.02 g	0.02 g
7	IT-1998-0103	Italy	09/09/1998	5.6	18.0	0.17 g	0.16 g
8	GR-1999-0001	Greece	07/09/1999	5.9	19.7	0.11 g	0.12 g
9	TK-1999-0294	Turkey	13/09/1999	5.8	13.8	0.08 g	0.32 g
10	IT-2009-0009	Italy	06/04/2009	6.1	26.2	0.03 g	0.02 g

The selection of records was performed by searching among the bidirectional registration of stations based on EC8 type A soils, consistently with the design soil type. Consistently with the choice of using EC8 Type I design spectrum, only earthquakes with magnitude between 5.5 and 7 and only registration of stations with epicentral distance between 10 and 30 km were considered. The 5%-damped response spectra of the selected records are reported in Figure 8.5a (North-South component) and 8.5b (East-West component). Both horizontal components of the selected records were simultaneously matched to the 5%-damped EC8 design spectrum at LS using wavelets through the RspMatchBi software (Grant 2010). It was observed that the resulting spectral shape of the matched record was independent on the target PGA. Hence, it is assumed as reference record set the one obtained by matching ground motions to the elastic spectrum associated with LS and anchored at a PGA equal to 0.15 g. The response spectra of the matched ground motions in the NS direction and in the EW direction are shown, together with the mean spectrum and the target response spectrum, in Figure 8.5c. Note that the record component registered in the NS direction is applied along X global direction, while the component registered in the EW direction was applied along Z global direction.

Incremental Dynamic Analyses (Vamvatsikos and Cornell 2002) were performed by scaling each selected and matched record for a set of pre-determined scale factors (SF) in order to obtain for each horizontal direction an incremental PGA (selected as Intensity

Measure) vs maximum IDR and maximum top displacement (selected as Engineering Demand Parameters) curve. A total of 32 scale factors ranging from 0.067 to 10 were considered. This allowed performing the IDAs for 32 values of PGA roughly equal in both directions and ranging from 0.010 g to 1.50 g, as reported in Table 8.6.
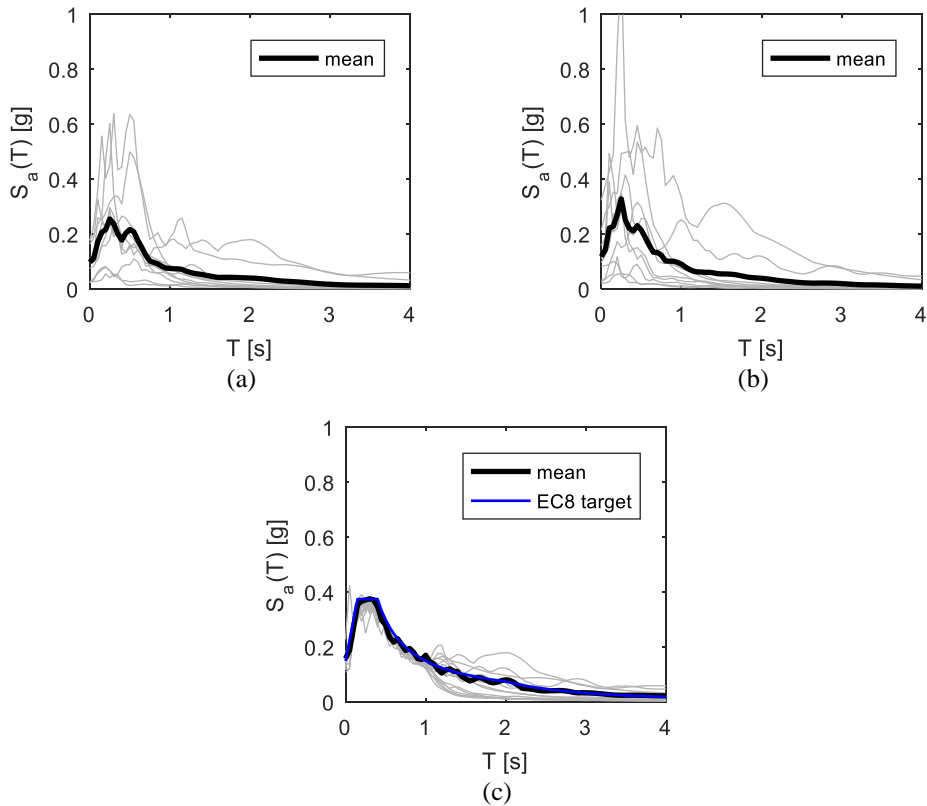
Figure 8.5. Selected records response spectra for NS components (a) and EW components (b). Response spectra of the selected records matched to EC8 design spectrum at LS with PGA equal to 0.15 g (c).

Table 8.6. Selected Records' scale factors (SF) and associated PGAs for Incremental Dynamic Analyses.

#	SF	PGA [g]	#	SF	PGA [g]	#	SF	PGA [g]	#	SF	PGA [g]
1	0.067	0.010	9	1.000	0.150	17	2.333	0.350	25	5.333	0.800
2	0.100	0.015	10	1.167	0.175	18	2.667	0.400	26	6.000	0.900
3	0.133	0.020	11	1.333	0.200	19	3.000	0.450	27	6.667	1.000
4	0.167	0.025	12	1.500	0.225	20	3.333	0.500	28	7.333	1.100
5	0.333	0.050	13	1.667	0.250	21	3.667	0.550	29	8.000	1.200
6	0.500	0.075	14	1.833	0.275	22	4.000	0.600	30	8.667	1.300
7	0.667	0.100	15	2.000	0.300	23	4.333	0.650	31	9.333	1.400
8	0.833	0.125	16	2.167	0.325	24	4.667	0.700	32	10.00	1.500

Note that IDAs were performed, for each case study building, on a W/ model, in which the degradation of IP and OOP behaviours due to the IP/OOP interaction was implemented, together with the infill removal routine, and on a W/O model in which only the infill removal routine at the attainment of the IP or OOP unchanging collapse displacement was implemented. All analyses were performed after the application of gravity loads which was followed by the introduction of infill walls in the structural model.

The analyses were carried out by applying mass- and tangent stiffness-proportional Rayleigh damping rules for two control frequencies. Modal analyses were performed on the elastic models of the infilled case-study frames. For all case-study buildings, three groups of modes were recognizable: a first group of global "lower" modes corresponding to lower frequencies/modes involving the entire structure; a second group of local modes involving groups of infills excited in the OOP direction corresponding to intermediate frequencies; a third group of global "higher" modes corresponding to higher frequencies/modes involving the whole structure. Frequencies associated to the second group are very close to each other and to the infill natural frequency in the OOP direction. Two different groups of "intermediate" local modes are registered when dealing with two-leaf infill layouts (WL and ML). For all these reasons, the frequencies corresponding to one "global" and to one "local" mode were selected as control frequencies. Namely, the first control mode corresponds the first natural frequency of the infilled structure, while the second control mode corresponds to the "intermediate" mode associated to the frequency closer to the infill natural frequency in the OOP direction, as reported, for example purposes, in Figure 8.6 for the case-study building 4P05_SL.
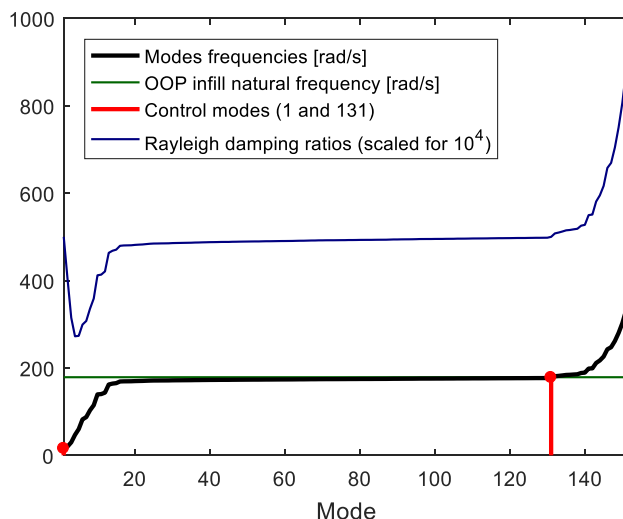
Figure 8.6. Mode frequencies, OOP frequency of the SL infill, control modes and Rayleigh damping ratios for the 4P05_SL case-study building.

In the case of two-leaf layouts, the control frequency selected among the intermediate ones was that associated with the slender and, most likely, more vulnerable leaf. The damping ratio assigned to control frequencies was equal to 5% both for the first global and for the second local control mode: the latter choice is due to the lack of exhaustive studies on the damping properties of infills excited in the OOP direction, which is worth to be investigated in the future.

8.5. GLOBAL RESPONSE OF THE CASE-STUDY BUILDINGS

In this section, the global seismic response of the case-study buildings is discussed by comparing their IDA curves. Remember that a total of 96 buildings was analysed (16 different RC frames x 3 infill layouts x 2 modelling strategies – W/O and W/) under the action of 10 bidirectional records scaled per 32 different scale factors. A total of more than 30 thousand time history analyses were performed. For the sake of simplicity, the IDA curves are not shown for all case-study buildings but only for some of them, in order to show in a simple and direct way how the IP/OOP interaction effects influence the seismic response of RC buildings.

In Figure 8.7, the IDA curves for building 8P35_WL are shown for both the W/O and the W/ models.
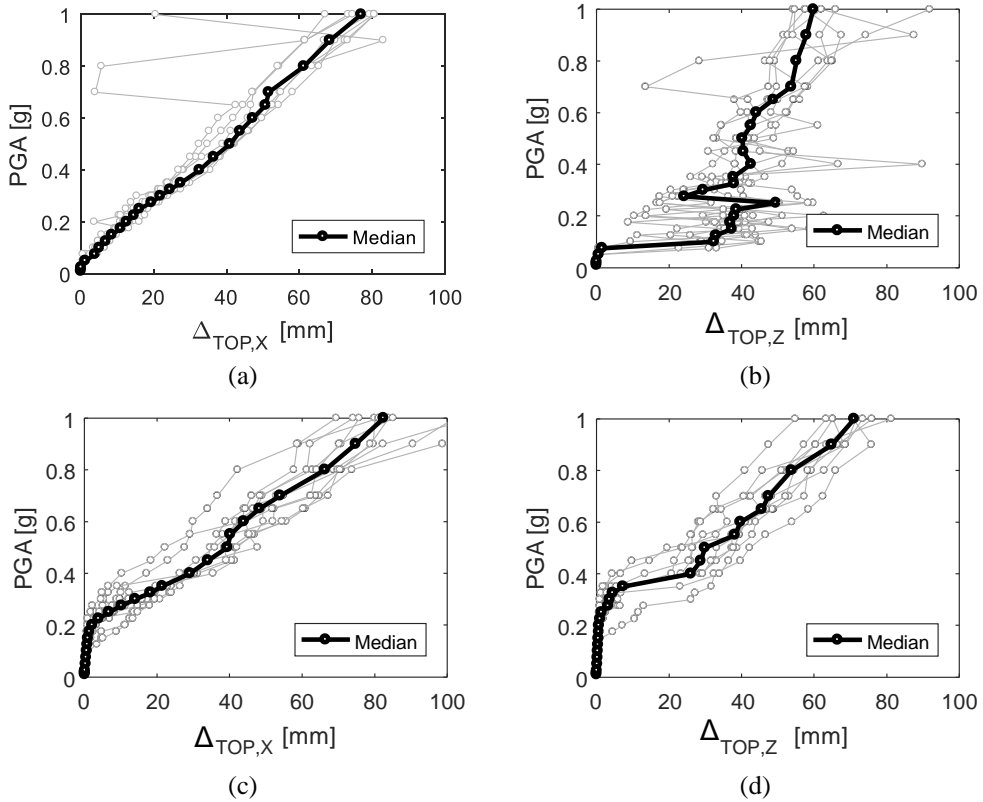
Figure 8.7. IDA curves for building 8P35_WL in the X (a-c) and Z (b-d) directions for the W/ (a-b) and the W/O (c-d) models.

The OOP collapses of infills (and their removal from the structural model) is visible from the sudden increase in the lateral displacement demand. Of course, this jerk is visible also in the IDA curves of the W/O model (Figure 8.7d), but for a higher PGA demand. It should be noted that, as expected, wide OOP collapses are registered in the more deformable direction of the building, i.e., along Z global direction.

In general, if the IP/OOP interaction effects are neglected, the lateral displacement demand acting on buildings is underestimated. For example, at PGA equal to 0.35 g, the median displacement demand in Z direction for 8P35_WL building is roughly equal to 10 mm according to the results of the analyses on the W/O model, while it is roughly equal to 35 mm for the W/ model.

Note also that, especially for the W/ model, the IDA curves are characterized by a jagged trend, with many "resurrections". This is quite expected, as the entity of the

IP/OOP interaction effects as well as the number and location of infills collapsed and removed from the structural model can vary significantly (and not necessarily "monotonically") at increasing intensity level. Remember that this is the result obtained on 8P35_WL case-study building, but that such trends have been observed for all case-study buildings. That being said, it is interesting to observe also the response of the 8P35_ML building in Figure 8.8.

It is quite interesting to observe that the median IDA curve for 8P35_ML building (W/ model) presents two sudden increments in the lateral displacement demand due to the collapse at different PGAs of the two leaves. Even WL buildings are infilled by two-leaf infills, but the thicknesses of WL leaves are very similar, hence they collapse at quite similar PGAs and the two "jumps" in the lateral displacement demand are not discernible. At high PGA demand, in the W/ models, some cases of dynamic instability are observed.
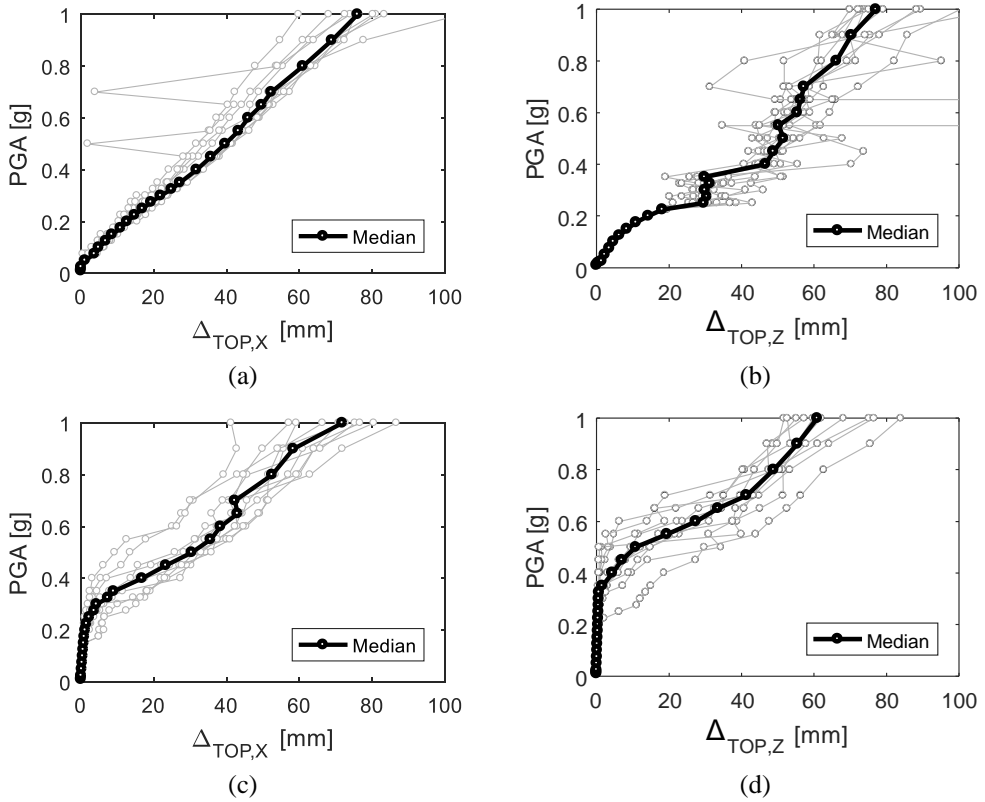
Figure 8.8. IDA curves for building 8P35_ML in the X (a-c) and Z (b-d) directions for the W/ (a-b) and the W/O (c-d) models.

The response of the 8P35_SL building is shown in Figure 8.9. As expected, the significant IP stiffness of the infill walls makes such building very stiff and the lateral displacement demand very low. The PGA corresponding to the OOP collapse of infills is significantly affected by record-to-record variability, hence there is not a unique "jump" in the displacement demand but many "resurrections" in the IDA curves, at very high PGA, as expected for such thick and robust infills characterized by a high OOP capacity and by a lower impact of the IP/OOP interaction effects (as shown in Chapter IV).
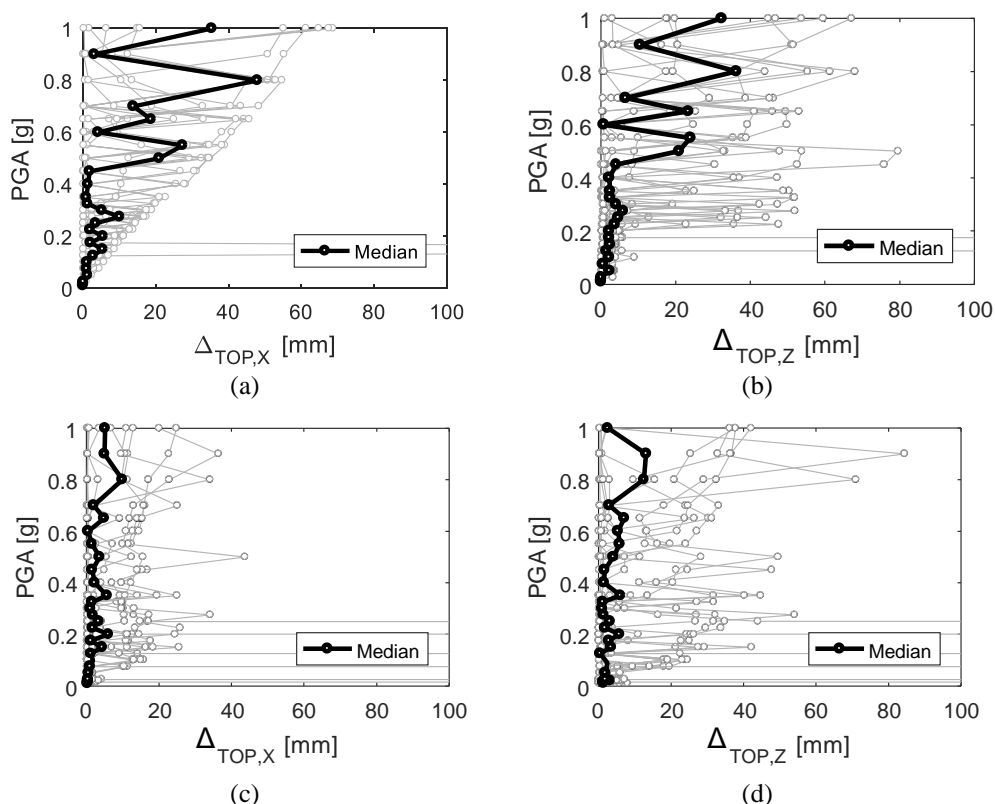
Figure 8.9. IDA curves for building 8P35_SL in the X (a-c) and Z (b-d) directions for the W/ (a-b) and the W/O (c-d) models.

8.6. ASSESSMENT OF THE OOP COLLAPSE PGA AND IDR

In this section, for each one of the 48 case-study infilled buildings, the PGA associated with the first OOP collapse of infills (PGA_c) and the IDR demand associated with the first infill collapsed due to OOP actions (IDR_c) is assessed. Clearly, for each case-study building, ten values of PGA_c and IDR_c are obtained from structural analyses (one for each record). The values herein compared and commented are the average of such ten values.

Clearly, both PGA_c and IDR_c are evaluated on the W/ and on the W/O model. This allows the assessment of the influence on such paramount values of the IP/OOP interaction. The values of PGA_c and IDR_c assessed on W/ models are compared with those obtained in a non-linear static framework reported in Chapter VII for the WL and

SL case-study buildings.

The results obtained in terms of PGA_c and of IDR_c are summarized in fragility curves showing the probability of OOP collapse of infills at increasing PGA demand and maximum IDR demand. In addition, frequency distributions showing the number of first OOP collapses registered during analyses for each storey of each case-study buildings are shown. Also these results are compared with the analogous ones obtained in a non-linear static framework and discussed in Chapter VII.

8.6.1. PGA_c assessment

In this section, the PGA at the first OOP collapse of infills (PGAc) is assessed for each case-study building. Of course, ten values are obtained for each case-study building, one for each record. The mean values are herein compared and discussed.

The PGA_c values on the W/O model of each case study building are reported in Table 8.7 and compared in Figures 8.10-11. It is worth to note that, even at PGA equal to 1.50 g, in many cases the OOP collapse was not observed for SL infills. Hence, the value reported in the "mean" column, in this case, is not the average of the PGA_c assessed for each record but the minimum value of the available results, in order to provide a value more similar to a lower bound of the real PGA_c of such type of infills. This circumstance is also pointed out in Figures 8.10-11, in which the PGA_c values reported for the SL layout are not represented by a continuous line but by a dashed line, instead.

Table 8.7. Values of PGA$_c$ [g] for all case-study buildings (W/O models).

Record	#1	#2	#3	#4	#5	#6	#7	#8	#9	#10	mean
2P05WL	0.550	0.500	0.500	0.600	0.600	0.650	0.700	0.550	0.700	0.700	0.605
2P15WL	0.550	0.500	0.500	0.600	0.600	0.650	0.700	0.550	0.700	0.700	0.605
2P25WL	0.550	0.500	0.500	0.600	0.600	0.650	0.700	0.550	0.700	0.700	0.605
2P35WL	0.500	0.500	0.500	0.600	0.650	0.650	0.750	0.650	0.600	0.700	0.610
4P05WL	0.650	0.650	0.700	0.500	0.550	0.400	0.350	0.550	0.500	0.650	0.550
4P15WL	0.600	0.550	0.800	0.450	0.550	0.600	0.450	0.800	0.650	0.700	0.615
4P25WL	0.650	0.800	0.450	0.600	0.400	0.500	0.350	0.800	0.500	0.600	0.565
4P35WL	0.650	0.550	0.550	0.600	0.600	0.600	0.500	0.650	0.550	0.650	0.590
6P05WL	0.600	0.550	0.400	0.600	0.300	0.500	0.350	0.400	0.500	0.400	0.460
6P15WL	0.500	0.550	0.550	0.700	0.400	0.450	0.275	0.400	0.450	0.550	0.483
6P25WL	0.650	0.650	0.450	0.650	0.400	0.700	0.500	0.550	0.450	0.450	0.545
6P35WL	0.550	0.600	0.450	0.600	0.500	0.900	0.450	0.600	0.400	0.600	0.565
8P05WL	0.400	0.400	0.325	0.350	0.350	0.400	0.300	0.550	0.500	0.350	0.393
8P15WL	0.550	0.400	0.275	0.450	0.550	0.550	0.300	0.450	0.500	0.550	0.458
8P25WL	0.600	0.400	0.350	0.500	0.500	0.700	0.400	0.450	0.600	0.550	0.505
8P35WL	0.600	0.300	0.450	0.500	0.550	0.700	0.550	0.600	0.800	0.700	0.575
2P05ML	1.400	1.000	1.300	0.900	0.500	0.700	0.450	0.900	1.100	1.100	0.935
2P15ML	0.900	1.200	0.800	1.100	0.700	0.900	0.550	1.000	1.100	1.000	0.925
2P25ML	1.300	0.700	0.900	0.900	0.500	0.900	0.450	1.100	1.100	0.900	0.875
2P35ML	0.900	0.800	0.800	1.200	0.700	0.800	0.450	1.100	1.200	1.100	0.905
4P05ML	0.900	0.800	1.000	0.800	0.700	0.900	0.650	0.800	0.700	1.000	0.825
4P15ML	0.700	0.800	1.200	0.700	0.900	0.600	0.600	1.000	1.300	0.800	0.860
4P25ML	0.900	1.200	0.900	0.650	0.800	0.800	0.650	1.200	0.900	1.100	0.910
4P35ML	0.800	0.800	1.100	1.100	0.800	0.900	0.550	0.900	1.000	1.100	0.905
6P05ML	0.800	1.000	0.650	0.900	0.450	0.700	0.600	0.600	0.600	0.450	0.675
6P15ML	1.000	0.650	0.900	1.200	0.600	0.700	0.350	0.700	0.900	0.800	0.780
6P25ML	0.600	0.650	0.550	0.800	0.600	0.700	0.600	0.600	1.000	0.550	0.665
6P35ML	0.800	1.000	1.000	0.700	0.550	0.800	0.800	0.900	0.650	0.700	0.790
8P05ML	1.000	0.650	0.600	0.650	0.550	0.600	0.500	0.700	0.700	0.600	0.655
8P15ML	0.600	0.450	0.400	0.700	0.600	0.700	0.350	0.700	0.650	0.700	0.585
8P25ML	0.700	0.600	0.550	0.800	0.600	0.900	0.650	0.800	1.000	0.800	0.740
8P35ML	1.000	0.500	0.550	0.800	1.000	1.000	0.700	0.800	1.000	1.100	0.845
2P05SL	n/a	n/a	n/a	n/a	1.200	n/a	1.100	n/a	n/a	n/a	1.100
2P15SL	n/a	n/a	n/a	n/a	1.400	n/a	0.800	n/a	n/a	n/a	0.800
2P25SL	n/a	n/a	n/a	n/a	1.200	n/a	1.300	n/a	n/a	n/a	1.200
2P35SL	n/a	n/a	n/a	n/a	n/a	n/a	1.400	n/a	n/a	n/a	1.400
4P05SL	n/a	n/a	n/a	n/a	n/a	1.400	1.400	1.500	n/a	n/a	1.400
4P15SL	n/a	n/a	n/a	n/a	n/a	1.400	1.100	n/a	n/a	n/a	1.100
4P25SL	n/a	n/a	n/a	n/a	n/a	n/a	1.200	n/a	n/a	n/a	1.200
4P35SL	n/a	n/a	n/a	n/a	1.200	n/a	n/a	n/a	n/a	n/a	1.200
6P05SL	1.400	n/a	n/a	n/a	1.000	1.500	1.000	1.300	n/a	1.400	1.000
6P15SL	n/a	n/a	n/a	n/a	1.100	1.500	1.100	1.200	1.500	n/a	1.100
6P25SL	n/a	n/a	1.400	n/a	1.500	n/a	1.100	1.300	n/a	1.100	1.100
6P35SL	n/a	1.400	n/a	n/a	1.300	n/a	1.400	n/a	n/a	1.400	1.300
8P05SL	n/a	1.400	1.300	1.500	1.100	1.200	1.200	n/a	1.400	1.100	1.100
8P15SL	n/a	0.900	0.800	n/a	n/a	n/a	1.000	1.100	n/a	1.200	0.800
8P25SL	n/a	1.300	1.400	n/a	n/a	n/a	1.400	n/a	n/a	1.400	1.300
8P35SL	n/a	1.200	1.300	n/a	n/a	n/a	n/a	n/a	n/a	1.500	1.200
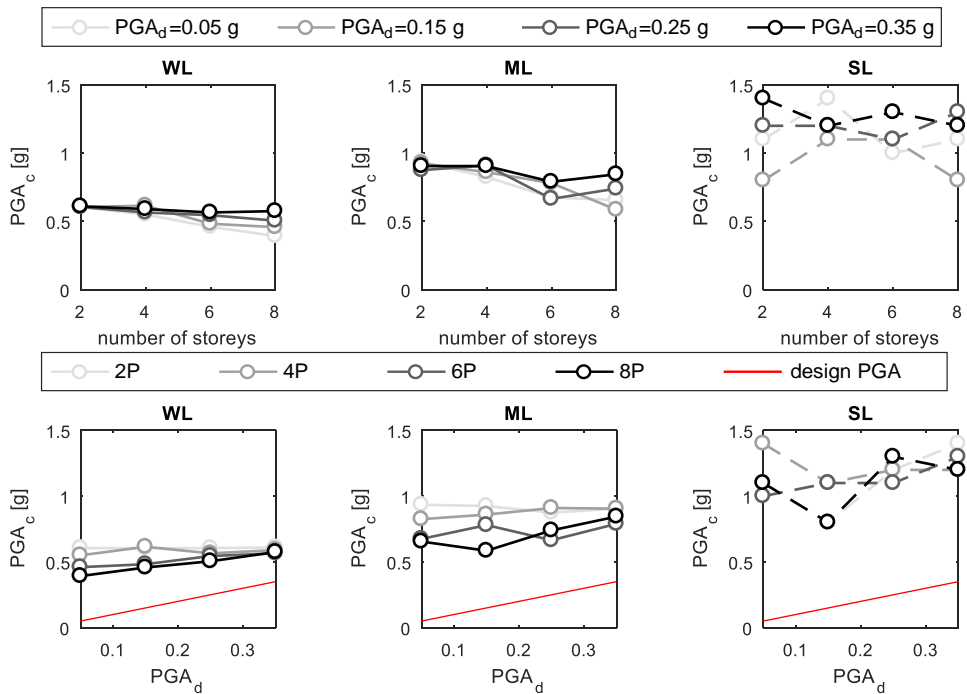
Figure 8.10. Mean PGA$_c$ values on the W/O models for all case-study buildings.
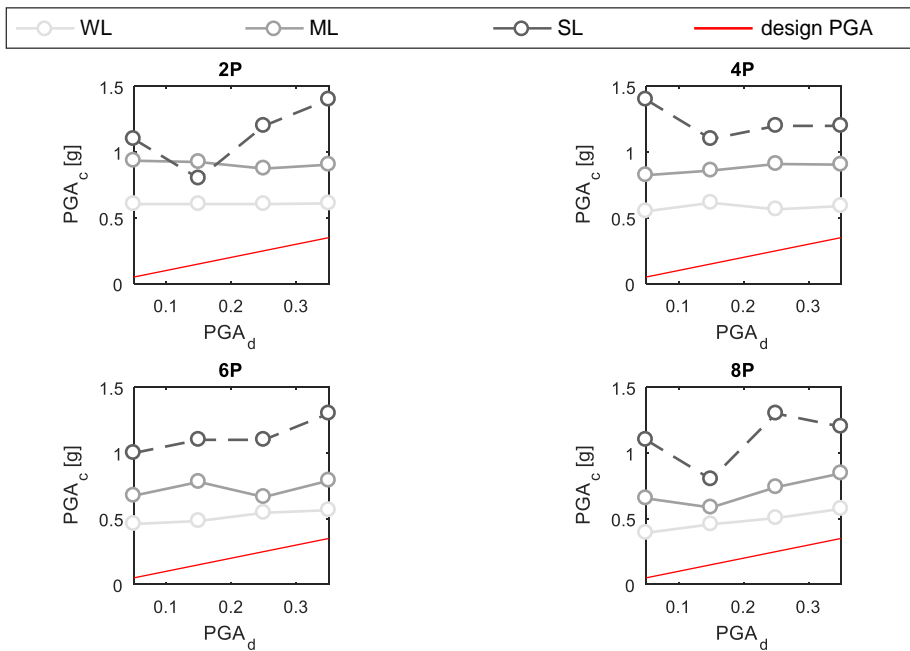
Figure 8.11. Mean PGA$_c$ values on the W/O models for all case-study buildings.

Remember that in W/O models the OOP collapse of infills always occurs at the building last storey. It is observed that PGA_c decreases at increasing number of storeys, which is expected, as in higher building the OOP seismic demand at the last storey is higher with respect to lower buildings. In addition, PGA_c does not show a clear tendency with the design PGA, most likely due to the influence of record-to-record variability on the OOP seismic demand, which is also dependent on the relationship existing between the OOP period of the infill and the vibration period of the building. Note that all trends for SL layouts are not very clear, most likely because the values reported and compared are not, as already stated, an average value but a lower bound value obtained from a reduced number of analyses performed up to the OOP collapse of such a type of infills.

Clearly, as expected, due to the higher OOP undamaged strength, SL buildings are provided with a significantly higher PGA_c with respect to WL and ML infills.

If the IP/OOP interaction is neglected, all buildings result safe with respect to the OOP collapse of infills, as for all infill layouts PGA_c is always higher than the design PGA at LS.

The PGA_c values on the W/ model of each case study building are reported in Table 8.8 and compared in Figure 8.12-13.

Table 8.8. Values of PGA$_c$ [g] for all case-study buildings (W/ models).

| Record	#1	#2	#3	#4	#5	#6	#7	#8	#9	#10	mean
2P05WL	0.275	0.275	0.275	0.275	0.150	0.250	0.100	0.275	0.275	0.275	0.243
2P15WL	0.275	0.275	0.275	0.275	0.150	0.250	0.100	0.275	0.275	0.275	0.243
2P25WL	0.275	0.275	0.275	0.275	0.150	0.250	0.100	0.275	0.275	0.275	0.243
2P35WL	0.300	0.275	0.275	0.300	0.175	0.250	0.125	0.275	0.275	0.275	0.253
4P05WL	0.250	0.225	0.250	0.175	0.175	0.200	0.125	0.200	0.225	0.275	0.210
4P15WL	0.250	0.250	0.275	0.200	0.200	0.225	0.150	0.275	0.250	0.275	0.235
4P25WL	0.250	0.275	0.225	0.200	0.200	0.250	0.125	0.300	0.250	0.275	0.235
4P35WL	0.250	0.275	0.275	0.275	0.200	0.250	0.150	0.275	0.275	0.275	0.250
6P05WL	0.200	0.200	0.175	0.200	0.100	0.200	0.100	0.175	0.150	0.150	0.165
6P15WL	0.225	0.200	0.225	0.250	0.175	0.225	0.100	0.200	0.200	0.175	0.198
6P25WL	0.225	0.225	0.200	0.250	0.175	0.250	0.150	0.200	0.200	0.175	0.205
6P35WL	0.225	0.225	0.225	0.225	0.200	0.300	0.200	0.200	0.200	0.225	0.223
8P05WL	0.200	0.100	0.100	0.150	0.125	0.150	0.100	0.225	0.225	0.150	0.153
8P15WL	0.200	0.100	0.075	0.200	0.200	0.250	0.100	0.225	0.250	0.175	0.178
8P25WL	0.200	0.125	0.125	0.250	0.200	0.250	0.175	0.225	0.250	0.175	0.198
8P35WL	0.200	0.125	0.125	0.225	0.250	0.250	0.225	0.250	0.275	0.250	0.218
2P05ML	0.450	0.350	0.400	0.400	0.225	0.325	0.200	0.350	0.350	0.325	0.338
2P15ML	0.400	0.350	0.350	0.350	0.275	0.350	0.150	0.400	0.350	0.325	0.330
2P25ML	0.450	0.325	0.350	0.350	0.200	0.400	0.175	0.325	0.400	0.350	0.333
2P35ML	0.400	0.350	0.350	0.400	0.225	0.300	0.200	0.325	0.400	0.350	0.330
4P05ML	0.325	0.325	0.300	0.275	0.275	0.275	0.225	0.300	0.325	0.350	0.298
4P15ML	0.325	0.300	0.400	0.325	0.300	0.275	0.225	0.450	0.400	0.350	0.335
4P25ML	0.300	0.400	0.300	0.275	0.300	0.350	0.225	0.450	0.350	0.400	0.335
4P35ML	0.350	0.325	0.350	0.350	0.250	0.275	0.225	0.325	0.400	0.325	0.318
6P05ML	0.275	0.300	0.275	0.300	0.175	0.275	0.200	0.250	0.225	0.200	0.248
6P15ML	0.300	0.300	0.325	0.400	0.225	0.275	0.150	0.275	0.300	0.250	0.280
6P25ML	0.275	0.225	0.250	0.325	0.250	0.325	0.200	0.250	0.325	0.200	0.263
6P35ML	0.325	0.300	0.350	0.275	0.250	0.350	0.250	0.325	0.250	0.250	0.293
8P05ML	0.325	0.200	0.175	0.225	0.200	0.225	0.175	0.300	0.300	0.225	0.235
8P15ML	0.275	0.150	0.125	0.300	0.275	0.325	0.125	0.250	0.300	0.275	0.240
8P25ML	0.275	0.200	0.225	0.350	0.250	0.400	0.225	0.300	0.350	0.250	0.283
8P35ML	0.300	0.225	0.250	0.300	0.300	0.350	0.300	0.350	0.400	0.325	0.310
2P05SL	0.800	0.900	0.700	0.700	0.500	0.800	0.450	0.700	0.700	0.800	0.705
2P15SL	1.000	0.900	0.800	0.800	0.500	0.650	0.325	0.800	0.900	0.900	0.758
2P25SL	1.100	0.800	0.900	0.700	0.400	0.700	0.450	0.650	0.700	0.900	0.730
2P35SL	1.000	0.700	0.900	0.900	0.500	0.600	0.450	0.800	0.800	0.650	0.730
4P05SL	0.800	0.650	0.800	0.700	0.700	0.600	0.550	0.650	0.800	0.800	0.705
4P15SL	0.650	0.650	0.900	0.700	0.700	0.600	0.450	0.900	0.700	0.900	0.715
4P25SL	0.700	0.900	0.650	0.650	0.650	0.800	0.500	1.200	0.900	0.900	0.785
4P35SL	0.800	0.800	0.650	0.800	0.500	0.650	0.550	0.800	0.900	0.700	0.715
6P05SL	0.550	0.800	0.700	0.700	0.350	0.650	0.350	0.550	0.550	0.400	0.560
6P15SL	0.650	0.700	0.650	0.800	0.450	0.650	0.400	0.500	0.600	0.600	0.600
6P25SL	0.700	0.600	0.600	0.700	0.600	0.800	0.350	0.550	0.700	0.450	0.605
6P35SL	0.900	0.600	0.650	0.550	0.500	0.700	0.600	0.700	0.650	0.600	0.645
8P05SL	0.700	0.500	0.400	0.500	0.400	0.500	0.350	0.600	0.600	0.400	0.495
8P15SL	0.650	0.325	0.325	0.600	0.550	0.700	0.350	0.450	0.600	0.500	0.505
8P25SL	0.650	0.350	0.550	0.700	0.600	0.900	0.400	0.650	0.900	0.550	0.625
8P35SL	0.700	0.500	0.450	0.700	0.800	1.000	0.550	0.700	1.000	0.650	0.705
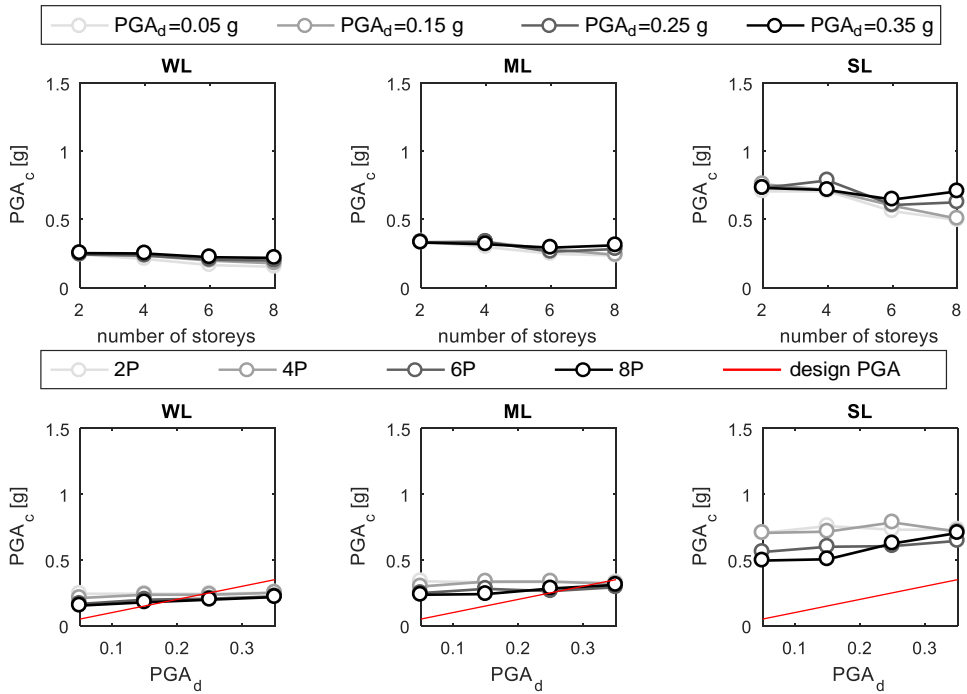
Figure 8.12. Mean PGA_c values on the W/ models for all case-study buildings.
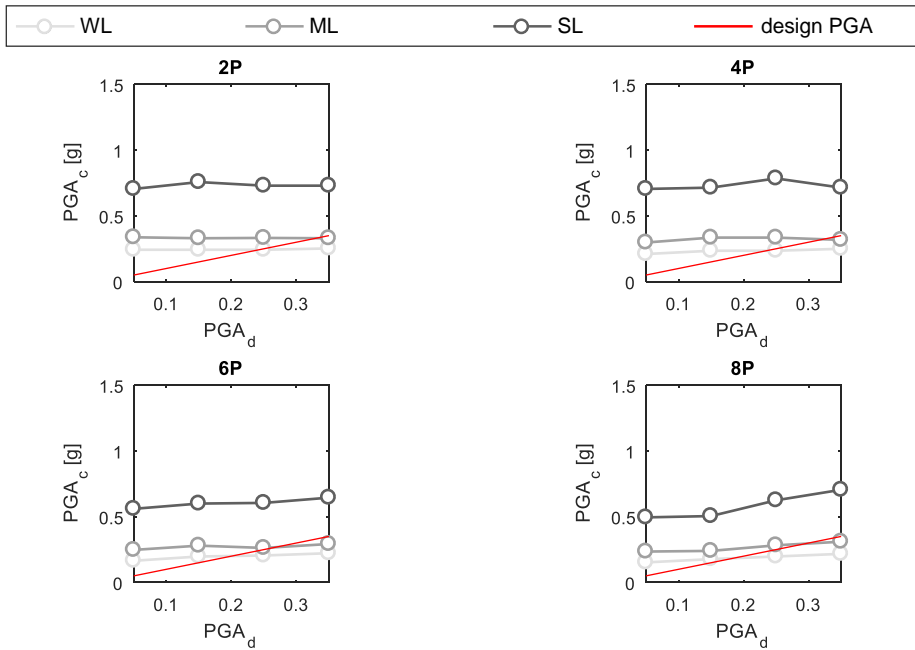
Figure 8.13. Mean PGA_c values on the W/ models for all case-study buildings.

It is observed that PGA_c is quite independent on the design PGA and on the total number of storeys of the building for WL and ML infills. However, some trends are slightly visible, with PGA_c decreasing at increasing number of storeys, which is expected, as higher buildings – being more deformable – are more prone to the IP/OOP interaction, and increasing at increasing design PGA, which is also expected, as buildings designed for higher seismic acceleration – being more stiff – are less prone to the IP/OOP interaction. Such trends were also visible in Chapter VII, in which PGA_c was assessed in a non-linear static framework. In addition, such trends are more visible for the SL buildings.

Clearly, as expected, due to the higher OOP undamaged strength and to the lower impact of the IP/OOP interaction effect, SL buildings are provided with a significantly higher PGA_c with respect to WL and ML infills.

As also observed in Chapter VII, mid- and high-rise buildings in mid- and high-seismicity zones are not safe with respect to the OOP failure of infills if WL and ML infills are used. Only SL infills are always safe with respect to the IP/OOP interaction, as also observed in Chapter VII, even if with a lower safety margin with respect to that assessed in a non-linear static framework.

It is clear from the comparison of the results obtained on the W/O and on the W/ models that accounting for the IP/OOP interaction is necessary to not perform an unsafe assessment of the seismic performance of buildings at LS.

In Figures 8.14 and 8.15, fragility curves relating the probability of OOP collapse to the PGA value are shown, separately for each infill layout considered. More specifically, in Figure 8.14 the fragility curves for the three infill layouts are compared for the W/ and the W/O models. Their parameters (the median and the logarithmic standard deviation) are reported in Table 8.9.

Each fragility curve contains in its parameters the record-to-record variability as well as the variability of PGA_c associated with the variation of the buildings' number of storeys and design PGA. In other words, one can enter such fragility curves only knowing the infill typology and without knowing the building number of storeys and design PGA, i.e., by assuming an equal probability that the considered building is characterized by a number of storeys equal to 2, 4, 6 or 8 and by a design PGA equal to 0.05 g, 0.15 g, 0.25 g and 0.35 g.

Table 8.9. Fragility curves parameters (PGA$_c$) determined based on the results of the non-linear time-history analyses.

	WL		ML		SL	
	W/O	W/	W/O	W/	W/O	W/
median	0.600	0.232	0.881	0.329	1.25	0.691
log. st. dev.	0.237	0.397	0.282	0.254	0.154	0.275
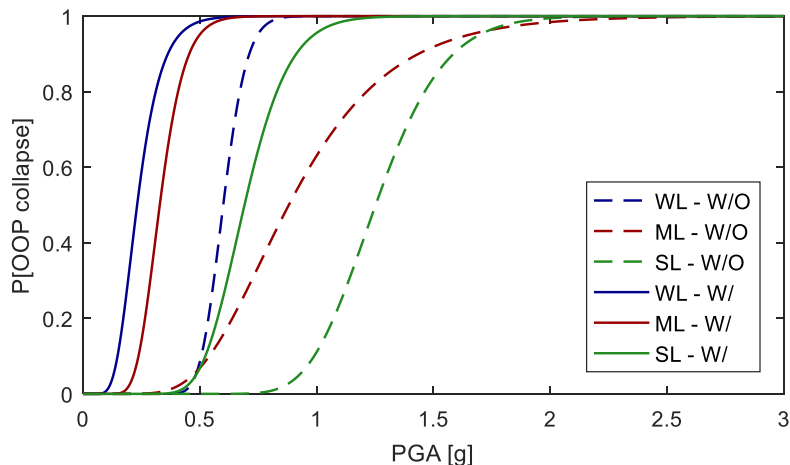
Figure 8.14. Fragility curves (PGA$_c$): comparison of the results obtained by means of non-linear time-history analyses on W/ models (continuous lines) and on W/O models (dashed lines) for all the case-study buildings.

As expected, a greater fragility is observed for W/ models. Remember that for the W/O models of SL buildings, the PGA values used for the construction of the fragility curves are more similar to a lower bound of the real PGA$_c$, and, hence, also the fragility curve reported is more similar to a "lower bound" fragility curve.

In Figure 8.15, the fragility curves for the WL and the SL layout obtained on the W/ model are compared with those obtained by applying the Reference Approach, i.e., with those determined in a non-linear static framework, shown in Chapter VII.
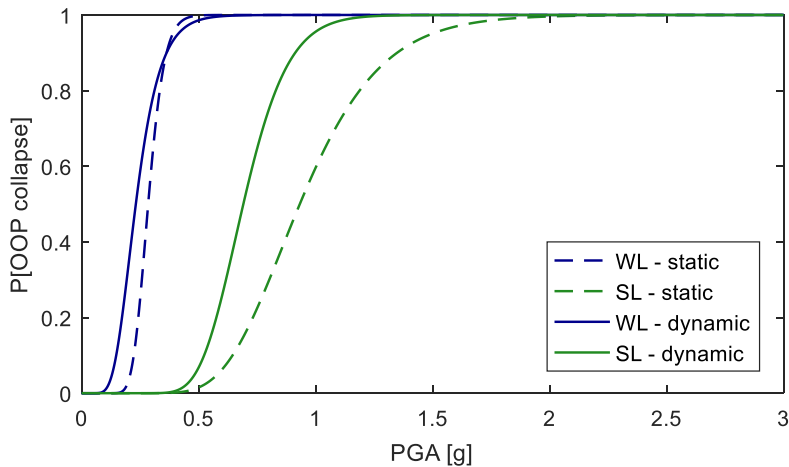
Figure 8.15. Fragility curves (PGA_c): comparison of the results obtained by means of non-linear time-history analyses (continuous lines) with those obtained by means of non-linear static analyses (dashed lines).

A greater fragility is observed for both WL and SL infills (especially for the least) when dealing with the results of non-linear time-history analyses. Most likely, this is due to the unconservative assumptions made to apply the so-called "Reference Approach" in Chapter VII and above all, among these, for the fact that the non-linear static approach adopted in Chapter VII does not account for the OOP damage effect on the IP response of infills. This circumstance, in fact, produces the underestimation of the infilled building lateral deformability, so the underestimation of drift demands and, hence, the underestimation of the IP/OOP interaction effects.

8.6.2. IDR$_c$ assessment

In this section, the IDR at the first OOP collapse of infills (IDR$_c$) is assessed for each case-study building. Of course, ten values are obtained for each case-study building, one for each record. The mean values are herein compared and discussed.

The IDR$_c$ values on the W/O model of each case study building are reported in Table 8.10 and compared in Figures 8.16-17. In the same Figures, the IDR$_c$ values are compared, for each infill layout, with the corresponding IDR at the IP collapse, i.e., at the complete loss of IP resistance, predicted by means of Panagiotakos and Fardis's model. It is observed that the OOP collapse of WL and ML infills always foreruns the IP collapse, while SL infills collapse for IP actions prior than for OOP actions.

As already stated in the previous subsection, even at PGA equal to 1.50 g, in many cases the OOP collapse was not observed for SL infills. Hence, the value reported in the "mean" column, in this case, is not the average of the IDR_c assessed for each record but the minimum value of the available results, in order to provide a value more similar to a lower bound of the real IDR_c of such type of infills. This circumstance is also pointed out in Figures 8.16-17, in which the IDR_c values reported for the SL layout are not represented by a continuous line but by a dashed line, instead.

Table 8.10. Values of IDR$_c$ [%] for all case-study buildings (W/O models).

| Record	#1	#2	#3	#4	#5	#6	#7	#8	#9	#10	mean
2P05WL	1.183	0.552	0.571	1.281	0.700	0.696	0.716	0.684	1.179	1.819	0.938
2P15WL	1.183	0.552	0.571	1.281	0.700	0.696	0.716	0.684	1.179	1.819	0.938
2P25WL	1.183	0.552	0.571	1.281	0.700	0.696	0.716	0.684	1.179	1.819	0.938
2P35WL	1.224	0.534	0.470	1.110	0.624	0.663	0.572	0.541	0.856	1.414	0.801
4P05WL	1.186	0.691	0.619	1.133	0.678	0.600	0.680	0.755	1.180	2.110	0.963
4P15WL	1.093	0.628	0.561	1.032	0.678	0.643	0.669	0.511	1.073	1.838	0.873
4P25WL	1.214	0.484	0.540	1.035	0.646	0.653	0.562	0.588	1.007	1.583	0.831
4P35WL	1.077	0.469	0.394	0.884	0.457	0.553	0.446	0.414	0.734	1.354	0.678
6P05WL	1.490	0.744	0.589	1.073	0.597	0.641	0.785	0.606	1.017	1.862	0.940
6P15WL	1.089	0.583	0.559	1.113	0.688	0.671	0.657	0.531	1.001	1.636	0.853
6P25WL	1.027	0.422	0.487	1.052	0.624	0.665	0.681	0.443	0.993	1.677	0.807
6P35WL	1.055	0.531	0.442	0.946	0.521	0.561	0.419	0.444	0.931	1.158	0.701
8P05WL	1.279	0.619	0.556	1.184	0.574	0.585	0.802	0.638	1.127	1.851	0.921
8P15WL	1.318	0.602	0.478	1.029	0.719	0.694	0.657	0.542	1.037	1.672	0.875
8P25WL	1.088	0.518	0.437	1.177	0.566	0.706	0.576	0.560	0.868	1.414	0.791
8P35WL	0.974	0.441	0.391	1.021	0.495	0.551	0.471	0.441	0.802	1.248	0.684
2P05ML	1.302	0.719	0.621	1.230	0.652	0.844	0.809	0.725	1.294	1.871	1.007
2P15ML	1.302	0.719	0.621	1.230	0.652	0.844	0.809	0.725	1.294	1.871	1.007
2P25ML	1.302	0.719	0.621	1.230	0.652	0.844	0.809	0.725	1.294	1.871	1.007
2P35ML	1.271	0.599	0.537	1.239	0.621	0.874	0.629	0.554	1.182	1.617	0.912
4P05ML	1.365	0.745	0.659	1.466	0.699	0.728	0.731	0.800	1.259	2.120	1.057
4P15ML	1.136	0.657	0.635	1.269	0.735	0.739	0.706	0.659	1.356	2.148	1.004
4P25ML	1.407	0.543	0.497	1.095	0.620	0.760	0.641	0.660	1.023	1.643	0.889
4P35ML	1.148	0.545	0.411	0.905	0.648	0.627	0.559	0.507	0.848	1.355	0.755
6P05ML	1.544	0.939	0.654	1.316	0.559	0.606	0.835	0.757	1.278	2.257	1.074
6P15ML	1.285	0.691	0.626	1.033	0.658	0.707	0.680	0.618	0.985	1.747	0.903
6P25ML	1.381	0.564	0.542	1.387	0.675	0.693	0.754	0.603	1.227	1.883	0.971
6P35ML	1.206	0.560	0.404	1.120	0.535	0.699	0.545	0.491	1.006	1.500	0.807
8P05ML	1.507	0.700	0.636	1.516	0.704	0.624	0.768	0.763	1.041	2.260	1.052
8P15ML	1.342	0.668	0.477	1.139	0.777	0.797	0.705	0.729	1.183	1.895	0.971
8P25ML	1.329	0.468	0.541	1.253	0.748	0.727	0.635	0.622	1.074	1.778	0.918
8P35ML	1.147	0.504	0.467	0.984	0.495	0.653	0.612	0.586	0.901	1.273	0.762
2P05SL	n/a	n/a	n/a	n/a	5.43	n/a	5.91	n/a	n/a	n/a	5.426
2P15SL	n/a	n/a	n/a	n/a	5.43	n/a	5.91	n/a	n/a	n/a	5.426
2P25SL	n/a	n/a	n/a	n/a	5.43	n/a	5.91	n/a	n/a	n/a	5.426
2P35SL	n/a	n/a	n/a	n/a	n/a	n/a	4.98	n/a	n/a	n/a	4.984
4P05SL	n/a	n/a	n/a	n/a	n/a	5.52	5.8	5.95	n/a	n/a	5.524
4P15SL	n/a	n/a	n/a	n/a	n/a	5.88	6.03	n/a	n/a	n/a	5.878
4P25SL	n/a	n/a	n/a	n/a	n/a	n/a	4.81	n/a	n/a	n/a	4.812
4P35SL	n/a	n/a	n/a	n/a	5.02	n/a	n/a	n/a	n/a	n/a	5.022
6P05SL	11.09	n/a	n/a	n/a	4.51	4.81	6.42	6.31	n/a	15.06	4.512
6P15SL	n/a	n/a	n/a	n/a	5.58	5.79	5.57	4.59	7.619	n/a	4.593
6P25SL	n/a	n/a	4.15	n/a	5.86	n/a	5.57	4.59	n/a	13.58	4.150
6P35SL	n/a	4.057	n/a	n/a	3.95	n/a	4.02	n/a	n/a	11.52	3.946
8P05SL	n/a	5.777	4.66	11.36	4.93	5.16	6.13	n/a	8.546	15.65	4.660
8P15SL	n/a	5.573	3.69	n/a	n/a	n/a	5.68	5.41	n/a	12.43	3.692
8P25SL	n/a	3.975	4.22	n/a	n/a	n/a	5.63	n/a	n/a	12.02	3.975
8P35SL	n/a	3.554	3.5	n/a	n/a	n/a	n/a	n/a	n/a	11.88	3.499
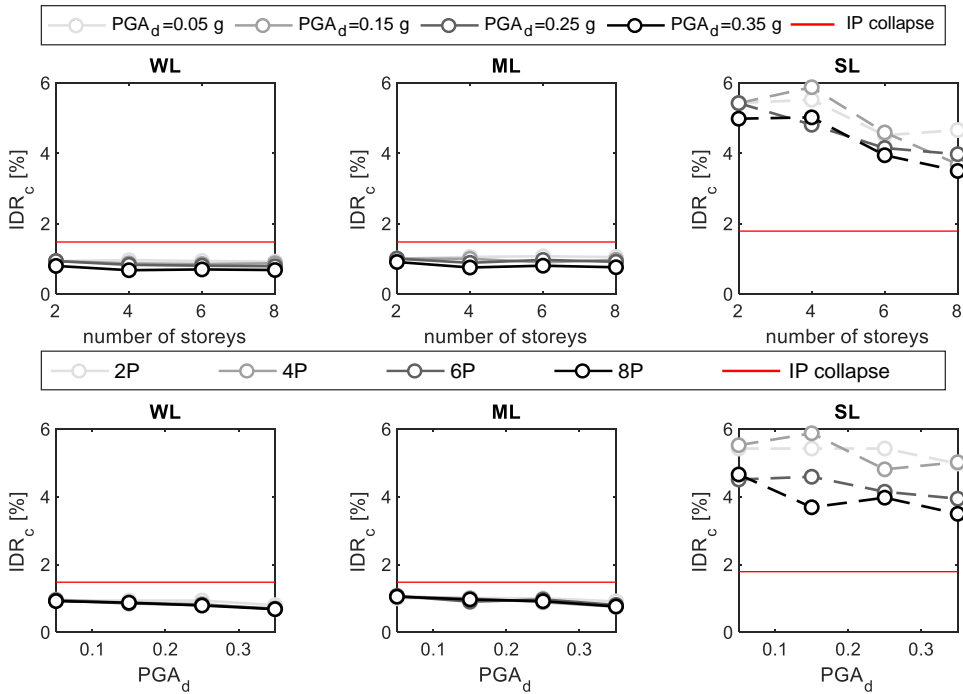
Figure 8.16. Mean IDR$_c$ values on the W/O models for all case-study buildings.
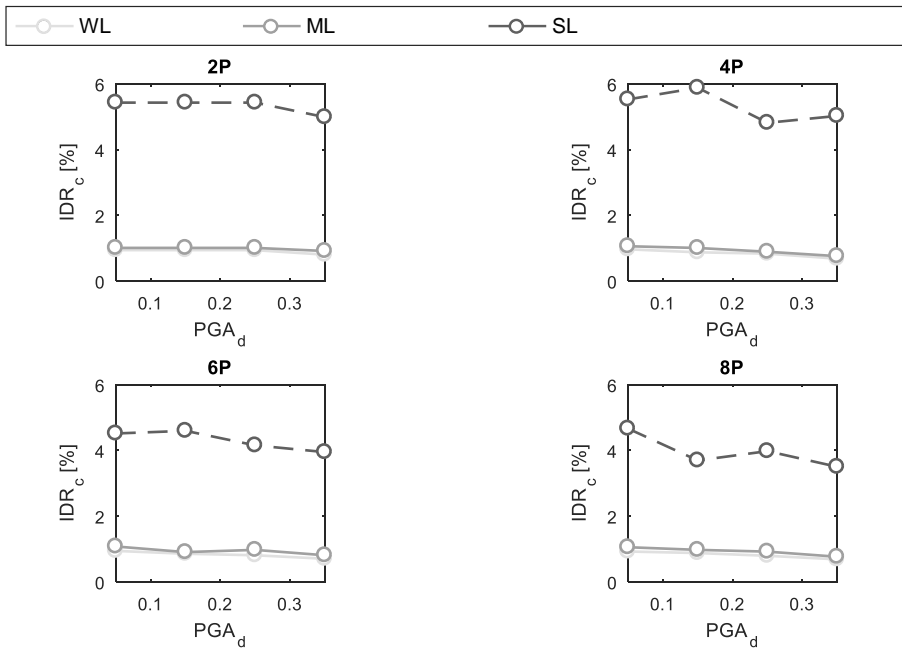
Figure 8.17. Mean IDR$_c$ values on the W/O models for all case-study buildings.

Remember that in W/O models the OOP collapse of infills always occurs at the building last storey. It is quite surprising to observe that the IDR capacity of infills with respect to the first OOP collapse is quite independent on the design PGA and on the number of storeys.

Clearly, as expected, due to the higher OOP undamaged strength, SL buildings are provided with a significantly higher PGA_c with respect to WL and ML infills. At such a higher PGA demand, a higher IDR demand is expected and, hence, a higher IDR_c, too.

The IDR_c values on the W/ model of each case study building are reported in Table 8.11 and compared in Figure 8.18-19. Also in this case, the IDR_c values are compared, for each infill layout, with the corresponding IDR at the IP collapse, i.e., at the complete loss of IP resistance, predicted by means of Panagiotakos and Fardis's model. It is observed that the OOP collapse of WL and ML infills always foreruns the IP collapse, while SL infills collapse for IP actions prior than for OOP actions.

Table 8.11. Values of IDR$_c$ [%] for all case-study buildings (W/ models).

| Record	#1	#2	#3	#4	#5	#6	#7	#8	#9	#10	mean
2P05WL	0.414	0.202	0.190	0.398	0.213	0.247	0.227	0.208	0.364	0.611	0.307
2P15WL	0.414	0.202	0.190	0.398	0.213	0.247	0.227	0.208	0.364	0.611	0.307
2P25WL	0.414	0.202	0.190	0.398	0.213	0.247	0.227	0.208	0.364	0.611	0.307
2P35WL	0.387	0.175	0.167	0.372	0.203	0.231	0.186	0.180	0.306	0.503	0.271
4P05WL	0.422	0.222	0.198	0.402	0.209	0.222	0.250	0.229	0.389	0.665	0.321
4P15WL	0.385	0.200	0.186	0.366	0.211	0.230	0.225	0.189	0.357	0.604	0.295
4P25WL	0.372	0.172	0.166	0.362	0.200	0.215	0.193	0.179	0.331	0.519	0.271
4P35WL	0.329	0.148	0.141	0.309	0.166	0.201	0.158	0.147	0.272	0.433	0.230
6P05WL	0.464	0.242	0.184	0.378	0.188	0.209	0.250	0.220	0.370	0.672	0.318
6P15WL	0.366	0.216	0.188	0.340	0.219	0.216	0.230	0.170	0.332	0.562	0.284
6P25WL	0.376	0.155	0.157	0.369	0.218	0.210	0.209	0.163	0.351	0.555	0.276
6P35WL	0.359	0.163	0.141	0.309	0.183	0.197	0.153	0.155	0.288	0.424	0.237
8P05WL	0.426	0.216	0.206	0.410	0.204	0.207	0.245	0.229	0.354	0.619	0.312
8P15WL	0.412	0.212	0.175	0.359	0.228	0.220	0.230	0.193	0.374	0.550	0.295
8P25WL	0.398	0.160	0.161	0.391	0.208	0.225	0.193	0.182	0.315	0.483	0.272
8P35WL	0.333	0.154	0.131	0.334	0.166	0.201	0.172	0.162	0.288	0.394	0.233
2P05ML	0.480	0.220	0.202	0.457	0.251	0.269	0.237	0.222	0.382	0.672	0.339
2P15ML	0.480	0.220	0.202	0.457	0.251	0.269	0.237	0.222	0.382	0.672	0.339
2P25ML	0.480	0.220	0.202	0.457	0.251	0.269	0.237	0.222	0.382	0.672	0.339
2P35ML	0.457	0.182	0.179	0.384	0.221	0.266	0.200	0.190	0.364	0.574	0.302
4P05ML	0.498	0.233	0.220	0.458	0.219	0.229	0.268	0.247	0.459	0.785	0.362
4P15ML	0.412	0.208	0.209	0.439	0.247	0.259	0.241	0.218	0.417	0.659	0.331
4P25ML	0.436	0.175	0.172	0.391	0.222	0.258	0.203	0.207	0.338	0.602	0.300
4P35ML	0.385	0.169	0.141	0.324	0.199	0.217	0.188	0.156	0.288	0.502	0.257
6P05ML	0.474	0.291	0.202	0.419	0.193	0.221	0.280	0.252	0.422	0.733	0.349
6P15ML	0.439	0.255	0.220	0.368	0.230	0.222	0.248	0.203	0.332	0.590	0.311
6P25ML	0.451	0.176	0.167	0.432	0.246	0.248	0.251	0.195	0.404	0.600	0.317
6P35ML	0.384	0.170	0.146	0.371	0.186	0.223	0.171	0.172	0.314	0.492	0.263
8P05ML	0.507	0.235	0.220	0.475	0.219	0.225	0.250	0.236	0.358	0.693	0.342
8P15ML	0.449	0.216	0.175	0.387	0.255	0.247	0.232	0.228	0.397	0.589	0.317
8P25ML	0.458	0.171	0.175	0.457	0.231	0.246	0.220	0.197	0.362	0.579	0.310
8P35ML	0.382	0.162	0.156	0.337	0.179	0.225	0.196	0.181	0.323	0.465	0.261
2P05SL	4.104	1.784	1.591	3.747	2.027	2.340	2.100	1.935	3.255	5.601	2.848
2P15SL	4.104	1.784	1.591	3.747	2.027	2.340	2.100	1.935	3.255	5.601	2.848
2P25SL	4.104	1.784	1.591	3.747	2.027	2.340	2.100	1.935	3.255	5.601	2.848
2P35SL	3.510	1.416	1.403	3.371	1.842	2.048	1.665	1.542	2.924	4.749	2.447
4P05SL	4.423	1.947	1.772	3.504	1.853	1.860	2.120	2.193	4.107	6.667	3.045
4P15SL	3.496	1.692	1.861	3.597	2.204	1.984	2.168	1.808	3.680	5.376	2.786
4P25SL	3.660	1.388	1.456	3.143	1.965	2.242	1.711	1.861	2.908	4.714	2.505
4P35SL	3.374	1.335	1.207	2.765	1.687	1.784	1.667	1.190	2.543	4.351	2.190
6P05SL	4.177	2.573	1.615	3.672	1.699	1.660	2.437	2.257	3.453	5.517	2.906
6P15SL	3.553	2.233	1.831	2.845	2.022	1.973	2.106	1.562	2.666	4.444	2.524
6P25SL	4.008	1.428	1.460	3.408	2.166	2.071	2.029	1.658	3.342	4.678	2.625
6P35SL	3.214	1.390	1.097	3.026	1.482	1.823	1.450	1.422	2.508	4.338	2.175
8P05SL	4.307	2.038	1.750	4.150	1.686	1.844	2.100	1.781	3.210	5.927	2.879
8P15SL	3.582	1.940	1.320	3.056	2.011	1.977	1.976	2.022	3.084	4.644	2.561
8P25SL	4.069	1.349	1.507	3.650	1.808	2.101	1.877	1.619	2.778	4.465	2.522
8P35SL	3.063	1.327	1.275	2.639	1.496	1.952	1.582	1.443	2.635	4.126	2.154
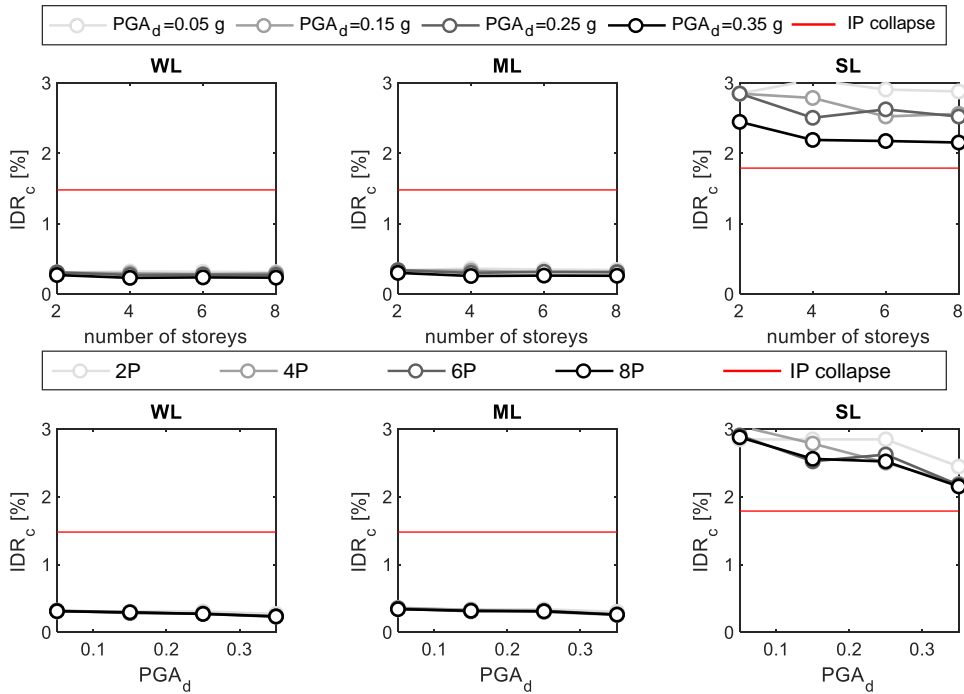
Figure 8.18. Mean IDR$_c$ values on the W/ models for all case-study buildings.
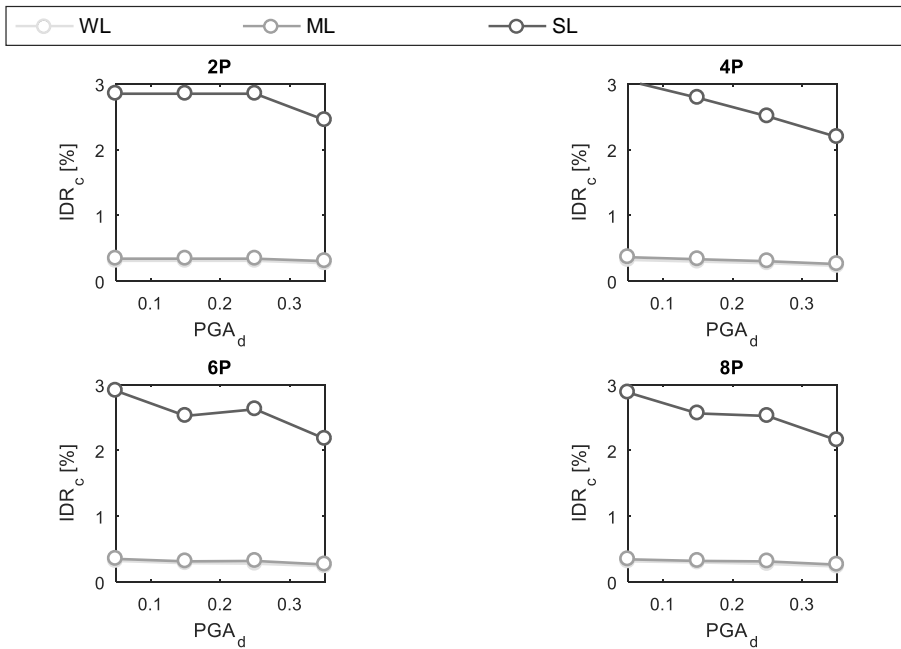
Figure 8.19. Mean IDR$_c$ values on the W/ models for all case-study buildings.

Also in this case, it is observed that IDR_c is quite independent on the design PGA and on the total number of storeys of the building for WL and ML infills. Clearly, as expected, due to the higher OOP undamaged strength and to the lower impact of the IP/OOP interaction effect, SL buildings are provided with a significantly higher IDR_c with respect to WL and ML infills. It is clear from the comparison of the results obtained on the W/O and on the W/ models that the IDR capacity with respect to the first OOP collapse is highly overestimated if the IP/OOP interaction effects are neglected.

In Figures 8.20 and 8.21, fragility curves relating the probability of OOP collapse to the IDR value are shown, separately for each infill layout considered.

More specifically, in Figure 8.20 the fragility curves for the three infill layouts are compared for the W/ and the W/O models. Their parameters (the median and the logarithmic standard deviation) are reported in Table 8.12.

Each fragility curve contains in its parameters the record-to-record variability as well as the variability of IDR_c associated with the variation of the buildings' number of storeys and design PGA. In other words, one can enter such fragility curves only knowing the infill typology and without knowing the building number of storeys and design PGA, i.e., by assuming an equal probability that the considered building is characterized by a number of storeys equal to 2, 4, 6 or 8 and by a design PGA equal to 0.05 g, 0.15 g, 0.25 g and 0.35 g.

Table 8.12. Fragility curves parameters (IDR_c) determined based on the results of the non-linear time-history analyses.

	WL		ML		SL	
	W/O	W/	W/O	W/	W/O	W/
median	0.776	0.261	0.867	0.288	6.02	2.39
log. st. dev.	0.405	0.397	0.402	0.410	0.379	0.414
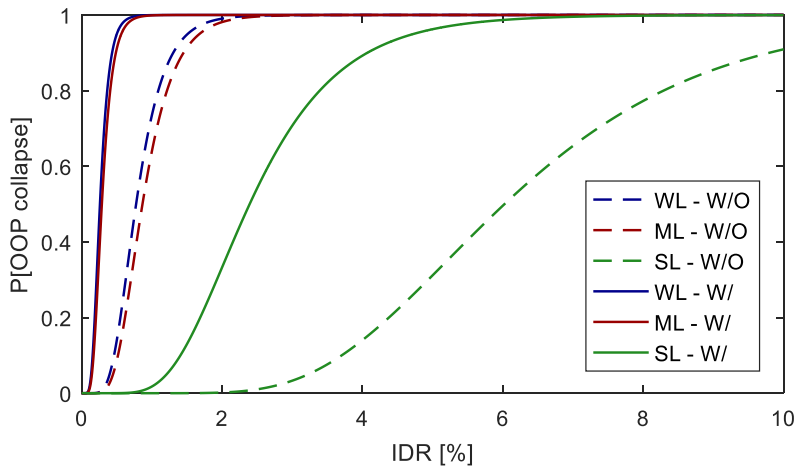
Figure 8.20. Fragility curves (IDR$_c$): comparison of the results obtained by means of non-linear time-history analyses on W/ models (continuous lines) and on W/O models (dashed lines) for all the case-study buildings.

As expected, a greater fragility is observed for W/ models. Remember that for the W/O models of SL buildings, the IDR values used for the construction of the fragility curves are more similar to a lower bound of the real IDR$_c$, and, hence, also the fragility curve reported is more similar to a "lower bound" fragility curve.

In Figure 8.21, the fragility curves for the WL and the SL layout obtained on the W/ model are compared with those obtained by applying the Reference Approach, i.e., with those determined in a non-linear static framework, shown in Chapter VII.
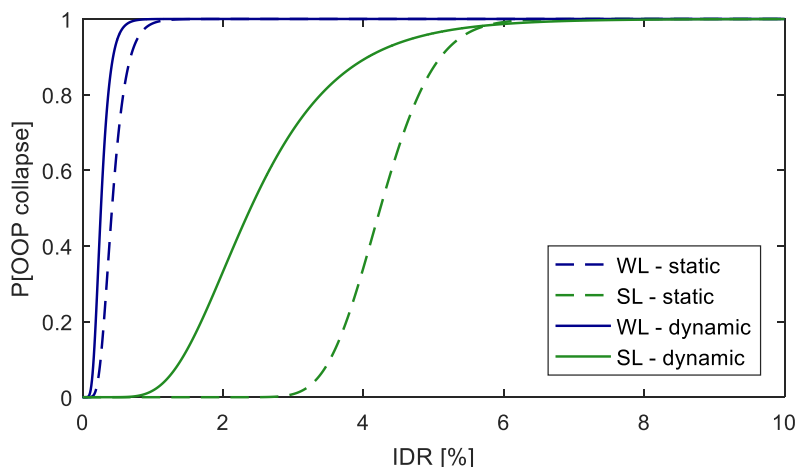
Figure 8.21. Fragility curves (IDR$_c$): comparison of the results obtained by means of non-linear time-history analyses (continuous lines) with those obtained by means of non-linear static analyses (dashed lines).

A greater fragility is observed for both WL and SL infills (especially for the least) when dealing with the results of non-linear time-history analyses, most likely due to the unconservative assumptions of the non-linear static approach, namely the absence of OOP effects on the IP behaviour of infills.

8.6.3. Location of the first OOP collapse

In this section, the issue of the location at which the first OOP collapse occurs is discussed. Of course, in the case of W/O models, the first OOP collapse always occurs at the building last floor. For what concerns W/ models, the first OOP collapse occurs at intermediate-high floors, at which the maximum IP/OOP interaction effect is expected.

Remember that in Chapter VII, it was shown that in a non-linear static framework the first OOP collapse always occurs for infills in the Z direction, at the second storey for 2- and 4- storey buildings, at the third-fourth storey for 6-storey buildings, between the third and the fifth storey for 8-storey buildings.

Also in this case, the first OOP collapse always occurs in the Z direction, i.e., along the buildings' more deformable direction. In Figure 8.22, the frequency distribution of first OOP collapses is shown for each case-study building. More specifically, for each one of the 48 case-study buildings, the storeys are shaded with different shades of grey

based on the number of records (out of ten) that were characterized by the occurrence of the first OOP collapse at that storey.

(a)

(b)

SL

2P05 4P05 6P05 8P05   2P15 4P15 6P15 8P15

2P25 4P25 6P25 8P25   2P35 4P35 6P35 8P35

☐ 0 out of 10 cases   ☐ 1-2 out of 10 cases   ☐ 3-4 out of 10 cases   ■ 5 or more out of 10 cases

(c)
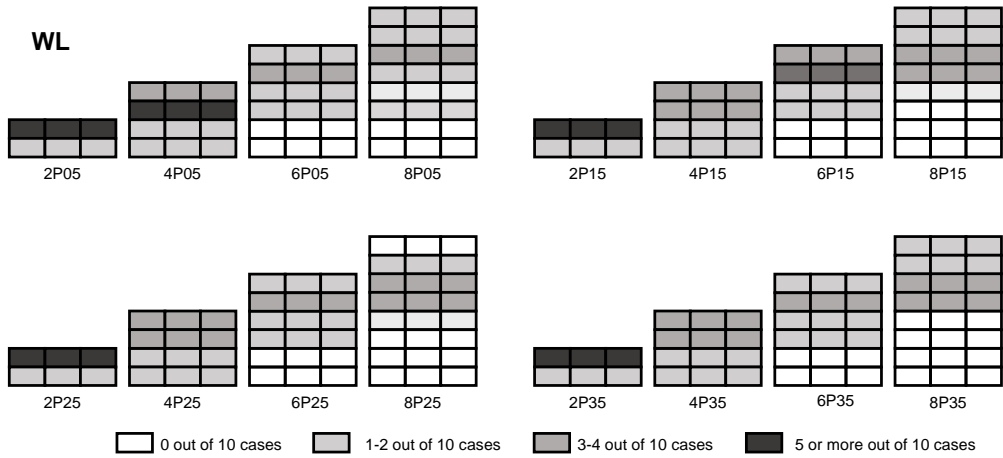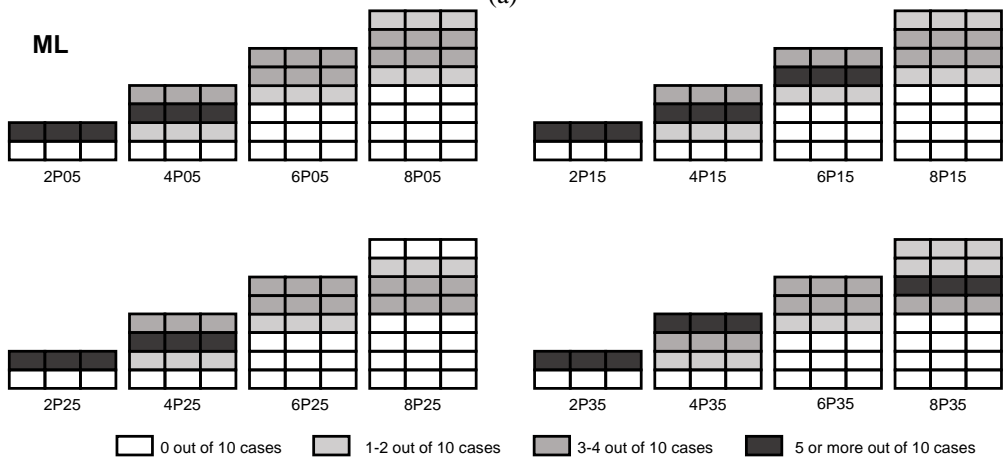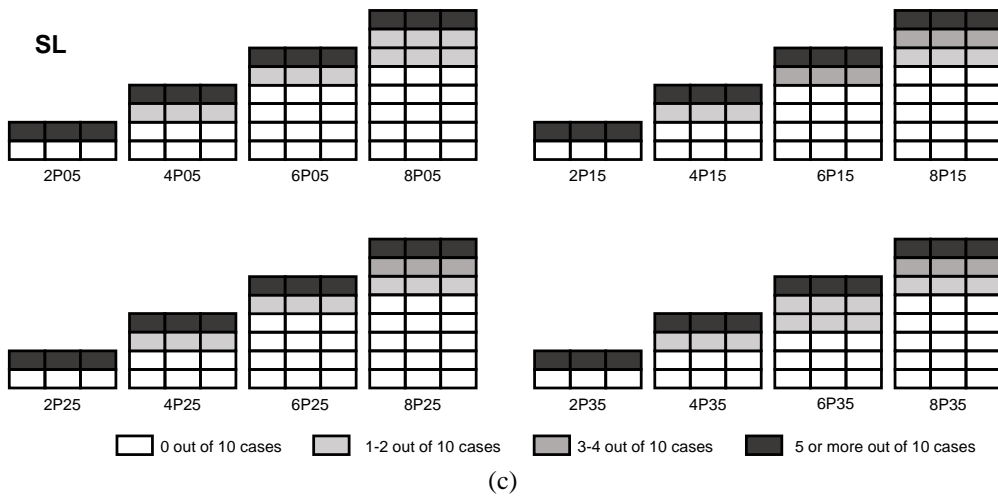
Figure 8.22. Frequency distributions of OOP collapses for all the case-study buildings. (W/ models)

It is observed that, in general, the first OOP collapse occurs at the building mid-height or at the upper storeys for WL and ML, while for SL buildings the first OOP collapse occurs, in most cases, at the very top of the building, i.e., at the last or second-to-last storey. Most likely, this occurs because for SL infills the impact of the IP/OOP interaction is very limited: hence, the first OOP collapse is generally due to "high" OOP displacement demand (typical of upper storeys) more than to "high" IP/OOP interaction effects (typical of intermediate storeys).

8.7. ASSESSMENT OF THE OOP BEHAVIOUR FACTOR AND EFFECTIVE STIFFNESS OF URM INFILLS

The main aim of this section is the definition of the behaviour factor associated with the OOP seismic response of URM infills.

Each IP-undamaged infill of the case-study buildings can be considered as a Single Degree Of Freedom (SDOF) dynamic system provided of a mass m^* equal to the mass participating to the first OOP vibration mode, of an initial stiffness, $K_{el,und}$, equal to the elastic stiffness of a plate calculated according to Timoshenko, of a certain strength, $F_{max,und}$, and of a certain displacement capacity $d_{u,und}$, both calculated through the formulations proposed in Chapter IV. This is completely correct for the IP-undamaged infill. As already stated, due to the OOP modelling strategy adopted for infill walls in

this study, the SDOF that represents them has an evolutionary behaviour during the non-linear time-history analyses and its displacement capacity, strength and initial stiffness varies during the analyses due to IP/OOP interaction.

Now, consider a specific record used for the non-linear time-history analysis of a single case-study building. As during IDAs the record is scaled, it is possible to define the lowest scale factor that multiplied for the unscaled record produces the first OOP infill collapse. Such collapse occurs at a certain storey of the case-study building. So, it is possible to associate to the specific record considered and to the specific case-study building:

i.   the storey at which the first OOP infill collapse occurs and the acceleration and displacement floor response spectrum corresponding to the scaled record. These floor spectra can be considered as capacity floor spectra for the specific record and for the specific "capacity condition" considered, i.e., the first OOP infill collapse;

ii.   the "residual" OOP initial stiffness, $K_{el,dam}$, reduced due to the IP action effects, that the infill/SDOF had when it collapsed;

iii.   the "residual" OOP strength, $F_{max,dam}$, reduced due to the IP action effects, that the infill/SDOF had when it collapsed;

iv.   the "residual" OOP displacement capacity, $d_{u,dam}$, reduced due to the IP action effects, that the infill/SDOF had when it collapsed.

As it is well-known, the behaviour factor of an SDOF is given by the ratio between the seismic force that the SDOF would have known if it was elastic, F_{el}, over its strength, F_{max}. So, it is possible to calculate the q-factor in two ways:

i.   if the IP/OOP interaction is not considered, it is possible to enter the capacity acceleration floor response spectrum obtained for the W/O model with the elastic period function of $K_{el,und}$. The elastic spectral acceleration considered is multiplied for the SDOF mass, m^*, and then divided by the strength of the IP-undamaged infill/SDOF, $F_{max,und}$, to obtain the q-factor in the W/O case, as shown in Figure 8.23;

ii.   if the IP/OOP interaction is considered, it is possible to enter the capacity acceleration floor response spectrum obtained for the W/ model with the elastic period function of $K_{el,dam}$. The elastic spectral acceleration

considered is multiplied for the SDOF mass, m^*, and then divided by the strength of the IP-damaged infill/SDOF, $F_{max,dam}$, to obtain the q-factor in the W/ case, as shown in Figure 8.23;
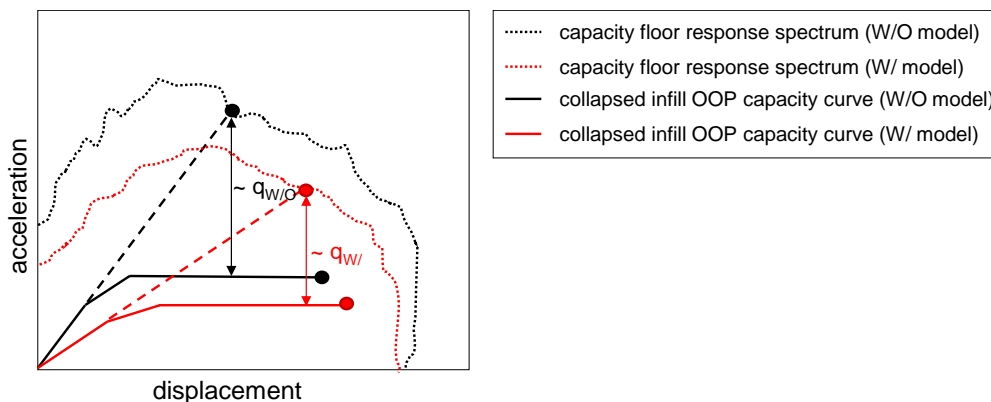
Figure 8.23. Determination of the behaviour factor for the W/O and the W/ model with reference to the OOP elastic stiffness of the IP-undamaged (W/O model) and of the IP-damaged (W/ model) infill.

The above approaches will be defined "straightforward approaches" for the evaluation of the q-factors and will be applied in the following subsection. Further approaches will be described in the next subsections.

8.7.1. Straightforward approaches for the evaluation of the q-factor

The values obtained for the q-factor are shown in Table 8.13 and in Figures 8.24-25 for the W/O models. As already stated in the previous subsection, even at PGA equal to 1.50 g, in many cases the OOP collapse was not observed for SL infills. Hence, the value reported in the "mean" column, in this case, is not the average of the q-factors assessed for each record but the minimum value of the available results, in order to provide a value more similar to a lower bound of the real q-factor of such type of infills. This circumstance is also pointed out in Figures 8.24-25, in which the q-factors values reported for the SL layout are not represented by a continuous line but by a dashed line, instead.

Table 8.13. Values of the q-factor obtained through the non-linear time-history analysis on the W/O models calculated by dividing the OOP seismic demand corresponding to the initial elastic stiffness of the IP-undamaged infill by its strength.

Record	#1	#2	#3	#4	#5	#6	#7	#8	#9	#10	mean
2P05WL	1.04	1.40	1.36	1.22	0.87	1.19	1.25	1.40	1.21	1.02	1.20
2P15WL	1.05	1.14	1.33	1.08	0.88	1.09	1.16	1.27	1.37	0.90	1.13
2P25WL	1.22	1.23	1.44	1.33	0.89	1.19	1.34	1.19	1.11	1.04	1.20
2P35WL	1.12	1.37	1.46	1.17	0.78	1.04	1.44	1.39	1.16	1.00	1.19
4P05WL	1.40	1.40	1.40	1.45	1.39	1.37	1.35	1.38	1.44	1.45	1.41
4P15WL	1.45	1.29	1.45	1.29	1.44	1.43	1.37	1.40	1.31	1.45	1.39
4P25WL	1.35	1.43	1.44	1.44	1.37	1.51	1.44	1.31	1.37	1.38	1.40
4P35WL	1.33	1.41	1.37	1.49	1.40	1.39	1.34	1.36	1.48	1.41	1.40
6P05WL	1.44	1.36	1.39	1.38	1.39	1.51	1.48	1.39	1.41	1.42	1.42
6P15WL	1.46	1.40	1.37	1.48	1.38	1.51	1.38	1.44	1.44	1.33	1.42
6P25WL	1.51	1.40	1.40	1.47	1.32	1.32	1.43	1.51	1.42	1.34	1.41
6P35WL	1.41	1.38	1.49	1.39	1.46	1.49	1.44	1.44	1.36	1.44	1.43
8P05WL	1.58	1.42	1.48	1.54	1.62	1.44	1.47	1.45	1.58	1.58	1.52
8P15WL	1.54	1.44	1.49	1.54	1.53	1.58	1.61	1.63	1.58	1.56	1.55
8P25WL	1.45	1.54	1.49	1.58	1.53	1.45	1.56	1.45	1.44	1.51	1.50
8P35WL	1.54	1.53	1.55	1.54	1.53	1.54	1.55	1.54	1.53	1.54	1.54
2P05ML	1.24	1.42	1.72	1.14	0.90	1.41	1.28	1.3	1.2	0.9	1.26
2P15ML	0.90	1.32	1.51	1.21	1.03	1.03	1.14	1.3	1.4	0.9	1.18
2P25ML	1.17	1.53	1.55	1.19	0.99	1.38	1.59	1.2	1.4	1	1.30
2P35ML	1.41	1.18	1.66	1.09	0.93	1.11	1.56	1.3	1.1	0.9	1.23
4P05ML	1.18	1.37	1.64	1.52	1.36	1.40	1.38	1.6	1.6	1.4	1.44
4P15ML	1.44	1.29	1.42	1.29	1.43	1.50	1.28	1.5	1.4	1.6	1.42
4P25ML	1.38	1.53	1.58	1.38	1.34	1.60	1.58	1.5	1.6	1.4	1.49
4P35ML	1.42	1.18	1.53	1.30	1.56	1.60	1.53	1.3	1.5	1.3	1.41
6P05ML	1.53	1.50	1.24	1.50	1.29	1.66	1.50	1.45	1.43	1.47	1.46
6P15ML	1.55	1.57	1.23	1.59	1.37	1.59	1.55	1.43	1.64	1.38	1.49
6P25ML	1.53	1.31	1.55	1.61	1.55	1.32	1.52	1.28	1.43	1.42	1.45
6P35ML	1.34	1.45	1.61	1.48	1.30	1.51	1.19	1.30	1.32	1.52	1.40
8P05ML	1.62	1.62	1.65	1.72	1.60	1.39	1.33	1.32	1.43	1.55	1.52
8P15ML	1.49	1.54	1.32	1.52	1.34	1.42	1.57	1.52	1.59	1.41	1.47
8P25ML	1.63	1.73	1.38	1.59	1.71	1.26	1.69	1.36	1.75	1.43	1.55
8P35ML	1.51	1.61	1.80	1.42	1.43	1.71	1.56	1.47	1.66	1.68	1.59
2P05SL	n/a	n/a	n/a	n/a	1.13	n/a	1.84	n/a	n/a	n/a	1.13
2P15SL	n/a	n/a	n/a	n/a	1.10	n/a	2.14	n/a	n/a	n/a	1.10
2P25SL	n/a	n/a	n/a	n/a	1.69	n/a	1.54	n/a	n/a	n/a	1.54
2P35SL	n/a	n/a	n/a	n/a	n/a	n/a	1.84	n/a	n/a	n/a	1.84
4P05SL	n/a	n/a	n/a	n/a	n/a	2.87	2.84	2.23	n/a	n/a	2.23
4P15SL	n/a	n/a	n/a	n/a	n/a	2.12	2.34	n/a	n/a	n/a	2.12
4P25SL	n/a	n/a	n/a	n/a	n/a	n/a	2.13	n/a	n/a	n/a	2.13
4P35SL	n/a	n/a	n/a	n/a	2.39	n/a	n/a	n/a	n/a	n/a	2.39
6P05SL	2.95	n/a	n/a	n/a	2.54	3.07	3.91	2.33	n/a	2.26	2.26
6P15SL	n/a	n/a	n/a	n/a	2.46	2.16	2.79	3.20	2.53	n/a	2.16
6P25SL	n/a	n/a	2.55	n/a	2.99	n/a	2.48	3.12	n/a	2.14	2.14
6P35SL	n/a	2.31	n/a	n/a	2.67	n/a	2.35	n/a	n/a	3.25	2.31
8P05SL	n/a	2.83	3.41	2.52	3.41	2.79	3.39	n/a	2.89	2.84	2.52
8P15SL	n/a	2.61	3.27	n/a	n/a	n/a	3.07	3.65	n/a	3.17	2.61
8P25SL	n/a	3.46	3.24	n/a	n/a	n/a	4.04	n/a	n/a	3.66	3.24
8P35SL	n/a	3.52	2.83	n/a	n/a	n/a	n/a	n/a	n/a	3.33	2.83
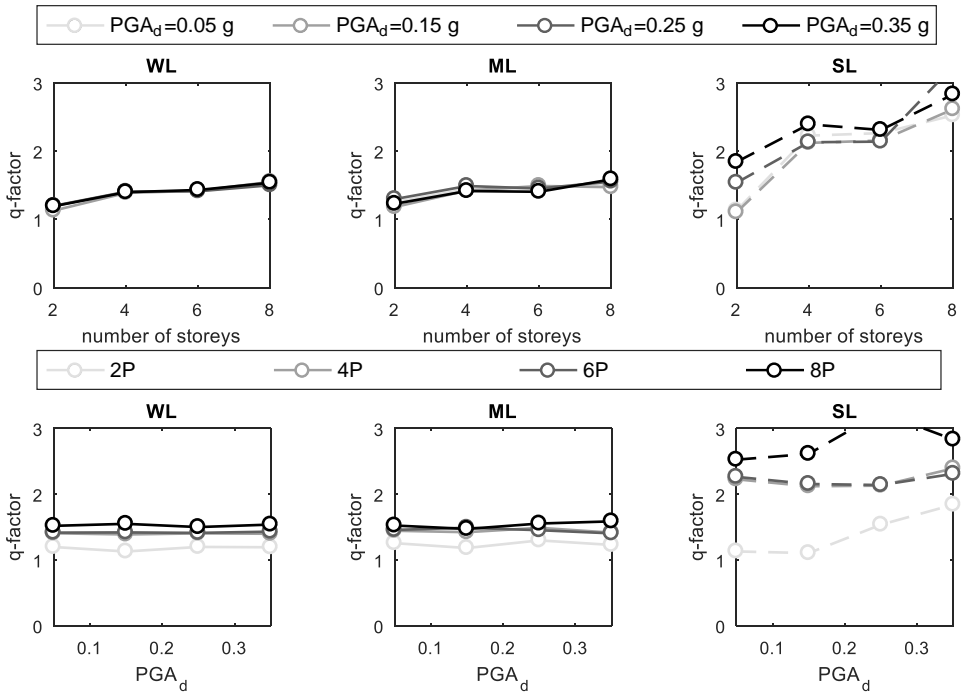
Figure 8.24. Mean q-factor values on the W/O models for all case-study buildings (straightforward approach).

Figure 8.25. Mean q-factor values on the W/O models for all case-study buildings
(straightforward approach)

It is observed that the average q-factor is quite independent on the design PGA of the building, while it has a noticeable dependence on the total number of storeys of the building for WL and ML infills. This occurs because at fixed design PGA and infill layouts, the first OOP collapse occurs at higher acceleration demand for higher buildings (remember that in W/O models the first OOP collapse always occurs at the last storey), while the strength capacity of the infill is not dependent on the building height. Trends are not so clear for SL buildings, as the values of q-factors obtained are derived from a small number of data.

The average q-factor obtained not accounting for the IP/OOP interaction effect is equal to 1.38 for WL buildings and to 1.42 for ML buildings. The lower bound q-factor for SL buildings is equal to 1.10.

The values obtained for the q-factor are shown in Table 8.14 and in Figures 8.26-27 for the W/ models.

Table 8.14. Values of the q-factor obtained through the non-linear time-history analysis on the W/ models calculated by dividing the OOP seismic demand corresponding to the initial elastic stiffness of the IP-damaged infill by its strength.

| Record	#1	#2	#3	#4	#5	#6	#7	#8	#9	#10	mean
2P05WL	1.29	1.58	1.69	1.37	1.01	1.43	1.57	1.58	1.48	1.17	1.42
2P15WL	1.23	1.40	1.53	1.32	1.00	1.31	1.51	1.61	1.62	1.08	1.36
2P25WL	1.39	1.54	1.92	1.45	1.12	1.38	1.58	1.45	1.36	1.33	1.45
2P35WL	1.44	1.58	1.72	1.36	0.90	1.34	1.71	1.72	1.48	1.19	1.44
4P05WL	1.58	1.57	1.64	1.63	1.57	1.62	1.66	1.59	1.71	1.62	1.62
4P15WL	1.64	1.57	1.64	1.56	1.63	1.62	1.62	1.67	1.55	1.55	1.60
4P25WL	1.60	1.57	1.68	1.59	1.67	1.69	1.65	1.56	1.58	1.54	1.61
4P35WL	1.56	1.57	1.55	1.69	1.55	1.67	1.54	1.57	1.66	1.55	1.59
6P05WL	1.81	1.69	1.88	1.75	1.77	1.91	1.84	1.81	1.75	1.73	1.79
6P15WL	1.82	1.83	1.75	1.78	1.71	1.80	1.73	1.76	1.89	1.75	1.78
6P25WL	1.77	1.83	1.82	1.87	1.74	1.71	1.75	1.90	1.84	1.80	1.80
6P35WL	1.74	1.73	1.88	1.89	1.81	1.75	1.70	1.74	1.77	1.85	1.79
8P05WL	1.90	1.86	2.02	1.97	1.93	1.85	1.92	1.81	1.93	1.93	1.91
8P15WL	1.90	1.85	1.91	2.01	1.90	1.96	1.89	1.95	1.93	1.99	1.93
8P25WL	1.90	1.93	1.93	1.92	1.89	1.94	1.93	1.86	1.80	1.98	1.91
8P35WL	2.02	1.99	2.04	1.98	1.86	1.92	1.87	1.86	1.93	1.89	1.94
2P05ML	1.29	1.53	1.83	1.22	0.93	1.48	1.34	1.41	1.22	1.01	1.33
2P15ML	0.99	1.44	1.52	1.22	1.06	1.08	1.30	1.44	1.44	0.91	1.24
2P25ML	1.28	1.60	1.57	1.22	1.10	1.44	1.65	1.17	1.41	1.12	1.36
2P35ML	1.48	1.31	1.79	1.21	0.92	1.12	1.55	1.54	1.15	0.97	1.31
4P05ML	1.24	1.38	1.59	1.51	1.41	1.47	1.39	1.66	1.76	1.46	1.49
4P15ML	1.58	1.31	1.46	1.29	1.44	1.58	1.33	1.62	1.44	1.60	1.47
4P25ML	1.49	1.53	1.71	1.47	1.37	1.72	1.66	1.48	1.66	1.52	1.56
4P35ML	1.49	1.27	1.58	1.45	1.67	1.68	1.54	1.27	1.53	1.35	1.48
6P05ML	1.80	1.68	1.47	1.63	1.49	1.91	1.63	1.75	1.70	1.72	1.68
6P15ML	1.71	1.82	1.50	1.84	1.64	1.86	1.82	1.62	1.89	1.60	1.73
6P25ML	1.88	1.56	1.79	1.82	1.88	1.56	1.65	1.49	1.66	1.54	1.68
6P35ML	1.57	1.63	1.92	1.78	1.56	1.67	1.38	1.58	1.51	1.79	1.64
8P05ML	1.91	1.98	1.80	1.96	1.76	1.69	1.62	1.49	1.70	1.84	1.78
8P15ML	1.67	1.83	1.57	1.79	1.60	1.64	1.82	1.82	1.80	1.73	1.73
8P25ML	1.99	1.92	1.62	1.79	2.05	1.45	2.02	1.62	1.88	1.59	1.79
8P35ML	1.70	1.79	2.04	1.64	1.70	1.99	1.69	1.77	1.98	1.92	1.82
2P05SL	0.86	1.37	1.58	1.02	0.94	1.15	1.39	1.41	1.52	1.17	1.24
2P15SL	1.02	1.44	1.26	1.15	0.82	1.07	1.24	1.27	1.18	0.98	1.14
2P25SL	1.09	1.34	1.74	1.10	1.08	1.19	1.24	1.22	1.11	1.24	1.24
2P35SL	1.23	1.32	1.39	1.18	0.79	1.02	1.18	1.61	1.06	0.92	1.17
4P05SL	1.36	1.18	1.54	1.26	1.05	1.40	1.41	1.48	1.40	1.18	1.33
4P15SL	1.23	1.14	1.24	1.01	1.26	1.45	1.22	1.64	1.37	1.30	1.29
4P25SL	1.51	1.54	1.53	1.42	1.44	1.62	1.45	1.38	1.37	1.59	1.49
4P35SL	1.51	1.41	1.18	1.39	1.53	1.23	1.12	1.14	1.31	1.45	1.33
6P05SL	1.52	1.37	1.58	1.57	1.40	1.69	1.87	1.36	1.83	1.21	1.54
6P15SL	1.48	1.20	1.39	1.58	1.57	1.18	1.67	1.66	1.40	1.57	1.47
6P25SL	1.71	1.71	1.44	1.48	1.53	1.45	1.36	1.56	1.54	1.39	1.51
6P35SL	1.50	1.45	1.33	1.64	1.35	1.57	1.33	1.56	1.31	1.49	1.45
8P05SL	1.55	1.69	1.57	1.33	1.74	1.46	1.53	1.39	1.71	1.43	1.54
8P15SL	1.25	1.52	1.73	1.61	1.33	1.60	1.62	1.70	1.80	1.86	1.60
8P25SL	1.60	1.77	1.58	1.53	1.71	1.82	1.75	1.41	1.67	1.55	1.64
8P35SL	1.40	2.01	1.51	1.54	1.80	1.79	1.65	1.54	1.44	1.52	1.62

Figure 8.26. Mean q-factor values on the W/ models for all case-study buildings
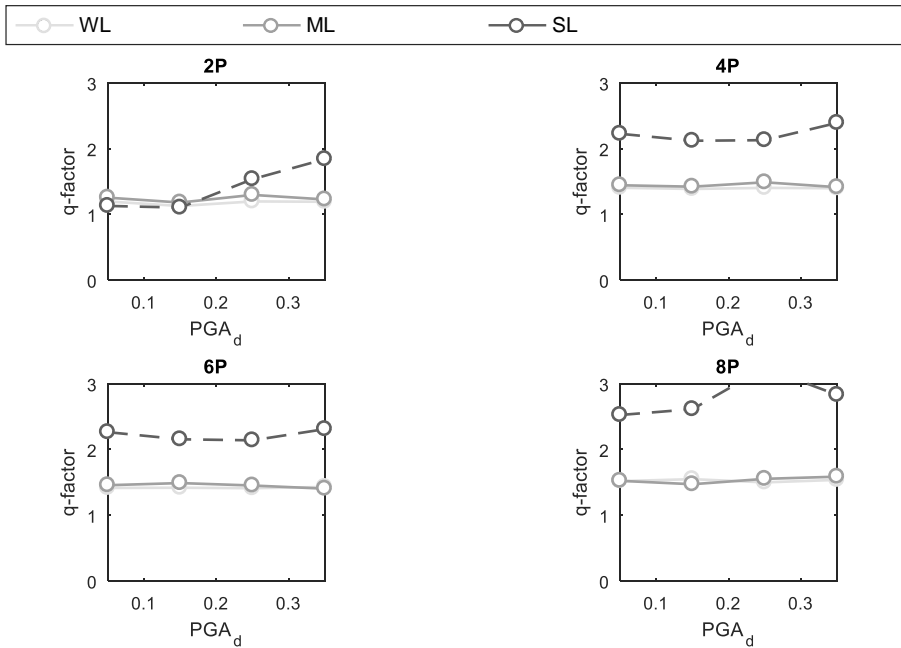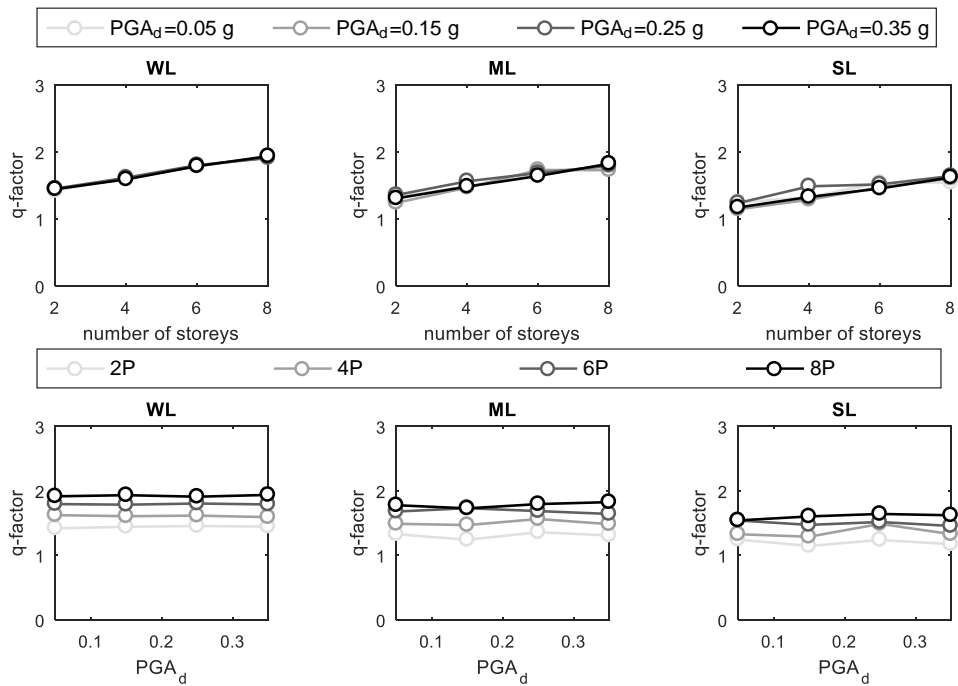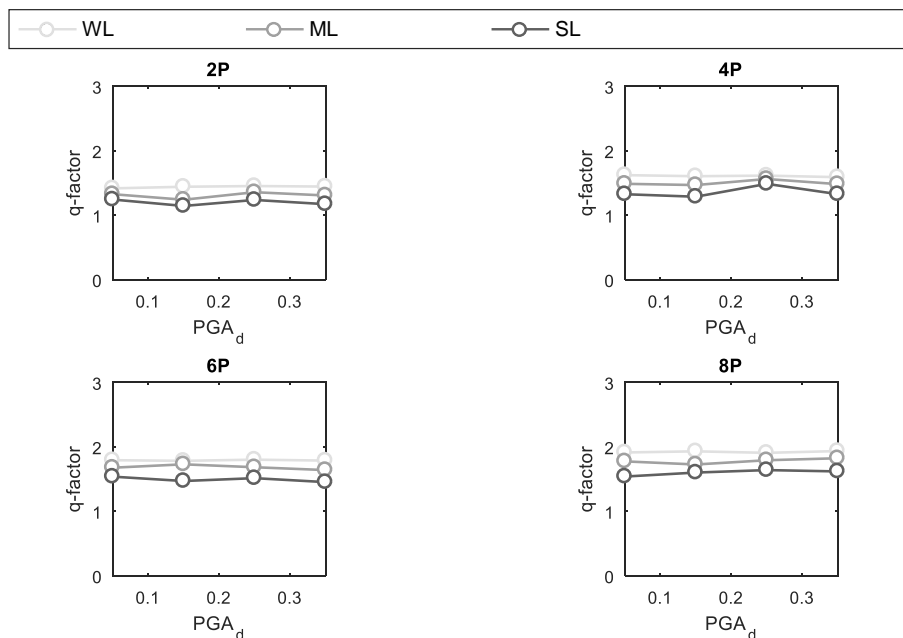(straightforward approach).

Figure 8.27. Mean q-factor values on the W/ models for all case-study buildings
(straightforward approach)

It is observed that the average q-factor is quite independent on the design PGA of the building, while it increases at increasing total number of storeys of the building. As shown in Figures 8.26-27, even if accounting for the IP/OOP interaction, most of the first OOP collapses occurs at higher storeys in higher buildings. Hence, it occurs, in general, for higher OOP seismic demand in higher building. On the other hand, it has been shown in the previous subsection that the IDR demand acting on the collapsed infill at the attainment of the first OOP collapse is quite similar for all case-study buildings. Hence, the residual OOP strength of the first collapsed infills is quite the same, independently on the building height. Hence, q-factors are higher for higher buildings.

The average q-factor obtained not accounting for the IP/OOP interaction effect is equal to 1.68 for WL buildings and to 1.57 for ML buildings and 1.41 for SL buildings.

8.7.2. Practice-oriented approach for the evaluation of the q-factor

Now, consider that in general, for the sake of simplicity, the IP/OOP interaction is not explicitly modelled. So, usually, $K_{el,dam}$ and $F_{max,dam}$ are not known by the practitioner. For this reason, the q-factor can be calculated by considering the OOP

seismic demand evaluated for the W/ model but entering the capacity acceleration floor spectrum with the vibration period associated with $K_{el,und}$ and dividing the elastic force by $F_{max,und}$, as reported in Figure 8.28.
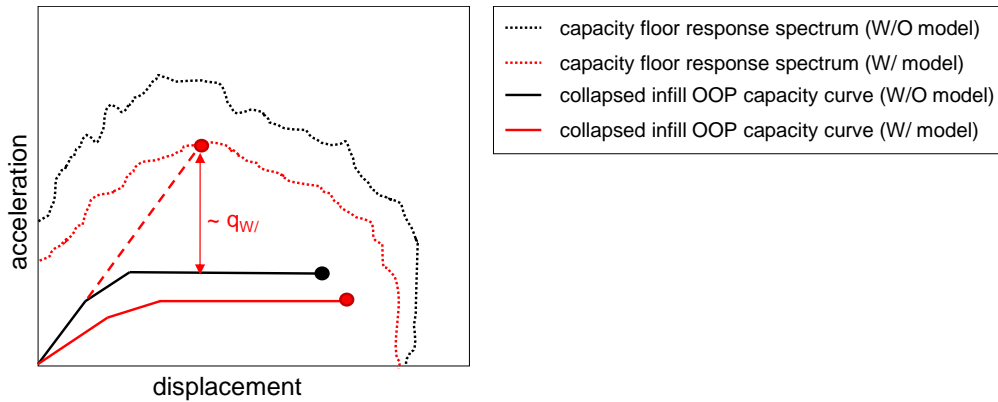
Figure 8.28. Determination of the behaviour factor for the W/ model with reference to the OOP elastic stiffness of the IP-undamaged infill.

In this case, it should not be surprising that q-factors even lower than the unit are obtained, as the OOP seismic demand considered is consistent with the one associated with an IP-damaged infill while the OOP strength considered is that associated with the IP-undamaged infill. This occurs as if the OOP seismic demand should be indeed increased to account for the detrimental effects of the IP/OOP interaction if such a demand is compared with the OOP strength of the IP-undamaged infill.

The values obtained for the q-factor are shown in Table 8.15 and in Figures 8.29-30 for the W/ models.

Table 8.15. Values of the q-factor obtained through the non-linear time-history analysis by calculating, for the W/ model, the OOP seismic demand corresponding to the initial elastic stiffness of the IP-undamaged infill and dividing the elastic force by the strength of the IP-undamaged infill.

Record	#1	#2	#3	#4	#5	#6	#7	#8	#9	#10	mean
2P05WL	0.98	1.18	1.26	1.01	0.74	1.05	1.19	1.17	1.10	0.89	1.06
2P15WL	0.89	1.06	1.15	0.99	0.74	0.99	1.09	1.16	1.18	0.83	1.01
2P25WL	1.05	1.17	1.37	1.11	0.80	1.01	1.20	1.05	1.01	0.96	1.07
2P35WL	1.05	1.18	1.25	1.04	0.69	0.99	1.28	1.24	1.06	0.86	1.07
4P05WL	1.16	1.16	1.24	1.24	1.20	1.19	1.21	1.18	1.26	1.20	1.20
4P15WL	1.22	1.16	1.22	1.14	1.21	1.22	1.17	1.22	1.17	1.16	1.19
4P25WL	1.16	1.20	1.25	1.22	1.21	1.26	1.22	1.14	1.18	1.17	1.20
4P35WL	1.14	1.18	1.19	1.26	1.19	1.25	1.17	1.18	1.25	1.16	1.20
6P05WL	1.36	1.27	1.35	1.32	1.35	1.36	1.37	1.35	1.29	1.27	1.33
6P15WL	1.34	1.37	1.26	1.36	1.26	1.37	1.29	1.29	1.35	1.27	1.32
6P25WL	1.36	1.34	1.32	1.36	1.28	1.28	1.31	1.37	1.35	1.29	1.33
6P35WL	1.28	1.28	1.37	1.35	1.31	1.34	1.31	1.32	1.29	1.34	1.32
8P05WL	1.45	1.40	1.44	1.41	1.47	1.37	1.42	1.37	1.42	1.42	1.42
8P15WL	1.47	1.37	1.40	1.47	1.40	1.45	1.45	1.47	1.47	1.49	1.44
8P25WL	1.40	1.43	1.47	1.42	1.44	1.40	1.41	1.39	1.37	1.45	1.42
8P35WL	1.45	1.43	1.48	1.44	1.41	1.43	1.39	1.41	1.44	1.43	1.43
2P05ML	0.99	1.14	1.32	0.92	0.68	1.07	1.01	1.08	0.91	0.72	0.98
2P15ML	0.75	1.09	1.17	0.90	0.77	0.79	0.94	1.11	1.09	0.70	0.93
2P25ML	0.93	1.18	1.20	0.94	0.82	1.06	1.22	0.86	1.03	0.83	1.01
2P35ML	1.06	0.97	1.31	0.88	0.71	0.84	1.19	1.10	0.87	0.70	0.96
4P05ML	0.94	1.06	1.22	1.13	1.07	1.10	1.03	1.19	1.26	1.08	1.11
4P15ML	1.15	0.96	1.05	1.00	1.09	1.20	0.98	1.19	1.09	1.21	1.09
4P25ML	1.08	1.13	1.26	1.10	1.03	1.23	1.21	1.12	1.21	1.09	1.15
4P35ML	1.11	0.94	1.17	1.03	1.23	1.27	1.13	0.98	1.15	0.97	1.10
6P05ML	1.32	1.25	1.08	1.24	1.08	1.40	1.25	1.26	1.24	1.27	1.24
6P15ML	1.31	1.35	1.07	1.42	1.17	1.40	1.31	1.18	1.35	1.18	1.27
6P25ML	1.36	1.18	1.32	1.35	1.35	1.14	1.27	1.10	1.19	1.18	1.24
6P35ML	1.15	1.26	1.37	1.28	1.14	1.26	1.06	1.16	1.13	1.30	1.21
8P05ML	1.40	1.45	1.38	1.45	1.33	1.24	1.16	1.10	1.28	1.36	1.32
8P15ML	1.25	1.33	1.13	1.36	1.15	1.21	1.31	1.35	1.33	1.27	1.27
8P25ML	1.42	1.47	1.22	1.38	1.49	1.12	1.46	1.18	1.44	1.22	1.34
8P35ML	1.31	1.36	1.52	1.18	1.25	1.45	1.29	1.31	1.43	1.43	1.35
2P05SL	0.66	1.01	1.21	0.79	0.68	0.87	1.05	1.02	1.11	0.89	0.93
2P15SL	0.78	1.03	0.92	0.86	0.60	0.77	0.92	0.91	0.90	0.75	0.84
2P25SL	0.82	1.02	1.26	0.84	0.81	0.86	0.91	0.90	0.81	0.90	0.91
2P35SL	0.92	0.96	1.04	0.88	0.61	0.78	0.91	1.16	0.77	0.69	0.87
4P05SL	0.97	0.90	1.15	0.94	0.80	1.07	1.05	1.11	1.00	0.90	0.99
4P15SL	0.88	0.83	0.91	0.78	0.92	1.07	0.87	1.24	1.02	0.93	0.95
4P25SL	1.12	1.14	1.09	1.06	1.03	1.16	1.08	0.99	1.05	1.15	1.09
4P35SL	1.11	1.03	0.84	1.02	1.13	0.91	0.83	0.84	1.01	1.07	0.98
6P05SL	1.15	1.02	1.17	1.17	1.06	1.20	1.37	1.00	1.32	0.93	1.14
6P15SL	1.09	0.89	1.06	1.15	1.12	0.89	1.24	1.20	1.03	1.12	1.08
6P25SL	1.23	1.24	1.03	1.06	1.16	1.06	1.01	1.16	1.11	1.02	1.11
6P35SL	1.16	1.08	0.98	1.24	0.97	1.21	1.01	1.14	0.99	1.13	1.09
8P05SL	1.15	1.21	1.14	1.01	1.30	1.05	1.11	1.06	1.27	1.06	1.14

continues

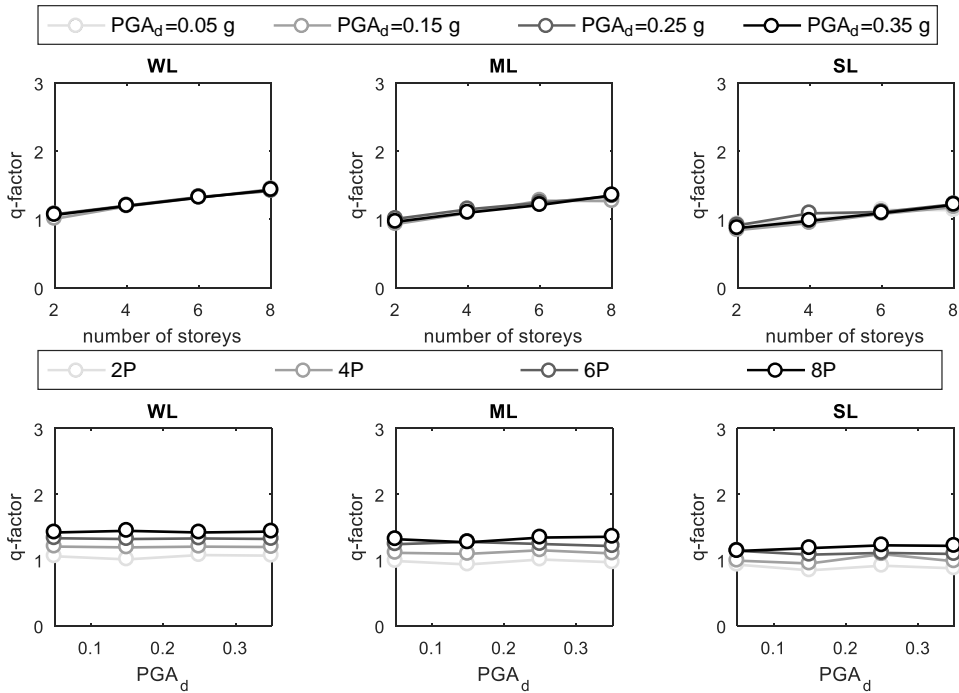| *follows*										
8P15SL	0.96	1.11	1.26	1.16	0.99	1.22	1.16	1.27	1.29	1.39	1.18
8P25SL	1.21	1.27	1.17	1.13	1.27	1.34	1.30	1.08	1.27	1.18	1.22
8P35SL	1.07	1.50	1.15	1.18	1.33	1.32	1.21	1.13	1.09	1.16	1.21

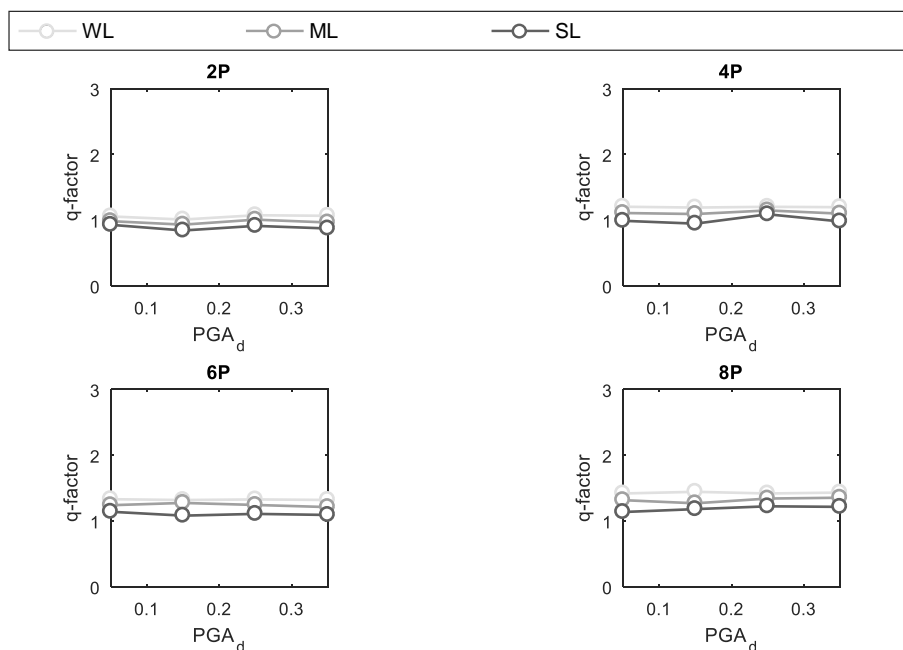Figure 8.29. Mean q-factor values on the W/ models for all case-study buildings (practice-oriented approach).

Figure 8.30. Mean q-factor values on the W/ models for all case-study buildings (practice-oriented approach).

It is observed that the average q-factor is quite independent on the design PGA of the building, while it increases at increasing total number of storeys of the building. As shown in Figures 8.29-30, even if accounting for the IP/OOP interaction, most of the first OOP collapses occurs at higher storeys in higher buildings. Hence, it occurs, in general, for higher OOP seismic demand in higher building. On the other hand, the OOP strength of the IP-undamaged infill is independent on the number of storeys. Hence, q-factors are higher for higher buildings.

The average q-factor obtained not accounting for the IP/OOP interaction effect is equal to 1.25 for WL buildings and to 1.16 for ML buildings and 1.05 for SL buildings.

8.7.3. Evaluation of the q-factor based on the OOP effective stiffness

The choice of the period at which the OOP seismic demand should be calculated is an open issue, as discussed in Chapter V. In this sense, the concept of effective stiffness of an SDOF can be used to provide a consistent approach that accounts, contemporarily, for the strength and displacement capacity of the infill/SDOF.

In other word, the OOP effective stiffness of the infill is the one associated to the period that is associated to a displacement demand obtained from the displacement capacity floor response spectrum equal to the OOP collapse displacement of the infill. In this case, the effective stiffness can be calculated both for W/O and for W/ model (Figure 8.31). Clearly, an implicit assumption made is a sort of "equal displacement rule", i.e., it is assumed that the displacement demand undergone by the elastic infill/SDOF is equal to that undergone by the non-linear SDOF. Further investigation are necessary concerning this issue.
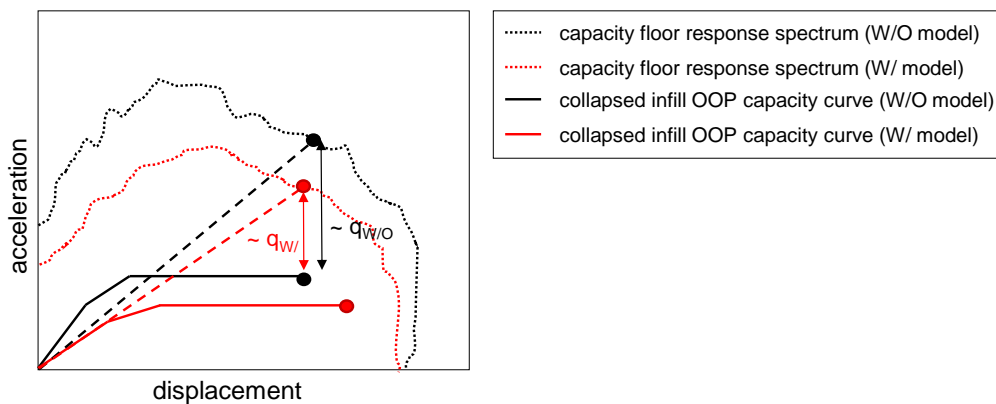
Figure 8.31. Determination of the behaviour factor for the W/O and the W/ model with reference to the OOP effective stiffness.

For the W/O model, in Table 8.16, the values obtained of the OOP effective stiffness obtained for the ten records and for each case-study building are normalized with respect the initial elastic stiffness as calculated for the analyses carried out for this Chapter, i.e., according to Timoshenko (1959)'s approach. As already stated in the previous subsection, even at PGA equal to 1.50 g, in many cases the OOP collapse was not observed for SL infills. Hence, the value reported in the "mean" column, in this case, is not the average of the K_{eff}/K_{el} ratios assessed for each record but the minimum value of the available results, in order to provide a value more similar to a lower bound of the real K_{eff}/K_{el} of such type of infills.

Table 8.16. Values of the effective stiffness K_{eff} normalized with respect to the elastic K_{el} stiffness of the IP-undamaged infill obtained through the non-linear time-history analysis on the W/O models.

Record	#1	#2	#3	#4	#5	#6	#7	#8	#9	#10	mean
2P05WL	0.32	0.31	0.28	0.36	0.29	0.45	0.32	0.50	0.33	0.20	0.34
2P15WL	0.30	0.34	0.35	0.45	0.17	0.31	0.32	0.49	0.39	0.27	0.34
2P25WL	0.35	0.36	0.29	0.30	0.29	0.41	0.37	0.31	0.27	0.26	0.32
2P35WL	0.36	0.31	0.58	0.26	0.18	0.22	0.58	0.54	0.26	0.25	0.35
4P05WL	0.31	0.61	0.54	0.47	0.46	0.37	0.55	0.40	0.53	0.30	0.45
4P15WL	0.29	0.43	0.44	0.41	0.37	0.26	0.31	0.56	0.33	0.33	0.37
4P25WL	0.47	0.60	0.41	0.26	0.45	0.48	0.45	0.40	0.46	0.30	0.43
4P35WL	0.43	0.31	0.50	0.37	0.32	0.33	0.37	0.58	0.35	0.54	0.41
6P05WL	0.29	0.32	0.36	0.45	0.28	0.36	0.53	0.49	0.31	0.33	0.37
6P15WL	0.35	0.39	0.35	0.36	0.53	0.31	0.25	0.35	0.42	0.40	0.37
6P25WL	0.52	0.38	0.53	0.36	0.31	0.43	0.28	0.27	0.34	0.41	0.38
6P35WL	0.39	0.37	0.62	0.46	0.39	0.45	0.32	0.55	0.29	0.44	0.43
8P05WL	0.43	0.25	0.61	0.56	0.43	0.35	0.45	0.34	0.44	0.32	0.42
8P15WL	0.36	0.54	0.34	0.49	0.33	0.42	0.33	0.35	0.53	0.34	0.40
8P25WL	0.49	0.44	0.59	0.46	0.34	0.52	0.55	0.54	0.57	0.51	0.50
8P35WL	0.56	0.69	0.28	0.54	0.45	0.51	0.31	0.51	0.31	0.52	0.47
2P05ML	0.23	0.44	0.29	0.47	0.21	0.33	0.27	0.44	0.32	0.39	0.34
2P15ML	0.27	0.47	0.53	0.46	0.29	0.29	0.21	0.37	0.42	0.21	0.35
2P25ML	0.33	0.41	0.30	0.36	0.33	0.43	0.48	0.32	0.44	0.35	0.38
2P35ML	0.47	0.37	0.58	0.26	0.33	0.31	0.43	0.31	0.35	0.30	0.37
4P05ML	0.48	0.30	0.46	0.51	0.29	0.48	0.38	0.41	0.64	0.53	0.45
4P15ML	0.27	0.28	0.65	0.46	0.38	0.33	0.29	0.41	0.62	0.49	0.42
4P25ML	0.33	0.51	0.40	0.30	0.46	0.37	0.45	0.47	0.45	0.47	0.42
4P35ML	0.33	0.26	0.41	0.37	0.36	0.26	0.43	0.34	0.34	0.53	0.36
6P05ML	0.41	0.47	0.56	0.37	0.44	0.59	0.34	0.47	0.49	0.54	0.47
6P15ML	0.30	0.37	0.34	0.29	0.47	0.40	0.39	0.47	0.54	0.36	0.39
6P25ML	0.52	0.39	0.58	0.71	0.41	0.38	0.57	0.46	0.33	0.44	0.48
6P35ML	0.25	0.32	0.37	0.55	0.42	0.45	0.32	0.48	0.26	0.54	0.40
8P05ML	0.39	0.60	0.41	0.44	0.47	0.53	0.32	0.45	0.52	0.47	0.46
8P15ML	0.40	0.47	0.34	0.39	0.52	0.39	0.47	0.52	0.58	0.24	0.43
8P25ML	0.52	0.65	0.31	0.45	0.40	0.45	0.44	0.34	0.55	0.35	0.45
8P35ML	0.57	0.31	0.53	0.65	0.42	0.62	0.50	0.42	0.64	0.50	0.52
2P05SL	n/a	n/a	n/a	n/a	0.05	n/a	0.06	n/a	n/a	n/a	0.05
2P15SL	n/a	n/a	n/a	n/a	0.03	n/a	0.11	n/a	n/a	n/a	0.07
2P25SL	n/a	n/a	n/a	n/a	0.09	n/a	0.06	n/a	n/a	n/a	0.07
2P35SL	n/a	n/a	n/a	n/a	n/a	n/a	0.09	n/a	n/a	n/a	0.09
4P05SL	n/a	n/a	n/a	n/a	n/a	0.11	0.16	0.13	n/a	n/a	0.13
4P15SL	n/a	n/a	n/a	n/a	n/a	0.11	0.06	n/a	n/a	n/a	0.09
4P25SL	n/a	n/a	n/a	n/a	n/a	n/a	0.11	n/a	n/a	n/a	0.11
4P35SL	n/a	n/a	n/a	n/a	0.09	n/a	0.00	n/a	n/a	n/a	0.05
6P05SL	0.14	n/a	n/a	n/a	0.10	0.15	0.16	0.10	n/a	0.11	0.13
6P15SL	n/a	n/a	n/a	n/a	0.10	0.08	0.12	0.19	0.09	n/a	0.11
6P25SL	n/a	n/a	0.09	n/a	0.09	n/a	0.08	0.07	n/a	0.09	0.09
6P35SL	n/a	0.11	0.00	n/a	0.08	n/a	0.12	n/a	n/a	0.13	0.09
8P05SL	n/a	0.15	0.17	0.12	0.17	0.10	0.14	n/a	0.10	0.11	0.13
8P15SL	n/a	0.13	0.20	n/a	n/a	n/a	0.18	0.14	n/a	0.07	0.14
8P25SL	n/a	0.10	0.19	n/a	n/a	n/a	0.16	n/a	n/a	0.12	0.14
8P35SL	n/a	0.10	0.10	n/a	n/a	n/a	n/a	n/a	n/a	0.13	0.11

The average K_{eff}/K_{el} ratio obtained not accounting for the IP/OOP interaction effect is equal to 0.40 for WL infills and to 0.42 for ML infills, while the minimum value registered for SL infills is 0.05. It is worth to mention that the average effective stiffness for WL and ML infills is roughly equal to their secant stiffness at peak load (which is equal, as reported in Chapter IV, to 0.40 times K_{el}). Note that the effective stiffness for SL is very low. This occurs because the OOP displacement capacity of such a type of infills is very high, hence a spectral displacement equal to the displacement capacity is attained only for very high values of the effective vibration period of the infill.

The values for the q-factor obtained from the W/O models by calculating the force demand acting on infills as a function of their effective stiffness are shown in Table 8.17 and in Figures 8.33-34. As already stated in the previous subsection, even at PGA equal to 1.50 g, in many cases the OOP collapse was not observed for SL infills. Hence, the value reported in the "mean" column, in this case, is not the average of the q-factors assessed for each record but the minimum value of the available results, in order to provide a value more similar to a lower bound of the real q-factor of such type of infills. This circumstance is also pointed out in Figure 8.33-34, in which the q-factors values reported for the SL layout are not represented by a continuous line but by a dashed line, instead.

Table 8.17. Values of the q-factor obtained through the non-linear time-history analysis on the W/O models calculated by dividing the OOP seismic demand corresponding to the effective period of the infill by its strength.

| Record	#1	#2	#3	#4	#5	#6	#7	#8	#9	#10	mean
2P05WL	0.87	1.16	1.07	0.93	0.73	0.93	0.90	1.16	0.98	0.67	0.94
2P15WL	0.84	1.06	1.02	0.99	0.78	1.09	0.86	1.18	1.17	0.76	0.97
2P25WL	0.88	0.96	1.18	0.93	0.73	1.15	0.96	0.97	0.91	0.96	0.96
2P35WL	0.87	1.39	1.37	0.93	0.81	0.96	1.39	1.07	1.06	0.95	1.08
4P05WL	1.29	1.28	1.26	1.13	1.04	1.22	1.22	0.95	1.23	1.19	1.18
4P15WL	1.12	1.02	1.24	1.08	1.30	1.16	1.15	1.38	1.09	1.06	1.16
4P25WL	1.34	1.49	1.08	1.17	1.27	1.30	1.49	1.14	1.14	1.13	1.25
4P35WL	1.29	1.14	1.17	1.25	1.05	1.13	1.09	1.43	1.53	1.14	1.22
6P05WL	1.45	1.27	1.17	1.17	1.15	1.17	1.40	1.31	1.26	1.11	1.25
6P15WL	1.27	1.21	1.35	1.48	1.21	1.18	1.08	1.48	1.16	1.20	1.26
6P25WL	1.49	1.05	1.32	1.36	1.13	1.13	1.11	1.16	1.20	1.23	1.22
6P35WL	1.35	1.13	1.55	1.19	1.51	1.18	1.36	1.38	1.17	1.35	1.32
8P05WL	1.63	1.19	1.46	1.61	1.41	1.11	1.28	1.47	1.48	1.45	1.41
8P15WL	1.38	1.10	1.36	1.14	1.49	1.47	1.36	1.09	1.12	1.18	1.27
8P25WL	1.22	1.34	1.55	1.26	1.32	1.12	1.49	1.39	1.12	1.08	1.29
8P35WL	1.33	1.59	1.21	1.35	1.39	1.42	1.29	1.36	1.20	1.31	1.35
2P05ML	1.01	1.43	1.41	0.89	0.70	1.19	1.05	1.18	0.98	0.95	1.08
2P15ML	0.70	1.15	1.37	1.17	1.00	1.07	0.87	1.20	1.24	0.77	1.06
2P25ML	1.02	1.42	1.40	1.03	0.96	1.22	1.63	1.28	0.96	0.99	1.19
2P35ML	1.33	1.13	1.41	0.85	0.95	1.05	1.46	1.28	0.96	0.74	1.12
4P05ML	1.10	1.12	1.30	1.33	1.07	1.36	1.13	1.37	1.40	1.39	1.26
4P15ML	1.30	1.04	1.30	1.06	1.15	1.31	1.19	1.47	1.35	1.39	1.26
4P25ML	1.39	1.36	1.61	1.10	1.17	1.55	1.12	1.14	1.50	1.52	1.35
4P35ML	0.96	0.93	1.25	1.14	1.56	1.28	1.31	1.01	1.30	1.14	1.19
6P05ML	1.34	1.46	1.29	1.45	1.06	1.49	1.37	1.11	1.04	1.27	1.29
6P15ML	1.27	1.27	1.02	1.17	1.19	1.37	1.40	1.25	1.37	1.24	1.25
6P25ML	1.52	1.14	1.26	1.63	1.68	1.14	1.40	0.95	1.38	1.07	1.32
6P35ML	1.25	1.08	1.57	1.37	1.41	1.24	0.87	1.24	1.17	1.42	1.26
8P05ML	1.32	1.41	1.45	1.42	1.38	1.40	1.26	1.08	1.49	1.29	1.35
8P15ML	1.41	1.47	1.05	1.26	1.51	1.15	1.42	1.32	1.32	1.01	1.29
8P25ML	1.68	1.58	1.37	1.37	1.42	1.15	1.67	1.33	1.48	1.33	1.44
8P35ML	1.44	1.19	1.58	1.47	1.31	1.54	1.22	1.28	1.45	1.28	1.40
2P05SL	n/a	n/a	n/a	n/a	0.15	n/a	0.23	n/a	n/a	n/a	0.15
2P15SL	n/a	n/a	n/a	n/a	0.15	n/a	0.28	n/a	n/a	n/a	0.15
2P25SL	n/a	n/a	n/a	n/a	0.22	n/a	0.24	n/a	n/a	n/a	0.22
2P35SL	n/a	n/a	n/a	n/a	n/a	n/a	0.29	n/a	n/a	n/a	0.29
4P05SL	n/a	n/a	n/a	n/a	n/a	0.33	0.45	0.32	n/a	n/a	0.32
4P15SL	n/a	n/a	n/a	n/a	n/a	0.37	0.33	n/a	n/a	n/a	0.33
4P25SL	n/a	n/a	n/a	n/a	n/a	n/a	0.34	n/a	n/a	n/a	0.34
4P35SL	n/a	n/a	n/a	n/a	0.39	n/a	n/a	n/a	n/a	n/a	0.39
6P05SL	0.48	n/a	n/a	n/a	0.37	0.48	0.43	0.29	n/a	0.34	0.29
6P15SL	n/a	n/a	n/a	n/a	0.40	0.31	0.36	0.49	0.38	n/a	0.31
6P25SL	n/a	n/a	0.36	n/a	0.42	n/a	0.30	0.33	n/a	0.26	0.26
6P35SL	n/a	0.33	n/a	n/a	0.42	n/a	0.35	n/a	n/a	0.40	0.33
8P05SL	n/a	0.43	0.59	0.42	0.58	0.48	0.52	n/a	0.35	0.40	0.35
8P15SL	n/a	0.41	0.53	n/a	n/a	n/a	0.51	0.54	n/a	0.36	0.36
8P25SL	n/a	0.50	0.51	n/a	n/a	n/a	0.54	n/a	n/a	0.44	0.44
8P35SL	n/a	0.49	0.36	n/a	n/a	n/a	n/a	n/a	n/a	0.38	0.36
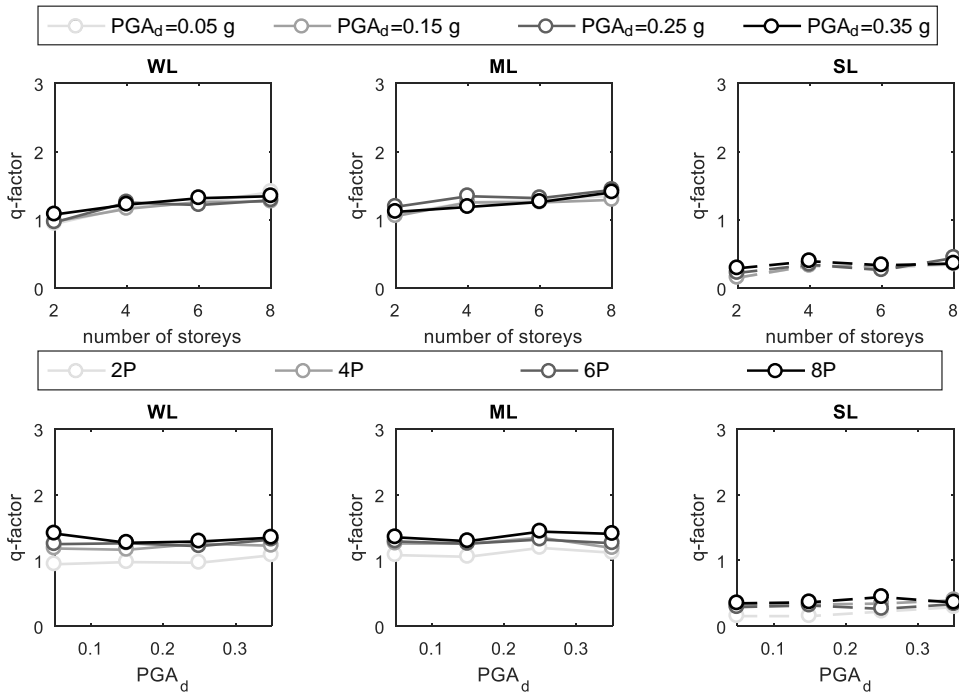
Figure 8.32. Mean q-factor values on the W/O models for all case-study buildings (effective stiffness approach).
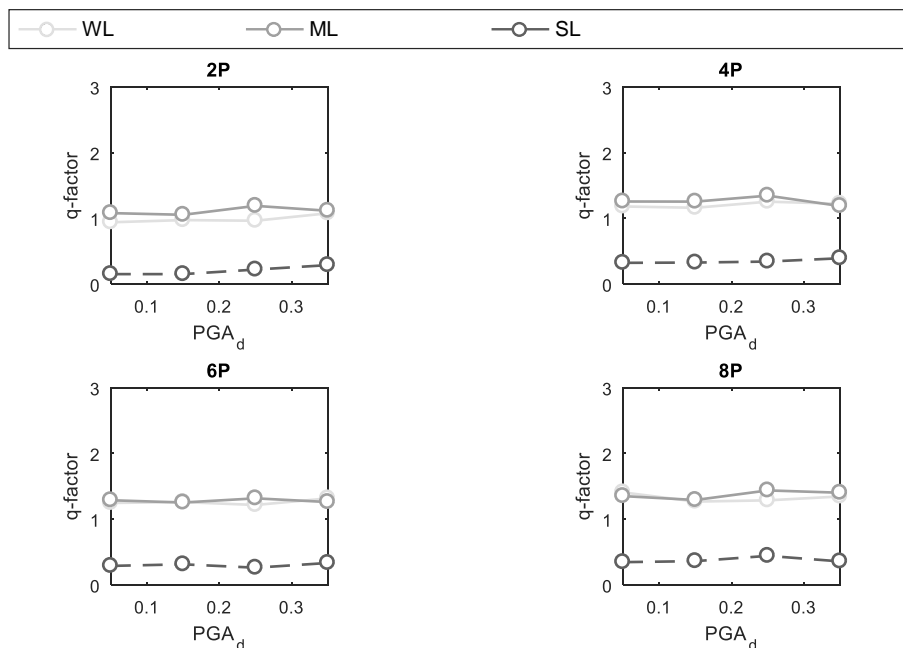
Figure 8.33. Mean q-factor values on the W/O models for all case-study buildings (effective stiffness approach).

It is observed that the q-factors for SL infills are often lower than the unit. This occurs because at very high (effective) period, the floor displacement demand is high (and equal to the OOP displacement capacity of the infill) but the floor acceleration demand is low and, namely, lower than that associated with the OOP strength of the IP-undamaged infill.

The average q-factor obtained not accounting for the IP/OOP interaction effect is equal to 1.20 for WL buildings and to 1.26 for ML buildings. The lower bound q-factor for SL buildings is equal to 0.15.

For the W/ model, in Table 8.18, the values obtained of the OOP effective stiffness obtained for the ten records and for each case-study building are normalized with respect the initial elastic stiffness as calculated for the analyses carried out for this Chapter, i.e., according to Timoshenko's approach.

Table 8.18. Values of the effective stiffness K_{eff} normalized with respect to the elastic K_{el} stiffness of the IP-undamaged infill obtained through the non-linear time-history analysis on the W/ models.

Record	#1	#2	#3	#4	#5	#6	#7	#8	#9	#10	mean
2P05WL	0.26	0.25	0.22	0.30	0.22	0.34	0.29	0.36	0.28	0.15	0.27
2P15WL	0.22	0.29	0.26	0.38	0.12	0.25	0.28	0.41	0.29	0.21	0.27
2P25WL	0.27	0.32	0.26	0.21	0.23	0.30	0.31	0.28	0.25	0.22	0.27
2P35WL	0.32	0.25	0.47	0.22	0.15	0.21	0.48	0.42	0.24	0.19	0.30
4P05WL	0.25	0.47	0.42	0.35	0.36	0.31	0.46	0.30	0.45	0.22	0.36
4P15WL	0.24	0.35	0.35	0.31	0.29	0.20	0.24	0.47	0.26	0.24	0.30
4P25WL	0.39	0.44	0.33	0.21	0.36	0.36	0.36	0.34	0.34	0.23	0.33
4P35WL	0.34	0.23	0.38	0.27	0.25	0.28	0.29	0.46	0.26	0.40	0.32
6P05WL	0.26	0.27	0.33	0.39	0.26	0.29	0.49	0.46	0.27	0.28	0.33
6P15WL	0.27	0.35	0.32	0.32	0.43	0.26	0.21	0.28	0.34	0.36	0.31
6P25WL	0.45	0.35	0.45	0.34	0.29	0.37	0.23	0.25	0.29	0.36	0.34
6P35WL	0.35	0.34	0.50	0.43	0.31	0.40	0.26	0.44	0.25	0.41	0.37
8P05WL	0.34	0.23	0.55	0.46	0.34	0.32	0.42	0.29	0.35	0.25	0.35
8P15WL	0.32	0.45	0.32	0.45	0.30	0.35	0.30	0.28	0.44	0.31	0.35
8P25WL	0.41	0.38	0.50	0.36	0.29	0.45	0.50	0.46	0.48	0.43	0.43
8P35WL	0.49	0.58	0.24	0.49	0.37	0.44	0.24	0.42	0.27	0.43	0.40
2P05ML	0.16	0.32	0.22	0.33	0.15	0.25	0.20	0.35	0.22	0.27	0.25
2P15ML	0.21	0.34	0.36	0.33	0.20	0.22	0.17	0.28	0.29	0.15	0.26
2P25ML	0.23	0.30	0.20	0.27	0.23	0.31	0.33	0.23	0.31	0.25	0.27
2P35ML	0.35	0.29	0.39	0.20	0.22	0.23	0.33	0.23	0.25	0.22	0.27
4P05ML	0.33	0.23	0.34	0.34	0.21	0.35	0.26	0.30	0.46	0.37	0.32
4P15ML	0.21	0.21	0.42	0.35	0.27	0.26	0.19	0.28	0.40	0.32	0.29
4P25ML	0.25	0.32	0.31	0.21	0.34	0.26	0.33	0.35	0.34	0.31	0.30
4P35ML	0.22	0.20	0.29	0.28	0.25	0.20	0.30	0.24	0.23	0.36	0.26
6P05ML	0.36	0.38	0.42	0.27	0.33	0.50	0.27	0.35	0.38	0.46	0.37
6P15ML	0.24	0.31	0.27	0.23	0.35	0.33	0.30	0.34	0.44	0.28	0.31
6P25ML	0.42	0.32	0.48	0.52	0.31	0.30	0.42	0.36	0.26	0.32	0.37
6P35ML	0.22	0.24	0.29	0.42	0.33	0.37	0.27	0.40	0.21	0.40	0.32
8P05ML	0.31	0.48	0.32	0.32	0.34	0.45	0.26	0.34	0.43	0.38	0.36
8P15ML	0.32	0.38	0.27	0.34	0.39	0.32	0.35	0.40	0.43	0.21	0.34
8P25ML	0.43	0.49	0.24	0.37	0.30	0.38	0.35	0.29	0.40	0.25	0.35
8P35ML	0.42	0.25	0.39	0.46	0.36	0.47	0.36	0.37	0.55	0.37	0.40
2P05SL	0.03	0.03	0.05	0.03	0.03	0.04	0.03	0.03	0.05	0.03	0.03
2P15SL	0.03	0.04	0.03	0.03	0.02	0.02	0.04	0.04	0.04	0.03	0.03
2P25SL	0.02	0.03	0.05	0.02	0.04	0.04	0.03	0.03	0.03	0.02	0.03
2P35SL	0.03	0.03	0.04	0.03	0.02	0.02	0.04	0.04	0.02	0.02	0.03
4P05SL	0.03	0.02	0.03	0.04	0.02	0.04	0.05	0.06	0.03	0.04	0.03
4P15SL	0.03	0.03	0.03	0.03	0.05	0.05	0.02	0.03	0.02	0.03	0.03
4P25SL	0.03	0.03	0.04	0.05	0.04	0.04	0.05	0.02	0.04	0.05	0.04
4P35SL	0.03	0.03	0.03	0.04	0.04	0.04	0.03	0.03	0.03	0.05	0.04
6P05SL	0.05	0.04	0.03	0.04	0.04	0.06	0.05	0.04	0.04	0.04	0.04
6P15SL	0.03	0.03	0.05	0.04	0.04	0.03	0.05	0.06	0.04	0.05	0.04
6P25SL	0.04	0.05	0.04	0.04	0.03	0.05	0.03	0.03	0.06	0.04	0.04
6P35SL	0.04	0.05	0.05	0.04	0.03	0.04	0.04	0.04	0.03	0.04	0.04
8P05SL	0.04	0.06	0.06	0.04	0.06	0.04	0.04	0.04	0.04	0.04	0.05
8P15SL	0.03	0.05	0.06	0.06	0.03	0.04	0.06	0.04	0.03	0.03	0.04
8P25SL	0.04	0.03	0.06	0.05	0.03	0.07	0.04	0.03	0.06	0.04	0.04
8P35SL	0.02	0.04	0.04	0.03	0.04	0.03	0.04	0.03	0.06	0.05	0.04

The average K_{eff}/K_{el} ratio obtained accounting for the IP/OOP interaction effect is equal to 0.33 for WL infills, to 0.31 for ML infills and to 0.04 for SL infills. The very low effective stiffness of SL infills has been already explained in the case of W/O models. The values of the effective stiffness evaluated for W/ models is generally lower than that obtained on W/O models. This occurs because the OOP model adopted is characterized by an OOP collapse displacement that increases at increasing IP damage level. Hence, the OOP collapse of infills occurs, in the case of W/ model, for a higher displacement demand than in the case of W/O models. This circumstance yields to higher values of the effective period and, so, to lower values of the effective stiffness of infills.

The values for the q-factor obtained from the W/ models by calculating the force demand acting on infills as a function of their effective stiffness are shown in Table 8.19 and in Figures 8.34-35.

Table 8.19. Values of the q-factor obtained through the non-linear time-history analysis on the W/ models calculated by dividing the OOP seismic demand corresponding to the effective period of the IP-undamaged infill by its strength.

Record	#1	#2	#3	#4	#5	#6	#7	#8	#9	#10	mean
2P05WL	0.82	0.95	0.98	0.85	0.59	0.83	0.89	0.92	0.84	0.64	0.83
2P15WL	0.77	1.05	0.95	0.94	0.61	0.96	0.86	1.03	1.04	0.74	0.89
2P25WL	0.84	0.96	1.13	0.81	0.64	1.01	0.92	0.80	0.79	0.98	0.89
2P35WL	0.91	1.15	1.27	0.88	0.65	0.91	1.26	1.03	0.90	0.88	0.99
4P05WL	1.05	1.15	1.10	0.91	0.90	1.07	1.13	0.89	1.10	1.07	1.04
4P15WL	0.97	0.94	1.08	0.87	1.15	0.97	0.93	1.23	0.92	0.95	1.00
4P25WL	1.20	1.13	0.98	0.94	1.14	1.06	1.21	0.92	0.90	0.94	1.04
4P35WL	1.06	1.02	0.99	0.98	0.96	1.00	1.02	1.13	1.21	0.99	1.04
6P05WL	1.25	1.20	1.03	1.02	1.13	1.05	1.20	1.16	1.07	1.02	1.11
6P15WL	1.20	1.32	1.28	1.32	1.11	1.19	0.99	1.25	1.06	1.21	1.19
6P25WL	1.29	1.01	1.34	1.34	1.01	1.01	1.01	1.08	1.27	1.17	1.15
6P35WL	1.27	0.95	1.34	1.27	1.23	1.04	1.20	1.27	1.05	1.16	1.18
8P05WL	1.43	1.11	1.35	1.36	1.41	1.09	1.25	1.29	1.31	1.18	1.28
8P15WL	1.28	1.09	1.17	1.18	1.31	1.45	1.32	1.07	1.10	1.24	1.22
8P25WL	1.18	1.16	1.43	1.07	1.34	1.13	1.39	1.23	1.19	1.13	1.22
8P35WL	1.27	1.43	1.18	1.24	1.28	1.42	1.18	1.26	1.06	1.32	1.27
2P05ML	0.79	1.06	1.00	0.80	0.55	0.83	0.81	0.90	0.78	0.73	0.82
2P15ML	0.58	0.98	1.11	0.85	0.70	0.80	0.79	0.91	0.93	0.66	0.83
2P25ML	0.85	1.09	0.99	0.89	0.72	1.02	1.14	0.87	0.79	0.84	0.92
2P35ML	0.93	0.93	1.20	0.69	0.67	0.82	1.09	0.97	0.68	0.62	0.86
4P05ML	0.80	0.89	0.92	0.96	0.89	1.07	0.82	1.08	1.13	0.99	0.96
4P15ML	0.98	0.76	1.05	0.87	0.97	1.09	0.95	1.16	1.04	1.04	0.99
4P25ML	1.11	1.04	1.22	0.81	1.00	1.22	0.91	0.89	1.21	1.14	1.05
4P35ML	0.83	0.83	1.01	0.93	1.22	0.94	0.94	0.70	1.01	0.93	0.93
6P05ML	1.29	1.23	1.10	1.18	0.95	1.22	1.07	1.00	0.95	1.17	1.12
6P15ML	1.04	1.18	0.84	1.05	1.07	1.10	1.18	1.09	1.08	1.05	1.07
6P25ML	1.33	0.95	1.18	1.27	1.34	0.94	1.07	0.88	1.08	0.91	1.10
6P35ML	1.00	1.01	1.40	1.09	1.15	0.97	0.76	1.04	1.04	1.33	1.08
8P05ML	1.19	1.21	1.21	1.33	1.14	1.13	1.21	0.82	1.24	1.09	1.16
8P15ML	1.17	1.20	0.91	1.05	1.17	1.03	1.18	1.27	1.06	0.99	1.10
8P25ML	1.44	1.32	1.18	1.24	1.15	0.93	1.39	1.20	1.14	1.05	1.20
8P35ML	1.26	1.09	1.35	1.20	1.14	1.40	1.11	1.22	1.47	1.09	1.23
2P05SL	0.09	0.13	0.17	0.09	0.09	0.13	0.13	0.15	0.15	0.14	0.13
2P15SL	0.10	0.14	0.14	0.13	0.08	0.12	0.13	0.12	0.13	0.10	0.12
2P25SL	0.11	0.16	0.18	0.12	0.12	0.14	0.14	0.13	0.12	0.12	0.13
2P35SL	0.12	0.14	0.14	0.11	0.09	0.11	0.13	0.16	0.10	0.08	0.12
4P05SL	0.14	0.12	0.16	0.15	0.11	0.13	0.16	0.17	0.14	0.13	0.14
4P15SL	0.14	0.14	0.14	0.09	0.15	0.17	0.12	0.16	0.12	0.15	0.14
4P25SL	0.18	0.18	0.18	0.17	0.14	0.18	0.16	0.13	0.13	0.15	0.16
4P35SL	0.16	0.17	0.11	0.16	0.18	0.12	0.10	0.12	0.15	0.16	0.14
6P05SL	0.17	0.12	0.15	0.17	0.16	0.18	0.17	0.12	0.21	0.13	0.16
6P15SL	0.15	0.11	0.15	0.18	0.17	0.14	0.17	0.19	0.15	0.16	0.16
6P25SL	0.19	0.19	0.14	0.13	0.18	0.16	0.12	0.14	0.18	0.14	0.16
6P35SL	0.15	0.14	0.15	0.19	0.14	0.15	0.14	0.15	0.15	0.13	0.15
8P05SL	0.16	0.17	0.19	0.16	0.20	0.17	0.18	0.14	0.17	0.16	0.17
8P15SL	0.15	0.18	0.19	0.17	0.15	0.17	0.19	0.18	0.18	0.16	0.17
8P25SL	0.14	0.17	0.19	0.16	0.16	0.22	0.17	0.15	0.20	0.16	0.17
8P35SL	0.12	0.23	0.15	0.16	0.16	0.16	0.17	0.17	0.17	0.15	0.16
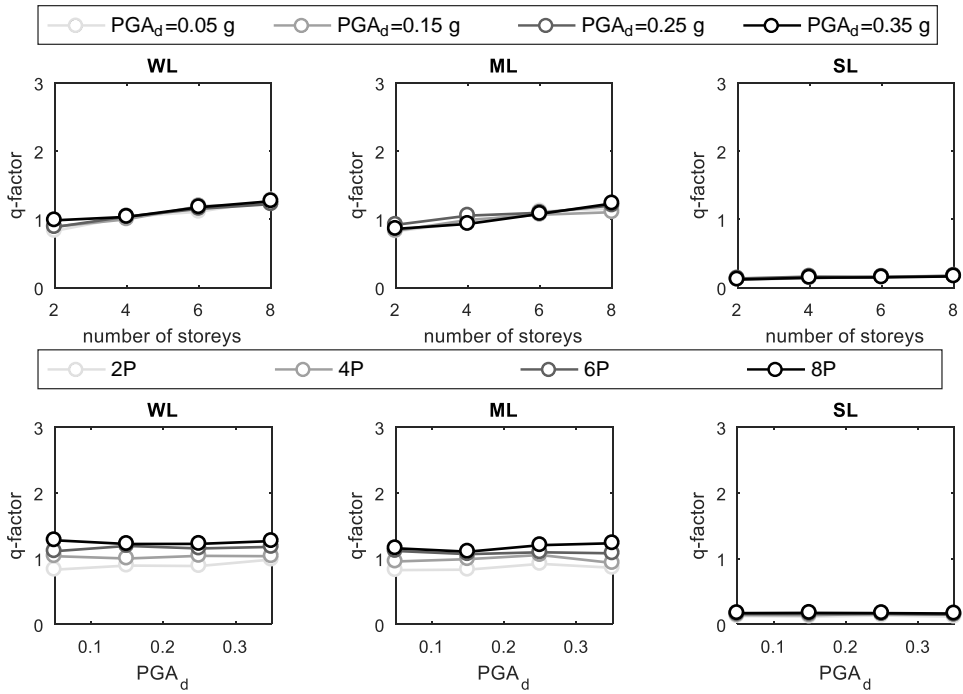
Figure 8.34. Mean q-factor values on the W/ models for all case-study buildings (effective stiffness approach).
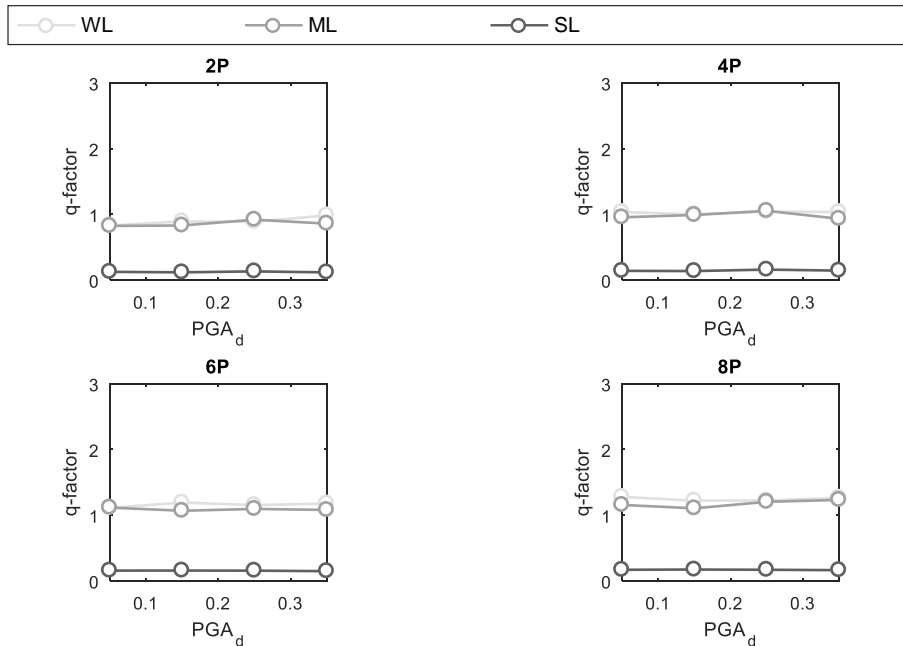
Figure 8.35. Mean q-factor values on the W/ models for all case-study buildings (effective stiffness approach).

Also in this case, it is observed that in many cases, especially for SL infills, q-factors are lower than the unit. This occurs because at very high period, such as the effective one, the floor displacement demand is high but the floor acceleration demand is low and, namely, lower than that associated with the OOP strength of the IP-undamaged infill.

The average q-factor obtained not accounting for the IP/OOP interaction effect is equal to 1.08 for WL infills, to 1.03 for ML infills, and to 0.12 for SL infills.

8.7.4. Final remarks and proposals

In this section, the results previously shown and discussed are summarized in order to define a proposal for the value of the OOP behaviour factor and of the effective stiffness of URM infills.

Remember that the effective stiffness has been evaluated as a fraction of the OOP initial stiffness of the IP-undamaged infill. Its value has been determined for both W/O and W/ models. The average values obtained for the considered infill layouts are reported, separately, in Table 8.20. Actually, the value reported for the SL infills in W/O models is not an average, but a lower bound of the K_{eff}/K_{el} ratio. Note that the average

values are not distinguished also for design PGA of the case-study building and/or for total number of storeys of the case-study building as it was observed that both of these parameters have only a slight influence on the value of the effective stiffness.

Table 8.20. Average values of the effective stiffness for all infill layouts.

	WL		ML		SL	
	W/O	W/	W/O	W/	W/O	W/
K_{eff}/K_{el}	0.40	0.33	0.42	0.31	0.05	0.04

It is observed that, on average, the effective stiffness is greater when evaluated on W/O models. This occurs because the proposed OOP model is characterized by an OOP conventional collapse displacement that can remain constant or increase at increasing IP displacement demand. Hence, infills collapsed in the W/O model are characterized by lower OOP displacement demand at collapse than in W/ model and, so, by a lower effective period.

For what concerns the behaviour factor, it has been evaluated in different ways on both W/O and W/ models:

i. With demand calculated based on the OOP elastic period of the IP-undamaged infill and capacity calculated based on the OOP strength of the IP-undamaged infill (for W/O models, within the "straightforward approach" and for W/ models, within the "practice-oriented approach");

ii. With demand calculated based on the OOP elastic period of the IP-damaged infill and capacity calculated based on the OOP strength of the IP-damaged infill (only for W/ models within the "straightforward approach");

iii. With demand calculated based on the OOP effective period of the infill and capacity calculated based on the OOP strength of the IP-undamaged infill (for both W/O and W/ model within the approach based on the "effective stiffness").

The 16th, 50th and 84th percentile values of the q-factors obtained for the considered infill layouts and accounting for the record-to-record variability are reported, separately, in Tables 8.21-23. Remember that the values reported for the SL infills in W/O models are derived based on a reduced dataset, as the collapse of SL infills was not always observed in W/O models. Note that the average values are not distinguished also for

design PGA of the case-study building and/or for total number of storeys of the case-study building as it was observed that both of these parameters have only a slight influence on the value of the q-factor. In other words, one can use such percentiles of the q-factor only knowing the infill typology and without knowing the building number of storeys and design PGA, i.e., by assuming an equal probability that the considered building is characterized by a number of storeys equal to 2, 4, 6 or 8 and by a design PGA equal to 0.05 g, 0.15 g, 0.25 g and 0.35 g.

Table 8.21. Values of the q-factor for all infill layouts: 16th percentile.

	WL		ML		SL	
approach	W/O	W/	W/O	W/	W/O	W/
straightforward	1.24	1.53	1.24	1.31	2.14	1.18
practice-oriented	-	1.12	-	0.98	-	0.88
effective stiffness	1.00	0.91	1.04	0.83	0.29	0.12

Table 8.22. Values of the q-factor for all infill layouts: 50th percentile.

	WL		ML		SL	
approach	W/O	W/	W/O	W/	W/O	W/
straightforward	1.41	1.72	1.43	1.59	2.79	1.42
practice-oriented	-	1.27	-	1.18	-	1.06
effective stiffness	1.18	1.08	1.28	1.04	0.38	0.15

Table 8.23. Values of the q-factor for all infill layouts: 84th percentile.

	WL		ML		SL	
approach	W/O	W/	W/O	W/	W/O	W/
straightforward	1.53	1.91	1.60	1.82	3.37	1.63
practice-oriented	-	1.41	-	1.35	-	1.21
effective stiffness	1.39	1.27	1.45	1.21	0.50	0.18

Based on the above results, the most appropriate and practical way to calculate in a linear elastic framework the OOP seismic demand on URM infills and to verify them against the seismic action by accounting for the IP/OOP interaction (but without explicitly modelling it) is, in the writer opinion:

i.   calculating the seismic demand as a function of the initial elastic stiffness of the IP-undamaged infill;

  ii. calculating the OOP capacity as a function of the OOP strength of the IP-undamaged infill;

  iii. assuming a behaviour factor equal to 1.

First of all, such suggestions derive from a simplification of the "practice-oriented" approach results. The value proposed for the behaviour factor is consistent with the 16th percentile of the values obtained through the analyses' results and it seems, to the writer judgment, sufficiently conservative for all infill layouts.

Such value of the behaviour factor can be considered as representative of a specific mechanical phenomenon. If the IP/OOP interaction is not explicitly modelled and the OOP seismic demand and capacity of infills is calculated as if the infill were not IP-damaged, the beneficial effects of the potential OOP ductility capacity of the infill should not be considered to perform a safety-sided simplified safety check. It is worth to mention that the value herein suggested for the behaviour factor is equal to that already assumed by NZSEE 2017.

The reader should be aware that the OOP seismic demand on infills, for a perfect closure on the suggested approach, should be calculated by means of appropriate floor spectra derived from the analyses herein performed. Ongoing research is focused also on this issue.

REFERENCES

- Calvi GM, Bolognini D. Seismic response of reinforced concrete frames infilled with weakly reinforced masonry panels. Journal of Earthquake Engineering 2001;5.2:153-185.
- Eurocode 6. Design of Masonry Structures. Part 1-1: General Rules for Reinforced and Unreinforced Masonry Structures. Brussels, 2005. 123 p.
- Eurocode 8. Design of structures for Earthquake Resistance. Part 1-1: General Rules, Seismic Actions and Rules for Buildings. Brussels, 2004. 229 p.
- Fardis MN (editor). Experimental and numerical investigations on the seismic response of RC infilled frames and recommendations for code provisions, ECOEST/PREC8 Report No.6, Laboratorio Nacional de Engenharia Civil Publications, Lisbon, 1996.
- Furtado A, Rodrigues H, Arêde A, Varum H. Experimental evaluation of out-of-plane capacity of masonry infill walls. Engineering Structures 2016;111:48-63.
- Grant DN, Response spectral matching of two horizontal ground-motion components. Journal of Structural Engineering, 137.3, 289-297, 2010.

- Guidi G, da Porto F, Dalla Benetta M, Verlato N, Modena C. Comportamento sperimentale nel piano e fuori piano di tamponamenti in muratura armata e rinforzata. Proceedings of the XV ANIDIS, L'Ingegneria Sismica in Italia, Padua, Italy, 2013, 30. (in Italian).
- Hak S, Morandi P, Magenes G. Out-of-plane experimental response of strong masonry infills. 2nd European Conference on Earthquake Engineering and Seismology, 2014.
- Haselton CB, Liel AB, Lange ST, Deierlein GG. Beam-column element model calibrated for predicting flexural response leading to global collapse of RC frame buildings. Pacific Earthquake Engineering Research Center 2007.
- Kadysiewski S, Mosalam KM. Modelling of unreinforced masonry infill walls considering in-plane and out-of-plane interaction. Pacific Earthquake Engineering Research Center 2009.
- Luzi L, Puglia R, Russo E & ORFEUS WG5 (2016). Engineering Strong Motion Database, version 1.0. Istituto Nazionale di Geofisica e Vulcanologia, Observatories & Research Facilities for European Seismology. doi: 10.13127/ESM
- McKenna F, Fenves GL, Scott MH. Open system for earthquake engineering simulation. University of California, Berkeley, CA, 2000.
- Mosalam K.M., Günay S. Progressive collapse analysis of reinforced concrete frames with unreinforced masonry infill walls considering in-plane/out-of-plane interaction. Earthquake. Spectra 2015;31.2,921-943.
- NZSEE 2017. New Zealand Society for Earthquake Engineering (NZSEE), Structural Engineering Society New Zealand Inc. (SESOC), New Zealand Geotechnical Society Inc., Ministry of Business, Innovation and Employment, Earthquake Commission. The Seismic Assessment of Existing Buildings (the Guidelines), Part C – Detailed Seismic Assessment, 2017. http://www.eq-assess.org.nz/
- Panagiotakos TB, Fardis MN. Seismic response of infilled RC frames structures. 11th World Conference on Earthquake Engineering. June 23-28, 1996, Acapulco, México.
- Timoshenko SP, Woinowsky Krieger S. Theory of plates and shells. McGraw-Hill, New York, 1959.
- Vamvatsikos D, Cornell CA. Incremental dynamic analysis. Earthquake Engineering and Structural Dynamics 2002;31.3:491-514.

Appendix A
Analytical derivation of mechanical-based OOP strength models

A.1. INTRODUCTION

In this Appendix, the analytical derivation of the mechanical-based OOP strength models presented in Chapter I is reported.

As reported also in Chapter 1, the mechanical strength formulations based on one-way arching action are McDowell et al.'s model (1956), Angel et al.'s model (1994), Eurocode 6's model (2004). The only mechanical-based strength formulation based on two-way arching action is that by Bashandy et al. (1995).

The derivation of all these formulations is herein described in detail. Although such derivation may be available elsewhere in the literature (especially for which concerns Angel et al.'s and Bashandy et al.'s model), presenting all of them with a unique notation and critical approach seems to the Author worthy to be included in this thesis and potentially useful to the interested reader.

A.2. OOP STRENGTH MODELS BASED ON ONE-WAY ARCHING ACTION

In this section, the OOP strength models accounting for one-way arching action are derived.

A.2.1. McDowell et al.'s strength model

Consider a unit-width masonry stripe constrained at the edges by stiff elements with length equal to h, thickness equal to t, material compressive strength f_m and elastic modulus E_m. It is assumed that the considered masonry stripe is subjected to an OOP uniformly distributed load. The contribution to the OOP strength of flexural mechanisms is neglected. Hence, when calculating the OOP strength, the considered masonry stripe is already cracked at its ends and mid-height. Of course, it is assumed that arching action occurs.

At the initial stage, the masonry stripe is separated in two parts with length h/2 and diagonal length L', as shown in Figure A.1 and reported in Equation 1.

$$L' = \sqrt{\left(\frac{h}{2}\right)^2 + t^2} \tag{1}$$
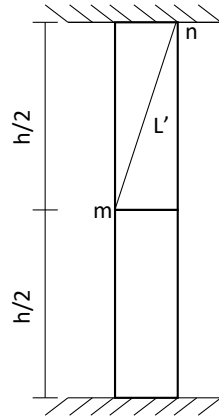
Figure A.1. McDowell et al.'s masonry stripe at the initial stage.

When the lateral OOP displacement of point m equals the infill thickness, t, the diagonal length equals h/2. Hence, when the OOP displacement of the infill centre equals t, the shortening strain of the diagonal ε_m can be expressed as reported in Equation 2.

$$\varepsilon_m = \frac{L' - h/2}{L'} = \frac{\sqrt{(h/2)^2 + t^2} - h/2}{\sqrt{(h/2)^2 + t^2}} \tag{2}$$

If the material was indefinitely elastic, the maximum compressive stress acting at the masonry part ends and producing such a diagonal shortening could be expressed through the simple elastic relation reported in Equation 3.

$$f_{max} = E_m \varepsilon_m \tag{3}$$

By a simple proportion, it is possible to calculate the lateral displacement x_y at which the maximum stress equals masonry compressive strength f_m, as reported in Equation 4.

$$\frac{x_y}{f_m} = \frac{t}{E_m \varepsilon_m} \rightarrow x_y = \frac{t f_m}{E_m \varepsilon_m} \tag{4}$$

It is assumed that the OOP strength of the infill is attained when the maximum compressive stress at each masonry part end equals f_m and when the OOP central displacement of the masonry stripe equals x_y. In addition, it is assumed that in such a state, the compressive stress distribution at each end of masonry parts can be represented by a stress block with height equal to $0.85f_m$ and base equal to $0.85c$, with c equal to the contact length. For all these reasons, the arching thrust according to McDowell et al.'s, C, is expressed as reported in Equation 5.

$$C = 0.85c \, 0.85f_m \tag{5}$$

Considering each masonry part, C acts at both of their ends with distance b, as reported in Figure A.2.
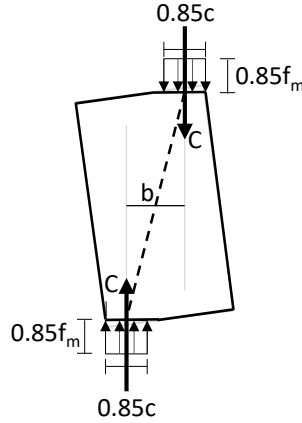
Figure A.2. McDowell et al.'s arching mechanism for a single masonry part.

Remember that at the attainment of the OOP strength, with reference to Figure A.1, point n has not moved while point m has shifted along the horizontal direction with a displacement equal to x_y. Hence, the initial distance between n and m is equal to t, while at the attainment of the OOP strength of the stripe it is equal to $t-x_y$. The centroid of C is applied, at the masonry part upper edge, at a distance equal to one half 0.85c from point n and at a distance equal to one half 0.85c from point m. Hence, the distance b between C directions can be expressed as reported in Equation 6.

$$b = t - x_y - \frac{1}{2}0.85c - \frac{1}{2}0.85c = t - x_y - 0.85c \tag{6}$$

The torque, M, can be expressed as reported in Equation 7.

$$M = C \cdot b = 0.85c\,0.85f_m\left(t - x_y - 0.85c\right) \tag{7}$$

In Equation 7 all values are known except c, the contact length. It is assumed that its value at the attainment of the OOP strength is such that the moment M is maximized. Hence, c is calculated by differentiating M with respect to c and by equating such derivative to zero. The value obtained for the contact length is reported in Equation 8.

$$c = \frac{1}{2 \cdot 0.85}\left(t - x_y\right) = \frac{1}{1.7}\left(t - x_y\right) \tag{8}$$

By substituting Equation 8 in Equation 7, the expression of M reported in Equation 9 is obtained.

$$M = \frac{1}{4} 0.85 f_m \left(t - x_y\right)^2 \tag{9}$$

The principle of virtual work is then applied. It is assumed that M acts on each of the two rotating masonry parts and that one-half of M, M_y, acts at each end of each masonry part, as reported in Equation 10.

$$M_y = \frac{1}{8} 0.85 f_m \left(t - x_y\right)^2 \tag{10}$$

The external work under uniformly distributed load calculated with reference to the mechanism shown in Figure A.3 is reported in Equation 11.
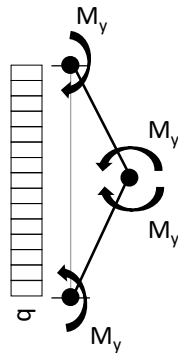
Figure A.3. Collapse mechanism for McDowell et al.'s masonry stripe.

$$L_e = q \frac{h^2}{4} \varphi \tag{11}$$

On the other hand, the internal work is reported in Equation 12.

$$L_i = 4 M_y \varphi \tag{12}$$

By equating Equation 11 and Equation 12, the value of q_{max} reported in Equation 13 is obtained.

$$q_{max} = \frac{16M_y}{h^2} \tag{13}$$

By substituting Equation 10 in Equation 13, a straightforward formulation for q_{max} is derived, as reported in Equation 14.

$$q_{max} = 1.7 \frac{f_m}{(h/t)^2} \left(1 - \frac{f_m}{E_m \varepsilon_m}\right)^2 \tag{14}$$

A.2.2. Angel et al.'s strength model

Consider a unit-width masonry stripe constrained at the edges by stiff elements with length equal to h, thickness equal to t, material compressive strength fm and elastic modulus E_m. It is assumed that the considered masonry stripe is subjected to an OOP uniformly distributed load. The contribution to the OOP strength of flexural mechanisms is neglected. Hence, when calculating the OOP strength, the considered masonry stripe is already cracked at its ends and mid-height. Of course, it is assumed that arching action occurs.

As shown in Figure A.4, the arching thrust T acts in a certain direction at each end of each rotating masonry segment. Such direction forms an angle called γ with the vertical direction, while the rotation angle of the masonry part is equal to θ. The contact length evaluated on the masonry segment undeformed shape is called b.
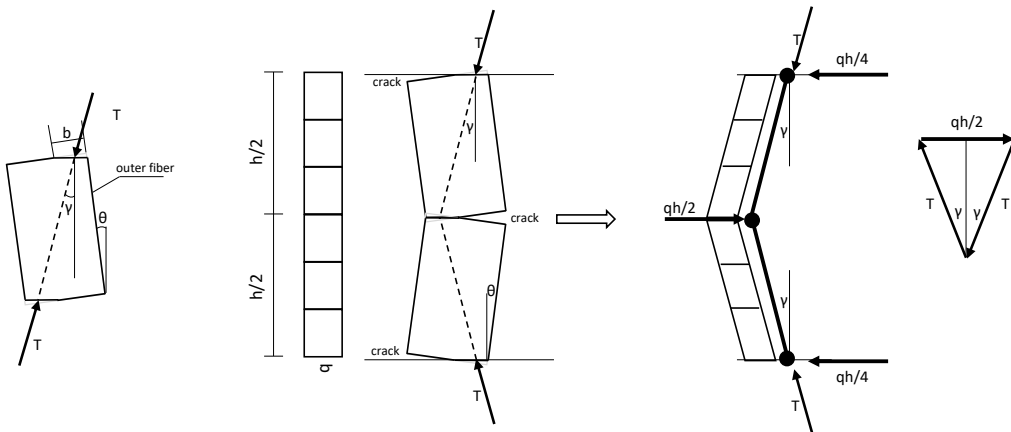
Figure A.4. Angel et al.'s arching mechanism.

In Figure A.4, the static scheme of the cracked masonry stripe is shown, too, together with the equivalent scheme considered by Angel et al. Under these assumptions, based on equilibrium, Equation 15 can be written.

$$\frac{qh}{2} = 2T\sin\gamma \tag{15}$$

It is assumed that the compressive stresses distribution acting along b is characterized by a maximum compressive stress equal to f_b and a medium compressive stress equal to fav. The k_1 ratio is hence defined as reported in Equation 16.

$$k_1 = \frac{f_{av}}{f_b} \tag{16}$$

As shown in Figure A.5, the resultant compressive action C acting perpendicular to the undeformed edge of the masonry part can be calculated as reported in Equation 17.
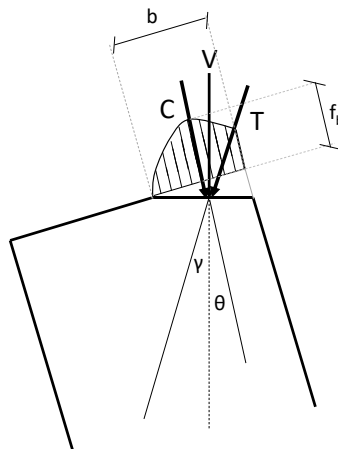
Figure A.5. Stresses and forces acting at one end of the upper masonry part according to Angel et al.

$$C = bf_{av} = bk_1f_b \tag{17}$$

It is assumed that C is the component acting along the masonry rotating part axis of a vertical action V. Hence, V can be expressed as reported in Equation 18.

$$V = C/\cos\theta = bk_1f_b/\cos\theta \qquad (18)$$

At the same time, also T is the component of V acting along the direction of arching thrust. Hence, T can be expressed as reported in Equation 19.

$$T = V\cos\gamma = C\cos\gamma/\cos\theta = bk_1f_b\cos\gamma/\cos\theta \qquad (19)$$

By substituting Equation 19 in Equation 15, the formulation reported in Equation 20 is obtained to express q.

$$\frac{qh}{2} = 2bk_1f_b\cos\gamma\sin\gamma/\cos\theta \rightarrow q = \frac{4bk_1f_b\frac{\cos\gamma}{\cos\theta}\sin\gamma}{h} = \frac{4\frac{b}{t}k_1f_b\frac{\cos\gamma}{\cos\theta}\sin\gamma}{h/t} \qquad (20)$$

Now, explicit formulations for calculating γ, b and θ are derived. As shown in Figure A.6, it is assumed that the outside fiber of the masonry segment is characterized by a linear distribution of strain equal to zero at the cracked end and to ε_{max} to the supported end.
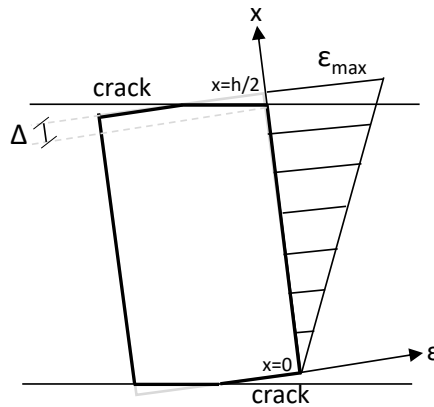
Figure A.6. Stresses and forces acting at one end of the upper masonry part according to Angel et al.

The shortening of the outside fiber evaluated along the masonry part axis, Δ, can be expressed as reported in Equation 21.

$$\Delta = \int_0^{h/2} \varepsilon(x)\,dx = \int_0^{h/2} \frac{\varepsilon_{max}}{h/2}\,x\,dx = \frac{2\varepsilon_{max}}{h} \int_0^{h/2} x\,dx = \frac{1}{4}\varepsilon_{max}h = ch \qquad (21)$$

In Equation 21, c is a dimensionless parameter equal to one-fourth of ε_{max}. In addition a further parameter is introduces, i.e., the distance of C application point from the outer fiber of masonry segment calculated along the undeformed edge of the masonry segment normalized with respect to b. Such parameter is named k_2.
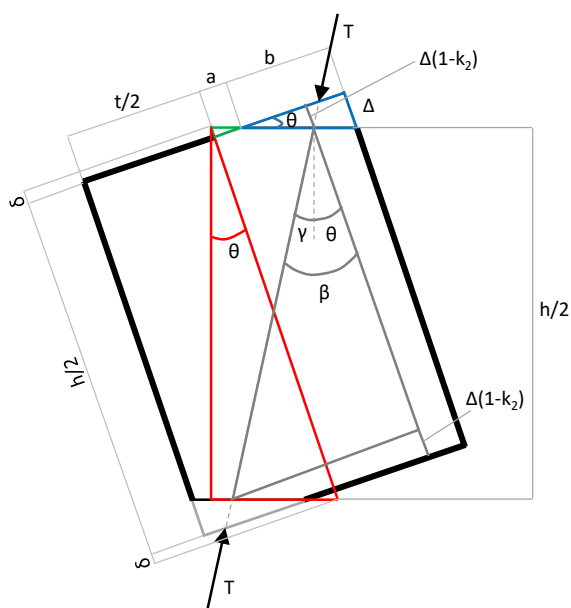
Figure A.7. Calculation of Angel et al.'s contact length b and θ and γ angles based on geometrical considerations.

Consider now Figure A.7 and, specifically, the red triangle. Equation 22 applies.

$$\left(\frac{h}{2} + 2\delta\right)\cos\theta = \frac{h}{2} \qquad (22)$$

From Equation 22 the expression of δ is derived as reported in Equation 23.

$$\delta = \frac{h}{4}\left(\frac{1}{\cos\theta} - 1\right) = \frac{h}{4}\left(\frac{1-\cos\theta}{\cos\theta}\right) \qquad (23)$$

From the green triangle in Figure A.7, the expression of δ reported in Equation 24 is derived.

$$\delta = a\tan\theta = a\frac{\sin\theta}{\cos\theta} \tag{24}$$

By comparing Equation 23 and Equation 24, the value of a is derived as reported in Equation 25.

$$\frac{h}{4}\left(\frac{1-\cos\theta}{\cos\theta}\right) = a\frac{\sin\theta}{\cos\theta} \rightarrow a = \frac{h}{4}\left(\frac{1-\cos\theta}{\sin\theta}\right) \tag{25}$$

It can be observed from Figure A.7 that a is defined as t/2-b. Hence, Equation 26 applies.

$$b = \frac{t}{2} - a = \frac{t}{2} - \frac{h}{4}\left(\frac{1-\cos\theta}{\sin\theta}\right) = \frac{t}{2} - \frac{h}{4}\left(\frac{1}{\sin\theta} - \frac{1}{\tan\theta}\right) \tag{26}$$

From the blue triangle in Figure A.7, the expressions of sinθ and tanθ are derived as reported in Equations 27 and 28.

$$\Delta = \sqrt{b^2 + \Delta^2}\sin\theta \rightarrow \sin\theta = \frac{\Delta^2}{\sqrt{b^2 + \Delta^2}} \tag{27}$$

$$\Delta = b\tan\theta \rightarrow \tan\theta = \frac{\Delta}{b} \tag{28}$$

By substituting Equations 27 and 28 in Equation 26, Equation 29 is obtained for b.

$$b = \frac{t}{2} - \frac{h}{4}\left(\frac{\sqrt{b^2 + \Delta^2}}{\Delta^2} - \frac{b}{\Delta}\right) \tag{29}$$

Some manipulation on Equation 29 together with the definition of the parameter c yield to the expression reported in Equation 30.

$$\left(1 - \frac{1}{4c}\right)b - \frac{t}{2} = -\frac{1}{4c}\sqrt{b^2 + \Delta^2} \tag{30}$$

By squaring both members of Equation 30 and with some other manipulation, Equation 31 is obtained.

$$\left(1 - \frac{1}{2c}\right)b^2 - t\left(1 - \frac{1}{4c}\right)b + \left(\frac{t}{2}\right)^2 - \left(\frac{h}{4}\right)^2 = 0 \tag{31}$$

The term $(h/4)^2$ can be rewritten as reported in Equation 32.

$$\left(\frac{h}{4}\right)^2 = \frac{1}{4}\left(\frac{h}{t}\right)^2\left(\frac{t}{2}\right)^2 \tag{32}$$

By substituting Equation 32 in Equation 31, Equation 33 is obtained.

$$\left(1 - \frac{1}{2c}\right)b^2 - t\left(1 - \frac{1}{4c}\right)b + \left(\frac{t}{2}\right)^2\left[1 - \frac{1}{4}\left(\frac{h}{t}\right)^2\right] = 0 \tag{33}$$

If in Equation 33 all terms are divided by t^2, Equation 34 is obtained.

$$\left(1 - \frac{1}{2c}\right)\left(\frac{b}{t}\right)^2 - t\left(1 - \frac{1}{4c}\right)\frac{b}{t} + \frac{1}{2}\left[1 - \frac{1}{4}\left(\frac{h}{t}\right)^2\right] = 0 \tag{34}$$

The feasible solution in b/t of Equation 34 is reported in Equation 35.

$$\frac{b}{t} = \frac{1}{2}\left[\frac{(1 - 4c)}{2(1 - 2c)} + \sqrt{\frac{1}{4(1 - 2c)^2} - \frac{c}{2(1 - 2c)}\left(\frac{h}{t}\right)^2}\right] \tag{35}$$

In Equation 35, c and its multiples can be neglected when added or subtracted from the unit. Hence, Equation 35 simplifies in Equation 36.

$$\frac{b}{t} \cong \frac{1}{2}\left[\frac{1}{2} + \sqrt{\frac{1}{4} - \frac{c}{2}\left(\frac{h}{t}\right)^2}\right] = \frac{1}{4}\left[1 + \sqrt{1 - 2c\left(\frac{h}{t}\right)^2}\right] \tag{36}$$

Based on Equation 36, the contact length is a function of masonry maximum strain and of the masonry stripe slenderness ratio.

From Equation 28, the value of the rotation θ can be derived as reported in Equation 37.

$$\Delta = b\tan\theta \rightarrow \tan\theta = \frac{\Delta}{b} = c\frac{h}{b} = c\frac{h/t}{b/t} \rightarrow \theta = \text{atan}\left(c\frac{h/t}{b/t}\right) = \text{atan}\left(c\frac{h/t}{b/t}\right) \tag{37}$$

By substituting Equation 36 in Equation 37, Equation 38 is obtained.

$$\theta = \text{atan}\left(c\frac{h/t}{\frac{1}{4}\left[1 + \sqrt{1 - 2c(h/t)^2}\right]}\right) \tag{38}$$

Based on Figure A.7, it is observed that the angle formed by the direction of the arching thrust with the vertical direction can be expressed as reported in Equation 39.

$$\gamma = \beta - \theta \tag{39}$$

The angle β can be defined by observing the grey triangle in Figure A.7. The length of the sides of this triangle are known. In fact, one of them is given by the infill thickness t reduced by two times the distance of the compression centroid from the outer fiber of the masonry segment, which is equal to k_2b. Hence, the first side of the triangle is $t-2k_2b$ long. The length of the second side of the grey triangle is equal to the initial length of the masonry part, h/2, reduced by two times the shortening of the fiber corresponding to the compression centroid, which is equal to $\Delta(1-k2)$. Hence, the second side of the triangle is $h/2-2(1-k_2)\Delta$ long. For the determination of β, Equation 40 is derived.

$$\tan\beta = \frac{t - 2k_2b}{h/2 - 2(1 - k_2)\Delta} \tag{40}$$

With some manipulation, Equation 40 can be rewritten as reported in Equation 41.

$$\tan\beta = \frac{2[1 - 2k_2(b/t)]}{(h/t)[1 - 4c(1 - k_2)]} \tag{41}$$

In Equation 41, c and its multiples can be neglected when added or subtracted from the unit. Hence, Equation 41 simplifies in Equation 42.

$$\tan\beta \cong \frac{2[1 - 2k_2(b/t)]}{(h/t)} \tag{42}$$

Hence, Equation 43 can be used to calculate β.

$$\beta = \text{atan}\left(\frac{2[1 - 2k_2(b/t)]}{(h/t)}\right) \tag{43}$$

For a given OOP displacement of the stripe centre, d_{OOP}, Equation 44 can be applied to calculate θ.

$$\theta = \text{atan}\left(\frac{2d_{OOP}}{h}\right) \tag{44}$$

At this point, one should define the stress-strain relationship for masonry under compression. This also means defining the values of k_1 and k2. For example, if the stress-stain relationship is triangular, k_1 is equal to 0.50 and k2 is equal to 0.33.

The OOP force-displacement relationship for the stripe can be calculated by following the procedure listed hereafter.

- i.   Define a value of the OOP displacement, d_{OOP};
- ii.   Calculate θ by means of Equation 44;
- iii.   Calculate c by applying a trial-and-error procedure on Equation 38;
- iv.   Calculate ε_{max} equal to 4c;
- v.   Enter masonry stress-strain relationship with $\varepsilon=4c$ and calculate the value of f_b;
- vi.   Calculate b/t from Equation 36;
- vii.   Calculate β from Equation 43;
- viii.   Calculate γ from Equation 39;
- ix.   Calculate q from Equation 20.

A direct strength formulation is also provided, based on some hypotheses.

From the application of the above procedure, it is possible to calculate also the OOP load q vs εmax diagram. According to Angel et al., the OOP load should be assumed equal to zero when ε_{max} equals masonry crushing strain, ε_{crush}, conservatively, provided that the arching action has not vanished due to snap-through, as explained in Chapter I.

The ε_{max} value at which the OOP strength is attained is called $\varepsilon_{max,1}$.

Angel et al. assume that $\varepsilon_{max,1}$ normalized with respect to ε_{crush} is a function of the infill slenderness ratio h/t according to Equation 45.

$$\frac{\varepsilon_{max,1}}{\varepsilon_{crush}} = 0.73 - 0.016(h/t) \tag{45}$$

Now consider Equation 20, recalled in Equation 46. Such Equation allows, based on the above procedure, the evaluation of the entire OOP force-displacement curve.

$$q = \frac{4(b/t)k_1 f_b \frac{\cos\gamma}{\cos\theta}\sin\gamma}{h/t} \tag{46}$$

For the direct calculation of q_{max}, the following assumptions are made by Angel et al. First, Equation 47 applies, i.e., it is assumed that γ and θ are very small angles.

$$\frac{\cos\gamma}{\cos\theta} \cong 1 \tag{47}$$

Based on Equation 47, Equation 46 can be rewritten as reported in Equation 48.

$$q = \frac{4(b/t)k_1 f_b \sin\gamma}{h/t} \tag{48}$$

It is assumed that the compression distribution at the masonry parts ends is triangular. Hence, k_1 is equal to 0.50 and k_2 is equal to 0.33. Equation 48 can be rewritten as Equation 49.

$$q = \frac{2(b/t)f_b \sin\gamma}{h/t} \tag{49}$$

The parameter c can be calculated directly for εmax equal to $\varepsilon_{max,1}$. In this case, it is indicated as c_1 and calculated as reported in Equation 50, based also on Equation 45.

$$c_1 = \frac{1}{4}\varepsilon_{max,1} = \frac{1}{4}[0.73 - 0.016(h/t)]\varepsilon_{crush} \tag{50}$$

Hence, at the attainment of the OOP strength, Equation 51 applies for the calculation of b/t.

$$\frac{b}{t} = \frac{1}{4}\left[1 + \sqrt{1 - 2c_1\left(\frac{h}{t}\right)^2}\right] \tag{51}$$

In addition, Equations 52 and 53 applies for the calculation of θ and β.

$$\tan\theta = c_1 \frac{h/t}{b/t} \tag{52}$$

$$\tan\beta = \frac{2[1 - 2k_2(b/t)]}{(h/t)} \rightarrow \frac{2 - (4/3)(b/t)}{(h/t)} \tag{53}$$

If it is assumed that also β is small, Equations 54-56 applies.

$$\tan\theta \cong \theta \tag{54}$$

$$\tan\beta \cong \beta \tag{55}$$

$$\sin\gamma = \sin(\beta - \theta) = \sin\left[\frac{2 - (4/3)(b/t)}{(h/t)} - c_1\frac{h/t}{b/t}\right] \rightarrow$$

$$\rightarrow \sin\left[\frac{2 - (4/3)\frac{1}{4}\left[1 + \sqrt{1 - 2c_1\left(\frac{h}{t}\right)^2}\right]}{(h/t)}\right.$$

$$\left. - c_1\frac{h/t}{\frac{1}{4}\left[1 + \sqrt{1 - 2c_1\left(\frac{h}{t}\right)^2}\right]}\right] \tag{56}$$

Based on Equation 50, c_1 is a function only of h/t and ε_{crush}. Based on Equation 51, b/t is a function of h/t and ε_{crush}. Based on Equation 56, $\sin\gamma$ is a function of h/t and $\varepsilon crush$. Now consider f_b in Equation 48. Clearly, it is the stress corresponding to $\varepsilon_{max,1}$. Hence, it depends on masonry behaviour, which depends on masonry mechanical properties (f_m and ε_{crush}) and on the value of $\varepsilon_{max,1}$, which depends on ε_{crush} and h/t. Hence,

the f_b/f_m ratio depends on ε_{crush} and on h/t. Equation 49 can be rewritten as reported in Equation 57.

$$q = \frac{2f_m(b/t)(f_b/f_m)\sin\gamma}{h/t} = \frac{2f_m}{h/t}\left[\left(\frac{b}{t}\right)\left(\frac{f_b}{f_m}\right)\sin\gamma\right] \tag{57}$$

Consider now the parameter λ reported in Equation 58.

$$\lambda = \left(\frac{b}{t}\right)\left(\frac{f_b}{f_m}\right)\sin\gamma \tag{58}$$

The parameter λ, based on the above discussion, is a function only of h/t and ε_{crush}. Equation 57 can be rewritten as reported in Equation 59.

$$q = \frac{2f_m}{h/t}\lambda \tag{59}$$

Angel et al. have calculated the values of λ as a function of h/t for ε_{crush} equal to 0.004. Equation 59 is corrected by means of two coefficients: R_1, which accounts for the IP/OOP interaction effects and has been calibrated based on experimental data; R_2, which accounts for the frame deformability effects and has been calibrated based on the parametric application of Dawe and Seah (1989)'s stripe model. If Equation 59 is multiplied by R_1 and R_2, Equation 60, which is Angel et al.'s strength direct formulation, is obtained.

$$q = R_1 R_2 \frac{2f_m}{h/t}\lambda \tag{60}$$

A.2.3. Eurocode 6 strength model

Eurocode 6 (2005), in section 6.3.2, proposes an expression to calculate the lateral specific strength of masonry walls in which arching action can occur; this relationship can be extended, potentially, to URM infills and is reported in Equation 61.

$$q_{max} = f_d \left(\frac{t}{l_a}\right)^2 \tag{61}$$

Consider a unit-width masonry stripe constrained at the edges by stiff elements with length equal to h, thickness equal to t and material compressive strength fm. In these hypotheses, Equation 61 can be rewritten as reported in Equation 62.

$$q_{max} = f_m \left(\frac{t}{h}\right)^2 \tag{62}$$

Equation 62 can be derived based on simple equilibrium conditions and on some assumptions. First, it is assumed that the considered masonry stripe is subjected to an OOP uniformly distributed load. The contribution to the OOP strength of flexural mechanisms is neglected. Hence, when calculating the OOP strength, the considered masonry stripe is already cracked at its ends and mid-height. Of course, it is assumed that arching action occurs. The compression stress distribution acting at each end of the two masonry segments is assumed as triangular, with maximum stress equal to fm and neutral axis depth equal to 0.30t. Under these hypotheses, the arching thrust value, called N_{ad}, is defined by the expression reported in Equation 63.

$$N_{ad} = \frac{1}{2} 0.3 t f_m = 0.15 t f_m = 1.5 \frac{t}{10} f_m \tag{63}$$

It is assumed that the masonry stripe resisting to lateral loads can be represented by arching thrusts and by the three-hinged arch that they form. The arch deflection, f, is assumed equal to 0.90t. If the angle defined by the arching thrusts and the vertical direction is small, the value of the end support vertical reaction H is roughly equal to the arching thrust. H can be expressed as a function of the external load as reported in Equation 64.

$$H = q \frac{h^2}{4} \tag{64}$$

It is assumed that H equals N_{ad} when q is equal to q_{max}. By equating Equations 63 and 64, Equation 65 is obtained.

$$q_{max} = 1.08 f_m \left(\frac{t}{h}\right)^2 \tag{65}$$

For simplicity, the coefficient 1.08 is reduced to one.

A.3. OOP STRENGTH MODELS BASED ON TWO-WAY ARCHING ACTION

In this section, the OOP strength model accounting for two-way arching action by Bashandy et al. is derived. Bashandy et al.'s model should be considered as an extension to infills in which two-way arching occurs of McDowell et al.'s model.

Consider an infill wall with height h, width w, thickness t made with masonry provided with compressive strength equal to f_{mv} and f_{mh} in the vertical and horizontal direction, respectively, and with elastic modulus equal to E_{mv} and E_{mh} in the vertical and horizontal direction, respectively. It is assumed that the idealized and regularized deformed shape of the infill wall is the hipped one represented in Figure A.8, with θ angle equal to 45°.
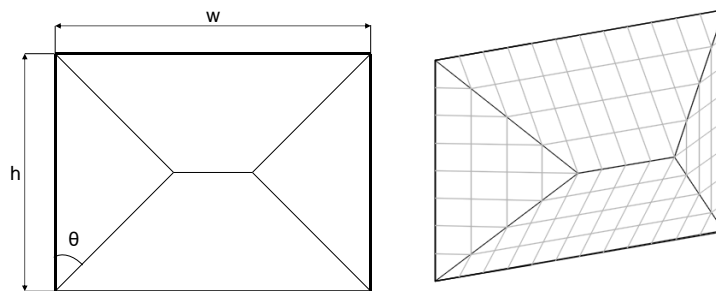
Figure A.8. Bashandy et al.'s OOP collapse mechanism.

It is assumed that the central displacement of the infill is equal to x_{yv}, which is calculated according to Equation 4 by using masonry properties in the vertical direction.

The infill wall is divided in vertical and horizontal unit-width stripes. Hence, each value of x corresponds to a vertical stripe, each value of y corresponds to a horizontal stripe. Each vertical stripe is characterized by a maximum OOP displacement δ_v, which is a function of x, while each horizontal stripe is characterized by a maximum OOP displacement δ_h, which is a function of y. The linear functions that express $\delta_v(x)$ and $\delta_h(y)$ are known, as they are determined by the definition of x_{yv} value and by the definition of the idealized and regularized deformed shape assumed.

It is assumed that a uniformly distributed load acts on each stripe. The uniformly distributed load acting on vertical stripes is named δq_v and its entity is a function of x, while the uniformly distributed load acting on horizontal stripes is named δq_h and its entity is a function of y.

Now, consider vertical stripes. As shown in Figure A.9, two types (type A and type B) of vertical stripes exist.
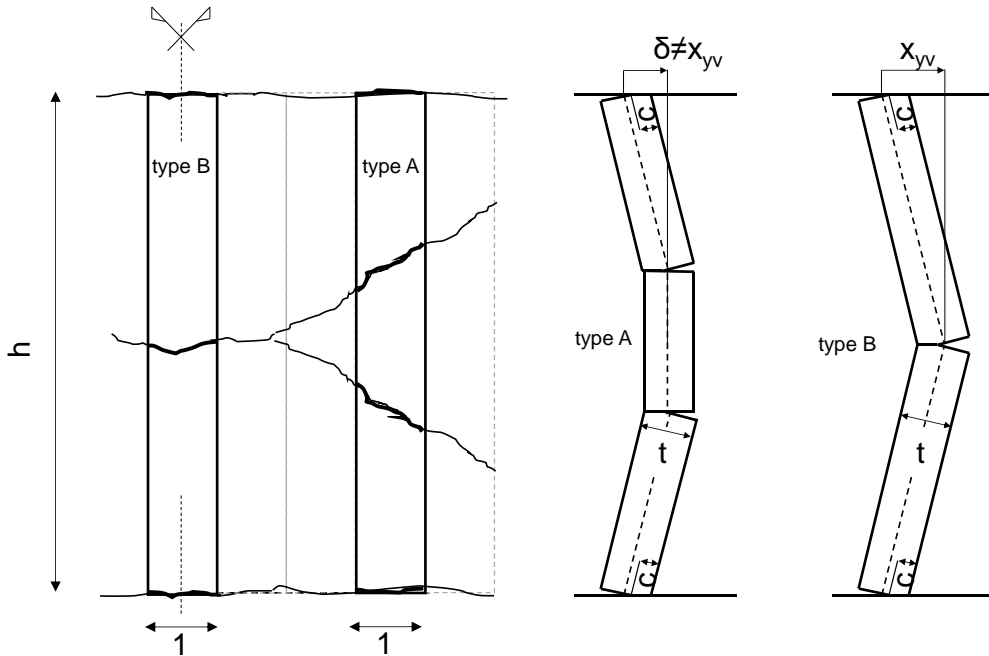
Figure A.9. Bashandy et al.'s stripe model.

Type A vertical stripes are characterized by a trapezoidal deformed shape with maximum OOP displacement varying from zero (edge stripes) to x_{yv}.

Consider now a Type A vertical stripe at abscissa equal to x. The uniformly distributed load acting on it is equal to $\delta q_v(x)$ and its maximum OOP displacement is equal to $\delta_v(x)$. The deformed shape along y of such a stripe, $d_v(x,y)$, is defined as reported in Equations 66 and 67.

$$d_v(x,y) = \frac{\delta_v(x)}{x} y \qquad\qquad \text{if } y \leq x \tag{66}$$

$$d_v(x,y) = \delta_v(x) \qquad\qquad \text{if } x \leq y \leq h/2 \tag{67}$$

Of course, the deformed shape is symmetric with respect to the horizontal axis passing from the stripe mid-height. Note also that Type A stripes' deformed shape is

characterized by three masonry parts at the ends of which M_A acts. M_A is calculated by applying Equation 68.

$$M_A(x) = \frac{\delta_v(x)}{x_{yv}} M_{yv} \tag{68}$$

In other words, it is assumed that the maximum moment due to arching action is a function of the OOP maximum displacement of the stripe and that it varies linearly from zero, at the infill vertical edge, to M_{yv}, which is calculated by applying McDowell's Equation 10 with masonry mechanical properties in the vertical direction. This assumption has not mechanical basis and is opposite to that proposed by Dawe and Seah, which assume that the moment due to arching thrusts is maximum at the very edge of the infill.

The external load made by $\delta q_{v,A}(x)$ on the considered Type A stripe is calculated as reported in Equation 69.

$$
\begin{aligned}
\delta l_{v,e}^A(x,y) &= 2\int_0^x \delta q_{v,A}(x)\, d_v(x,y)dy + \int_0^{h-2x} \delta q_{v,A}(x)\, d_v(x,y)dy = \\
&= 2\int_0^x \delta q_{v,A}(x)\frac{\delta_v(x)}{x}y\, dy + \int_0^{h-2x} \delta q_{v,A}(x)\,\delta_v(x)dy = \\
&= 2\delta q_{v,A}(x)\frac{\delta_v(x)}{x}\int_0^x y\, dy + \delta q_{v,A}(x)\delta_v(x)\int_0^{h-2x} dy = \\
&= 2\delta q_{v,A}(x)x + \delta q_{v,A}(x)\delta_v(x)(h-2x)
\end{aligned}
\tag{69}
$$

The internal work for a Type A vertical stripe is reported in Equation 70.

$$\delta l_{v,i}^A(x,y) = 4M_A\frac{\delta_v(x)}{x} \tag{70}$$

Of course, both the external work and the internal work are only a function of x. By equating Equation 69 and Equation 70, the formulation for $\delta q_{v,A}(x)$ valid for Type A vertical stripes and reported in Equation 71 is derived.

$$\delta q_{v,A}(x) = \frac{4M_A}{hx - x^2} \tag{71}$$

By substituting Equation 68 in Equation 71, Equation 72 is derived.

$$\delta q_{v,A}(x) = \frac{8M_{yv}}{h}\frac{x}{hx - x^2}$$

(72)

It can be observed that the load acting on the stripe is a function of x, hence it is different for each stripe.

Type B vertical stripes are characterized by a triangular deformed shape with maximum OOP displacement equal to x_{yv}. Note also that Type B stripes' deformed shape is characterized by two masonry parts at the ends of which M_{yv}, calculated by applying Equation 10 with masonry properties in the vertical direction, acts.

Consider now a Type B vertical stripe at abscissa equal to x. The uniformly distributed load acting on it is equal to $\delta q_v(x)$ and its maximum OOP displacement is equal to xyv. The deformed shape along y of such a stripe, $d_v(x,y)$, is defined as reported in Equation 73.

$$d_v(x, y) = \frac{x_{yv}}{x}y \qquad\qquad \text{if } y \le h/2$$

(73)

Of course, the deformed shape is symmetric with respect to the horizontal axis passing from the stripe mid-height.

The external load made by $\delta q_{v,B}(x)$ on the considered Type B stripe is calculated as reported in Equation 74.

$$\delta l_{v,e}^B(x, y) = 2\int_0^{h/2} \delta q_{v,B}(x)\, d_v(x, y)dy = 2\int_0^{h/2} \delta q_{v,B}(x)\frac{x_{yv}}{x}ydy =$$
$$= 2\delta q_{v,B}(x)\frac{x_{yv}}{x}\int_0^{h/2} y\, dy = \frac{1}{2}\delta q_{v,B}(x)x_{yv}h$$

(74)

The internal work for a Type B vertical stripe is reported in Equation 75.

$$\delta l_{v,i}^A(x, y) = 8M_{yv}\frac{x_{yv}}{h}$$

(75)

Of course, both the external work and the internal work are only a function of x. By equating Equation 74 and Equation 75, the formulation for $\delta_{qv,B}(x)$ valid for Type B vertical stripes and reported in Equation 76 is derived.

$$\delta q_{v,B}(x) = \frac{16 M_{yv}}{h^2} \tag{76}$$

It can be observed that the load acting on the stripe is not a function of x, hence it is equal for each stripe.

The contribution to the entire infill wall OOP strength provided by vertical stripes, F_V, can be obtained by integrating $\delta q_v(x)$ along the infill width, as reported in Equation 77.

$$F_v = 2 \int_0^{h/2} h \delta q_{v,A}(x) dx + \int_0^{w-2h} h \delta q_{v,B}(x) dx = 16 M_{yv} \ln 2 + 16 M_{yv} \frac{w-h}{h} \tag{77}$$

Horizontal stripes are, all of them, Type A stripes. All the Equations above defined for vertical stripes are valid provided that w is substituted by h, h by w, x by y, y by x. However, some discussion is needed concerning the value of the moment acting at masonry parts ends.

In the case of vertical stripes, it was assumed that M_{yv} acts at the ends of central stripes while a fraction varying from zero to one of M_{yv} act at the ends of lateral stripes. In other words, it was assumed that the value of the moment depends linearly on the OOP maximum displacement of the stripe. Remember that M_{yv} can be attained only if the OOP displacement is equal to x_{yv}.

In the horizontal direction, masonry is generally provided with different properties with respect to vertical direction. Hence, the maximum moment due to arching thrusts can be calculated by applying McDowell et al.'s Equation 10 with masonry properties in the horizontal direction. This moment will be attained only if the OOP maximum displacement of the considered stripe is equal to x_{yh}, which can be calculated by applying McDowell et al.'s Equation 4 to the horizontal direction.

However, it should be noted that, according to Bashandy et al., the OOP strength is attained when the infill central displacement equals x_{yv}. So, it is assumed that the maximum horizontal moment acting at the ends of the horizontal masonry parts is equal to a fraction x_{yv}/x_{yh} of M_{yh}. Of course, all the non-central horizontal stripes are characterized by maximum moment, which is a fraction of x_{yv}/x_{yh} times M_{yh} and it is assumed that such a fraction varies linearly from zero at the infill horizontal edges to one at the infill centre.

Based on these assumptions, the uniformly distributed load acting on each horizontal stripe is, also in this case, calculated by applying the principle of virtual works and is

reported in Equation 78.

$$\delta q_{h,A}(y) = \frac{8M_{yh}}{h} \frac{y}{wy - y^2} \frac{x_{yv}}{x_{yh}} \tag{78}$$

By integrating $\delta q_{h,A}$ on the entire height of the infill, the contribution of horizontal stripes to the OOP strength of the infill is obtained as reported in Equation 79.

$$F_h = \frac{16M_{yh}}{h} \frac{x_{yv}}{x_{yh}} \ln\left(\frac{w}{w - h/2}\right) \tag{79}$$

The OOP strength of the infill is provided by the summation of the contribution of vertical and horizontal stripes. Hence, Equation 80 is obtained.

$$F_{max} = 16M_{yv}\ln2 + 16M_{yv}\frac{w - h}{h} + \frac{16M_{yh}}{h}\frac{x_{yv}}{x_{yh}}\ln\left(\frac{w}{w - h/2}\right) \tag{80}$$

With some manipulation, Equation 81 is obtained.

$$F_{max} = 16\frac{M_{yv}}{h^2}\left[h^2\ln2 + h^2\left(\frac{w - h}{h}\right) + wh\left(\frac{M_{yh}}{M_{yv}}\frac{x_{yv}}{x_{yh}}\right)\ln\left(\frac{w}{w - 0.5h}\right)\right] \tag{81}$$

REFERENCES

- Angel R, Abrams DP, Shapiro D, Uzarski J, Webster M. Behaviour of reinforced concrete frames with masonry infills. University of Illinois Engineering Experiment Station. College of Engineering. University of Illinois at Urbana-Champaign., 1994.
- Bashandy T, Rubiano NR, Klingner RE. Evaluation and analytical verification of infilled frame test data. Phil M. Ferguson Structural Engineering Laboratory, University of Texas at Austin. 1995.
- Dawe JL, Seah CK. Out-of-plane resistance of concrete masonry infilled panels. Canadian Journal of Civil Engineering 1989;16(6):854–864.
- Eurocode 6. Design of Masonry Structures. Part 1-1: General Rules for Reinforced and Unreinforced Masonry Structures. Brussels, 2005. 123 p.
- McDowell EL, McKee KE, Sevin E. Arching action theory of masonry walls. J. Struct. Div 1956;82.2:915.

Appendix B
Specimens' cracking patterns and damage evolution

For each experimental test carried out at the Department of Structures for Engineering and Architecture of University of Naples Federico II, the evolution of damage observed during experimental tests is herein reported.

The nature of the test (IP or OOP) to which the cracking pattern are referred is declared in the caption to the Figures. The force and displacement reported in the Figures are the IP force and the IP displacement of the RC frame upper beam cross-section centroid for the IP tests, the OOP force and the OOP displacement of the infill centre for the OOP tests.

F=19.4 kN   d=3.3 mm   F=22.0 kN   d=5.3 mm   F=20.3 kN   d=6.0 mm

F=19.4 kN   d=7.8 mm   F=18.1 kN   d=10.3 mm   F=18.0 kN   d=13.2 mm

F=17.1 kN   d=16.3 mm   F=16.3 kN   d=28.7 mm   F=13.5 kN   d=40.5 mm

F=6.3 kN   d=61.4 mm   F=4.4 kN   d=76.9 mm
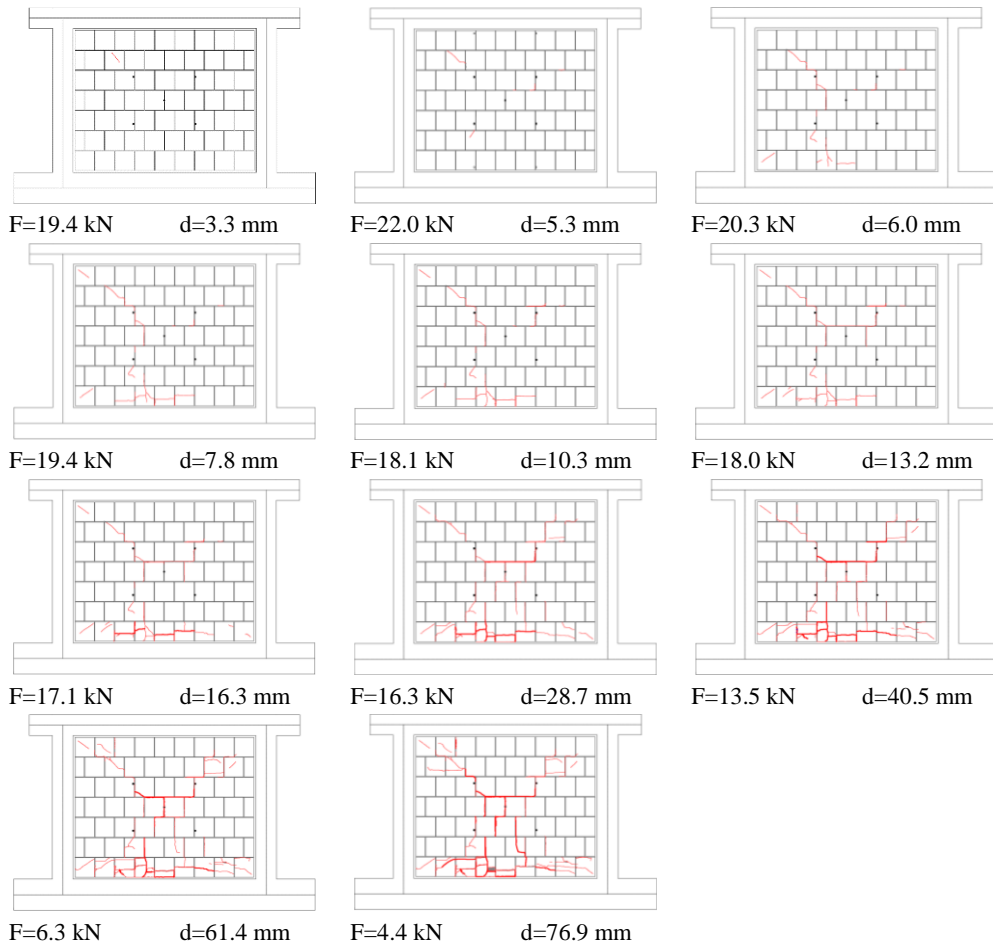
Figure B.1. OOP test 80_OOP_4E.

F=12.2 kN   d=5.4 mm   F=13.0 kN   d=6.5 mm   F=13.4 kN   d=7.5 mm

F=16.1 kN   d=10.6 mm   F=17.2 kN   d=13.5 mm   F=17.6 kN   d=15.7 mm

F=13.3 kN   d=17.7 mm   F=11.4 kN   d=21.8 mm   F=11.0 kN   d=26.7 mm

F=10.6 kN   d=34.6 mm   F=9.8 kN   d=42.3 mm   F=8.3 kN   d=51.3 mm

F=6.5 kN   d=58.4 mm
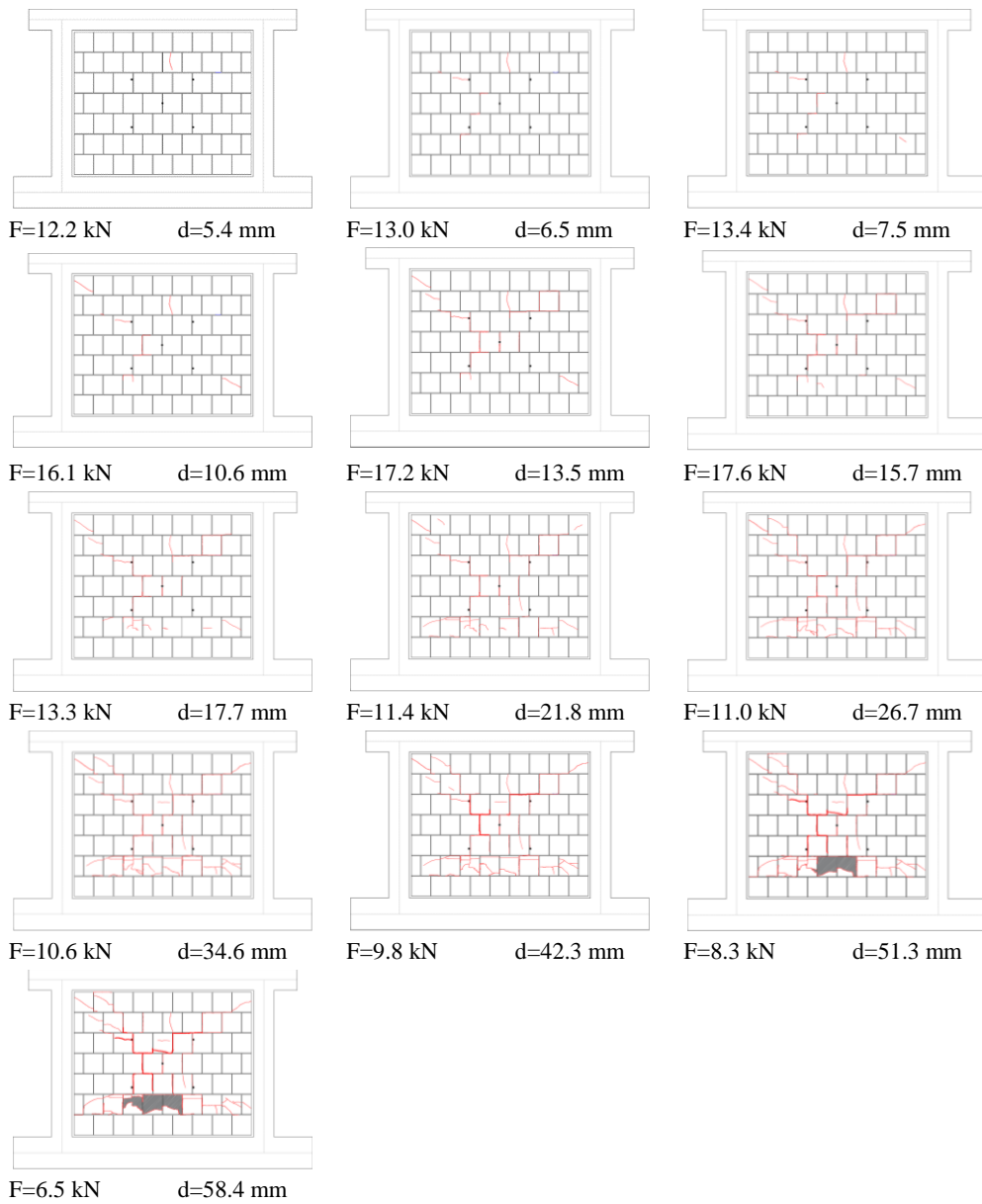
Figure B.2. OOP test 80_OOP_3E.

F=18.2 kN   d=14.9 mm   F=18.4 kN   d=20.1 mm   F=16.4 kN   d=30.0 mm

F=12.2 kN   d=40.0 mm   F=8.5 kN   d=50.0 mm   F=6.1 kN   d=58.2 mm

F=4.6 kN   d=65.4 mm
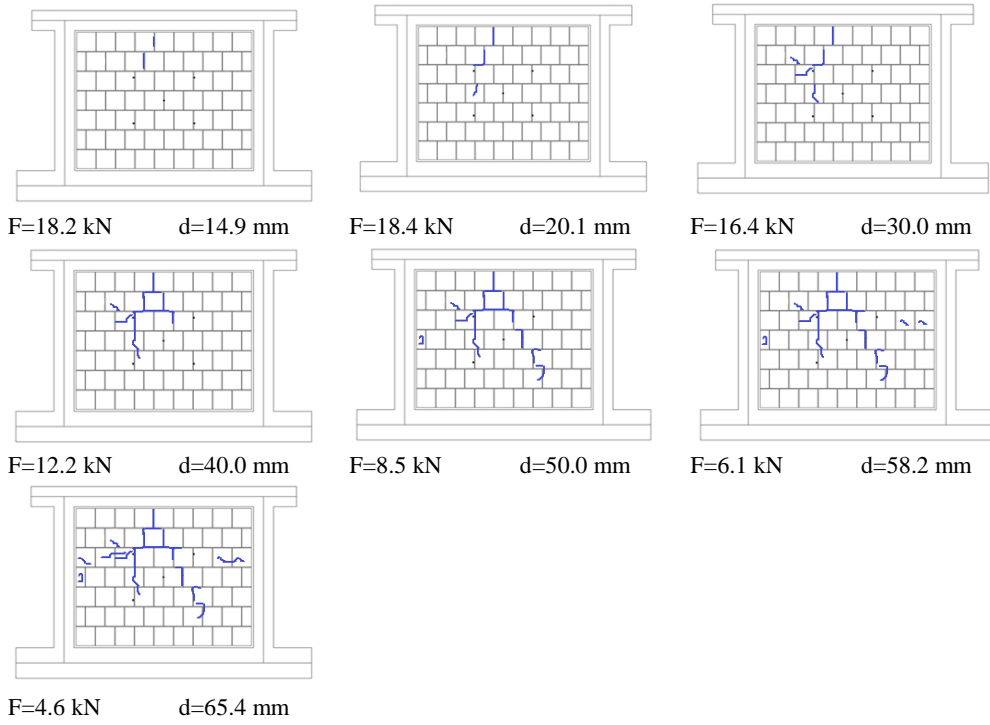
Figure B.3. OOP test 80_OOP_3Eb.

F=11.7 kN   d=3.0 mm   F=11.5 kN   d=4.3 mm   F=12.7 kN   d=6.2 mm

F=14.4 kN   d=11.9 mm   F=14.6 kN   d=14.2 mm
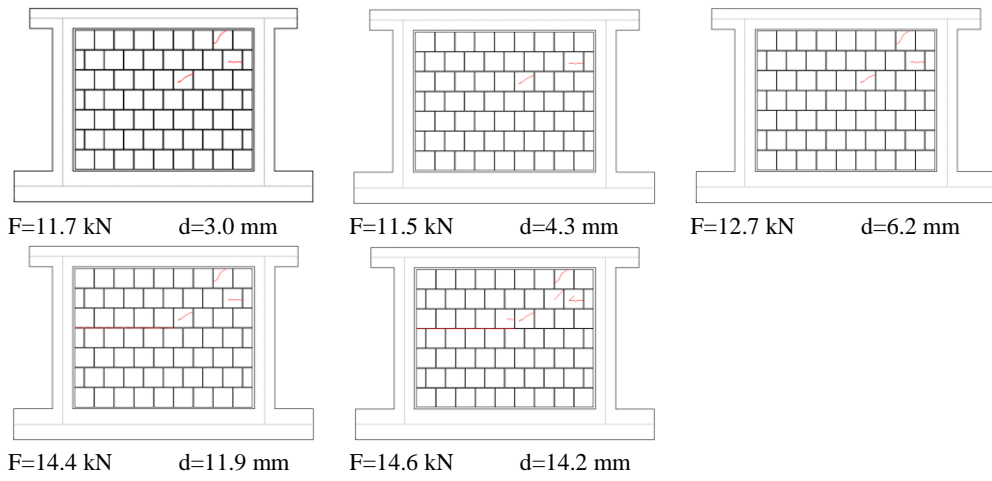
Figure B.4. OOP test 80_OOP_2E.

first cycle
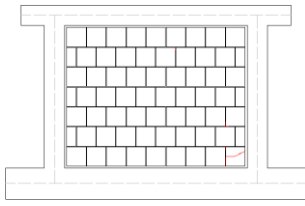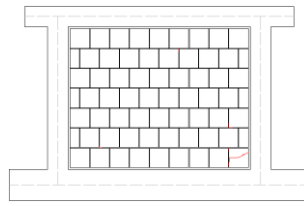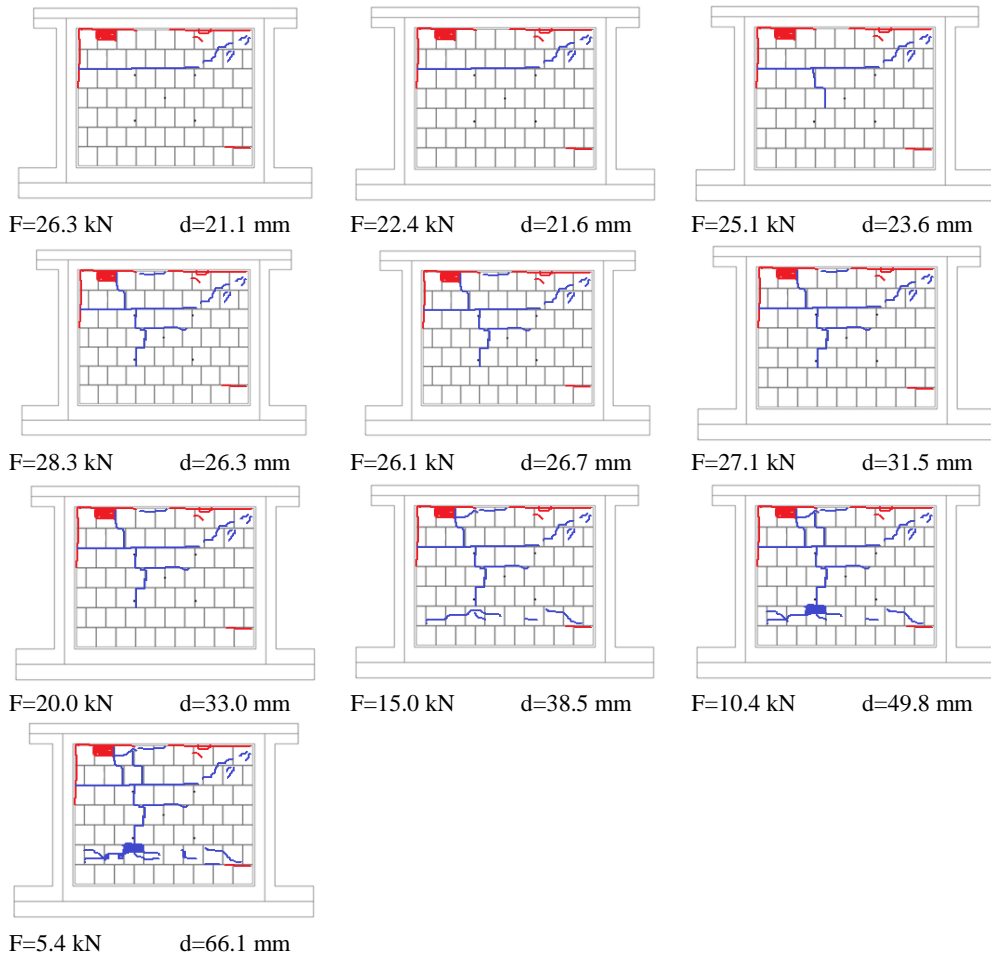
F=+55.3 kN   d=+1.3 mm   F=-58.0 kN   d=-1.3 mm

second cycle
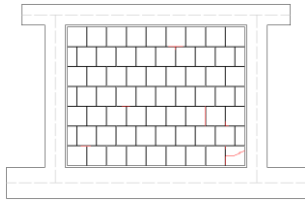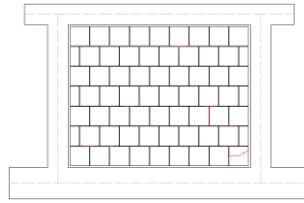
F=+79.3 kN   d=+3.0 mm   F=-79.1 kN   d=-3.1 mm

Figure B.5. IP test 80_IP+OOP_L.

F=12.6 kN   d=1.8 mm   F=23.4 kN   d=6.8 mm   F=17.2 kN   d=8.9 mm

F=14.2 kN   d=23.6 mm   F=11.3 kN   d=29.6 mm   F=9.8 kN   d=36.5 mm

F=7.1 kN   d=43.5 mm   F=3.1 kN   d=70.5 mm
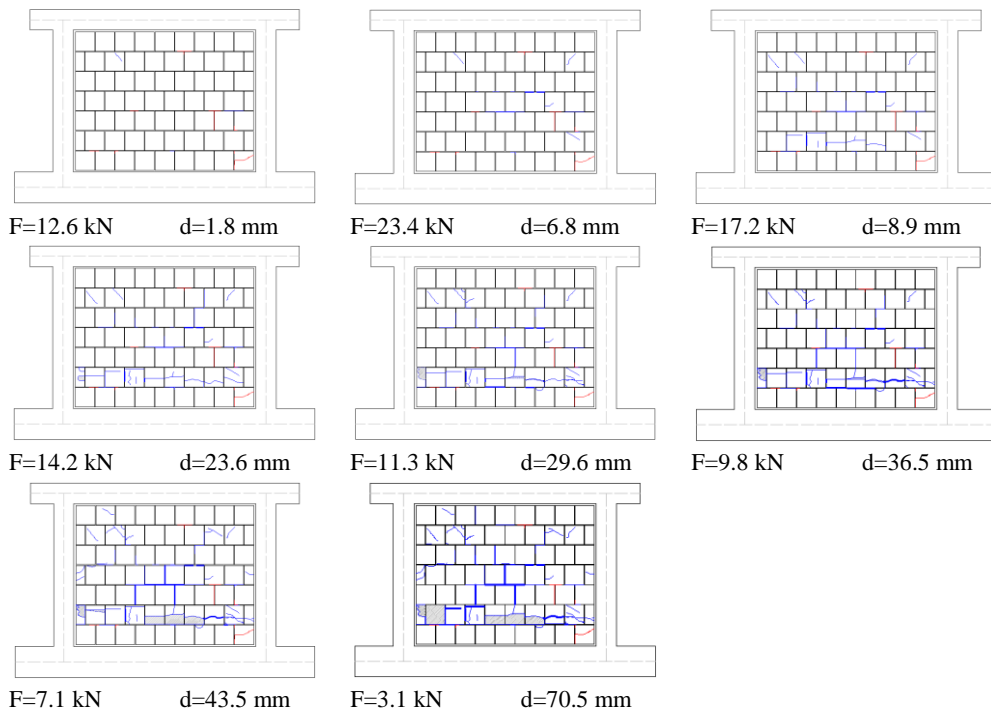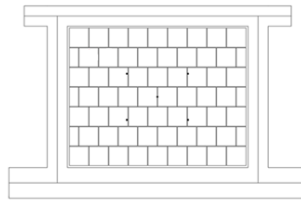
Figure B.6. OOP test 80_IP+OOP_L.

first cycle
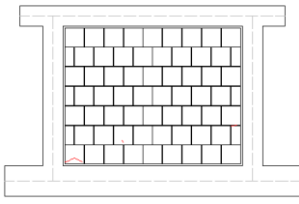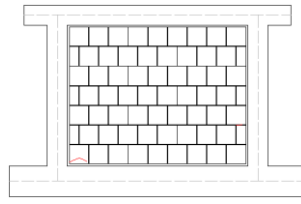
F=+62.2 kN   d=+1.3 mm   F=-62.2 kN   d=-1.2 mm

second cycle
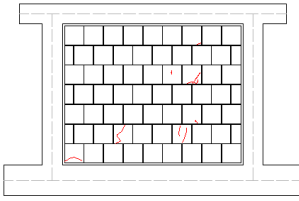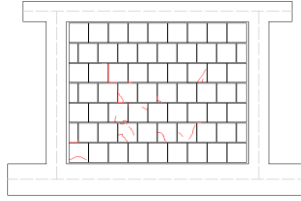
F=+76.2 kN   d=+3.0 mm   F=-83.5 kN   d=-2.9 mm

third cycle
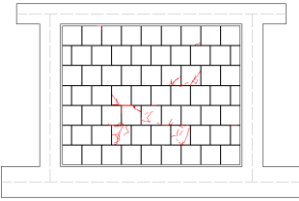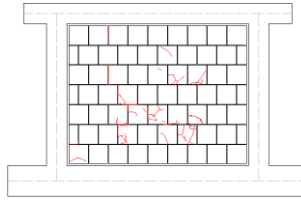
F=+90.1 kN   d=+4.8 mm   F=-86.6 kN   d=-4.7 mm

fourth cycle
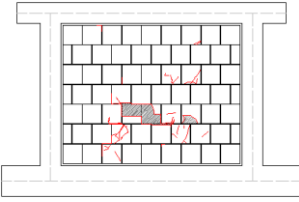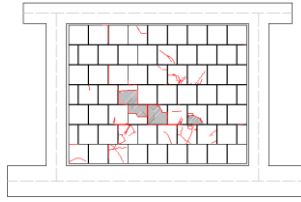
F=+88.6 kN   d=+6.8 mm   F=-85.9 kN   d=-6.6 mm

Figure B.7. IP test 80_IP+OOP_M.

F=5.2 kN d=4.3 mm   F=8.5 kN d=11.6 mm   F=10.5 kN d=32.0 mm

F=10.3 kN d=36.7 mm   F=9.8 kN d=39.7 mm   F=9.2 kN d=43.4 mm

F=7.1 kN d=55.6 mm   F=4.7 kN d=70.1 mm   F=3.9 kN d=77.4 mm
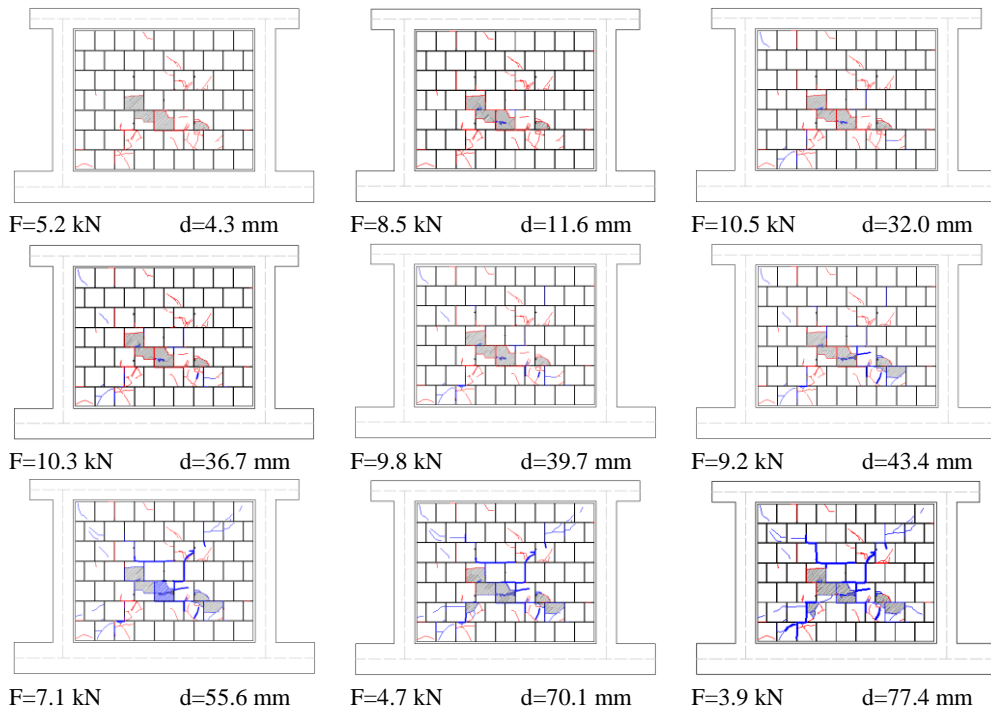
Figure B.8. OOP test 80_IP+OOP_M.

first cycle
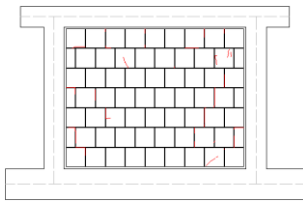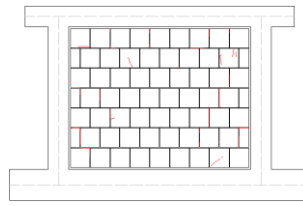
F=+49.1 kN   d=+1.2 mm   F=-43.1 kN   d=-1.4 mm

second cycle
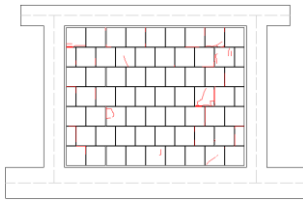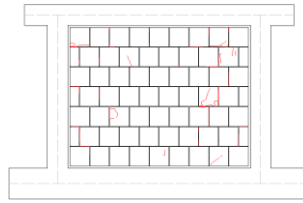
F=+74.7 kN   d=+2.8 mm   F=-72.8 kN   d=-3.0 mm

third cycle
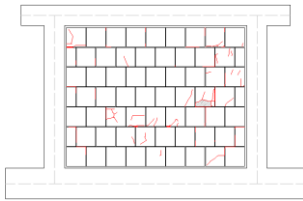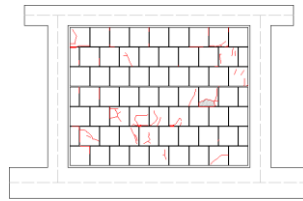
F=+88.3 kN   d=+4.7 mm   F=-84.4 kN   d=-4.7 mm

fourth cycle
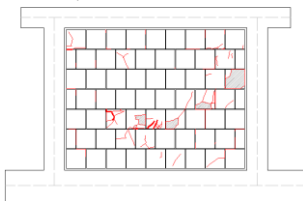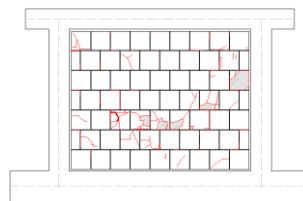
F=+103 kN   d=+6.5 mm   F=-83.9 kN   d=-6.6 mm

Figure B.9a. IP test 80_IP+OOP_H (1st to 4th cycle).

fifth cycle
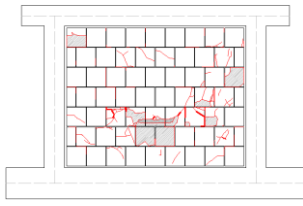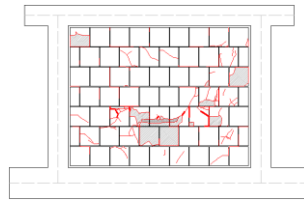
F=+100 kN   d=+8.5 mm   F=-72.8 kN   d=-8.7 mm

sixth cycle
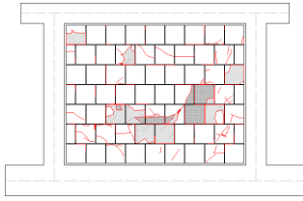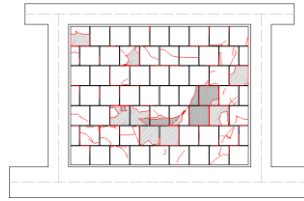
F=+90.4 kN   d=+10.6 mm   F=-69.5 kN   d=-10.6 mm

Figure B.9b. IP test 80_IP+OOP_H (5th and 6th cycles).

F=2.5 kN d=9.3 mm	F=4.6 kN d=17.4 mm	F=5.9 kN d=25.8 mm
F=5.3 kN d=29.3 mm	F=4.5 kN d=33.7 mm	F=3.5 kN d=40.0 mm
F=2.8 kN d=43.0 mm	F=1.6 kN d=53.9 mm	F=1.4 kN d=55.3 mm
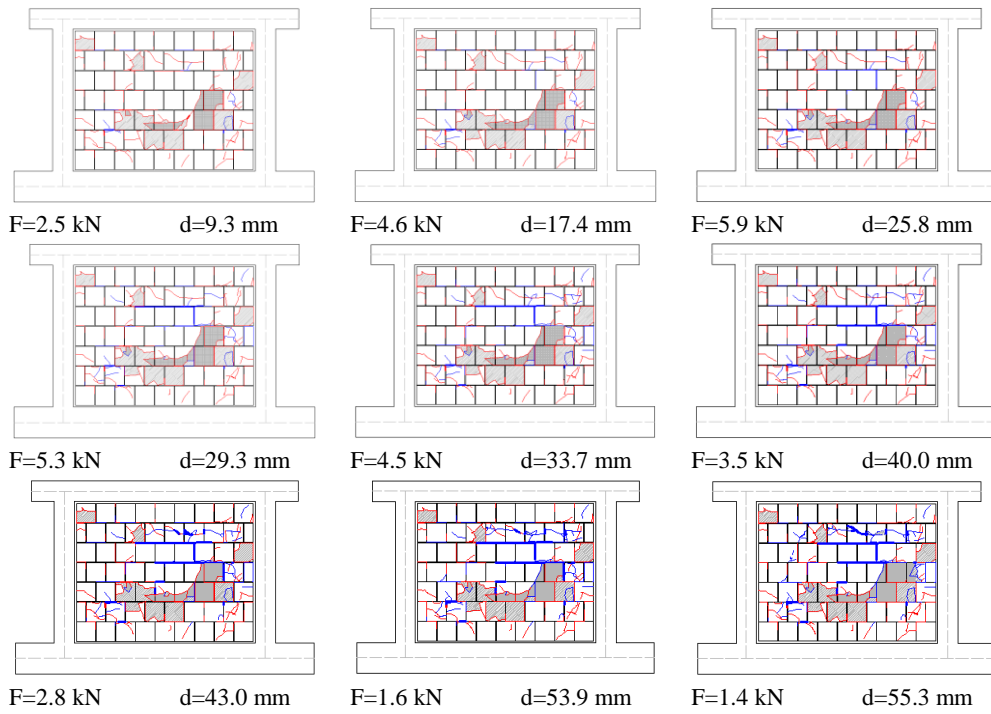
Figure B.10. OOP test 80_IP+OOP_H.

F=27.5 kN   d=2.5 mm   F=41.8 kN   d=8.0 mm   F=36.2 kN   d=12.5 mm

F=34.8 kN   d=17.5 mm   F=34.3 kN   d=20.0 mm   F=29.3 kN   d=27.0 mm

F=16.3 kN   d=37.5 mm
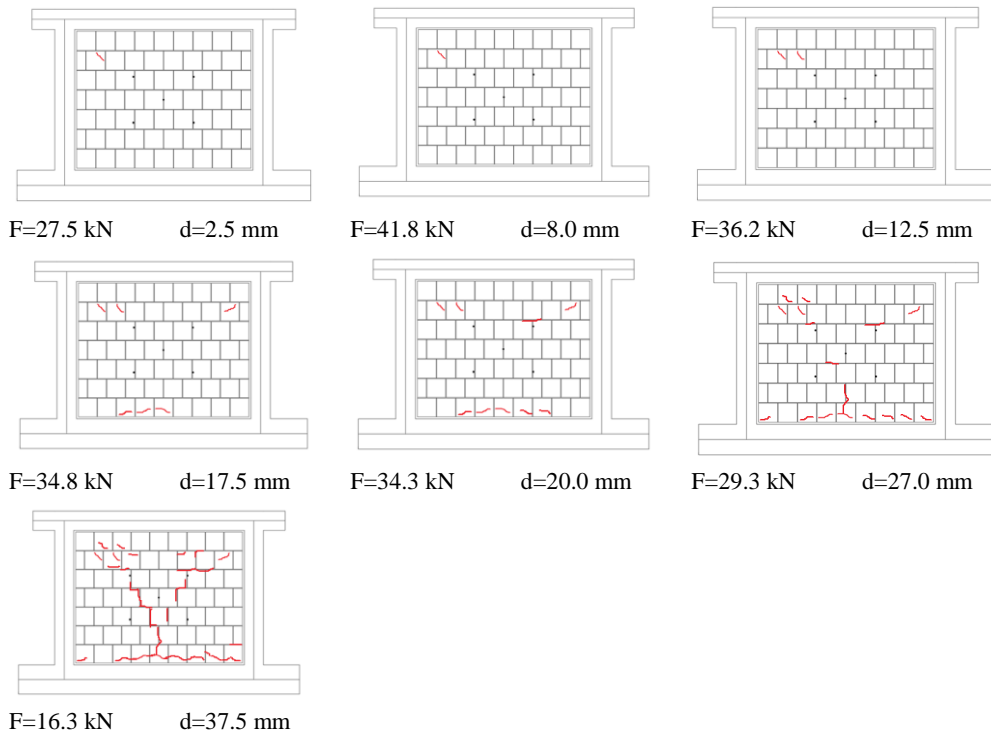
Figure B.11. OOP test 120_ OOP_4E.

F=19.5 kN   d=4.3 mm   F=31.1 kN   d=11.5 mm   F=33.6 kN   d=16.4 mm

F=33.0 kN   d=20.0 mm   F=23.7 kN   d=28.0 mm
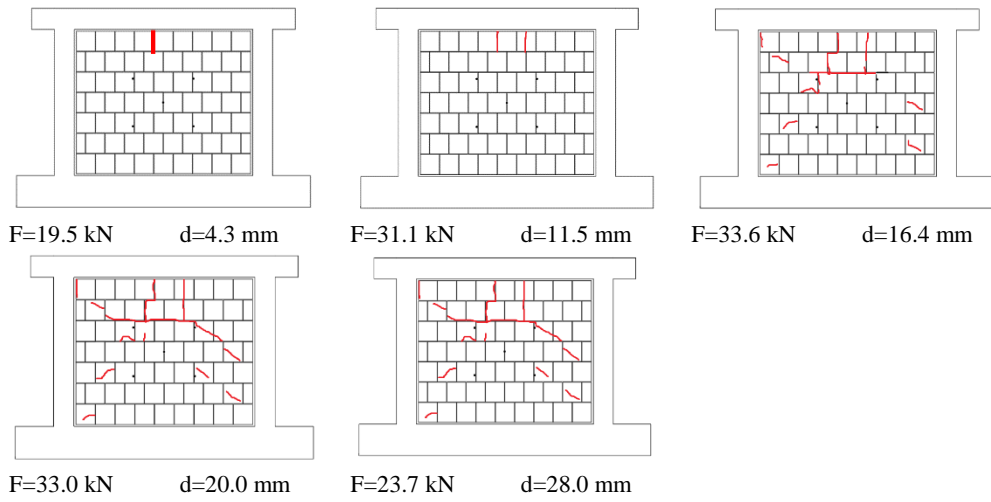
Figure B.12. OOP test 120_ OOP_3E.

F=18.5 kN   d=5.5 mm   F=24.0 kN   d=9.5 mm   F=24.6 kN   d=10.2 mm

F=14.2 kN   d=14.6 mm
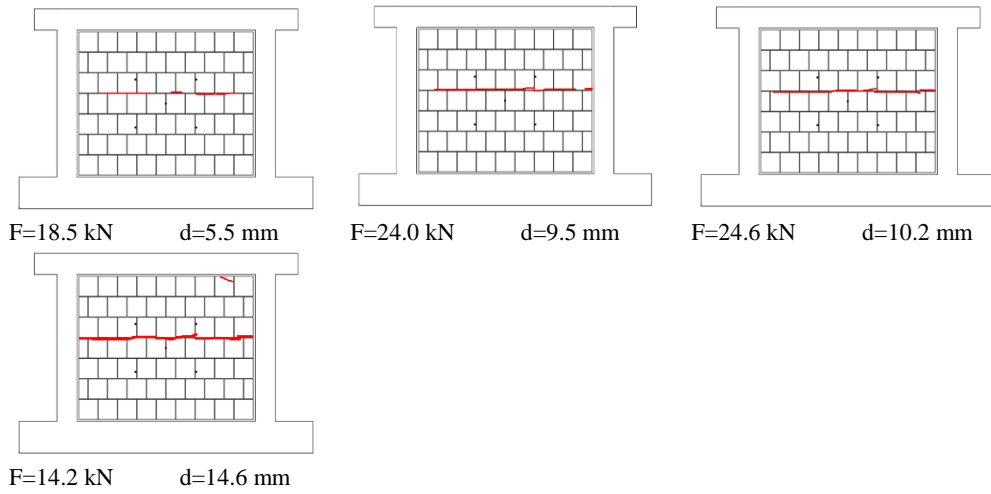
Figure B.13. OOP test 120_ OOP_2E.

first cycle
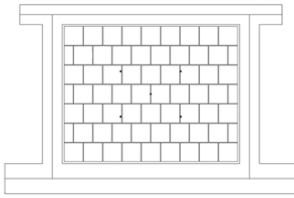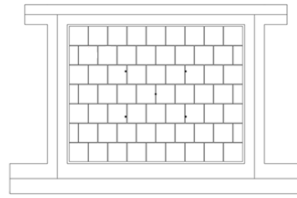
F=+68.9 kN   d=+1.3 mm   F=-64.8 kN   d=-1.1 mm

second cycle
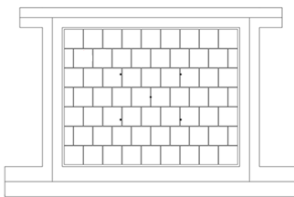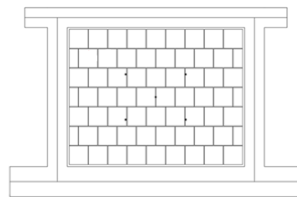
F=+93.5 kN   d=+2.8 mm   F=-97.6 kN   d=-2.7 mm

third cycle
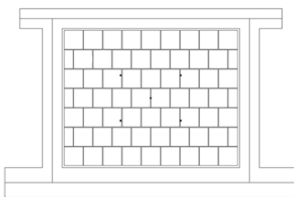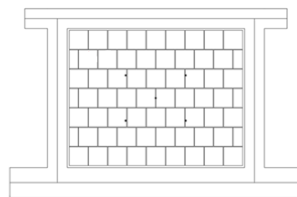
F=+108 kN   d=+4.7 mm   F=-111 kN   d=-4.2 mm

Figure B.14. IP test 120_IP+OOP_L.

F=41.3 kN   d=9.7 mm   F=28.4 kN   d=12.7 mm   F=26.4 kN   d=17.8 mm

F=19.7 kN   d=19.6 mm   F=19.0 kN   d=22.1 mm
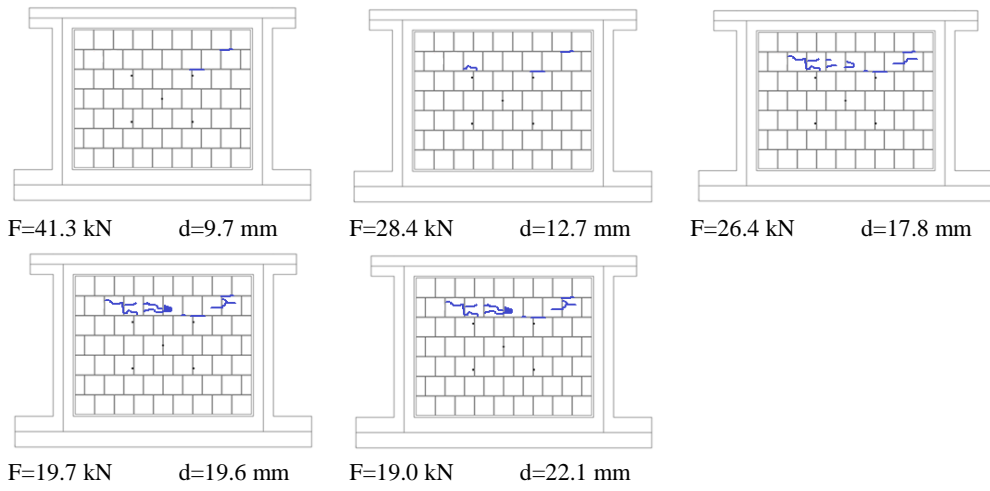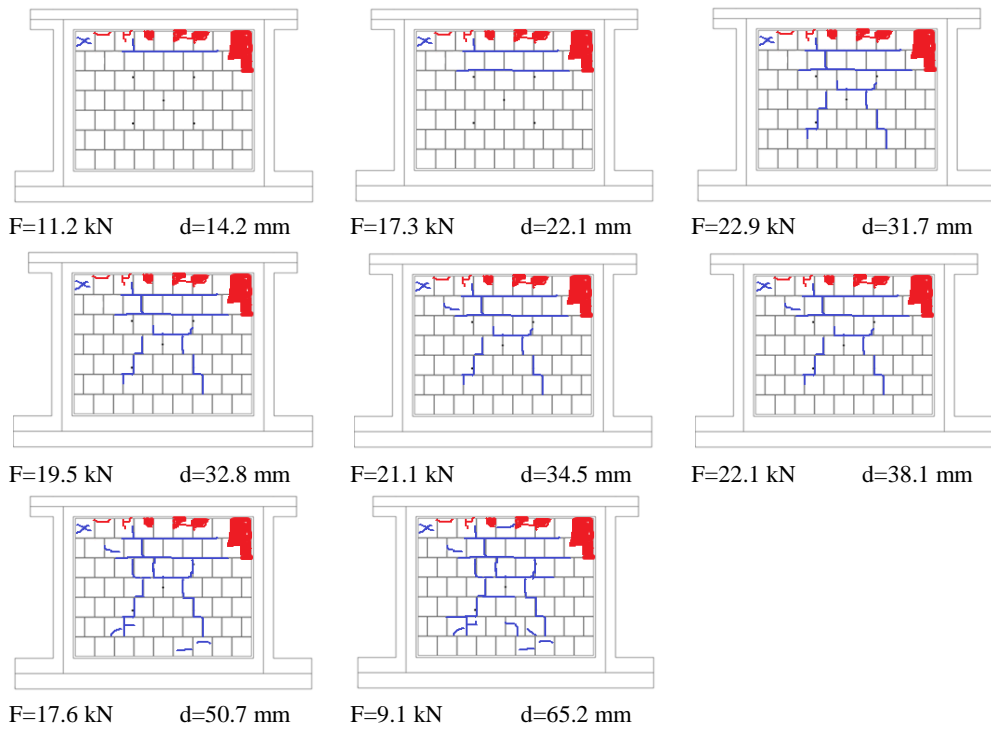
Figure B.15. OOP test 120_IP+OOP_L.

first cycle
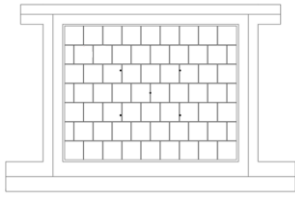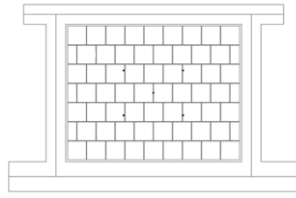
F=+67.9 kN   d=+0.9 mm   F=-63.1 kN   d=-1.1 mm

second cycle
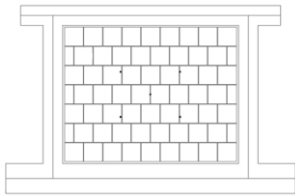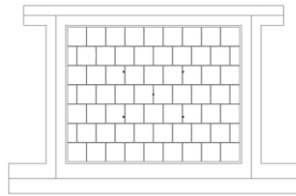
F=+105 kN   d=+2.2 mm   F=-88.5 kN   d=-2.5 mm

third cycle
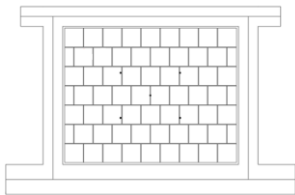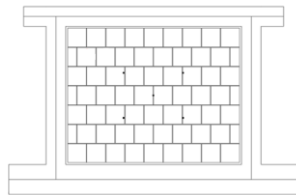
F=+115 kN   d=+3.8 mm   F=-90.1 kN   d=-4.3 mm

fourth cycle
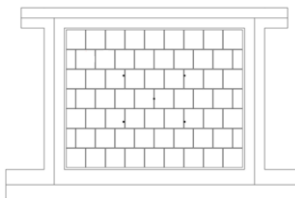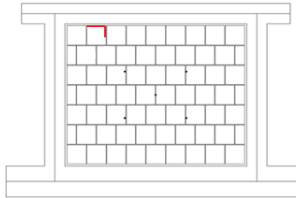
F=+116 kN   d=+5.7 mm   F=-89.6 kN   d=-6.1 mm

Figure B.16a. IP test 120_IP+OOP_M (1st to 4th cycle).

fifth cycle
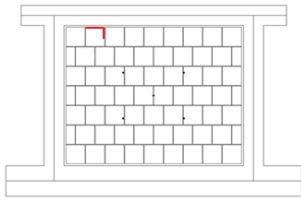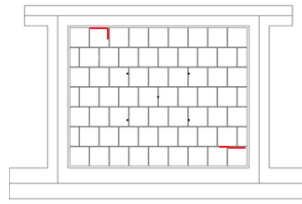
F=+121 kN   d=+7.5 mm   F=-93.7 kN   d=-7.9 mm

sixth cycle
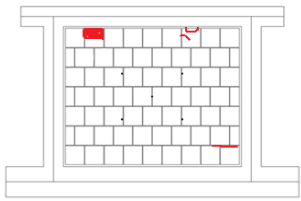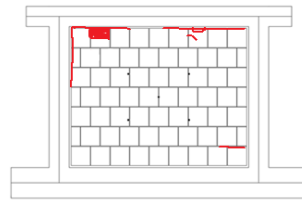
F=+120 kN   d=+9.5 mm   F=-95.9 kN   d=-9.6 mm

Figure B.16b. IP test 120_IP+OOP_M (5th and 6th cycles).

F=26.3 kN   d=21.1 mm   F=22.4 kN   d=21.6 mm   F=25.1 kN   d=23.6 mm

F=28.3 kN   d=26.3 mm   F=26.1 kN   d=26.7 mm   F=27.1 kN   d=31.5 mm

F=20.0 kN   d=33.0 mm   F=15.0 kN   d=38.5 mm   F=10.4 kN   d=49.8 mm

F=5.4 kN   d=66.1 mm

Figure B.17. OOP test 120_IP+OOP_M.

first cycle
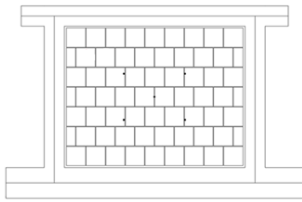
F=+60.7 kN   d=+1.3 mm   F=-57.9 kN   d=-1.1 mm

second cycle
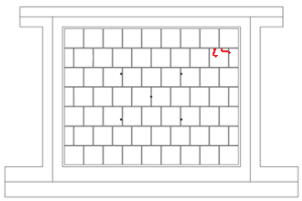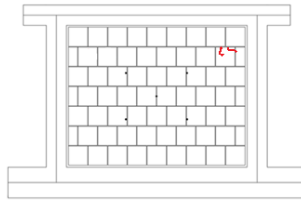
F=+90.8 kN   d=+2.8 mm   F=-83.5 kN   d=-2.7 mm

third cycle
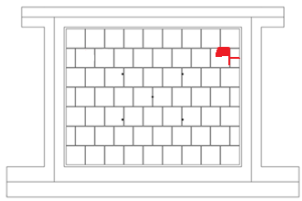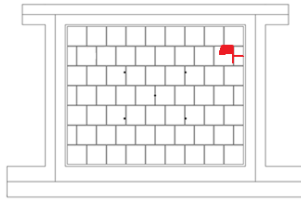
F=+100 kN   d=+4.5 mm   F=-91.8 kN   d=-4.4 mm

fourth cycle
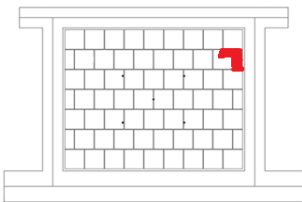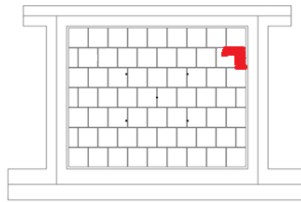
F=+100 kN   d=+6.3 mm   F=-91.8 kN   d=-6.2 mm

Figure B.18a. IP test 120_IP+OOP_H (1st to 4th cycle).

fifth cycle
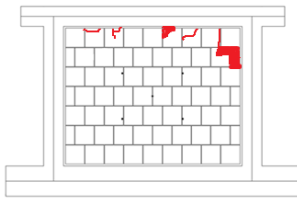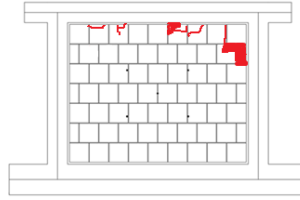
F=+98.8 kN   d=+8.2 mm   F=-92.5 kN   d=-8.0 mm

sixth cycle
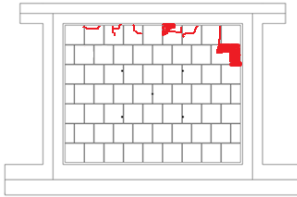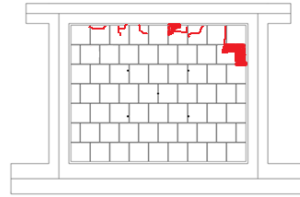
F=+98.8 kN   d=+10.0 mm   F=-96.2 kN   d=-9.7 mm

seventh cycle
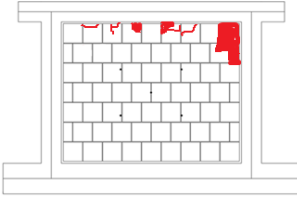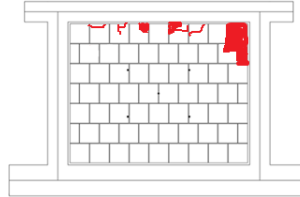
F=+112 kN   d=+13.6 mm   F=-110 kN   d=-13.1 mm

eighth cycle
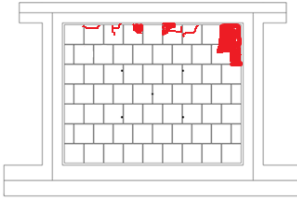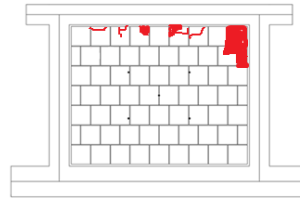
F=+119 kN   d=+17.5 mm   F=-120 kN   d=-16.4 mm

Figure B.18b. IP test 120_IP+OOP_H (5th and 8th cycles).

F=11.2 kN   d=14.2 mm   F=17.3 kN   d=22.1 mm   F=22.9 kN   d=31.7 mm

F=19.5 kN   d=32.8 mm   F=21.1 kN   d=34.5 mm   F=22.1 kN   d=38.1 mm

F=17.6 kN   d=50.7 mm   F=9.1 kN   d=65.2 mm

Figure B.19. OOP test 120_IP+OOP_H.

first cycle
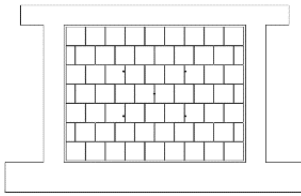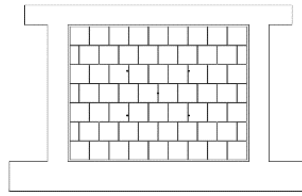
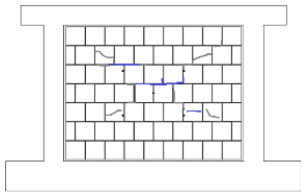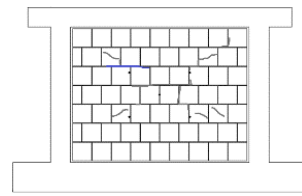| F=+23.3 kN   d=+4.3 mm | F=-25.0 kN   d=-3.6 mm | F=0 kN   d=+0.9 mm |
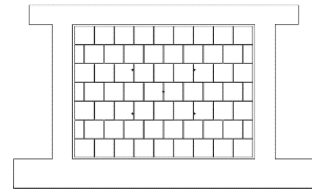
second cycle
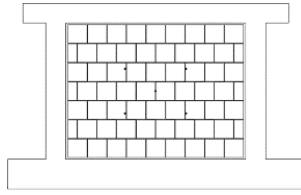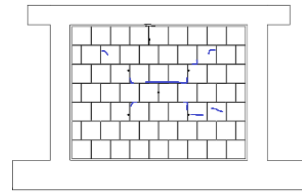
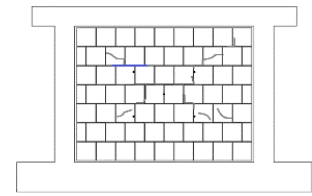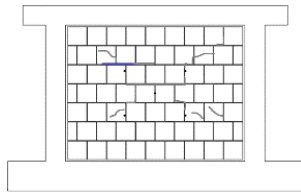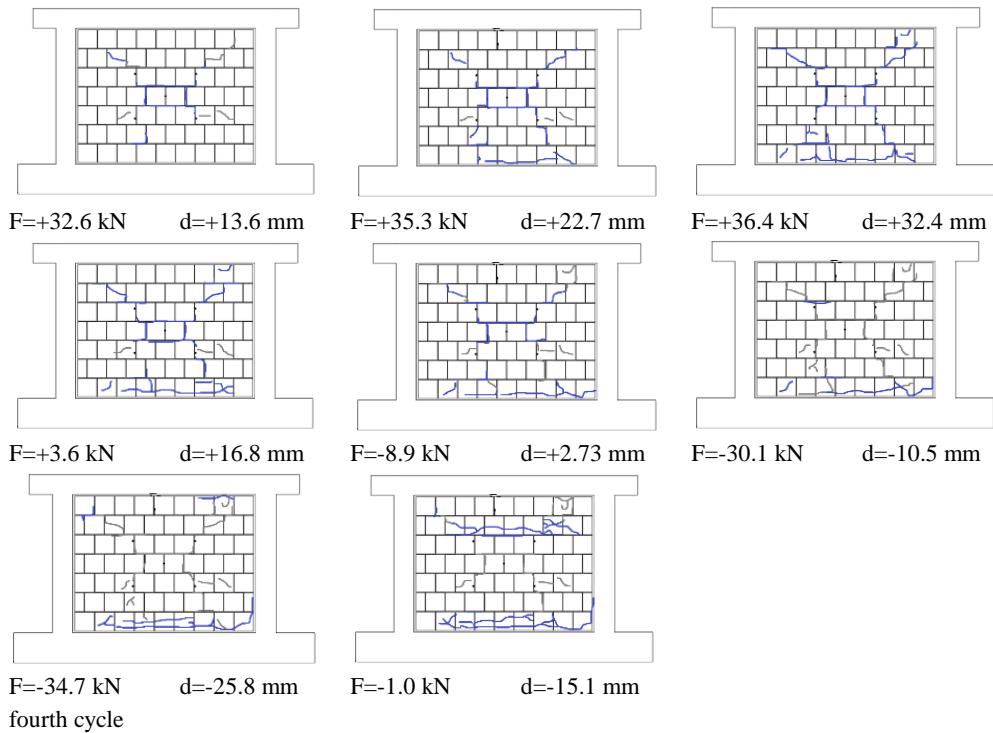| F=+21.5 kN   d=+4.3 mm | F=+29.5 kN   d=+7.7 mm | F=+36.4 kN   d=+11.0 mm |

| F=+7.6 kN   d=+5.0 mm | F=-23.2 kN   d=-4.0 mm | F=-39.7 kN   d=-9.0 mm |
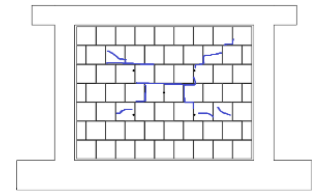
F=-8.2 kN   d=-4.7 mm

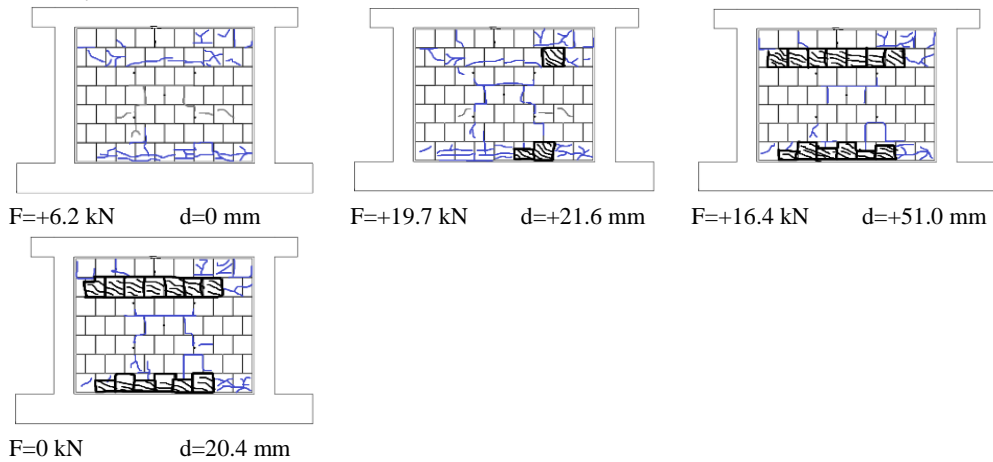Figure B.20a. OOP test 120_OOP_4E_cyclic (1st and 2nd cycles).

third cycle

F=+32.6 kN   d=+13.6 mm

F=+35.3 kN   d=+22.7 mm

F=+36.4 kN   d=+32.4 mm

F=+3.6 kN   d=+16.8 mm

F=-8.9 kN   d=+2.73 mm

F=-30.1 kN   d=-10.5 mm

F=-34.7 kN   d=-25.8 mm

F=-1.0 kN   d=-15.1 mm

fourth cycle

F=+6.2 kN   d=0 mm

F=+19.7 kN   d=+21.6 mm

F=+16.4 kN   d=+51.0 mm

F=0 kN   d=20.4 mm

Figure B.20b. OOP test 120_OOP_4E_cyclic (3rd and 4th cycles).

Appendix C
DIST-UNINA experimental tests' results

For each experimental test carried out at the Department of Structures for Engineering and Architecture of University of Naples Federico II, the OOP measures of the instruments (vertical axis) are herein reported as a function of the OOP central displacement (horizontal axis).

In the following Figures, the instruments are named according to the layout reproduced in Figure C.1. Remember that LVDT IP_up was used only for the tests on the 120 mm-thick infills.
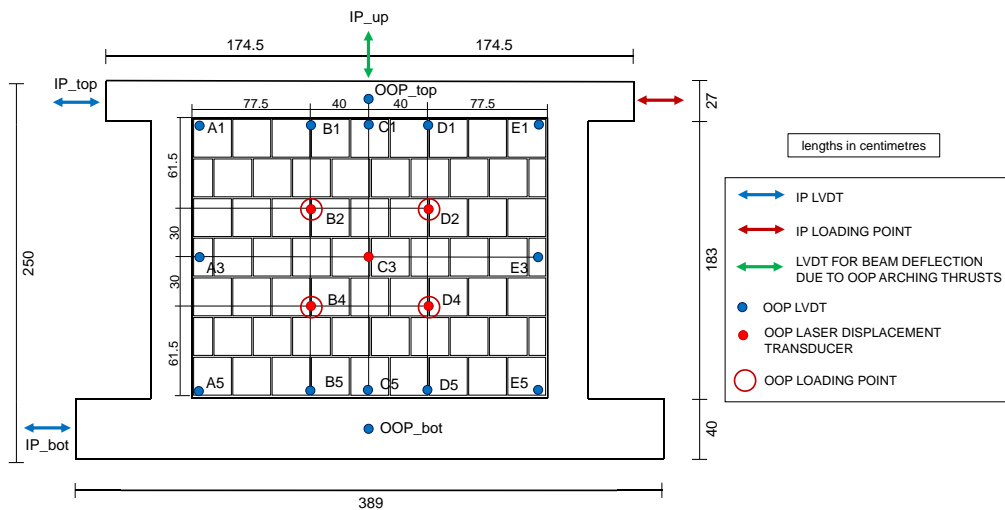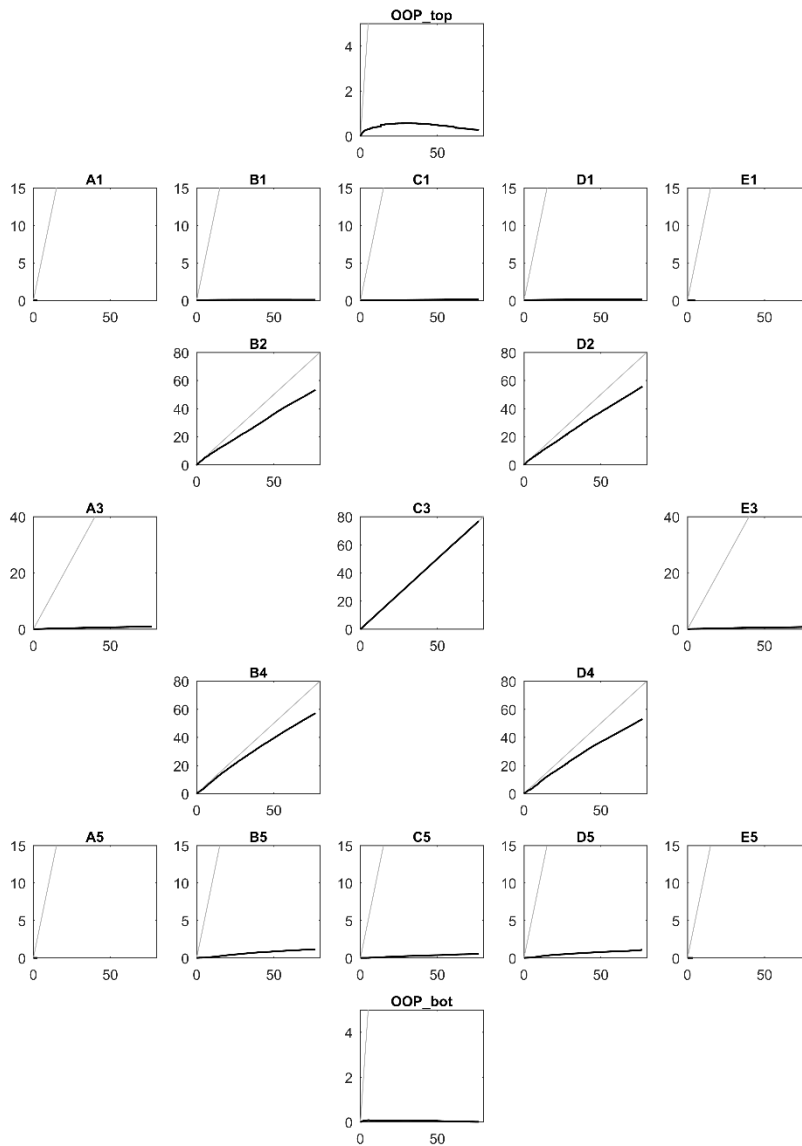

Figure C.1. Instrumentation layout.

Figure C.2. Test 80_OOP_4E.The vertical axis refers to the displacement read by the considered instrument, the horizontal axis refers to the OOP central displacement.

Figure C.3. Test 80_OOP_3E. The vertical axis refers to the displacement read by the considered instrument, the horizontal axis refers to the OOP central displacement.

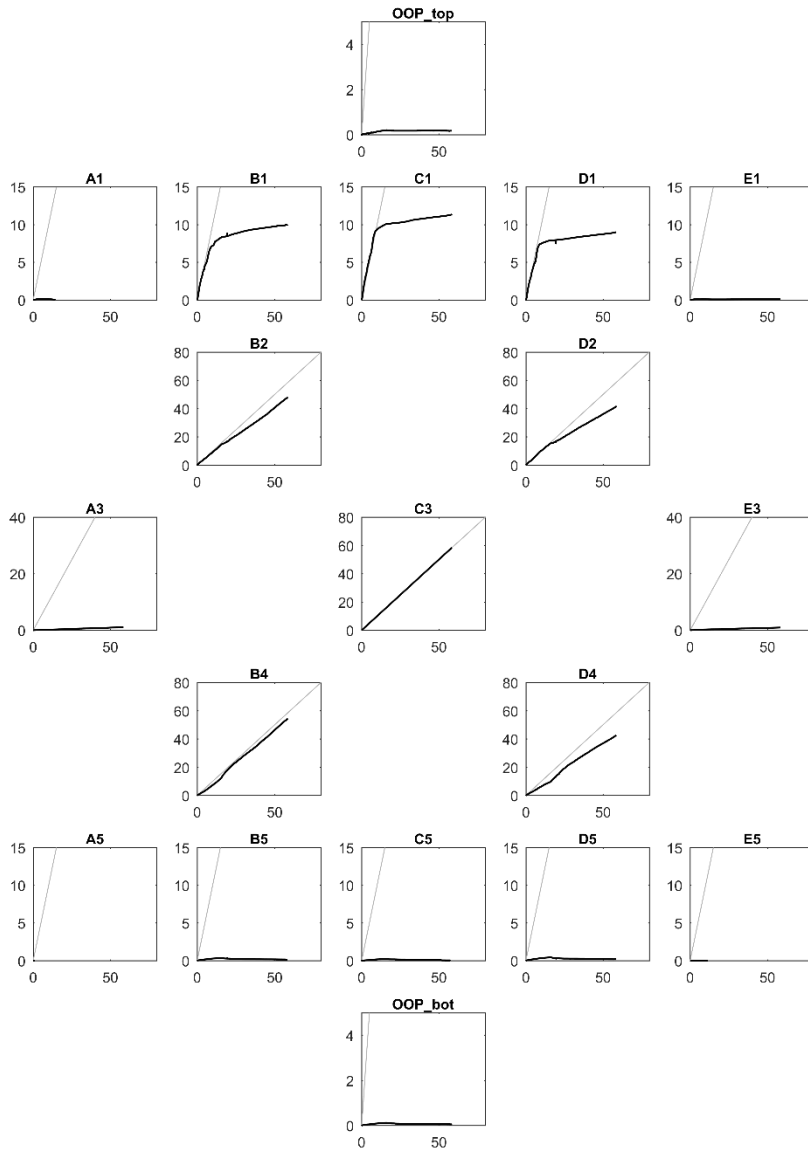Figure C.4. Test 80_OOP_3Eb. The vertical axis refers to the displacement read by the considered instrument, the horizontal axis refers to the OOP central displacement. Instruments B1, C1 and D1 reached the end of their measurement range.

Figure C.5. Test 80_OOP_2E. The vertical axis refers to the displacement read by the considered instrument, the horizontal axis refers to the OOP central displacement.
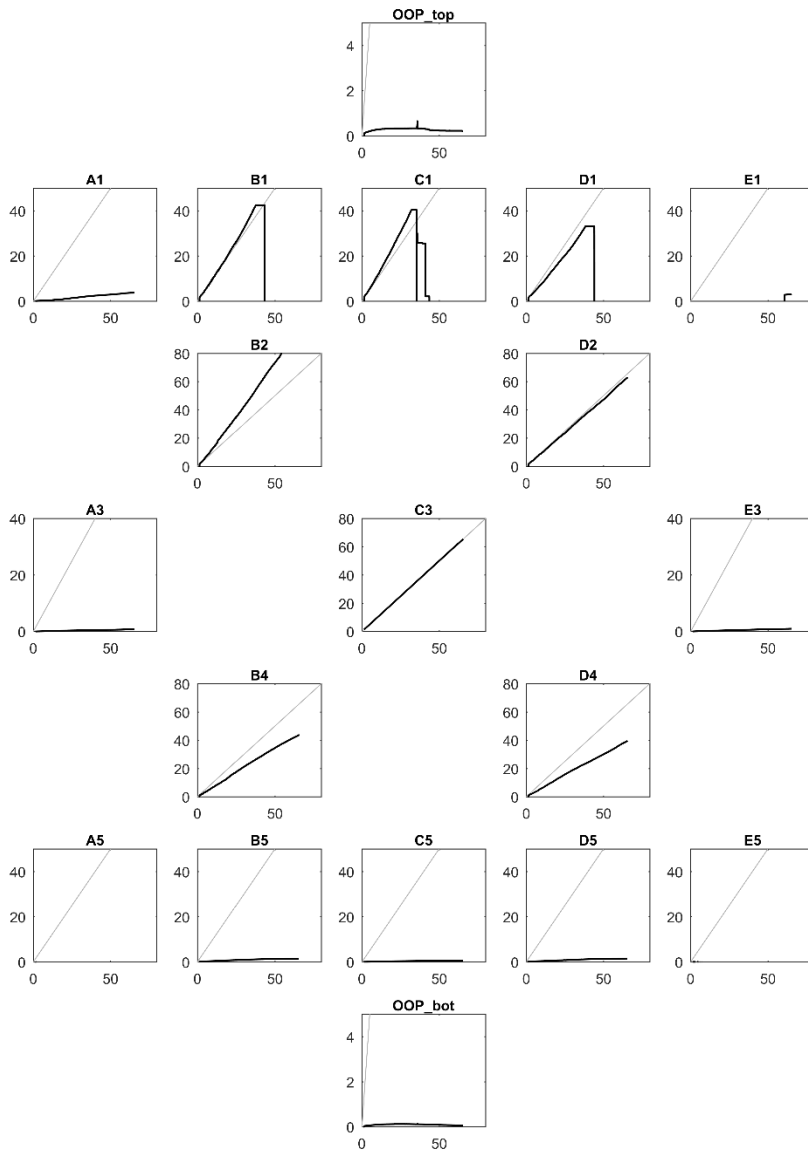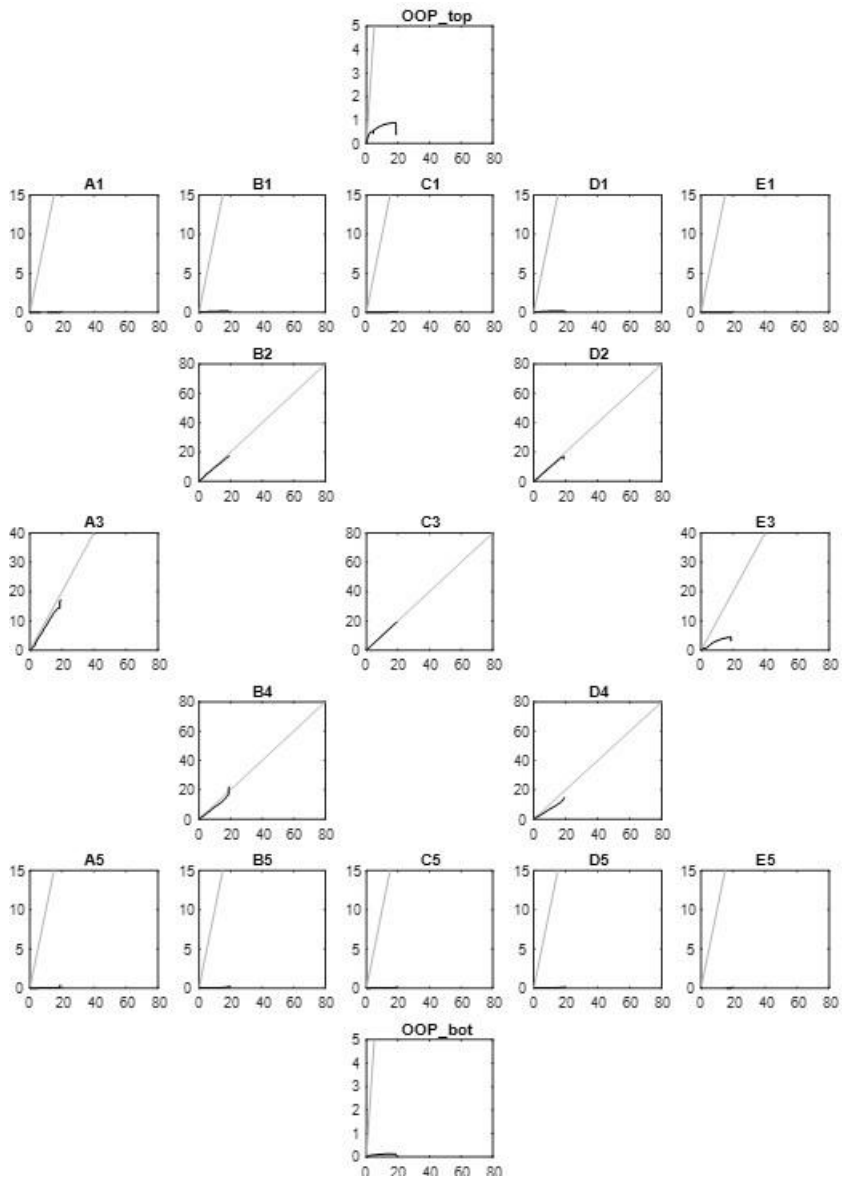
Figure C.6. Test 80_IP+OOP_L. The vertical axis refers to the displacement read by the considered instrument, the horizontal axis refers to the OOP central displacement.

Figure C.7. Test 80_IP+OOP_M. The vertical axis refers to the displacement read by the considered instrument, the horizontal axis refers to the OOP central displacement.

Figure C.8. Test 80_IP+OOP_H. The vertical axis refers to the displacement read by the considered instrument, the horizontal axis refers to the OOP central displacement.
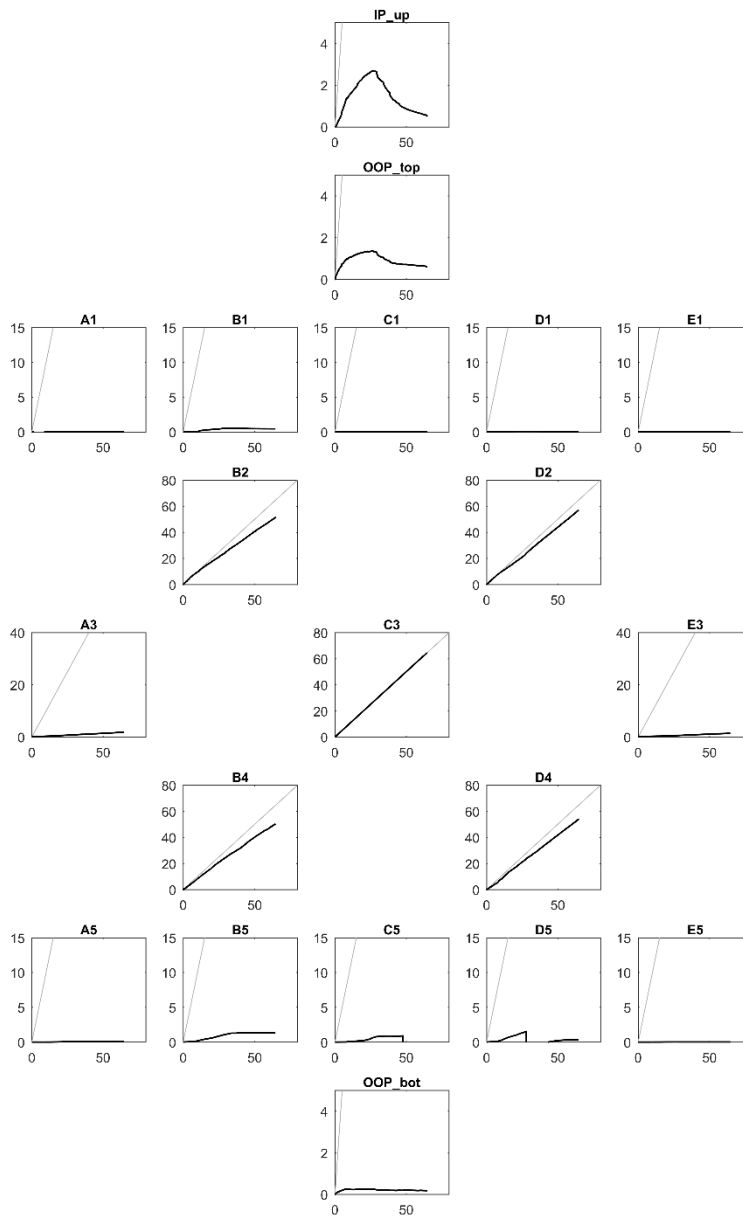
Figure C.9. Test 120_OOP_4E. The vertical axis refers to the displacement read by the considered instrument, the horizontal axis refers to the OOP central displacement.
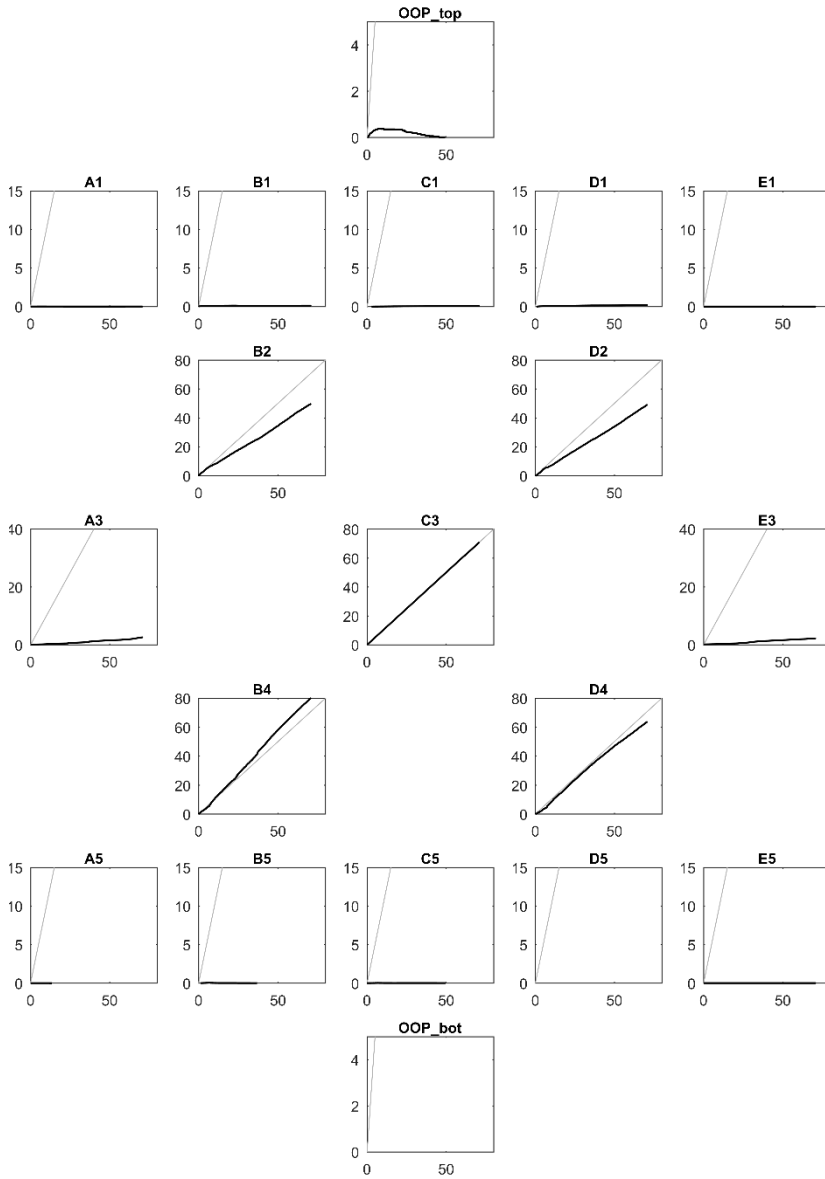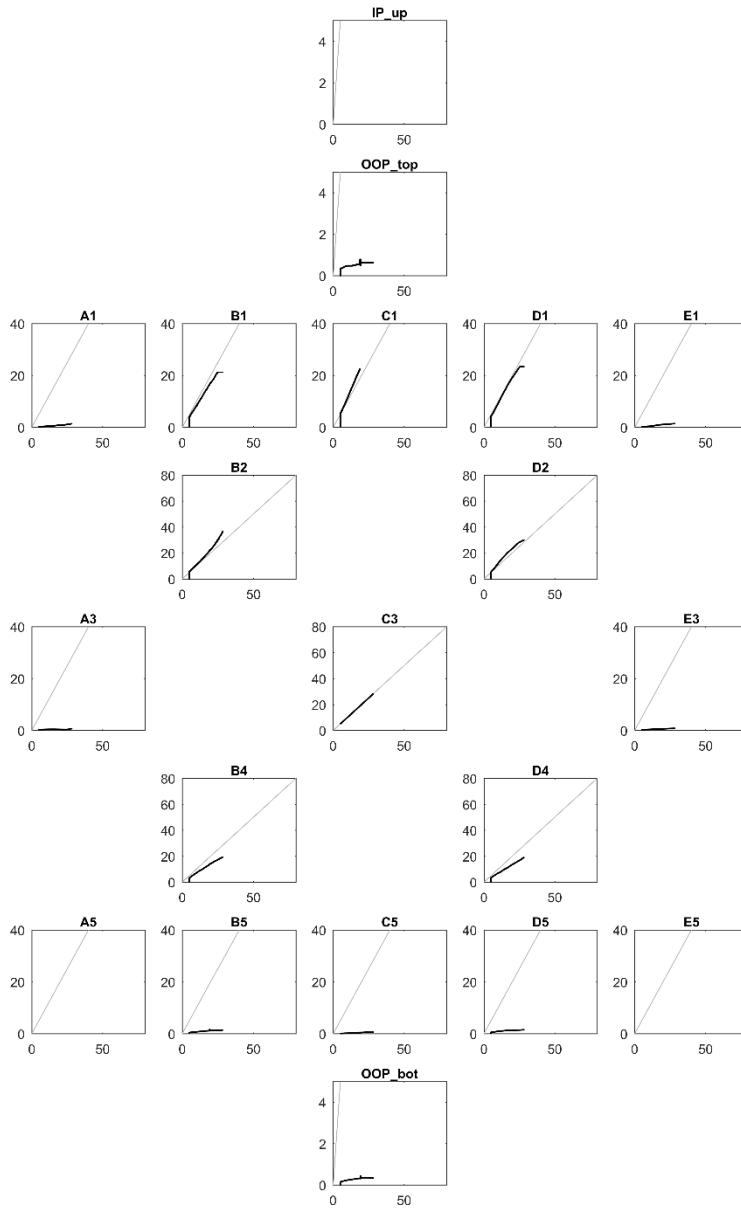
Figure C.10. Test 120_OOP_3E. The vertical axis refers to the displacement read by the considered instrument, the horizontal axis refers to the OOP central displacement.
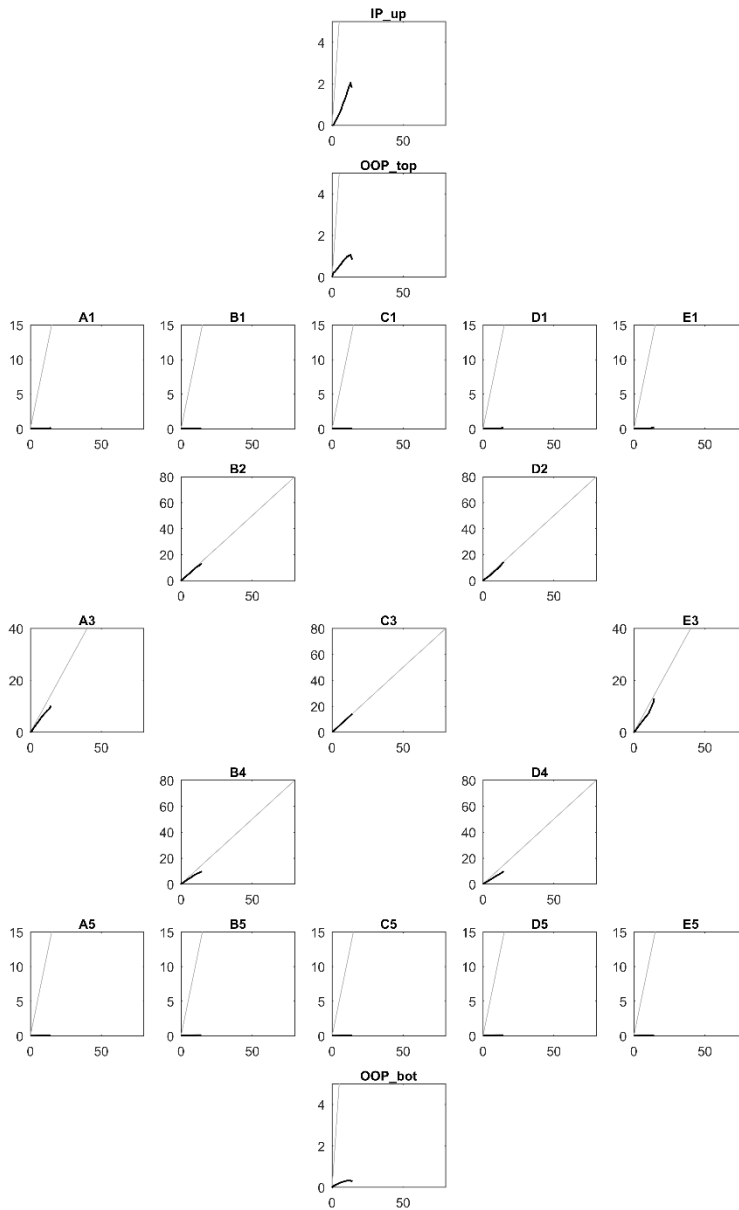
Figure C.11. Test 120_OOP_2E. The vertical axis refers to the displacement read by the considered instrument, the horizontal axis refers to the OOP central displacement.
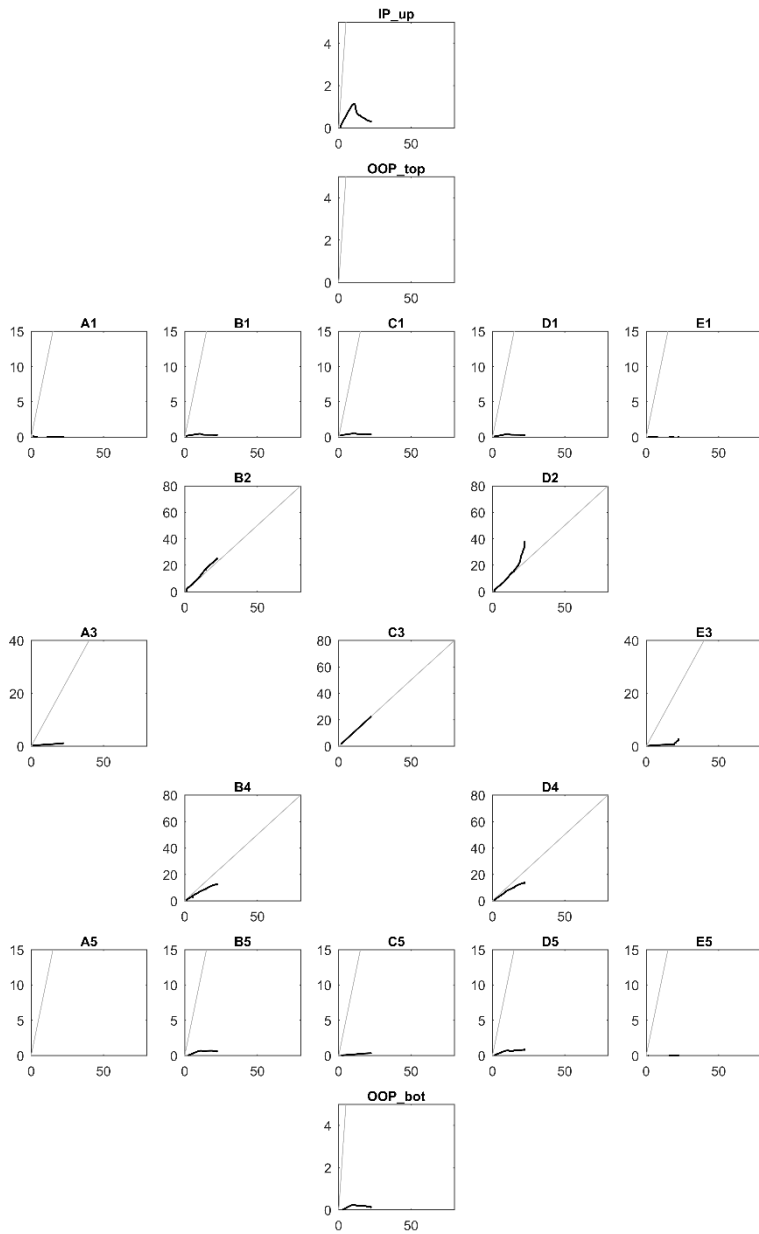
Figure C.12. Test 120_IP+OOP_L. The vertical axis refers to the displacement read by the considered instrument, the horizontal axis refers to the OOP central displacement.
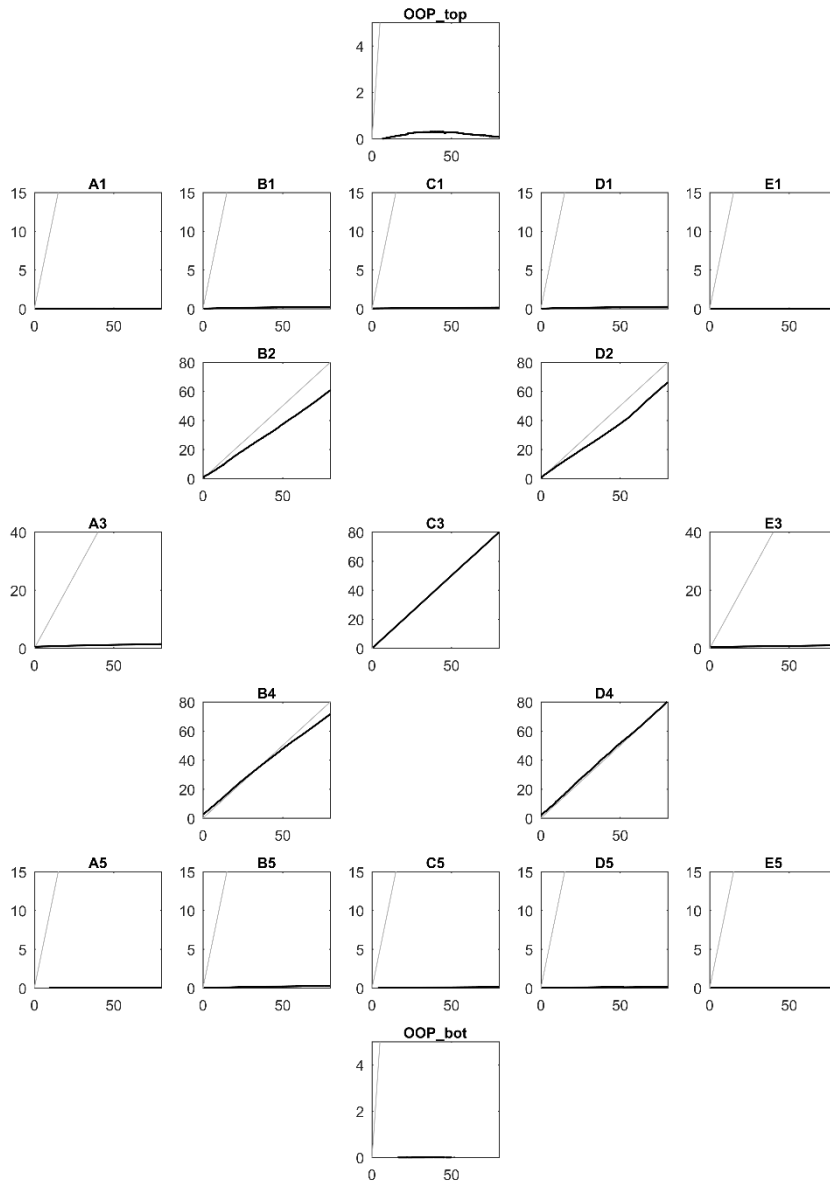
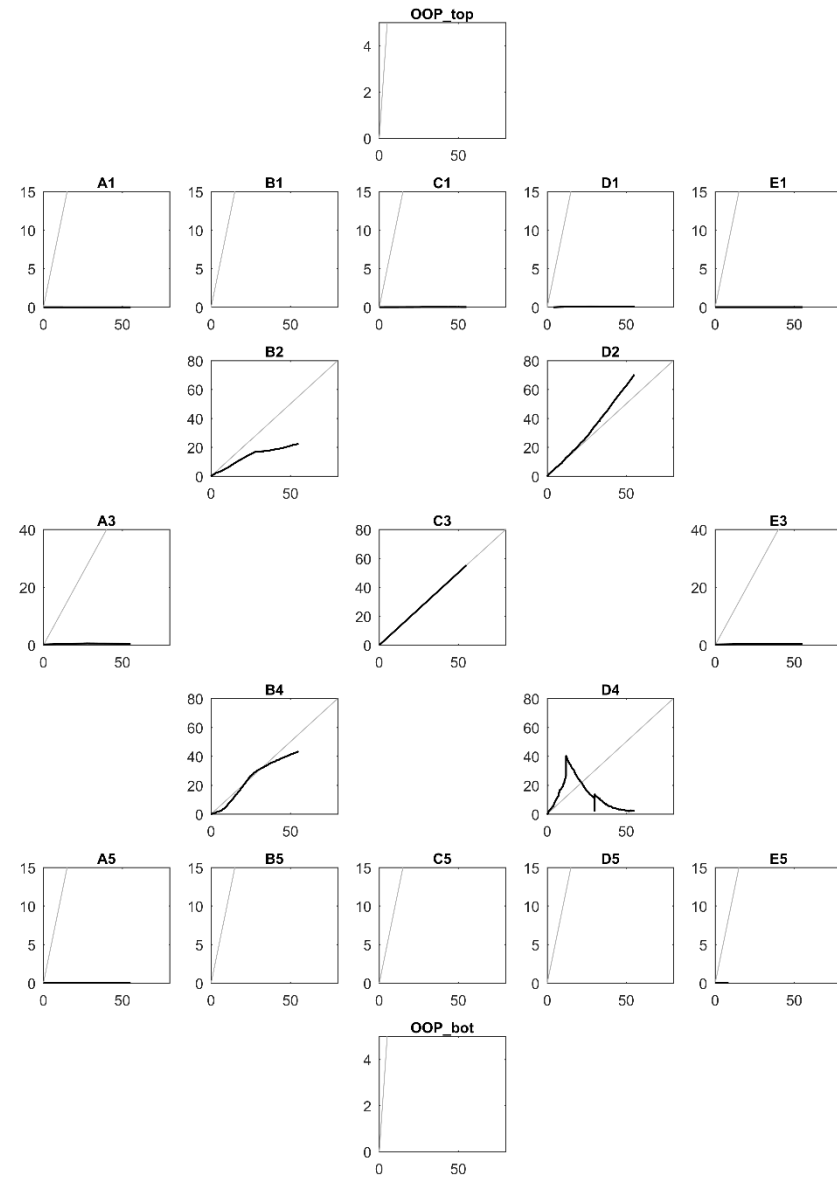Figure C.13. Test 120_IP+OOP_M. The vertical axis refers to the displacement read by the considered instrument, the horizontal axis refers to the OOP central displacement. Instruments B1, C1 and D1 reached the end of their measurement range.
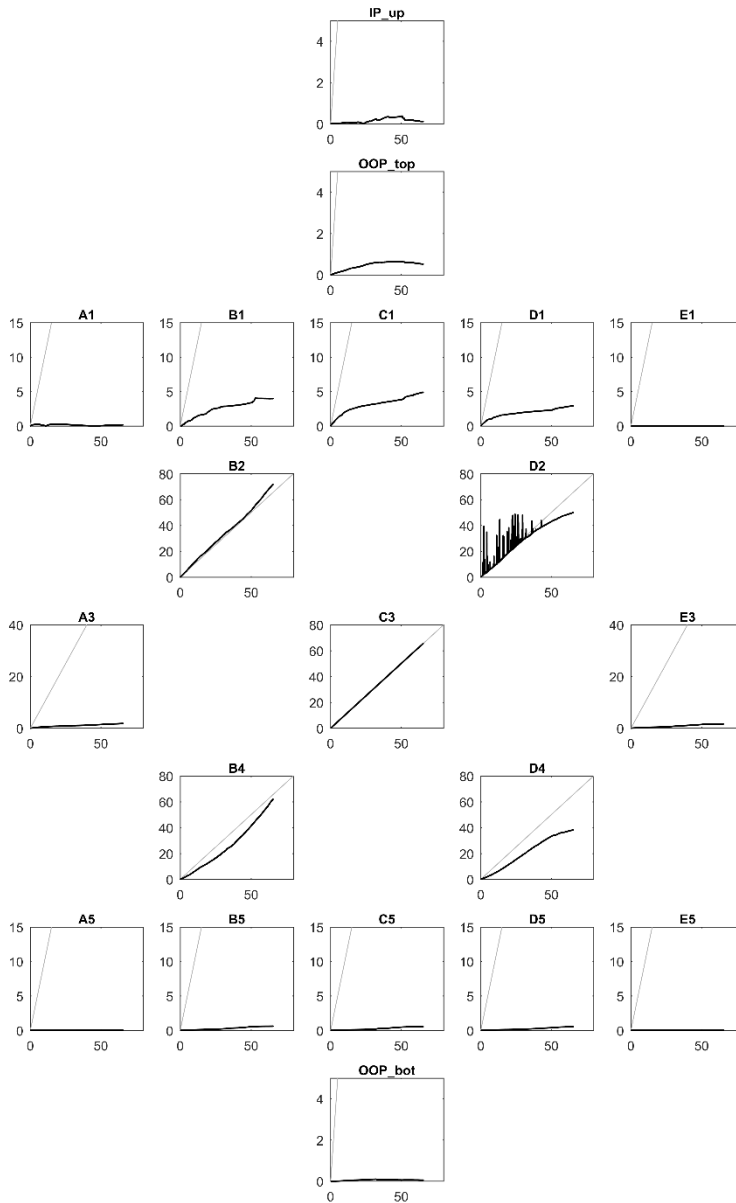
Figure C.14. Test 120_IP+OOP_H. The vertical axis refers to the displacement read by the considered instrument, the horizontal axis refers to the OOP central displacement. Instruments B1, C1 and D1 reached the end of their measurement range.
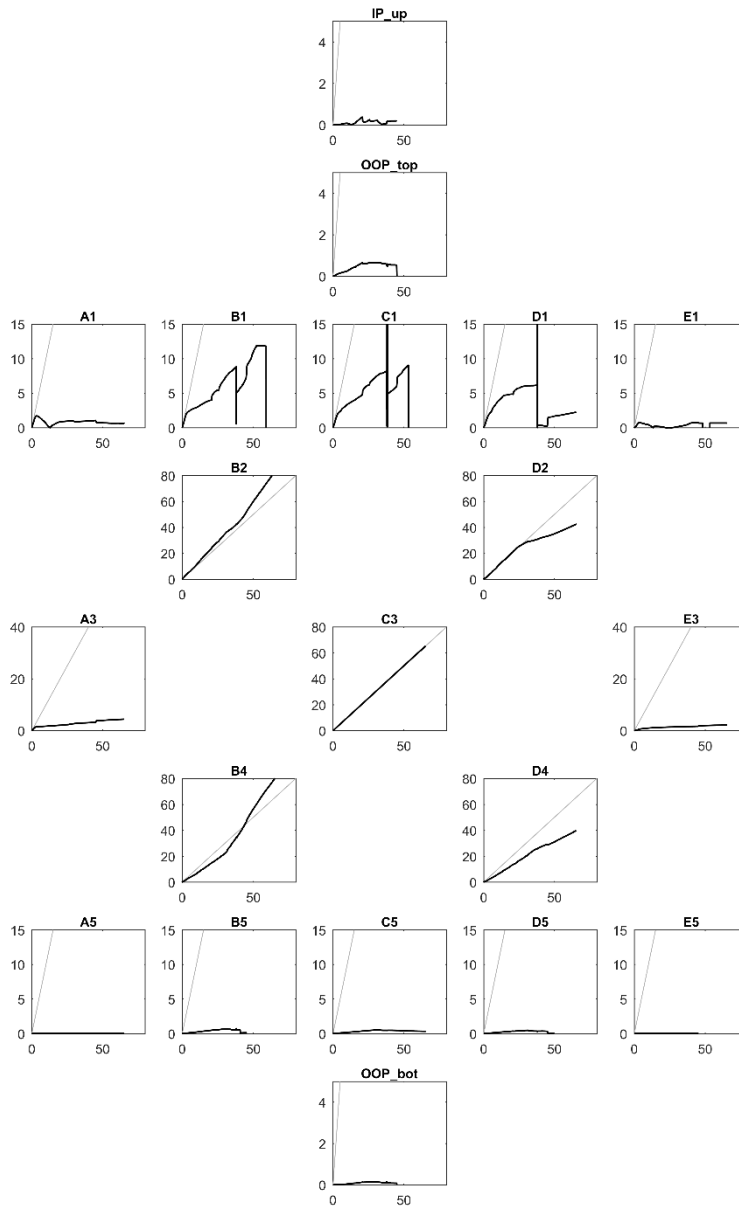
Appendix D
Experimental database specimens' properties

In this appendix, the geometric and mechanical properties of the specimens that entered the experimental database discussed and analysed in Chapter IV are reported. Namely, both infills' and confining frames' properties are reported in two separate tables. The experimental results associated with each specimen are reported in detail in Chapter IV.

In the following Tables:

- t is the infill thickness;
- h is the infill height;
- w is the infill width;
- h/t and w/t are the vertical and horizontal slenderness ratio of the infill, respectively;
- f_{mv} and f_{mh} are masonry compressive strength in the vertical and in the horizontal direction, respectively;
- E_{mv} and E_{mh} are masonry elastic modulus in the vertical and in the horizontal direction, respectively;
- I_b and J_b are the frame upper beam cross-section inertia and torsional constant, respectively;
- I_c and J_c are the frame columns' cross-section inertia and torsional constant, respectively;
- E_b and E_c are the elastic modulus of the frame beams' and columns' material.

Some mechanical properties are reported with an asterisk (*). This means that the value reported has not been provided by the Authors but they have been assumed by the writer based on the criteria reported in Chapter IV.

Table D.1. Specimens' geometric and mechanical properties (infill walls).

#	Author	specimen	type	t [mm]	h [mm]	w [mm]	h/t	w/t	f_{mv} [MPa]	E_{mv} [MPa]	f_{mh} [MPa]	E_{mh} [MPa]
1	da Porto et al.	FOB1	2E	300	2520	1000	8.4	3.3	2.62	2620	-	-
2	da Porto et al.	FOB2	2E	300	2520	1000	8.4	3.3	2.62	2620	-	-
3	da Porto et al.	FOB3	2E	300	2520	1000	8.4	3.3	2.62	2620	-	-
4	Hak et al.	TA5	2E	350	2950	1380	8.4	3.9	4.64	5299	1.08	494
5	DIST-UNINA	80_OOP_2E	2E	80	1830	2350	22.9	29.4	1.81	1090	2.45	1255
6	DIST-UNINA	120_OOP_2E	2E	120	1830	2350	15.3	19.6	2.21	1770	-	-
7	Dawe and Seah	WE2	4E	190	2800	3600	14.7	18.9	28.1	23000	18.40	17400
8	Dawe and Seah	WE4	4E	140	2800	3600	20.0	25.7	22.7	13800	18.40	17400
9	Dawe and Seah	WE5	4E	90	2800	3600	31.1	40.0	20.2	15600	18.40	17400
10	Dawe and Seah	WE8	4E	140	2800	3600	20.0	25.7	27.4	16200	18.40	17400
11	Angel et al.	1	4E	48	1625	2440	33.9	50.8	11.6	7848	14.00*	11355*
12	Flanagan and Bennett	18	4E	195	2240	2240	11.5	11.5	5.59	5300	3.01	2160
13	Flanagan and Bennett	25	4E	93	2240	2240	24.1	24.1	5.59	5300	3.01	2160
14	Calvi and Bolognini	10	4E	115	2750	4200	23.9	36.5	1.10	1873	1.11	991
15	Varela-Rivera et al.	E-1	4E	150	2720	3670	18.1	24.5	2.84	2948*	3.40*	2780*
16	Varela-Rivera et al.	E-2	4E	150	2880	3770	19.2	25.1	2.84	2948*	3.40*	2780*
17	Varela-Rivera et al.	E-3	4E	120	2880	3770	24.0	31.4	2.45	2543*	3.00*	2398*
18	Varela-Rivera et al.	E-4	4E	150	2720	2850	18.1	19.0	2.84	2948*	3.40*	2780*
19	Varela-Rivera et al.	E-5	4E	150	2720	2950	18.1	19.7	2.84	2948*	3.40*	2780*
20	Varela-Rivera et al.	E-6	4E	120	2720	2950	22.7	24.6	2.45	2543*	3.00*	2398*
21	Furtado et al.	Inf_02	4E	150	2300	4200	15.3	28.0	0.53	1418	0.64*	519*
22	DIST-UNINA	80_OOP_4E	4E	80	1830	2350	22.9	29.4	1.80	1517	2.21	1188
23	DIST-UNINA	120_OOP_4E	4E	120	1830	2350	15.3	19.6	1.65	1455	2.12	1262

Table D.2. Specimens' geometric and mechanical properties (confining frames).

#	Author	specimen	type	I_b [cm^4]	J_b [cm^4]	E_b [MPa]	I_c [cm^4]	J_c [cm^4]	E_c [MPa]
1	da Porto et al.	FOB1	2E	-	-	-	-	-	-
2	da Porto et al.	FOB2	2E	-	-	-	-	-	-
3	da Porto et al.	FOB3	2E	-	-	-	-	-	-
4	Hak et al.	TA5	2E	125052	211338	32308	125052	211338	32308
5	DIST-UNINA	80_OOP_2E	2E	32805	39243	32308	32805	39243	32308
6	DIST-UNINA	120_OOP_2E	2E	32805	39243	34819	32805	39243	34819
7	Dawe and Seah	WE2	4E	4540	22	200000	1880	41	200000
8	Dawe and Seah	WE4	4E	4540	22	200000	1880	41	200000
9	Dawe and Seah	WE5	4E	4540	22	200000	1880	41	200000
10	Dawe and Seah	WE8	4E	4540	22	200000	1880	41	200000
11	Angel et al.	1	4E	59937	82597	36689	71925	121553	36689
12	Flanagan and Bennett	18	4E	11900	31	200000	703	26	200000
13	Flanagan and Bennett	25	4E	11900	31	200000	703	26	200000
14	Calvi and Bolognini	10	4E	714583	282663	30379	67500	114075	30379
15	Varela-Rivera et al.	E-1	4E	10000	12149	9614	10000	12149	9614
16	Varela-Rivera et al.	E-2	4E	80000	34386	10943	15625	10065	10943
17	Varela-Rivera et al.	E-3	4E	64000	18688	11124	10000	12149	11124
18	Varela-Rivera et al.	E-4	4E	10000	12149	9782	19531	17609	9782
19	Varela-Rivera et al.	E-5	4E	19531	17609	10425	19531	17609	10425
20	Varela-Rivera et al.	E-6	4E	15625	10065	11638	15625	10065	11638
21	Furtado et al.	Inf_02	4E	312500	281737	24700	67500	114075	24700
22	DIST-UNINA	80_OOP_4E	4E	32805	39243	32308	32805	39243	32308
23	DIST-UNINA	120_OOP_4E	4E	32805	39243	34819	32805	39243	34819